Akhyar *Editor*

Proceedings of the 2nd International Conference on Experimental and Computational Mechanics in Engineering

ICECME 2020, Banda Aceh, October 13–14

∑ Springer

Lecture Notes in Mechanical Engineering

Akhyar
Editor

Proceedings of the 2nd International Conference on Experimental and Computational Mechanics in Engineering

ICECME 2020, Banda Aceh, October 13–14

Springer

Editor
Akhyar
Syiah Kuala University
Aceh, Indonesia

Preface

We are proud to present these updated research papers of the *Lecture Note in Mechanical Engineering* which contains 47 scientific papers. The papers discuss the latest research results or latest trends and development in the fields of computational mechanics, metallurgy and material science, energy, manufacturing processing systems, industrial and system engineering, biomechanics, artificial intelligence, micro-/nanoengineering, microelectromechanical system, machine learning, mechatronics, and engineering design. This book provides information about research activities in various countries since the authors of the papers came from Indonesia, Malaysia, Japan, India, Thailand, and Taiwan.

The editor would like to extend gratitude to Prof. Louis Cacetta from Curtin University—Australia, Prof. Yoshikazu Nakai from Kobe University—Japan, Prof. Chetan Singh Solanki from IIT Bombay—India, Assoc. Prof. Ir. Ts. Dr. Mohd Rizal Alkahari from Universiti Teknikal Malaysia Melaka (UTeM)—Malaysia, and Assoc. Prof. Anupun Terdwongworakul, Ph.D., from Kasetsart University—Thailand, for sharing his knowledge and insights in the keynote address. A special thank is awarded to the reviewers and editorial team, for their effort in the review and editing of the papers. The editor would also like to express their appreciation to the staff of Scientific.Net for their full cooperation during the preparation of this collection of research papers.

Aceh, Indonesia
Dr. Akhyar
Chairman
Dr. Mohd. Iqbal
Chief Editor

Contents

Contents

Effect of Densification Pressure on Physical and Combustion Properties of Binderless Briquettes Made from Rice-Husk and Coffee-Pulp

Alchalil, Adi Setiawan, Juwaini, and Taufiq Bin Nur

Abstract Agricultural residues such as rice husk and coffee pulp are abundantly available highlighting its potential as source of renewable energy. Utilizing this kind of biomass as a raw material for bio-briquettes can be considered as an effective way to minimize their wastage. This study aims to examine the characteristics of bio-briquettes produced from rice husk and coffee pulp through a cold-forming process at a pressure of 100, 150 and 200 kg/cm^2 without binder. Prior to briquetting process, coffee pulp was sun-dried, ground and sieved to mesh 20 while rice husk was dried and carbonized before grinding and sieving. Mixtures of 50% rice husk char-50% coffee pulp and 100% coffee pulp were made by adding water followed by molding and drying processes. Characterization of the briquette employs a number of techniques including DSC, TGA, bomb calorimeter and proximate analyses as well as mechanical testing. The results show that the calorific value of 100% coffee-skin briquette is 4764 cal/g containing 16.5 wt% of moisture, 12 wt% ash. The rate of combustion is 0.019 g/s with ignition time of 196 s. Varying briquetting pressure results in a change in ignition time of bio-briquettes as the density is increased. However, no significant change was observed on the rate of combustion upon increasing the briquetting pressure. This investigation concludes the potential use of agriculture residues as raw material for solid biomass fuel production.

Alchalil · A. Setiawan (✉) · Juwaini
Mechanical Engineering Department, Faculty of Engineering, Universitas Malikussaleh, Bukit Indah, Muara Satu, Lhokseumawe 24352, Indonesia
e-mail: adis@unimal.ac.id

T. B. Nur
Mechanical Engineering Department, Faculty of Engineering, Universitas Sumatera Utara, Padang Bulan, Medan 20155, Indonesia

1 Introduction

Rice and coffee agro-industries contribute significant amount of residues which potentially can be used as source of renewable energy. Increases in their consumption lead to increases in annual production of both commodities as well as amount of residues. This has received tremendous attention both in developed and developing countries to optimize utilization of this biomass energy source. Indeed, the use of agricultural residues helps in resolve the competition between energy and food crops for cultivable land [1]. Although agricultural residues are the most potential sources of biomass energy, their efficient exploitation for energy is rarely implemented.

In fact, rice industry produces significant amounts of waste which mostly in the form of rice straw, rice husk and rice husk ash. Rice straw is the stem of the plant that is left after harvesting the grain where each kilo of paddy rice produces 0.41–3.96 kg of rice straw. Rice husk is identified as the outer layer of rice seed which removed during the grinding process. For each tons of harvested rice, contributes 20–33% of the grain weight [2]. On the other hand, processing of coffee produces waste of around 30–50% of its total weight depending on the type of processing [3]. Coffee pulp and husk are the main residues obtained after removing coffee beans during the dry or wet process. These residues need an effective method of use as disposing this residual into the environment brings environmental problems.

In many countries, a number of studies have been devoted to investigate the potential utilization of agricultural wastes however profitable and technically feasible methods are still under development. Currently, there are a number of methods have developed for utilizing agro-industry-by-products including (1) mushroom cultivation, (2) production of enzymes, (3) biofuel production, (4) organic acid production, (5) bioactive compounds, (6) dietary fiber, (7) composting and vermicomposting [4]. Among these options, the conversion of coffee waste into biofuel looks like more potential and applicable for agriculture regions.

Basically, these biomass wastes can be directly used as fuel, however the combustion process cannot be maximized due to several factors, including high ash content, low density, non-competitive calorific value per unit volume, higher moisture contains and produces smoke [5]. Thus, briquetting is one of the most common strategies used for enhancing fuel quality and helps in establishing more effective fuel distribution, storage and utilization. Recent investigation has been reported about densification of biochar produced from coffee-pulp [6, 7] highlighting potential strategy of coffee-agro-industry by-product utilization.

In this study, rice husk and coffee pulp were processed into a higher-energy-density fuel through densification process in absence of binder to produce a bio-briquette. The main objective is to examine the effect of pressure applied on physical properties of bio-briquettes produced through the cold-forming process as well as finding the combustion characteristic of briquettes.

2 Experimental Methods

2.1 Preparation of Bio-briquettes

Rice husk raw material was sourced from Aceh Utara District while residue of Arabica coffee was collected from Bener Meriah District of Aceh Province, Indonesia. Initially, rice husk was carbonized and ground while coffee skin was sun-dried and ground. Both materials was sieved to mesh 20 and mixed by adding water sufficiently. The mixture consisted of 50% coffee pulp and 50% rice husk. As shown in Fig. 1a, cold-forming process of briquettes employed a home-made briquetting machine which consists of four piston dies, a rigid frame structure and hydraulic jack. Densification was carried out at a pressure of 100, 150 and 200 kg/cm² and later denoted as RC100, RC150 and RC200, respectively. Another set of briquettes was prepared under similar procedure and size with a raw material of 100% coffee pulp. The sample was later named as CP100, CP150 and CP200. All briquettes were then naturally dried for five days. Figure 1b displays bio-briquette products after pressing where briquette diameter is 45 mm and height 60 mm.

2.2 Briquettes Testing and Characterization

In order to understand the physical and chemical properties of binderless briquette produced from coffee pulp and rice-husk, thermogravimetric analysis (TGA) was performed under Shimadzu DTG-60 machine by purging with nitrogen at a flow rate of 20 ml/min and heating rate of 20 °C/min. Shimadzu DSC-60 helps in thermal analysis of briquettes in air at a flow rate of 20 ml/min and heating rate of 15 °C/min. In any TGA and DSC experiments, about 10 mg of sample was placed
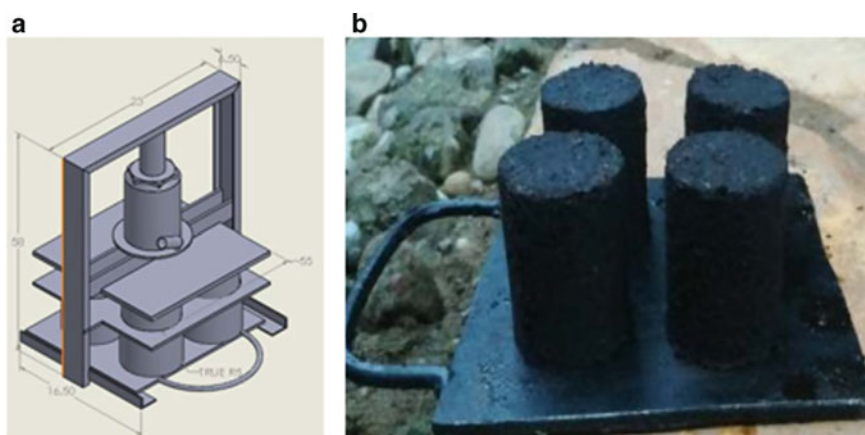
Fig. 1 **a** Briquettes pressing machine and **b** bio-briquettes products

in aluminum crucible. Bomb calorimeter estimated the caloric value of briquettes. Ignition time, flame duration and rate of combustion of the briquette were also tested. Mechanical properties were analyzed in term of compression strength, size stability and porosity.

3 Result and Discussion

Thermo-physical properties of bio-briquettes was assessed initially under thermo-gravimetry and differential scanning calorimeter analyses at temperature up to 600 °C with heating rate of 20 °C/min and 15 °C/min, respectively. Figure 2 displays decreases in weight as a function of temperature of RC150 and CP 150 samples. Both thermogram graphs show significant loss of weight during heating in nitrogen. Comparing these two graphs indicates a lower decomposition rate observed from RC150 briquette which is mostly due to carbonization process of rice husk during preparation. There are three-stage of weight loss observed i.e. room temperature to 220 °C, 220 °C < T < 350 °C and 350 °C < T < 600 °C. This thermal degradation profile is relatively similar to what has been reported in the literature [8]. During the first stage, *ca.* 8% of both samples weight is lost which is mostly due to removal of moisture and weak-bonded compounds. The weight of CP150 sample is significantly lost (24%) within the second stage while RC150 sample lost only 9% of its weight in this region due to most of volatile matter is decomposed. Decrease in weight is continued upon heating to 600 °C where respectively 11.6% and 14.2% of RC150 and CP150 sample weight are lost during last stage. Most of biomass is typically contained a high volatile matter compared to coal, thus reactivity of fuel derived from biomass is better [9].

Figure 3 shows DSC curves of RC150 and CP150 samples upon heating up to 600 °C at a rate of 15 °C/min. DSC curve of RC150 sample indicates an
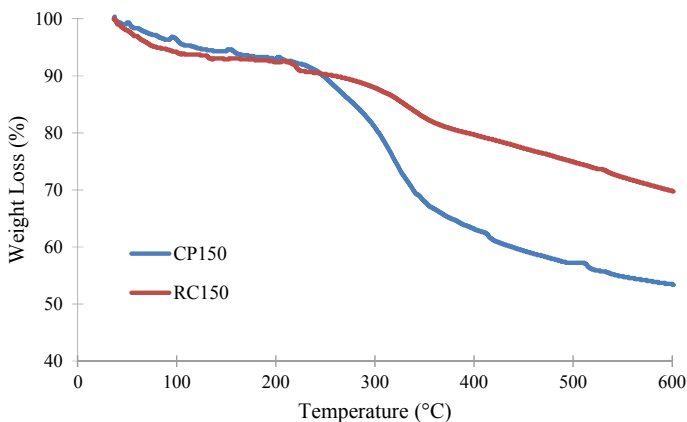
Fig. 2 TG curve of binderless briquettes at heating rate of 20 °C/min
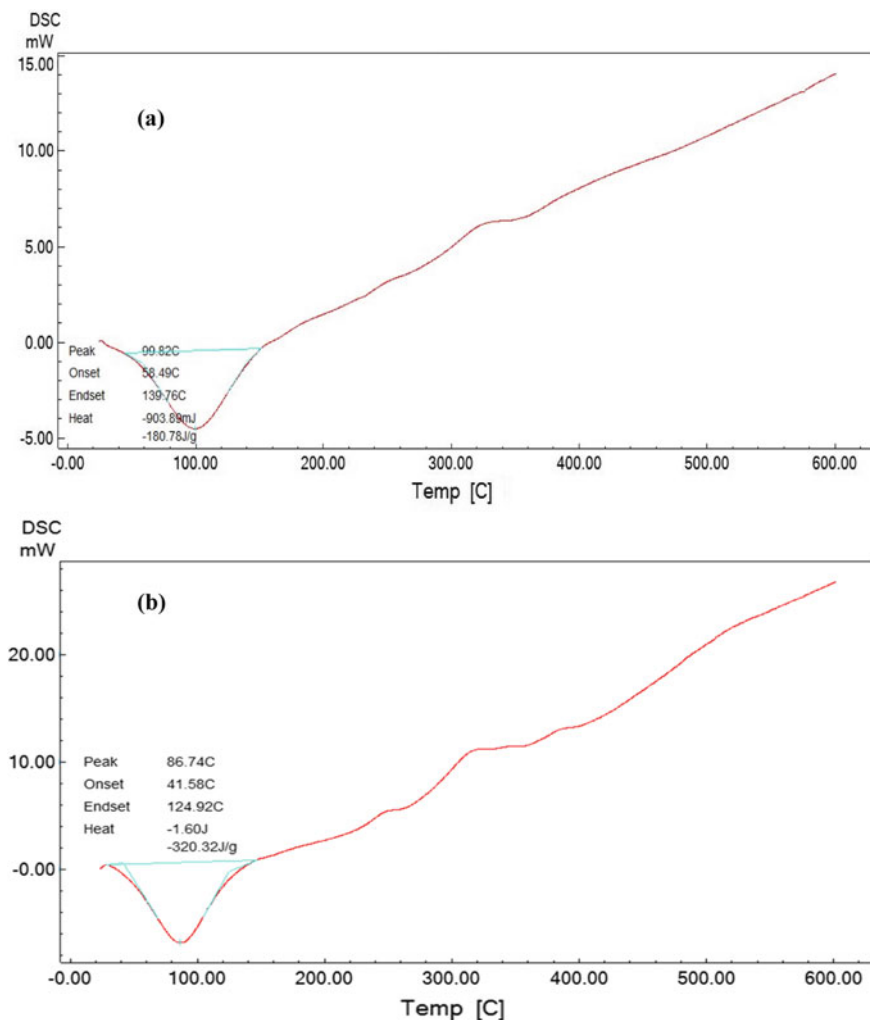
Fig. 3 DSC curve of **a** RC150 and **b** CP150 briquettes at heating rate of 15 °C/min

endothermic reaction takes place within a temperature range of 58.5–139.8 °C where the maximum peak is at 99.8 °C. While, CP150 briquette experiences an endothermic reaction at temperature range of 41.6–124.9 °C and maximum peak at 86.7 °C. From both samples, exothermic reaction is started above 125 °C. Integration of area within endothermic curve suggests amount of heat adsorbed by RC150 and CP150 samples are 180.8 J/g and 320.3 J/g respectively. These amounts of heat are mostly required for removing moisture content and other weak-bond species.

Table 1 Water and ash content of binderless briquettes

Sample code	Water content (wt%)			Density (g/cm^3)	Ash content (wt%)
	Mixture	After press	After drying		
RC100	60	28.6	11.8	0.38	18.8
RC150	60	26.6	11.4	0.37	19.2
RC200	60	23.3	11.7	0.33	24
CP100	80	66.6	15.7	0.28	10
CP150	80	65	16.5	0.3	12
CP200	80	60	14.8	0.31	13

Heating value of coffee-skin briquette was analyzed using bomb calorimeter resulting higher heating value of 4058 cal/g and 3705 for RC and CP briquettes, respectively. Table 1 summarizes density, water and ash content of each samples. Initially, 80% of mixture is water. After pressing process, water content is decreased to 60 ∼ 66.6%. A decrease in water content is obviously observed when briquetting pressure is increased. After drying, the average water contents is ranging from 11.4 to 16.5 wt%. Density of briquette is obviously affected by briquetting pressure. CP200 briquettes recorded the greatest density (0.31 g/cm^3), then CP150 (0.30 g/cm^3) and CP100 briquettes (0.28 g/cm^3). RC briquettes has slightly higher density compared to CP briquettes. The resulting density is mostly affected by particle size and moisture content of the raw material The percentage of ash measured after burning the sample at 600 °C for 4 h is 10 wt% for CP100 sample. The amount of ash is slightly higher for higher briquetting pressure which is due to higher briquette density.

The combustion properties of rice husk and coffee-pulp briquettes have been investigated and summarized in Table 2. Results show that the ignition time is ranging from 192 to 252 s. The higher pressure for briquetting, the longer time is needed for ignition. Flame duration for one piece of CP100 briquette is 1380 s, while increasing briquetting pressure to 200 kg/cm^2 leads to a longer duration of flame, i.e. 1470 s. In average, the rate of combustion of three kinds of sample is 0.020 g/s.

Table 2 Combustion properties of binderless briquettes

Sample code	Ignition time (s)	Flame duration (s)	Rate of combustion (g/s)
RC100	360	2405	0.016
RC150	372	2618	0.012
RC200	450	2854	0.011
CP100	195	1380	0.021
CP150	196	1415	0.019
CP200	252	1470	0.02

Table 3 Size stability and porosity of binderless briquettes

Sample code	Compression strength (kg/cm^2)	Size stability (%)	Porosity (%)
RC100	1.56	99.00	91
RC150	2.04	99.24	80
RC200	2.87	99.30	75
CP100	0.07	82.09	98
CP150	0.07	87.42	95
CP200	0.1	94.00	92

Correlation between briquetting pressure and size stability as well as porosity is explained by data in Table 3. Briquette CP100 has size stability of 82.09% while pressing briquette at 150 kg/cm^2 and 200 kg/cm^2 enhances the size stability to 87.42% and 94.00% respectively. As suggested in the literature that lower weight to mass reductions leads to a higher durability at higher hydraulic pressures of the briquettes [10]. As can be seen in this table, higher densification pressure results in smaller porosity. In term of compression strength, this kind of briquette has low ability to receive compressive load since no binder was added during production. The maximum compression strength is only 0.10 kg/cm^2 obtained from CP200 sample. This low compressive strength has correlation to higher percentage of porosity measured from any type of sample. Indeed, higher porosity benefits ignition of the briquette as shown in Table 2 where all samples can be ignited within 252 s.

4　Conclusion

Rice husk and coffee-pulp have been used as raw material for bio-briquettes and tested to identify its properties. The calorific value of 100% coffee-pulp briquette is 4764 cal/g containing in average 15.67 wt% of moisture, 11.67 wt% ash. The rate of combustion is 0.019 g/s with ignition time of 196 s. Varying briquetting pressure results in a change in ignition time of bio-briquettes as the density is increased. However, no significant change was observed on the rate of combustion upon increasing the briquetting pressure. Results show a potential use of agro-industry residues as feedstock for solid biomass fuel production.

References

1. Fritsche UR, Sims REH, Monti A (2010) Direct and indirect land-use competition issues for energy crops and their sustainable production—an overview. Biofuels, Bioprod Biorefin 4:692–704
2. Rambo MKD, Cardoso AL, Bevilaqua DB, Rizzetti TM, Ramos LA, Korndorfer GH, Martins AF (2011) Silica from rice husk ash as an additive for rice plant. J Agron 10:99–104
3. Oliveira LS, Franca AS (2014) An overview of the potential uses for coffee husks. Elsevier Inc
4. Janissen B, Huynh T (2018) Resources, conservation and recycling chemical composition and value-adding applications of coffee industry by-products: a review. Resour Conserv Recycl 128:110–117
5. Haykiri-Acma H, Yaman S (2010) Production of smokeless bio-briquettes from hazelnut shell. In: Proceedings of the world congress on engineering and computer science, vol II, pp 20–22
6. Setiawan A, Hayat F, Faisal, Nur TB (2019) Combustion characteristics of densified bio-char produced from Gayo Arabica coffee-pulp: effect of binder. IOP Conf Ser Earth Environ Sci 364
7. Setiawan A, Juwaini, Nayan A, Faisal, Fauzan (2018) Mechanical and physical properties of bio-briquette produced from Gayo Arabica coffee-skin. In: 1st International conference on multidisciplinary engineering (ICoMdEn). Lhokseumawe, p 13
8. Singh YD, Mahanta P, Bora U (2017) Comprehensive characterization of lignocellulosic biomass through proximate, ultimate and compositional analysis for bioenergy production. Renew Energy 103:490–500
9. Mckendry P (2002) Energy production from biomass (part 1): overview of biomass 83:37–46
10. Amarasekara A, Tanzim FS, Asmatulu E (2017) Briquetting and carbonization of naturally grown algae biomass for low-cost fuel and activated carbon production. Fuel 208:612–617

Characteristics of Lightweight Bricks Composed of Clay and Diatomite

Muttaqin Hasan, Taufiq Saidi, Husaini, Muhammad Jamil, and Zikratul Rhina

Abstract The widely used conventional bricks are made from clay. However, the apparent density of bricks made of clay is high due do the high bulk density of clay. In this study, the diatomite which has low bulk density was used to replace the clay partially and totally in order to produce lightweight brick. The purpose of this study therefore was to obtain the characteristic (i.e. apparent density, specific gravity, absorption, single and paired compressive strength) of bricks composed of clay and diatomite. Five clay to diatomite ratios in volume which are 1: 0; 0.75: 0.25; 0.50: 0.50; 0.25: 0.75 and 0: 1 were prepared and tested in accordance with the standards. Analysis of variance was performed in order to see the significance of the influence of diatomite content on the characteristic of the bricks. The test results showed that lightweight bricks can be produced by composing of the clay and the diatomite. The bulk density and specific gravity of the bricks decreased with increasing in diatomite content. In contrary, however, the absorption of the bricks increased with increasing in diatomite content. The diatomite content did not affect the compressive strength of bricks. According to SNI 15-2094-2000 all bricks composed at different clay to diatomite ratio can be classified as one class, which is Class 50. Using regression analysis, the relationships between diatomite content and apparent density, specific gravity and absorption of bricks as well as relationship between single and pair bricks compressive strength were proposed.

M. Hasan (✉) · T. Saidi · M. Jamil · Z. Rhina
Department of Civil Engineering, Universitas Syiah Kuala, Banda Aceh, Indonesia
e-mail: muttaqin@unsyiah.ac.id

Husaini
Department of Mechanical Engineering, Universitas Syiah Kuala, Banda Aceh, Indonesia

1 Introduction

Bricks have been used as material construction since 7500 BC. They were found at Tell Aswad, in the upper Tigris region and in southeast Anatolia close to Diyarbakir [1]. Conventionally, bricks were made from clay. The clay is mixed with water and formed in the prims shape, then burned in the furnace usually at the temperature of 600–800 °C for 3 or 4 days. Nowadays, in Indonesia and other developing countries, bricks are widely used as building walls. Its function is only considered as insulating wall between rooms and outer wall without being intended to carry loads. However, the wall itself overloads the supporting beams which are a part of the building structure system to withstand gravity loads and lateral loads in the form of wind pressure and earthquake. The greater the weight of the wall, the greater the load that must be carried by the beams and other the structural systems. Since the clay has a large bulk density, then the clay bricks have a large apparent density and hence a large load must be carried by the building structures. In order to reduce the load on the structures, it is necessary to find other materials that are lighter to make the bricks.

Diatomite which is a siliceous sedimentary rock formed from accumulation of skin deposition or fossil skeleton of aquatic plants is a lightweight material with bulk density ranging between 417 and 767 kg/m^3 [2, 3] is expected to be a raw material for making lightweight bricks. However, very few studies have examined the use of diatomite as a material for making lightweight bricks [4]. Mostly researches were conducted in utilizing diatomite as cementitious material in composite cement [5–7], mortar [8], high strength concrete [9–11] and ultra-high strength concrete production [12]. This research, however was conducted to study the compressive strength, water absorption, apparent density and specific gravity of lightweight bricks composed of clay and diatomite.

2 Experimental Program

Five types of bricks at different clay to diatomite volume ratio as shown in Table 1 were prepared. Beside clay and diatomite, sand with particle size less than 1 mm and water were also used. The diatomite was collected from Beureunut Village, Aceh Besar District, Indonesia while clay, sand and water were available at the

Table 1 Material volume ratio of studied bricks

Brick type	Clay	Diatomite
Type 1	1.00	0.00
Type 2	0.75	0.25
Type 3	0.50	0.50
Type 4	0.25	0.75
Type 5	0.00	1.00

Table 2 Liquid limit, plastic limit and plasticity index of clay

Properties	Test result
Liquid limit (%)	71.86
Plastic limit (%)	27.14
Plasticity index (%)	44.73

Table 3 Bulk density of clay, diatomite and sand

Materials	Bulk density (kg/m^3)
Clay	1465
Diatomite	1437
Sand	735

conventional brick factories located in Miruek Taman Village, Aceh Besar District, Indonesia. The liquid limit, plastic limit and plasticity index of clay were tested in accordance with SNI 1966:2008 and SNI 1967:2008 [13, 14] and the results are shown in Table 2 while the bulk density of clay, diatomite and sand were tested in accordance with SNI 03-4804-1998 [15] and the results are shown in Table 3.

Brick specimens with the size of $210 \times 110 \times 45$ mm^3 were prepared at the brick factory. Clay and diatomite were ground and mixed together with sand and sufficient water to have a homogeneous plastic material. The material then was formed in timber moulds. The moulds were previously swept with ash so that the material did not stick when formed and resulted in smooth and neat bricks. The bricks were then gradually dried in a place protected from the sun so that they did not experience crack. After the bricks were dry enough, then they were burned in a furnace with the temperature of 600 °C for 4 days. Later, the bricks were cooling down in room temperature before tested. For each type of brick, 30 specimens were prepared. The mix proportion of the materials are shown in Table 4.

The apparent density of the specimens was tested in accordance with SNI 15-2094-2000 [16] while the specific gravity was tested in accordance with ASTM C373-18 and ASTM C67/C67M-2020 [17, 18]. The steps for testing apparent density and specific gravity were the same and used the same tools. Five specimens were tested for each type of bricks. The specimens were dried in the oven with the temperature of 100 °C for 24 h and weighed (M_d). The specimens were then cooled to room temperature and then put in a container that has been hung in a vessel filled with water and allowed to stand for a while so that the water enters completely, which was marked by the loss of water bubbles. The weight of the specimens while

Table 4 Mix proportion for 30 specimens of bricks

Brick type	Clay (kg)	Diatomite (kg)	Sand (kg)	Water (kg)
Type 1	45.68	0.00	14.94	8.90
Type 2	34.26	5.73	14.94	11.40
Type 3	22.84	11.45	14.94	15.90
Type 4	11.42	17.18	14.94	16.40
Type 5	0.00	22.91	14.94	22.00

hanging in the water was also measured (M_b). The specimens were then removed from the water and wiped with a water absorbent cloth and weighed (M_c). Apparent density (Q_{sch}) and specific gravity (T) were calculated by the following equations:

$$Q_{sch} = \frac{M_d}{M_c - M_b} d_w \tag{1}$$

$$T = \frac{M_d}{M_d - M_b} \tag{2}$$

where d_w = density of water (1000 kg/m^3).

The water absorption test was conducted in accordance with SNI 15-2094-2000 [16]. Five specimens for each type of bricks were tested. The specimens were immersed in water for 24 h, the surface of the specimens was wiped with a water absorbent cloth and the weight of the specimens was measured (A). The specimens were then dried in the oven with the temperature of 100 °C and weighed (B). The water absorption (P_e) was calculated by the following equation:

$$P_e = \frac{A - B}{A} 100\% \tag{3}$$

Compressive strength test was performed on single bricks and paired bricks. The single brick compressive strength test was conducted in accordance with ASTM C C67/C67M-2020 [18]. The surface of the specimens was smoothed and levelled up. The specimens were put between two plates of loading machine and the compression load was applied until the specimens get failure. Five specimens were tested for each type of bricks. The paired brick compressive strength was tested in accordance with SNI 15-2094-2000 [16]. Five specimens were tested for each type of bricks. The specimens were cut at the centre into two pieces. One piece of the specimens was put into another piece with space of 6 mm. On the space a mortar with the ratio of 1 cement and 3 sand was filled. After the mortar getting hard, the specimen was cured in the water for 24 h followed by cured in the room temperature for 7 days. The compression load was applied on the specimens using universal testing machine until the specimens get failure. The compressive strength (f_c') was calculated by the following equation:

$$f_c' = \frac{P_{max}}{F} \tag{4}$$

where: P_{max} = maximum load and F = the section area of the specimens.

3 Experimental Results and Discussion

3.1 The Variation of Experimental Data

To see the variation of the data obtained which means the specimens were prepared well, the data of apparent density, specific gravity and water absorption with their statistical analysis including standard deviation (SD) and coefficient of variation (CV) is presented in Tables 5, 6 and 7. The coefficient of variation of all data was less than 10% with only one data exceeded this ratio. This means that the data obtained has no significant variation.

3.2 Apparent Density

The average apparent density of all types of bricks are shown in Fig. 1a. This figure shows that the apparent density of bricks decreased with the increase in diatomite content. By replacing the clay with diatomite totally reduced the apparent density of bricks by 30.78%. This means that lightweight bricks can be produced by replacing the conventionally used clay with the diatomite. To see the influence of diatomite content on the apparent density of bricks, an analysis of variance was conducted and the result is presented in Table 8. It was found that the $F_o > F_o$ (0.05); (4.20) with means that the diatomite content significantly affected the apparent density of

Table 5 Data of apparent density

Brick type	Apparent density (kg/m^3) for specimen						SD (kg/m^3)	CV (%)
	#1	#2	#3	#4	#5	Average		
Type 1	1710	1680	1710	1700	1680	1696	13.56	0.80
Type 2	1500	1510	1510	1520	1510	1510	6.32	0.42
Type 3	1370	1350	1370	1360	1340	1358	11.66	0.86
Type 4	1320	1350	1310	1320	1330	1326	13.56	1.02
Type 5	1190	1200	1180	1150	1150	1174	20.59	1.75

Table 6 Data of specific gravity

Brick type	Specific gravity for specimen						SD	CV (%)
	#1	#2	#3	#4	#5	Average		
Type 1	2.25	2.27	2.26	2.20	2.28	2.25	0.03	1.24
Type 2	2.19	2.21	2.21	2.20	2.20	2.20	0.01	0.34
Type 3	2.17	2.20	2.19	2.17	2.17	2.18	0.01	0.58
Type 4	2.15	2.20	2.18	2.17	2.16	2.17	0.02	0.79
Type 5	2.17	2.17	2.17	2.14	2.10	2.15	0.03	1.28

Table 7 Data of water absorption

Brick type	Water absorption (%) for specimen						SD (%)	CV (%)
	#1	#2	#3	#4	#5	Average		
Type 1	14.95	15.90	16.12	14.49	8.48	13.99	2.82	20.15
Type 2	22.69	22.87	22.69	22.10	22.24	22.52	0.29	1.31
Type 3	28.24	32.16	28.44	28.77	33.53	30.23	2.19	7.23
Type 4	31.13	30.10	32.38	30.89	31.04	31.11	0.73	2.36
Type 5	40.13	38.47	39.93	42.87	40.90	40.46	1.44	3.56
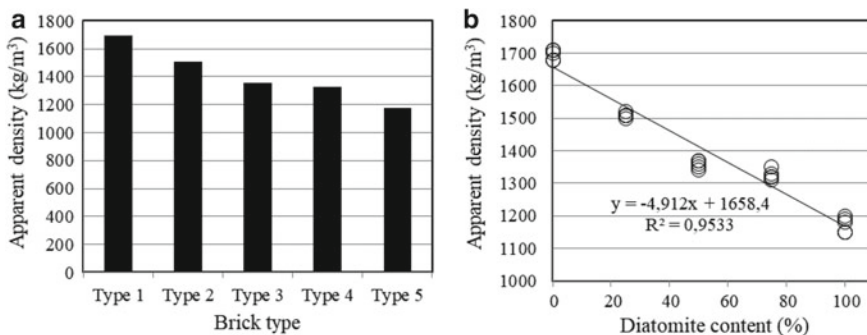
Fig. 1 a Apparent density; **b** relationship between apparent density and diatomite content

Table 8 Analysis of variance on the influence of diatomite content on apparent density of bricks

Variance source	Sum of square	df	Mean square	F_o	F_o (0.05); (4.20)
Treatments	0.786	4	0.197	812.05	2.87
Error	0.005	20	0.000		
Total	0.791	24			

bricks at significance level of 5%. Using the linear regression analysis as shown in Fig. 1b, the relationship between apparent density and diatomite content can be written as follows:

$$Q_{sch} = 1658.4 - 4.912D_c \qquad (5)$$

where Q_{sch} = apparent density of bricks (kg/m^3) and D_c = diatomite content (%).

3.3 Specific Gravity

The average specific gravity of all types of bricks are shown in Fig. 2a. This figure shows that the specific gravity of bricks decreased with the increase in diatomite content. The result of analysis of variance shown in Table 9 indicates that the diatomite content significantly affected the specific gravity of bricks at significance level of 5%. Using the linear regression analysis as shown in Fig. 2b, the relationship between specific gravity of bricks and diatomite content can be written as follows:

$$T = 2.238 - 0.0009D_c \tag{6}$$

where T = specific gravity of brick and D_c = diatomite content (%).

3.4 Water Absorption

The average water absorption of all bricks tested in this study is shown in Fig. 3a. This figure shows that the water absorption of bricks increased with the increase in diatomite content. The result of analysis of variance shown in Table 10 indicates that the diatomite content significantly affected the specific gravity of bricks at a significance level of 5%. Using the linear regression analysis as shown in Fig. 3b, the relationship between water absorption of bricks and diatomite content can be written as follows:

$$P_e = 15.354 + 0.2461D_c \tag{7}$$

where P_e = specific gravity of brick and D_c = diatomite content (%). Because of the high absorption of lightweight bricks made of diatomite, they cannot be used for
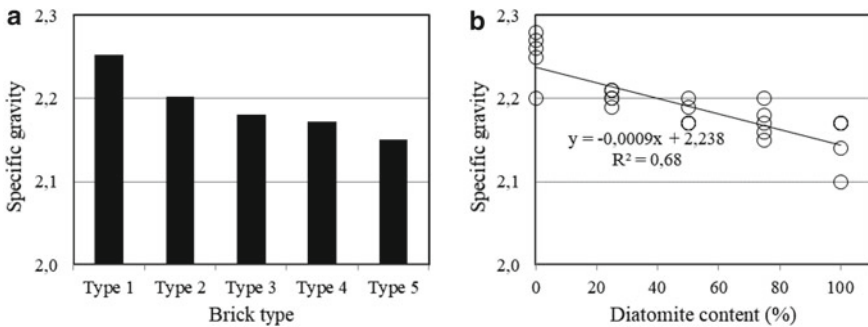
Fig. 2 a Specific gravity; b relationship between specific gravity and diatomite content

Table 9 Analysis of variance on the influence of diatomite content on brick specific gravity

Variance source	Sum of square	df	Mean square	F_o	F_o (0.05); (4.20)
Treatments	0.020	4	0.005	8.208	2.87
Error	0.012	20	0.001		
Total	0.033	24			
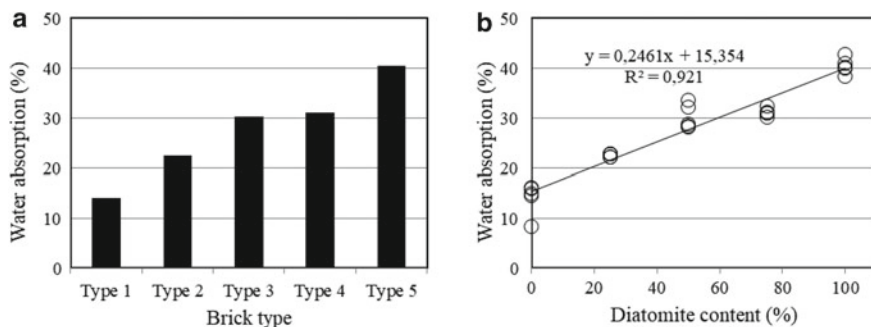
Fig. 3 **a** Water absorption; **b** relationship between water absorption and diatomite content

Table 10 Analysis of variance on the influence of diatomite content on brick absorption

Variance source	Sum of square	df	Mean square	F_o	F_o (0.05); (4.20)
Treatments	1978.44	4	494.61	128.30	2.87
Error	77.10	20	3.86		
Total	2055.54	24			

trasram masonry, bathroom walls and masonry in the ground with need impermeability. The application of this lightweight bricks is for normal masonry only with including the building wall.

3.5 Compressive Strength

The average compressive strength of all bricks tested in this study is shown in Fig. 4a. This figure shows that the compressive strength of paired bricks was lower than that of single bricks. This lower of paired brick compressive strength is attributed to the lower strength of mortar between the two pairs of bricks. When the compression test was conducted the age of the mortar was still 7 days. As well known the mortar reaches its optimum compressive strength at the age of 28 days. Therefore, it is recommended the compression test of paired bricks would be conducted when the age of the mortar reaches 28 days. The analysis of variance
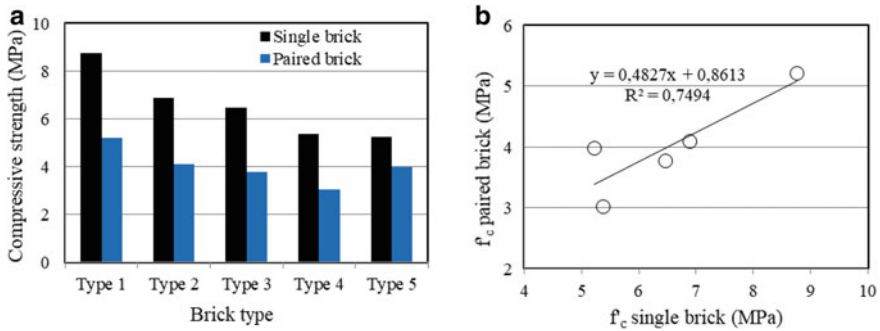
Fig. 4 **a** Compressive strength; **b** relationship between compressive strength of paired and single bricks

results for the influence of diatomite content on the compressive strength of single and paired bricks are shown in Tables 11 and 12. Table 11 shows that the $F_o < F_o$ (0.05); (4.20) with means that the diatomite content did not significantly affect the compressive strength of single bricks at significance level of 5%. According to the compressive strength obtained, all the bricks can be classified in one class which is Class 50 (SNI 15-2094-2000). However, the analysis of variance result presented in Table 12 shows that the diatomite content significantly affected the compressive strength of paired bricks at a significance level of 5%. Using the linear regression analysis as shown in Fig. 4b, the relationship between compressive strength of paired bricks and that of single bricks can be written as follows:

$$f'_p = 0.4827 f'_s + 0.8613 \tag{8}$$

Table 11 Analysis of variance on the influence of diatomite content on single brick compressive strength

Variance source	Sum of square	df	Mean square	F_o	F_o (0.05); (4.20)
Treatments	40.45	4	10.11	2.82	2.87
Error	71.63	20	3.58		
Total	112.08	24			

Table 12 Analysis of variance on the influence of diatomite content on paired brick compressive strength

Variance source	Sum of square	df	Mean square	F_o	F_o (0.05); (4.20)
Treatments	40.45	4	10.11	2.82	2.87
Error	71.63	20	3.58		
Total	112.08	24			

where: f'_p = compressive strength of paired bricks and f'_s = compressive strength of single bricks.

4   Conclusions

Based on the results presented above, the following conclusions can be drawn:

1. The diatomite content affected the apparent density and specific gravity of bricks significantly. The apparent density and specific gravity of bricks decreased with increasing in diatomite content. By replacing the clay with diatomite totally, the apparent density of bricks reduced by 30.78%. Therefore, lightweight bricks can be produced by replacing the clay with diatomite partially or totally.
2. The water absorption of bricks increased with increasing in diatomite content. Therefore, due to the high absorption of lightweight bricks made of diatomite, they cannot be used trasram masonry, bathroom walls and masonry in the ground with need impermeability.
3. The diatomite content did not affect the compressive strength of bricks. Based on the compressive strength, lightweight bricks composed of diatomite and clay can be classified at the same class with conventionally clay bricks, which is Class 50.

References

1. https://www.en.wikipedia.org/wiki/Brick
2. Posi P, Lertnimoolchai S, Sata V, Chindaprasirt P (2013) Pressed lightweight concrete containing calcined diatomite aggregate. Constr Build Mater 47:896–901
3. Hasan M, Saidi T, Muyasir A, Alkhali YR, Muslimsyah M (2020) Characteristis of calcined diatomaceous earth from Aceh Besar District—Indonesia as cementitious binder. IOP Conf Ser Mater Sci Eng 933:012008
4. Pimraksa K, Chindaprasirt P (2009) Lightweight bricks made of diatomaceous earth, lime and gypsum. Ceram Int 35:471–478
5. Hasan M, Saidi T (2020) Properties of blended cement paste with diatomite from Aceh Province Indonesia. IOP Conf Ser Mater Sci Eng 796:012034
6. Kastis D, Kakali G, Tsivilis S, Stamatakis MG (2006) Properties and hydration of blended cements with calcareous diatomite. Cem Concr Res 36:1821–1826
7. Fragoulis D, Stamatakis MG, Papageorgiou D, Chaniotakis E (2005) The physical and mechanical properties of composite cements manufactured with calcareous and clayey Greek diatomite mixtures. Cem Concr Compos 27:205–209
8. Saidi T, Hasan M (2020) The effect of partial replacement with diatomaceous earth (DE) on the compressive strength and absorption of mortar. J King Saud Univ Eng Sci. https://doi.org/10.1016/j.jksues.2020.10.003

9. Hasan M, Muyasir A, Saidi T, Husaini, Azzahra R (2020) Properties of high strength concrete with calcined diatomaceous earth as cement replacement under compression. Def Diff Forum 402:7–13

10. Tagnit-Hamou A, Petrov N, Luke K (2003) Properties of concrete containing diatomaceous earth. ACI Mater J 100:73–78

11. Hasan M, Riski ADD, Saidi T, Husaini, Rahman PN (2020) Flexural and splitting tensile strength of high strength concrete with diatomite micro particles as mineral additive. Def Diff Forum 402:50–55

12. Saidi T, Hasan M, Riski ADD, Ayunizar RR, Mubarak A (2020) Mix design and properties of reactive powder concrete with diatomaceous earth as cement replacement. IOP Conf Ser Mater Sci Eng 933:012007

13. SNI 1966:2008. Cara uji penentuan batas plastis dan indeks plastisitas tanah. Badan Standardisasi Nasional

14. SNI 1967:2008. Cara uji penentuan batas cair tanah. Badan Standardisasi Nasional

15. SNI 03-4804-1998. Pengujian berat isi dan rongga udara dalam agregat. Badan Standardisasi Nasional

16. SNI 15-2094-2000. Bata merah pejal untuk pasangan dinding. Badan Standardisasi Nasional

17. ASTM C373-18 2018. Standard test methods for determining of water absorption and associated properties by vacuum method for pressed ceramic tiles and glass tiles and boil method for extruded ceramic tiles and non-tile fired ceramic whiteware products

18. ASTM C67/C67M-20. Standard test methods for sampling and testing brick and structural clay tile

Thermal Characteristics of Oil Palm Wood and Ramie Fiber as Raw Materials for Thermal Insulation Bio Board

I. Mawardi, Samsul Rizal, S. Aprilia, and M. Faisal

Abstract The wise use of insulation materials in buildings not only reduces energy consumption but also reduces greenhouse gas emissions and increases the thermal comfort of the room. Oil palm wood fiber and ramie fiber have great potential as a basis for the thermal insulation bio board. The thermal stability of the base material is essential to study. The purpose of this study was to analyze the thermal characteristics of oil palm wood and ramie fiber as raw material for the thermal insulation bio board. Thermal characteristics were tested by thermogravimetric analysis (TGA) and differential scanning calorimetry (DSC). Oil palm wood fiber and ramie fiber as the base material get treatment before being tested. Oil palm wood fiber is immersed in 120 °C hot water for 30 and ramie fiber in 5% NaOH solution at the same time. The results of the TGA analysis show that the thermal stability of OPW fibers with treatment is better, 248 °C than the OPW without treatment at 235 °C. Likewise, ramie fiber with 5% NaOH mixture has better thermal stability, 280 °C than untreated ramie fiber, which produces a peak temperature of 272 °C. DSC analysis showed that the maximum temperature peaks occurred at 409 °C and 408 °C for OPW and hemp fiber treated, respectively. The thermal stability of fibers will increase with pretreatment compared to untreated fibers.

Keywords Oil palm wood · Ramie fiber · Thermal insulation · Bio board

I. Mawardi
Doctoral Program, School of Engineering, Post Graduate Program, Universitas Syiah Kuala, Banda Aceh 23111, Indonesia

S. Rizal
Department of Mechanical Engineering, Universitas Syiah Kuala, Banda Aceh 23111, Indonesia

S. Aprilia · M. Faisal (✉)
Department of Chemical Engineering, Universitas Syiah Kuala, Banda Aceh 23111, Indonesia
e-mail: mfaisal@unsyiah.ac.id

1   Introduction

Building, industry, and transportation are the three sectors that consume the most energy. These three sectors are the main contributors to CO_2 emissions, which cause global warming. Buildings can consume 47.6% of energy and produce CO_2 emissions of 44.6% [1]. The high energy consumption in buildings is inseparable from the increasing human population and the need for a place to live (buildings), indirectly narrowing green space and increasing energy consumption due to human activities, indoors and outdoors. Energy consumption is dominated by energy use for lighting, air conditioning (AC), space heating, and the use of other electronic devices.

At present, energy efficiency in buildings is a primary concern in social and economic development [2–4]. One of the energy efficiency techniques in buildings is the application of insulation materials [5–7]. The use is carried out by covering the building with insulation materials. Synthetic or inorganic materials such as; glass wool, rock wool, polyurethane foam, extruded polystyrene (XPS), and expanded polystyrene (EPS) have been widely used as thermal insulation materials, at present [7, 8]. Although inorganic materials have low thermal conductivity and density, the use of these materials harms the environment, is not renewable, the production process is high, and cannot be recycled. Therefore, the use of organic materials such as natural fibers as building insulation materials is one of the essential factors in creating a healthier and more sustainable environment.

Natural fibers such as ramie fiber and oil palm trunk have great potential and are promising as raw materials for environmentally friendly thermal insulation materials. The availability and readily biodegradable are the advantages of natural fibers. Many researchers have published the results of insulation material research using organic materials/natural fibers instead of inorganic materials. Wei et al. [9] have developed a new thermal insulation material from rice straw. The study was conducted by looking at the influence of several variables such as high-frequency heating, board density, particle size, and ambient temperature on the mechanical and physical properties of rice straw insulation material. The results showed that the optimal mechanical and physical properties of the boards were obtained with a moisture content of 14%, a density of 250 kg/m^3, and L-type particle size. Besides, thermal insulation boards have thermal conductivity ranging from 0.051 to 0.053 W/mK. Zhou et al. [10] have published environmentally friendly thermal insulation materials from natural fibers. Thermal insulation boards are formed from non-adhesive cotton stalk fibers. The board is formed by hot pressing. The insulation boards produced have a density of 150–450 kg/m^3 and have thermal conductivity values ranging from 0.0585 to 0.0815 W/mK. The value of thermal conductivity has a strong linear correlation with density.

Panyakaew and Fotios [11] have developed thermal insulation boards from coir and bagasse fibers. The insulation material is formed without the use of chemical binders and with low density. Their experimental results showed that the insulation boards from coir and bagasse fibers had thermal conductivity values ranging from

0.046 to 0.068 W/mK. These results approach conventional insulation materials such as cellulose fibers and mineral wool. Korjenic et al. [12] have published the use of hemp, flax, and hemp to develop new insulation materials from renewable resources. Specimens were formed using polystyrene adhesive (PS). Experimental results show that the optimal combination of natural materials has thermal and mechanical properties comparable to conventional insulation materials such as polyurethane, polystyrene, and mineral wool. Manohar et al. [13] also have biodegradable insulation material from coir fiber and bagasse fiber. The results showed that the thermal conductivity at 70 kg/m^3 of bagasse and coir fiber was 0.05094 W/mK (24 °C) and 0.04884 W/mK (21.8 °C), respectively.

Research the thermal insulation materials from renewable natural materials continue to develop. In addition to the use of natural fibers, but biomass such as wood and date palms has been reported. The natural fibers were also investigated [14, 15], which uses wood waste as an alternative material for thermal insulation materials for buildings. Waste wood used comes from primary production sources without treatment. Particle sizes range from 1 to 4 mm. The results showed that the thermal conductivity of 0.048–0.055 W/mK. Dates with comparable gypsum adhesive can replace conventional insulation materials. Thermal insulation material from date palms with gypsum adhesive is safe for humans [16].

In addition to the date palm tree, [17] has mixed bio-based local material, sawdust, and palm fiber as a mixture of concrete blocks. Sawdust and coir fiber are processed to form composite building blocks. Experiments were carried out to determine the thermal conductivity, compressive strength, and density of sand concrete. The results of the research show that incorporating bio-based materials into concrete reduces density and thermal conductivity, thereby reducing the burden of heat-transmitting walls.

In addition to wood and date palm trunks, palm oil trunks have enormous potential to be developed as raw material for insulation materials. Indonesia, in 2019 has an area of 14.67 million hectares of oil palm plantations [18]. An average rejuvenation rate of 4% per year is carried out from the total plantation area [19]. Rejuvenation results can produce a volume of oil palm wood of around 200 m^3/ha. The vast potential of oil palm wood has not been utilized optimally. Loh [20] has published the potential of Malaysian palm oil biomass as a renewable energy source. Overall, oil palm biomass has great potential as one of the largest alternative energy sources for commercial exploitation. The use of palm oil receptor rods into an economically valuable product such as particle board has been developed.

The thermal insulation boards are influenced by the thermal characteristics of the forming material. The thermal characteristics of oil palm trunk and ramie fiber as raw material for bio board insulation material are needed to obtain data on fiber degradation to heat. Thermal degradation analysis and microstructure testing for various local fibers from different trees have been carried out [21]. Kabir [22] have reported the structural composition and thermal decomposition of fibers made from chemically treated ramie. Differential thermogravimetric analysis (DTGA) shows that the primary degradation of fibers occurs at temperatures between 250 and 375 °C. Thermal characteristics and mechanical properties of coir fibers treated with

alkali fibers have been reported [23, 24], where they use differential calorimetry and infrared spectroscopy. Ali and Alabdulkarem [23] also have the characteristic thermal features of date palm fibers. Thermogravimetric analysis (TGA and DTGA) shows the degradation and decomposition of the fiber starting at 232 °C, where the sample is only about 8.5% of the mass obtained. Differential analysis of calorimetric scanning (DSC) is carried out and shows what is meant by endothermic starting at 243–382 °C with a peak at 369 °C. In addition to natural fibers, thermogravimetric analysis and analysis of differential scanning calorimetry for sheep wool, goat wool, and horse mane that have been reported [25]. Horse mane shows more stability up to the temperature of 375 °C as compared to sheep and goat wool.

This study analyzes the thermal characteristics of oil palm wood and ramie fiber as raw material for the thermal insulation bio board. Thermogravimetric analysis (TGA) and differential scanning calorimetry (DSC) tests performed to determine the thermal characteristics of the bio board forming materials.

2 Experimental

2.1 Materials

Oil palm wood (OPW) and ramie fiber are the primary raw material for forming the thermal insulation bio board. Oil palm wood is taken from oil palm trunks on 25–30 years old from North Aceh, Aceh. Oil palm trunks are cut based on the height (bottom, middle, and edge) and the trunk (peripheral, central, inner). The oil palm wood used is taken in the middle on the position and center of the cross-section, and then cut and crushed into particles. The particles treatment in hot water at a temperature of 120 °C for 30 min. Particles dried up to 10–15% moisture content. Ramie fiber comes from Sleman, Yogyakarta. It is the treatment in NaOH 5% solution for 30 min, then rinsed with distilled equates and then dried until it reached a moisture content of 10–15%. Figures 1 and 2 show oil palm wood and ramie fiber that are untreated and treated.

2.2 Thermogravimetric Analysis (TGA)

The most commonly used thermal analysis method is thermogravimetric analysis (TGA). TGA is an analytical technique to determine the thermal stability of a material and fraction in terms of decreasing mass that occurs due to decomposition or burning. Materials decomposed at high temperatures are said to have high thermal stability and vice versa. The thermogravimetric analyzer was conducted using Shimadzu DTG-60. TGA testing follows ASTM E1131-08 standards. It is measures the amount of change in the mass of a material as a function of

OPW untreated   OPW treatment
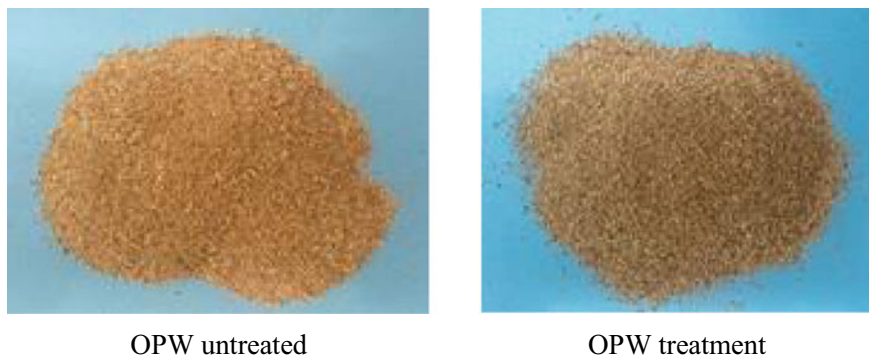
Fig. 1 OPW untreated and treatment hot water 120 °C, 30 min

Ramie fiber untreated   Ramie fiber treatment

Fig. 2 Ramie fiber untreated and treatment 5% NaOH, 30 min

temperature rise or exothermic as a function of time in the nitrogen atmosphere. The sample weight used was 2.0 mg and was heated from 40 to 1000 °C, with a heating rate of 40 °C/min.

2.3 Differential Scanning Calorimetry (DSC)

Another method for analyzing material properties thermal is differential scanning calorimetry (DSC). DSC measures the enthalpy changes in a sample due to changes in physical and chemical properties as a function of temperature or time. DSC testing will show thermal stability associated with phase change, in this case, melting. Material that melts at higher temperatures is said to have high thermal stability and vice versa. It is testing was carried out using Shimadzu DSC-60, and analysis was carried out following the ASTM D3418-08 standard. The sample

weight used was 2.0 mg. The sample is heated in a DSC oven in an aluminum container under atmospheric nitrogen pressure. Heating is carried out to a temperature of 600 °C, with a heating rate of 40 °C/min.

3   Results and Discussion

The thermal analysis aims to determine the thermodynamic process of raw materials because bio board production uses temperature (hot press), which can affect the quality of the material, especially mechanical properties. Thermogravimetric analysis (TGA) and differential scanning calorimetry (DSC) methods are widely used to analyze the thermal properties. Therefore, the thermal properties of the base material need to be analyzed to determine the ability of the base material to provide heat load both before and after the production process.

Figures 3 and 4 show the TGA curve of OPW fiber and ramie fiber. The TGA curve is divided into three stages of degradation, the first stage (a–b), the second stage (c–d), and the third stage (d–e). TGA curves of OPW fiber untreated and treatment are shown in Fig. 3. The first stage degradation occurs in the temperature range of 40–92 °C for OPW untreated and 40–90 °C for OPW treatment. The loss of mass in the first stage was caused by the loss of water from the sample. The second stage, which is the main stage, occurs at 235–392 °C for OPW untreated and 248–415 °C for OPW treatment. At this stage, there is damage to the fiber and microfibrils of the fiber structure. In this area, decomposition occurs due to hemicellulose decomposition and is accompanied by loss of OPW fiber mass. Degradation of remaining OPW mass loss in the third stage, at temperatures of 392–580 °C for OPW untreated and 415–600 °C for OPW treatment. The start temperature of a drastic decrease indicates the thermal stability of the material. Thermal stability is said to be high if mass reduction occurs at higher temperatures. Figure 3, thermal stability occurs at a temperature of 235 °C for OPW untreated and 248 °C for OPW treatment.

TGA thermogram of ramie fiber similar OPW fiber (Fig. 4). Losing a certain amount of ramie fiber mass in the first stage takes longer. The first stage of degradation of ramie fiber untreated ranges from temperatures 40–115 °C and 40–135 °C for ramie fiber with treatment. In the second stage, degradation occurs at temperatures of 272–408 °C for ramie fiber untreated and 280–416 °C for ramie fiber with treatment. The third stage, which is the residual mass loss of fibers, occurred at a temperature of 408–600 °C for ramie fiber untreated and 416–600 °C for ramie fiber with treatment. In Fig. 4, the peak temperature (272 °C), which is the thermal stability of the ramie fiber untreated, occurs and 280 °C for the ramie fiber with the treatment.

DSC testing will show thermal stability associated with phase change, in this case, melting. Material that melts at higher temperatures is said to have high thermal stability and vice versa. Differential scanning calorimetry (DSC) for OPW fiber and ramie fiber is shown in Figs. 5 and 6. Figure 5 shows the DSC curve of OPW

Fig. 3 TGA curves of OPW fibers **a** untreated **b** treatment hot water

(a)

(b)
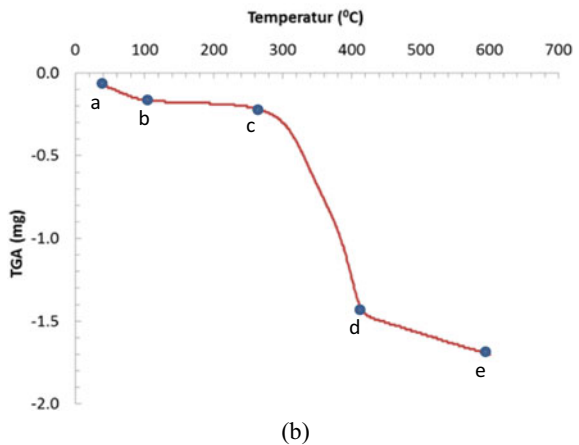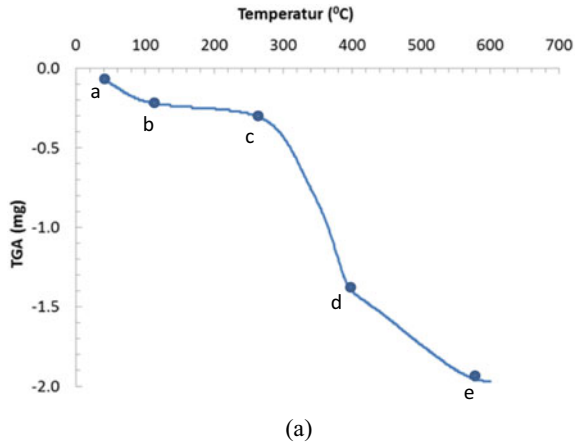
without treatment and OPW with treatment with 120 °C hot water. Endothermic reactions occur at temperatures of 40–150 °C for OPW untreated and 40–153 °C for OPW with treatment. The exothermic reaction states that the material has been degraded to occur at a temperature of 390–420 °C for OPW untreated, with peak temperatures of 402 °C and 385–438 °C with peak temperatures of 409 °C for OPW with treatment.

Figure 6 shows the ramie fiber DSC curve, similar to the OPW fiber DSC curve. Endotherms for ramie fiber untreated occur at 55–150 °C and 60–160 °C for ramie fiber with 5% NaOH treatment. Simultaneously, exothermic occurs at 395–425 °C for ramie fiber untreated and 390–435 °C for ramie fiber with treatment. The exothermic peak temperature of ramie fiber untreated and with NaOH 5% treatment, respectively, at 402 °C and 408 °C.

Fig. 4 TGA curves of ramie fibers **a** untreated **b** treatment NaOH 5%

(a)

(b)
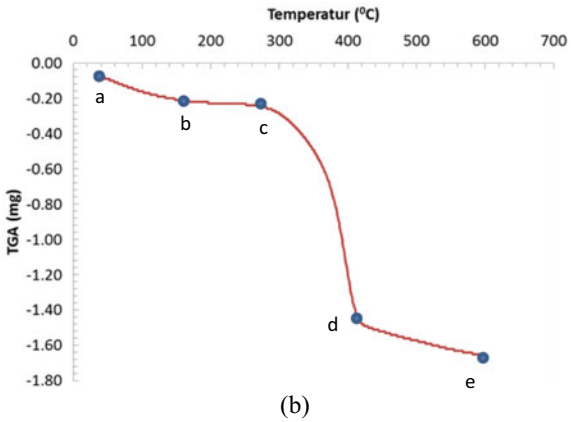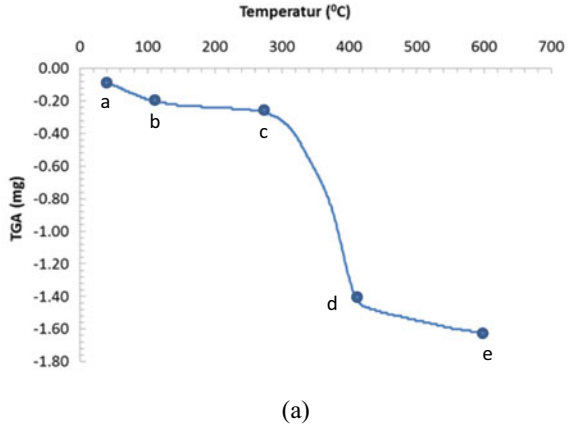
4 Conclusions

Material development for thermal insulation bioboard is influenced by the thermal characteristics of the constituent material. TGA analysis showed that untreated OPW fibers degraded at a lower temperature, 235 °C compared to OPW fibers that had been treated in hot water (248 °C). Likewise, ramie fibers with 5% NaOH treatment and without treatment experienced degradation, respectively at 280 °C and 272 °C. From the DSC analysis, it shows that OPW fibers which have been treated in hot water and ramie fibers with 5% NaOH treatment produce higher peak temperatures than untreated fibers, at temperatures of 409 °C and 408 °C, respectively. Both results of the analysis show that OPW fibers that have been treated in hot water and ramie fibers with 5% NaOH treatment have better thermal stability than untreated fibers. The thermal degradation of the two fibers (OPW and ramie) is very important initial information in the development of thermal insulation bioboard materials based on OPW and ramie fibers.
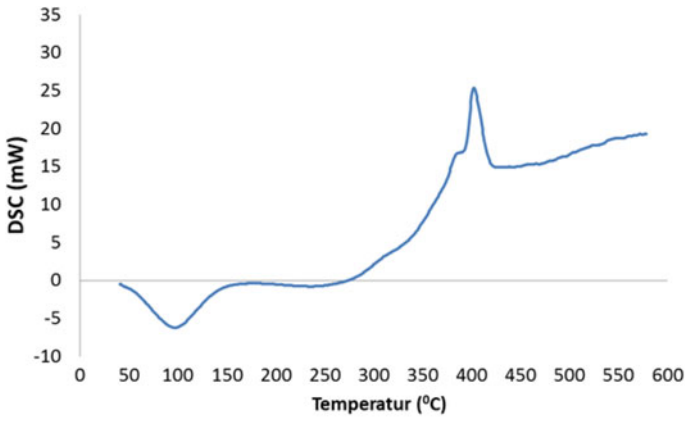
(a)
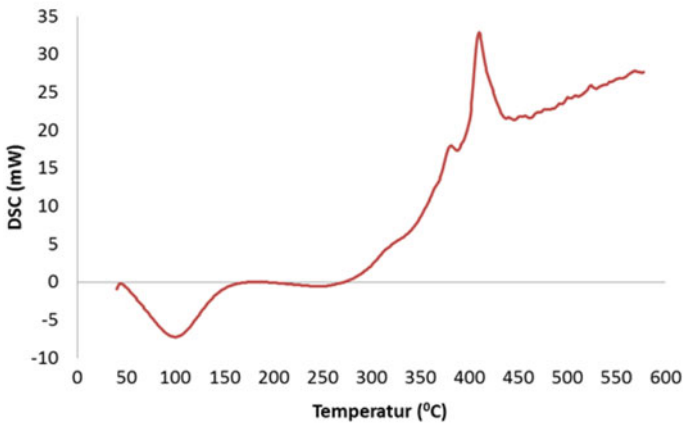
(b)

Fig. 5 DSC curves of OPW fibers **a** untreated **b** treatment hot water
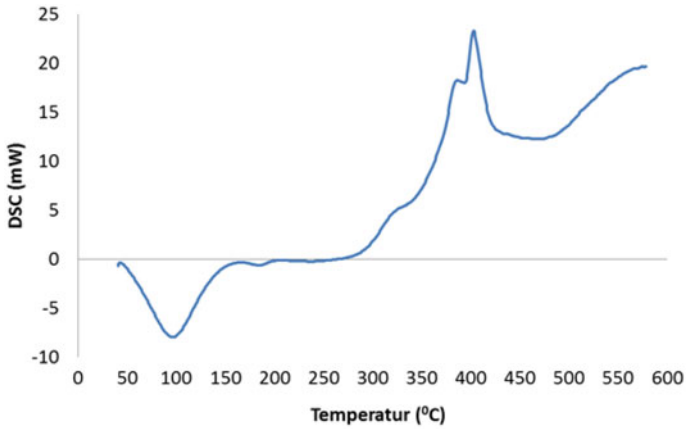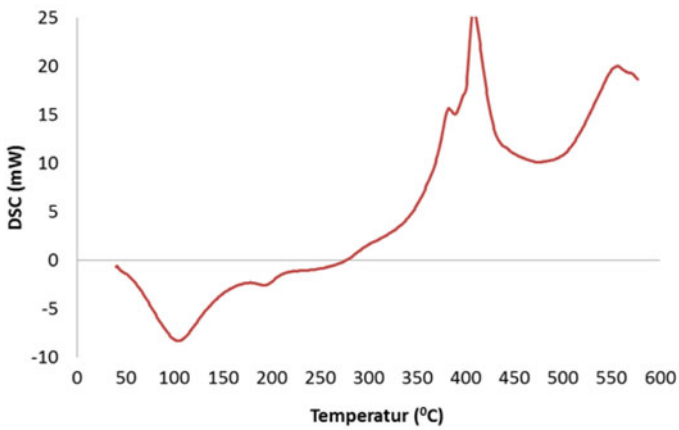
Fig. 6 DSC curves of ramie fibers **a** untreated **b** treatment 5% NaOH

References

1. Florea I, Manea DL (2019) Analysis of thermal insulation building materials based on natural fibers. Procedia Manuf 32:230–235
2. Geng Y, Ji W, Lin B, Hong J, Zhu Y (2018) Building energy performance diagnosis using energy bills and weather data. Energy Build 172:181–191

3. Viot H, Sempey A, Mora L, Batsale JC, Malvestio J (2018) Model predictive control of a thermally activated building system to improve energy management of an experimental building: Part I—Modeling and measurements. Energy Build 172:94–103
4. Zhang Y, Bai X, Mills FP, Pezzey JCV (2018) Rethinking the role of occupant behavior in building energy performance: a review. Energy Build 172:279–294
5. La Rosa AD et al (2014) Environmental impacts and thermal insulation performance of innovative composite solutions for building applications. Constr Build Mater 55:406–414
6. Sadineni SB, Madala S, Boehm RF (2011) Passive building energy savings: a review of building envelope components. Renew Sustain Energy Rev 15(8):3617–3631
7. Aditya L et al (2017) A review on insulation materials for energy conservation in buildings. Renew Sustain Energy Rev 73:1352–1365
8. Jelle BP (2011) Traditional, state-of-the-art and future thermal building insulation materials and solutions–properties, requirements and possibilities. Energy Build 43(10):2549–2563
9. Wei K, Lv C, Chen M, Zhou X, Dai Z, Shen D (2015) Development and performance evaluation of a new thermal insulation material from rice straw using high frequency hot-pressing. Energy Build 87:116–122
10. Zhou X, Zheng F, Li H, Lu C (2010) An environment-friendly thermal insulation material from cotton stalk fibers. Energy Build 42(7):1070–1074
11. Panyakaew S, Fotios S (2011) New thermal insulation boards made from coconut husk and bagasse. Energy Build 43(7):1732–1739
12. Korjenic A, Petránek V, Zach J, Hroudová J (2011) Development and performance evaluation of natural thermal-insulation materials composed of renewable resources. Energy Build 43 (9):2518–2523
13. Manohar K, Ramlakhan D, Kochhar G, Haldar S (2006) Biodegradable fibrous thermal insulation. J Brazilian Soc Mech Sci Eng 28(1):45–47
14. Cetiner I, Shea AD (2018) Wood waste as an alternative thermal insulation for buildings. Energy Build 168:374–384
15. Ginting A, Mawardi I, Jannifar A, Hasyim SS, Anzieb MR (2019) Effectiveness of die hole on wood pellet density quality improvement. IOP Conf Ser: Earth Environ Sci 268(1):12166
16. Braiek A, Karkri M, Adili A, Ibos L, Ben Nasrallah S (2017) Estimation of the thermophysical properties of date palm fibers/gypsum composite for use as insulating materials in building. Energy Build 140:268–279
17. Opoku R, Obeng GY, Darkwa J, Kwofie S (2020) Minimizing heat transmission loads and improving energy efficiency of building envelopes in sub-Saharan Africa using bio-based composite materials. Sci African, e00358
18. Pertanian DJPK (2018) Statistik Perkebunan Indonesia 2017–2019 (kelapa sawit). Direktorat Jenderal Perkebunan Kementerian Pertanian, Jakarta
19. Hambali E, Rivai M (2017) The potential of palm oil waste biomass in Indonesia in 2020 and 2030. IOP Conf Ser: Earth Environ Sci 65(1):12050
20. Loh SK (2017) The potential of the Malaysian oil palm biomass as a renewable energy source. Energy Convers Manag 141:285–298
21. Bilba K, Arsene M-A, Ouensanga A (2007) Study of banana and coconut fibers: botanical composition, thermal degradation and textural observations. Bioresour Technol 98(1):58–68
22. Kabir MM (2012) Effects of chemical treatments on hemp fiber reinforced polyester composites. University of Southern Queensland
23. Ali ME, Alabdulkarem A (2017) On thermal characteristics and microstructure of a new insulation material extracted from date palm trees surface fibers. Constr Build Mater 138:276–284
24. Mawardi I (2018) Effect of fiber fibrillation on impact and flexural strength of coir fiber reinforced epoxy hybrid composites. IOP Conf Ser: Mater Sci Eng 334(1):12079
25. Ahmed A, Qayoum A, Mir FQ (2019) Investigation of the thermal behavior of the natural insulation materials for low temperature regions. J Build Eng 26:100849

Effect of Soil Composition on the Corrosion Rate of Underground Water Distribution Pipes in Natural Environment

Reza Putra, Muhammad, Syifaul Huzni, and Syarizal Fonna

Abstract The distribution of raw water in the fertilizer industry in the North Aceh area that uses pipes has been used for approximately 33 years. The majority of the pipe material is concealed under the soil which is one of many media that contributes in external corrosion on metals. This research has been conducted to see the effect of soil properties on different environments on the rate of corrosion that occurs in carbon steel materials. The corrosion rate is calculated by the weight loss method which refers to ASTM G 162. The tested specimens use SA 283 standard carbon steel pipe with the time of buried specimens for 3 months or 2160 h. This research was conducted on 5 different soil sites along the pipe buried line. The results show the highest corrosion rate (0.45 mm/yr) that occurs during the experiment. It's believed that the soil has the highest redox potential with a high acidity level as well. In general, all land in underground pipelines has the potential to cause external corrosion of underground pipes.

Keywords Corrosion · Corrosion rate · Redox potential · Soil properties

1 Introduction

Within the fertilizer industry, the use of pipelines is an element that plays an important role. The pipeline is used as a distribution tool for various industrial needs, one of which is water to meet the needs of factories and housing complexes. This water need is channeled through a steel pipe from the river which is located ±24 km from the factory location, namely on the Peusangan river (Bireuen

R. Putra (✉) · Muhammad
Mechanical Engineering, Faculty of Engineering, Universitas Malikussaleh,
Kota Lhokseumawe 24351, Indonesia
e-mail: reza.putra@unimal.ac.id

S. Huzni · S. Fonna
Mechanical Engineering, Faculty of Engineering, Universitas Syiah Kuala,
Banda Aceh 23111, Indonesia

Regency). At the time of construction, the pipe has been protected from corrosion by the coating and cathodic protection systems. This underground pipeline has been carrying out its functions for more than 33 years. Based on the initial evaluation that has been done, the soil resistivity value along the pipe installation path and the measurement results of cathodic protection on underground pipes monitored through a 25 point test box shows the results of over-protection in several locations [1].

Pipelines that transfer and dispense water, gas, oil, petroleum products and other types of fluids are very helpful in reducing transportation costs. Long pipelines and diverse environments over a long period of time can reduce the quality of pipe material. Corrosion is the main factor that must be anticipated in a pipeline that is buried in the ground. Corrosion affects all pipelines and equipment which are buried in the ground or submerged in water because generally pipe material is made of steel metal [2]. In the case of pipelines carrying fluids with flammability, high pressure or potentially polluting the environment, pipe safety is the most important thing. The design and selection of the best systems and materials for pipelines and corrosion protection systems is the main focus that needs to be considered in the industry [2, 3].

Corrosion in a pipeline network was a decreased the quality of the pipe material and related systems due to its interaction with the environment. The failure that occurs in pipelines caused by corrosion, and the number of repair costs to billions of dollars per year [3]. At the end of 2017, there were 28 accidents caused by pipeline failure in the United States. Based on data summarized by the US Department of Transportation in charge of the safety of hazardous materials and piping (PHMSA), in 2010 to 2016 there have been 752 cases of accidents caused by the failure of piping systems [4].

Corrosion is a destructive attack of material resulting from the reaction of metals with their environment and potential natural hazards associated with the production and transportation facilities of pipelines [2]. This corrosion problem has become a significant problem in industries throughout the globe [3]. Corrosion attacks are responsible for most failures in metal materials and with these corrosion reactions metals lose strength, ductility, and other mechanical properties. The problem on underground structures such as pipelines is a serious problem for engineers, the government and the general public. The failure of the pipeline will result in environmental pollution, loss of life and enormous property. Unprotected pipes, buildings, and other engineered structures construct in corrosive environments generally have a shorter life period [5].

The type of corrosion in piping networks is generally related to internal and external factors. Internal factors that are closely related to corrosion are the oxygen content of the fluid reaction carried, the use of different materials in the piping network, flow rate, pressure and temperature of the fluid. External factors include fabrication and installation processes, work environment, soil factors such as pH and moisture for buried pipes or water chemistry in the case of submerged pipes [6]. This corrosion can cause the loss of uniform material along the surface of the pipe, resulting in continuous thinning of the pipe wall [5], where excessive thinning walls

can cause leakage or rupture of pipelines. Almost all aqueous environments can increase corrosion, which occurs under many complex conditions in oil, gas production, processing, and piping systems. The handling costs and maintenance costs in each industry are quite large in overcoming corrosion problems every year [3].

The soil is a very influential environment as a medium for the occurrence of corrosion reaction processes. Different soil properties in an environment generally accelerate the growth of corrosion rates in an embedded metal material. More acidic soils show a serious risk of corrosion of general structural materials such as steel, cast iron, and zinc coating. Land resistivity has historically been the main indicator of soil corrosion. Other parameters commonly used to evaluate the potential of soil corrosion are pH, Redox potential, soil resistivity, chloride content and sulfide content [3].

Resistivity is often used as an indicator of corrosion that occurs in the soil. Its caused by ionic current flows are associated with soil corrosion reactions, high soil resistivity can slow corrosion reactions. Soil resistivity can be measured by the four pin Wenner technique, known as an electromagnetic measurement. This method allows measurement in an easy way at different soil depths.

Corrosion rates are measured by the penetration depth of the surface which is usually expressed in millimeters per year or miles per year. The selection of suitable pipe materials and an amalgamation of corrosion protection methods such as cathodic protection and the appropriate type of surface coating can reduce or even prevent corrosion of the outer surface of the pipe that is in contact with the soil. However, even with the best efforts, corrosion may still occur due to inadequate cathodic protection (CP) and/or poor coating conditions on the pipe surface [7].

Wang et al. [8] evaluated the corrosion behavior of X70 steel pipes buried in red soil environments. Corrosion kinetics was evaluated by measuring weight loss. The results show that in red soils, the corrosion rate of X70 steel decreases over time, and follows the exponential decay law. General corrosion with non-uniform and localized pitting occurs on the steel surface. α-FeOOH is a product that dominates during corrosion throughout the buried period, and corrosion products show good protective properties. Potentiodynamic polarization tests revealed that icorr decreased with time, indicating an increase in corrosion resistance.

Vanaei et al. [9] use the In-Line Inspection (ILI) technique in predicting corrosion rates in pipes. This corrosion growth model refers to the model in the previous study that has been used namely linear corrosion growth rate model, non-linear corrosion growth rate model, Markov model, Monte-Carlo method, TI-GEVD model, TD-GEVD, and BMWD model. The field data used was data on the gas pipeline between 1996 and 2006 in the southern region of Mexico. The results showed that the Markov model was more precise in corrosion and the reliability of the pipeline defect rate evaluation when cooperated with the Monte Carlo framework reliability.

Biezma et al. [10] have predicted external corrosion rates based on a combination of measurements of six soil parameters. The method used shows a relationship that is relatively easy to operate in an industrial world that focuses on optimizing security and sustainability of the service. The soil parameters included

in fuzzy logic experts are systems that vary from those used by previous researchers who have opted for a fuzzy approach, introducing important factors, such as sulfate and chloride concentration, moisture content, that has been proven to be of high importance in underground pipe corrosion.

In this work, a case study is presented with the aim of sharing knowledge with a corrosion growth rate that is passed by the pipeline in different soil environments. The study of soil as a medium is important to take into account a large amount of buried pipes. The deterioration of that kind of structures representing environmental problems, safety, and the economy through the years.

2   Experimental

2.1   Material

The material used in this study was a 30-inch diameter carbon steel pipe with a thickness of 15 mm with ASTM SA 283 grade D standard with a tensile strength between 415 and 550 Mpa [11]. This material was analyzed for its chemical composition using metal analyzer presented in Table 1. This material is cut into a coupon with an average size of 25 × 50 mm using a saw. The used of saws in the cutting process to avoid changes in structure due to the influence by heat. Before Burying, these specimens have been cleaned and weighed to determine the initial weight of each coupon [12]. Media land as a place for burying test coupons has chosen adjacent to the location of the pipeline. Environmental conditions vary along the pipeline to see the effect of soil on corrosion. The five variations of the selected soil environment are rice fields, topsoil, ponds, clay, and irrigation. All test coupons are buried at a depth of 80 cm from the ground.

2.2   Resistivity Test

The Wenner method has been used to determine soil resistivity in accordance with ASTM G57-95a [13]. This method uses a 4-pole digital resistance meter. The tool used in this study is the Earth Tester tool from the Megger DET4TD2 brand. This method uses four probes that enter the test area. In this case, the probe is used to connect electrical contacts with the earth. The Megger Test Tool then injects a constant current through the ground through a tester and two external probes (C_1 and C_2), and the current flowing through the earth (resistive material) develops a

Table 1 Chemical composition of SA 283 carbon steel grade D

C	Si	Mn	P	S	Fe
0.28	0.42	0.59	0.0007	0.005	Balance

voltage or potential difference. The potential is measured between pins P_1 and P_2 as seen in Fig. 1. From the current (I) and voltage (V) values, an apparent resistivity (R) value is calculated.

Almost all corrosion is an electrochemical reaction, so all that affect the speed of a chemical reaction or the amount of current flowing will affect the rate of corrosion. The corrosion rate is directly proportional to the amount of current flowing in the cell electrochemical corrosion. If the current can be measured, an exact calculation of metal loss can be determined. This means that a measurement in amperes or milliamperes is mathematically calculated in kilograms (pounds) per year. Different metals have different corrosion rates [13].

In this study, the corrosion rate of the pipe was represented based on the perspective involving the specimen directly, by measuring the mass loss caused by corrosion. Sample preparation and cleaning using the ASTM G 01 test standard [13]. This corrosion rate testing method involves the process of burying material samples (coupons) in the soil along the pipeline in 5 different locations until the sample material (coupon) is corroded. Over time, the specimen will experience thinning due to loss of mass. The standard for this method is ASTM G 162 [14].

2.3   Corrosion Test

The coupons were buried for 3 months or 2160 h. Measurement of mass loss is obtained by comparing the weight of the coupon before and after testing. Corrosion rates due to soil variations in these locations, for metals tested, can be determined and represented in units of penetration per year (millimeters per year), namely Corrosion rate (mm/yr) = $(K \times W)/(A \times T \times D)$, where K = a constant (8.76×104), T = time of exposure to the nearest 0.01 h, A = area in cm^2 to the nearest 0.01 cm^2, W = mass loss in gr, to nearest 1 mg, and D = density in g/cm^3 [15]. The rate of testing and testing is done with the ASTM G 51. The pH value of
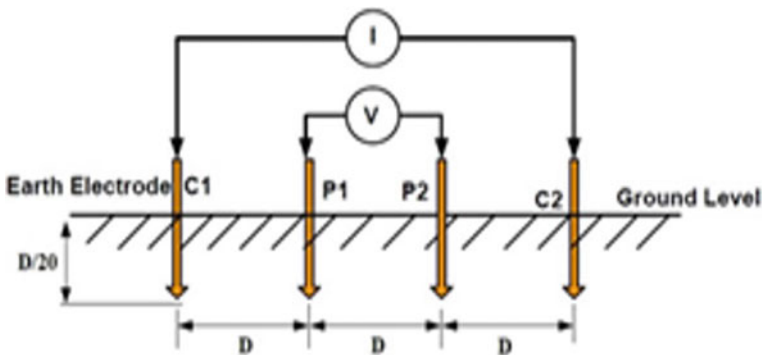
Fig. 1 ASTM G57-95a Wenner four point method

the soil is calculated to be a corrosion rate on the coupon. pH measurements were using a glass electrode. pH values are shown as an average of 4 measurements.

The location of buried coupons on the path through which the underground pipes pass. The location was chosen based on different environmental factors such as rice fields, ponds, irrigation and community farms. four coupons were buried in the soil for each location. The study sites are located in Aceh Utara with latitude 5° 13′ N and 5° 14′ N, and longitude 96° 57′ E and 96° 59′ E.

3 Result and Discussion

3.1 Soil Texture

This study provides information about the texture, physical and chemical properties of the soil against the corrosion rate that occurs in the test coupons and their comparison with the nature of the soil. The results of testing the soil texture properties are presented in Fig. 2. In general, the soil in the underground pipe location is sandy and clay type, where the sand content is above 50% with a plasticity below 40%. The high sand content indicates that the tested soil is soil on the surface. The value of soil texture generally indicates the condition of the land which is an area of rice fields and ponds.

Other external factors that affect soil characteristics are very diverse including temperature and soil moisture content. At ground level, temperatures range from 25 to 34 °C, while at 80 cm depth the temperature varies between 22 and 29 °C. When the research conducted in March to June which is the transition period of the season is very influential on rainfall. The rainfall affects the level of soil moisture up to 6%.

	1	2	3	4	5
Dust (%)	23.29	6.855	13.94	8.52	22.595
Clay (%)	38.295	32.995	31.365	13.98	15.385
sand (%)	38.415	60.15	54.695	77.5	62.02
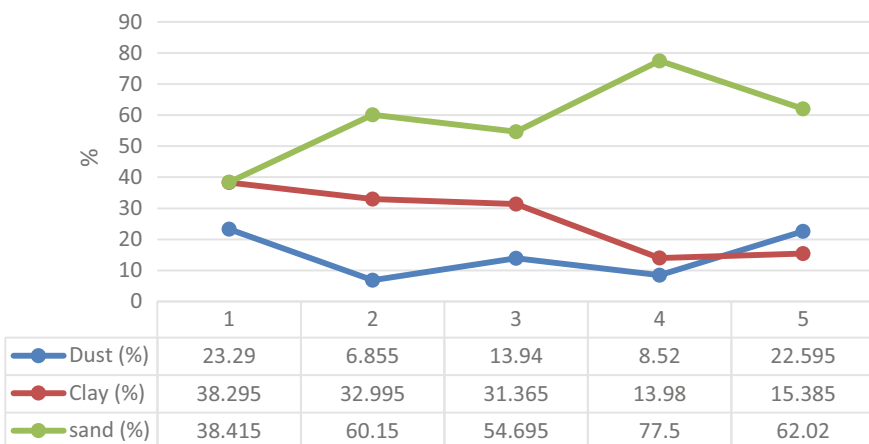
Fig. 2 The texture of experimental soil

This rain also affects the acidity of the soil, which shows that the content of rainwater contains a high C_l where the test location is also close to the coastline (approximately 2 km). Furthermore, the acidity of the soil obtained in the field shows the effect of fertilizers and microorganism with a pH range of 3.8–6.2. The chemical composition of each of these soils is presented in Table 2.

3.2 Corrosion Rate

To see the corrosion rate that occurs at different locations, the test coupon that has been buried for 2160 h is removed and cleaned of rust products. After cleaning, the entire test coupon is weighed again to get the weight difference (gr). The values presented in Fig. 3 below represent the value of the average weight loss for each test coupon in different types of soil.

Figure 3 shows the value of heavy losses that occurred in the SA283 test specimen after going through the buried period of 2160 h. The highest weight loss value at Paloh Awe location 1.77 gr indicates this location has a high level of corrosion. Observation in the field shows that this area is the location of rice fields with conditions of watery clay. The smallest weight loss in the Reulet 2 area of 1.08 gr also indicates that this location is inclined to external corrosion attacks, i.e. from the ground.

From the measurement of soil resistivity using the Wenner method at 150 cm depth, it can be seen that the lowest resistivity value is 57.42 Ωcm which indicates this environment is at the soil level with extremely corrosive. This can be affected by the position of pipelines in relatively wet rice fields and irrigation. A high resistivity value can be seen at Pinto Makmur 2 with the value of 2241.94 Ωcm which indicates poor corrosion level take place within this location. The comparison between the corrosion rate and soil resistivity can be presented as in Fig. 4.

The histogram graph in Fig. 4 shows the corrosion rate that occurred in SA 283 material in 5 different locations. The value of the corrosion rate is influenced by the type of soil which is at a different location and is also influenced by changes in the weather at the study site during the study period. Therefore, the chemical properties of the soil will be compared with the corrosion rate to obtain a correlation between

Table 2 Chemical and physical analysis of experimental soil

No.	Location	Condition	pH	Potential redox (mV)	Resistivity (Ωcm)
1	Reulet Barat 1	Silty clay soil	5.67	38.1	1796.90
2	Reulet Barat 2	Loamy soil	5.85	27.2	442.65
3	Paloh Awe	Silt clay soil	3.84	61.6	57.42
4	Pinto Makmur 1	Sandy soil	4.96	38.2	385.22
5	Pinto Makmur 2	Humus soil	6.22	40.3	2241.94

Fig. 3 The average of weight loss specimen
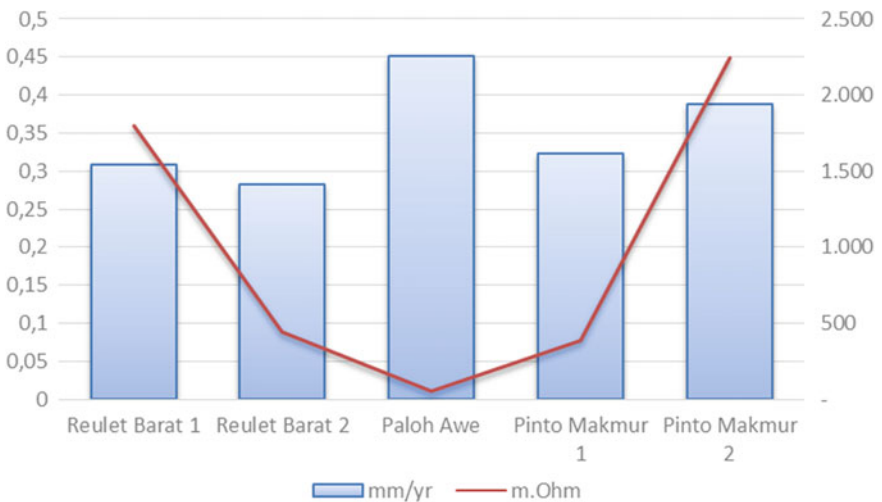
Fig. 4 Comparison of corrosion rates with soil resistivity

the main causes of corrosion growth. Comparison between the corrosion rates that occur with soil acidity (pH) can be plotted as shown in Fig. 5.

The biggest corrosion rate is 0.45 mm/yr which occurs in the Paloh Awe area which has a clay texture of 31.3%. The condition of clay has a smaller particle size than sand so that it can inhibit the flow of water in the soil. Water as an electron-carrying medium makes this type of soil a potential medium for corrosion to occur compared to other locations. However, at the location of West Reulet 1, the highest clay value is 38.3% but has a corrosion rate of only 0.3 mm/yr. According

	1	2	3	4	5
mm/yr	0,308403734	0,283161182	0,450766689	0,323320548	0,388088438
pH	5,67	5,85	3,84	4,96	6,22
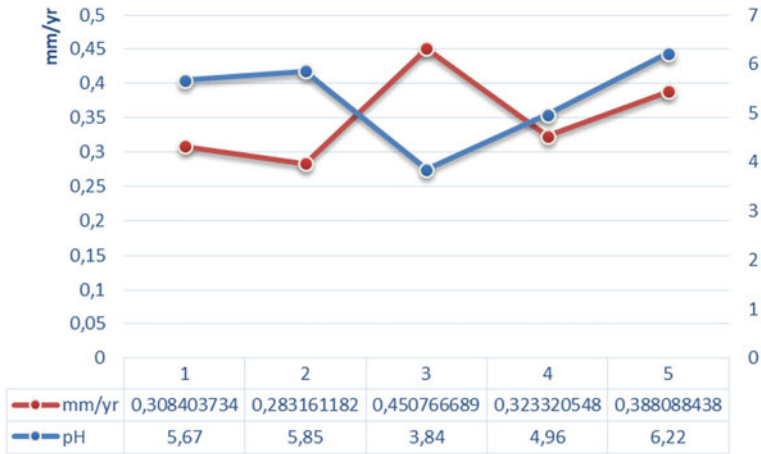
Fig. 5 Comparison of corrosion rates with pH

to the rating in the category of internal corrosion, the value of the corrosion rate between 0.3 to 1 mm/year indicates a medium corrosion rate [2]. According to previous literature and research, the level of acidity of the soil influences the growth of corrosion rates in the range of values below pH 4. The relationship between corrosion rate and redox potential in a soil can be seen in Fig. 6.

Figure 6 shows a significant correlation between corrosion rates that occur with the value of redox potential in each study location. The biggest potential value is 61.6 mV which is proportional to the highest corrosion rate that occurs at 0.45 mm/yr

	1	2	3	4	5
mV	38,1	27,2	61,6	38,2	40,3
mm/yr	0,308403734	0,283161182	0,450766689	0,323320548	0,388088438
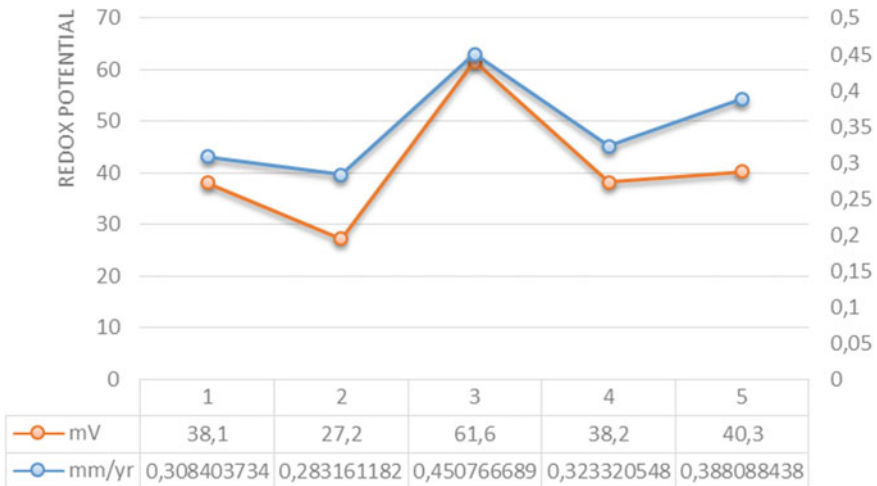
Fig. 6 Comparison of corrosion rates with redox potential

in the Paloh Awe location which has a type of wet silt clay soil. The location of Reulet 2 with the type of humus shows the lowest potential value of 27.2 mV and has the lowest corrosion rate of 0.43 mm/yr. Reduced potential values at the study site showed a significant relationship to the growth of the corrosion rate. This is based on the electron requirements in the corrosion process available with high redox potential values in a location/place. In general the acidity and redox potential of the soil from the study location showed an influence on the growth of the corrosion rate in the pipe material if it is not protected.

4   Conclusion

The results of this research have been carried out related to soil composition for corrosion rates along with underground pipelines with weight loss methods. It can be concluded that the pipeline has the potential for external corrosion of it to be caused by soil. External corrosion from soil varies in each location with the composition of the soil itself. The corrosion rate of 0.45 mm/year is the highest value for SA 283 material at Paloh Awe location. The highest acidity value and potential redox are also obtained at the same location. In general, all land in underground pipelines has the potential to cause external corrosion of underground pipes. Optimization of the existing protection system and further research on the potential for internal corrosion in pipe material needs to be done.

References

1. Putra R, Muhammad, Huzni S, Ali N, Fonna S (2018) AIP Conf Proc 1977:1–7
2. Fontana M (1986) Corrosion engineering. McGraw Hill, New York
3. Roberge P (2000) Handbook of corrosion engineering. McGraw Hill, New York
4. Pipeline and Hazardous Materials Safety Administration. Available: https://www.phmsa.dot. gov/about-phmsa/offices/office-pipeline-safety
5. Guma NT, Mohammed US, Tanimu AJ (2016) AJER 2:109–119
6. Mohtadi-Bonab AM, Eskandari M, Szpunar AJ (2014) Mater Sci Eng 620:97–106
7. Popoola TL, Grema SA, Latinwo KG, Gutti B (2013) Intr J Industr Chem 4:35
8. Wang S, Du S, Li X, Liu Z, Zhu M, Zhang D (2015) Prog Nat Sci Mater Int 25:242–250
9. Vanaei RH, Eslami A, Egbewande A (2017) Int J Press Vess Pip 149:43–54
10. Biezma M, Agudo D, Barron G (2018) Int J Press Vess Pip 163:55–62
11. ASTM (2003) Standard specification for low and intermediate tensile strength carbon steel plates
12. ASTM (1999) Standard practice for preparing, cleaning, and evaluating corrosion test 90
13. ASTM (2001) Field measurement of soil resistivity using the Wenner four-electrode method

14. ASTM G 162 (2004) Standard practice for conducting and evaluating laboratory corrosions tests 99
15. Cor E (2004) Standard practice for laboratory immersion corrosion testing of metals 72

Finite Element Model of Magnetic Induction Tomography for Low Conductivity Sample

Liyana Isamail and Muhamad Husaini Abu Bakar

Abstract Magnetic Induction Tomography (MIT) is a contactless and non-invasive method that is sensitive to the conductivity properties of an object. The application of the MIT in the biomedical field is in high demand, especially for brain monitoring and tumour imaging. However, the implementation of MIT for bone imaging application is not popular. In this paper, the performance of MIT for bone imaging is studied. The objective of this paper is to study the eddy current distribution for the bone with varying shape, size and location. The conductivity of the other tissue also will be considered to see its effect on the eddy current distribution. The model in this paper used one excitation coil of the 10 AWG copper wire with 10 turns. The frequency and current used in this study are 1 MHz and 1 A. The results show that the eddy current analysis able to detect the different shape, size and location of the bone. The eddy current density of the bone is 0.509 A/m^2 for the size of 1 cm, which located at the centre of ROI. The value increases when the size of the bone is bigger and located near the transmitter coil. It also shows that the conductivity of the tissue affects the eddy current distribution.

Keywords Magnetic induction · Tomography · Finite element · Low conductivity

1 Introduction

Magnetic induction tomography (MIT) has received much attention in recent years due to its low cost, non-invasive and non-contact imaging method [1–6] in biomedical applications. MIT is an imaging technique that use eddy current effect to image the passive electromagnetic properties of an object, especially conductivity [7]. The components of the MIT systems are excitation and receiver coil, interfaces electronic and a host computer (Fig. 1). The transmitter coil used to generate the

L. Isamail · M. H. Abu Bakar (✉)
System Engineering and Energy Laboratory, Universiti Kuala Lumpur Malaysian Spanish Institute, Kulim Hi-Tech Park, 09000 Kulim, Kedah, Malaysia
e-mail: muhamadhusaini@unikl.edu.my
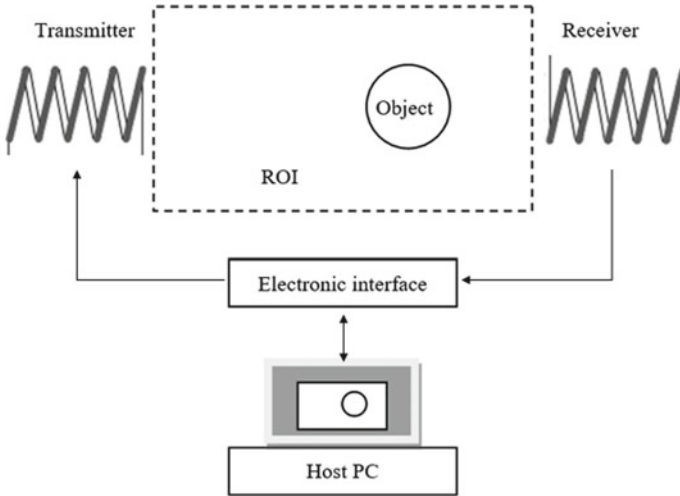
Fig. 1 Component of magnetic induction tomography system

alternating primary magnetic field. Then, the induced eddy current will create a secondary magnetic field.

MIT has been proposed for various medical applications, such as monitoring temporal changes in the volume of hematoma in the head [8], measure intracranial fluid-volume shifts [9], detect and identify stroke in human brain [10, 11], imaging lung structure [12] and anomalous mapping conductivity in the heart [13].

However, most of the research does not appear focused on bone imaging. The paper presents the study of MIT for bone imaging using Finite Element Method Magnetics (FEMM) software, which is open-source software. This paper aims to study the eddy current distribution of the bone with different shape, size and location. The study also used a different conductivity sample to see its effect on the eddy current distribution. Then, the results are used to mapping the image of the sample.

2   Finite Element Model for Magnetic Induction Tomography

The simulation used the Finite Element Method Magnetics (FEMM) software which is open-source. This study uses the 10 AWG copper wire, the number of turns is 10 with 1 A of current and the frequency is set to 1 MHz. Four models were developed to study the eddy current distribution on the varying shape, diameter, location and conductivity.

The shape used in the first model is circle and square with a constant diameter of 1 cm, location centred at 2.5 and conductivity of 0.0244 S/m (Fig. 2). The second model is in a square shape with a varying diameter of 1, 2 and 3 cm (Fig. 3). The
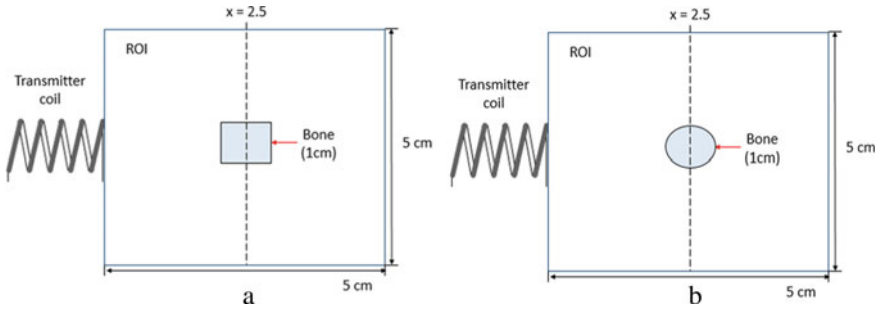
Fig. 2 Model 1 configuration, **a** square shape bone and **b** circle shape bone
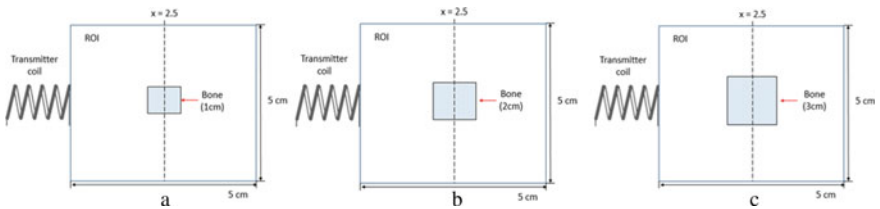
Fig. 3 Model 2 configuration, **a** 1 cm bone, **b** 2 cm bone and **c** 3 cm bone
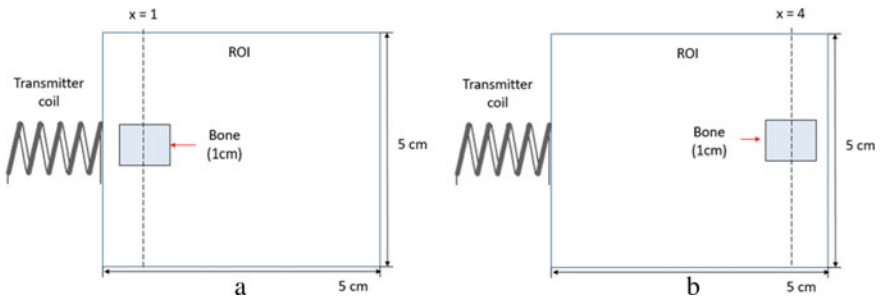
Fig. 4 Model 3 configuration, **a** centre of bone at position x = 1 and **b** centre of bone at position x = 4

location and conductivity are fixed. In the third model, the shape, diameter and conductivity of the bone are fixed. However, the centre of the bone is located at x = 1 and x = 4 (Fig. 4).

Figure 5 shows the model 4 configuration of the 2D tissue model consists of skin, fat, muscle and bone. The dielectric properties, such as conductivity was considered in this study. According to Ref. [14], the conductivity of skin, fat, muscle and bone at 1 MHz was 0.0132 S/m, 0.0441 S/m, 0.503 S/m and 0.0244 S/m respectively. The eddy current distribution for different conductivity is studied in this model.
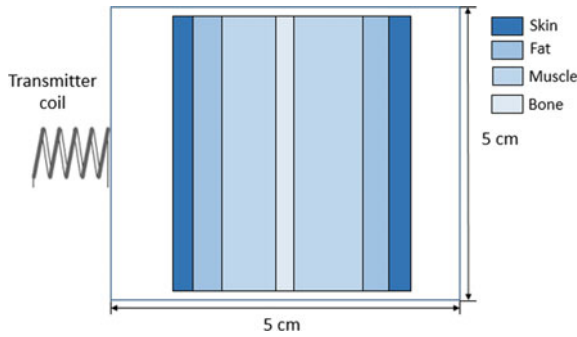
Fig. 5 Model 4 configuration of the 2D tissue model

3 Result and Discussion

3.1 Eddy Current Distribution for Varying Bone Shape

Figure 6a, b shows the current density for the bone with a different shape. Since the conductivity, location and size of the bone are similar, the value of the eddy current density does not change. The current density of each bone is 0.509 A/m^2. Figure 6c, d show the image of the sample that mapped by using the eddy current
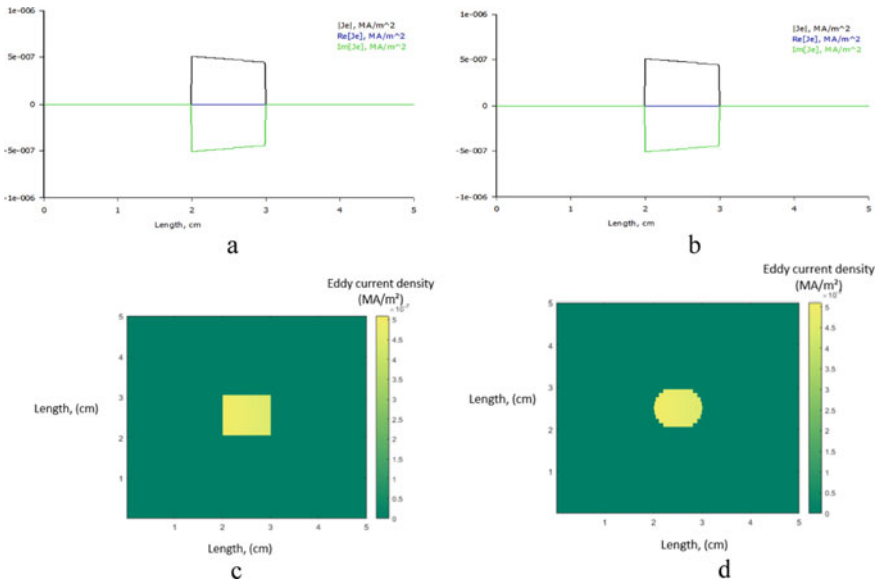
Fig. 6 **a** Eddy current distribution graph for square shape bone, **b** eddy current distribution graph for circle shape bone, **c** image for square shape bone and **d** image for circle shape bone

distribution data in the MATLAB software. The data collected able to provide the shape of the bone.

3.2 Eddy Current Distribution for Varying Bone Diameter

Figure 7a–c shows the current density graph for bone with a diameter of 1 cm, 2 cm and 3 cm, respectively. The induced eddy current density of the bone decrease from 0.589 A/m^2 (for 3 cm bone) to 0.547 A/m^2 (for 2 cm bone) and 0.509 A/m^2 (for 1 cm bone). The magnitude of the primary magnetic field that flows through the large bone is higher due to its location that is near the transmitter coil. This is the same as the study in [15] where the simulation focused on the eddy current analysis for breast cancer. Figure 7d–f shows the image from the data collected for different bone size. The image shows that the size of the bone can be identified.
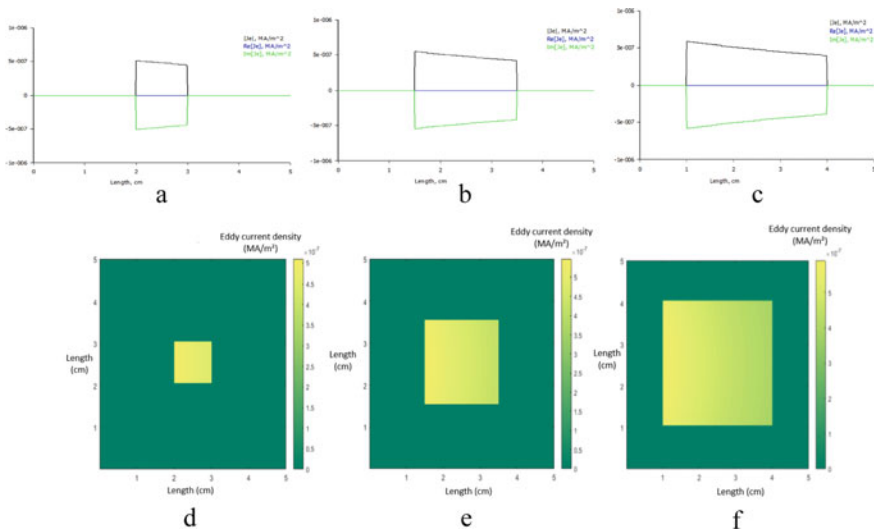
Fig. 7 **a** Eddy current distribution for 1 cm bone, **b** eddy current distribution for 2 m bone, **c** eddy current distribution for 3 cm bone, **d** image for 1 cm bone, **e** image for 2 cm bone and **f** image for 3 cm bone

3.3 Eddy Current Distribution for the Different Bone Location

Figure 8a, b shows the graph for eddy current density for 1 cm bone located at the left and right side of the ROI. The eddy current at the left side is approximately 0.638 A/m^2 and decreased to 0.419 A/m^2 for the right side. The value is higher for the left side is due to the higher induced current density. The result is expected since the study in Fig. 7a shows the same result. Figure 8c, d shows the image from the eddy current density. From the data provided, the system able to identify the location of the bone.
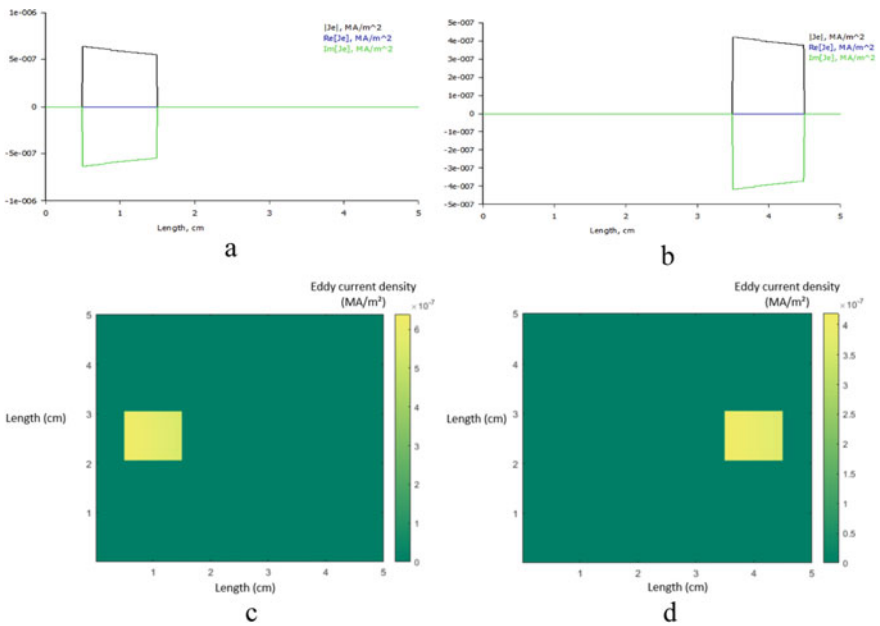
Fig. 8 **a** Eddy current distribution for the centre of bone at position x = 1, **b** eddy current distribution for the centre of bone at position x = 4, **d** image for centre of bone at position x = 1, **e** image for centre of bone at position x = 4
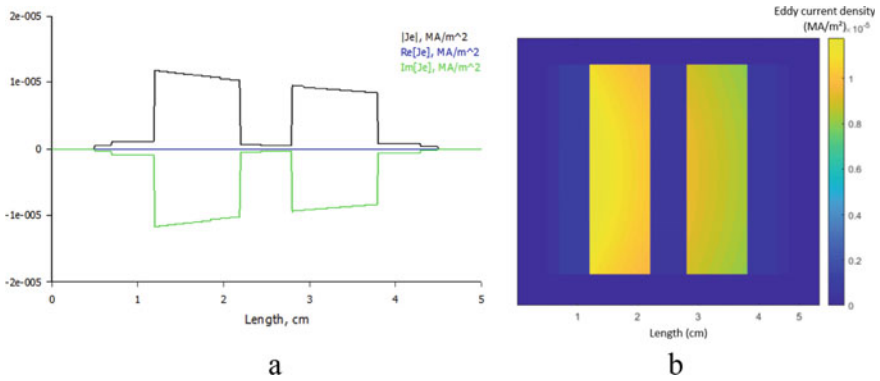
Fig. 9 **a** Eddy current distribution graph for different sample conductivity and **b** image of the various sample conductivity

3.4 Eddy Current Distribution for Different Conductivity of Tissue Model

Figure 9a shows the current density graph for a different tissue sample. The eddy current for skin (dry) is the lowest at 0.345 A/m^2 because the conductivity of the tissue is the lowest among all. The highest eddy current value is 11.783 A/m^2 for the muscle since the conductivity is the highest. For the fat and bone, the eddy current is 1.116 and 0.496 A/m^2. Figure 9b shows the image of different type and conductivity of the tissue. Based on the results, the tissue can be distinguished since it has different conductivity.

4 Conclusion

The simulation shows that the eddy current distribution is capable of providing data for the shape, size, location of the bone. Other than that, it also indicates that the conductivity of the tissue influence the eddy current distribution. This type of information is crucial in bone imaging. For the next phases, some modification to the study of the system is needed for the successful application for bone imaging.

References

1. Luo H, Jiang X (2016) The magnetic induction tomography measurement system based on Helmholtz coil. In: Proceedings—2015 8th international conference on biomedical engineering and informatics BMEI 2015, no Bmei, pp 29–33
2. Xiao Z, Tan C, Dong F (2017) Effect of inter-tissue inductive coupling on multi-frequency imaging of intracranial hemorrhage by magnetic induction tomography. Meas Sci Technol 28 (8)
3. Wang L (2018) Three-dimensional holographic electromagnetic imaging for accessing brain stroke. Sensors 18(11)
4. Wubuli S, Roula A, Mamatjan Y (2018) Rapid estimation of object movements in magnetic induction tomography. Int J Biomed Eng Technol 27(4):290
5. Ma L, Banasiak R, Soleimani M (2016) Magnetic induction tomography with high performance GPU implementation. Prog Electromagn Res B 65(1):49–63
6. Al-Hawari M, Aulia AI, Rudin A, Rohmadi, Muttakin I, Taruno WP (2018) Receiver circuit design for signal conditioning in magnetic induction tomography system. In: Proceedings 2017 5th international conference on instrumentation, communications, information technology, and biomedical engineering ICICI-BME 2017, Nov, pp 230–235
7. Ma L, Soleimani M (2017) Magnetic induction tomography methods and applications: a review. Meas Sci Technol 28(7)
8. Oziel M, Korenstein R, Rubinsky B (2018) Non-contact monitoring of temporal volume changes of a hematoma in the head by a single inductive coil: a numerical study. IEEE Trans Biomed Eng, 1
9. Griffith J et al (2018) Non-invasive electromagnetic skin patch sensor to measure intracranial fluid-volume shifts. Sensors 18(4):1–17
10. Hopfer M, Planas R, Hamidipour A, Henriksson T, Semenov S (2017) Electromagnetic tomography for detection, differentiation, and monitoring of brain stroke: a virtual data and human head phantom study. IEEE Antennas Propag Mag 59(5):86–97
11. Semenov S, Hopfer M, Planas R, Hamidipour A, Henriksson T (2017) Electromagnetic tomography for brain imaging: 3D reconstruction of stroke in a human head phantom. In: 2016 IEEE conference on antenna measurements and applications CAMA 2016, pp 1–4
12. Wang L, Al-Jumaily AM (2017) Imaging of lung structure using holographic electromagnetic induction. IEEE Acc 5
13. Deans C, Marmugi L, Hussain S, Renzoni F (2016) Optical atomic magnetometry for magnetic induction tomography of the heart. Quantum Opt 9900:99000F
14. Lloyd BA, Dielectric properties. Available: https://itis.swiss/virtual-population/tissue-properties/database/dielectric-properties/
15. Ann HJ, Su-Shi LS, Zakaria Z (2017) Non-invasive breast cancer assessment using magnetic induction spectroscopy technique. Int J Integr Eng 9(2):54–60

Airside Heat Transfer and Pressure Drop on the Spiral Finned-Tube Compact Heat Exchanger with Sharp Turns

Dedi Afandi, Ahmad Syuhada, and Sarwo Edhy Sofyan

Abstract This study aims to examine the airside heat transfer and pressure drop on the outer surface of a spiral finned-tube compact heat exchanger with sharp turns. The heat exchanger is made of a tube with sharp turns with an inside and outside diameter, namely 0.02, and 0.022 m. The length of the heat exchanger is 0.3 m with a turn length of 0.082 m and the total length of the heat exchanger is 6 m. The heat exchanger fins are made of aluminum with a thickness of 0.0003 m and the fin diameter is 0.042 m. The fin pitch of the heat exchanger tested was varied, namely 0.01, 0.02, 0.03, 0.05, and 0.07 m. Water is heated by a heater to a temperature of 80 °C and then circulated into the heat exchanger with a mass flow rate of 0.39 kg/s. The air inlet temperature is constant, and the air outlet temperature is measured using a thermocouple. The air velocity was varied, namely 2.4, 2.8, and 3.4 m/s. The results showed that to some extent the smaller the pitch between the fins, the higher the heat transfer rate. While the pressure drop is being higher as the pitch between the fins decreases. Heat exchanger with a pitch of 0.02 m produced the highest heat transfer rate compared to other configurations. The pressure drop in the heat exchanger with a pitch of 0.02 m is also lower than that at a pitch of 0.01 m. These results indicate the optimum fin pitch for this study is 0.02 m, where the high heat transfer rate with the low-pressure drop is more effective for industrial thermal system applications.

Keywords Compact heat exchanger · Fin pitch · Heat transfer rate · Pressure drop

D. Afandi · A. Syuhada (✉) · S. E. Sofyan
Department of Mechanical and Industrial Engineering, Universitas Syiah Kuala,
Jl. Tgk. Syech Abdurrauf No. 7 Darussalam, Banda Aceh 23111, Indonesia
e-mail: syuhada_mech@yahoo.com

1 Introduction

The compact heat exchanger (CHE) is widely applied in the industry, the use of CHE, in particular, can be found in power generation [1], chemical processes [2], air conditioning [3, 4], heat recovery [5], cryogenic [6], and other industrial processes. CHE characteristics are characterized by high surface area and heat transfer rate per unit volume [7].

Many factors affect the performance of the heat transfer rate on the heat exchanger, including the convection heat transfer coefficient (h), heat transfer surface area, and temperature differences. The greater the convection heat transfer coefficient, the higher the heat transfer rate. The convection heat transfer coefficient is influenced by the dimensions of the heat exchanger and the fluid flow regime [8]. In turbulent regime, the resulting convection heat transfer coefficient will be greater [9]. One way to increase the turbulence of fluid flow through the inner surface of the heat exchanger tube is by using a sharp turning technology [10]. To increase the turbulence of fluid flow on the outer surface of the heat exchanger, it is usually done adding fins.

Innovations to improve heat exchanger performance are continuously being developed. Increasing the surface area of heat transfer will increase the efficiency produced by a heat exchanger [11]. The use of nanofluids can also improve the heat exchanger performance [12]. Providing disruption to the flow of fluid through the heat exchanger can increase the resulting efficiency [13]. Vortex and swirl generators are widely applied to improve the performance of heat exchangers [14].

The study of convection heat transfer involving CHE with sharp turns technology has been carried out by Syuhada et al. [15]. The results show that CHE with a tube pass length of 10–16 times the hydraulic diameter produces the optimal heat transfer rate. Carija et al. [16] performed a heat transfer analysis on a flat and louvered fin heat exchanger. Syuhada et al. [17] have studied the effect of pitch on convection heat transfer in spiral finned-tube heat exchangers. The effect of adding fins with other geometries such as wavy fin, plain fin, offset strip fin, rectangular fin, and annular fin has been previously studied [18–21]. These types of fins are widely used to improve the performance of the heat exchanger. The effect of fin pitch with offset strip fin and serrated fin on plate heat exchanger has been carried out [22, 23]. The effect of fin pitch with wavy fin, crimped spiral fin, continuous flat fin, and discrete flat fin on tube-type heat exchanger has also been done before [24–26]. The addition of fins on the outer surface of the heat exchanger can increase the surface area of the heat transfer so that the heat transfer rate also increases. However, it also results in a decrease in the pressure of the fluid flow through it [27].

Based on previous research that examined the effect of fin pitch on tube-type heat exchangers with wavy fin, continuous flat fin, and discrete flat fin types. Research on the effect of fin pitch on different heat exchanger configurations with different fin types needs to be developed. Therefore, research on the effect of fin pitch on the spiral finned-tube CHE heat exchanger with sharp turns needs to be done. This study aims to examine the effect of the fin pitch configuration (0.01,

0.02, 0.03, 0.05, and 0.07 m) on the spiral finned-tube CHE on heat transfer and the pressure drop of the airside.

2 Experimental Set Up

In this study using a CHE type heat exchanger made of Galvanized with an inside diameter and an outside diameter of the tube, namely 0.02 and 0.02 m. The total length of the heat exchanger is 6 m with a tube pass length of 0.3 m. The fins are made of aluminum with a thickness of 0.0003 m and the fin diameter is 0.042 m. The fin pitch was varied, namely 0.01, 0.02, 0.03, 0.05, and 0.07 m. The heat exchanger configuration is shown in Fig. 1.

Water is heated by a heater to a temperature of 80 °C and then circulated into the heat exchanger using a pump with a mass flow rate of 3.9 kg/s. The temperature of the water that enters the heat exchanger is maintained at 80 °C. The thermocouple is placed at the inlet and outlet of the heat exchanger to measure the temperature of the inlet and outlet of the water. The air exhaled by the fan is circulated in a cross-flow through the heat exchanger. The air inlet temperature is constant and the air outlet temperature is measured using a thermocouple. The air velocity was varied, namely 2.4, 2.8, and 3.4 m/s. The research schematic is shown in Fig. 2.

3 Data Reduction

The heat transfer rate from high-temperature fluid to low-temperature fluid is calculated using the following equation [28]:
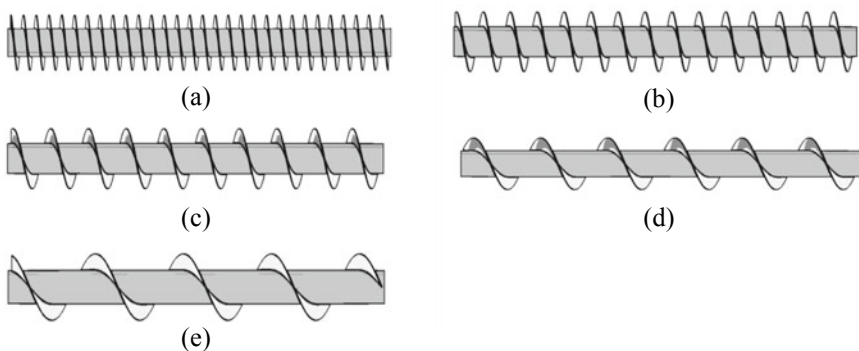
Fig. 1 Heat exchanger configuration with a fin pitch of **a** 0.01 m, **b** 0.02 m, **c** 0.03 m, **d** 0.05 m, **e** 0.07 m
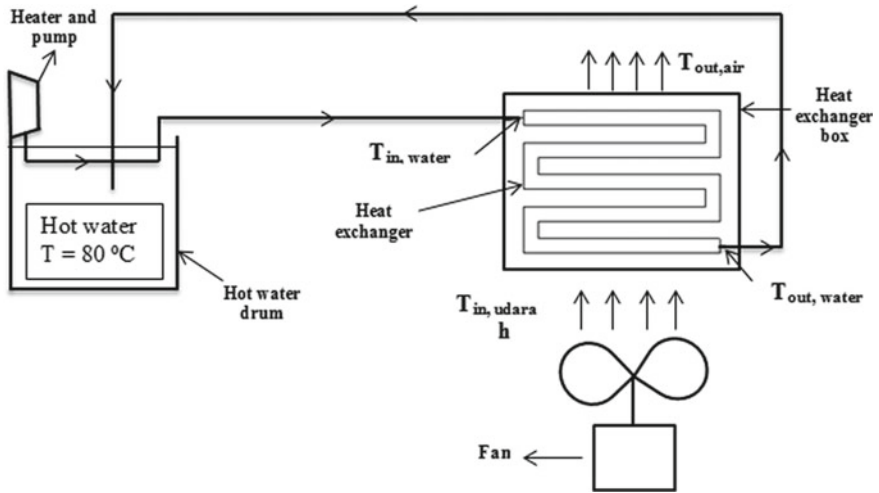
Fig. 2 Schematic of research

$$\dot{Q} = \dot{m} \cdot C_p \cdot (T_i - T_o) \tag{1}$$

where $\dot{Q}$ is the rate of heat transfer (W) from high-temperature fluid to low-temperature fluid, $\dot{m}$ is the mass flow rate (kg/s) of water flowing in the heat exchanger. C_p is the specific heat of water (J/kg K) at temperatures of 80 °C and T_i, T_o is the water inlet and outlet temperatures (°C).

The convection heat transfer coefficient is calculated using the following equation [28]:

$$h = \frac{Q}{A \cdot \Delta T_m} \tag{2}$$

where ΔT_m defined by heat exchanger surface temperature (T_s) minus ambient temperature (T_∞), to calculated T_s and T_∞ using the following equation [28]:

$$T_s = \frac{T_{in,water} + T_{out,water}}{2} \text{ and } T_\infty = \frac{T_{in,air} + T_{out,air}}{2} \tag{3}$$

The pressure drop on the outer surface of the heat exchanger (airside) can be calculated using the following equation [27]:

$$\Delta p = \xi \cdot \frac{L}{d_e} \cdot \frac{\rho w^2}{2} C_{N_r} \tag{4}$$

where ΔP defined by the pressure drop (N/m^2) on the airside, ξ is the friction factor, L is the heat exchanger length (m), d_e is the equivalent diameter (m), ρ is the air density (kg/m^3), w is the air velocity (m/s), and C_{N_r} is the correction factor.

Reynolds number for the flow through the outer surface of the heat exchanger is calculated using the following equation [27]:

$$\text{Re} = \frac{\rho \cdot w \cdot d_e}{\mu} \tag{5}$$

where μ is the absolute viscosity of dynamic fluids (Ns/m^2) of air evaluated at ambient temperature and w defined by the fluid velocity at the minimal cross-sectional area (m/s).

The ratio of heat transfer surface of a row of a tube to frontal free flow area is calculated using the following equation [27]:

$$W = \frac{d_o \pi \cdot \left(s_f - \delta_f\right) + \left(D^2 - d_o^2\right) \cdot \frac{\pi}{2} + D \cdot \pi \cdot \delta_f}{(s_1 - d_o) \cdot \left(s_f - \delta\right) + \delta \cdot (s_1 - D)} \tag{6}$$

where W is defined by the ratio of heat transfer surface of a row of a tube to frontal free flow area, s_f is the fin pitch (m), δ_f is the fin thickness (m), D is the fin diameter (m), d_o is the tube diameter (m), and s_1 is the transversal pitch tube (m).

The equivalent diameter of the heat exchanger can be calculated using the following equation [27]:

$$d_e = 4 \cdot r_e = 4 \cdot \frac{V_f}{S_{he}} = 4 \cdot \frac{\varepsilon}{S_V} \tag{7}$$

where the equivalent diameter d_e is the ratio of the volume occupied by the air to the surface area that sweeps (m). The equivalent diameter can be defined by the volumetric porosity (ε) and the specific surface area (S_V).

The specific surface area S_V is a ratio of airside heat exchanger surface to the total heat exchanger volume (m^2/m^3), that calculated using the following equation [27]:

$$s_V = \frac{S_{he}}{V_t} = \frac{d_o \pi \cdot \left(s_f - \delta_f\right) + \left(D^2 - d_o^2\right) \cdot \frac{\pi}{2} + D \cdot \pi \cdot \delta_f}{s_1 \cdot s_2 \cdot s_f} \tag{8}$$

The volumetric porosity ε is defined as a ratio of heat exchanger free volume (unoccupied by tube bundle) to total heat exchanger volume, volumetric porosity is calculated using the following equation [27]:

$$\varepsilon = \frac{V_f}{V_t} = 1 - \frac{\frac{\pi}{4} \cdot \left[d_o^2 \cdot \left(s_f - \delta\right) + D^2 \cdot \delta\right]}{s_1 \cdot s_2 \cdot s_f} \tag{9}$$

The length of the heat exchanger is calculated using the following equation [27]:

$$L = N_r \cdot s_2 \tag{10}$$

where L is the length of the heat exchanger (m), N_r is number of tube row and s_2 is defined by longitudinal pitch tube (m). For the heat exchanger with tube row less than 5 row, the correction factor (C_{N_r}) is adding to calculation.

4   Result and Discussion

Figure 3 shows the relationship between the heat transfer rate and the pressure drop of airflow that passes through the outer surface of the heat exchanger at air velocities of 2.4, 2.8, and 3.4 m/s. The heat transfer rate increases as the pitch between the fins decrease to a certain extent. Based on Eq. (2) the heat transfer rate is also influenced by the heat transfer surface area, where the greater the heat transfer surface area, the higher the heat transfer rate. The smaller the pitch between the fins, the greater the heat transfer surface area so that the heat transfer rate will also be higher. However, under certain conditions, the fin pitch is too small resulting in a larger boundary layer so that the heat transfer coefficient decreases [25, 26]. This causes the heat transfer rate to decrease as the heat transfer coefficient decreases.

From Fig. 3 it can also be seen that the smaller the pitch between the fins, the higher the pressure drop will be. This is influenced by the Reynolds number and airflow resistance that occurs. Based on Eq. (5) at the air velocity of 2.4 m/s the Reynolds number produced by a heat exchanger with a pitch of 0.01 m, 0.02 m, 0.03 m, 0.05 m, and 0.07 m respectively, i.e. 7352, 11,778, 14,713, 18,365, and 20,546. At air velocity 2.8 m/s the Reynolds number increased by 14.2% compared to an air velocity of 2.4 m/s. Reynolds number at air velocity of 3.4 m/s increased by 17.6% compared to an air velocity of 2.8 m/s. The greater the pitch between the fins, the higher the Reynolds number produced by the airflow after passing through the outer surface of the heat exchanger. This is due to the resistance that occurs is getting smaller so that the pressure drop is also getting smaller. Meanwhile, the higher the air velocity, the greater the pressure drop that occurs, because air velocity is one of the main factors affecting the pressure drop. Too large a pressure drop is also undesirable because of the fan power required to distribute the airflow increases.

These results indicate that the heat exchanger with a 0.02 m fin pitch has the most optimal results which produce the highest heat transfer rate with a lower pressure drop. Meanwhile, the heat exchanger with a 0.01 m fin pitch experienced a
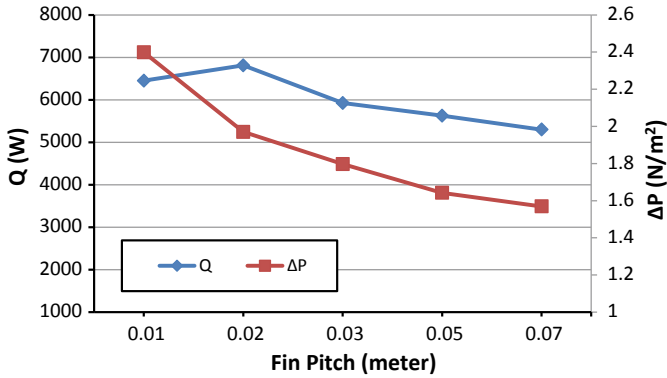
(a)
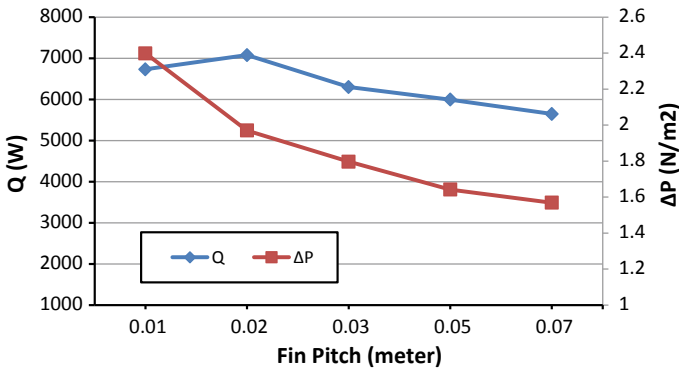
(b)
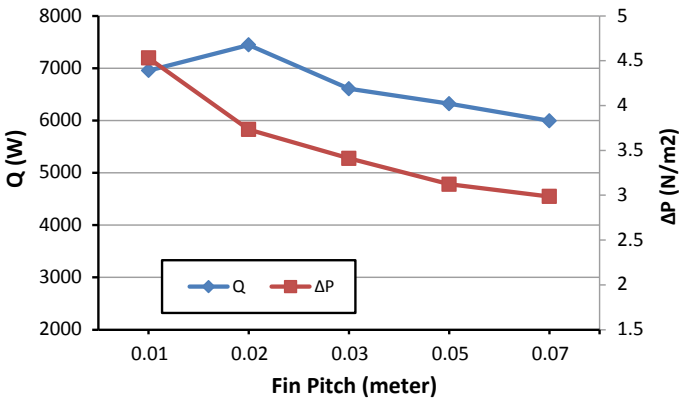
(c)

Fig. 3 The relationship between heat transfer rate and pressure drop of airflow on the outer surface of the heat exchanger at air velocity **a** 2.4 m/s, **b** 2.8 m/s, **c** 3.4 m/s

higher pressure drop with a lower heat transfer rate than the heat exchanger with a pitch of 0.02 m. In a heat exchanger with a pitch of 0.03, 0.05, and 0.07 m, the heat transfer rate and pressure drop were lower than at a pitch of 0.02 m.

5   Conclusion

For this research, it can be concluded that the heat transfer rate is influenced by the pitch between the fins were to a certain extent the smaller the pitch between the fins, the higher the heat transfer rate. The smaller the pitch between the fins, the greater the thickness of the boundary layer so that the convection heat transfer coefficient decreases. The pressure drop increases as the pitch between the fins decreases and vice versa, so that in a heat exchanger without fins the pressure drop on the outer surface is negligible. The heat exchanger with a pitch of 0.02 m produced the highest heat transfer rate with a lower pressure drop compared to a pitch of 0.01 m. While at a pitch of 0.03, 0.05, and 0.07 m, the heat transfer rate and pressure drop were lower.

References

1. Mortean MVV, Cisterna LHR, Paiva KV, Mantelli MBH (2019) Thermal and hydrodynamic analysis of a cross-flow compact heat exchanger. Appl Therm Eng 150(January):750–761. https://doi.org/10.1016/j.applthermaleng.2019.01.038
2. Gorobets V, Bohdan Y, Trokhaniak V, Antypov I (2019) Investigations of heat transfer and hydrodynamics in heat exchangers with compact arrangements of tubes. Appl Therm Eng 151:46–54. https://doi.org/10.1016/j.applthermaleng.2019.01.059
3. Yadav MS, Giri SA, Momale VC (2017) Sizing analysis of louvered fin flat tube compact heat exchanger by genetic algorithm. Appl Therm Eng 125:1426–1436. https://doi.org/10.1016/j.applthermaleng.2017.07.119
4. Zeeshan M, Nath S, Bhanja D (2017) Numerical study to predict optimal configuration of fin and tube compact heat exchanger with various tube shapes and spatial arrangements. Energy Convers Manag 148:737–752. https://doi.org/10.1016/j.enconman.2017.06.011
5. Gholami A, Mohammed HA, Wahid MA, Khiadani M (2019) Parametric design exploration of fin-and-oval tube compact heat exchangers performance with a new type of corrugated fin patterns. Int J Therm Sci 144(July 2018):173–190. https://doi.org/10.1016/j.ijthermalsci.2019.05.022
6. Manjunath K, Sharma OP, Kaushik SC (2020) Entropy generation and thermoeconomic analysis of printed circuit heat exchanger using different materials for supercritical CO_2 based waste heat recovery. Mater Today Proc 21:1525–1532. https://doi.org/10.1016/j.matpr.2019.11.077
7. Baek S, Lee C, Jeong S (2014) Effect of flow maldistribution and axial conduction on compact microchannel heat exchanger. Cryogenics (Guildf) 60:49–61. https://doi.org/10.1016/j.cryogenics.2014.01.003
8. Abbas A, Lee H, Sengupta A, Wang CC (2020) Numerical investigation of thermal and hydraulic performance of shell and plate heat exchanger. Appl Therm Eng 167:114705. https://doi.org/10.1016/j.applthermaleng.2019.114705

9. Nagaosa RS (2017) Turbulence model-free approach for predictions of air flow dynamics and heat transfer in a fin-and-tube exchanger. Energy Convers Manag 142:414–425. https://doi.org/10.1016/j.enconman.2017.03.063

10. Hirota M, Fujita H, Syuhada A, Araki S, Yoshida T, Tanaka T (1999) Heat/mass transfer characteristics in two-pass smooth channels with a sharp 180-deg turn. Int J Heat Mass Transf 42(20):3757–3770. https://doi.org/10.1016/S0017-9310(99)00057-5

11. Muszynski T, Andrzejczyk R (2019) Experimental study on single phase operation of microjet augmented heat exchanger with enhanced heat transfer surface. Appl Therm Eng 155 (March):289–296. https://doi.org/10.1016/j.applthermaleng.2019.03.125

12. Sheikholeslami M, Sadoughi MK (2018) Simulation of CuO-water nanofluid heat transfer enhancement in presence of melting surface. Int J Heat Mass Transf 116:909–919. https://doi.org/10.1016/j.ijheatmasstransfer.2017.09.086

13. Wu JM, Zhang H, Yan CH, Wang Y (2012) Experimental study on the performance of a novel fin-tube air heat exchanger with punched longitudinal vortex generator. Energy Convers Manag 57:42–48. https://doi.org/10.1016/j.enconman.2011.12.009

14. Sheikholeslami M, Gorji-Bandpy M, Ganji DD (2015) Review of heat transfer enhancement methods: Focus on passive methods using swirl flow devices. Renew Sustain Energy Rev 49:444–469. https://doi.org/10.1016/j.rser.2015.04.113

15. Syuhada A, Maulana MI, Adria A (2019) Experimental analysis of the effect of tube pass length on the characteristics of heat transfer in U-sharp turned channels. J Adv Res Fluid Mech Therm Sci 60(1):124–131

16. Čarija Z, Franković B, Perčić M, Čavrak M (2014) Heat transfer analysis of fin-and-tube heat exchangers with flat and louvered fin geometries. Energy Econ 45:160–167. https://doi.org/10.1016/j.ijrefrig.2014.05.026

17. Syuhada A, Afandi D, Sofyan SE (2020) Convective heat transfer study on the spiral finned tube heat exchanger under various fin pitch arrangements. IOP Conf Ser Earth Environ Sci 463(1). https://doi.org/10.1088/1755-1315/463/1/012024

18. Hwang SW, Kim DH, Min JK, Jeong JH (2012) CFD analysis of fin tube heat exchanger with a pair of delta winglet vortex generators. J Mech Sci Technol 26(9):2949–2958. https://doi.org/10.1007/s12206-012-0702-2

19. Ke H et al (2019) Thermal-hydraulic performance and optimization of attack angle of delta winglets in plain and wavy finned-tube heat exchangers. Appl Therm Eng 150(March 2018):1054–1065. https://doi.org/10.1016/j.applthermaleng.2019.01.083

20. Benítez T, Sherif SA, Benítez J (2019) Heat and mass transfer on rectangular and annular finned surfaces of heat exchangers operating under frosting conditions. Int J Heat Mass Transf 136:99–115. https://doi.org/10.1016/j.ijheatmasstransfer.2019.02.005

21. Ozturk MM, Doğan B, Erbay LB (2019) Performance analysis of a compact heat exchanger with offset strip fin by non-uniform uninterrupted fin length. Appl Therm Eng 159 (March):113814. https://doi.org/10.1016/j.applthermaleng.2019.113814

22. Jiang Q, Zhuang M, Zhu Z, Shen J (2018) Thermal hydraulic characteristics of cryogenic offset-strip fin heat exchangers. Appl Therm Eng 150(Dec 2018):88–98. https://doi.org/10.1016/j.applthermaleng.2018.12.122

23. Li K, Wen J, Yang H, Wang S, Li Y (2019) Sensitivity and stress analysis of serrated fin structure in plate-fin heat exchanger on cryogenic condition. Int J Therm Sci 145(March 2019). https://doi.org/10.1016/j.ijthermalsci.2019.106013

24. Kim Y et al (2004) Effects of fin and tube alignment on the heat transfer performance of finned-tube heat exchangers with large fin pitch. no 1978:1–8

25. Pongsoi P, Pikulkajorn S, Wongwises S (2012) Effect of fin pitches on the optimum heat transfer performance of crimped spiral fin-and-tube heat exchangers. Int J Heat Mass Transf 55(23–24):6555–6566. https://doi.org/10.1016/j.ijheatmasstransfer.2012.06.061

26. Dong J, Su L, Chen Q, Xu W (2013) Experimental study on thermal-hydraulic performance of a wavy fin-and-flat tube aluminum heat exchanger. Appl Therm Eng 51(1–2):32–39. https://doi.org/10.1016/j.applthermaleng.2012.09.018

27. Genic SB, Jacimovic BM, Latinovic BR (2006) Research on air pressure drop in helically-finned tube heat exchangers. Appl Therm Eng 26(5–6):478–485. https://doi.org/10.1016/j.applthermaleng.2005.07.017
28. Bejan A (1995) Heat transfer, second edition

Preparation of Chitosan-Silver Nanoparticles Immobilized onto Pumice for Antibacterial Testing Against *Escherichia coli*

M. Adlim, M. I. Hidayat, N. Azmi, and R. F. I. Ramayani

Abstract Immobilization of chitosan-silver colloidal nanoparticles (AgNPs) onto pumice was carried out to determine the effectiveness against *Escherichia coli*. AgNPs was synthesized with photo-irradiation method due to low cost, simple and environmentally friendly and using chitosan as the stabilizing agent. The Chi-AgNPs colloid was characterized by using UV-Vis spectrophotometry method. The surface of AgNPs immobilized on chitosan coated pumice (AgNPs-[chi-Pum]) was observed by using SEM method. Chi-AgNP-Pumice inhibited and reduced up to 68.75% of *Escherichia coli* concentration (MPN/100 mL) in 30 minutes incubation. The results indicate that immobilization was compatible and the AgNPs-[chi-Pum] significantly reduced *Escherichia coli* concentration in aquatic pollution.

ketwords Antibacterial · Colloidal nanoparticles · Photo-irradition · Water pollution

1 Introduction

Saving a clean and hygienic water is a major prevention of health risks to avoid disease in human body. These health risks associated with the intake of microorganisms in contained water. The absence of fecal coliforms per 100 mL of water is established as a microbiological limit for drinking water [1]. That is given the correlation between the presence of both fecal contamination and disease-causing microorganisms [2]. It is important to learn about drinking water treatment to solve diverse problems, such as preserving antimicrobial activity to reduce bacteria in

M. Adlim (✉) · N. Azmi · R. F. I. Ramayani
Chemistry Department, FKIP, Universitas Syiah Kuala, Darussalam,
Banda Aceh 23111, Indonesia
e-mail: adlim@unsyiah.ac.id

M. I. Hidayat
Chemistry Department, FMIPA, Universitas Syiah Kuala, Darussalam,
Banda Aceh 23111, Indonesia

water and helping the human's crisis of clean water, so in the future we can produce hygienic water from the nature.

Filtration technology can be improved by the immobilization of antimicrobial agents in filtering material aimed to kill and inactivate microorganisms. Silver nanoparticles (AgNPs) have received much attention due to their good antimicrobial agents [3, 4]. AgNPs has a broad antimicrobial spectrum and outstanding activity that they can kill bacteria [5, 6], fungi [7, 8] and virus [9, 10]. The high surface area of AgNPs offer better contact with microorganisms, which penetrate inside the bacteria and interact with protein in the cell and leading to death. AgNPs can control the release of Ag^+ that contributing to antimicrobial endurance, so it is better compare to bulk metal or salts [11]. Although AgNPs are highly toxic to many microorganisms, they have low toxicity toward human cells, so it is becoming a major reason to use silver.

The present research is what reported [12], as an example of immobilization of natural antimicrobial agents that of attempting a lysozyme to a porous ceramic filter to enhance antibacterial properties for water treatment purposes. Recently, a new antimicrobial system based on the covalent immobilization of EOCs on silica supports to enhance antimicrobial effect against microorganisms in both in vitro and in vivo studies [13]. On the other hand, there has been no report about AgNPs immobilized onto pumice surface and using chitosan to stabilize nanoparticles [14–17]. Chitosan (Chi) is a natural renewable resource obtained from the deacetylation of chitin and it has been used as stabilizer for preparation of metal and non metal nanoparticles. In this study, we synthetized the Chi-AgNPs and immobilized them onto pumice. Furthermore, we explore the antibacterial property of prepared material (Chi-AgNPs onto pumice) against *E. coli* bacteria. Chitosan itself has already antimicrobial activity in nature [18]. Thus, contributing the antibacterial property to our prepared material that can expand its commercial application especially in aquatic zone.

2 Materials and Methods

Chitosan medium molecular weight (400,000, Fluke). CH_3COOH (99.8%; Merck KGaA) was used to dissolve chitosan. $AgNO_3$ (Merck KGaA) was used as source of silver ions. Pumice (Alue Naga Beach, Aceh Besar) was used as solid support material of silver nanoparticle. *E. coli* suspension was used to antibacterial test, Mueller hinton agar (MHA) and Eosine methylene blue (EMB) were used as bacterial growth medium, Mc Farland standard, alcohol sterilization and aquabidest.

Microscope (Olympus CXZI) was used to look at bacterial culture. Spectrophotometer UV-Vis (Shimadzu model no. UV1601) was used to determine surface plasmon resonance of silver nanoparticle. Scanning electron microscope (JEOL JSM 6510 LA) was used to evaluate the surface morphology of prepared AgNPs-[Chi-Pumice].

2.1   Preparation of Pumice

Pumice used was taken from Alue Naga beach area (googlemap; 5.605255768040228, 95.34585675631982 Pantai Alue Naga, Alue Naga, Banda Aceh City, Aceh), Syiah Kuala district, Aceh Besar. Pumice was washed and soaked to water for 24 h. Pumice was dried under the sunlight and it was mashed to smaller pieces. Pumice was sieved with a 10 mesh sieve and dried at room temperature for 3×24 h. The dried pumice was placed in an oven at 105 °C until a constant weight. Pumice samples were stored in a desiccator before being used for immobilization experiment.

2.2   Preparation of Chitosan Solution

Chitosan (0.6 g) was dissolved into 20 mL of 1.5% CH_3COOH solution as a stock solution. The chitosan stock solution was diluted with 1.5% CH_3COOH solution until the volume reached 100 mL. The solution was stirred using a magnetic stirrer until it was clear and evenly mixed.

2.3   Immobilization of Silver Nanoparticles onto Chitosan Coated Pumice

A solution of 10 mL of 0.1 M $AgNO_3$ was added to 20 mL of chitosan solution into Erlenmeyer flask. This mixture was irradiated with a 100 watt Tungsten lamp light for 7 hours while stirring to form a brownish yellow colloidal nanoparticle (Ag^o-Chi). The spectra of colloidal Ag^o-Chi was analyzed by using UV-Vis spectrophotometer. Then this sample was labelled as AgNPs-Chi. Coating process was carried out through soaking 2 g of pumice into 15 mL of AgNPs-Chi, and then allowed to dry. The prepared material was named AgNPs-[Chi-Pumice] and was observed using SEM to look at chitosan coating around the pumice surface.

2.4   Antibacterial Activity

The prepared material Ag^o-[Chi-Pumice] was evaluated for its antibacterial activity, which is tested against E. coli by observing the inhibitory growth. The apparatus used were washed and sterilized using an autoclave. The bacteria were bred in a petri dish using MHA nutrient agar media with a standard concentration of Mc Farland 2, and then agar media that contained E. coli bacteria were divided into 4 observation spots. Antibacterial testing of E. coli in more detail shown in Table 1.

Table 1 Antibacterial testing against *E. coli* in MHA agar media

Spot 1	Spot 2	Spot 3	Spot 4
+0.05 g Ag^o-[*Chi-Pumice*]	+1 drop AgNPs solution	+1 drop AgNO$_3$ solution	+0.05 g pumice 10 mesh

Furthermore, to test the effectiveness of AgNPs-[Chi-Pumice] as an antibacterial in the aquatic zones, so their activity was tested in MHA liquid as a bacterial growth media.

Two grams of AgNPs-[Chi-Pumice] was weighed and it put into a column until it reached a height of 10 cm. Next, 50 mL of bacterial suspension on MHA liquid medium with Mc Farland 6 standard was inserted into a column that contained AgNPs-[Chi-Pumice], and then left the column with incubation period of 10, 20, and 30 min before the bacterial suspension was lowered. The bacterial suspension that descended from column was then collected in a sample bottle and diluted with aquabidest until the volume reached 150 mL. Furthermore, bacteria were measured their fecal coliform levels that remained after the testing process using SNI standard (item 01-2897-1992 point 3.1).

Table 1 contains data on the type and quantity of material to test against *E. coli* on the MHA agar media. Spot 1 was a testing point for 10 mesh pumice granules, which were immobilized with 0.05 g of chitosan-silver nanoparticles. As a control of errors and biases that might occur during the testing process, it was repeated until 3 times so that the results obtained were more optimal and accurate.

3 Result and Discussion

3.1 Immobilization of Chitosan-Silver Nanoparticle onto Pumice

AgNO$_3$ solution used as precursors of silver nanoparticles formation. To avoid the aggregates of silver nanoparticles, so it used chitosan as stabilizer agent [19]. Chitosan had many functions such as high biocompatibility and biodegradability, and non-toxicity [18]. Nowadays, people are looking for a green product with environmentally friendly, good antimicrobial and barrier property to reduce the environmental problems [20]. In the experiment, the reduction Ag$^+$ was carried out by photo-irradiation method to 0.1 M AgNO$_3$ and used 100 W Tungsten lamp light for 7 h to form silver nanoparticles that produced brownish yellow. Thus, photo-irradiation was effective for reduction of silver ions. Photo-irradiation method was chosen due low cost, simple and environmentally friendly procedure. The immobilization processed of colloidal AgNP-Chi onto pumice show stable particles of AgNPs-[Chi-Pumice] which indicate compatibility mixture of AgNO3-chitosan-pumice in appropriated concentration size and sequence procedure.

3.2 UV-Vis Spectrum of AgNPs and SEM Analysis of AgNPs-[Chi-Pumice]

The UV-Vis spectra characterization of silver nanoparticle showed the absorbance peak at wavelengths around 430 nm with absorbance of 1.698 at 7 h synthesis (Fig. 1). These wavelengths were the characteristic of surface plasmon resonance (SPR) of silver nanoparticles [21]. According to previous research [22], the highest absorbance of silver nanoparticles is around the wavelength of 390–470 nm when measured with a UV-Vis instrument. Measurement was carried out using Shimadzu UV-Vis spectroscopy (UV1601 model) with a golden yellow base color of silver nanoparticles as solution testing and aquadest as blank.

The AgNPs-Chi on the pumices surface was proven by SEM analysis by observing the layer of chitosan coated on the pumice surface. SEM analysis was done with enlargement 10.000 times in a vertical cross section position. As shown in Fig. 2a the sharp and hollow surface characteristic of pumice. Surface pumice looks rough and there was no chitosan coat. However, the presence of chitosan layer that attached to the surface and pores of pumice (Fig. 2b) and this layer was characterized by the presence of a white film that coats the pumice surface. Cross section of pumice immobilized appears to have chitosan particles and is finer when compared to pumice surface without immobilization.

3.3 Antibacterial Test

Antibacterial test of AgNPs-[Chi-Pumice] against *E. coli* on MHA agar media was carried out by the Kirby Bauer method with bacterial colony standard of Mc
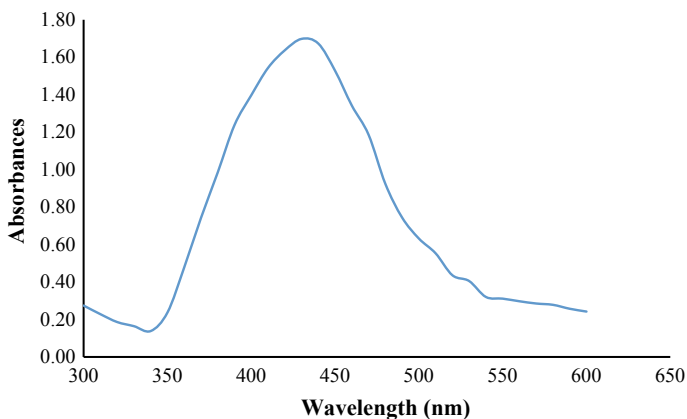
Fig. 1 UV-Vis spectra of silver nanoparticles

(a)   (b)
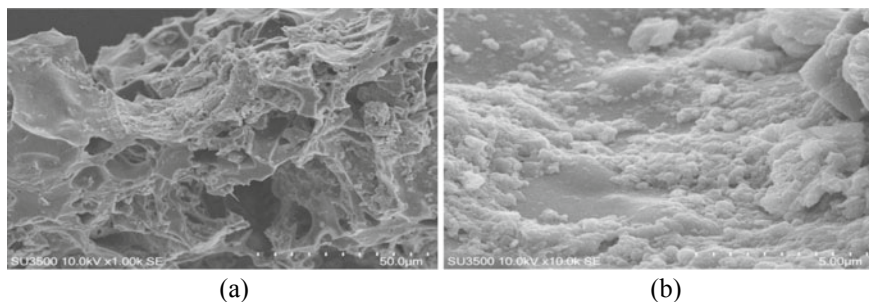
Fig. 2 SEM analysis of pumice without AgNPs-Chi (**a**) and with AgNPs-Chi immobilization (**b**)

Farland 2. Point tested was consisted of AgNPs-[Chi-Pumice], AgNPs, 0.1 M AgNO$_3$ solution and 10 mesh pumice granules. The process of testing a liquid sample was done by injection first on paper discs, whereas the solid sample directly tested on bacteria. Samples that have been placed on the bacterial spot are labeled and stored in incubator (upside down petri dish position), so that there was no residual liquid sample that drips on bacterial media and that measurement of activity zone can be maximized. Sample incubation was carried out for 24 h started from the injection period of sample on bacterial media. The result of inhibition zone shown in Fig. 3. Antibacterial test was carried out 3 times (a, b and c), so that the results obtained were reliable. Antibacterial properties showed positive reactions on AgNPs-[Chi-Pumice] samples and AgNPs on disc paper. This was evidenced by the formation of clear zone around bacteria in both samples. The AgNPs synthesized using photo-irradiation was showed a good antibacterial property against *E. coli* bacteria. This might be due to the superior antibacterial properties of AgNPs, which killed the surrounding bacteria in the media [23]. AgNPs can interact with sulfur-containing proteins in the cell membrane to change its permeability and made cell leaking [24].

Immobilization process of AgNPs onto pumice surface did not show a sign of decreasing antibacterial properties of AgNPs. Thereby it has the potential for a bactericide in the aquatic zones. Table 2 contains data of antibacterial test that observed through inhibition zone of each sample. The test of AgNPs was not only carried out in agar media, but also on liquid that aimed to simulate antibacterial properties of AgNPs in aquatic zones (Scheme 1). Antibacterial test on liquid media of AgNPs-[Chi-Pumice] is expected as exterminator of *E. coli* in the aquatic phase and this was done by intensifying the contact between *E. coli* bacteria and AgNPs-[Chi-Pumice] in the column. The concentration of *E. Coli* before and after passing the AgNPs-[Chi-Pumice] column was compared. Incubation time was 10, 20 and 30 min to observe the effect of incubation to the reduced concentration of *E. coli* bacteria. The result of AgNPs-[Chi-Pumice] against *E. coli* on MHA liquid media shown in Table 3. The best result was achieved at 30 min with a decrease amount of bacterial concentration was 68.75% that is applicable in liquid phase to reduce *E. coli* bacteria (Fig. 4).
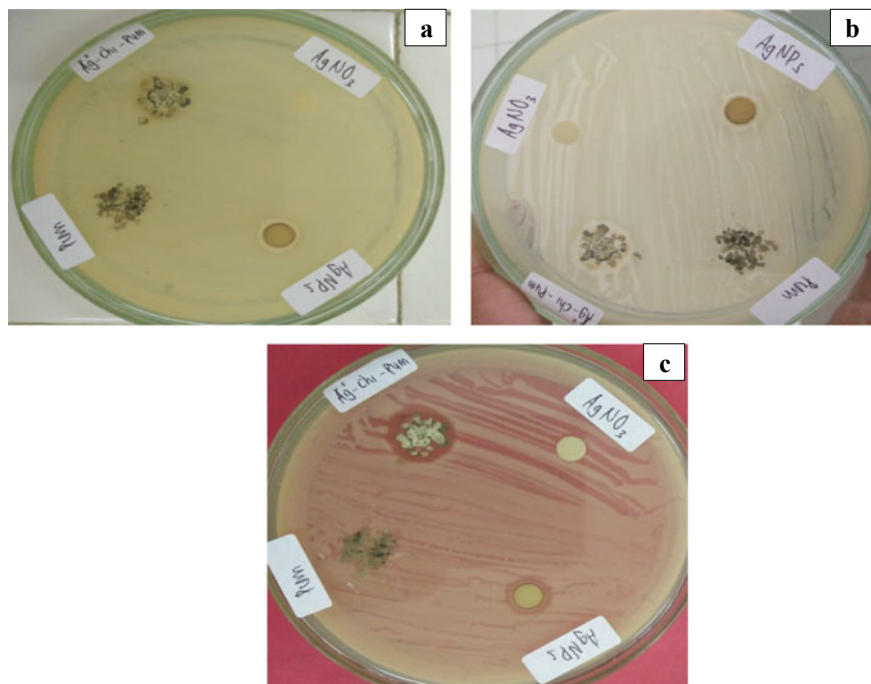
Fig. 3 Antibacterial test in the first (**a**), (**b**) second and third (**c**) experiments

Table 2 The result of *E. coli* clear zone

Sample	Inhibition zone diameter (mm)					
	Horizontal			Vertical		
	P1	P2	P3	P1	P2	P3
Ag°-[Chi-Pumice]	14.1	13.9	7.8	14.5	14.1	8.2
AgNPs	9.5	9.7	7.9	8.3	8.3	8.0
AgNO$_3$ solution	–	–	–	–	–	–
Pumice	–	–	–	–	–	–

Table 3 The result of Ag°-[Chi-Pumice] against *E. coli* on MHA liquid media

Sample	Incubation (min)	Initial concentration (MPN/100 mL)	Last concentration (MPN/100 mL)
E. coli + AgNPs-[*Chi-Pum*]	10	1600	900
E coli + AgNPs-[*Chi-Pum*]	20	1600	600
E coli + AgNPs-[*Chi-Pum*]	30	1600	500
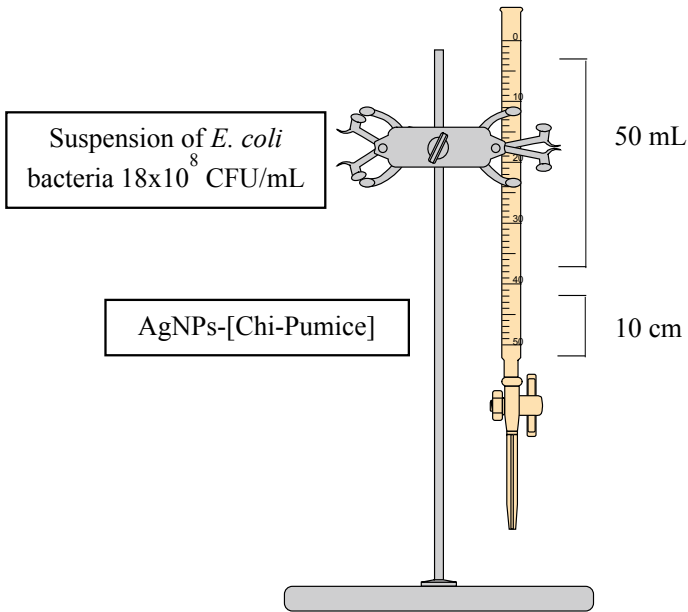
Fig. 4 AgNPs-[Chi-Pumice] is applied in column filter simulation for antibacterial water treatment

4 Conclusion

The synthesis of chitosan-silver nanoparticle by photo-irradiation has been confirmed by the UV-Vis spectra and immobilized the chitosan-Ag^o on pumice was successfully conducted. The properties of AgNPs-[Chi-Pumice] as antibacterial of *E. coli* on MHA liquid media reached the maximum condition at 30 min incubation time. AgNO$_3$ did active inhibit bacteria but Ago in form of AgNPs-[Chi-Pumice] inhibit and reduced 68.75% of the E-coli growth from initial colony concentration even at very low concentration of silver nanoparticles. AgNPs-[Chi-Pumice] is applicable used in a column filter for water treatment.

References

1. World Health Organization (2017) Drinking-water. Retrieved 10 Nov, 2017 from http://www.who.int/mediacentre/factsheets/fs391/en/
2. Tallon P, Magajna B, Lofranco C, Leung KT (2005) Water, Air, and Soil Pollut 166:139
3. Sondi L, Salopek-Sondi B (2004) J Colloid Interf Sci 275:177
4. Rai M, Yadav A, Gade A (2009) Biotechnol Adv 27:76
5. Feng QL, Wu J, Chen GQ, Cui FZ, Kim TN, Kim JO (2000) J Biomed 52:662

6. Senthilkumar P, Yaswant G, Kavitha S, Chandramohan E, Kowsalya G, Vijay R, Sudhagar B, Kumar DS, Santhosh R (2019) Inter J Bio Macromol 141:290
7. Pinto VV, Ferreira MJ, Silva R, Santos HA, Silva F, Pereira CM (2010) Coll Surf A Physicochem Eng Asp 364:19
8. Zhang W, Mou Z, Wang Y, Chen Y, Yang E, Guo F, Sun D, Wang W (2019) Mater Sci Eng C 97:486
9. Elechiguerra JL, Burt JL, Morones JR, Camacho-Bragado A, Gao X, Lara HH, Yacaman MJ (2015) J Nanobiotechnol 3:1
10. Chen N, Zheng Y, Yin J, Lia X, Zheng C (2013) J Virology Methods 193:470
11. Tolaymat T, El-Badawy A, Genaidy A, Scheckel K, Luxton T, Suidan M (2010) Sci Tot Environ 5:999
12. Kroll S, Brandes C, Wehling J, Treccani L, Grathwohl G, Rezwan K (2012) Environ Sci Technol 46:8739
13. Ribes S, Ruiz-Rico M, Pérez-Esteve É, Fuentes A, Talens P, Martínez-Máñez R, Barat JM (2017) Food Control 81:181
14. Adlim A (2006) J Sains Teknol 12:185
15. Adlim M, Zarlaida F, Khaldun I, Fadila NA, Bakar NHHA (2019) Environ Technol Innov 13:74
16. Adlim M, Zarlaida F, Rahmayani RFI, Wardani R (2019) Environ Technol Innov 16:100442
17. Adlim M, Zarlaida F, Khaldun I, Dewi R, Karina S, Omar AF (2019) Indones J Chem 19 (2):386
18. Joz MH, Babaei A, Arab BZ, Shahrampour D, Zabihi E, Jafari SM (2019) Carbohyd Polym 225:115220
19. Raveendran P, Fu J, Wallen SL (2006) Green Chem 8:34
20. Cazón P, Velazquez G, Ramírez JA, Vázquez M (2017) Food Hydrocolloids 68:136
21. Wu M, Shibata H, Kihara J, Honda Y, Arase S (2008) Langmuir 24:10494
22. Khatami M, Pourseyedi S, Khatami M, Hamidi H, Zaeifi M, Soltani L (2015) J Bioresour Bioprocess 2:1
23. Wang R, Song X, Xiang T, Liu Q, Su B, Zhao W, Zhao C (2017) Carbohyd Polym 168:310
24. Duran N, Duran M, de Jesus MB, Seabra AB, Favaro WJ, Nakazato G (2016) Nanomedicine 12:789

Study of the Effect Sudu Length on Electricity Power Generated by Wind Speed in Banda Aceh Beach

Abdul Munir, Ahmad Syuhada, and Muhammad Ilham Maulana

Abstract Wind is a renewable energy that has great potential with wind speed potential in Banda Aceh ranging from 4 to 6 m/s which blows between 4 and 6 h/day and blows speed of 6–9 m/s between 1 and 2 h/day. Studies on the use of wind energy and wind turbines have been extensively researched. This research discusses the effect of blade length on the electric power produced. The research was conducted at Ulee Lhee beach in Banda Aceh. The wind turbine used is a horizontal type with a blade length ratio of 1.25, 1.50 and 1.75 m and the number of blades 3, 4 and 5 to obtain the data results of wind speed and turbine rotation. Analysis of electrical energy data was carried out on a 3-blade and 4-blade wind turbine by installing a 2000 W generator with 1600 W power and using a transmission ratio of 1: 5. Data collection was carried out from February to August 2020 at wind speeds of 3–8 m/s. The measurement results show that the 3-blade and 4-blade wind turbines with a blade length of 1.25 m produce optimal turbine rotation at wind speeds of 4–6 m/s compared to 4 blades and 5 blades with blade lengths of 1.50 and 1.75 m

Keywords Wind turbine · Wind speed · Blade length · Electrical energy

1 Introduction

Wind is a renewable energy that has great potential with potential wind speeds in Indonesia, wind speeds ranging from 2 to 6 m/s within 6 h/day so it is very feasible to build a small wind power plant (10 kW) to moderate (10–100 kW), while the province of Aceh, especially the city of Banda Aceh, the coastal part of the average wind speed of 4 m/s, wind speed between 4 and 6 m/s which blows between 4 and 5 h/day and wind speed of 7–9 m/s blows for 1–2 h/day.

A. Munir · A. Syuhada (✉) · M. I. Maulana
Department of Mechanical and Industrial Engineering, Syiah Kuala University,
Jl. Tgk. Syech Abdurrauf, No. 7 Darussalam, Banda Aceh 23111, Indonesia
e-mail: syuhada_mech@yahoo.com

Fachri and Hendrayana [1] Analyzing Wind Potential with Weibull Distribution for the Banda Aceh Bayu Power Plant. It shows that the average wind speed in Banda Aceh every year is 4.5 m/s and the most frequency occurs at speeds of 1.5–3.5 m/s [2].

Ryski [3] conducted a Feasibility Study on the Potential of Wind Energy in the Area of the University of Tanjung Pura Pontianak to be Utilized as Electrical Energy, showing the average wind speed at an altitude of 20 m at 2.3 m/s using secondary data from NASA and included in the class 3 (three) wind category, can produce an annual electric power of 86.19 kWh/year applied to the AWI-E1000T micro wind turbine [4].

Tambrin et al. (2011) analyzed the Energy Potential in Supporting the Electricity of the Border Area of Sambas Regency, showing that the average wind velocity of 2.9 m/s at an altitude of 20 m was applied with the AWI-E1000T micro wind turbine, so the energy obtained was 1861 kWh/year [5].

Septiawan et al. [6] conducted a Study on the Potential of Wind Energy in Merak Banten to generate electrical energy, showing an average wind of 7.2 m/s applied to the FD16-20 kW wind turbine, producing 422–14,595 W of electric power [7].

Syuhada et al. (2019) Studied the potential of wind velocity in the Banda Aceh coast to the ability to generate electrical energy by horizontal axis wind turbines, at wind speeds of 3–9 m/s get optimal wind power at wind speeds of 6 m/s, with 392.73 W value because at a speed of 5–6 m/s the wind can blow 4–6 h/day and wind speeds of 6–9 m/s the wind potential is 1–2 h/day [8]. Based on the above phenomena, this research will conduct a study of the effect of blade length on the electric power generated by the wind speed at Banda Aceh Beach. Based on the potential wind speed on the coast of Banda Aceh the test is carried out on a wind turbine which has a blade length of 1.25, 1.50 m with a number of 3 blades that will be tested at wind speeds ranging from 3 to 8 m/s. The blade material is made of local wood, namely meranti wood. Meranti wood is a versatile wood, has a hard texture and is easy to shape, has an economical selling value that is easily found in Aceh. The shape of the turbine blades is taken from the provisions of the NACA 4418 type airfoil with a horizontal shaft. This study aims to determine the electrical power generated by a 2000 W generator with a load of 1600 W on a wind turbine with blade length of 1.25, 1.50 and 1.75 m.

2   Methodology

In this test the parameters measured are wind speed, turbine shaft rotation, electric generator shaft, and the voltage generated by the generator. Testing was carried out from February to August 2020 on the coast of Ulee Lheue, Banda Aceh City, Indonesia. To measure wind speed (m/s) a digital anemometer is used. Measurement of the height of the wind speed is 20 m above sea level, equivalent to the wind turbine shaft. To measure the shaft rotation speed (rpm) used a laser tachometer.

Measurement of electric voltage (V) using a voltmeter and measuring electric current (A) using a clammeter by installing a clam meter on the cable and connecting it directly to the generator.

In this study, the wind turbine used a horizontal airfoil type turbine with a 2000 W generator with the following specifications.

a. Blades: 3

- Material: meranti wood
- Blade length: 1.25, 1.50 and 1.75 m.
- Blade width: 20 cm
- Maximum blade thickness: 2 cm
- Airfoil type: NACA 4418.

b. Pitch angle: 10°
c. Turbine body frame: 5 mm iron plate and iron hollow 2 cm
d. Rotor: 4 mm iron plate and r 20 cm
e. Guide tail: 1 mm iron plate
f. Stanchion: 10 cm iron pipe
g. Generator: 1 phase induction

- Capacity: 2000 W
- Speed: 1000–6000 rpm
- Frequency: 50/60 Hz
- Current: 8 A.

h. Controler System: Automatic Voltage Regulator
i. Transmission: Belt Pulley ratio 1: 5 (Fig. 1).

Fig. 1 Horizontal wind turbine
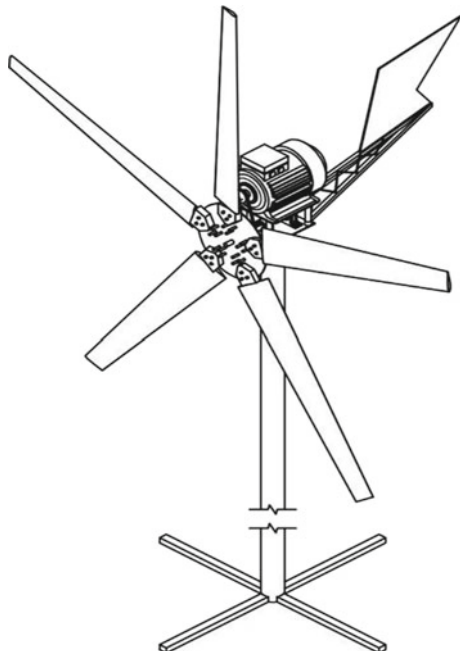
3   Experimental Results

This study examines and analyzes the wind speed potential on the coast of Banda Aceh against the ability to generate electrical energy using horizontal shaft wind turbines. Because of that, the measured parameters are wind speed, turbine rotation and voltage generated by the generator and the electric current produced.

3.1   The Effect of Wind Speed on the Electric Voltage with 3 Blades at a Blade Length of 1.25, 1.50 and 1.75 m Is Shown in Fig. 2 Below

Based on Fig. 2 above, it can be seen that at wind speeds of 3–3.5 m/s the generator has not yet produced electrical power, so the required generator rotation is 1000–6000 Rpm. Then a wind turbine with 3 blades at a blade length of 1.25 m produces a voltage at a wind speed of 4 m/s of 95 V, a wind turbine with a blade length of 1.50 m produces a voltage at a wind speed of 4.5 m/s of 90.23 V and a wind turbine with a blade length of 1.75 m produces a voltage at a wind speed of 5 m/s of 118 V. While the highest voltage that can be generated by a wind turbine with a blade length of 1.25 m is 219 V at a wind speed of 8 m/s, a wind turbine with a blade length of 1.50 m at a wind speed of 7 m/s and the wind turbine can produce as much as 219 V. And a blade length of 1.75 m produces 199 V with a wind speed of 6.5 m/s.
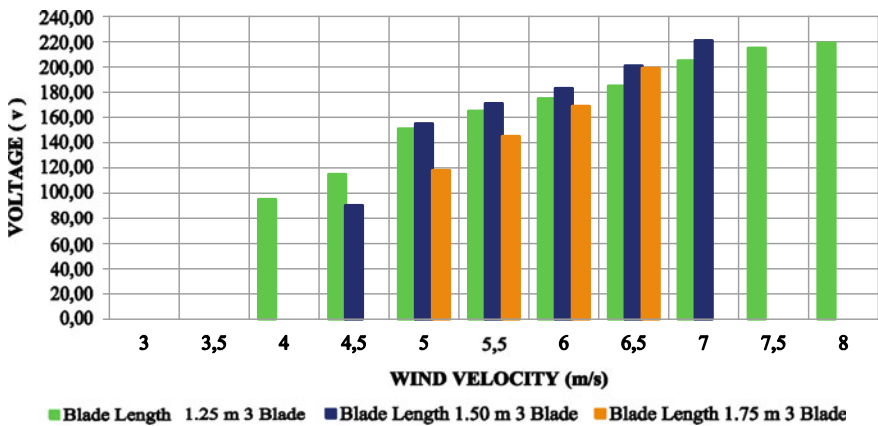
Fig. 2   Effect of wind speed on electric voltage with 3 blades at a blade length of 1.25 m, 1.50 m, and 1.75 m

3.2 The Effect of Wind Speed on the Electric Voltage with 4 Blades at a Blade Length of 1.25, 1.50 and 1.75 m Is Shown in Fig. 3 Below

Based on Fig. 3, it can be seen that the wind turbine with 4 blades at a blade length of 1.25 m, at a wind speed of 3–3.5 m/s the generator also does not produce electric power. A wind turbine with 4 blades at a blade length of 1.25 m produces a voltage at a wind speed of 4 m/s of 98 V, a wind turbine with a blade length of 1.50 m produces a voltage at a wind speed of 4.5 m/s 115 V and a wind turbine with a blade length of 1.75 m produces a voltage at a wind speed of 5 m/s of 95 W. While the highest voltage that can be produced by a wind turbine with a blade length of 1.25 m is 223 V at a wind speed of 8 m/s, a wind turbine with a blade length of 1.50 m wind speed of 6.5 m/s generates a voltage as wide as 221 V. And a blade length of 1.75 m produces 210 V with a wind speed of 7 m/s.

3.3 The Effect of Wind Speed on Electric Power with 3 Blades at a Blade Length of 1.25, 1.50 and 1.75 m Is Shown in Fig. 4 Below

Based on Fig. 4, it can be seen that the electric voltage is directly proportional to the electric power produced, the greater the voltage the greater the electric power produced. At a wind speed of 3–3.5 m/s the generator has not yet produced electric power, so the 3 blade wind turbine with a blade length of 1.25 m produces electric power at a wind speed of 4 m/s of 694 W, a wind turbine with a length 1.50 m blades generate electric power at a wind speed of 4.5 m/s of 659 W and a wind
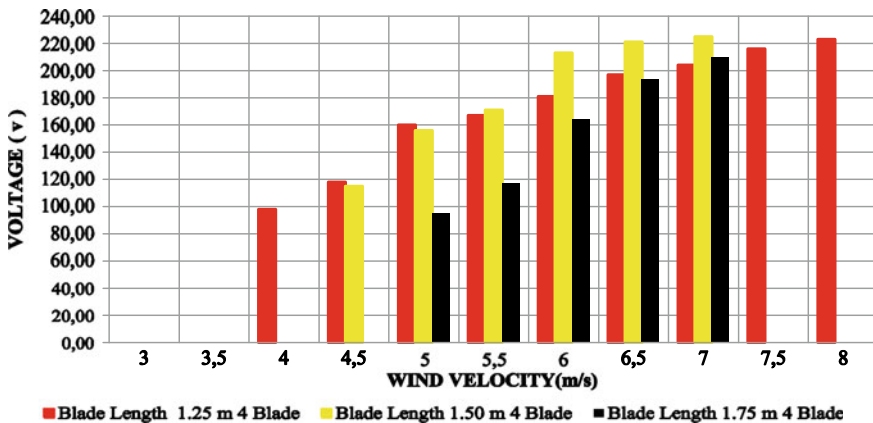
Fig. 3 Effect of wind speed on electric voltage with 4 blades at a blade length of 1.25 m, 1.50 m, and 1.75 m
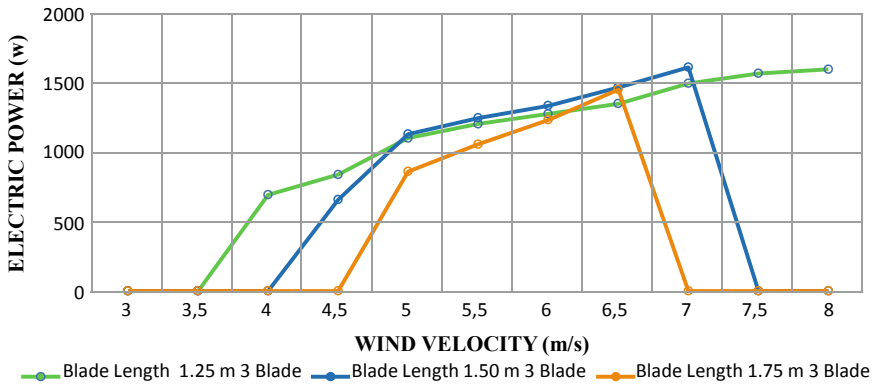
Fig. 4 Effect of wind speed on electric power with 3 blades at a blade length of 1.25 m, 1.50 m, and 1.75 m

turbine with a blade length of 1.75 m produces electric power at a wind speed of 5 m/s of 861 W. While the highest electric power that can be generated by a wind turbine with a blade length of 1.25 m is 1599 W at a wind speed of 8 m/s, a wind turbine with a blade length of 1.50 m can produce 1467 W of electric power at a wind speed of 6.5 m/s. And a blade length of 1.75 m produces 1453 W with a wind speed of 6.5 m/s.

3.4 The Effect of Wind Speed on Electric Power with 4 Blades at a Blade Length of 1.25, 1.50 and 1.75 m Is Shown in Fig. 5 Below

Based on Fig. 5, it can be seen that the 4-blade wind turbine with a length of 1.25 m at a wind speed of 3–3.5 m/s the generator has not yet produced electric power, the wind turbine with a blade length of 1.25 m can generate electric power at a speed 4 m/s wind of 715 W, a wind turbine with a blade length of 1.50 m produces electric power at a wind speed of 4.5 m/s of 840 W and a wind turbine with a blade length of 1.75 m produces electric power at wind speed 5 m/s of 694 W. While the highest electric power that can be generated by a wind turbine with a blade length of 1.25 m is 1628 W at a wind speed of 8 m/s, a wind turbine with a blade length of 1.50 m can produce an electric power of 1613 W at a wind speed of 6.5 m/s. And a blade length of 1.75 m produces 1533 W with a wind speed of 6.5 m/s.
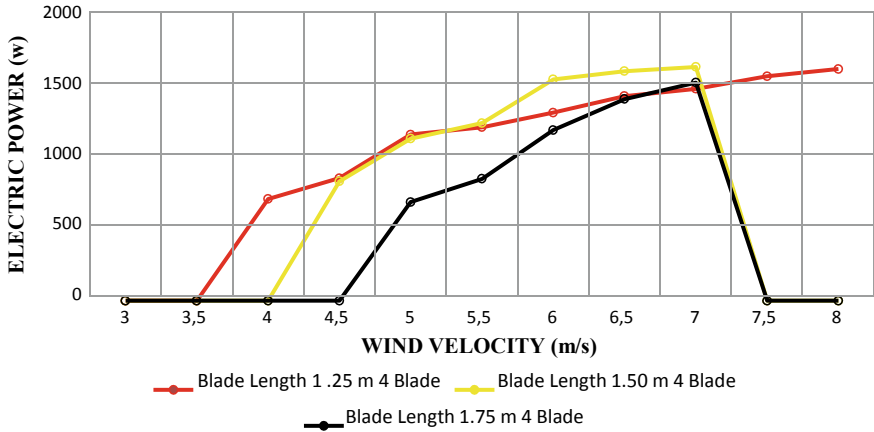
Fig. 5 Effect of wind speed on electric power 4 blades at a blade length of 1.25 m, 1.50 m, and 1.75 m

4 Discussion

Based on the measurement results, it is clear that the number of blades, the length of the turbine blades and the wind speed greatly affect the performance of the wind turbine and the electrical energy generated. The 3-blade and 4-blade wind turbines with a blade length of 1.25 m can generate electrical energy at wind speeds of 4 m/s while the 3 and 4-blade wind turbines with 1.50 blades can generate electrical energy at wind speeds of 4.5 m/s and turbines. 3 blades and 4 blades with a blade length of 1.75 m can generate tension at wind speeds of 5 m/s.

The electrical energy generated by a 3-blade and 4-blade wind turbine with a blade length of 1.25 m starts at a wind speed of 4–8 m/s while the 3 and 4 blade wind turbine with a blade length of 1.50 m starts at a speed wind 4.5–6.5 m/s and wind turbine 3 blades and 4 blades with a blade length of 1.75 m starting at a wind speed of 5–7 m/s.

5 Conclusion

Based on the above discussion, it can be concluded that the wind turbine that can produce optimal electricity is a wind turbine with 3 blades and 4 blades at a blade length of 1.25 m which can be driven by wind speeds ranging from 4 to 8 m/s. while the wind turbine blade length of 1.50 m and blade length of 1.75 m with blades 4 and 5 can generate electrical energy at wind speeds ranging from 5 to 6 m/s. So according to data on the coastal wind speed of Banda Aceh city, wind speeds of 3–4 m/s can blow 2–3 h/day, wind speeds of 4–6 m/s can blow for 4–6 h/day and wind

speeds of 6–9 m/s can blow for 1–2 h/day, thus a suitable turbine for use on the coast of Banda Aceh City is a 1.25 m long wind turbine with 3 and 4 blades.

References

1. Fachri MR, Hendrayana, Analysis of wind potential with weibull distribution for Bayu power plants in Banda Aceh (Electronics Engineering, Syiah Kuala University)
2. Manwell JF (2002) Wind energy explained theory, design and application. John Wiley and Sons, Ltd., Amherst
3. Ryski (2016) Feasibility study on the potential of wind energy in the Tanjung Pura University area (Pontianak)
4. Tambrin et al. (2017) Analysis of energy potential in supporting electricity in the border area of sambas regency (Mechanical Engineering Study Program)
5. Saputra M (2013) Analysis of Meulaboh city wind power generation system (Faculty of Engineering, Syiah Kuala University)
6. Septiawan et al. (2016) Study of the potential of wind energy to generate electrical energy in Merak Banten
7. Syuhada A, Maulana MI, Fuadi Z (2017) Analysis of wind energy potential for agriculture pump in mountain area Aceh Besar. AIP Conf Proc 1855(1):070007
8. Syuhada A, Maulana M I, Fuadi Z (2020) The potential of wind velocity in the Banda Aceh coast to the ability to generate electrical energy by horizontal axis wind turbines. IOP Conf Ser: Mater Sci Eng 788:012082

Study of Temperature Uniformity on the Multi-shelf Type Drying System

Dina Shabri, Ahmad Syuhada, and Razali

Abstract The study of temperature uniformity on multi-shelf drying equipment, using fuel as the drying energy was done. This study uses a 10-level dryer. The system of heat divider to the drying chamber is equipped with a sharp turn channel to equalize the temperature in the drying chamber. The hot gas distribution system is conducted by natural convection. This drying equipment system is also equipped with a combustion chamber, heat level, hot gas divider channel, drying chamber, and chimney. The type of fuel can be selected from LPG, fuel oil, and other solid fuels. In this test, the temperature in the drying chamber can be used between 60 and 90 °C. With a 60–90 °C, the temperature in the combustion chamber is 400–500 °C, the temperature in the hot gas channel is from 120 to 90 °C and the exhaust chamber temperature is 50–75 °C. From the test results, it was found that the temperature in the drying chamber between the first shelf to the highest shelf was 1 °C vertically, and the temperature difference was 0.2–0.5 °C horizontally. It can be said that the temperature distribution in the drying chamber is uniform. After being tested, the drying capacity for fish is 50–80 kg, drying time is 10–12 h with the water content of dried fish reach 12–15%. For drying fish 50 kg, requires 4 kg of LPG.

Keywords Temperature uniformity · Multiple-shelf dryer · Fuel energy · Heating channel · Sharp turn system

1 Introduction

Traditionally, drying is done by drying in the sun, where the temperature that can be accepted by the drying object is only around 40–45 °C. The heat transfer system for drying in the sun is a radiation module, which is when the drying is done, the drying

D. Shabri · A. Syuhada (✉) · Razali
Department of Mechanical and Industrial Engineering, Syiah Kuala University,
Jl. Tgk. Syech Abdurrauf No. 7 Darussalam, Banda Aceh 23111, Indonesia
e-mail: syuhada_mech@yahoo.com

object must be reversed [1], because the part of the object facing the sun will dry quickly, and the part that is not exposed to the sun does not dry out. Another disadvantage of solar energy is that drying energy can only be obtained in summer [2–6]. The good drying temperature is between 60 and 80 °C. To increase the drying temperature using solar thermal energy, a solar collector drying system has been developed, the temperature of the drying air that comes out of the collector can reach 80 °C by using absorbers and other technologies [7–10]. The disadvantage of drying technology using a collector is that the drying capacity still small and cannot be used during cloudy and rainy seasons for drying [11, 12].

To overcome the disadvantages of using solar energy, drying using heat energy from fuel combustion has been developed. By using the heat energy of a fuel, the drying temperature can be adjusted according to the need and the heat can take place continuously. Usually, a drying system using combustion energy is conducted by forced convection using a fan [13], which results in uneven drying. Accordingly, to get even drying results can be done with a natural convection system. Natural drying equipment using fuel energy has been conducted, this system is made with 7-shelf drying equipment, where the temperature variation between levels reaches 3–4 °C [14].

With the said background, the author conducted an experimental study of temperature uniformity in a multi-shelf drying chamber using fuel as the drying energy. In this study, the dryer is used with 10-levels, each level has a shelf where the dryer object is placed. The hot gas divider system to the drying chamber is equipped with a sharp turn channel [15, 16] with varying lengths to uniform the temperature in the drying chamber. The hot gas divider system is conducted by natural convection. This drying equipment system is also equipped with a combustion chamber, heat guide, hot gas divider channel, drying chamber, and chimney. The type of fuel used is LPG.

2 Experimental Set Up

The research was conducted at the Thermal Engineering Laboratory of the Mechanical Engineering Study Program, Department of Mechanical and Industrial Engineering, Faculty of Engineering, Syiah Kuala University, starting from equipment planning, manufacturing, data collection, and data processing. With the following stages.

2.1 Research Tools

The dryer designed is shown in Fig. 1, with its main part consisting of 5 (five) parts, namely (1) the combustion chamber as a source of heat production, (2) drying chamber, (3) hot gas divider channel, (4) shelf where a drying object is placed and

Part list:
1. Combustion chamber
2. Drying chamber
3. Hot gas divider channel
4. Shelf
5. Chimney

(a)   (b)
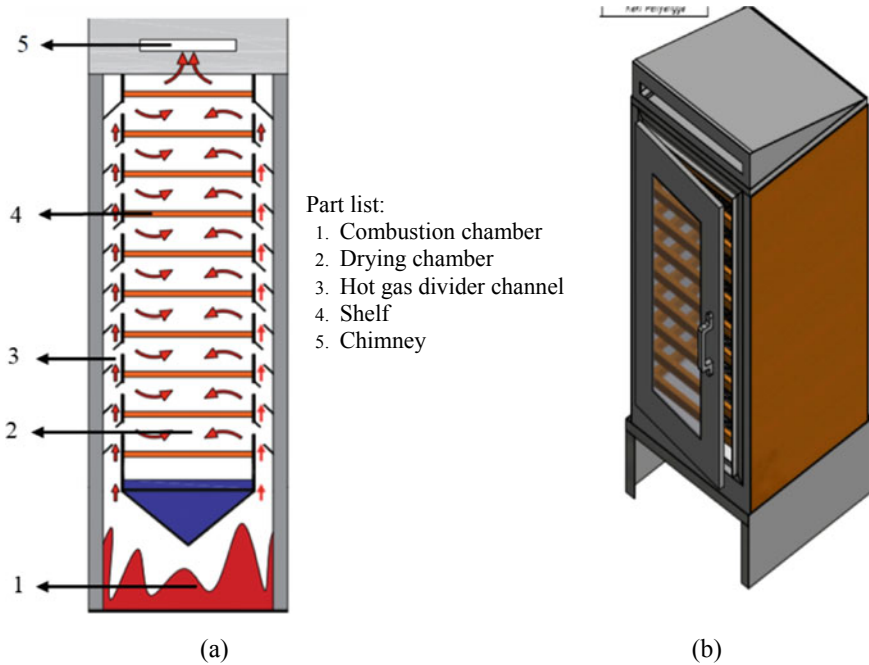
Fig. 1 Dryer **a** the main part of the dryer, **b** the 3D design of the dryer designed

(5) a chimney to remove water vapor. This dryer frame material is made of elbow metal, the walls are made of zinc plate and coated with plywood as heat insulation. The dryer with dimensions measuring 832 mm long, 820 mm wide, 1.440 mm high, 10-shelf has a drying capacity of 80 kg, the dimensions of the combustion chamber is 872 mm × 864 mm × 325 mm.

The hot gas divider channel is formed by a sharp turn channel. This sharp turn channel made 18 pieces at each shelf level on the right and left sides of the inner and outer walls of the drying chamber with a zinc plate thickness of 0.3 mm and an angle of 45° aims to change the flow of hot laminar gas that comes out of the combustion chamber into the drying chamber so that it can produce even heat in the drying chamber and the resulting temperature is close to uniform so that it can speed up drying time and produce good dry products as needed.

The variations in the length of the fins for sharp turns on the inner wall of the drying chamber are 10 mm on hot gas channel 1, 2, 3, length of the fins 20 mm on hot gas channel 4, 5, 6, 7 and lenght of the fins 15 mm on hot gas channel 8, 9. Meanwhile, the hot gas channel 10 is closed so that there is no heat loss (Fig. 2).
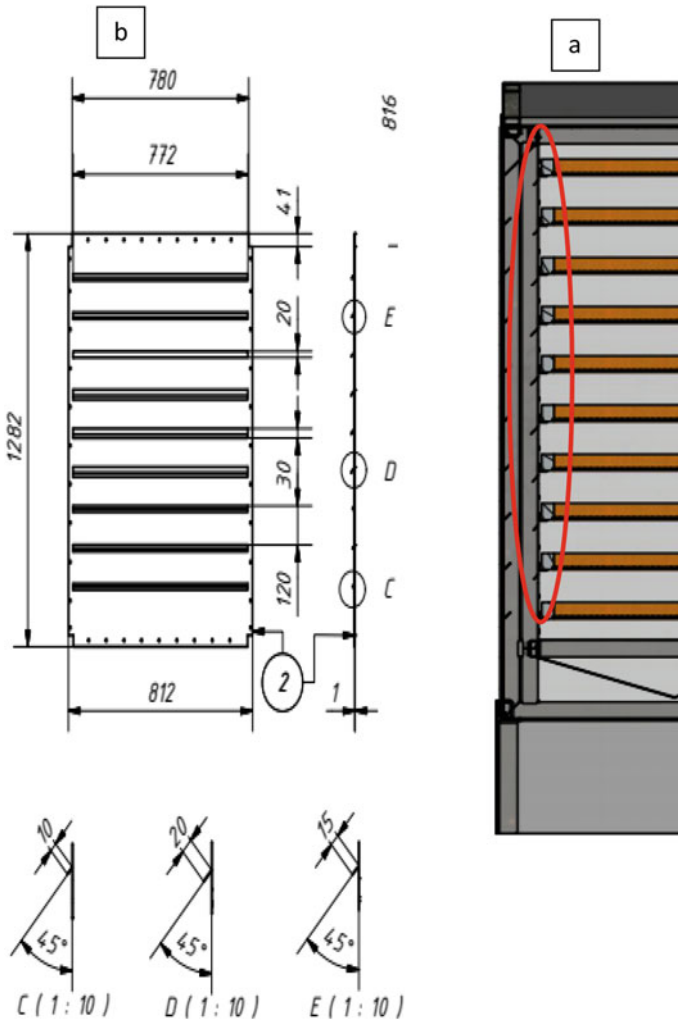
Fig. 2 a Sharp turn channel, **b** sharp turn channel and variations of fins length

2.2 The Test of the Dryer

In this test, the temperature distribution was conducted in the drying chamber. This temperature distribution measurement includes with no dryer load and with dryer load. The drying load that used was 50 kg of fresh fish. However, the drying capacity of the tools tested was 50–80 kg. The type of fuel used can be selected for LPG. The temperature tested in the drying chamber is between 70 and 90 °C. The measurement points on the dryer test are given in Fig. 3.

Description:
1. T.combustion chamber
2. T.inlet
3. Shelf 1
4. Channel 1
5. Shelf 3
6. Shelf 5
7. Channel 2
8. Shelf 6
9. Shelf 7
10. Channel 3
11. Shelf 9
12. Channel 4
13. T.outlet

(a) Measurement point vertically   (b) Measurement point horizontally
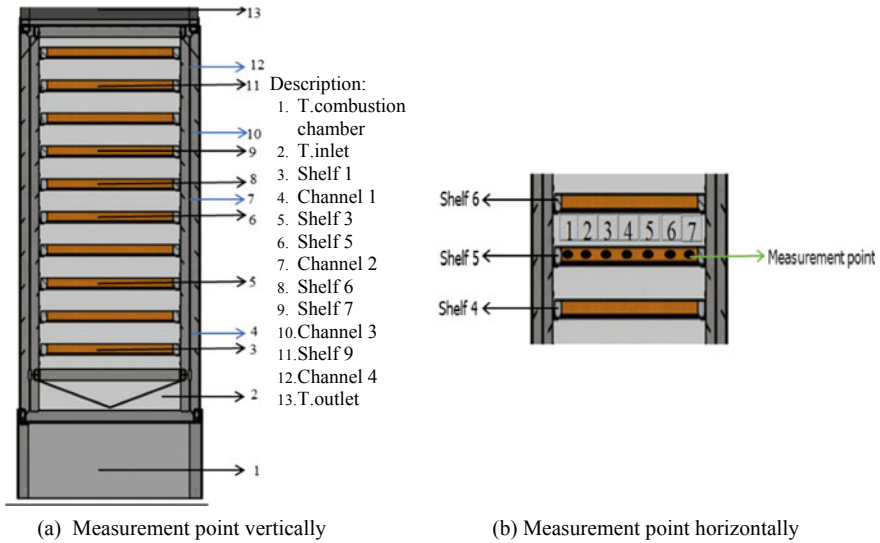
Fig. 3 Measurement points on the dryer test, **a** measurement point vertically, **b** measurement point horizontally

3 Result and Discussion

3.1 The Test Result

In this test, the measurement of the temperature distribution was conducted on a multi-shelf drying equipment (10-levels). The test conditions were carried out in two conditions; measuring the temperature distribution at no load and measuring the drying rate.

3.1.1 Measurement of Temperature Distribution in the Heating Channel

In this section, the temperature distribution of the multi-shelf drying equipment has been tested. The purpose of this study is to obtain a uniform temperature distribution in the drying chamber. The working principle of this drying equipment is to use hot gas from the combustion of fuel as the heat energy for drying. The heat source for this drying system is the result of the combustion of fuel in the combustion chamber with a combustion temperature of 400–450 °C. The hot gas from the combustion chamber then funneled into the hot gas channel towards the drying chamber. The standard point of this test is the temperature of 70, 80, and 90 °C in the drying chamber. The temperature distribution points of the hot gas channel are as shown in Fig. 3a. After the test the temperature distribution, the results can be

Fig. 4 Temperature
distribution in the hot gas
channel
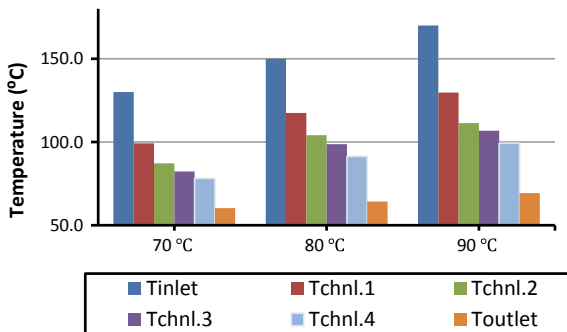
seen as in Fig. 4. In the dryer, the test was conducted on the temperature distribution of the hot gas channel into the drying chamber at no-load conditions.

From the test results, at the 70 °C drying chamber temperature, the combustion chamber temperature is 400 °C, at T.inlet the temperature is 125 °C, channel1 99 °C, channel2 87 °C, channel3 82 °C, channel4 78 °C while at T.out 60 °C. From this graph, it is clear that the temperature distribution between T.inlet and T.out is appropriate, meaning that the temperature from point 1 decreases gradually [1] according to the distribution of hot gas which is divided by a sharp turn channel towards the drying chamber. From Fig. 4, it is clear that the distribution of the test temperature at 80 and 90 °C, the temperature distribution characteristics tend to be the same as the 70 °C test.

3.1.2 Measurement of Temperature Distribution in the Drying Chamber

The Vertical Temperature Distribution of the Drying Chamber

The measurement point in this vertical temperature distribution test is as described in Fig. 3a, for this test the measurement point is only conducted at 6 points; shelf 1, shelf 3, shelf 5, shelf 6, shelf 7, and shelf 9. The test was conducted for 30 min and tested at a temperature of 75 °C. The first test is tested after a stable temperature (10 min after heating the combustion chamber), starting at a drying chamber temperature of about 75 °C. In the first minute, the temperature distribution is obtained at shelf 1 74.4 °C, shelf 9 75.2 °C and the average temperature of the six measurement points is 74.8 °C (Fig. 5).

Horizontal Temperature Distribution of the Drying Chamber

The measurement of the temperature distribution horizontally in the drying chamber conducted as many as 7 measuring points as shown in Fig. 3b. Measurements were

Fig. 5 Vertical temperature distribution of the drying chamber
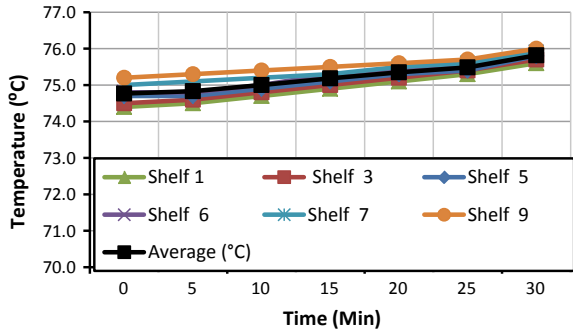
made in the central area of the drying chamber, which is on a level 5-shelf. The temperature distribution variations tested were 70, 80, and 90 °C. The measurement results can be seen in Fig. 6. At the test temperature of 70 °C, the highest point was 70.2 °C and the lowest was 69.9 °C and the average was 70 °C. From Fig. 6, it is clear that for the test at temperatures of 80 and 90 °C, the temperature distribution characteristics tend to be the same as the 70 °C test.

3.2 The Drying System Performance Test

Based on the graphs of the test results, this multi-shelf type dryer, both in the hot gas channel and in the drying chamber, has a good temperature distribution, therefore the drying system performance will be tested by observing the drying rate. The object used for the dryer was 50 kg of fresh fish even though the capacity of the dryer able for drying up to 80 kg of fresh fish. The consumption of LPG during 10 h of drying 50 kg of fresh fish requires 4 kg of LPG fuel. The shelf where the fish is placed was conducted on the sample shelf 3, shelf 5, shelf 7, and shelf 9 as shown in Fig. 3a.

Fig. 6 Horizontal temperature distribution of the drying chamber
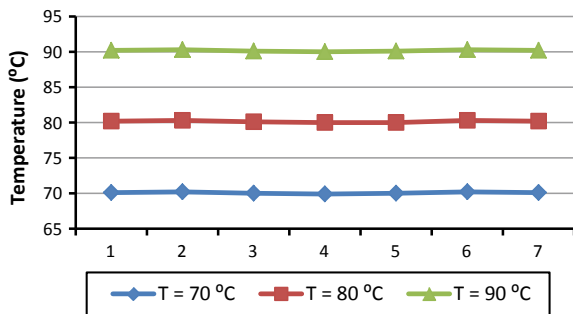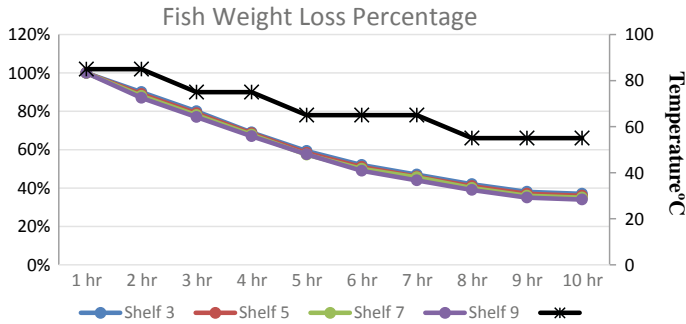
Fig. 7 Fish drying rate at the time

A good drying system for fresh fish is conducted with a higher initial temperature to a lower temperature [17]. The temperature distribution in the drying chamber after inserted the fish shown in Fig. 7 (black line). This test started with a temperature of 85 °C and after two hours the temperature gradually reduced to 75, 65 and 55 °C and the temperature maintained at 55 °C until the drying completed. This process is conducted so that the absorption of water content on the surface of the fish becomes faster, while in the next process the amount of water absorbed decreasing because the water content in the fish has reduced as the temperature decreases [18].

Figure 7 (shelf 3, shelf 5, shelf 7, shelf 9) shows the decrease in water content in the drying object faster in the first four hours; at a temperature of 85 and 75 °C than in the next process with a lower temperature.

The rapid decrease of water content is caused by a large amount of water content in the drying object along with the high drying temperatures [19]. Thus it can be seen that the higher the air temperature at the beginning of the drying process, the more water is absorbed on the surface of the object [19]. The subsequent drying rate is smaller at a drying chamber temperature of 65 °C and finally 55 °C because the water content of the drying object is low and the drying temperature is also low [20]. If the drying conducted at a high temperature for the drying object that has reduced the water content, this will cause the surface of the drying object to be drier so that heat cannot permeate the drying object [21], this is called thermal stress [22] and must be avoided in the drying process.

3.3   Discussion

In the no-load test, it can be seen that the working ability of the dryer such as the distribution of hot airflow in the drying chamber and temperature uniformity between the shelves in the drying chamber has been reached very well. The temperature setting from high to low temperature is faster than from low temperature to a higher temperature [23], so it can save fuel as an energy source and use a shorter time.

The drying rate at the time is influenced by several factors such as the length of drying time required for the drying object, the drying chamber temperature, and the decrease in the mass of the drying object at the time. Based on the data analysis, it is shown that the more the hot steam in the drying chamber, the faster the drying rate at the time required [24].

4   Conclusion

From the no-load test result data analysis, it can be seen that the temperature variation in the vertical range between the lowest and the highest is small than 1 °C, and the lowest and highest horizontal temperature ranges are also below 0.5 °C. After observing the vertical and horizontal ranges are very small in terms of heat uniformity in a drying chamber, the temperature in the drying chamber of the 10-shelf drying equipment can be stated as uniform.

From the test results to see the drying rate of the dryer between shelf-1 to shelf-9, the temperature difference is very small, which means it can be said that the drying rate is the same. Thus it can be stated that this drying chamber temperature can be considered uniform.

References

1. Ohijeagbon IO, Lasode OA, Adebayo S, Ajayi OO, Omotosho OA (2018) Data on drying kinetics of a semi-automated gas-fired fish dryer. Data Brief 18:641–647. https://doi.org/10.1016/j.dib.2018.03.072
2. Sary R, Syuhada A (2019) Study of fish drying process using multilevel shelves with wood fuel. In: Prosiding SNTTM XVIII. 9–10 Oktober 2019
3. Beigi M (2016) Energi efficiency and moisture diffusivity of apple slices during convective drying. J Food Sci Technol 36(1):145–150. https://doi.org/10.1590/1678-457X.0068
4. Jain D, Pathare PB (2007) Study the drying kinetics of open sun drying of fish. J Food Eng 78(4):1315–1319
5. Doymaz I, Ismail O (2011) Drying characteristics of sweet cherry. J Food Process Preser. J Food Bioprod Process 89:31–38
6. Chand TK, Scholar, PD, Mohanty MK, Prof A, Mohanty RC (2018) Exergy and energy analyses and evaluate drying parameters to develop a stastistical model for a solar dryer in fish drying. Int J Res Eng Appl Manage (IJREAM) ISSN: 2454–9150, 04(03)
7. Mehta P, Samaddar S, Patel P, Markam B, Maiti S (2018) Design and performance analysis of a mixed mode tent-type solar dryer for fish-drying in coastal areas. J Solar Energy 170:671–681. https://doi.org/10.1016/j.solener.2018.05.095
8. Prakash TB, Satyanayarana S (2014) Performance analysis of solar drying system for Guntur chili. Int J Latest Trends Eng Technol 4:283–298
9. Syuhada A, Maulana MI (2018) Absorber thickness effect on the effectiveness of solar collectors to production hot air for drying. In: E3S Web of Conferences 67, 04028, 3rd i-TREC

10. Ji Xu, Li M, Wang Y, Ling D, Luo X (2016) Performance characteristics of solar drying system for agricultural products. Bul Chem Commun 48:120–125. https://doi.org/10.1051/e3sconf/20186704028

11. Demiray E, Tulek Y (2012) Thin-layer drying of tomato (lycopersicum esculentum mill. Cv. Rio grande) slices in a convective hot air dryer. J Heat Mass Transfer 48(5):841–847, http://dx.doi.org/10.1007/s00231-011-0942-1

12. Alleyne FS, Milezarek R (2015) Design of solar thermal dryers for 24 hour food drying. United state department of agriculture. J Heating Process Food Res Unit

13. Setyawan EY et al (2018) Performance of turmeric dryer cabinets with Lpg fuel using temperature control and air speed. In: IOP conference series: materials science and engineering 420(1). https://doi.org/10.1088/1757-899x/420/1/012044

14. Jangsawang W (2017) Meat products drying with a compact solar cabinet dryer assessing the feasibility of using the heat demand-outdoor a long-term district heat demand forecast. Energy Procedia 138:1048–1054. https://doi.org/10.1016/j.egypro.2017.10.103

15. Syuhada A, Maulana MI (2018) Characteristics of heat transfer on solar collector channel by using a sharp turn. AIP Conf Proc 1984(020003):2018. https://doi.org/10.1063/1.5046587

16. Syuhada A, Maulana MI (2018) Study of heat transfer characteristics on sharp turn channels for solar collectors. J Adv Res Fluid Mech Thermal Sci 45(I):82–91. ISSN: 2289-7879

17. Oliveira SM, Ramos IN, Brandão TRS, Silva CLM (2015) Effect of air-drying temperature on the quality and bioactive characteristics of dried galega kale (Brassica oleraceaL. var. Acephala). J Food Process Preserv 39(6):2485–2496. https://doi.org/10.1111/jfpp.12498

18. Aritesty E, Wulandani D (2014) Performance of the rack type-greenhouse effect solar dryer for wild ginger (curcuma xanthorizza roxb.) drying. Energy Procedia 47:94–100. https://doi.org/10.1016/j.egypro.2014.01.201

19. Diamante L, Durand M, Savage G, Vanhanen L (2010) Effect of temperature on the drying characteristics, colour and ascorbic acid content of green and gold kiwifruits. Int Food Res J 17(2):441–451

20. Jabeen R, Aijaz T, Gul K (2015) Drying kinetics of potato using a self-designed cabinet dryer. Cogent Food Agri Food Sci Technol Res Article 1(1):1–5. https://doi.org/10.1080/23311932.2015.1036485

21. Patrón-Vázquez J et al (2019) The effect of drying temperature on the phenolic content and functional behavior of flours obtained from lemon wastes. J Agron 9(9):1–16. https://doi.org/10.3390/agronomy9090474

22. Inyang U, Oboh I, Etuk B (2017) Drying and the different techniques. Int J Food Nutr Saf 8(1):45–72

23. Marey S, Shoughy M (2016) Effect of temperature on the drying behavior and quality of citrus peels. Int J Food Eng 12(7):661–671. https://doi.org/10.1515/ijfe-2015-0296

24. Putra RN, Ajiwiguna TA (2017) Influence of air temperature and velocity for drying process. Procedia Eng 170:516–519. https://doi.org/10.1016/j.proeng.2017.03.082

Design and Analysis of Automatic Fish Dryer Prototype

Kevin Raynaldo, Richie Andrianto, and Steven Darmawan

Abstract Indonesia has lots of natural resources especially in marine sector such as yellowstripe scad and long-jawed mackerel. Those fish are usually dried by fisherman for longer storage using conventional drying by heat from the sun. This conventional drying method takes hours, about two or three days depends on sun heat intensity. Based on that problem, mechanical drying system may overcome the problem. Automatic fish dryer is designed to dry the fish effectively with even heat distribution with palette rotation system which is hoped to increase productivity and economic potential for coastal communities. The prototype is designed theoretically with mechanical design to generate part specification including heater, shaft, electric motor, bearing, pulley and transmission. CFD method to discover the heat distribution inside with 5,239 nodes and STD k-ε turbulence model. A 400 mm × 500 mm × 420 mm prototype is generated to dry 2 kg of long-jawed mackerels in 5.3 h with 0.00419 g/s for drying mass flow rate from 70 to 30% water content. CFD simulation shows the exhaust fan need to be installed at outlet for better water-vapor flow distribution. This research indicates that automatic fish dryer can dry 4 times faster than conventional drying system.

Keywords Fish dryer · Prototype · Mechanical design · CFD

1   Introduction

Indonesia is a country which has lots of natural resources especially in marine sector that is referred to as maritime country. Some fish which has important role to coastal communities are yellowstripe scad (*Selaroides leptolepis*) and long-jawed mackerel (*Rastrelliger*). Based on Sungailiat Archipelago Fishing Port data, the amount of yellowstripe scad catches in 2018 reaches 539.011 tons [1]. Then, long-jawed

K. Raynaldo (✉) · R. Andrianto · S. Darmawan
Study Program of Mechanical Engineering, Faculty of Engineering, Universitas Tarumanagara, Jalan Letjen S. Parman No. 1, Jakarta Barat 11440, Indonesia
e-mail: kevin.515170004@stu.untar.ac.id

mackerel is wide-spread in Indonesia such as in Pekalongan, Central Java with average catches from 2007 until 2016 reaches 1,386.199 tons per year [2].

Those fish are usually dried by fisherman for longer storage. However, that drying usually uses heat from the sun that takes longer time, about two or three days in accordance with the sun heat intensity. Another problem is when the rainy season coming that makes the sun heat intensity reduced, so the drying can fail and cause putrefaction to the fish.

Based on those problems, automatic fish dryer was designed to reduce water content in the fish from about 50–80% into less than 25%. It will inhibit bacterial activity and also the putrefaction [3]. It is recommended to set the drying temperature less than 85 °C in order to maintain fish nutritional quality [3].

The objectives in this study are to design automatic fish dryer prototype with mechanical concept that can dry the fish by heating evenly as well as numerically analysis the heat distribution with CFD method. Then, the prototype can reduce the drying time become 4 h that the fish water content reduced from 70 to 30%. Furthermore, it is able to increase productivity and also economic potential for coastal communities especially fisherman. Fish dryer already exists before, but new thing comes in our prototype especially the utilization of palette rotation mechanism for heating evenly without any changes in fish position. On the other hand, automatic fish dryer prototype can be used to get effective way in fish drying either rainy season or dry season. It also can encourage entrepreneurship sector because of its reasonable price.

Nomenclature			
q	Sensible heat rate (Watt)	c_p	Specific heat (J/kg °C)
Q	Sensible heat (Joule)	ΔT	Temperature changes (°C)
t	Drying time (s)	T_e	Equivalent torque (Nm)
m	Mass (kg)	M	Bending moment load (Nm)
T	Torque load (Nm)	d_2	Driven pulley diameter (inch)
d	Shaft diameter (mm)	$\bar{V}$	Linear velocity of v-belt (m/s)
$\bar{\tau}$	Allowable shear stress (MPa)	L	Pitch length of v-belt (mm)
C	Allowable dynamic load (N)	x	Distance between driver shaft and driven shaft (mm)
F_e	Equivalent dynamic load (N)	r_1	Driver pulley radius (mm)
K	Dynamic factor for bearing (=3 for ball bearing)	r_2	Driven pulley radius (mm)
n_1	Electrical motor revolution (rpm)	m_0	Fish mass before drying (g)
n_2	Fish palette system revolution (rpm)	m_1	Fish mass after drying (g)
d_1	Driver pulley diameter (inch)		

2 Methods

In this study, automatic fish dryer is made as prototype and object of analysis that can be considered for development with larger scale and more products [4]. Components and dimensions of automatic fish dryer are obtained from machine elements calculation and engineering approach [5, 6]. Furthermore, the selection of heating element is conducted with heat transfer model [7, 8].

Methods of collecting the data to calculate the automatic fish dryer performance is done by experiments [4, 9]. To get the drying mass flow rate distribution in dryer room, a simulation using CFD is conducted [4].

2.1 Mechanical Design

In the process of automatic fish dryer design, there are some elements to be considered as conceptual design as follows:

- Sketch of the automatic fish dryer can be seen below (Fig. 1).
- The system is only used for yellowstripe scad which has 15 cm length and 4.5 cm width in average and long-jawed mackerel with 20 cm length and 6 cm width in average. The data is obtained from directly measurement of the fish.
- Heating load calculation is influenced by fish, fish palette, and heater plate while target temperature is set by 70 °C.
- The maximum mass of fish that will be dried is 2 kg which is divided to four sections and each section mass is 500 g. The amount of yellowstripe scad that can be dried is around 33 fish with 3,300 J/kg °C specific heat [10] while the amount of long-jawed mackerel is 12 fish with 3,500 J/kg °C specific heat [10].
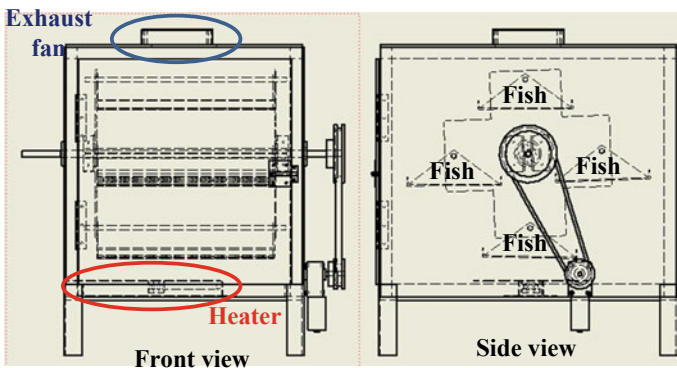
Fig. 1 Sketch of automatic fish dryer. The dimension is 400 mm (front length) × 500 mm (side width) × 420 mm (height). There are four sections of fish palette for drying process
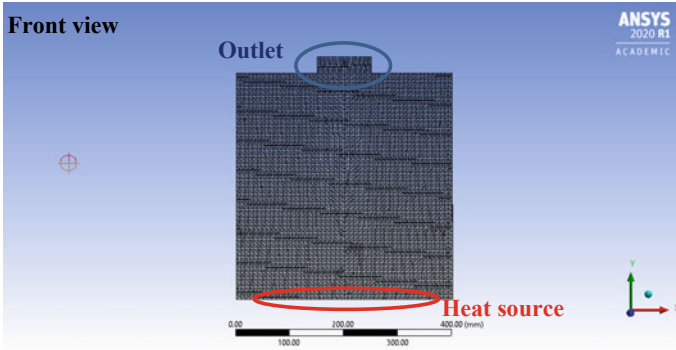
Fig. 2 Triangular computational grid of palette rotation area

- The rotation velocity of the fish palette is 30 rpm.
- The transmission system used for palette rotation mechanism is pulley and v-belt.

2.2 CFD Simulation

The geometry model for CFD simulation is the area in the middle section of prototype (palette rotation area) with 400×420 mm dimension without the palette that can describe drying mass flow rate into velocity model [11]. The computation model and solver preference are done with ANSYS Fluent (student version) 2020 R1. The mesh conducted is triangular with 5,239 nodes in the X-Y plane (2D) as shown by Fig. 2. Turbulence model for this study plays important roles in CFD analysis hence the turbulence model choice is necessary [12]. The turbulence model for palette rotation area geometry is STD k-ε which obtains convergence result. STD k-ε model is common in many turbulence models and has good performance in general flow [13]. The fluid is water-vapor which is assumed to be steady-state, ambient temperature and pressure is set to 25 °C, 1 atm respectively. The drying mass flow rate is set by 0.00419 g/s that is obtained from experiments.

3 Result and Discussion

3.1 Mechanical Design

There are some parameters to be considered in components selection and dimensions calculation such as heating load calculation, shaft calculation, electrical motor selection, bearing calculation, and calculation of pulley and v-belt transmission.

Table 1 Result of heating load calculation with setting time for 4 h

No.	Component	Variables				q (Watt)
		m (kg)	T_1 (°C)	T_2 (°C)	c_p (J/kg °C)	
1	Long-jawed mackerel	2	20	70	3,300	24.31
2	Four fish palettes (woven wire mesh—material: stainless steel 304) [14]	0.2	25	70	500	1.25
3	Heater plate (material: zinc, galvanize sheet) [15]	0.3	25	70	389.8	0.365
Total heating load (q_{total})						25.925

3.1.1 Heating Load Calculation

There are four main components for heating load calculation such as yellowstripe scad, long-jawed mackerel, fish palette, and heater plate. Sensible heat equation used in this calculation can be shown below [7, 8]:

$$q = \frac{Q}{t} = \frac{m.c_p.\Delta T}{t} \tag{1}$$

From the Eq. (1), sensible heat rate of each component can be obtained. The heat transfer model used for those components take 4 h as setting time. For the fish, heating load data will be taken from long-jawed mackerel because it has higher value than yellowstripe scad. Long-jawed mackerel have 24.31 W heating load, while yellowstripe scad have 22.92 W heating load.

From Table 1, total heating load will be multiplied with 1.25 as service factor [16], so the total heating load (q_{total}) becomes 32.406 W. Based on this calculation, the 100 W heater is selected refers to market availability. In theoretically with that heater, the drying time will be shorter becomes 0.972 h.

3.1.2 Shaft Calculation

Shaft is used as main element in palette rotation system to generate effective drying process. It has Aluminium 6061-T6 with 276 MPa for yield strength and the allowable shear stress obtained in the amount of 80.04 MPa.

Based on Fig. 3, the total torque can be calculated with friction coefficient for single row radial deep groove ball bearing in the amount of 0.0015 [17]. The total torque is obtained in the amount of 2.938×10^{-4} Nm with service factor of 1.25. Furthermore, the result of shaft bending moment calculation is 9.555 Nm with service factor of 1.25.

Then, the shaft calculation uses Guest Theory which affected by combination load: torque load and bending moment load for ductile base material [6].

Fig. 3 Free body diagram of
fish pallet rotation system.
Each point in A, B, C and D
have the same force in the
amount of 7.84 N. That
mechanism is a balance
system that makes torque
equals to zero. The available
torque is just affected by
friction force to bearing
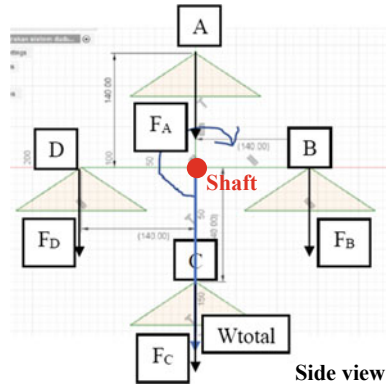
$$T_e = \sqrt{M^2 + T^2} \tag{2}$$

$$d = \sqrt[3]{\frac{16.T_e}{\pi.\bar{\tau}}} \tag{3}$$

From Eq. (2), equivalent torque (T_e) can be calculated and the result is 9.555 Nm.
Besides, from Eq. (3) the shaft diameter (d) can be obtained in the amount of
8.47 mm. Therefore, shaft with 10 mm diameter is chosen because of ease in
turning process and fulfil the design need.

3.1.3   Electrical Motor Selection

Electrical motor is chosen because of ease in installation and have appropriate
specification. The power needed to rotate the palette system when drying is
37.504 W. The most appropriate motor that fulfil that needs is electrical DC motor
with 115 W [18].

3.1.4   Bearing Calculation

Bearing used in fish palette rotation mechanism is single row radial deep groove ball
bearing 6900 type. This bearing has 2,691.04 N for allowable dynamic load [19] and
38.22 N for equivalent dynamic load that obtained from calculation of fish palette
rotation mechanism. Bearing lifetime can be calculated from equation below [6].

$$L = \left(\frac{C}{F_e}\right)^K \times 10^6 \text{ revolution} \tag{4}$$

From Eq. (4), the bearing lifetime is obtained in the amount of 3.491×10^{11} revolution.

3.1.5 Calculation of Pulley and v-Belt Transmission

Driven shaft revolution that used in palette rotation mechanism can be calculated from equation below [5].

$$\frac{n_2}{n_1} = \frac{d_1}{d_2} \tag{5}$$

From the Eq. (5) and these data: $n_1 = 160$ rpm; $d_1 = 2$ inch; $d_2 = 10$ inch, driven shaft revolution (n_2) is obtained in the amount of 32 rpm which is close to 30 rpm in initial planning condition.

Then, the linear velocity of v-belt can be calculated using equation below [5].

$$\bar{V} = \frac{\pi.d_2.n_2}{60 \times 100} \tag{6}$$

From the Eq. (6), the linear velocity of v-belt is obtained in the amount of 0.425 m/s. Then, pitch length of the v-belt can be calculated using Eq. (7) below [5].

$$L = \pi.(r_2 + r_1) + 2x + \frac{(r_2 - r_1)^2}{x} \tag{7}$$

Based on the Eq. (7) and initial planning condition for $x = 250$ mm, pitch length of the v-belt (L) is obtained in the amount of 1,019.826 mm. Pitch length of the v-belt chosen is 1,026 mm for type-A in accordance with IS: 2494–1974 standard [5].

3.1.6 Drying Time

Drying process in automatic fish dryer is assumed to be steady-state condition. Twelve long-jawed mackerels were taken as sample in an experiment which has 140 g mass for each fish before drying and were assumed to have 70% water content. The drying process was followed by palette rotation mechanism in the velocity of 30 rpm. A 100 W heater used to generate 67 °C in average for drying room temperature. The drying time was set by 1 h that close to 0,972 h from calculation at the end of Sect. 3.1.1. There must be an adjustment in drying time because in 1 h, the water content only became 62.5% (125 g).

From Table 2, to obtain 30% water content for the fish, it needs 5.3 h drying time from linear approach.

Table 2 Adjustment in drying time to obtain 30% water content

Data source	Drying time (h)	Mass before drying (g)	Water content before drying (%)	Mass after drying (g)	Water content after drying (%)
Experiment	1	140	70	125	62.5
Approach	5.3	140	70	60	30

3.1.7 Actual and Theoretical Comparison

In actual drying condition, temperature in drying room is only 67 °C while theoretically the temperature is set by 70 °C. The drying time for 67 °C has been calculated before in the amount of 5.3 h. So, when the temperature is 70 °C theoretically, the drying time becomes 5.073 h. There is temperature deviation that can be calculated using equation below.

$$\text{Relative deviation} = \left| \frac{T_{\text{actual}} - T_{\text{theoretical}}}{T_{\text{theoretical}}} \right| \times 100\% \qquad (8)$$

Based on the Eq. (8), the relative deviation of performance in actual and theoretical is 4.29%.

3.2 CFD Simulation of Drying Performance

3.2.1 Drying Mass Flow Rate

Drying mass flow rate of automatic fish dryer can be calculated theoretically using equation below.

$$\text{Drying mass flow rate} = \frac{\Delta m}{\Delta t} = \frac{m_0 - m_1}{t} \qquad (9)$$

Drying mass flow rate from long-jawed mackerel sample to reduce the water content from 70 to 30% for 5.3 h can be obtained from Eq. (9), and the drying mass flow rate is 0.00419 g/s. The main objective of the CFD simulation is to preliminary discover the heat distribution inside the system. In order to get the flow distribution that can describe the drying mass flow rate in drying room, CFD simulation of velocity is conducted as represented in Figs. 6 and 7. Analysis is focused on the water-vapor flow from inlet (assumed near the base of machine) to outlet where an exhaust fan is installed.

Figures 6 and 7 show the velocity of water-vapor flow in the middle section of prototype without palette that generated by STD k-ε model. Heat is well distributed from the heat source to each palette and sucked by the fan.

Fig. 4 Drying system of automatic fish dryer
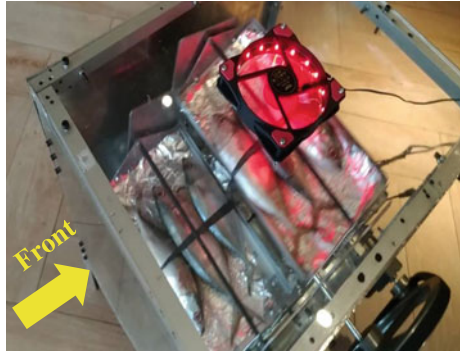
Fig. 5 Fish drying process

Fig. 6 Contour of particles velocity. The maximum value of particles velocity is 1.155×10^{-4} m/s at the outlet of automatic fish dryer
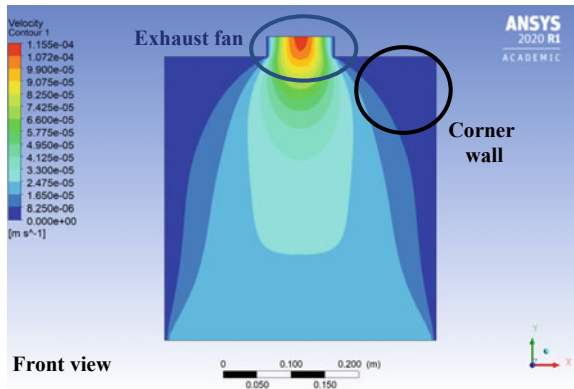
The system simulated is palette rotation area which is the most ideal place to analysis drying system performance. The simulation shows that there is water-vapor flow concentration at exhaust fan with 1.155×10^{-4} m/s for maximum particles velocity and 4.190014×10^{-6} kg/s for mass flow rate at the outlet. Furthermore,

Fig. 7 Vector of particles velocity. The particles are assumed to consist of drying mass flow rate from the fish
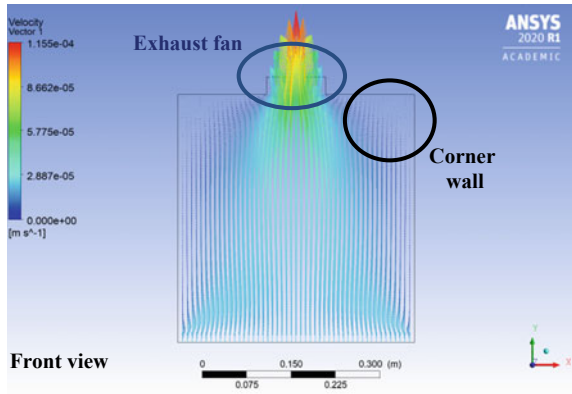
Fig. 8 Contour of total temperature without palette
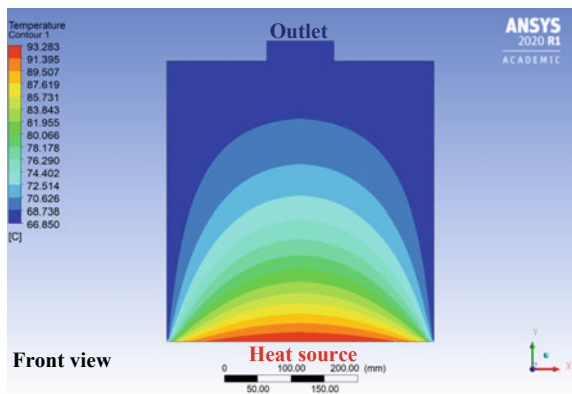
the flow distribution at corner wall area becomes obstructed which marked by the less of particles velocity in the amount of 8.25×10^{-6} m/s and it is almost 0 m/s near the wall. It implies that there is residual of water-vapor particles that accumulated at the corner wall of drying room. Therefore, a development from this study can be conducted to improve the flow distribution near corner wall by using bigger exhaust fan or adding more exhaust fans. However, the fish palette rotation mechanism can increase the water-vapor flow performance that makes drying time faster which vector of velocity can be shown in Fig. 7. It shows particles movement consists of water vapor from the fish to exhaust fan that influenced by palette rotation mechanism to increase drying performance. These CFD simulation results without the fish inside contributed as a preliminary design consideration. CFD simulation with the fish will be done in further research.

3.2.2 Effectiveness Level

Conventional drying system needs average in 2 days which can be assumed optimal drying time from 07.00 until 16.30 WIB in a day (9.5 h per day), so 2 days equals to 19 h drying. On the other hand, automatic fish dryer prototype needs 5.3 h to dry the fish that shown by Table 2. Based on this data, automatic fish dryer is 3.585 times (≈4 times) faster than conventional drying system which uses heat from the sun.

4 Conclusion

Design and analysis of automatic fish dryer is conducted to make prototype that can dry the fish by heating evenly and can be developed with larger scale and more products. The prototype can increase productivity and economic potential for coastal communities because of the effective way in drying. Furthermore, the comparison between prototype and conventional drying can be obtained. The prototype has some main design parameters to be considered, such as 100 W heater, 10 mm diameter shaft with Aluminium 6061-T6, 115 W electrical DC motor, single row radial deep groove ball bearing 6900 type, and 1,026 mm pitch length of type-A v-belt. Then, the relative deviation performance of automatic fish dryer in actual and theoretical is 4.29%. From the experiment, the prototype can dry the sample of fish (long-jawed mackerel) in 5.3 h with 0.00419 g/s for the drying mass flow rate. Besides, CFD simulation shows that there is water-vapor concentration at an exhaust fan while the flow near corner wall becomes obstructed that makes the particles accumulated. It implies that the drying performance still can be developed by using bigger exhaust or adding more exhaust fans to increase the particles velocity and makes the mass flow rate distribution more evenly when leave drying room. However, the fish palette rotation system has been effective to increase drying performance and can heat the fish evenly. This research indicates that automatic fish dryer can dry 4 times faster than conventional drying system which uses heat from the sun. Furthermore, this prototype has reasonable price for only 1.5 million Rupiah.

References

1. Rianto Y, Sukamto Y, Sunarto (2019) Laporan Tahunan Statistik: Pelabuhan Perikanan Nusantara Sungailiat pada 2018. In: Statistical Annual Report: Sungailiat Archipelago Fishing Port in 2018, Marine and Fisheries Ministry, Sungailiat
2. Amalia AP (2017) Analisis Hasil Tangkapan dan Pola Musim Penangkapan Ikan Kembung (Rastrelliger spp.) Yang Didaratkan di Pelabuhan Perikanan Nusantara (PPN) Pekalongan, Jawa Tengah. In: Analysis of Catch Result and Fishing Season Patterns for Long-Jawed Mackerel (Rastrelliger spp.) at Pekalongan Archipelago Fishing Port, Central Java. Universitas Brawijaya, Malang

3. Ekadewi AH, Philip K, Suryanty A. Desain dan pengujian sistem pengering ikan bertenaga surya. In: Design and testing fish dryer solar powered system. Universitas Kristen Petra, Surabaya

4. Romero VM, Cerezo E, Garcia MI, Sanchez MH (2014) Simulation and validation of vanilla drying process in an indirect solar dryer prototype using CFD Fluent program. Energy Procedia 57:1651–1658

5. Khurmi RS, Gupta JK (2005) A text book of machine design. Eurasia Publishing House PVT LTD, New Delhi

6. Agustinus PI (2009) Book of machine elements. Studi Program of Mechanical Engineering, Jakarta

7. Holman JP (2010) Heat Transfer Tenth Edition. McGraw-Hill

8. Yunus AC (2015) Heat and mass transfer fundamental and application, 5th edn. McGraw-Hill Educatuion, New York

9. Kuhe A, Ibrahim JS, Tuluen LT, Akanji SA (2019) Simulation od prototype active agricultural solar dryer with slit-type transpired solar collector. AZOJETE 15(3):750–761

10. EngineeringToolbox (2003) Specific heat of food and foodstuff [online]. Available: https://www.engineeringtoolbox.com/specific-heat-capacity-food-d_295.html

11. Steven D, Harto T (2019) CFD investigation of flow over a backward-facing step using an RNG k-ε turbulence model. Int J Technol 10(2):280–289

12. Steven D (2020) Reynolds number effects on swirling flows intensity and reattachment point over a backward-facing step geometry using STD k-ε turbulence model. IOP Conf Ser: Mater Sci Eng 852:012073

13. Matt C (2009) An evaluation of turbulence models for the numerical study of forced and natural convective flow in atria. Queen's University, Kingston

14. Matweb. 304 Stainless steel properties [online]. Available: http://www.matweb.com/search/datasheet.aspx?MatGUID=abc4415b0f8b490387e3c922237098da&ckck=1

15. Matweb. Zinc Properties [online]. Available: http://www.matweb.com/search/DataSheet.aspx?MatGUID=8909140a76074049809ad74d536ed606&ckck=1

16. Winsmith. Service factor selection [online]. Available: http://dpk3n3gg92jwt.cloudfront.net/domains/winsmith3d/Service_Factor.pdf

17. Amroll. Friction and frequency factors [online]. Available: https://www.amroll.com/friction-frequency-factors.html

18. Aslong. Aslong DC worm gear specification [online]. Available: http://m.aslong.net/en/pd.jsp?pid=99

19. NTN (2009) Ball and roller bearings: catalogue A-1000-XI. Equal Oppurtunity Employer, USA

Experimental Study the Effect of Reduction Temperature of Iron Ore Briquettes on Minimum Energy of Reduction

T. H. A. Furqan, Khairil, and Nurdin Ali

Abstract Analysis of the reduction kinetics of iron ore briquettes which are reduced at high temperature is determined by experimental methods to calculate the activation energy. The method used is to directly reduce the iron ore briquettes in a reduction kitchen with a temperature of 950–1250 °C and see the mass decrease that occurs. The briquettes are mixed with coal as a reducing agent and providing thermal energy and using asphalt as an adhesive with a composition of 95:0:5, 70:20:5 and, 55:40:5. The results obtained showed that the highest mass reduction occurred in briquettes with a composition of 55:40:5 at a temperature of 1250 °C and the resulting activation energy was 3.126–5.911 kJ/mol. From these results, it shows that the reduction temperature greatly affects the results of mass reduction and the minimum amount of energy required for the reduction to occur.

Keywords Briquette · Direct reduction · Activation energy

1 Introduction

The use of iron in Indonesia continues to increase every year. To suppress steel imports, the government issued regulations which are expected to be able to suppress steel imports and increase local steel production [1]. To produce iron ore as raw material for steel, it can be done in several ways. Among them, Blast Furnace (blast furnace), Direct Reduction Iron (Direct Reduction), Smelting Iron (Smelting Iron). Direct Reduction is a process used to convert pellets into sponges. The reducing gas that can be used is usually hydrogen or CO gas which can be produced by heating liquefied natural gas (LNG) with water vapor in a reactor. One of the

T. H. A. Furqan (✉) · Khairil (✉) · N. Ali
Mechanical and Industrial Engineering Department, Universitas Syiah Kuala,
Darussalam, Banda Aceh, Indonesia
e-mail: hakimalfurqan31@gmail.com

Khairil
e-mail: khairil@unsyiah.ac.id

efforts to fulfill the desire to be able to produce high quality, efficient, and can reduce the impact of emissions on the environment is by smelting iron ore using coal as a basis both as a provider of thermal energy and as a provider of reducing gas.

The direct reduction process is one of the processes to obtain sponge iron as raw material for steel making. Previously, a study on iron ore reduction by Nurdin Ali studied the reduction behavior of iron ore and low rank coal briquettes in Aceh using temperatures of 550, 650, 750 °C [2]. He et al. also conducted direct reduction research at temperatures of 650–850 °C [3]. Meanwhile Guo et al. 2017 conducted a study of direct reduction at temperatures of 850 and 1050 °C using simulations [4]. From the four studies, both experimentally and in a simulation, it shows that as the temperature increases, the reduction characteristics will get better which showed results in the form of an increase in the quality of sponge iron. Generated for each temperature rise. The use of temperatures that are getting closer to iron smelting temperature can improve the quality of sponge iron which is much better.

However, to find out the in-depth results of the reduction process, it is necessary to test the sample after the reduction process is complete to see the characteristics of the reduction process itself. Therefore, it is necessary to have research to determine the results of iron ore reduction by looking at its reduction behavior.

2 Experimental Method

2.1 Samples Preparations

The main ingredients of iron ore briquettes are iron ore and coal originating from the Aceh region. As seen in Fig. 1, iron ore and coal are ground to make the mixture evenly when it becomes briquettes and use asphalt as the adhesive. Supporting equipment is also used in the briquette-making process such as press tools, briquette molds, asphalt heaters, scales and tumbler testing tools to determine the strength of briquettes when rotated at a certain rotation.

Fig. 1 Briquette raw materials **a** iron ore, **b** coal
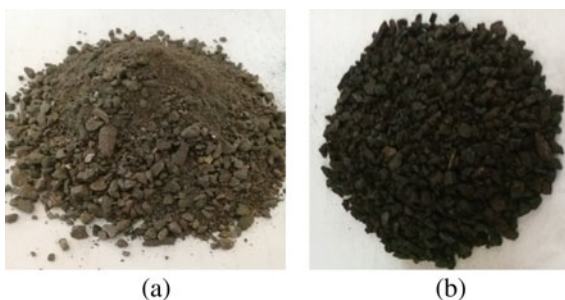
2.2 Experimental Set Up

In this test using furnace that uses LPG gas and compressed air from the compressor for the combustion process, air and controls are manually adjusted using a flowmeter. Figure 2 shows the kitchen schematic used and the description of its components is presented in Table 1.

After setting the furnace, the sample is entered. The process of mass reduction is read by the scale and recorded directly by a computer connected to the digital scale.

3 Results and Discussion

3.1 Effect of Temperature on Mass Reduction

Mass reduction was observed using a scale that is directly connected to the test sample. The mass drop is calculated using Eq. 1.
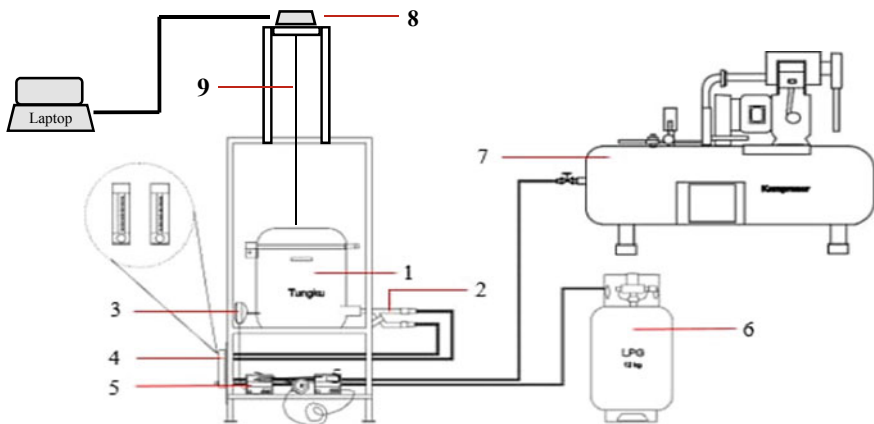
Fig. 2 Schematic of reductions furnace

	Number	Description
Table 1 Furnace description	Number	Description
	1	Furnace
	2	Burner
	3	Thermocouple
	4	Flowmeter
	5	Thermocouple display
	6	LPG fuel
	7	Compressor
	8	Digital scales
	9	Connectors from scales to briquette
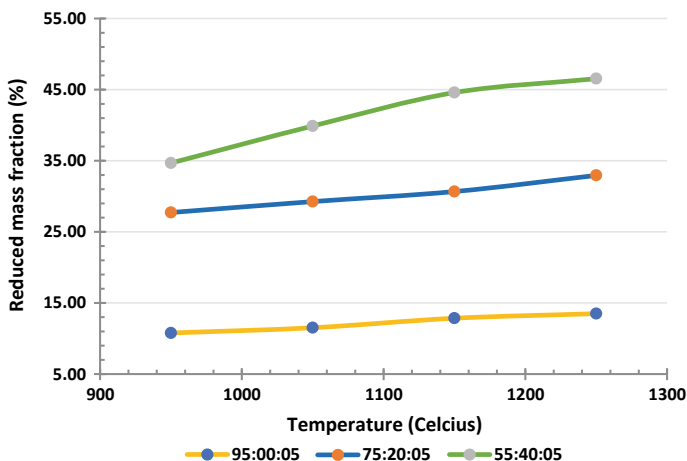
Fig. 3 The effect of mass reduction on reduction temperature

$$f = \frac{(M_0 - M_t)}{M_0} \tag{1}$$

where M_0 is the initial mass of the briquette before reduction (gr), M_t is the mass of briquette at any certain time (gr). The results obtained are the analysis of the effect of reduction temperature on the rate of mass loss as well as reduction kinetics and activation energy.

As seen in Fig. 3, the addition of coal to the briquettes gives a very significant difference. The higher the temperature and composition of the coal, the more reduction will occur.

The mixture of coal in iron ore briquettes affects the decrease in briquette mass at the time of reduction. Briquettes with a composition of 55:40:5 are the briquettes with the highest mass loss, which is 46.54% at a temperature of 1250 °C which is caused by the content of coal which has a high heating value and impurities that burn out during reduction.

3.2 Effect of Temperature on Reduction Rate

The mass reduction data were used as fractional reduction data. Previous researchers Takouda et al. [6] and McKewan [7] have determined a mathematical model for calculating fractional reduction based on chemical reaction control. To calculate α the following equation is used.

$$1 - (1 - f)^{1/3} = \alpha = kt \qquad (2)$$

This equation has also been investigated by Themelis and Gauvin who explained that the rate of reduction is controlled by the rate of reaction on the surface so that the rate of reduction towards the center of the particle will be constant with time. The results of these calculations are shown in Figs. 4, 5, 6.
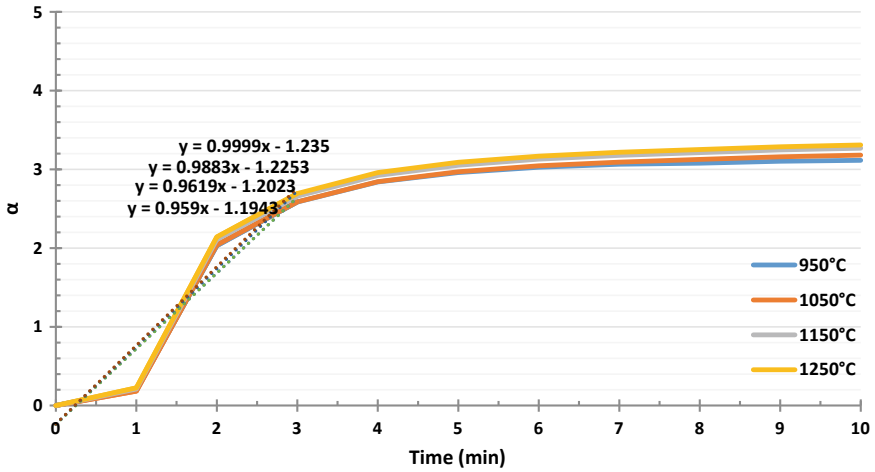
Fig. 4 The ratio of α to time for 95:0:5
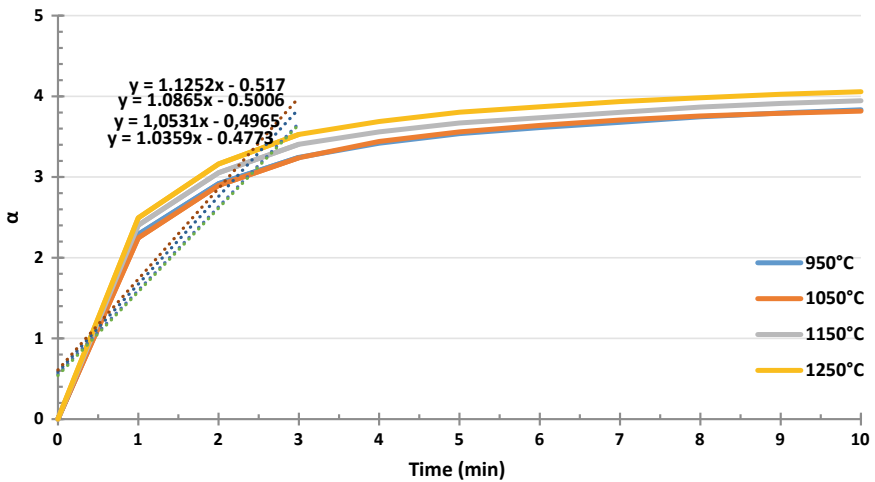
Fig. 5 The ratio of α to time for 75:20:5
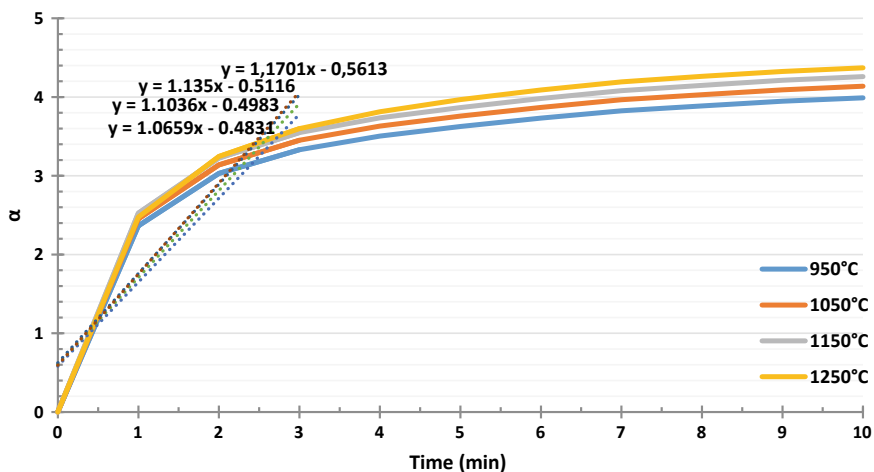
Fig. 6 The ratio of α to time for 55:40:5

In Fig. 4, we can see that the briquette sample needs a little time to start reacting at the initial stage of reduction, this is because the composition of the briquette does not contain too many volatile substances, however, after a slightly uniform combustion occurs in the next minute, the fast reduction process is normal. The resulting linear line shows the value of x which is not up to 1, this will affect the placement of the graph when calculating the activation energy values.

In contrast to the 95: 0: 5 composition in Fig. 4, fast reduction occurs immediately in the early minutes of the reduction process at compositions of 75:20:5 and 55:40:5 (Figs. 5, 6), this occurs because of the more volatile matter that contained in the briquette which is able to reduce quickly, the substance comes from coal which is mixed into the briquette.

From the results of the straight line equation, it can be seen in Fig. 3 that the rate constants are obtained for each composition (Table 2).

The temperature difference affects the rate of reduction in briquettes during the reduction process. The reduction process of briquettes with a composition of 55:40:5 at a temperature of 1250 °C is able to produce the highest reduction rate constant of 1.1701.

3.3 Activation Energy

The Arrhenius equation is used to calculate the minimum energy required for reduction [5].

Table 2 Rate constants for each test temperature

Temperature (K)	Rate constants	ln k	1/T
95:0:5			
1223	0.9590	−0.0418642	0.00082
1323	0.9619	−0.03884478	0.00076
1423	0.9889	−0.01116206	0.00071
1523	0.9999	−0.00010001	0.00066
75:20:5			
1223	1.0359	0.035270614	0.00082
1323	1.0531	0.051738195	0.00076
1423	1.0865	0.082961521	0.00071
1523	1.1252	0.117960798	0.00066
55:40:5			
1223	1.0659	0.063819513	0.00082
1323	1.1036	0.098577563	0.00076
1423	1.1350	0.126632651	0.00071
1523	1.1701	0.157089215	0.00066
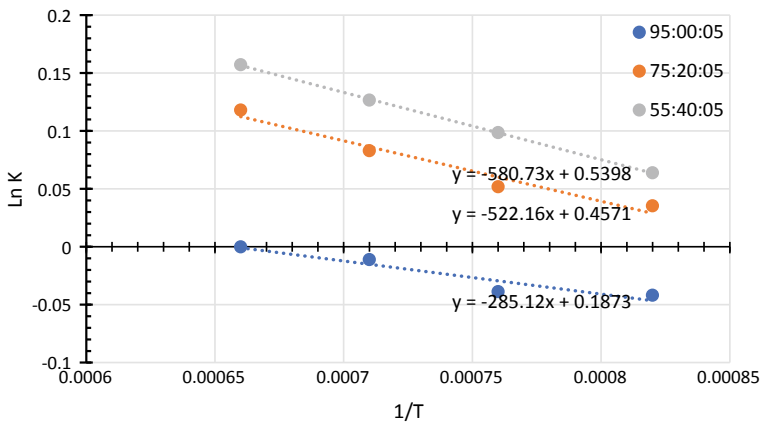
Fig. 7 Arrhenius plots (ln k vs 1/T) for each composition

$$\ln k = \ln A - \frac{E_a}{R_u T} \tag{3}$$

where E_a is activation energy (kJ/mol), R_u is the universal gas constant, T is the absolute temperature (K). The plot of ln k versus 1/T values obtained in Fig. 4 are used to find the activation energy value. Based on Table 2, the arrhenius plot is obtained at a temperature of 950–1250 °C for each composition as shown in Fig. 7.

Table 3 Activation energy value of iron ore briquettes

No	Composition (Iron ore:coal:asphalt)	Activation energy (kJ/mol)
1	95:00:5	2370
2	75:20:5	4341
3	55:40:5	4828

The slope value in the image shows different variations, for the 95:0:5 composition it is in the minus part of the graph, this has also been obtained in previous studies [2]. Based on the previous studies this has no effect on the calculation of the activation energy.

The straight line equation obtained is used to calculate the amount of activation energy. Table 3 shows the activation energy values obtained for each composition.

The results showed that the activation energy of iron ore briquettes was 2370–4828 kJ/mol at a temperature of 950–1250 °C. When coal is added to briquettes, the required activation energy is increases. The activation energy value is lower than Runsheng et al. [8], which reduced it by using coal at a temperature of 570–740 °C which obtained an activation energy value of 35.2 kJ/mol. Meanwhile Guo et al. [3] conducted research at a temperature of 1050 °C which produced an activation energy of 97.53 kJ/mol. Qiang et al. [9] conducted research using a temperature of 700–1000 °C to obtain an activation energy value of 120.58 kJ/mol.

4   Conclusion

The mixture of coal in iron ore briquettes affects the decrease in briquette mass at the time of reduction. Briquettes with a composition of 55:40:5 are the briquettes with the highest mass loss, which is 46.54% at a temperature of 1250 °C which is caused by the content of coal which has a high calorific value and impurities that burn out during reduction. The temperature difference affects the rate of reduction in briquettes during the reduction process. The reduction process of briquettes with a composition of 55:40:5 at a temperature of 1250 °C is able to produce the highest reduction rate constant of 1.1701. The difference in composition and temperature results in varying activation energy values. The greater the amount of coal contained, the greater the minimum energy required for the reduction reaction. The highest activation energy value occurred at the composition 55:40:5 at 4828 kJ/mol and the lowest at the composition 95:0:5 at 2370 kJ/mol.

References

1. Permendagri (2018) Ketentuan Impor Besi atau Baja, Baja paduan, dan Produk Turunannya, vol 110. Indonesia
2. Ali N, Khairil, Saputra M (2018) Perilaku Reduksi Briket Bijih Besi dan Batubara Peringkat Rendah Aceh. Jurnal Rekayasa Kimia dan Lingkungan, 51–59
3. He S, Sun H, Hu C, Li J, Zhu Q, Li H (2017) Direct reduction of fine iron ore concentrate in a conical fluidized bed. Powder Technol 161–168
4. Guo D, Li Y, Cui B, Chen Z, Luo S, Zhu H, Hu M (2017) Direct reduction of iron ore/biomass composite pellets using simulated biomass derived syngas: experimental analysis and kinetic modelling. Chem Eng J 822–830
5. Khairil (2013) Buku ajar Teknik Pembakaran Bahan Bakar Padat. Syiah Kuala University Press, Banda Aceh
6. Takuoda M, Yoshikoshi H, Ohtani M (1973) Kinetic of the reduction of iron ore. Transactions ISIJ 13:350–363
7. McKewan WM (1960) Kinetics on iron oxide reduction. Transa Metall Soc AIME 2–6
8. Runsheng X, Bowen D, Wei W, Johannes S, Zhengliang X (2018) Effect of iron ore type on thermal behaviour and kinetics of coal-iron ore briquettes during coking. Fuel Process Technol 11–20
9. Qiang H, Dingding Y, Yingpu X, Youjian Z, Haiping Y, Yingquan C, Hanping C (2018) Study on intrinsic reaction behaviour and kinetics during reduction of iron ore pellets by utilization of biochar. Energy Convers Manage 1–8

Techno-Economic Analysis for Energy Fulfillment in the University Farm

Maidi Saputra and Hamdani Umar

Abstract Renewable energy is energy sources that will not run out naturally. The using of a hybrid generating system can be a solution to increase the using of renewable energy sources in the electricity sector. The purpose of this study is the modeling of hybrid system power plants and determining the most optimal system configuration according to cost calculations. The electrical energy requirement in an agricultural unit is the electricity requirement in the compost house and the energy to run pumps for irrigation on agricultural land that the average electricity consumption per hour is 165.44 kWh/d, the average electricity demand is 6.89 kW, and a peak load during usage is 20.46 kW. The average radiation value is 4.71 kWh/m^2/day, the level of brightness is at an average value of 0.472 and the average wind speed is 3.30 m/s. Total Net Present Cost (NPC) value is \$211,894.30 and a Cost of Energy (CoE) is \$0,424 which is the average electricity generation each month by each component consists of solar cells and generators are 21,264 kWh/yr (47.1%) and 23,866 kWh/yr (52.9%), respectively.

Keywords Renewable energy · Hybrid systems · Techno-Economic analysis · University farm

1 Introduction

Renewable energy is energy sources that will not run out naturally. Renewable energy comes from natural elements that are available on the surface of the earth in large numbers, such as the sun, wind, streams, oceans, plants, and so forth [1].

M. Saputra (✉)
Department of Mechanical Engineering, Teuku Umar University,
Kampus Alue Peunyareung, Aceh 23615, Indonesia
e-mail: maidisaputra@utu.ac.id

H. Umar
Department of Mechanical Engineering, Universitas Syiah Kuala,
Jl. Tgk. Syech Abdul Rauf No. 7, Darussalam, Banda Aceh 23111, Indonesia

Hybrid system power generation combines several generating systems, both from renewable sources and those from fossils [2, 3]. The using of hybrid generating system can be a solution to increase the using of renewable energy sources in the electricity sector, as well as being an advantage in the future [2].

The using of electrical energy at a university farm is for compost houses and pump operations for irrigation/sprinklers and other needs, with a total of about 21.4 kW.

1.1 Absorption of Solar Radiation by PV Modules

Solar panels that produced the electrical energy are related to the amount of sunlight that can be received by the solar panels. The data of sunlight intensity that was measured or was found in the meteorological and geophysical board can only provide the amount of energy that was absorbed by the solar panel for horizontal position, but in reality, the position of solar panel installation gave a tilted angle to achieve optimal values [4]. The Perez model gives:

$$\varepsilon \equiv \frac{\left[(G_{dh} + G_{bh})/G_{dh} + 1.041\theta_z^3\right]}{\left[1 + 1.041\theta_z^3\right]} \tag{1}$$

$$\Delta \equiv \frac{G_{dh}.m}{G_{on}} = \frac{G_{dh}.m}{G_0/\cos\theta_z} = \frac{G_{dh}}{G_0} \tag{2}$$

where m is air mass.

The coefficient of brightness reduction and brightness coefficient, respectively F1 and F2 are functions of sky clarity. This relationship is referred as the Perez coefficient and the use of the Perez coefficient is given in Table 1.

$$F_1 = F_{11}(\varepsilon) + F_{12}(\varepsilon) \cdot \Delta + F_{13}(\varepsilon) \cdot \theta_z \tag{3}$$

$$F_2 = F_{21}(\varepsilon) + F_{22}(\varepsilon) \cdot \Delta + F_{23}(\varepsilon) \cdot \theta_z \tag{4}$$

Table 1 The Perez model coefficients for solar irradiance calculation

ε	F11	F12	F13	F21	F22	F23
1–1.065	−0.008	0.588	−0.062	−0.060	0.072	−0.022
1.065–1.23	0.130	0.683	−0.151	−0.019	0.066	−0.029
1.23–1.5	0.330	0.487	−0.221	0.055	−0.064	−0.026
1.5–1.95	0.568	0.187	−0.295	0.109	−0.152	−0.014
1.95–2.8	−0.873	−0.392	−0.362	0.226	−0.462	0.001
2.8–4.5	1.132	−1.237	−0.412	0.288	−0.823	0.056
4.5–6.2	1.060	−1.600	−0.359	0.264	−1.127	0.131
6.2–	0.678	−0.327	−0.250	0.156	−1.377	0.251

1.2 Wind Energy Conversion System

Several factors affect the output power which was generated by the wind turbine. The factors that influence the output power are the efficiency of aerodynamic power, mechanical transmission ηm, and the efficiency of electrical energy conversion ηg. Besides, the power of the wind turbine is also influenced by the condition of the area where the wind turbine is installed, as well as the height of the hub which shows the position of the generator against the ground surface [4].

The equation that gives the calculation result of the installed wind turbine power is explained by:

$$P_W(v) = \begin{cases} P_R \cdot \frac{v - v_C}{v_R - v_C} & (v_C \leq v \leq v_R) \\ P_R & (v_R \leq v \leq v_F) \\ 0 & (v \leq v_C \text{ and } v \geq v_F) \end{cases} \tag{5}$$

where PR is the rated electrical power; v_C is the cut-in wind speed; v_R is the rated wind speed; and v_F is the cut-off wind speed.

Wind speed profile has greatly affected the power of the wind turbine which was produced. This wind speed profile is strongly influenced by the vertical profile of the wind speed in a homogeneous flat terrain region, such as desert, grassland, flat field, and others. The following equation gives the basic shape of the vertical profile of the wind speed [4]:

$$\frac{v}{v_r} = \left(\frac{z}{z_r} \right)^\alpha \tag{6}$$

where v is the wind speed at hub height z (the height of the turbine above the ground), m/s; vr is the wind speed measured at the reference height zr, m/s; α is the power law exponent.

1.3 Hybrid Optimization Model for Electric Renewables (HOMER)

Hybrid Optimization Model for Electric Renewables (HOMER) is a software developed by the US National Renewable Energy Laboratory (NREL) to design micro power systems and to facilitate comparison of power generation technology [2, 3, 5]. HOMER models are the power of system based on physical behavior and overall costs, where the total overall costs are installation and operation costs [6].

Previous studies have provided results and conclusions about the HOMER program in the development of the hybrid system [1, 2, 3, 7, 8].

The purpose of this study is a modeling of hybrid system power plants and determining the most optimal system configuration according to cost calculations.
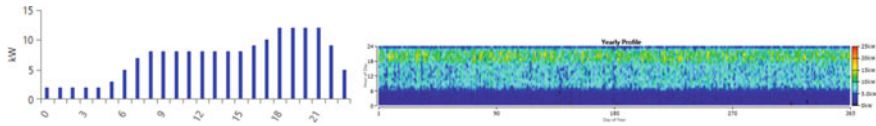
Fig. 1 Daily average load profile and yearly average load profile

2 Research Methods

2.1 Load and Energy Resources

2.1.1 Electrical Load

Basically, the necessity for electrical energy in agricultural land is not so large compared to the necessity for electrical energy in the housing sector both in rural and urban areas. The electrical energy requirement that must be met in an agricultural unit is the electricity requirement in the compost house and the energy to run pumps for irrigation on agricultural land. Daily and monthly energy requirements are shown in Fig. 1.

The annual electrical energy requirements at the university farm that are shown in Fig. 1 show that the average electricity consumption per hour is 165.44 kWh/d, the average electricity demand is 6.89 kW, and a peak load during usage is 20.46 kW. Based on the usage profile for a year shows that the usage of electrical energy in the university farm unit increased at 18:00 because at that time all equipment worked optimally, such as pumps and sprinkles used for watering plants and water distribution to agricultural land.

2.1.2 Solar Global Horizontal Irradiance (GHI) Resource

The Global Solar Horizontal Irradiance (GHI) Resource shows daily radiation data for a year at the study site. This data also shows the level of sun brightness index which is the necessary information about the availability of solar radiation on the earth's surface and change in atmospheric conditions [8, 9]. From the data on the potential of solar radiation and the level of brightness in a year, as that is shown in Fig. 2 shows that the average radiation value is 4.71 kWh/m^2/day, with the highest radiation value being found in February of 5180 kWh/m^2/day and the lowest radiation value being found in November of 4230 kWh/m^2/day. The brightness value of the sun at intervals of a year shows the level of brightness is at an average value of 0.472 with the highest brightness value in February of 0.513 and the lowest brightness value in October of 0.433. From the data of radiation value and brightness level given, it shows that there is a linear correlation between the level of solar radiation with the level of brightness that occurs in the same month.
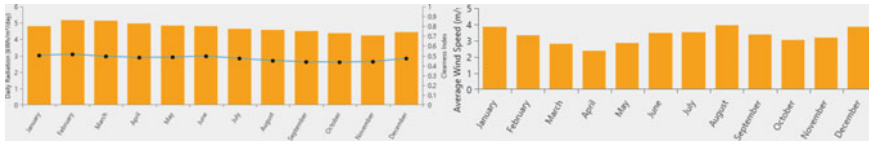
Fig. 2 Monthly average solar global horizontal irradiance (GHI) data and monthly average wind speed data

2.1.3 Wind Resource

Wind speed data shows monthly wind speed for a year. From the data that is shown in Fig. 2 shows that the average wind speed is 3.30 m/s. The highest wind speed in August is 3930 m/s and the lowest wind speed in April is 2380 m/s. Measurement of wind speed is done with the parameters of altitude above sea level is 0 m and the height of the anemometer at the time of measurement is 50 m. The value of the variation of wind speed to height for the wind speed profile is taken logarithmic and surface roughness length is 0.01 m [10, 11]. The advanced parameter that gives a Weilbull K value is 2, an autocorrelation factor is 0.85 and the diurnal pattern strength is 0.25 (values are in the range of 0.0–0.40 [10, 11]).

2.1.4 Fuel Resource

In this study, the diesel fuel which is taken has the properties, it appears that the Lower Heating Value of the diesel fuel is 43.20 Mj/kg, the density of the diesel fuel is 820 kg/m^3, the carbon content of the diesel fuel is 88% and the sulfur content of diesel fuel is 0.4%. The purchase price of diesel fuel at the time of doing this research and the additional possibility of inflation due to price changes are caused by various factors that equal to 0.7 $/L.

2.2 Hybrid System Components

Hybrid system components are designed to consist of the flat-plate PV, wind turbines, generators, batteries and converters; it is shown in Fig. 3. From the hybrid system design, it can be seen that the system is designed to meet off-grid generating systems for wind turbines, PV and generators. This hybrid system aims to meet the increasing number of energy that comes from a renewable energy system, then generators are used as energy reserves if energy from renewable sources is insufficient to produce energy. Each component included in the hybrid system is explained below.

Fig. 3 Hybrid system schematic
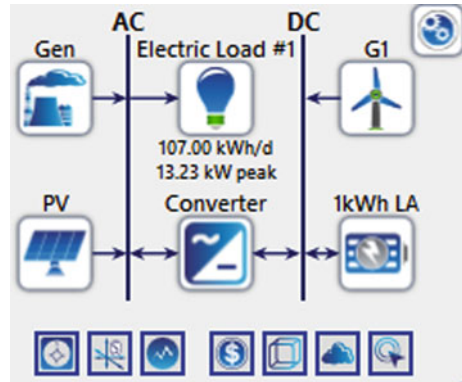
2.2.1 Wind Turbine

In this study, the selected wind turbine is Generic type 1 kW with the abbreviation G1 and the power capacity is 1 kW. For the value installed wind turbine costs that are for the purchase of one wind turbine unit is $7,000.00, the cost of replacing the turbine when it has expired is $7,000.00, and operational and maintenance value is $140.00 per year. The operating life of the installed wind turbine is around 20 years and the height of the wind turbine tower against the ground is 17 m.

The installed wind turbine power output converts energy from the wind speed which is received by the wind turbine. Wind turbines generate power based on the air velocity that received and it is shown in Fig. 4. From the picture, it can be seen that the Generic 1 kW type wind turbine provides increased power at wind speeds of 10 m/s, and the turbine power starts to decrease at the prevailing wind speed of 15 m/s, this value applies with the assumption that air density is at standard conditions.
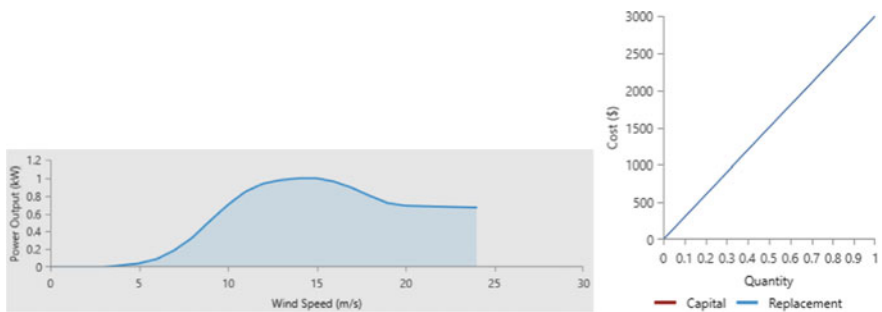
Fig. 4 Wind turbine power curve and cost curve

2.2.2 Photovoltaic

In this study, a flat plate type solar panel is used in combination with wind turbines and generators to meet the electrical energy needs on agricultural land. The name of the solar panel is Generic flat-plate PV, and the current capacity is 1 kW. The installation cost required for 1 kW solar panel is $3,000.00, the replacement cost if it has reached the usage age limit for 25 years that is $3,000.00, and operating costs and maintenance are $10.00 per year.

2.2.3 Generator

The use of generators in this study aims to provide enough energy needed in the University farm that is equal to 21.4 kW. Energy generation from renewable energy sources does not guarantee the adequacy of the energy generated, because solar panel generation systems cannot generate electricity at night and the energy from wind turbines is very dependent on the availability of wind energy in nature. The electric generator used is auto size generator type, fuel type is diesel, the price is 0.7 $/L, and it has properties such as Lower Heating Value of 43.2 Mj/kg, Density of 820 kg/m^3, the carbon content of 88%, and the sulfur content of 0.4%. The cost of generators required with a capacity of $ per kW consists an installation cost of $500.00, replacement costs if a usage period of 15,000.00 h has been reached $500.00, and operational and maintenance costs are $0.030.

2.2.4 Storage Batteries

Batteries are used meeting electrical energy needs when electricity supply cannot be directly from the available energy source. Batteries are used storing electrical energy, which is generated by generating sources, such as wind turbines, solar panels, and generators. In this research, the type of battery used is Generic 1 kWh Lead Acid, with battery properties are a nominal voltage of 12 V, a nominal capacity of 1 kWh and a maximum capacity of 83.4 Ah. The cost required per 1 unit of battery consists an installation fee of $300.00, replacement costs if a life span of 10 years has been reached of $240.00, and operational and maintenance costs are $10.00 per year.

2.2.5 Converter

A converter is used as a modifier of DC power, which is generated by renewable energy sources into the form of AC power. In this study, the type of converter used is a system converter with the cost required for a capacity of 1 kW, including installation costs is $300.00, replacement costs if a time limit for the use of 15 years has been reached for $300.00. The efficiency of the inverter and rectifier are 95% and 90%, respectively.

3 Results and Discussions

3.1 Sensitivity Cases Analysis

Sensitivity cases do a combination of variable sensitivity values. When we determine the value of some wind speed and several values of the price of fuel, sensitivity cases will multiply each value according to the number of combinations of each value. Then Homer will do the optimization process for all the entered sensitivity values. In the sensitivity analysis, the value of the price of diesel fuel and average wind speed is taken into consideration in determining the configuration of the system. The value of the price of diesel fuel which was taken at the time of the design of this system was 0.7 $/L, and the average value of the entered wind speed was 3.30 m/s. for the proses of sensitivity analysis, the price value of diesel fuel was taken varies which is 0.35; 0.70 and 1.40 $/L, and the wind speed values were taken vary, namely 3.00; 3.30 and 8.00 m/s. The sensitivity analysis results are shown in Fig. 5, showing there are variations in the optimization results of each sensitivity value; there is the amount of power generated from each type of power plants, such as solar cells, wind turbines, and generators. The resulting costs show that the lowest Cost of Energy (CoE), Net Present Cost (NPC), Operating Cost and Initial Capital values occur in the combination of sensitivity values for diesel fuel prices of 0.350 $/L and average wind speeds of 3.30 m/s, as well as the most significant cost incurred in the sensitivity analysis for diesel fuel prices of 1.40 $/L and average wind speeds of 8.00 m/s.

The results of the sensitivity analysis are given in the form of a surface plot graph which is shown in Fig. 5, showing that the sensitivity variable is given by the y-axis is the average wind speed (m/s), and the x-axis gives the price of diesel fuel ($/L). The value of the variable was plotted in the form of a surface graph for the Cost of Energy (CoE) value that is combined with the Total Net Present Cost (NPC) value.

3.2 Optimization Results

Optimization results are given for system configuration with a variable value of diesel fuel price sensitivity of 0.700 $/L, and average wind speed is 3.30 m/s that is
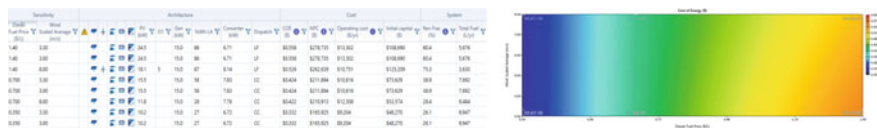
Fig. 5 Sensitivity cases analysis result and surface plot graph for cost of energy (CoE) with superimposed total net present cost (NPC)

PV (kW)	G1	Gen (kW)	1kWh LA	Converter (kW)	Dispatch	COE ($)	NPC ($)	Operating cost ($/yr)	Initial capital ($)	Ren Frac (%)	Total Fuel (L/yr)
15.5		15.0	58	7.83	CC	$0.424	$211,894	$10,816	$73,629	38.9	7,692
14.8	1	15.0	57	7.73	CC	$0.443	$221,341	$11,192	$78,267	37.7	7,852
		15.0	23	3.23	CC	$0.475	$237,363	$17,366	$15,370	0	14,699
	1	15.0	23	3.25	CC	$0.494	$246,650	$17,544	$22,376	0	14,655
		15.0			CC	$0.536	$267,379	$20,329	$7,500	0	17,477
0.0131		15.0			CC	$0.536	$267,384	$20,327	$7,539	0	17,473
0.144		15.0		0.104	CC	$0.555	$276,984	$20,531	$14,531	0	17,456
0.144	1	15.0		0.102	CC	$0.555	$277,052	$20,502	$14,963	0	17,413
54.3			213	15.9	CC	$0.666	$321,294	$7,022	$231,527	100	0
58.5	1		192	14.2	CC	$0.698	$336,597	$7,216	$244,350	100	0

Architecture — Cost — System

Fig. 6 Optimization system analysis results

shown in Fig. 6. The optimization results give an order based on the lowest value of the Total Net Present Cost (NPC) and Cost of Energy (CoE), which is a total Net Present Cost value of $211,894.30 and a Cost of Energy of $0,424. The architecture systems which are obtained from the optimization of many components are a generator of 15.0 kW, a solar cell of 15.5 kW, a battery of 15 strings, a converter of 7.83 kW, and the generating method of charging cycle.

The cost summary provides total Net Present Cost values and Annual cost values for each component, such as Autosize Genset, Generic 1 kWh Lead Acid, Generic flat-plate PV, and Converter systems. The total Net Present Cost and the Annual cost which are the optimization results of the system are $211,894 and $16,576, respectively, as shown in Fig. 7. The types of costs that are shown in the cost summary diagram consist a Capital cost, Operation costs, Replacement costs, Salvage costs and Resource cost. Capital cost on the value of the Net Present Cost and the Annual cost gives each a value of 34.75%, respectively, based on the total costs required. This cost shows that the capital cost is a value that is very important to be prepared and it becomes the basis for system development.

The average electricity generation each month by each component consisting of solar cells and generators are 21,264 kWh/yr and 23,866 kWh/yr, respectively. The color code shows the orange color as the value of power which was generated by a solar cell that is 47.1% and the green color as the value of power which was generated by a generator is 52.9%, as shown in Fig. 7. From the image data which was provided shows that the power generation which was generated by the generator having a high value compared to the generation of power which was generated by solar cells, this is influenced by less solar radiation during power
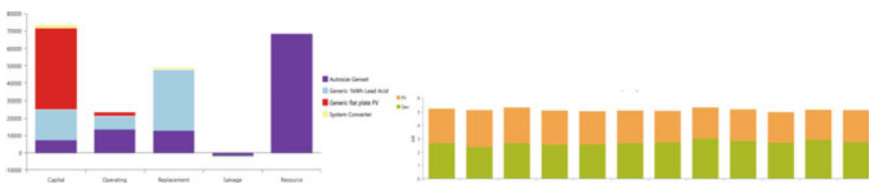
Fig. 7 Cost summary by cost type and monthly average electric production

generation. The yearly power consumption which was required by the university farm is 39,055 kWh/yr for AC power. The power which was generated by the system is 45,130 kWh/yr, so there is excess electricity that can be stored in the battery by 1882 kWh/yr or by 4.17%.

4   Conclusion

This study aims to analyze the Techno-Economic Analysis for Energy Fulfillment at the University Farm, which is carried out by modeling a hybrid system of power plants and determining the most optimal system configuration according to cost calculations. The annual electrical energy requirement as average electricity consumption per hour is 165.44 kWh/d. Global Solar Horizontal Irradiance (GHI) Resource shows that the average radiation value is 4.71 kWh/m^2/day. Wind speed data shows monthly wind speed for a year that the average wind speed is 3.30 m/s. The sensitivity analysis results show variations in the optimization results of each sensitivity value; there is the amount of power generated from each type of power plants, such as solar cells, wind turbines, and generators. Optimization results are given for system configuration with a variable value of diesel fuel price sensitivity of 0.700 $/L, and average wind speed is 3.30 m/s. Total Net Present Cost value is $211,894.30 and a Cost of Energy is $0,424 which is obtained from the optimization of many components are a generator of 15.0 kW, a solar cell of 15.5 kW, a battery of 15 strings, a converter of 7.83 kW, and the generating method of charging cycle. The average electricity generation each month by each component consists of solar cells and generators are 21,264 kWh/yr (47.1%) and 23,866 kWh/yr (52.9%), respectively. The yearly power consumption which was required by the university farm is 39,055 kWh/yr for AC power and the power which was generated by the system is 45,130 kWh/yr, so there is excess electricity that can be stored in the battery by 1882 kWh/yr or by 4.17%.

References

1. Lund H (2007) Renewable energy strategies for sustainable development. Energy 32(6):912–919. https://doi.org/10.1016/j.energy.2006.10.017
2. Shahzad MK, Zahid A, Rashid T, Rehan MA, Ali M, Ahmad M (2017) Techno-economic feasibility analysis of a solar-biomass off grid system for the electrification of remote rural areas in Pakistan using HOMER software. Renew Energy 106:264–273. https://doi.org/10.1016/j.renene.2017.01.033
3. Sen R, Bhattacharyya SC (2014) Off-grid electricity generation with renewable energy technologies in India: an application of homer. Renew Energy. https://doi.org/10.1016/j.renene.2013.07.028
4. Yang H, Lu L, Zhou W (2007) A novel optimization sizing model for hybrid solar-wind power generation system. Sol Energy 81(1):76–84. https://doi.org/10.1016/j.solener.2006.06.010

5. HOMER 404
6. Okonkwo EC, Okwose CF, Abbasoglu S (2017) Techno-economic analysis of the potential utilization of a hybrid PV-wind turbine system for commercial buildings in Jordan. Int J Renew Energy Res 7(2):908–914
7. Bai S, Rao KVS (2014) Design and integration of solar-biomass hybrid energy system for drip irrigation pumping. J Chem Pharm Sci 247–248
8. Adaramola MS, Agelin-Chaab M, Paul SS (2014) Analysis of hybrid energy systems for application in southern Ghana. Energy Convers Manag 88(2014):284–295. https://doi.org/10.1016/j.enconman.2014.08.029
9. Cotfas, DT, Cotfas PA, Kaplani E, Samoila C (2014) Monthly average daily global and diffuse solar radiation based on sunshine duration and clearness index for Brasov, Romania. J Renew Sustain Energy 6(5). https://doi.org/10.1063/1.4896596
10. Askari IB, Ameri M (2012) Techno-economic feasibility analysis of stand-alone renewable energy systems (PV/bat, wind/bat and hybrid PV/wind/bat) in Kerman, Iran. Energy Sources Part B Econ Plan Policy 7(1):45–60. https://doi.org/10.1080/15567240903330384
11. Akinyele D, Belikov J, Levron Y (2018) Challenges of microgrids in remote communities: a STEEP model application. Energies 11(2):1–35. https://doi.org/10.3390/en11020432
12. Technology roadmap solar photovoltaic energy. Current

Thermal Performance of a Heat-Pipe Evacuated-Tube Solar Collector

Wayan Nata Septiadi, I. Ketut Gede Wirawan, I. Putu Agus Saskara Yoga, Gerardo Janitra Puriadi Putra, and Sulthan Alif Ramadhan Lazuardy

Abstract The heat pipe solar water heater utilizes an evaporator to capture heat which is then used to heat water in the condenser section. The greater the heat that is able to be absorbed on the evaporator, can improve the overall performance of the solar water heater. Fins are added to the evaporator to increase the heat absorption area, but the shape of the fins can also affect the amount of heat absorbed. This research was conducted to determine the effect of fin shape on heat absorption in the evaporator section. Fins on the evaporator are made in a circular and flat shape with a width of 43 mm, a length of 516 mm for a flat fin and a diameter of 43 mm totaling 50 for a circular fin. From the test results it was found that the circular fin can reduce thermal resistance 43.48% greater than the flat fin and 9.89% of the solar water heater heat pipe without fins.

Keywords Heat pipe · Vacuum tube · Solar collector

1 Introduction

In general, the energy used in various human activities is energy that comes from fossils. In fact, fossil fuel combustion can cause serious health and developmental harms through its emission of carbon dioxide (CO_2) which is toxic for humans and the major pollutant of climate change [1]. In Indonesia for example, Surabaya is one

W. N. Septiadi (✉) · I. K. G. Wirawan
Department of Mechanical Engineering, Udayana University, Kampus Bukit Jimbaran, Badung, Bali 80361, Indonesia
e-mail: wayan.nata@gmail.com; wayan.nata@unud.ac.id

I. P. A. S. Yoga
Master Program of Mechanical Engineering, Udayana University, Kampus Sudirman, Denpasar, Bali, Indonesia

G. J. P. Putra · S. A. R. Lazuardy
Bachelor Program of Mechanical Engineering, Udayana University, Kampus Bukit Jimbaran, Badung, Bali, Indonesia

of the most populated and polluted city, second only to Jakarta. The main air pollutants found in Surabaya is carbon monoxide (CO), lead (Pb), nitrogen oxyde (NO_2), ozone (O_3), particulate matter (PM) and sulfur dioxide (SO_2) [2]. This pollutant mainly produced by vehicle engines, industrial activity and diesel electricity generators.

Indonesia is a tropical country in equator. Solar energy has enough potential to generate electrical energy since Indonesia has average sunshine of 6–7 h per day and can be utilized through solar panel for electrical energy for 5–6 h a day [3]. One of the uses of sunlight is as a source of electricity. Sunlight is also used as an energy source in heating water, both hot water in households and hot water in hotels using a solar water heater [4].

The solar water heater that is widely used is a solar water heater conventional where the working fluid is circulating in the solar collector using a pump so that it still uses electrical energy, which mostly comes from fossil energy. To reduce the use of electrical energy sourced from fossils, many have been developed solar water heaters using evacuated tube collectors that utilize natural fluid circulation. Because the circulation of the working fluid in the evacuated tube collectors only takes advantage of the effect of gravity and the vapor and liquid trajectory on the path, which causes dryness and the collector becomes malfunctioning [5].

To solve the problem of fossil energy, a heat pipe finned with the axis of the capillary developed as a tube was collector tube for solar water heater. The capillary axis is a porous medium that can separate the vapor path leading to the condenser and the liquid passage leading to the evaporator, where the capillary axis is one of the factors that greatly determines the performance of the heat pipe which of course will also affect the performance of the solar water heater [6].

According to N. Putra, et al., the development of a heat pipe with a capillary axis is *screen mesh* still not optimal because the *screen mash* has low capillarity so that the working fluid circulation is not optimal which results in the transfer of heat to the condenser is also not optimal. In addition, the collector is only a pipe cylinder, so that a lot of sunlight is still overlooked due to the limited area of the sun's heat catchment [7].

The research of solar collectors is currently focused on innovation and modifying current solar collector. For example the evacuated tube solar collector with u-tube [8], evacuated tube solar collector based on mini channels [9], evacuated tube solar collector with a variety of absorber tube shape [10], and even incorporating some technology into a solar collector such as nanofluid [11, 12] and phase change material [13, 14].

2 Experimental Setup

The solar collector is made using a copper heat pipe with a diameter of 10 mm length 700 mm. The insulator part is made using a glass tube with the size of the outer diameter is 60 mm and a length of 600 mm. This tube is closed with a plange
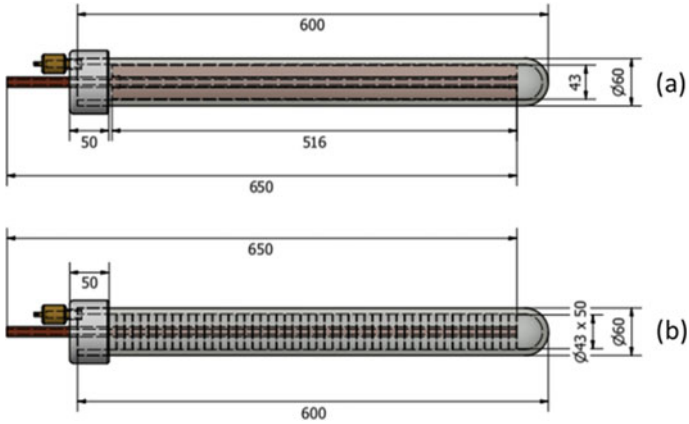
Fig. 1 Flat fin (**a**) and circular (**b**) heat pipe

equipped with a vacuum valve as shown Fig. 1. This solar collector section will be fitted into a water heating system based on finned heat pipes.

This water heating system consists of 4 (four) tubes, each of which contains a heat pipe. The evaporator part of the heat pipe inserted in a pipe with a diameter of 100 mm as a place to accommodate heated water as shown in Fig. 2. The detailed tube collector of the designed water heater presented in Table 1.

The heat pipe of the designed water heater made from oxygen-free copper with 700 mm in length and 10 mm in diameter. The working fluid used in the solar collector water heater is purified water and pressurized below 5×10^{-3} Pa. The maximum working temperature for this specific material is 300 °C. The vertical
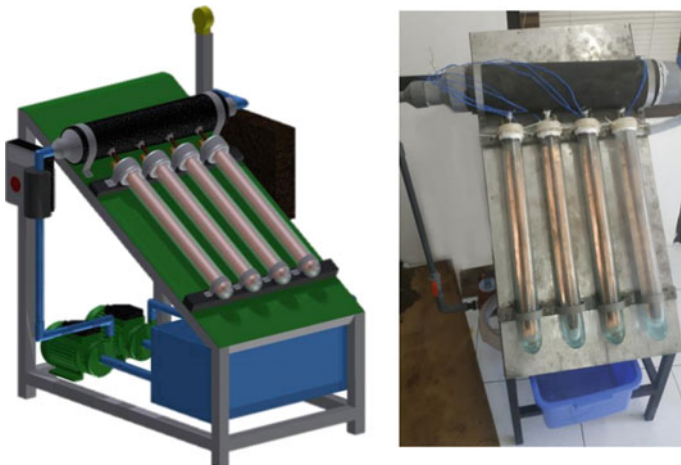
Fig. 2 Water heating system with solar collector based on heat pipe fin

Table 1 Tube collector specification

Length	Outer diameter	Weight	Material	Pressure
600 mm	60 mm	1100 gr	Glass	<1 atm
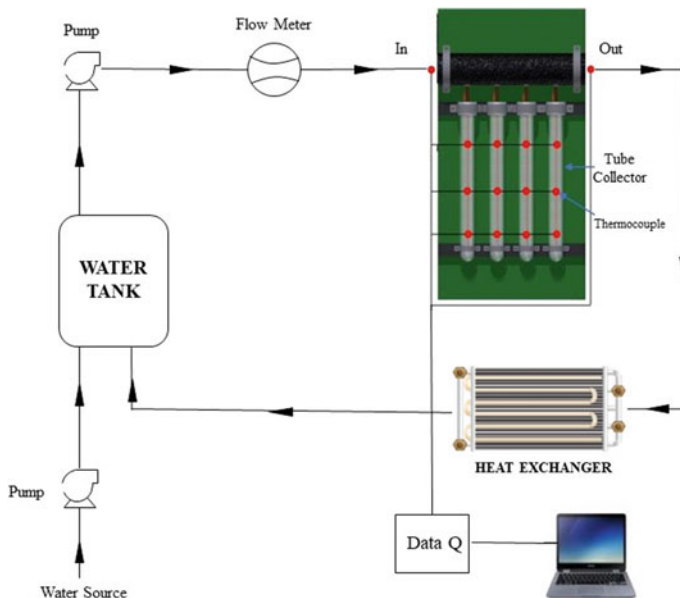
Fig. 3 Solar collector experimental scheme

installation angle for the heat pipe varied at 20°–70°. There are 2 type of fins used in the sun collector. It has 50 pieces of circular fin with 43 mm diameter and a sheet shaped fin with 516 mm in length and 43 mm in wide. The experimental scheme is presented in Fig. 3.

The experimental setup of the solar collector is referred to the real application of the solar collector. The water from water source streamed into the condenser section of the solar collector to catch the heat through natural convection process. Hot water coming from the condenser section called the water output then cooled in the heat exchanger to be streamed back to the condenser section. The pump is needed to vary the water flow rate. The data obtained from this experiment is evaporator temperature, condenser temperature, water output temperature, and the water flow rate. The data obtained using thermocouples through the data acquisition system into the laptop using LabView application.

Heat received by heat pipe depends on the solar heat flux and heat pipe surface area. Figure 4 shows the solar heat flux measured with solar energy meter from 9.00 am to 2.30 pm WITA.
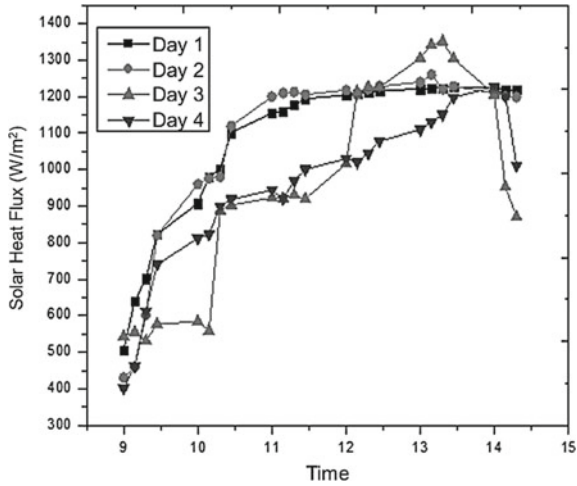
Fig. 4 Solar heat flux

The graph in Fig. 4 shows that the solar heat flux is tend to increase from 9 am to around 2 pm central Indonesia time. The results are affected by the weather that changes almost every day. The highest average solar heat flux obtained in 4 days is recorded at around 2 pm even though the highest solar heat flux recorded at 1 pm in the third day.

The graph in Fig. 5 shows the temperature distribution of evaporator section, Fig. 6. Shows the temperature distribution of condenser section, and Fig. 7. Shows the water output temperature distribution on flat and circular fin heat pipe. The graph shows that the temperature of each section is increasing every hour from 9 am to 2.00 central Indonesian time. The highest temperature recorded in each graph occurred around 2 to 2.30 pm. The highest evaporator temperature obtained
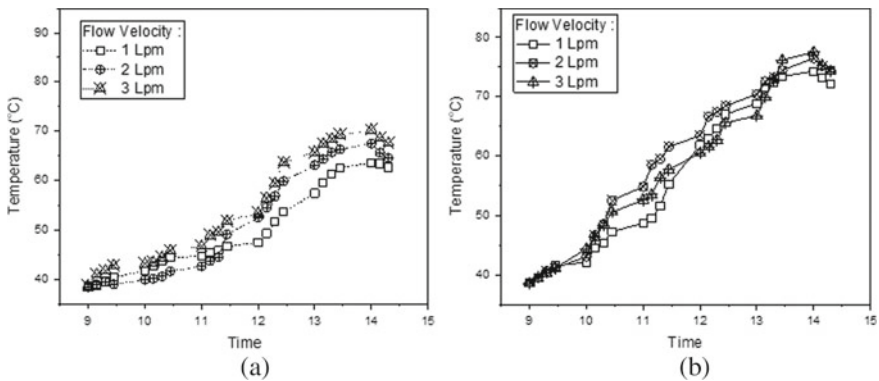
Fig. 5 Evaporator temperature of flat fin (**a**) and circular fin (**b**) evaporator temperature with water flow velocity variable
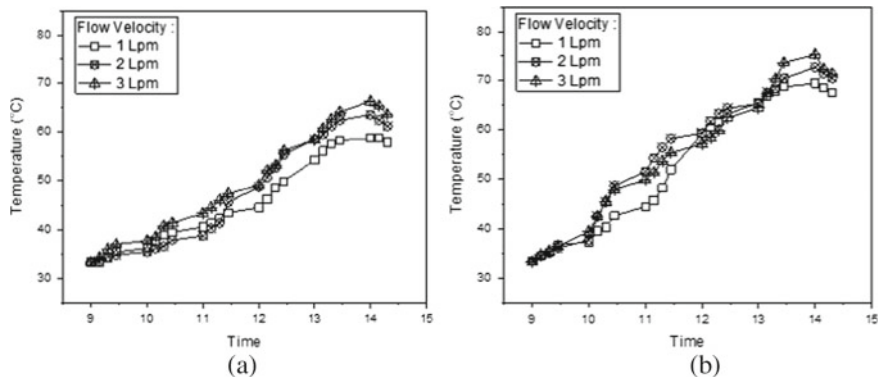
Fig. 6 Condenser temperature on flat fin (**a**) and circular fin (**b**) with water flow velocity variable
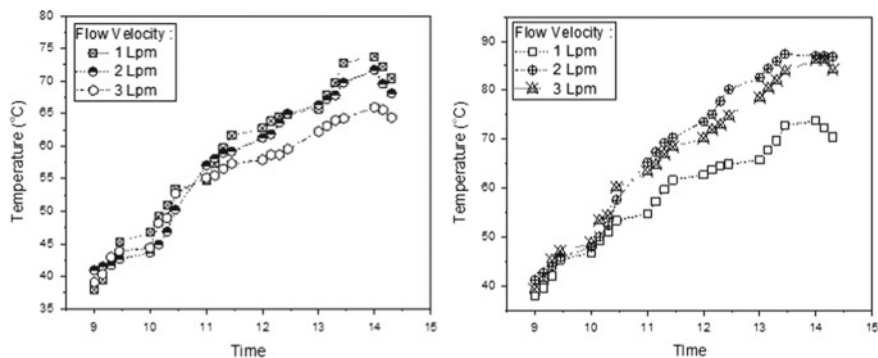
Fig. 7 Water output temperature on flat fin (**a**) and circular fin (**b**)

is 70.27 °C at 3 Lpm using flat fin heat pipe and 77.56 °C at 3 Lpm using circular fin heat pipe. The highest condenser temperature obtained is 66.33 °C at 3 Lpm using flat fin heat pipe and 75.34 °C at 3 Lpm using circular fin heat pipe. The highest water output temperature obtained is 73.75 °C at 1 Lpm using flat fin heat pipe and 86.88 °C at 2 Lpm using circular fin heat pipe.

The water flow velocity mainly affect the heat transfer process at the condenser section and water output temperature. Based on the mathematical model provided by Sabharwall et al., mass flow rate and velocity affect heat transfer coefficient. Increase in mass flow rate while maintaining constant velocity resulting in a decrease in the value of the heat transfer coefficient. But, the increase in mass flow rate results the increase of velocity, could improve the heat transfer coefficient [15]. The substantial advantage on heat transfer could obtained by increasing velocity. But, the result shows that the water output temperature at the highest water flow velocity recorded lower than lower water flow velocity. This result could caused by the water flow itself. Increase in heat transfer rate is more significant under turbulent flow condition [16].

Fig. 8 Evaporator temperature comparison based on fin shape at 3 Lpm water flow velocity
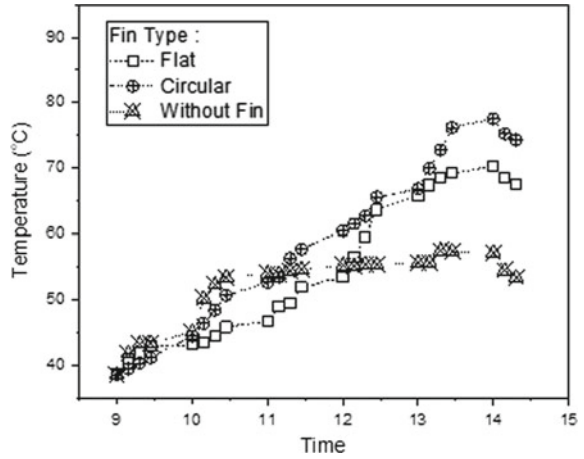
Fig. 9 Condenser temperature comparison at 3 Lpm water flow velocity
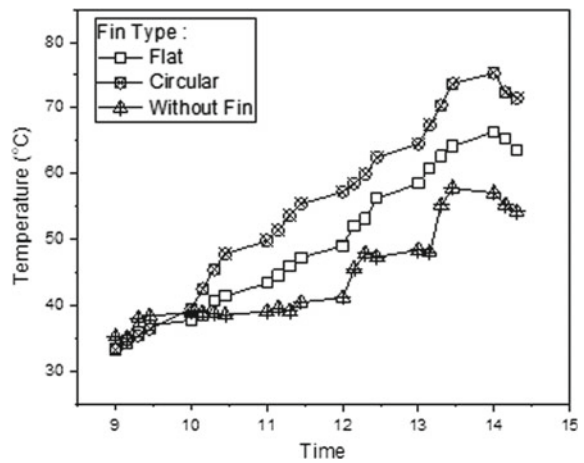
Fig. 10 Comparison of output water temperature based on fin shape at 3 Lpm water flow velocity
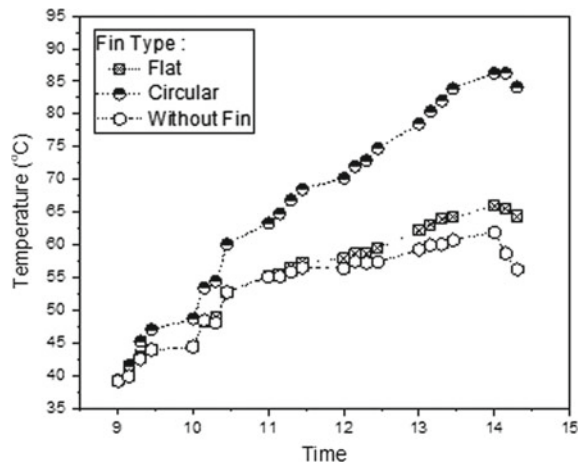
Fig. 11 Thermal resistance comparison between flat fin and circular fin solar water heater
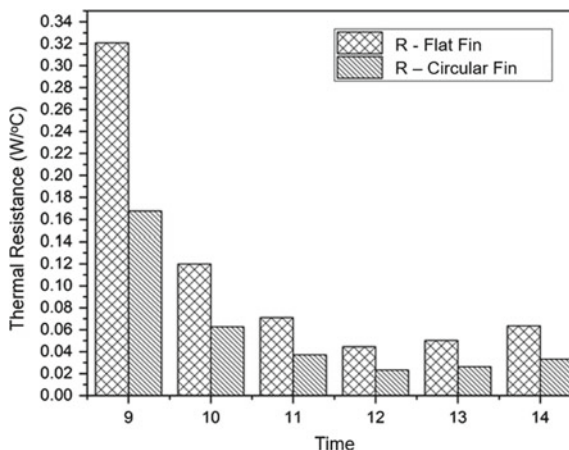
The graph provided above are temperature data comparison between evaporator section, condenser section and water output temperature based on fin shape at 3 Lpm water flow velocity as showed in Figs. 8. 9, 10. From the evaporator graph, it shows that the temperature of heat pipe with flat fin, circular fin, and without fin is pretty much similar in 9 am to 10 am central Indonesia time. Daghigh et al. in their research about solar collector stated that the greater the solar energy, the greater the heat captured by the heat pipe solar collector [17]. The data obtained is directly proportional to the solar heat flux provided in Fig. 4 especially for the evaporator section which directly capture the heat from the solar heat flux. The circular heat pipe shows the higher temperature than the flat fin and without fin heat pipe starting from 1 pm to 2 pm central Indonesia time. This phenomena occurred because the circular fin heat pipe has wider surface area to handle the solar heat flux.

From the experimental data obtained, solar water heater thermal resistance based on fin shape obtained. The thermal resistance comparison between flat fin and circular fin solar water heater can be seen in Fig. 11.

The use of flat and circular fins in the Solar Water Heater provides different thermal resistance values, namely the use of circular fins gives a thermal resistance value of 91.28% lower than the use of horizontal fins at 3 Lpm conditions. The same conditions also occur at 2 and 1 Lpm flows where the thermal resistance of the heat pipe on the Solar Water Heater with circular fins is lower than that of the solar water heater with flat fins.

The graph in Fig. 11 shows that the thermal resistance is reduced while the temperature data shows temperature increase between 9 to 12 am central Indonesia time and the thermal resistance increases with increasing temperature after 12 pm. Some research has similar pattern on thermal resistance result. Chen et al. research has the same data trend. They found that as the heat load is increasing, the thermal resistance is decreasing [18]. Meanwhile, in Septiadi et al. research about heat resistance stated that this behaviour happened only before the heat pipe reach maximum heat load. After the maximum heat load passed, the heat resistance will
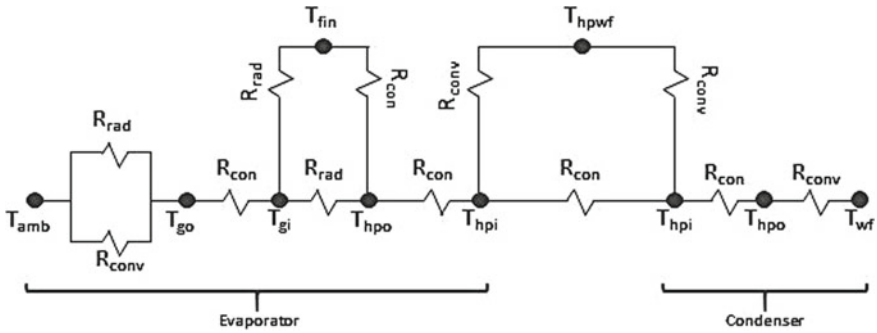
Fig. 12 Electrical analogy of tube evacuated heat pipe

increase as the heat load increase [19]. This behaviour happened after 12 pm which can be concluded that the heat load at that time was the maximum heat load can be handled by the heat pipe since based on the data, the temperature keep increasing until 14 pm.

Electrical analogy in Fig. 12 shows the heat transfer process with heat resistance occurred during the process. This electrical analogy contains the process of transferring heat from the sun and air (T_{amb}) to the outer surface of the glass (T_{go}) and by conduction, heat enters the inner surface of the glass (T_{gi}). The space in the evacuated tube is in a vacuum. Hence, heat transfer from the inner surface of the glass occurs radiantly to the fins (T_{fin}) and the outer surface of the heat pipe (T_{hpo}), after which the heat transfers to the inner surface of the heat pipe (T_{hpi}) by conduction. This process occurred in the evaporator section of the solar collector.

Heat that is on the inner surface of the heat pipe (T_{hpi}) is transferred along the heat pipe and transferred by convection to the working fluid of the heat pipe (T_{hpwf}). After the working fluid changes in phase to vapor and moves to the condenser, the steam heat transfers by convection to the inner surface of the heat pipe on the condenser (T_{hpi}) and conduction moves to the outer surface of the heat pipe (T_{hpo}) until finally the heat transfers conventionally to the water flow (T_{wf}). This process occurred in condenser section of the heat pipe.

According to Elsheniti et al. thermal resistance on the solar collector is closely related to the heat loss in the solar collector manifold. The mathematical model combining liquid film in the evaporator and nucleate in pool boiling calculation and other mathematical model presented by Elsheniti et al. has a huge correlation with heat pipe heat rate. In order to get both thermal resistance value, the heat pipe heat rate value must be obtained with calculations involving the heat loss manifold value [20].

3   Conclusion

The conclusions obtained from this study are as, the addition of fins on the evaporator can reduce thermal resistance on the solar water heater. The flat fin can reduce thermal resistance 9.89% and the circular fin can reduce the thermal resistance 43.48% compared to the finless evaporator. The fin shape of the solar water heater affects heat absorption in the evaporator with circular fins which can increase heat absorption by 39.46% and flat fins can increase heat absorption by 29.30% compared to heat pipes without fins.

References

1. Perera FP (2017) Multiple threats to child health from fossil fuel combustion: impacts of air pollution and climate change. Environ Health Perspect 125(2):141–148
2. Dewi BN, Syafei AD, Ciptaningayu TN (2019) Pedestrian exposure to nitrogen dioxide (NO2) and carbon monoxide (CO): a case study of Surabaya, Indonesia. IOP Conf Series: Earth Environ Sci 340(1):12012
3. Ho SM, Lomi A, Okoroigwe EC, Urrego LR (2019) Investigation of solar energy: the case study in Malaysia, Indonesia, Colombia and Nigeria. Int J Renew Energy Res 9(1)
4. Bourke G, Bansal P (2012) New test method for gas boosters with domestic solar water heaters. Sol Energy 86(1):78–86
5. Too YCS, Morrison GL, Behnia M (2009) Performance of solar water heaters with narrow mantle heat exchangers. Sol Energy 83(3):350–362
6. Kaya T, Goldak J (2006) Numerical analysis of heat and mass transfer in the capillary structure of a loop heat pipe. Int J Heat Mass Transf 49(17–18):3211–3220
7. Putra N, Septiadi WN, Rahman H, Irwansyah R (2012) Thermal performance of screen mesh wick heat pipes with nanofluids. Exp Therm Fluid Sci 40:10–17. https://doi.org/10.1016/j.expthermflusci.2012.01.007
8. Ma L, Lu Z, Zhang J, Liang R (2010) Thermal performance analysis of the glass evacuated tube solar collector with U-tube. Build Environ 45(9):1959–1967
9. Sharma N, Diaz G (2011) Performance model of a novel evacuated-tube solar collector based on minichannels. Sol Energy 85(5):881–890
10. Kim Y, Seo T (2007) Thermal performances comparisons of the glass evacuated tube solar collectors with shapes of absorber tube. Renew Energy 32(5):772–795
11. Jamil M, Sidik NC, Yazid MM (2016) Thermal performance of thermosyphon evacuated tube solar collector using TiO_2/water nanofluid. J Adv Res Fluid Mech Therm Sci 20(1):12–29
12. Sharafeldin MA, Grof G (2018) Evacuated tube solar collector performance using CeO_2/water nanofluid. J Clean Prod 185:347–356
13. Mehla N, Yadav A (2017) Experimental analysis of thermal performance of evacuated tube solar air collector with phase change material for sunshine and off-sunshine hours. Int J Ambient Energy 38(2):130–145
14. Abokersh MH, El-Morsi M, Sharaf O, Abdelrahman W (2017) An experimental evaluation of direct flow evacuated tube solar collector integrated with phase change material. Energy 139:1111–1125

15. Sabharwall P, Utgikar V, Gunnerson F (2009) Effect of mass flow rate on the convective heat transfer coefficient: analysis for constant velocity and constant area case. Nucl Technol 166 (2):197–200
16. Pranit M, Yadav AP, Patil PA (2015) Comparative study between heat transfer through laminar flow and turbulent flow. Int J Innov Res Sci 4(4):2223–2226
17. Daghigh R, Shafieian A (2016) Theoretical and experimental analysis of thermal performance of a solar water heating system with evacuated tube heat pipe collector. Appl Therm Eng 103:1219–1227
18. Chen J-S, Chou J-H (2014) Cooling performance of flat plate heat pipes with different liquid filling ratios. Int J Heat Mass Transf 77:874–882
19. Septiadi WN, Ula WAW, Wulandari I, Tnunay IA, Murti MR (2019) Thermal resistance analysis of central processing unit cooling system based on cascade straight heat pipe. IOP Conf Series Mater Sci Eng 539(1):12036
20. Elsheniti MB, Kotb A, Elsamni O (2019) Thermal performance of a heat-pipe evacuated-tube solar collector at high inlet temperatures. Appl Therm Eng 154:315–325

An Experimental Model for the Prediction of Chip Thickness in Steel Turning

L. B. Abhang, Mohd. Iqbal, and M. Hameedullah

Abstract In this research paper, a statistical exponential model was prepared for the determination of chip thickness during turning process of alloy steel by response surface methodology (RSM) with design of experiment method. The relationship between the chip thickness and machining conditions were analyzed. In the prediction of predictive models, cutting speed, feed rate, depth of cut and tool geometry (effective tool nose radius) were considered as input model variables and chip thickness was considered as response variable in the output form. The determined statistical model shows that the feed rate is the main influencing factor on chip thickness followed by tool nose radius and depth of cut. It increases with increase in feed rate but decreases with increase in cutting velocity and tool nose radius, respectively. The predicted values were found similar to the actual values.

Keywords Chip thickness · Response surface methodology · Factorial design · ANOVA

1 Introduction

Turning process is one of the most common processes applied for machine elements manufacturing in metal cutting industries, i.e. aerospace, automotive, and shipping. In turning/machining process, the work piece is rotated and the cutting tool trav-

L. B. Abhang
Department of Mechanical Engineering, Pravara Rural Engineering College, Loni, SPPU, Pune, Maharashtra, India
e-mail: abhanglb@yahoo.co.in

Mohd. Iqbal (✉)
Mechanical and Industrial Engineering, Faculty of Engineering, Universitas Syiah Kuala, Banda Aceh, Indonesia
e-mail: mohd.iqbal@unsyiah.ac.id

M. Hameedullah
Department of Mechanical Engineering, Aligarh Muslim University, Aligarh, India

elling to the left, removes a surface layer (chip), of the work piece material. The chip quality (chip thickness) is an important parameter to evaluate the productivity of machine tools as well as machined components. The comparison of chip produced is one of the major parameters in metal cutting industries. In other words, from the point of view of quality machining, interaction between the cutting tool and work material in metal cutting operations in material science. Chip size and thickness during turning processes are an integral part of many manufacturing operation. It is important to study the many factors influencing these operations in order to achieve better performance and economy. In metal cutting occurring plastic deformation of materials, work hardening, heat generation, and tool wear [1]. Finding a range of machining conditions that will give maximum efficiency can help manufactures produce more economically during machining process, chip thickness has great affects on mach inability i.e. cutting force, tool wear, surface smoothness, power requirement, like specific power etc. which affects on the performance of machining process. During machining chip, thickness affects the cutting materials. During machining two actions are there, one is rubbing and second one is chip removal. When increasing rubbing action the cutting force increases its affects on formation of burrs and decreasing surface smoothness. Therefore, the prediction and analysis of chip study is important in metal cutting. The chip size and colours are depends on machining variables and environmental conditions.

Tungsten carbide cutting tools are used in metal cutting industry to machine alloy steels due to their strength and toughness properties. To optimize their use, it is essential to control and properly select the machining variables applied in cutting operations to obtain higher material removal rate and proper type of chip for higher machinability. Therefore, chip thickness is considered significantly important for evaluating productivity of any cutting operation leading to the need to formulate prediction model for chip thickness as function of operating conditions. In machinability studies, statistical design of experiments such as factorial design and response surface methodology are used quite extensively. The methodology gives the required information about the main and interaction effects on the response [2]. Many researchers have applied response surface methodology for modelling and analysis of process parameters during machining of different materials. Zhou et al. [3] used response surface methodology for modelling the machining parameters for micro milling forces. Lu et al. [4], studies the influence of cutting parameters, considering the spindle speed, the feed rate per tooth, and the axial cutting depth, on surface Vickers hardness and predicts the Vickers hardness of the machined surface on Inconel 718 by RSM.

Przestackil et al. [5] obtained minimum uncut chip thickness and cutting forces during laser assisted turning. Author [6–8] prepared surface roughness and power prediction model for alloy steel with dry and different environment conditions. The author also [9] used the grey relational analysis technique and determined the optimum turning process parameters. Bhushan [10] applied Response surface methodology (RSM) for modelling surface roughness and tool life during turning composite materials with carbide tool.

However, little work on the machining of steel have been given to the prediction and analysis of turning parameters, cutting forces and chip-tool contact length in orthogonal cutting. Reddy has made analysis of surface roughness and chip thickness during end milling on Aluminium 6351-t6 alloy. He has applied Taguchi design of experiment method for study the quality response [11].

Fredink et al. [12] studied minimum chip thickness during longitudinal turning of duplex stainless steel. They have explored how the value of h_{1min} changes with varying process parameters.

Anurag et al. [13] used Taguchi optimization approach for turning of Ti-6Al-4 V ELI (grade 23) titanium alloy workpiece with coated carbide tool under dry condition. They have studied effect of turning parameters on chip thickness and chip reduction coefficient during machining process [14]. Mishra [14] has performed machining on composite materials and observed that there are different types of chip generated during machining.

Iqbal et al. [15] investigated hole delimitation in drilling Kevlar composite panel by HSS drill tool. They have employed 12 mm diameter of drill and a 4 mm thick Kevlar composite panel for experimental work. Abhang et al. [16] applied the simple multi-objective optimization technique on the basis of ratio analysis (MOORA) for solving multi-criteria (objective) optimization problem in the machining process. In this research paper experimental analysis are done on machining of EN-31 steel alloy with carbide inserts under without lubricating machining. The machining parameters studied are cutting speed, fed rate, depth of cut and effective tool nose radius. Chip thickness values were measured and statistically analyzed through statistical MINI-TAB-18 [17] software.

Response surface methodology (RSM) is a statistical method applied for developing statistical model. In RSM responses are influenced on several variables and the objective is to optimized easily. RSM involves, dependent and independent variables and response studied properly. The experimental values were collected from actual experiment and data utilized to build mathematical model by regression method. All these variables are measurable; the response surface expressed as:

$$Y = \emptyset(v, f, d, r) + \in \tag{1}$$

where, the parameters (v, f, d, and r) are speed, feed, depth of cut and tool nose radius etc. of the metal cutting processes, and ϵ is the error, which is normally distributed with mean = 0 according to observed response Y and $\emptyset$ is the response function. The relationship between surface roughness and other independent variables are modelled as shown in Eq. (2)

$$Ra = c\left(v^a\ f^b\ d^c\ r^d\right) \tag{2}$$

where (c is constant, a, b, c, and d, are the exponents).

2 Experimental Procedure

Experimental work a commercial alloy steel work piece (EN-31 steel alloy) is used for machining. Engine lathe machine (LTM-20) is used for test with tungsten carbide tools under without lubricating conditions. The work piece taken 400 mm in length and 50 mm in diameter, for machining, to maintain the stiffness of chuck/ work piece/cutting tool system, L/D ratio was kept as 8. During machining test samples were trued, cantered and cleaned. En-31 steel is used widely in automotive sectors. The cutting tools used during machining are CNMA 120404, CNMA 120408, CNMA 120412 and carbide tip. The tool holder used for machining was WIDAX SCLCR 12, Fo9 (ISO-designated) recommended in metal cutting industries. In this work, four parameters namely cutting speed, feed rate, depth of cut and tool nose radius of the cutting tool were selected for the experimentation. The range of each parameter was set at three different levels, namely low, medium and high based on preliminary test as shown in Table 1. Statistical technique composite factorial design of experiment with eight added centre points ($2^4 + 8$) used in this work. The complete design consists of 24 experiments as shown in Table 2.

Table 1 Level designation of different process variables

Level	Cutting speed (m/min)	Feed rate (mm/rev)	Depth of cut (mm)	Tool nose radius (mm)
−1	39	0.06	0.2	0.4
0	112	0.10	0.4	0.8
1	189	0.15	0.6	1.2

−1 represents the level for minimum value, 0 for the middle value, 1 the maximum value of the range of the parameters

Table 2 Completed design matrix

Sr. No.	X_1 V (m/min)	X_2 F (mm/rev)	X_3 D (mm)	X_4 R (mm)	*Chip thickness t_c (mm) (response)
1	−1	−1	−1	−1	0.472
2	−1	−1	−1	+1	0.453
3	−1	−1	+1	−1	0.475
4	−1	−1	+1	+1	0.428
5	−1	+1	−1	−1	0.550
6	−1	+1	−1	+1	0.510
7	−1	+1	+1	−1	0.539
8	−1	+1	+1	+1	0.501
9	+1	−1	−1	−1	0.470
10	+1	−1	−1	+1	0.443

(continued)

Table 2 (continued)

Sr. No.	X_1 V (m/min)	X_2 F (mm/rev)	X_3 D (mm)	X_4 R (mm)	*Chip thickness t_c (mm) (response)
11	+1	−1	+1	−1	0.455
12	+1	−1	+1	+1	0.436
13	+1	+1	−1	−1	0.535
14	+1	+1	−1	+1	0.521
15	+1	+1	+1	−1	0.520
16	+1	+1	+1	+1	0.483
17	0	0	0	0	0.500
18	0	0	0	0	0.473
19	0	0	0	0	0.475
20	0	0	0	0	0.492
21	0	0	0	0	0.486
22	0	0	0	0	0.500
23	0	0	0	0	0.479
24	0	0	0	0	0.480

*Average of three experimental results

A randomized experimental test has been done to overcome the experimental error due to machining set-up or manual operator error. Chips were collected at the end of each experiment and the chip thickness was measured using calibrated slider calliper as recommended by Sreenivasulu [11]. Collecting data from each test experiment, average chip thickness were measured of five readings of each chip produced during machining test as shown in Table 3.

3   Results and Discussion

Microsoft excel (MS Office-2010) and Mini-Tab-18 program were used in models training [17]. Model adequacy checking for significance of regression model and model coefficients, as well as test for lack-of-fit [2, 7, 13]. Analysis of variance (ANOVA) test is for checking the effect of each parameters on response.

The fit model is statistically significant for analysis of chip thickness at 95% confidence level for having p-values less than 0.05. The multiple regression coefficient of model is 95.20%. This means that the model can explain the variation to the extend of 95.20%. The value of R-sq(adj) is 94.47%. So it means model is more accurate to represent the En-31 steel turning process. Model F-value of 21.64 implies that model is significant. Lack-of-fit is not significant relative to the pure error. There is a 74% chance that a lack-of-fit value this large could occur due to noise. Non- significant lack-of-fit is good in model. Predicted R^2 of 0.9311 is in

Table 3 Experimental data for average chip thickness

Exp No.	Chip thickness (mm) Response for Run1	Chip thickness (mm) Response for Run2	Chip thickness (mm) Response for Run3	Average Chip thickness (mm) Average response
1	0.470	0.472	0.474	0.472
2	0.451	0.452	0.456	0.453
3	0.473	0.478	0.474	0.475
4	0.421	0.427	0.436	0.428
5	0.550	0.549	0.551	0.550
6	0.511	0.510	0.500	0.510
7	0.538	0.539	0.540	0.539
8	0.499	0.500	0.503	0.501
9	0.468	0.474	0.467	0.470
10	0.440	0.448	0.441	0.443
11	0.451	0.460	0.456	0.455
12	0.430	0.442	0.435	0.436
13	0.534	0.538	0.533	0.535
14	0.520	0.523	0.520	0.521
15	0.518	0.523	0.519	0.520
16	0.480	0.485	0.484	0.483
17	0.510	0.499	0.498	0.500
18	0.470	0.472	0.477	0.473
19	0.469	0.476	0.480	0.475
20	0.494	0.490	0.493	0.492
21	0.485	0.480	0.493	0.486
22	0.499	0.520	0.499	0.500
23	0.477	0.482	0.479	0.479
24	0.479	0.483	0.477	0.480

reasonable agreement with the adjusted R^2 of 0.9447 (Table 4). As seen from Fig. 1, the predicted chip thickness using the RSM model is closely match with the experimental values.

$$tc = 0.6838\left(V^{-0.010} * F^{0.148} * D^{-0.0275} * R^{-0.0566}\right) \tag{3}$$

From the exponential model it is observed that the factor with highest value of coefficient posses the most dominating effect over the chip thickness (response). From the model, it is observed that feed has the most significant effect over chip thickness, followed by the cutting speed and tool nose radius. However, depth of cut have very little effect on chip thickness as compared to other machining parameters during test. The normal probability plot of residuals for chip thickness as shown in Fig. 2. The normal probability plot is used to vary the normality

Table 4 Analysis of variance for chip thickness (RSM model)

Source	DF	SS	MS	F-value	P-value
Model	11	0.022473	0.002043	21.64	0.000
Linear	04	0.022073	0.000907	9.61	0.000
Square	01	0.000008	0.000008	0.08	0.776
Interaction	06	0.000392	0.000065	0.69	0.661
Residual error	12	0.001	0.000094	–	–
Lack-of-fit	05	0.000317	0.000063	0.54	0.74 ns*
Pure error	07	0.000816	0.000117	–	–
Total	23	0.023606	–	–	–

Note Rsq = 95.20%, Rsq (Pred.) = 93.11%, Rsq (adj) = 94.47%
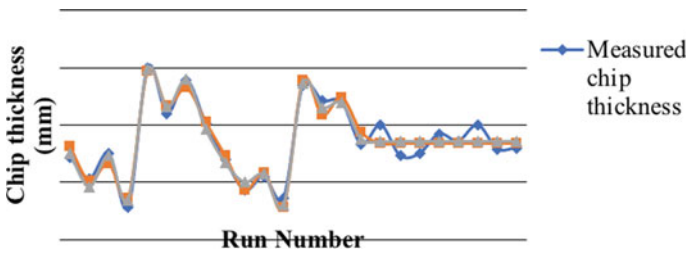
Fig. 1 Comparison between experimental results and values predicted by mathematical model for chip thickness
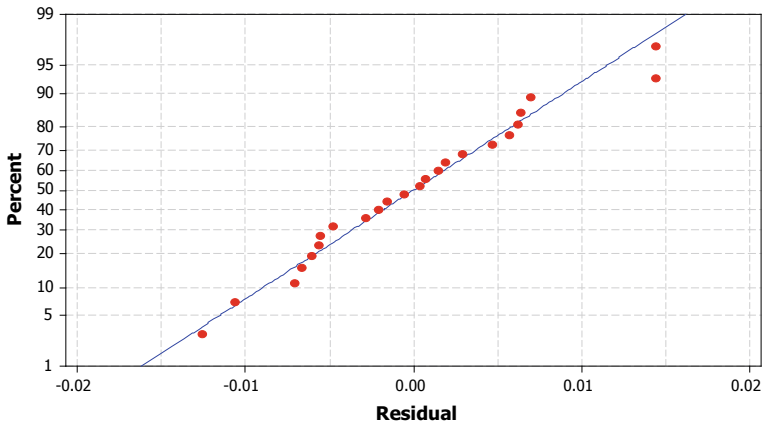
Fig. 2 Normal probability plot of the residuals (response is chip thickness)
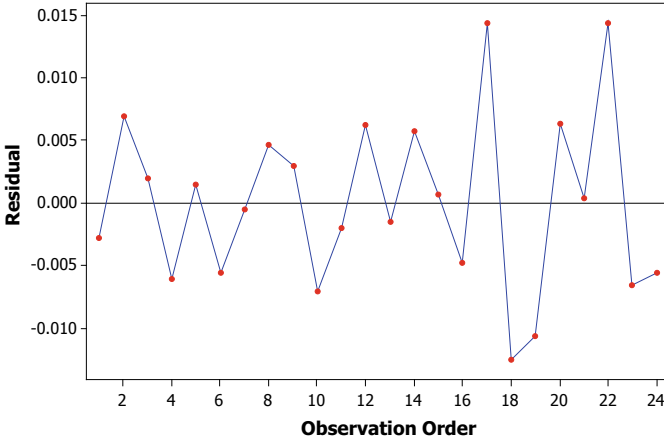
Fig. 3 Residual versus order of the data (response is chip thickness)
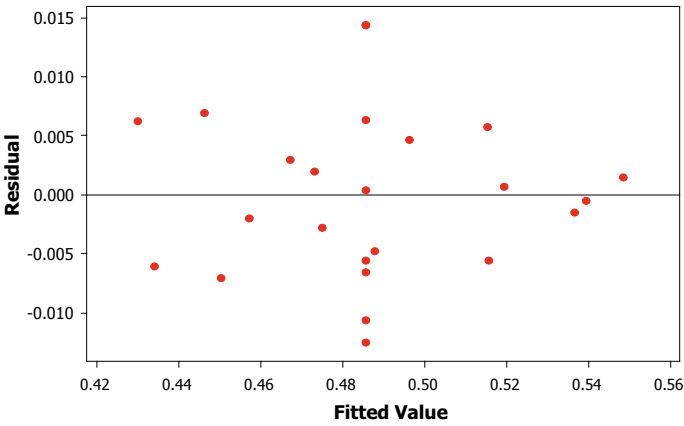
Fig. 4 Residual versus the fitted values (response is chip thickness)

assumption. Figure 3 shows that residuals are falling on a straight line, which means the errors are normally distributed. Figure 4 represents the residuals versus fitted responses for chip thickness values, which shows only the maximum variation of −0.010 to +0.015 mm (logarithmic scale) in chip thickness between the measured and the fitted values. It is seen that no obvious patterns or unusual structure implying models are accurate.

Equation (3) is used to develop the contour plots in terms of the process variables are shown in Fig. 5a–c. From the plots observed that the chip thickness decreases with increase in cutting speed and tool nose radius and the chip thickness increases with increase in feed rate.

Fig. 5 **a** Contour plot of chip thickness versus cutting speed (m/min) and feed rate (mm/rev), **b** contour plot of chip thickness versus cutting speed (m/min) and depth of cut (mm), **c** contour plot of chip thickness versus cutting speed (m/min) and tool nose radius (mm/rev)
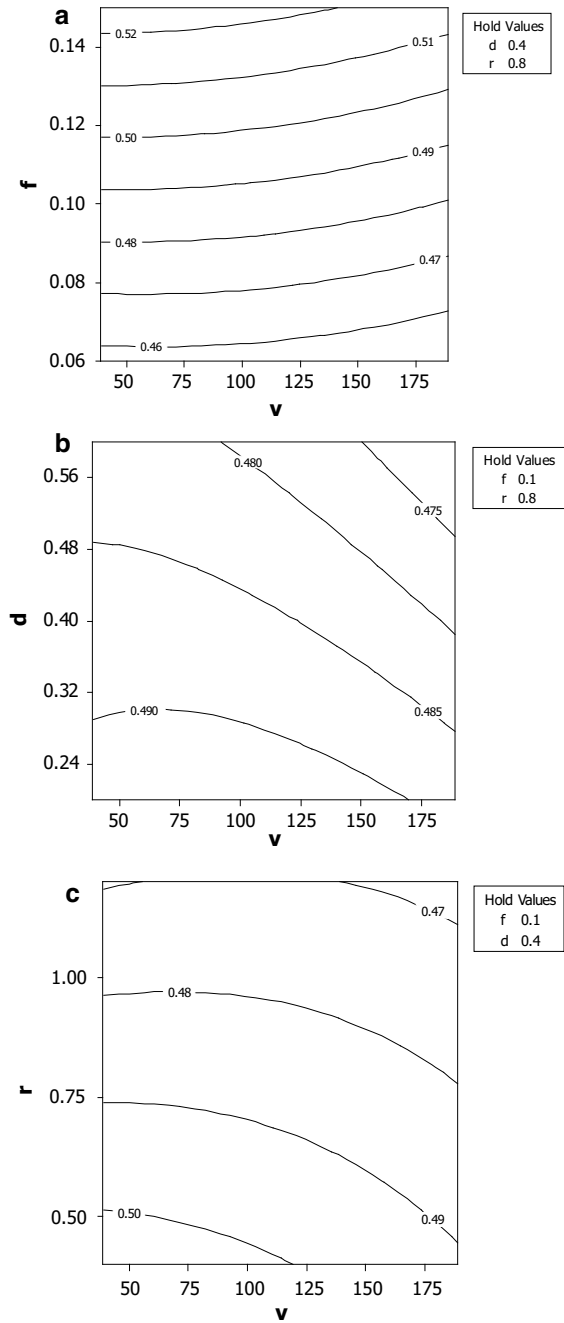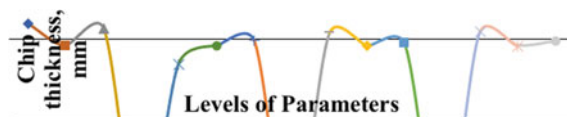
Fig. 6 Effect of machining parameters on chip thickness (1 represents the level for minimum value, 2 for the middle value, 3 the maximum value of the range of the parameters)

Table 5 Alternative solutions of optimum conditions

Sol^n	V (m/min)	F (mm/rev)	D (mm)	R (mm)	tc (mm)	Desirability
1	189	0.06	0.6	1.2	0.4298	0.985
2	39	0.06	0.6	1.2	0.4312	0.950
3	39	0.06	0.2	1.2	0.4340	0.852

Note V—cutting speed (m/min), F—feed rate (mm/rev), D—depth of cut (mm) and R—nose radius (mm), D = desirability

It is clear from above figures that lower chip thickness produced by higher cutting speed, depth of cut and lower feed rate as well as using a larger tool nose radius. Figure 6 shows the effect of machining parameters on chip thickness. From this figure, a minimum chip thickness can be produced by lower feed rate (0.06 mm/rev), higher cutting speed (V3 = 189 m/min), higher depth of cut (0.6 mm) followed by tool nose radius (1.2 mm).

After building the regression model, a numerical optimization technique using desirability functions to optimize the machining parameters and response. Table 5 shows three alternative solutions of the optimization approach used to determine the optimum machining conditions and response. Table 5 revealed that highest desirability obtained at high level of cutting speed, low level of feed rate, high level of depth of cut and tool nose radius. There are the optimal conditions to obtain high value of desirability (0.985). The minimum chip thickness obtained is 0.4298 mm at a cutting speed of 189 m/min, feed rate 0.06 mm/rev, depth of cut 0.6 mm and tool nose radius 1.2 mm as shown in Fig. 7. The chips produced during machining with optimum conditions (V, F, D and R) as shown in Fig. 8.

4 The Validation of the Optimal Experimental Results

After identifying the most effective parameters, the final phase is to verify the regression models of the chip thickness by conducting confirmation experiments and comparing the results of these validation runs with respect to the model predicted values. According to Table 6, a cutting speed 189 m/min, a feed rate 0.06 mm/rev, depth of cut 0.6 mm and tool nose radius 1.2 mm are taken for experimentation. The predicted and experimental values of chip thickness are close with each other as shown in Table 6.

Optimal D 0.98514	High Cur Low	v 189.0 [189.0] 39.0	f 0.150 [0.060] 0.060	d 0.60 [0.60] 0.20	r 1.20 [1.20] 0.40

Composite
Desirability
0.98514

tc
Minimum
y = 0.4298
d = 0.98514
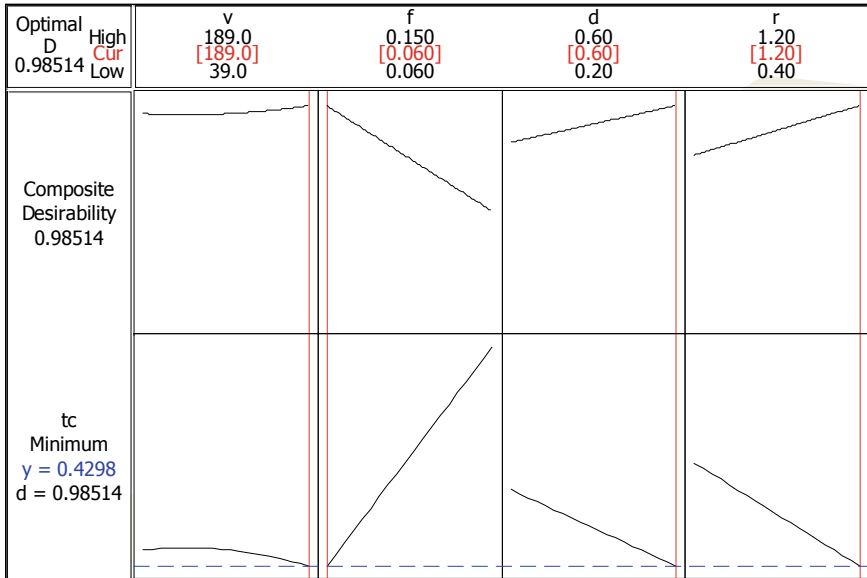
Fig. 7 Optimum global results
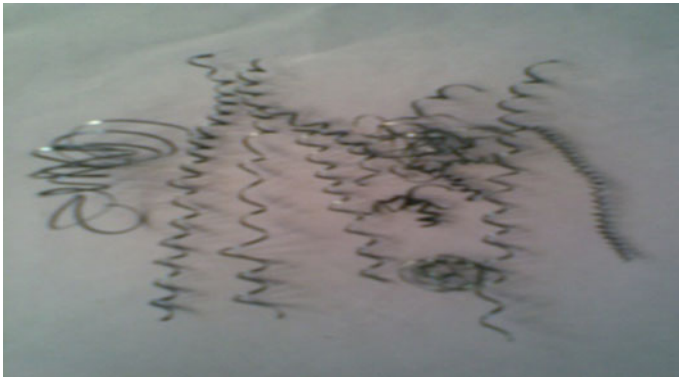
Fig. 8 Chips produced during optimum machining conditions

Table 6 Optimal setting and confirmation runs showing results for the chip thickness (mm)

Sol^n	V (m/min)	F (mm/rev)	D (mm)	R (mm)	tc (mm) Exp.	tc (mm) Pred.	Desirability
1	189	0.06	0.6	1.2	0.428	0.4298	0.985
2	39	0.06	0.6	1.2	0.430	0.4312	0.950
3	39	0.06	0.2	1.2	0.439	0.4340	0.852

5 Conclusions

- The mathematical models were found to be adequately representing the chip thickness with experimental results. The predicted equations clearly show that the cutting speed, feed rate and depth of cut were main influencing factor on the chip thickness. It increased with increasing feed rate but decreased with increasing the tool nose radius and cutting speed. Low value of chip thickness at high tool nose radius (1.2 mm) and high cutting speed (189 m/min).
- The optimization of metal cutting parameters for machining of En-31 steel alloy is carried out using global desirability based technique. The optimal conditions reduce the chip thickness in machining of EN-31 steel alloy within the machining parameters considered.
- Response surface methodology design of experiments actually save lot of time and cost of the experiments. From this design of experiments, lot of useful information is collected such as developed mathematical models of chip thickness and counter plots.
- The counter and the counter plot show the safe zone, to produce the optimum chip thickness with optimum machining parameters. This reduces the machining time, operation efforts, cost and save the cutting tools. A good combination among the cutting speed, feed rate, depth of cut and tool nose radius can achieve required chip thickness within machining variables.

References

1. Kalpakjian S (2000) Manufacturing process for engineering materials, 3rd edn, pp 467–4727. Addison-Wesley, Menlo Park, Calif, USA
2. Montgomery DC (2010) Design and analysis of experiments, 3rd edn. John Willy and Sons, New York, USA, pp 521–568
3. Zhou M, Chen Y, Zhang G (2020) Force prediction and cutting-parameter optimization in micro-milling Al7075-T6 based on response surface method. J Micro Mach 11(8):766. https://doi.org/10.3390/mi11080766
4. Lu XH, Jia ZY, Wang H, Feng YX, Liang SY (2019) The effect of cutting parameters on micro-hardness and the prediction of Vickers hardness based on a response surface methodology for micro-milling Inconel 718. Measurement 140:56–62
5. Przestacki D, Chwalczuk T, Wojciechowski S, (2017) The study on minimum uncut chip thickness and cutting forces during laser-assisted turning of WC/NiCr clad layers. Int J Adv Manuf Technol 91:3887–3898. https://doi.org/10.1007/s00170-017-0035-5
6. Abhang LB, Hameedullah M (2019) Wear behaviour of carbide tool during machining of steel SSRN: https://ssrn.com/abstract=3332379
7. Abhang LB, Hameedullah M (2011) Statistical modelling of surface roughness produced by wet turning using soluble-oil water mixture lubricant. Int J Manuf Mater Sci 1(1):26–30

8. Abhang LB, Hameedullah M (2010) Chip-tool interface temperature prediction model for turning process. Int J Eng Sci Technol 2(4):382–393

9. Abhang LB, Hameedullah M (2011) Empirical modeling of turning parameters using grey relational analysis. Appl Mech Mater 110–116:2596–2603

10. Bhushan RK (2020) Multi-response optimization of parameters during turning of AA7075/SiC composite for minimum surface roughness and maximum tool life. Silicon. doi: s12633-020-00640

11. Sreenivasulu R (2016) Taguchi based optimization for surface roughness and chip thickness during end milling process on aluminium 6351-t6 alloy. Independent J Manage Prod 7(4)

12. Shultheiss F, Agmell M, Bushlya V, Stahl J-E (2018) Analysis of the minimum chip thickness during turning of duplex stainless steel. Proc Instit Mech Eng Part B J Eng Manuf 13

13. Kumar AR, Joshi KK, Das RK (2018) Analysis of chip reduction coefficient in turning of Ti-6Al-4 V ELI. In: The 3rd international conference on materials and manufacturing engineering. IOP Publishing

14. Mishra A (2016) Overview study of the machining of composite materials. Int J Res EngTechnol 4(7):1–8

15. Iqbal M, Tadjuddin M, Abhang LB (2020) Investigation of hole delamination in drillingkeblar composite panel using HSS drill tool. Defect Diffus Forum 402:108–114

16. Abhang LB, Iqbal M, Hameedullah M (2020) Optimization of machining process parameters using moora method. Defect Diffus Forum 402:81–89

17. Minitab: version-18 Document, 2018, www.minitab.com

The Effect of Atmosphere Media on Temperature and Mass of Torrefacted Coffee Beans

Faisal, Khairil, Husni Husin, and Y. Abubakar

Abstract Torrefaction of coffee beans is a practicable way of producing various coffee products. Considering the fact that the variation of atmosphere media in biomass torrefaction results in changes in its characteristics, therefore, it is expected that atmosphere variations during torrefaction of coffee beans would also impact the characteristics and taste of the coffee products. Based on this, the purpose of this study was to determine the effect of atmosphere variations on the temperature and mass of torrefacted coffee beans. The study involved conducting a thermogravimetric test on Arabica coffee beans with atmosphere variations using argon, nitrogen and air at temperature rates of 10 and 20 °C/min. The data obtained were tabulated and statistically analyzed using the Kruskal-Wallis method at a temperature range of ≤ 250 °C. Results with both temperature rates showed the p values for the temperature were 0.308 and 0.311 while the p values for each coffee mass were 0.000. In conclusion, there was no significant effect of the atmosphere vari-

Faisal
Doctoral Program, School of Engineering, Universitas Syiah Kuala,
Banda Aceh 23111, Indonesia

Faisal
Department of Mechanical Engineering, Universitas Malikussaleh,
Lhokseumawe 24352, Indonesia

Khairil (✉)
Department of Mechanical Engineering, Universitas Syiah Kuala,
Banda Aceh 23111, Indonesia
e-mail: khairil@unsyiah.ac.id

H. Husin
Department of Chemical Engineering, Universitas Syiah Kuala,
Banda Aceh 23111, Indonesia

Y. Abubakar
Department of Agricultural Product Technology, Universitas Syiah Kuala,
Banda Aceh 23111, Indonesia

151

In conclusion, there was no significant effect of the atmosphere vari-

ation on the temperature but had a significant effect on the mass reduction of coffee beans torrefacted in argon, nitrogen and air media.

1   Introduction

Coffee is the second most popular and traded commodity in the world after oil [1]. It has some advantageous features which makes it more desirable than other commodities [2]. Coffee also has many product variations but sometimes inadequate in terms of production. Also, different plant varieties, height, planting location [3], method of processing [4], mixtures and compositions used during its production, all result to the difference in the coffee products [5, 6]. According to a previous study, one of its variants currently used as a solution in the production of coffee beans for exports were the specialty coffee products, higher in terms of quality, price and with unique taste [7].

Harvested coffee usually go through several stages of processing before consumption [2, 8]. One of these is the roasting stage conducted at a maximum temperature of 165–250 °C and in the open atmosphere. This temperature is usually reduced from the maximum temperature to 90 °C in a few moments (<1.5 min), when the coffee beans are put into the roasting drum. It is then increased again to the maximum temperature in about 12–15 min. The green coffee beans normally change color and give coffee aroma when roasted [9]. Also, temperature and time always have effect on the taste and aroma of the manufactured coffee products during the heating process [10]. In general, an exothermic process occurs during this heating thereby causing various reactions, which impact on the products and the quality of its taste [4, 6].

However, torrefaction of coffee beans could be used to substitute the roasting process [11]. Torrefaction is an exothermic process with the use of temperature lower than that of pyrolysis [12], usually <260 °C [13]. This process is commonly used to increase the characteristic value of biomass fuel. It is divided into two based on the atmosphere fluid used, these are wet and dry torrefaction. The wet torrefaction uses water vapor media at high pressure as its atmosphere fluid, while the dry type consists of non-oxidative and oxidative torrefaction. The non-oxidative uses inert gases such as nitrogen, argon, etc. as the atmosphere fluid but oxidative torrefaction uses air or oxygen. The torrefaction process is carried out at a relatively low temperature. Even with air or oxygen fluids, there are usually no oxidation reaction as it is conducted below the ignition point. However, several tests have shown that oxidation occurs on the surface of the biomass [14]. In general, torrefaction has a similarity slice with pyrolysis and roasting. The non-oxidative type has a similarity slice close to the pyrolysis process but with a lower temperature, then, the oxidative type is similar to the roasting process.

Generally, the various types of atmosphere media used during biomass torrefaction produce different characteristics of the products [15]. Considering the fact that variations in the types of atmospheric media usually impact the characteristics

of the torrefacted biomass, it is assumed it could also affect that of the torrefacted coffee, especially the taste quality. Based on these considerations, the aim of this study was to determine the effect of atmosphere variations on the temperature and mass of torrefacted coffee beans.

The use of a pilot scale reactor during biomass torrefaction with a larger mass could provide more complete data. However, the torrefaction process could also be studied using the Thermogravimetric Analysis (TGA) test method with a small sample mass. This TGA test is needed to obtain data on the characteristics of the material to be torrefacted accurately and more quickly, mainly by measuring and illustrating changes in sample mass versus time and temperature with high accuracy. Therefore, the TGA test on coffee bean products would be able to determine its thermal degradation and mass reduction. The two main variables usually examined are the effect of atmospheric variations on changes in temperature and mass of the torrefacted coffee beans.

2 Research Methods

The sample material was subjected to the TGA testing process to obtain its characteristics. The material used in this study was an exported quality Arabica coffee beans, known as Specialty Arabica Green Bean, obtained from Gayo, Central Aceh, in Aceh Province. The bean samples were made into powder form and placed in an aluminum container.

Prior to the torrefaction process, about 5 mg of the sample mass was measured and its container placed in a tube attached to a digital scale. During the process, the gas was allowed to flow into the tube at a rate of 20 ml/min. Considering the relationship between temperature and time of the roasting process, the estimated range of
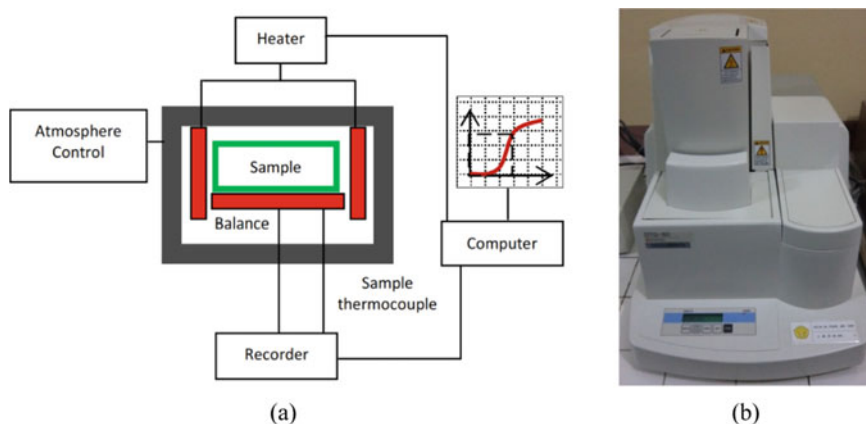
Fig. 1 a The working principle of the TGA test tool and b photo of the TGA test tool

temperature rates for torrefaction with TGA were measured around 10–20 °C/min. The gases used include argon, nitrogen and air. Then, the final temperature of the torrefaction process was ≤ 360 °C. The working principle of the TGA tool is shown in Fig. 1a while the (b) part is a photo of the TGA test tool, Shimadzu DTG-60 with Serial No: C30564800501TK, found in the Testing Laboratory, Department of Chemical Engineering, Politeknik Negeri Lhokseumawe, Aceh, Indonesia.

Data obtained were tabulated and analyzed to measure the effect of atmosphere variations on changes in temperature and mass of the torrefacted coffee beans. The data for the effect of atmospheric variations on the temperature and mass of torrefacted coffee beans through TGA at a temperature of ≤ 250 °C were subjected to statistical analysis. This was adjusted to the temperature range for the roasting process generally carried out to obtain torrefacted coffee products with good quality and not over-processed.

3   Results and Discussion

The graphs in Fig. 2 shows the relationship between changes in temperature and mass of torrefacted coffee beans with variations in atmosphere media at temperature rates of (a) 10 °C/min and (b) 20 °C/min. Based on the graphs, the curve of temperature-time relationship for each atmosphere variation increased linearly with time. Also, the three curves were seen almost coinciding with each other from the beginning to the end of the torrefaction process. This shows that there was only a slight difference in temperature changes over time due to atmosphere variations. These figures also show that the coffee mass (TGA) relationship with time has a continuous difference, which change from the beginning to the end of the torrefaction process. In addition, the mass percent of coffee continuously decreased with increase in time and temperature of torrefaction.

The TGA versus time graphs for both argon and air have similar pattern where the argon gas curve was always above the air curve in both figures. Also, the two curves traverse on parallel paths with a position which was farther away from one another. However, the TGA versus time graph for nitrogen has a different pattern from that of argon and air. Initially, the nitrogen curve was above that of argon with a slight difference when the minutes was ≤ 600 and temperature ≤ 130 °C, as shown in Fig. 3a or minutes ≤ 375 and temperature ≤ 155 °C, as shown in Fig. 3b. Subsequently, the graph tends to coincide with the argon gas graph until 1775 min and at a temperature of 260 °C, as shown in Figs. 2a and 3a. This continued to be under the argon gas curve with a greater difference in distance until the end of the process. Also, the nitrogen gas curve in Figs. 2b and 3b coincided with that of argon only at a small temperature interval of 155–175 °C and then continued to be below the argon gas curve. Even at 400 min and a temperature of 275 °C, it was below the air graph with an increasing distance until the end of the process.

According to Fig. 3a and b, the torrefaction process experienced two stages of thermal decomposition. The first was dehydration, where water evaporated up till
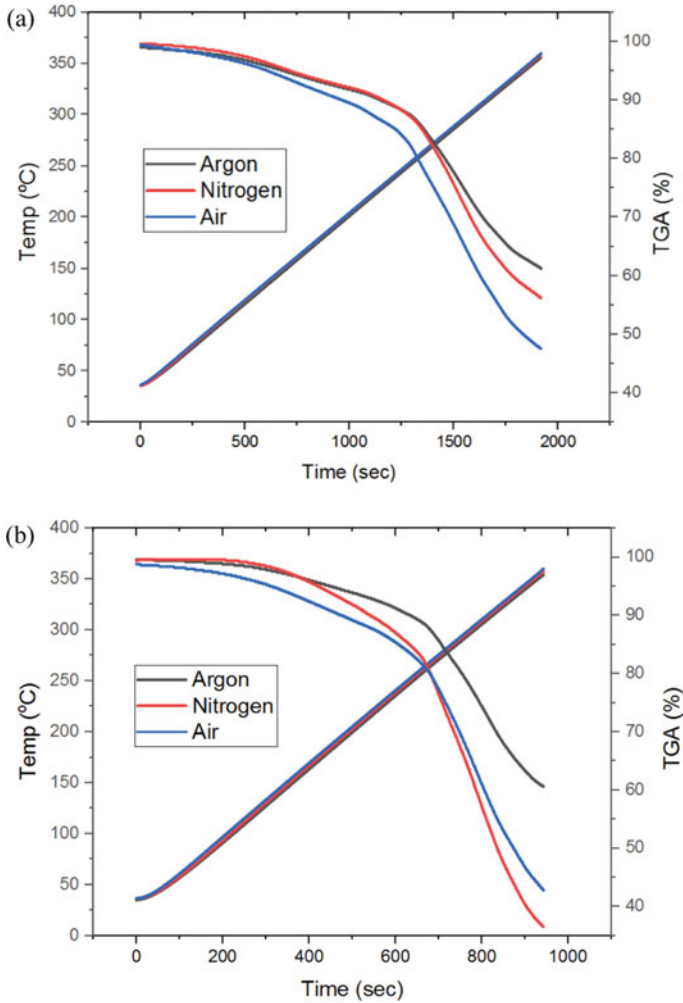
Fig. 2 Graphs showing the relationship between temperature, mass reduction (TGA) and time with variations in atmosphere media used during the torrefaction process at temperature rates of **a** 10 °C and **b** 20 °C/min

100 °C. This was followed by the evaporation of volatile substances up to a temperature of 250 °C. The first stage is shown by the gentle slope of the mass reduction curve. The torrefacted coffee beans then entered the second stage, known as devolatilization. The volatile substances in the coffee beans drastically evaporated at this stage. Devolatilization of the torrefacted coffee beans occurred at a temperature ≥ 250 °C until the process was completed, indicated by the sharp decrease in the slope of the TGA curve. The maximum torrefaction temperature of coffee beans was 360 °C which was less than the ignition point temperature at
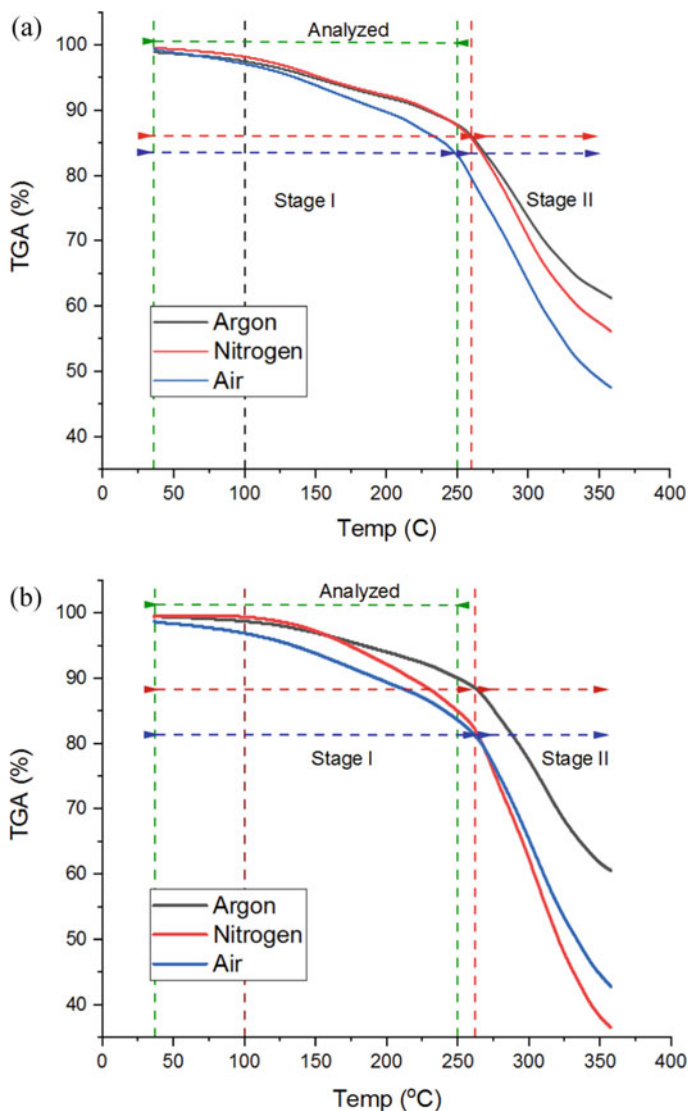
Fig. 3 The graphs showing the relationship of mass reduction (TGA) to temperature with variations in atmosphere media in the torrefaction process at temperature rates of **a** 10 °C and **b** 20 °C/min

380 °C [16, 17]. However, the statistical analysis of data on the effect of atmosphere variations on temperature and mass was limited to ≤ 250 °C.

Tables 1 and 2 show the results of statistical analysis for the temperature of the torrefacted coffee beans at temperature rates of 10 and 20 °C/min for argon, nitrogen and air. The data obtained were not normally distributed, at p (probability) = 0.000. Then, the statistical analysis used, i.e., Kruskal-Wallis test, which is

Table 1 Kruskal-Wallis analysis on the temperature of the torrefacted coffee beans at a temperature rate of 10 °C/min with atmosphere variations

Types of atmosphere	N	Temperature (°C)		P
		Mean ± SD	Median (minimum–maximum)	
Argon	1269	138.5990 ± 62.44780	138.4500 (35.88–246.82)	0.308
Nitrogen	1269	141.4736 ± 62.94791	141.8500 (35.61–249.77)	
Air	1269	142.1924 ± 62.41038	142.3700 (36.70–250.00)	
Total	3807			

Table 2 Kruskal-Wallis analysis on the temperature of the torrefacted coffee beans at a temperature rate of 20 °C/min with atmosphere variations

Types of atmosphere	N	Temperature (°C)		P
		Mean ± SD	Median (minimum–maximum)	
Argon	627	133.0628 ± 63.76554	131.8400 (35.10–244.85)	0.311
Nitrogen	627	135.6598 ± 64.46498	135.0300 (37.02–248.12)	
Air	627	138.4721 ± 64.51471	138.2100 (36.68–250.22)	
Total	1881			

an alternative to the ANOVA test, showed that the p values were 0.308 and 0.311. These mean that there is no significant difference of temperature in the variations of argon, nitrogen and air.

Tables 3 and 4 show the results of statistical analysis for the mass of the torrefacted coffee beans at temperature rates of 10 and 20 °C/min for argon, nitrogen and air. Similarly, the data obtained were not normally distributed, at $p = 0.000$, therefore, were again subjected to the Kruskal-Wallis test. This resulted to a p value of 0.000, meaning that the mass reduction percent showed a significant difference with the atmosphere variations.

Table 3 Kruskal-Wallis analysis for the mass reduction of torrefacted coffee beans at a temperature rate of 10 °C/min with atmosphere variations

Types of atmosphere	N	Mass reduction (%)		P
		Mean ± SD	Median (minimum–maximum	
Argon	1269	94.931 ± 3.2293	95.600 (88.0–99.0)	0.000
Nitrogen	1269	95.399 ± 3.4304	96.000 (87.8–99.6)	
Air	1269	93.665 ± 4.4835	94.600 (83.4–99.4)	
Total	3807			

Kruskal-Wallis test. Post hoc Mann-Whitney test: argon versus nitrogen $p = 0.000$; argon versus air, $p = 0.000$; nitrogen versus air, $p = 0.000$

Table 4 Kruskal-Wallis analysis for the mass reduction of the torrefacted coffee beans at a temperature rate of 20 °C/min with atmosphere variations

Types of atmosphere	N	Mass reduction (%)		p
		Mean ± SD	Median (minimum–maximum	
Argon	627	97.600 ± 2.7320	97.600 (90.2–99.6)	0.000
Nitrogen	627	98.200 ± 4.2404	98.200 (85.4–99.6)	
Air	627	95.000 ± 4.3507	95.000 (84.0–98.8)	
Total	1881			

Kruskal-Wallis test. Mann-Whitney post hoc test: argon versus nitrogen $p = 0.013$; argon versus air, $p = 0.000$; nitrogen versus air, $p = 0.000$

The results were further subjected to the Mann-Whitney post hoc test in order to determine the significant differences between the atmospheric media used in the study. Based on the tests involving mass data with temperature rate of 10 °C/min, the p value of argon versus nitrogen, argon versus air, and nitrogen versus air was 0.000. This means that there was a significant difference among these three comparisons at $p < 0.05$ [18]. Then, the Mann-Whitney post hoc test a temperature rate of 20 °C/min showed that argon versus nitrogen, argon versus air, and nitrogen versus air had a p value of 0.013, 0.000, and 0.000 respectively. This means that there was also a significant difference among these three comparisons at $p < 0.05$.

Furthermore, the mass reduction percent of the torrefacted coffee beans with argon, nitrogen, and air were 11, 11.8, and 16% respectively at temperature rate of 10 °C/min and 9.4, 14.2 and 14.8% at temperature rate of 20 °C/min. These were obtained from the difference between the maximum and minimum values.

4   Conclusions

The following conclusions were drawn based on the findings of this study:

1. The mass reduction during the torrefaction process with air was always greater than argon in both the dehydration and devolatilization stages.
2. The mass reduction of the torrefacted coffee beans with nitrogen had a different pattern from argon and air. Then, at the initial stage of dehydration, the mass reduction was lower in argon and air, but increased at mid-dehydration equaled to that in argon at temperature rate of 10 °C/min, and then greater than argon at 20 °C/min. During the devolatilization stage, the mass reduction was greater than argon at a temperature rate of 10 °C/min and then greater than both argon and air at 20 °C/min.
3. The results of the statistical analysis obtained from the thermogravimetric test showed that the atmospheric variations had no significant effect on the temperature but had a significant effect on the mass reduction of the torrefacted coffee beans.

4. The mass reduction of the torrefacted coffee beans with atmosphere variations showed a significant difference among argon versus nitrogen, argon versus air and nitrogen versus air, at $p < 0.05$ for both temperature rate of 10 and 20 °C/min.
5. Finally, the mass reduction percent of the torrefacted coffee beans with argon, nitrogen, and air were 11, 11.8 and 16% respectively at temperature rate of 10 °C/min and 9.4, 14.2 and 14.8% at 20 °C/min.

References

1. Mussatto SI, Machado EMS, Martins S, Teixeira JA (2011) Production, composition, and application of coffee and its industrial residues. Food Bioprocess Technol 4(5):661
2. Murthy PS, Naidu MM (2012) Sustainable management of coffee industry by-products and value addition—a review. Resour Conserv Recycl 66:45–58
3. Avelino J et al (2005) Effects of slope exposure, altitude and yield on coffee quality in two altitude terroirs of Costa Rica, Orosi and Santa María de Dota. J Sci Food Agric 85(11):1869–1876
4. Abubakar Y, Hasni D, Muzaifa M, Widayat HP (2019) Effect of varieties and processing practices on the physical and sensory characteristics of Gayo Arabica specialty coffee. IOP Conf Ser Mater Sci Eng 523(1):12027
5. Farah A, Monteiro MC, Calado V, Franca AS, Trugo LC (2006) Correlation between cup quality and chemical attributes of Brazilian coffee. Food Chem 98(2):373–380
6. Abubakar Y, Karim A, Fahlufi F (2011) Flavor of arabica coffee grown in Gayo Palteau as affected by varieties and processing techniques. In: Proceedings of the annual international conference, Syiah Kuala University-Life Sciences & Engineering Chapter, vol 1, no 1
7. Sunarharum WB, Williams DJ, Smyth HE (2014) Complexity of coffee flavor: a compositional and sensory perspective. Food Res Int 62:315–325
8. Roseberry W (1996) The rise of yuppie coffees and the reimagination of class in the United States. Am Anthropol 98(4):762–775
9. Baggenstoss J, Poisson L, Kaegi R, Perren R, Escher F (2008) Coffee roasting and aroma formation: application of different time—temperature conditions. J Agric Food Chem 56 (14):5836–5846
10. Hečimović I, Belščak-Cvitanović A, Horžić D, Komes D (2011) Comparative study of polyphenols and caffeine in different coffee varieties affected by the degree of roasting. Food Chem 129(3):991–1000
11. Misra M, Mohapatra SK, Kondamudi NV (2013) Methods, systems, and apparatus for obtaining biofuel from coffee and fuels produced therefrom. Google Patents
12. Kumar G et al (2017) A review of thermochemical conversion of microalgal biomass for biofuels: chemistry and processes. Green Chem 19(1):44–67
13. Vakalis S et al (2019) The 'COFFEE BIN' concept: centralized collection and torrefaction of spent coffee grounds. Environ Sci Pollut Res 1–9
14. Barskov S et al (2019) Torrefaction of biomass: a review of production methods for biocoal from cultured and waste linocellulosic feedstocks. Renew Energy
15. Ho S-H, Zhang C, Tao F, Zhang C, Chen W-H (2020) Microalgal Torrefaction for solid biofuel production. Trends Biotechnol

16. Roberts TA, Buckland I, Shirvill LC, Lowesmith BJ, Salater P (2004) Design and protection of pressure systems to withstand severe fires. Process Saf Environ Prot 82(2):89–96
17. Field P (1987) Explosibility assessment of industrial powders and dusts. HMSO Books, P. O. Box 276, London SW 8 5 DT, England
18. Walpole RE, Myers RH (1995) Probability and statistics for engineers and scientists

Boundary Element Inverse Analysis (BEIA) Simulation for Detecting Corrosion Location in Reinforced Concrete

Syahrul Fathi, M. Abrar Masykuri, Israr Bin M. Ibrahim, Syarizal Fonna, and Syifaul Huzni

Abstract The purpose of this research is to develop the Boundary Element Inverse Analysis (BEIA) for detecting corrosion location of reinforcing steel in concrete. In this study, the locations of corrosion to be detected were limited into only two corrosion locations. BEIA is based on Boundary Element Method (BEM) and Particle Swarm Optimization (PSO). BEM is used to calculate the potential value on a concrete surface. Then, PSO is used to evaluate the cost function to detect corrosion of reinforcing steel in the concrete. BEIA was performed by using several electrical potential data of the concrete surface. The numerical simulation results show that the developed BEIA has successfully identified two locations of corrosion on the reinforcing steel. Hence, it shows that BEIA is a promising method for detecting rebar corrosion.

Keywords Rebar corrosion · Boundary element method · Optimization · Particle swarm optimization · Inverse analysis

1 Introduction

Every infrastructure can be affected by corrosion which leads to a country's losses. Generally, the losses caused by corrosion range from 1 to 5% of gross national product (GNP) [1]. According to experts, the damage caused by corrosion in Indonesia can reach up to 1.5% of GNP [2].

Based on the Badan Informasi Geospasial (BIG), Indonesia is the country with the second longest coastline in the world (around 99,093 km) [3]. Hence, the environment poses a risk of corrosion losses caused by sea water. This losses can affect reinforced concrete infrastructure such as buildings, bridges, tunnels and other structures. Corrosion in reinforced concrete causes a decrease in the strength

S. Fathi · M. A. Masykuri · I. Bin M. Ibrahim · S. Fonna (✉) · S. Huzni
Department of Mechanical and Industrial Engineering, Universitas Syiah Kuala, Jl. Tgk. Syech Abdul Rauf No 7, Banda Aceh 23111, Indonesia
e-mail: syarizal.fonna@unsyiah.ac.id

of the infrastructure thus shortening the service life [4]. Therefore, corrosion in reinforced concrete needs to be detected as early as possible so that corrective action can be taken immediately [5].

The widely used technique in detecting corrosion in reinforced concrete is the half-cell potential mapping method which refers to ASTM C876 [6]. The result obtained from this technique is the level of probability of corrosion based on the potential value of the concrete surface [7]. In the case of uniform corrosion, this technique gives good results in detecting corrosion, where the potential value of the concrete surface is almost the same as that of the reinforcing surface [8]. However, problem arises when detecting localized corrosion, that is, corrosion with a small anode-cathode ratio, because the potential of the concrete surface differs greatly from the surface of the reinforcement [9]. In addition, the problem of corrosion detection in reinforced concrete is an ill-posed problem that cannot be solved by direct methods such as the half-cell potential mapping method [10]. Thus, the method is less effective in detecting local corrosion.

Fonna [5, 9, 11] has developed an inverse method for detecting localized corrosion of reinforced concrete. This method is based on the boundary element method (BEM) and particle swarm optimization (PSO) and is also called the boundary element inverse analysis (BEIA). BEIA is run using several potential measurement data on concrete surface. However, the capacity of BEIA is still very limited, which only capable of detecting a single corrosion location [11]. BEIA needs further development due to the fact that corrosion occurs in various places, sizes and shapes. The purpose of this research is to improve the ability of BEIA so that it is capable of detecting multiple locations of corrosion in reinforced concrete. In this study, the corrosion locations to be detected were limited to two corrosion locations.

2 Methodology

BEIA was developed with a combination of the Boundary Element Method (BEM) and Particle Swarm Optimization (PSO) for detecting corrosion in reinforced concrete. Research on BEIA has been carried out in previous studies [5, 9, 11].

BEIA is run based on the flow chart shown in Fig. 1. The initial step is to determine the required parameters such as Z, j_{max}, ε_0, a_1, a_2, and W_j. The parameter Z is the number of particles, j_{max} is the maximum iteration, a_1 and a_2 are constant values, W_j is the Weight Inertia value. Then, the initial corrosion locations (X_j) were randomly guessed on the concrete surface. These locations are the "particles". BEM is run to calculate the potential value on the concrete surface for each particle.

The next step is to input N measured electrical potential data $\left(\bar{\phi}\right)$ on the concrete surface. The objective function (ε) value for each particle is calculated by following Eq. (1).
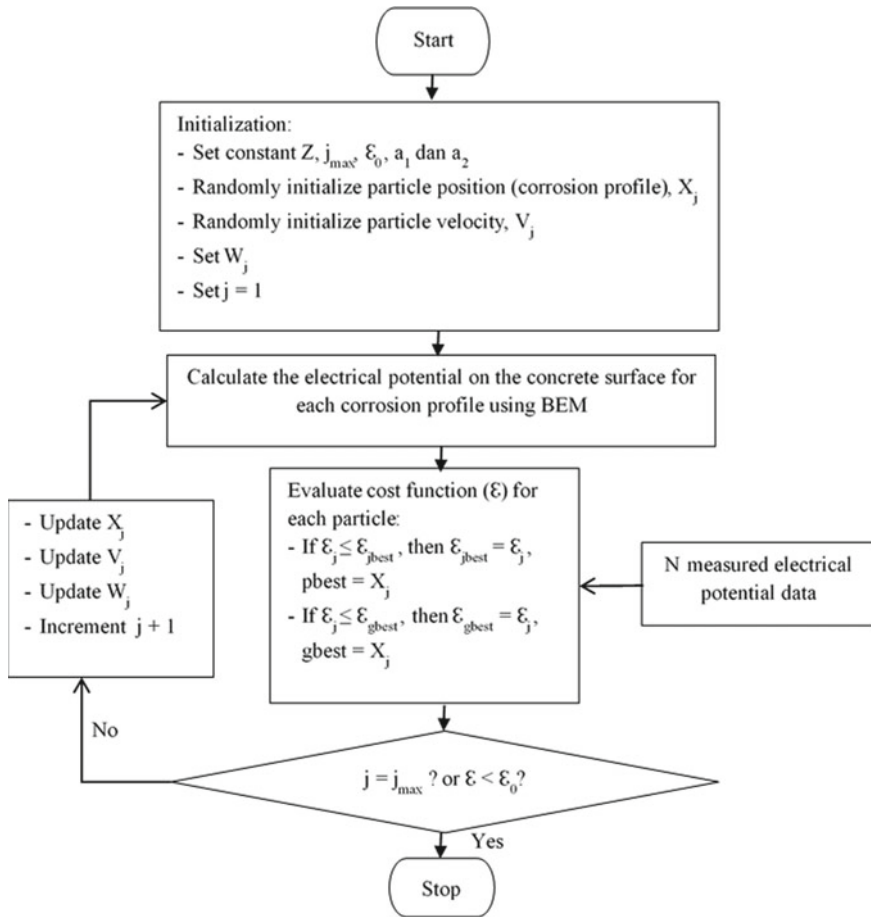
Fig. 1 The flowchart of BEIA

$$\varepsilon(X) \sum_{l=1}^{N} = \left[\frac{\phi_l - \bar{\phi}_l}{\bar{\phi}_{\max}} \right]^2 \qquad (1)$$

In this equation, X represents the corrosion location on the reinforcing steel. ϕ and $\bar{\phi}$ are potential values calculated using BEM and measured potential data such as using half-cell potential mapping. $\bar{\phi}_{\max}$ is the highest measured electrical potential value among N. The objective function value is evaluated for each particles from each iteration with predetermined conditions.

When the maximum iteration has been reached, the simulation has been completed. However, if this is not achieved then the iteration continues by updating X_j and V_j. The change in position and velocity of each particle for each iteration follows Eqs. (2) and (3). In this equation, X_{j+1} = next particle position, X_j = current particle

position, V_{j+1} = next particle velocity, V_j = current particle velocity, W_j = Weight Inertia, a_1 and a_2 = constant, r_1 and r_2 = random numbers (0–1), *pbest* = local best particle position, *gbest* = global best particle position, and j = iteration.

$$X_{j+1} = X_j + V_{j+1} \tag{2}$$

$$V_{j+1} = WV_j + a_1 r_1 \left(pbest - X_j\right) + a_2 r_2 \left(gbest - X_j\right) \tag{3}$$

The value of ε is continuously evaluated following the flow diagram in Fig. 1. So that each particle can locate the corrosion when the stopping criterion has been reached.

The case study used in this research is a model of reinforced concrete which refers to the previous study [11] with a length of 400 cm, a width of 30 cm and a height of 30 cm. Then the reinforced concrete geometry was simplified into two dimensions as shown in Fig. 2. It can be seen in Fig. 2 that the location of the corrosion is still unknown. In this study, corrosion was detected using the developed BEIA method.

Furthermore, reinforced concrete geometry was meshed using constant element. The coordinates, nodes and elements were arranged in order, then integrated into the BEIA code. To run the BEIA simulation, potential data on the concrete surface obtained from field measurements are required. However, in this case the potential data from the field measurement results were taken from the BEM simulation results assuming the corrosion was at X_1 = 100 and X_2 = 300 cm.

Potential data from the BEM simulation results were obtained as in Fig. 3. The potential data were rounded-off into three-digit precision to imitate the measured data in the field. For this study, 15 potential data points were chosen for BEIA simulation from BEM simulation results. The BEIA was performed based on those 15 potential data points.
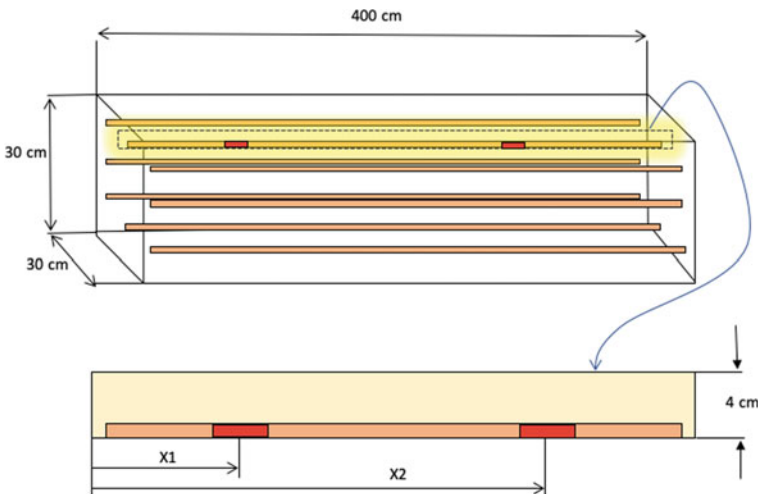
Fig. 2 Model of corrosion of reinforcing steel in the concrete structure
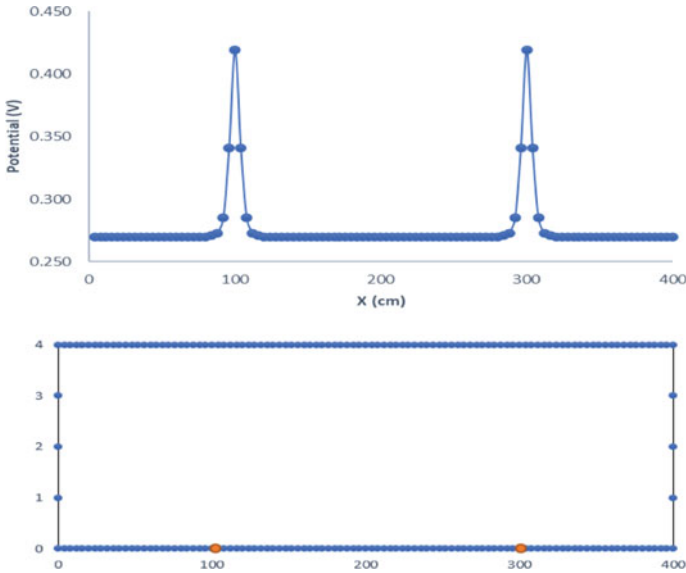
Fig. 3 Potential distribution on the concrete surface for the RC model using BEM

3 Results and Discussion

The results generated from the Boundary Element Inverse Analysis (BEIA) simulation can be seen in Figs. 4, 5, 6. The figures show the movement of particles at each iteration.

Figure 4a shows that twenty (20) particles were randomly scattered in the searching area along the rebar with various locations for the first iteration. Both corrosion locations (X_1 and X_2) were represented by each particle. On the subsequent iterations, each particle has started to form a group as shown in Fig. 4b. However, the positions of the particles were not at the actual corrosion location yet.
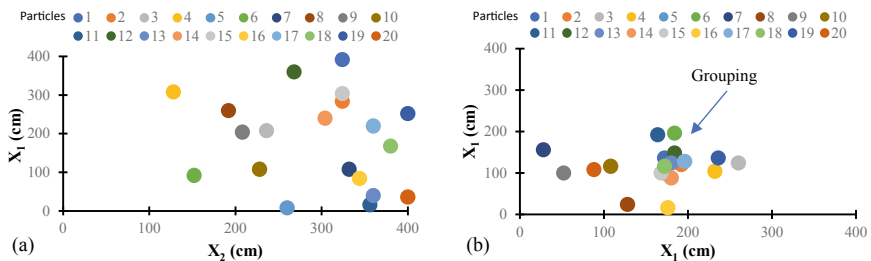
Fig. 4 BEIA simulation results: **a** 1st iteration; **b** 10th iteration
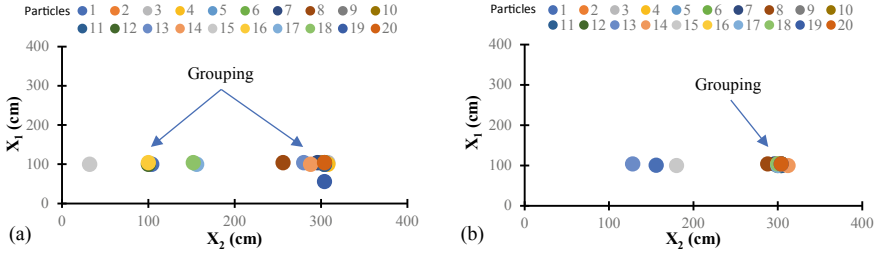
Fig. 5 BEIA simulation results: **a** 25th iteration; **b** 50th iteration
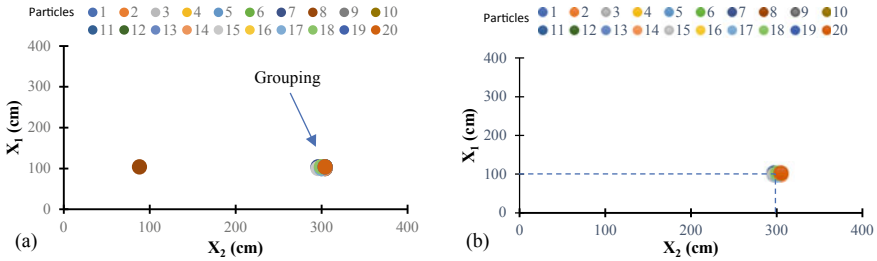
Fig. 6 BEIA simulation results: **a** 75th iteration; **b** 100th iteration

Then, in the 25th iteration, the particles become less-scattered as shown in Fig. 5a. Here, almost all particles have found the X_1. There were two large group of particles that correspond to X_2. After the 50th iteration, most particles have clustered around the corrosion locations (X_1 and X_2) as depicted in Fig. 5b. There were only three particles that were still outside of the group. However, it indicated that the corrosion locations were starting to be located by the particles.

As the iteration continues, the clustering becomes dense, which means that the corrosion location has been determined by almost all particles, as shown in Fig. 6a. There was only one particle that still is outside the group in the 75th iteration. In the 100th iteration (Fig. 6b), all particles have converged in certain position that were the corrosion location (X_1 and X_2). Comparison of actual corrosion locations ($X_1 = 100$ and $X_2 = 300$ cm) and the BEIA result yields error of $\leq 5\%$. Thus, the result is acceptable [9, 11].

Figure 7 shows the cost function values for all particles with increasing iteration. The criterion for finding the corrosion location was set at the cost function value of $<10^{-1}$. The figure shows that all particles start to have the cost function value of $<10^{-1}$ after 94th iteration. It means that after 94th iteration, all particles already converged, and the corrosion locations have been detected. The same implication can be also be found from Fig. 6b the locations of corrosion were identified on 100th iteration.
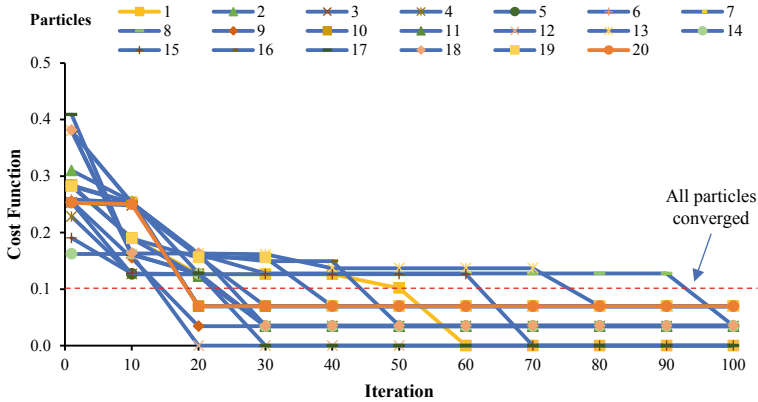
Fig. 7 The cost function of particles in searching for two corrosion location for RC model

4 Conclusion

BEIA was developed by combining BEM and PSO to detect the locations of corrosion in reinforced concrete. The development of BEIA has been successfully carried out. The BEIA effectively performed in locating two locations of corrosion with good accuracy and an error of $\leq 5\%$. Hence, the developed BEIA can be used to detect corrosion in reinforced concrete. Further study is needed to improve the capability of BEIA to detect multiple locations of corrosion in reinforced concrete.

References

1. Roberge PR (2008) Corrosion engineering: principles and practices. McGraw-Hill, New York
2. Darmawan MS (2006) Model korosi untuk struktur beton bertulang di lingkungan air laut. Seminar nasional rekayasa perencanaan VIII, UPN Jatim, Surabaya (in Indonesian)
3. Badan Informasi Geospasial, *no year*, Garis Pantai Indonesia Terpanjang Kedua. http://big.go.id (*in Indonesian*)
4. Moreno E, Cobo A, Palomo G, Gonzalez MN (2014) Mathematical models to predict the mechanical behaviour of reinforcements depending on their degree of corrosion and the diameter of the rebars. Constr Build Mater 61:156–163
5. Fonna S, Huzni S, Ridha M, Ariffin AK (2013) Inverse analysis using particle swarm optimization for detecting corrosion profile of rebar in concrete structure. Eng Anal Boundary Elem 37:585–593
6. Kelvin (2012) Probe electrode for contactless potential measurement on concrete—properties and corrosion profiling application. Corros Sci 56:26–35
7. Ridha M, Fonna S, Huzni S, Ariffin AK (2013) Corrosion risk assessment of public building affected by the 2004 tsunami in Banda Aceh. J Earthquake Tsunami 7(1):1–2

8. Marinier P, Isgor OB (2013) Model-assisted non-destructive monitoring of reinforcement corrosion in concrete structures, nondestructive testing of materials and structure. In: Büyüköztürk O et al (eds) RILEM Bookseries, pp 719–724. Springer-Verlag

9. Fonna S (2014) Boundary element method and particle swarm optimization for inverse analysis to identify reinforced concrete corrosion. In: Doctoral dissertation, University Kebangsaan Malaysia (UKM) (in Malay)

10. Fonna S, Ibrahim IM, Ridha M, Huzni S, Ariffin AK (2016) Simulation of the ill-posed problem of reinforced concrete corrosion detection using boundary element method. Int J Corros, article id 6392702

11. Fonna S (2018) Boundary element inverse analysis for rebar corrosion detection: study on the 2004 tsunami—affected structure in Aceh. Case Stud Constr Mater 8:292–298

Performance of Ultrasonic Atomization on Mini Sea Water Humidification and Dehumidification Technology

I. D. G. Agustriputra, Putu Wijaya Sunu, Sudirman, Nyoman Sugiartha, I. Wayan Temaja, and Wayan Nata Septiadi

Abstract Ultrasonic atomization is one of methods to generate very narrow droplets on atmospheric pressure and ambient temperature. Droplets are ejected on low velocities and microns size distribution. Sea water distillation process removed salts and minerals from sea water as saline water. Normal salinity of the sea water is about 3500–4000 ppm. Many kinds of technology had been developed to convert saline water into fresh water with various methods and apparatus. This project was performed an experimental to observe the performance of new technology within humidification and dehumidification process that is assisted by ultrasonic humidifier. It has been performed a mini humidification and dehumidification technology which utilized a commercial ultrasonic humidifier with power rating 10 watts and resonance frequency of 1.65 MHz. This work also analyses measurement of the production of fresh water by their quality and quantity. Quality of the fresh water has been indicated by salt concentrations of output of mini seawater humidification and dehumidification technology and also number of output fresh water flow rate as their quantity. It has been measured about 1150–1165 ppm and the rate of fresh water production about 65–84 ml/h by single unit of ultrasonic humidifier.

1 Introduction

Water is a part of life and our life necessities. There are two main problems for sustainable fresh water supply, scarcity of fresh water and increasing demand of fresh water for the population. The world's water consumption is enormous and spread across various applications and industries. Maintenance costs of equipment

I. D. G. Agustriputra (✉) · P. W. Sunu · Sudirman · N. Sugiartha · I. Wayan Temaja
Department of Mechanical Engineering, Bali State Polytechnic, Jl. Kampus Bukit Jimbaran,
Badung-Bali, Indonesia
e-mail: dewagedeagustriputra@pnb.ac.id

W. N. Septiadi
Mechanical Engineering, Udayana University, Kampus Bukit Jimbaran,
Badung-Bali, Indonesia

are one of the biggest problems that has been faced to develop technology of fresh water production. Fresh water is generally characterized by concentrations of dissolved salts and other total dissolved solid. Though seawater and brackish water excludes specifically by the terms. Indonesia is an archipelago which has a large amount of seawater. Separation technique to distilled water from seawater were performed by using many different kind of systems [1]. One of the methodologies is humidification and dehumidification (HDH) for distillation of sea water. Many researchers have designed HDH desalination system and their target was to reduce the power consumption or increasing use of free renewable energy [1–4]. Along with these development steps, various design and capacity becomes important parameter for sustainable technology and appropriated by user in different culture.

Several Technology was developed by atomization process on distillation system for extraction and separation binary liquids solutions. One of atomization process had been applied an ultrasonic vibration which produced by piezoelectric disc. Unlike conventional atomization, ultrasonic atomization of liquid can be more energy efficient and requires only electrical energy which it's transmitted to a piezoelectrically vibrating disk [5]. There are no moving parts and only mechanical vibrations generated by the supplied electrical energy are used for the generation of the droplets. Ultrasonic atomization is the ejection of fine droplets from a liquid film formed on an ultrasonically vibrating surface. The ejection of the droplets from a vibrating surface has been explained by a combination of two major hypothesis viz. capillary wave hypothesis and cavitation hypothesis. The capillary wave hypothesis, which can't be observed visually, considers the formation of a capillary wave consisting of peaks and troughs on a vibrating surface. The cavitation hypothesis suggests that droplet formation is controlled by cavitation, a phenomenon which is basically the formation of cavities in the liquid film on the vibrating surface of the atomizer. The collapse of these bubbles, especially near the surface, it's expelled directly from the droplets by a cavitation event around the oscillating piezoelectric disk [4, 6, 7].

However, cavitation are difficult to control in a random droplet size distribution from ultrasonic atomizer. Consequently, the narrow size distribution of droplets observed from ultrasonic atomizer have been difficult to explained by the cavitation theory. On this project work, we carry out experiments on ultrasonic atomization to investigate humidification process at excitation frequency of 1.65 MHz, to provide insight into the dynamics of ultrasonic atomization. We base our analysis on cavitation wave mechanism which is responsible for fog formation on sea water humidification and dehumidification technology. This choice have been considers by recent works that had been proposed, such as: utilization ultrasonic atomization on solar still technology, enrichment of ethanol solutions and also others work to investigate increasing of humidification process by ultrasonic atomization [1, 8, 9]. This experimental study was conducted to analyses production of fresh water and reduced of salt concentrations as the process of desalination output quality. A portable ultrasonic humidifier had been utilized to increase humidity in humidification chamber [1, 6]. The thickness of sea water layer and mass flow rate of the air will be important parameter on design for application of ultrasonic humidifier.

2 Literature Review

Ultrasonic Atomization has been used in a large number of applications, as the droplets generated are very large in number and small in size, typically only a few micrometers in diameter. The most common commercial applications are in room humidifiers for domestic use and in the delivery of aerosol drugs such as in asthma treatment. Room humidifier have been used on room air conditioning system, mostly utilized in subtropic for domestic appliances and also for fresh fruits and vegetable supply chain. The generation of a very fine mist also finds application in the fumigation of fresh food and in the sanitization of food service equipment. The mist generated by acoustic atomization has a very large surface area per unit volume of solution, due to the small diameter of the droplets. This means that surface-active species such as amino acids and peptides will be preferentially concentrated within this mist. This approach has been used to concentrate the ethanol in rice wine and the amino acids tryptophan and phenylalanine from dilute aqueous solutions. Series of experiments were performed to analyze the influence of physical parameters such as temperature, carrier gas flow and position of mist collection on the enrichment of ethanol distillation. Besides, droplet size measurements of the atomized mists and visualization of the oscillating fountain jet formed during ultrasound application were utilised to understand the separation mechanism [5, 10]. However, the level of concentrations that can be achieved is limited by the rate of mass transfer of generated mist through the liquid to the surface of the droplets as their form [8].

So far, there is no general consensus in the literature on the actual mechanism that is responsible for ultrasonic atomization. Evidence for cavitation has been reported only in situations where the forcing acceleration is very high, such as in horn atomizers. On the other hand, there are no evidence of cavitation was reported in the case of ultrasonic atomization which occurred on surface of vibrating piezoelectric disc. Sea water desalination plant is a technology for separation of fresh water from sea water. Amount of salt will be removed by distillation process or others similar separation process. Solar still is common technology as a conventional method. This technology had been developed significant by various research and methods cause of utilization of solar thermal energy which has been free energy [8, 11, 12]. Utilization of ultrasonic atomization becomes favorable technology in recent years for application on several fields such as humidification [13], aroma diffusion, dust control and nanoparticles separation. Advantages of ultrasonic atomization separation are easy operation, available to heat-sensitive materials, and maintenance free. An ultrasonic atomization process utilized more efficient electric energy, generating mist by mechanical vibrations which supplied by electrical power.

3 Testing Method and Experimental

In this experimental we were looking into whether we consider to examine 'ul-ultrasonic humidifier' presumably as an evaporation (or humidification) process on partly of mini sea water humidification and dehumidification technology. We assume that the ultrasonic transducer contributed as a mechanical work through vibrations to generate the mist or fog water on the air circulation of the carrier gas.

3.1 Materials and Equipments

A commercially available mist-maker or ultrasonic humidifier (also known as nebulizer) was used to carry out the experiments. The resonant frequency of the disc was f = 1.65 MHz with a working disc diameter of 20 mm and power rating about 10–15 W. Acrylic materials utilized for construction of design two chamber on prototype mini humidification and dehumidification technology Micro dc sub-mersible pump was utilized to drain water to the surface of 20 mm piezoelectric. Dry air was blown by single blower unit to ducting and PWM module applied to speed controller of the blower unit (Fig. 1). DC power supply has been used to supply an electrical power for ultrasonic generator (24 V) and blower.

1. Ultrasonic humidifier	5. Dc Blower 5015 24 volt
2. Piezo electric disc	6. Sand filter dehumidifier chamber
3. Air blower intake	7. Blower ssuction pipe
4. Bafel humidification chamber	8. Fresh water out
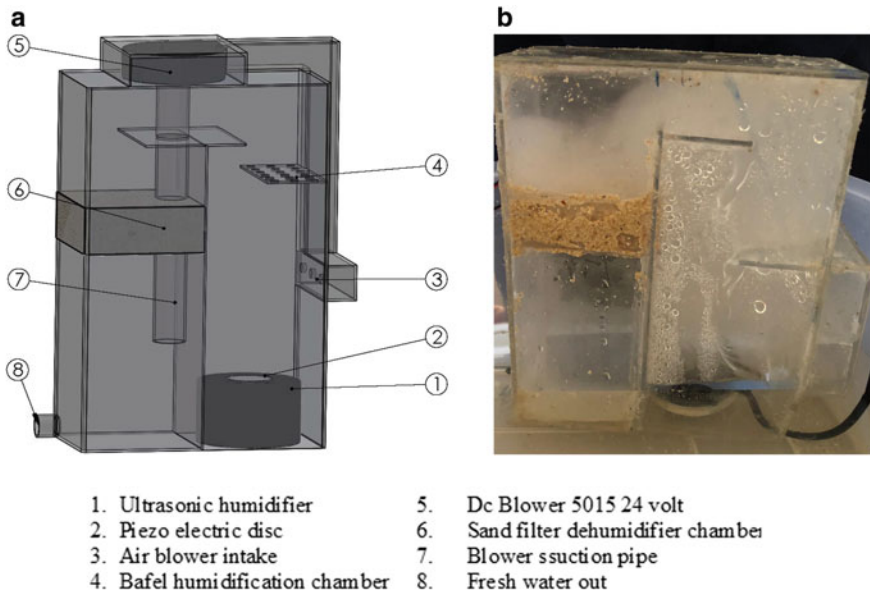
Fig. 1 **a** Schematic figure of mini humidification and dehumidification technology; **b** Prototype mini sea water humidification and dehumidification technology

3.2 Experimental Setup

The dry air was driven into humidifier through intake manifold of the air blower. After ultrasonic atomization, humid air mixed with water vapor were injected in humidifier chamber through "upside chamber" dry air temperature and relative humidity were measured. Figure 1 shows schematic (a) and model test (b) of mini humidification and dehumidification in vertical plane, respectively. During measurement process, dry air was directly humidified on the humidification chamber. The experiments were conducted to evaluate the overall performance on application ultrasonic atomization for humidification process and salt concentrations on output of fresh water. The dry air temperature, relative humidity, and energy consumption as input electrical current to ultrasonic generator, were measured continuously in duct system of two chambers.

3.3 Measurement Procedure and Data Analysis

Measurements were made to determine the effect of water layer thickness and mass flow rate that occurs on relative humidity and air temperature. Measurement procedure is by observing the limits of water layer thickness so that it's generated fountain fog as visual observation. Next procedure is to control the blower's rotation speed using the PWM module. After observations were determinate, data of measurement have been collected from several sensor which installed in humidification dehumidification chamber.

We have been designed arduino environment for an embedded system on measuring system and collecting data this experiment. 3 thermocouple type K with max 6675 module were utilized to measure temperature of air flow on mini seawater humidification and dehumidification technology. 2 humidity sensors type SHT 11 has been used for measure relative humidity and dry bulb temperature. Arduino uno R3 installed for collecting and digital reading all sensors and module. Arduino uno R3 was configured by IDE environment software for create an embedded system. Max 6675 module supported for Serial Peripheral Interface (SPI) data transfer and SHT 11 configured by analog data transfer to arduino base system.

Based on the measured results (dry temperature and relative humidity), the absolute humidity (humidity ratio or moisture content), and partial pressure of water vapor could be obtained by following equations:

$$\omega = \frac{0.622\varphi}{(P_b - P_{sw}\omega)} \tag{1}$$

where ω is humidity ratio (kg/kg), φ is relative humidity, P_b is atmospheric pressure (Pa), Psw is partial pressure of water vapor (Pa), then it has been determinate by dry air function (T);

$$\ln P = C_8/T + C_9 + C_{10}T + C_{11}T^2 + C_{12} \ln T \tag{2}$$

and coefficient of $C_8 = -6069.9385$; $C_9 = 21.2409643$; $C_{10} = 0.027111929$; $C_{11} = 1.673952 \times 10^{-5}$; and $C_{12} = 2.433502$, which could be utilized to describe the relationship between air temperature and partial pressure of water vapor.

Measurement of salt concentrations utilized a digital salinometer and also number of productivities fresh water measured by measuring cup and stopwatch. It is not easy to measure on side the fresh water out (Fig. 1) by digital measurement.

4 Result and Discussion

Firstly, it is necessary to measure the electric current to the ultrasonic humidifier module for limits of sea water layer thickness. The limits of the test are referred to the limits on the thickness of the sea water layer for humidification chamber and air mass flow rate which has been set on the prototype of mini sea water humidification and dehumidification technology.

According to electrical current measurement (Table 1), the limits on the thickness of the water layer and air mass flow rate are considered on gain of electrical supply and observations about fog formation. We have decided to the testing limit of water layer thickness on 3–5 cm and also air mass flow rate on 0.0000558– 0.000372 kg/s. Water layer thickness influenced on increasing of electrical current up to 0.01 A at thickness 4–5 cm water layer.

On this experiment we have been collected data relative humidity and dry air temperature from sensors SHT 11 and then, data have been determined for moisture content of dry air. Based on the psychrometric of the air we calculate flow rate of the moisture content. Figure 2 shows that rise of moisture content by gained of ultrasonic humidifier on the chamber. On the higher limit of mass flow rate increased their moisture content but lower mass flow rate reduced moisture content

Table 1 Electrical current supply to ultrasonic humidifier module

Sea water thickness (cm)	Electric current (A)
3	0.42
3.5	0.42
4	0.42
4.5	0.42
5	0.43
5.5	0.43
6	0.43
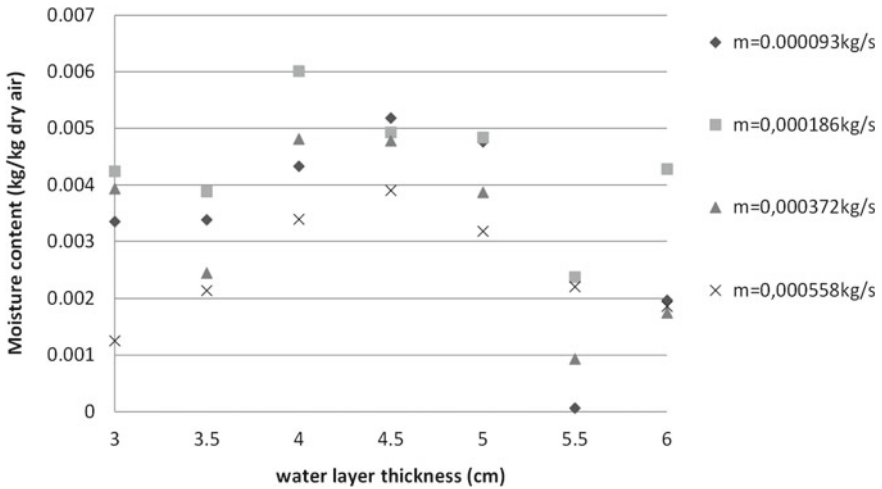
Fig. 2 Gained of moisture contents on mini sea water humidification and dehumidification technology

of dry air on humidification process. Humidification process have been determined for effective limits of water layer thickness about 3.5–4.5 cm and also air mass flow rate about 0.0186 kg/s.

Temperature difference of dry air is deviation of dry air temperature between dry air temperature in suction blower and temperature humid air on the humidifier chamber. Figure 3 shows that almost all the testings are increased their temperature of dry air. Electrical equipment produced heat which transferred to sea water on humidification and dehumidification chamber. Increasing of temperature have been
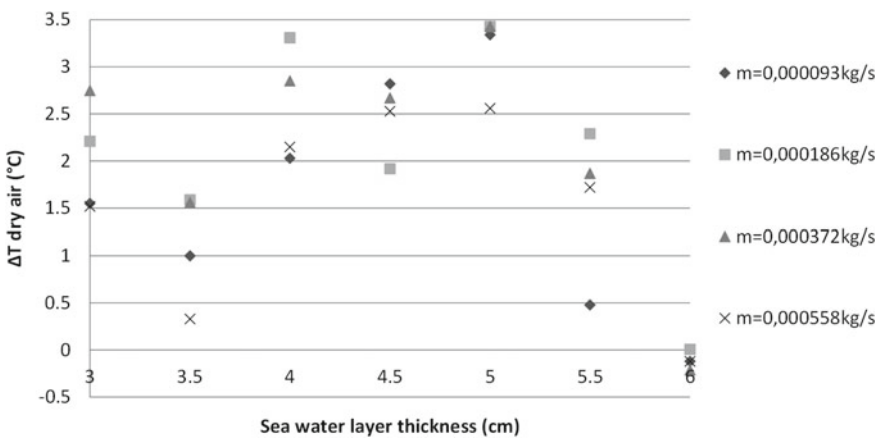
Fig. 3 Temperature deviation on mini sea water humidification and dehumidification technology

Table 2 Salts concentrations and flow rate

No. experiment	Salt concentrations (ppm)	Flow rate (ml/h)
1	1164	60
2	1165	67
3	1160	68
4	1158	74
5	1155	75
6	1152	80
7	1150	84
8	1154	81
9	1150	78
10	1152	80

held on 4.5 cm water layer thickness and it's maximized on 5 cm water layer thickness. Air mass flow rate about 0.000186 kg/s shows that the temperature deviation is higher relatively than others air mass flow rate.

Performance of mini sea water humidification and dehumidification indicated by measurement of fresh water output flow rate and reduction of salt concentrations as quality of fresh water production. Measurement had been performed by 30 min of time interval and we have been observed repetition for 10 times measurement. Base on preliminary testing we have decided to adjusted 4 cm thickness of sea water layer on the surface of piezo electric disc.

Based on Table 2, this prototype could be reduced the salt concentrations of sea water. It's normally, about 4000–5000 ppm which has been reduced up to 1150–1165 ppm of salt concentrations on fresh water outputs. Productivity of fresh water is about 60–84 ml/h. Post-treatment of this fresh water is needed to meet the requirement of fresh water outputs for water consumption. Even though development of this technology is still promising for utilizations of free renewable energy (PV power) and also sustainable fresh water supply for coastal area. Pressure difference between humidification and dehumidification chamber will be influenced of rise of fresh water productivity and also carrier gas properties which is circulated. It's a major objective for next project on over all investigation of this technology.

5   Conclusion

On this paper, the utilization of ultrasonic humidifier for mini seawater humidification and dehumidification technology had been tested their performance experimentally. It performed shows that ultrasonic humidifier on humidification and dehumidification process had been reduced sea water salinity up to 1150 ppm and maximum fresh water productions is 84 ml/h.

References

1. Shehata AI, Kabeel AE, Khairat Dawood MM, Abo Elazm MM, Abdalla AM, Mehanna A (2019) Energy Convers Manage 201:112–142
2. Rahimi-Ahar Z, Hatamipour MS, Ahar LR (2020) Prog Energy Combust Sci 80:100850
3. Dumka P, Jain A, Mishra DR (2020) J Energy Storage 30:101541
4. El-Said EMS, Abdelaziz GB (2020) J Clean Prod 256:120609
5. Spotar S, Rahman A, Gee OC, Jun KK, Manickam S (2015) Chem Eng Process Process Intensif 87:45–50
6. Yasuda K, Honma H, Asakura Y, Koda S (2010) Symp Ultrason Electron 31:363–364
7. Khmelev VN, Shalunov AV, Golykh RN, Nesterov VA, Dorovskikh RS, Shalunova AV (2017) Eng. Phys. Thermophys 90(4):831–844
8. Dumka P, Mishra DR (2020) Energy 190:116398
9. Shehata AI et al (2020) Energy Convers Manage 208:112592
10. Lozano A, García JA, Alconchel J, Barreras F, Calvo E, Santolaya JL (2017) 6–8
11. Zhang Y, Sivakumar M, Yang S, Enever K, Ramezanianpour M (2018) Desalination 428:116–145
12. Rahbar N, Esfahani JA, Asadi A (2016) Energy Convers Manage 118:55–62
13. Putra IDGAT et al (2020) J Phys: Conf Ser 1450:012050

Experimental Research of Solar Cooker with High Solar Energy Concentration Using Parabolic Dish

Muhammad Amin, Fazri Amir, Nasruddin A. Abdullah, Agus Putra A. Samad, Hamdani Umar, and Aron Okto Tri Yanto Sirait

Abstract The problem on energy consumption in the household, especially in cooking activities is the air pollution. Therefore, the priority to overcome the matter is by creating a solar cooker that can produce a high temperature energy which can be applied for cooking, boiling, and frying. The concept of Concentrating Solar Power (CSP) is to produce maximum temperature, and it was achieved using an environmentally friendly parabolic dish solar cooker. The purpose of this study was to determine the performance of environmentally friendly parabolic dish solar cookers. In his study, a parabolic dish equipped with a solar reflector film was used to reflect solar radiation. The samples used were water and oil. The parameter measurements were temperature distribution of solar cookers and the efficiency of solar cookers. At the end of this study, fish as a food product was tested to fry using the solar cooker. Based on the test, it found that the solar cooker has an efficiency of 20.5% at a solar radiation of 887.9 Wm^{-2} with an ambient temperature between 32.7 and 36.2 °C. The fried fish has a normal flesh texture and flavour. It indicated that this type of solar cooker is suitable to be used as cooking, boiling, and frying tool. Thus, this solar cooker can be recommended as a cooking tool for the needs of households and home industries.

M. Amin (✉) · F. Amir · N. A. Abdullah · A. O. T. Y. Sirait
Department of Mechanical Engineering, Faculty of Engineering,
Universitas Samudra, Kota Langsa 24416, Indonesia
e-mail: muhammadamin@unsam.ac.id

A. P. A. Samad
Department of Aquaculture, Faculty of Agriculture, University of Samudra,
Kota Langsa 24416, Indonesia

H. Umar
Department of Mechanical Engineering, Universitas Syiah Kuala,
Banda Aceh 23111, Indonesia

1 Introduction

Energy consumption in cooking activities plays an important role in household [1]. In developing countries, such as Indonesia, most household energy consumption is used for cooking purposes [2]. Nowadays, some underdeveloped and most developed regions in Indonesia still use wood-burning cookers [3]. Mostly, the smoke from wood contains toxic particles and compounds which are not good for the human health, especially the eyes and lungs [4]. Moreover, the smoke can produce CO_2 emissions that affect bad impact on the earth where climate change can occur erratically [5]. Therefore, the use of renewable energy is the best alternative as a source of energy to replace wood fuel.

The sun is an abundant source of energy that never runs out. It also very easy to obtain, inexpensive, has no effect on economic conditions, politics and pressure from richer countries. Indonesia is a country with an astronomical position on the equator, 6º of North Latitude to 11º South Latitude and 95º of East Longitude to 141º East Longitude which are on the path of energy sources [6]. The geographical position of Indonesia, which is crossed by the equator, causes very long solar irradiance and abundant energy sources and sunny weather each year, so that the heat in the sun can be used as an alternative energy. Indonesia has an average of 4.8 KWhm^{-2} intensity of solar radiation per day in all regions [6]. Solar energy is a good choice as an alternative energy source for cooking and heating water. There are many social and economic benefits for cooking and heating water using solar energy. Therefore, it is necessary to design techniques for an effective solar cooker for cooking purposes.

Solar cookers are simple devices that use environmental friendly and pollution-free, because solar energy does not consume any type of fuel [7]. Solar cookers are suitable for all locations with sufficient solar radiation throughout the year, especially in the tropics [8] and are very well used for areas that do not yet have electricity networks as reported Akayleh et al. [9]. The solar cooker was firstly made as a solar collector and then used to cook by a Swiss geologist in 1767 [10]. Furthermore, in 1878 India produced a mass production of these solar cookers [11]. At that time, solar cookers were generally used by the community for household needs such as cooking and boiling food. The advantages of solar cookers are cheap, simple design, easy to assemble, low maintenance, comfortable, safe cooking and free from pollution [12]. The temperature obtained by a solar cooker can reach 260–538 °C [13, 14] depending on the type of solar cooker used. The temperature on a solar cooker obtained easily when using solar Concentrating Solar Power (CSP) technology.

The principle of this CSP system is solar energy collected by a len/glass, then the len/glass reflects solar radiation to the focus point until an increase in energy flux occurs. This energy flux produces high temperatures [15]. The high temperature can be used for cooking purposes. CSP technology is commonly used a type of parabolic reflector, electric tower, parabolic plate, and using Fresnel Reflector [16].

Moussaoui et al. making a solar cooker system using a parabolic. The obtained temperature averages above 200 °C [17].

The solar cooker also has a pretty good performance compared to other cookers in general. Onokwai et al. made solar cookers that have good performance with efficiencies of 44.2% [18]. The time needed for a solar cooker to cook, boil, and fry is relatively short. The solar cooker made by Coccia et al. is able to boil 1 kg of water in just 11 min [19], the solar cooker Bhave and Thakare could cook 140 grams of rice in 30 min [20].

Based on the analysis above, whereas a solar cooker can be used to cook, boil, and fry, then a study on solar cooker is important to be done in order to produce a new type of solar cooker which suitable to Indonesian climate. Thus, the purpose of this study is to examine the performance of a parabolic dish type solar cooker as an environmentally friendly new technology. In his study, a parabolic dish equipped with a solar reflector film to reflect solar radiation that produces high temperatures.

2 Methodology

2.1 Experimental Set Up

This research is an experimental research. The test instrument studied was a solar cooker using a parabolic dish type CSP technology. All components of this solar cooker consist a satellite dish, solar reflector film, a buffer, and a pot for placing loads. The assembly system for the test equipment is a parabola made of circular steel plates coated with a solar reflector film. The image and its size are shown in Fig. 1 which consists of (a) side view, (b) front view, (c) top view, and (d) three-dimensional complete image. The sun tracking system is used manually which can be adjusted using a hydraulic system and the angle is adjusted using an arc that is adjusted to the latitude of the sun. In this study, the location of the focus point of the test equipment used equation [18]:

$$f = \frac{D^2}{16h} \tag{1}$$

whereas,

f   Where the focus point (m)
D   Aperture diameter (m)
h   Depth of the dish (m)
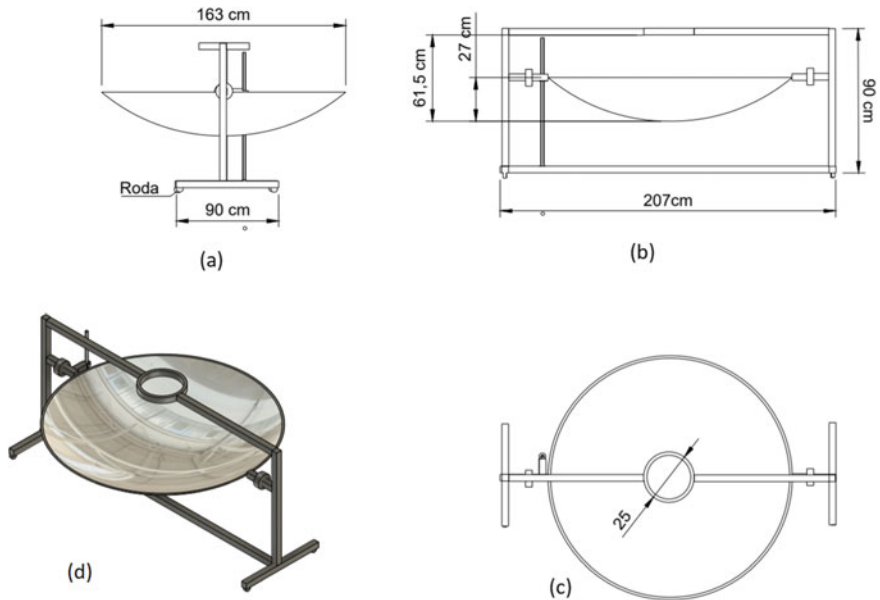
Fig. 1 Solar cooker instrument using parabolic dish

2.2 Procedure

In this research, the solar dish type parabolic was tested in 3 (three) stages. The first stage was measuring the temperature distribution above the parabolic area without any loads. It was done to determine the temperature distribution obtained on the solar cooker. The location of the focus point obtained was then compared with Eq. (1). The second stage was to test the performance of the solar cooker with a load. In this test, the loads used were water and oil with a mass of 1 kg each. The performance of the solar cooker tested was its efficiency only with a sample in the form of water and then analyzed using equation [18]:

$$\eta = \frac{mC(T_e - T_w)}{IA\Delta t} \tag{2}$$

whereas:

η Solar cooker efficiency (%)
m   Mass of the water (kg)
T_e Water boiling temperature (°C)
T_w Initial water temperature (°C)
C   Water specific heat capacity at constant pressure (4.186 kJ kg^{-1} °C^{-1})
I   Incoming average solar radiation (Wm^{-2})
A   Aperture area of the dish (m^2)

$$A = \frac{\pi D^2}{4} \tag{3}$$

The third stage was carried out the same as in the second stage. In this third stage, focus on seeing the final results of fish frying.

The first stage of this test was carried out from morning to evening, starting at 09.00 a.m. until 18.00 pm during the hot weather. The temperature data were obtained using a k-type thermocouple which was installed at several points as shown in Fig. 2a. The thermocouple is linked to the Agilent 34970A data acquisition type. Data is recorded every 1 (one) minute. The data was then processed in graphical form using a computer device. The graph that is displayed in the form of the y-axis represents the temperature and the x-axis represents time. The time taken is the average time per hour. The method of placing the focus point was by placing several thermocouples at several points where a plus sign shaped iron has been installed on the surface of the dish. The second stage of this test was using the samples (water and oil) as shown in Fig. 2b. Then the data in the form of temperature and time were taken and displayed in a graph and then analyzed and calculated the performance of the solar cooker in the form of efficiency only. The third stage is carried out the same as in the second stage. In this third stage, it is only to see the final result of frying fish.

In this study, the solar tracking system was set manually by rotating the angle by $3°$ continuously. The lever is rotated by monitoring the temperature of the focus point due to changes position of the sun latitude. The intensity of solar radiation was obtained using the HOMER energy software application by determining the coordinates of the research sites. The place of research is in the coordinates $4°$ 27, $5'$ N, $97°$ 56.3$'$ E then the data was taken according to the testing time.

(a)   (b)

Fig. 2 Solar cooker parabolic dish test **a** without any loads, **b** with loads

3   Results and Discussions

Figure 3a shows temperature distribution of the solar cooker without load. The temperature was measured using a k-type thermocouple which spread at several points as shown in Fig. 3b. The placement of the thermocouple at these points was intended to determine the highest temperature position. The points were given the notation T_1 to T_9 with a distance of 0.1 m. Based on the test, the highest temperature was obtained at T_1. T_1 was the focus point which exactly 0.6 m from the center of the parabola. Based on Eq. (1) the focus point also located at a distance of 0.61 m. The temperature of T_1 can reach 400 °C, much different compared with T_2 to T_9. These results proved that the placement of the pot was in accordance with the calculations and experimentally. In addition, the results of Fig. 3a explained that the temperature distribution of the solar cooker (T_1) has a temperature that good enough to be tested using loads. This research was conducted from 09.00 a.m. to 18.00 p. m. which was conducted on July 2, 2020 with a maximum solar radiation intensity of 785.8 Wm^{-2}. The results of measuring the intensity of solar radiation were not much different from the results of the test Sianturi et al. [21]. The ambient temperature (T_a) ranges from 34 to 35 °C. The temperature distribution of the solar cooker (T_1) reached 100–400 °C which could be operated for 6 h. Based on these data, this solar cooker can be carried out further research with loads.

Figure 4 showed the performance of a solar cooker with water and oil samples. The water tested was done on July 9, 2020 as shown in Fig. 4a. The experiment was carried out starting at 12.23 pm. when the weather was hot for 24 min. The Average solar radiation intensity was 887.9 Wm^{-2} with ambient temperature (T_a) between 32.7–36.2 °C. At first, the water was put into the pot; the initial temperature of water (T_w) at that time was 32 °C. Due to the high intensity of solar radiation, caused an increase in the pot's temperature (T_p) from 35.2 to 113.5 °C for 1 min. In these conditions the CSP system works to cause heat transfer, radiation and convection. The reflection from the solar reflector which focused on the pot was changed into heat. Therefore, the temperature in the pot increasing to heat the pot. Then it affects the water temperature. In this study, the boiling water was left constant for several minutes. The time needed to boil 100 °C of water was 12.5 min. So that the efficiency of the solar cooker based on Eqs. (2) and (3) is obtained 20.5%. Pot average temperature (T_p) was 324.7 °C. The working principle in this study is the same as that described in the research of Rekha and Sukchai [22]. Meanwhile, the oil sample test was carried out on July 11, 2020 as shown in Fig. 4b. Testing time starts at 11.52 a.m. on a hot 40-minute day. The Average solar radiation intensity at that time was 923.9 Wm^{-2} with an ambient temperature between 34 and 36.5 °C. Initially the oil was put into a pot where the initial oil temperature (To) was 34 °C and continues to increase to 108.8 °C within 7 min. Oil temperature (T_o) continue to increase until above 200 °C within 15 min. The maximum oil temperature obtained was 248.8 °C at 25 min and at 40 min the oil temperature was constant at 230 °C. During 40 min of this test, the average
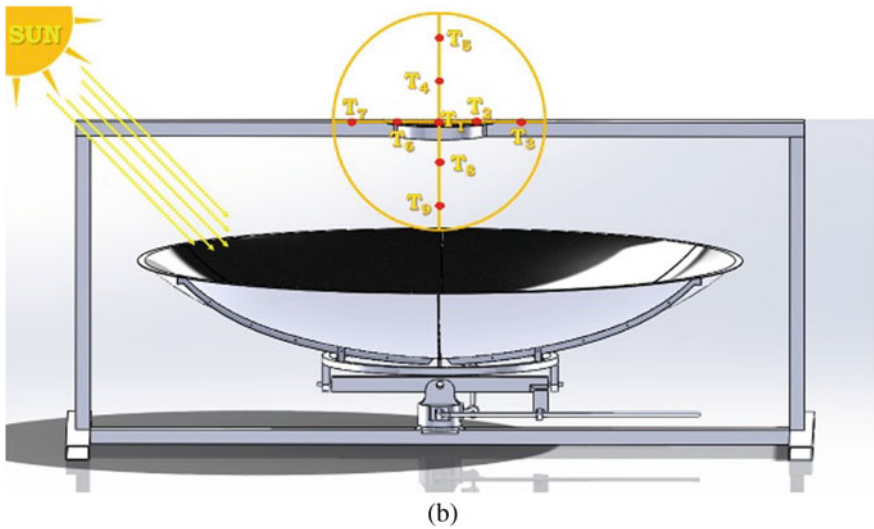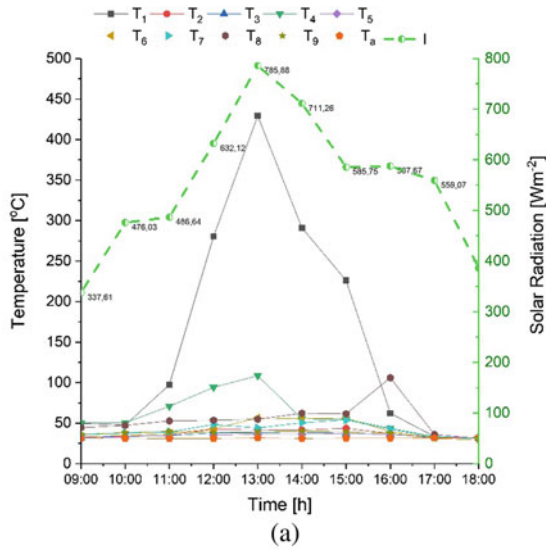
Fig. 3 a Solar cooker distribution without loads; b Thermocouples positioning to detect the highest temperature

temperature of the pot was 270.7 °C. Based on these results, the solar cooker is very possible for frying applications.

After testing the parabolic dish type solar cooker using oil, then the solar cooker was applied to test with food products. The food product tested in this study was fresh fish with a mass of 0.3 kg. Initially, the fresh fish were cook using frying pan filled with oil. The oil temperature at that time was 140 °C and frying pan

(a) water   (b) oil
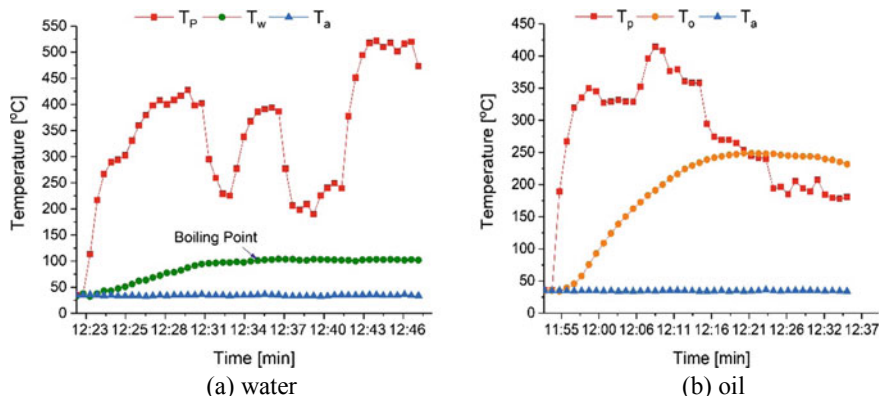
Fig. 4   Solar cooker performances using different samples

(a) The cooking process   (b) Fresh fish   (c) Fried fish
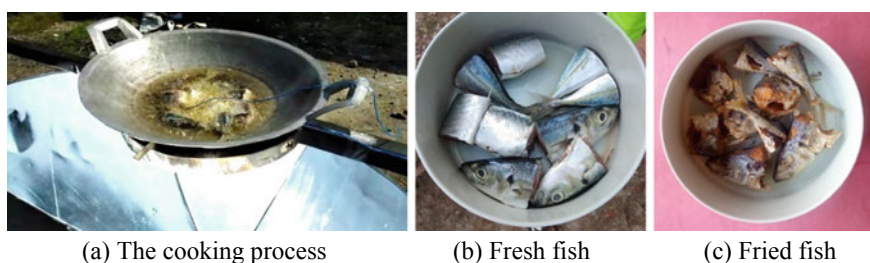
Fig. 5   The cooking process of fresh fish to be fried fish using parabolic solar cooker

temperature was 191 °C. The process of frying fish into fried fish using a parabolic dish type solar cooker takes 15 min. The process is shown in Fig. 5. The result of the fried fish was still in accordance with the standard of fried fish in general. The same thing was done by Zafar et al., whereas in their research solar cookers were applied to cook rice and roast chicken. The result is that cooking rice and roasting chicken takes 60 and 90 min, respectively [23].

4   Conclusions

Research on solar cookers using CSP system equipped with parabolic dish has been successfully tested. This solar cooker does not use any fuel, it only uses solar energy. Therefore, this solar cooker can be proved to be an environmentally friendly cooker. From this study, found that the temperature of the solar cooker could reach an average of 100 °C and the maximum temperature reached 500 °C. This solar cooker can be operated within 6 h per day during high solar radiation

intensity. The efficiency of solar cookers obtained 20.5%. Meanwhile, the test results of food products using a parabolic dish type solar cooker were carried out with a sample of wet frying fish. The final result obtained fried fish which has the same texture and flavour as fried fish in general. Therefore, this solar cooker is suitable to be applied as a tool for cooking, boiling, and frying. This solar cooker can also be recommended as an environmentally friendly cooker for household and home industry needs.

References

1. Paudel U, Khatri U, Pant KP (2018) Understanding the determinants of household cooking fuel choice in Afghanistan: a multinomial logit estimation. Energy 156:55–62 Aug.
2. Narayan S, Doytch N (2017) An investigation of renewable and non-renewable energy consumption and economic growth nexus using industrial and residential energy consumption. Energy Econ. 68:160–176 Oct.
3. Astuti SP, Day R, Emery SB (2019) A successful fuel transition? Regulatory instruments, markets, and social acceptance in the adoption of modern LPG cooking devices in Indonesia. Energy Res Soc Sci 58:101248 Dec.
4. Mazorra J, Sánchez-Jacob E, de la Sota C, Fernández L, Lumbreras J (2020) A comprehensive analysis of cooking solutions co-benefits at household level: healthy lives and well-being, gender and climate change. Sci Total Environ 707:135968 Mar.
5. Deka P, Hoque RR (2015) Chemical characterization of biomass fuel smoke particles of rural kitchens of South Asia. Atmos Environ 108:125–132
6. Rumbayan M, Abudureyimu A, Nagasaka K (2012) Mapping of solar energy potential in Indonesia using artificial neural network and geographical information system. Renew Sustain Energy Rev 16(3):1437–1449, 01 Apr 2012 Pergamon
7. Arunachala UC, Kundapur A (2020) Cost-effective solar cookers: a global review. Solar Energy 207:903–916. Elsevier, 01 Sep 2020
8. Pranesh V, Velraj R, Christopher S, Kumaresan V (2019) A 50 year review of basic and applied research in compound parabolic concentrating solar thermal collector for domestic and industrial applications. Solar Energy 187:293–340. Elsevier, 15 Jul 2019
9. Akayleh AS, Al-Soud MS, Al-Jufout SA (2020) Design and development of a solar-based cooker with a mechanical sun tracking system. Int J Ambient Energy 41(7):808–812 Jun.
10. Jebaraj S, Iniyan S (2006) Renewable energy programmes in India. Int J Glob Energy Issues 26(3–4):232–257
11. Aramesh M et al (2019) A review of recent advances in solar cooking technology. Renew Energy 140:419–435 Sep.
12. Saxena A, Karakilcik M (2017) Performance evaluation of a solar cooker with low cost heat storage material. Int J Sustain Green Energy 6(4):57 Jul.
13. Edmonds I (2018) Low cost realisation of a high temperature solar cooker. Renew Energy 121:94–101 Jun.
14. Islam R, Chowdhury T, Chowdhury H, Chowdhury P, Hasnat A, Barua B (2018) Barriers against the development of solar cooker & its solution. Int Conf Mech, Indus Energy Eng 2018:1–5
15. He YL et al (2020) Perspective of concentrating solar power. Energy 198:117373 May

16. Zhang HL, Baeyens J, Degrève J, Cacères G (2013) Concentrated solar power plants: review and design methodology. Renew Sustain Energy Rev 22:466–481 Jun.
17. El Moussaoui N et al (2020) Feasibility of a new design of a Parabolic Trough Solar Thermal Cooker (PSTC). Solar Energy 201:866–871. Elsevier, 01 May 2020
18. Onokwai AO, Okonkwo UC, Osueke CO, Okafor CE, Olayanju TMA, Dahunsi SO (2019) Design, modelling, energy and exergy analysis of a parabolic cooker. Renew Energy 142:497–510 Nov.
19. Coccia G, Di Nicola G, Pierantozzi M, Tomassetti S, Aquilanti A (2017) Design, manufacturing, and test of a high concentration ratio solar box cooker with multiple reflectors. Sol Energy 155:781–792 Oct.
20. Bhave AG, Thakare KA (2018) Development of a solar thermal storage cum cooking device using salt hydrate. Sol Energy 171:784–789 Sep.
21. Sianturi Y, Marjuki, Sartika K (2020) Evaluation of ERA5 and MERRA2 reanalyses to estimate solar irradiance using ground observations over Indonesia region. AIP Conf Proc 2223(1):020002
22. Santhi Rekha SM, Sukchai S (2018) Design of phase change material based domestic solar cooking system for both indoor and outdoor cooking applications. J Sol Energy Eng Trans ASME 140(4), Aug 2018
23. Zafar HA, Khan MY, Badar AW, Tariq R, Butt FS (2018) Introducing a novel design in the realm of box type solar cookers: an experimental study. J Renew Sustain Energy 10 (4):043707 Jul.

Investigation the Effect of Concrete Element Size on the Potential Distribution of RC Cathodic Protection Simulation Using BEM 3D

Iqbal Tanjung, Affandi, Syifaul Huzni, and Syarizal Fonna

Abstract The boundary element method (BEM) has been widely used as a technique to evaluate the performance of cathodic protection (CP) in reinforced concrete (RC) structures. The concrete element size is one of the parameters that is suspected to affect the performance of the BEM. The objective of this study is to investigate the effect of concrete element size on the electrical potential distribution of RC. The geometry used in this study is a concrete beam with nine reinforcing steel that is applied with CP. The geometry was built and meshed using the open-source software Salome mecca 8.3. Triangular elements were selected during the meshing process and then five variations of concrete mesh size were defined for this study. The simulation results show that the sacrificial anode is active in performing protection and the reinforcing steel is in a well-protected condition for all variations ($\leq$ −850 mV vs. Cu/CuSO$_4$). Furthermore, the electrical potential becomes evenly distributed when the concrete element size is smaller. However, it is still tolerable because the distribution pattern that occurs is conformable with the characteristics of common corrosion distribution.

Keywords Corrosion · Boundary element method · Reinforced concrete · Cathodic protection

I. Tanjung · Affandi
Department of Mechanical Engineering, University of Muhammadiyah Sumatera Utara, 20238 Medan, Indonesia

S. Huzni · S. Fonna (✉)
Department of Mechanical and Industrial Engineering, Universitas Syiah Kuala, Darussalam, 23111 Banda Aceh, Indonesia
e-mail: syarizal.fonna@unsyiah.ac.id

1 Introduction

Concrete has been used as a construction material for 3500 years. This material is believed to have built the pyramids, the Roman Colosseum, and others. Concrete is a composite material, namely the arrangement of cement, sand, coarse aggregate, and water. Throughout the development of technology to increase the tension mechanical properties and high loading capabilities, reinforcing steel (rebar) has been selected as a reinforcement in the concrete [1].

The high alkaline nature of the concrete initially provides passive protection for rebar against corrosion. However, environments with high humidity, high temperature, intense wet conditions, and hygroscopic conditions can bring damage to the oxide layer of the rebar surface. This is the beginning of the decline in the alkaline condition of concrete to pH < 14 and the corrosion of reinforced concrete (RC) could be initiated. The study stated that corrosion causes a loss of 3–4% of GDP in a country, so corrosion is a serious problem that needs to be controlled [2].

Corroded rebar induced deterioration in the RC structure produces a new product which has a greater volume than the original material, which makes cracks in the concrete structure that can generate damage and thereafter lead to the failure of the RC structure. To prevent corrosion of RC structures, generally, rebar is
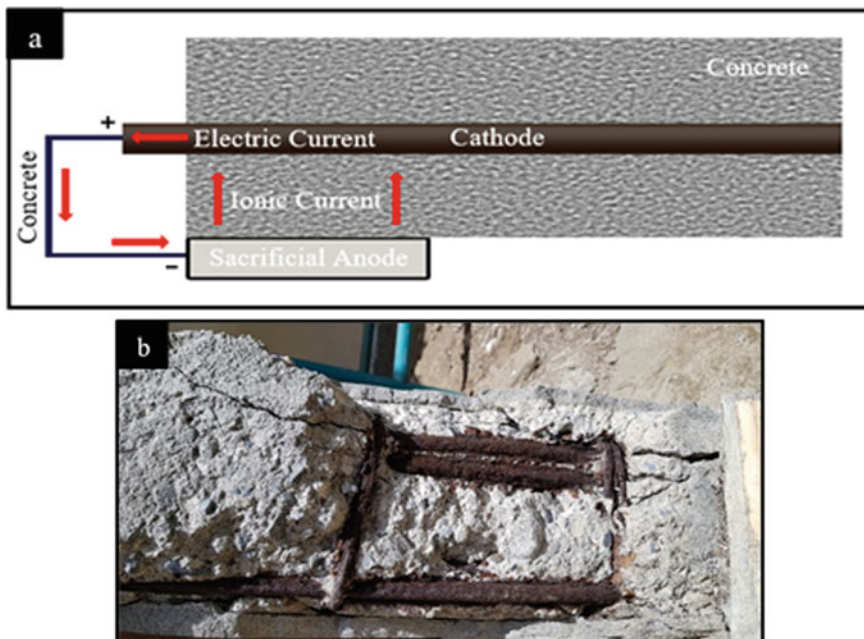
Fig. 1 **a** SACP applications on RC. **b** Damaged structure by corrosion

implemented using a corrosion protection system such as a sacrificial anode cathodic protection (SACP). This system has been widely applied in various concrete structures and has succeeded in preventing corrosion of the rebar. However, this system also has a weakness, i.e. it can only be evaluated when it has already been implemented [3, 4]. The Examples of SACP applications on RC and damaged structure by corrosion can be seen in Fig. 1.

In attempts to solve this problem, many researchers used numerical methods to solve a corrosion-engineering problem. One of the numerical methods used in solving corrosion-engineering problems is the boundary element method (BEM) [5]. This method is successfully used in solving some corrosion-engineering problems such as corrosion engineering on a pile pump and a pier structure. Thus, the development of the effectiveness of BEM is one of the most important studies. Development to increase the effectiveness of BEM has been conducted by Fonna et al. They evaluated the performance of BEM by observing the influence of the type of anode, the distance of anode to cathode, the size of the anode, and the concrete conductivity value to the protection potential of SACP [6, 7].

Iqbal et al. also carried out similar development. They observed the effect of the mesh ratio to the distribution of the RC potential applied with SACP [8]. However, some parameters such as the effect of the concrete element size to the RC potential distribution needs to be studied further. The objective of this study is to investigate the effect of concrete element size on the potential distribution of RC simulations applied with SACP using BEM.

2 Research Method

The Domain (Ω) in this study is a model of an RC beam that is applied electrically with SACP. The domain is considered in a steady-state so that it has a constant conductivity value. After it is defined, domains can be transformed into mathematical models using Laplace equations as shown in Eq. 1. The relationship between electrical potential and current density occurring in all domains is enclosed in Eq. 2, as well as for the all boundary conditions are set in the Eqs. (3–5).

$$\nabla^2\phi = \frac{\partial^2\phi}{\partial x^2} + \frac{\partial^2\phi}{\partial y^2} + \frac{\partial^2\phi}{\partial z^2} = 0 \quad (\Omega) \tag{1}$$

$$i = -\kappa\frac{\partial\phi}{\partial n} \quad \left(\text{A/m}^2\right) \tag{2}$$

$$i = i_0 = 0 \quad \Gamma_1 \quad \left(\text{A/m}^2\right) \tag{3}$$

$$\phi = -f_c(i) \quad \Gamma_2 \quad (\text{V}) \tag{4}$$

$$\phi = -f_a(i) \quad \Gamma_3 \quad (\text{V}) \tag{5}$$

where ϕ is the electrical potential, i is the current density of the domain, κ is the conductivity of the concrete, n is the normal vector and Γ is the boundary condition of the domain. By determining the boundary conditions of the domain, Eq. 1 can be solved using a matrix equation by following the standard formula for the BEM derivative as shown in Eq. 6. Hereafter, the potential value for the entire domain surface can be determined [5–9]. The model of SACP for RC is shown in Fig. 2.

$$\kappa[\text{H}] \left\{ \begin{array}{c} \phi \\ -f_c(i) \\ -f_a(i) \end{array} \right\} - [G] \left\{ \begin{array}{c} i_o \\ i_c \\ i_a \end{array} \right\} = 0 \quad (\Omega) \tag{6}$$

3 Case Study

The test object in this study was a RC beam with 9 rebar which is applied with SACP. The dimensions of the RC beam refer to previous research by Mahasiripan et al. [10] where the dimensions of the concrete beam were (100 mm × 100 mm × 1000 mm). The diameter and length of the rebar were $\Phi12$ mm and 80 mm and the dimension of sacrificial anode was ($\Phi25 \times 50$ mm). The model and geometry of the RC can be seen in Fig. 3a and 3b, respectively.

The rebar and the sacrificial anode used in the study were mild steel and Zn, respectively. The distance between the anode and the reinforcing steel was 20 mm for each variation. The geometry was built and meshed using the open-source software Salome Mecca 8.3. During the meshing process, five variations of the
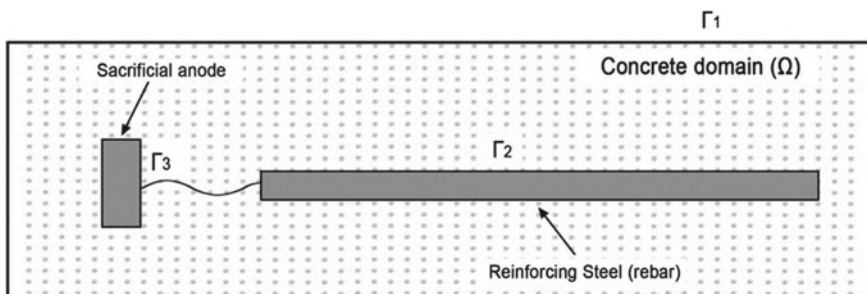

Fig. 2 The model of SACP for RC
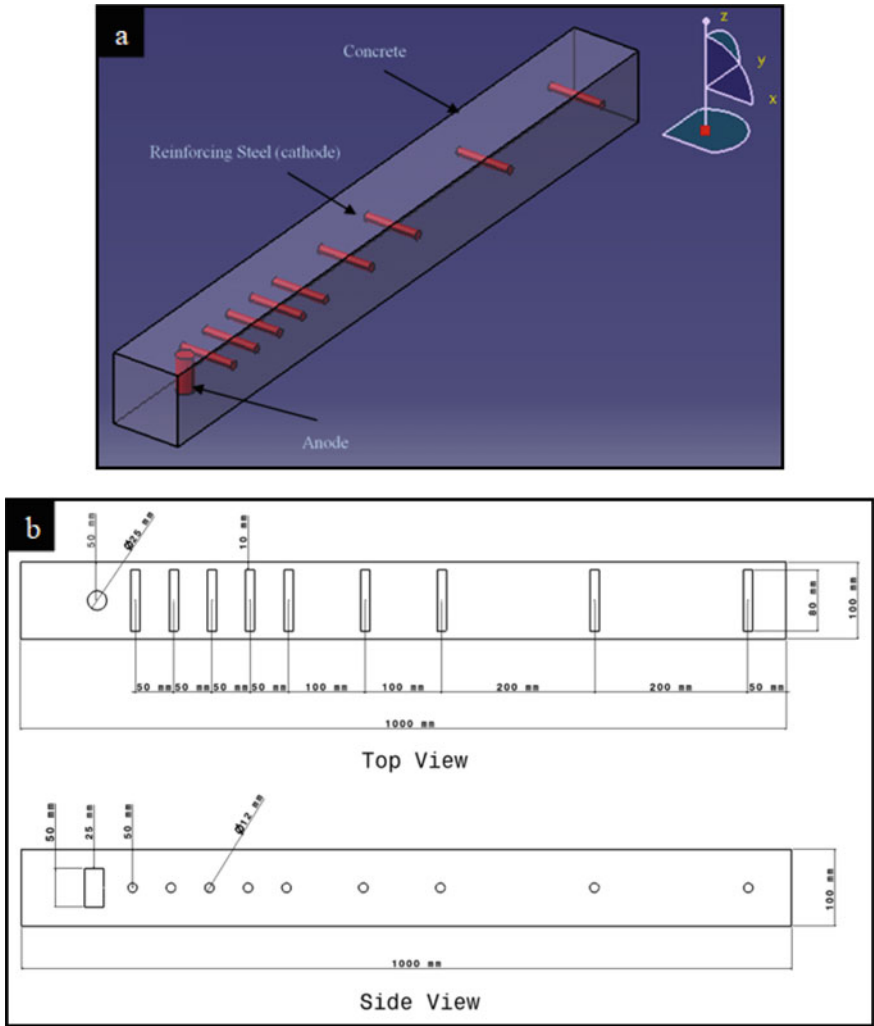
Fig. 3 a Modeling of RC. **b** Geometry of RC

Table 1 The variation of concrete element length for the study

Mesh length			
Variation	Anode/cathode (mm)	Concrete (mm)	Number of element
1	14	50	774
2	14	40	1074
3	14	30	1590
4	14	20	2538
5	14	10	6810

length of the concrete elements were tested, and the length of the anode/cathode elements was constant. In this study, the type of element used was a triangular element. After the built and meshing process finished, the data was incorporated into BEM code which afterward run the code using the FORTRAN compiler. The variation of mesh length of the concrete element and mesh length of anode/cathode element is tabulated in Table 1.

4 Result and Discussion

The successfulness of SACP in performing protection was observed based on the electrical potential value of the sacrificial anode and the rebar. The anode is active for protection if its electrical potential value ranged between (−1000 mV to −1200 mV) [1], whilst the rebar is categorized as protected from corrosion if the electrical potential value was ($\leq$ −850 mV vs. Cu/CuSO$_4$) [11]. The simulation results show the sacrificial anode has the electrical potential value in the range of −1000 mV to −1200 mV, whilst the reinforcing steel has the electrical potential value in the range of −900 mV to −920 mV for each variation. These indicates that the sacrificial anode is active in performing protection and the reinforcing steel is in a well-protected condition from corrosion. These results are consistent with the experiments conducted by Mahasiripan [10], so BEM has been used successfully in this study.

Hereafter, the effect of concrete element size is observed based on potential different value and the distribution of electrical potential that occurs throughout the concrete surface. In this study, it is assumed that the source of corrosion is only from the Zn sacrificial anode.

Figure 4 shows the potential distribution of variation 1 and 2. By observing the results in Fig. 4a, b shows that the distribution of electrical potential on the surface of the concretes have a relatively similar pattern. The simulation results describe the value of the highest electrical potential located in the area adjacent to the sacrificial anode. This case is a common corrosion potential distribution pattern [5]. The simulation results show the concrete surfaces have a potential value in the range of −897.72 mV to −1081.01 mV for variation 1 and −890.70 mV to −1084.38 mV for variation 2.

Figure 5 shows the potential distribution in variations 3, 4 and 5. The different distribution pattern was found for each variation respectively. By observing Fig. 5a, it shows there are points of higher electrical potential on the RC side. Furthermore, these points are more visible in variations 4 and 5 as shown in Fig. 5b, c. These points are the area directly adjacent to the rebar. This case indicates the potential distribution on the concrete surface is more even, where the area adjacent to the corrosion source has a more negative value than other areas [12]. The simulation results show the concrete surfaces have a potential value in the range of −893.51 mV to −1084.68 mV for variation 3, −893.52 mV to −1085.37 mV for variation 4, and −892.66 mV to −1086.09 mV for variation 5.
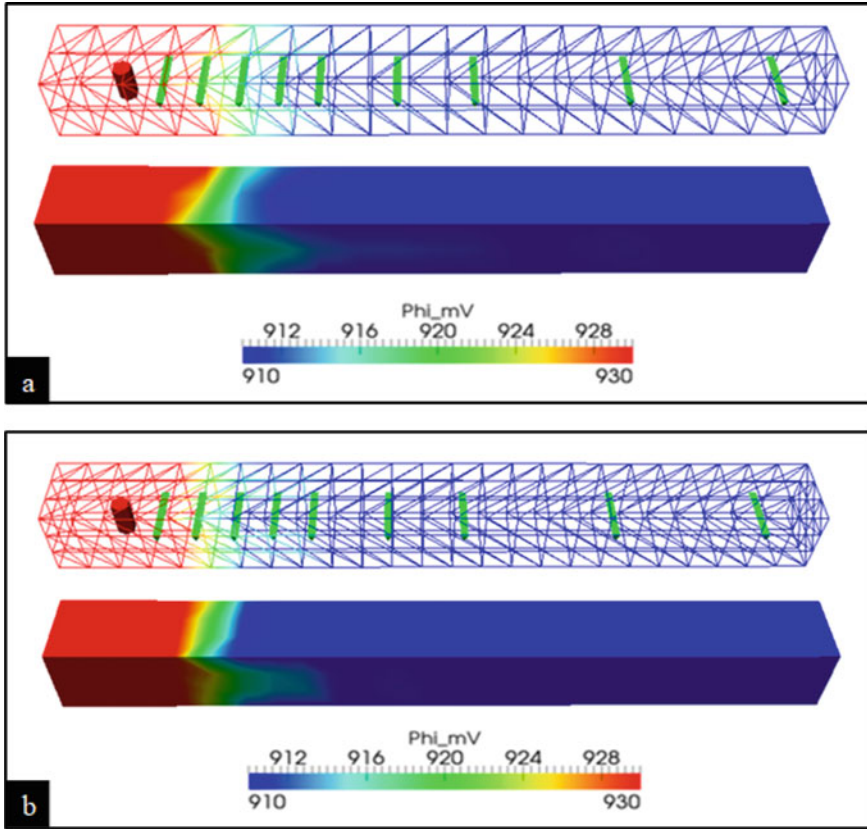
Fig. 4 Potential distribution for: **a** variation 1, **b** variation 2

The potential difference value for each variation is shown in Fig. 6. From the simulation result, it can be seen that the potential difference value decreases as the element size used in the simulation gets smaller. This is consistent with the potential distribution previously discussed. The electrical potential distributes more evenly when the potential difference value from the simulation results is smaller [6]. However, this decreased value is not significant and can still be tolerated because the distribution pattern that occurs conformable with the characteristics of common corrosion distribution and also within protection criteria.
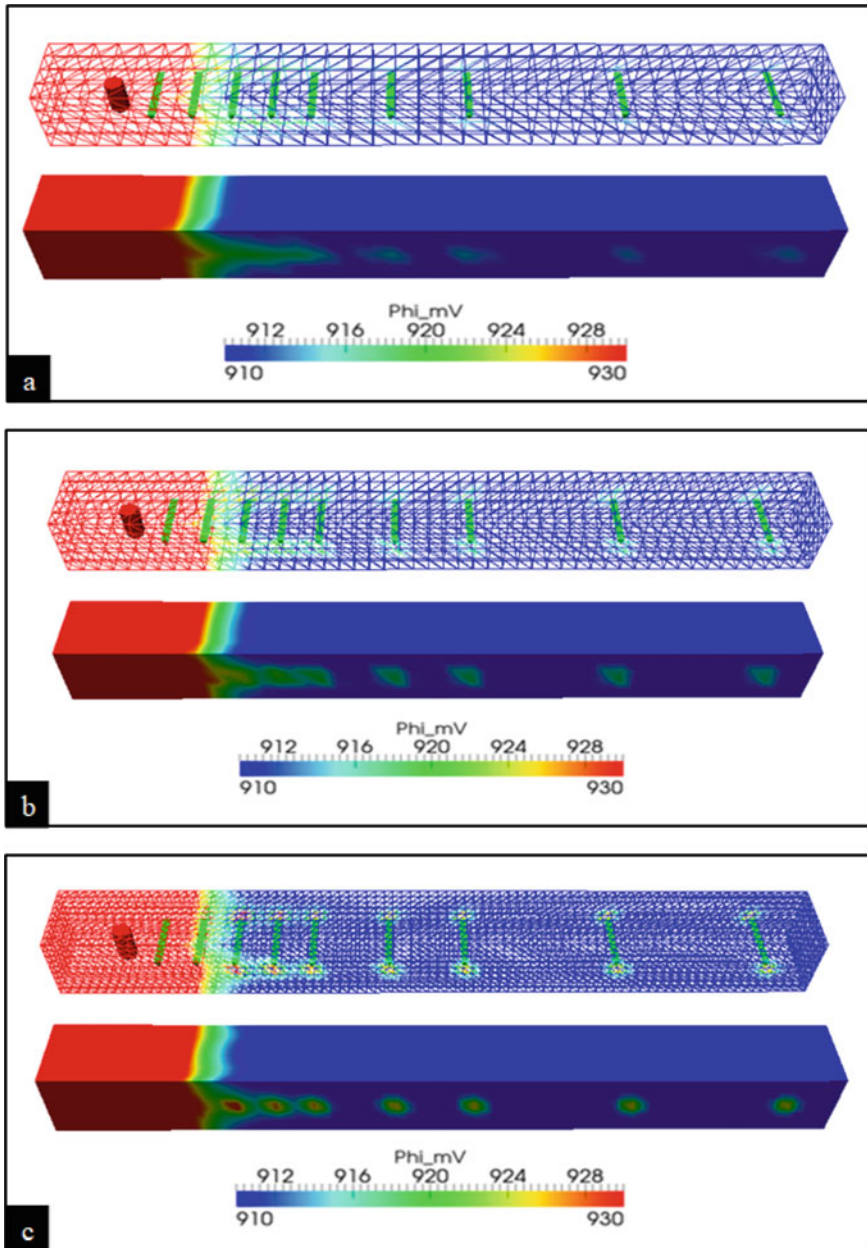
Fig. 5 Potential distribution for: **a** variation 3, **b** variation 4 and **c** variation 5

Fig. 6 The influence of concrete element size on the potential distribution of RC
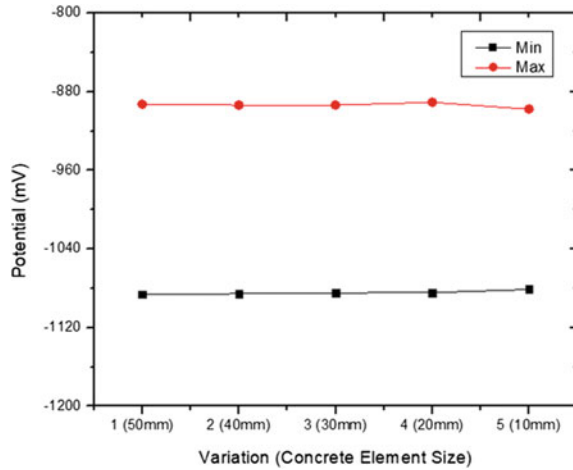
5 Conclusion

In conclusion, BEM has been used successfully in this study for analysing the effect of concrete element size on the potential distribution of RC. In this study, the concrete elements size affects the potential distribution pattern of RC. However, this influence is still tolerable because it is within a reasonable limit.

References

1. Roberge PR (2000) Handbook of corrosion engineering. Mcgraw-Hill, New York, NY
2. Ahmad A (2006) Principles of corrosion engineering and corrosion control. Elsevier
3. Ridha M, Safuadi M, Huzni S, Israr I, Ariffin AK, Daud AR (2011) The evaluation of cathodic protection system design by using boundary element method. Adv Mater Res 339:642–647
4. Safuadi M, Fonna S, Ridha M, Ariffin AK, Daud AR (2014) Infinite boundary element formulation for the analysis of CP system for submersible pump. Appl Mech Mater 471:313–318
5. Aoki S, Kishimoto K (1990) Application of BEM to galvanic corrosion and cathodic protection. Springer, pp 65–86
6. Fonna S, Huzni S, Putra MA, Kurniawan R (2018) Simulation the effect of anode-cathode displacement and anode type on reinforced concrete cathodic protection using BEM. In: MATEC Web of Conferences, vol 197, p 12001
7. Fonna S, Huzni S, Zaim A, Ariffin AK (2017) Simulation of cathodic protection on reinforced concrete using BEM. J Mech Eng SI4 2:111–122
8. Tanjung I, Fonna S, Huzni S (2019) Study on the effect of mesh ratio to the potential distribution of RC cathodic protection using BEM. IOP Conf Ser: Earth Environ Sci 364 (1):12022
9. Brebbia CA, Dominguez J (1992) Boundary elements: an introductory course. McGraw-Hill, Southampton, UK

10. Mahasiripan A, Tangtermsirikul S, Sancharoen P (2014) A study of different sacrificial anode materials to protect corrosion of reinforcing steel in concrete. Sci Technol Asia 16–25
11. NACE standard 2007 NACE International TX: NACE, 12–17 Houston
12. Ihsan M, Fonna S, Kurniawan R, Fuadi Z, Ariffin AK (2019) Computational modelling for RC cylindrical column corrosion using axisymmetric BEM. In: 2019 IEEE International Conference on Cybernetics and Computational Intelligence (CyberneticsCom), pp 82–86

Design and Calibration of Temperature Monitoring Device for a Cold Box with Hydrated Salts as Phase Change Material (PCM)

Gunawati, M. N. Nasruddin, Adi Setiawan, K. Sebayang, A. Makruf, and Zakaria

Abstract Development of Phase Change Material (PCM) for cold storage application requires devices for monitoring the changes in temperature during the charging and discharging processes. This device helps to understand the behaviour of PCM during the solidifying-liquefying process and predicts how long PCM can store the energy. The aims of this study were to design and prepare a temperature monitoring system using DS18B20 sensors for recording and displaying the temperature changes at six points within a box cooled by salt hydrate PCM. Thermistor types were used as temperature gauges due to their lower prices and flexibility. Six DS18B20 sensors were programmed with Arduino Uno as microcontroller. Output temperature measurement values in degrees Celsius were stored in a computer using PLX-DAQ software. Calibration of temperature measurement was performed by comparing the measurement results of the DS18B20 sensor and a commercial thermometer data logger using the Root Mean Square Error (RMSE) method. Results show that the first DS18B20 sensor was RMSE 1.75, the second sensor was 0.98, the third sensor was 1.2, the fourth sensor was 1.21, the fifth sensor was 1.24, and the sixth sensor was 1.7. The changes in temperature measured by the DS18B20 sensor were successfully recorded for three days without any interruption.

Gunawati · M. N. Nasruddin (✉) · K. Sebayang
Doctoral Program in Physics, Faculty of Mathematics and Natural Sciences, Universitas Sumatera Utara, Padang Bulan, 20155 Medan, Indonesia
e-mail: nasnoer1955@gmail.com

Gunawati · A. Makruf · Zakaria
Department of Physics, Faculty of Mathematics and Natural Sciences, Universitas Syiah Kuala, Darussalam, 23111 Banda, Aceh, Indonesia

A. Setiawan
Mechanical Engineering Department, Faculty of Engineering, Universitas Malikussaleh, Bukit Indah, 24352 Lhokseumawe, Indonesia

1   Introduction

There are many thermometers in the market ranging from cheap to expensive ones, analogue to digital ones. Yet, it depends on the needs of users to decide which one they need. In addition to thermometers, various effective and modern tools for measuring temperature are available, such as thermocouples, *Resistance Temperature Detectors* (RTDs), and thermistors. All these three devices have their own advantages and limitations. Thermocouple has a strong resistance to temperature when measuring, medium accuracy, and is expensive while a *Resistance Temperature Detector* (RTD) has a high accuracy, less resistance to low temperatures, and is relatively expensive. Meanwhile, a thermistor has medium resistance and accuracy, and its price is relatively cheap [1]. Therefore, this device is more appropriate to be used in this study.

In a recent study conducted by Gunawati et al. [2] to test the temperature stability in a cold box made from PCM (Phase Change Material) from local hydrated salt, a digital thermocouple was used with a manual recording process for 8 h. In another study conducted by Gunawati [3], temperature measurements were carried out using a commercial digital thermometer (MASTECH MS6514) where the data was automatically stored in Microsoft Excel, which can only record data for 8 h. In both studies, temperature measurements were still carried out through the process of recording for 4 different points, once every 5 min for 8 h. If the temperature measurement is conducted for more than 8 h, it will complicate the measurement. Hence, a device which can store the measurement results automatically is desirable. In addition, a study carried out by Rozaq [4] to test the characterization sensor of the waterproof DS18B20 was used to measure water temperature. The calibration results using a thermometer show that the error rate of using one DS18B20 sensor is less than 2%.

Based on the aforementioned explanation, a study to design a temperature monitoring device for a PCM in a cold box was undertaken [5, 6]. The output will be displayed and saved automatically into the computer, so there is no need to record the measurements manually, and the measurement period can be done more than 8 h with more than 4 observation points. Six DS18B20 sensors were used to facilitate measurement at several points of observation as this sensor can be used to measure temperatures from −55 to 125 °C.

The aims of this research were to design and manufacture a temperature measuring device using the DS18B20 sensor as well as its display in the form of data logger, in order to calibrate and test the ability of the temperature measuring device in a cold box with 10% hydrated salt as the PCM. The test needs to be conducted to find out whether the DS18B20 sensor can work effectively in hydrated salt with the temperature ranging from −55 to 125 °C.

2   Method

A number of materials such as cables, 56 Ω resistors, DS18B20 sensors, Arduino Uno modules, which are assembled on a circuit board, were used to design the measuring device. After finishing the design, a program with Arduino software was compiled to display the output of the assembled tool. The output of the device is a display of 6 temperature measurement points as shown in Fig. 1.

After the programming was complete, the calibration was carried out by comparing the measurement results of the temperature measuring device using sensor with the commercial temperature device, MASTECH MS6514. Then, a test for measuring the temperature rate in a cold box with hydrated salt of 10% water as PCM was carried out.

3   Results and Discussion

3.1   Design and Installation of Monitoring Device

Figure 1 shows a schematic diagram of the temperature monitoring device that has been designed. There is a cold box with six measurement points using six DS18B20 sensors as detectors for temperature values and the Arduino Uno as a microcontroller. The detection results are then sent to the output on the computer screen. The resulting output is the temperature in Celsius which will be stored directly in the computer.

The results of the design framework can be seen in Fig. 2, connected using a PCB board and soldered so that it is not easily separated. Six DS18B20 sensors were connected by one-wire, meaning that they can be connected at one point only; there is no need for many cables. The red wire functions as power that is connected to the 5 V Arduino Uno, the black one is the ground cable connected to the GND Arduino Uno, and the yellow one is the data receiver output cable connected to

Power (3 − 5.5)	: ———	
Output	: ———	
Ground	: ———	

1. Water container   5. Outside box
2. Wooden case   6. PCM bottle
3. Styrofoam
4. Inside cold-box
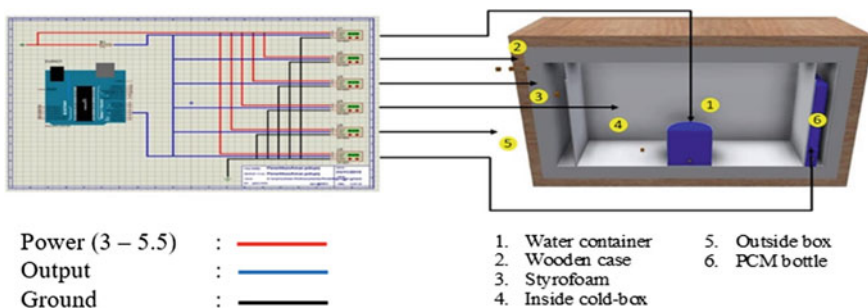
Fig. 1 Sensors measuring points and data acquisition scheme

Fig. 2 The circuit of temperature monitoring device

Arduino pin number 3. To make all the functions of the circuit work, several cables and resistors are needed. Resistors serve as pull-ups so that the data reception process runs smoothly while the cable serves to connect the Arduino Uno to DS18B20 sensor and to the output.

After completing the design of the DS18B20 sensor, it was then connected to the cold box with measurement points. There are 6 measurement points: the water temperature, the wood temperature in the cooler, the temperature of the Styrofoam in the cold box, the interior temperature in the cold box, the temperature in the PCM bottle, and finally the ambient temperature. The location of the measurement points can be seen in Fig. 1, and the cold box that has been made and connected to the DS18B20 sensor can be seen in Fig. 2.

Arduino Uno software has a direct connection with the Arduino Uno device. This connection can be adjusted in the devices by changing the board and processor according to the type of Arduino used. DS18B20 sensor initially uses the "DallasTemperatur.h" library which functions to detect the type of sensor DS18B20 and "OneWire.h" as a sensor control [7]. One DS18B20 sensor can connect to 1 cable, but this study needed 6 sensors requiring a lot of cables. Thus, the library "OneWire.h" was used so that 6 DS18B20 sensors can be connected to one cable.

Furthermore, in the program, it was defined that the output was connected to the Arduino Uno pin, which has 12 pins. In this study, the output was connected to the 3rd Arduino Uno pin. The number of sensors was then defined. For example, when using 3 sensors, "temperature 1, temperature 2, and temperature 3" were measured. For more details, the main program of the sensor can be seen in Appendix 1, which has been successfully executed so that the sensor can read, display, and save the results of the temperature measurement in the computer. After the main program was finished, it was followed by setting the output in the next part of the program, instructing the pin to display in Celsius. Measurement results can also be displayed in Kelvin, Fahrenheit, and Réaumur. However, the program was displayed in Celsius. Then, the program was repeated with "loop", to enable the variation of

duration such as every 1 s, 10 s, 1 min, 5 min, and other variations. The complete output setting program can be seen in Appendix 2.

3.2 Calibration

Calibration was undertaken by comparing the measurement results of DS18B20 sensor with measurements from commercial instruments (Mastech MS6514). As shown in Figure 3 and 4, the calibration process was carried out by measuring cold water from the refrigerator at a temperature of 6.4 °C, with 300 grams of the mass of water. The temperature was recorded from the time it was removed from the refrigerator until it reached equilibrium temperature [8]. Figure 5 is a graph of the results of the cold water calibration.

Calibration was also carried out for hot water temperature, with the same mass as cold water, which is 300 grams. The temperature was recorded from 68.1 °C until it reached the equilibrium temperature. Figure 6 is the result of the hot water calibration.

The temperature of the cold water and hot water was taken 60 times a minute during the calibration process using the DS18B20 sensor. It was also carried out on 5 other DS18B20 sensors with the same method. The results on the first DS18B20
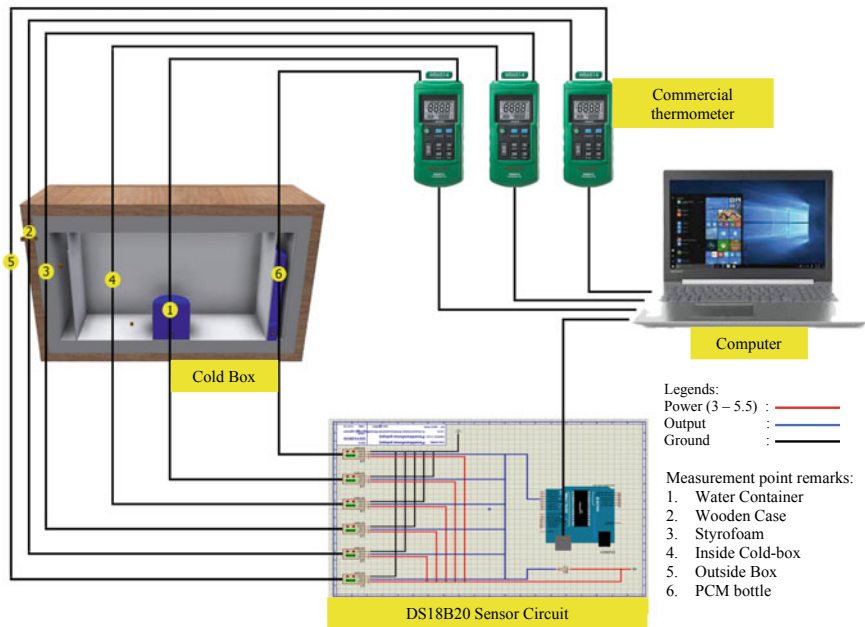
Fig. 3 The scheme of temperature sensors calibration

Fig. 4 Callibration set-up

Table 1 RMSE values of DS18B20 sensors

Sensor	Minimum difference	Maximum difference	RMSE
1	0.01	3.32	1.75
2	0.22	2.35	0.98
3	0.07	2.30	1.2
4	0.26	2.36	1.21
5	0.26	2.75	1.24
6	0.34	3.24	1.7

sensor for measuring the cold and hot water were used to look for the RMSE (Root Mean Square error) value. The value of sensor 1 can be calculated using the equation below:

$$\text{RMSE} : \sqrt{\frac{\sum_{i=1}^{n}(X_W - X_T)^2}{n}} = \sqrt{\frac{184.82}{60}} = \sqrt{3.08} = 1.75$$

Table 1 shows the RMSE value of 6 DS18B20 sensors. To obtain more accurate measurement results, the RMSE value was used to find errors in the sensor results so that they could be fixed. From this table, it can be seen that the RMSE value was below 2% and this is in accordance with previous research [4].

The RMSE value obtained was re-measured to find the difference in the results before and after the calibration. The measurement results after being calibrated are closer to those measured with commercial device which means the error from the sensor is reduced. The value of the calibrated measurement results can be seen in Figs. 7 and 8.
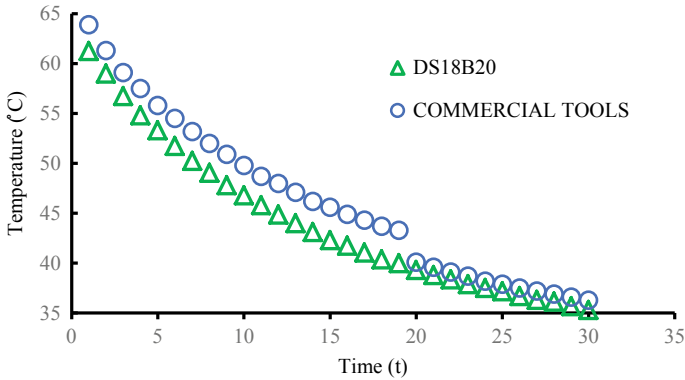
Fig. 5 Temperature measurement data of cold water using sensor DS18B20
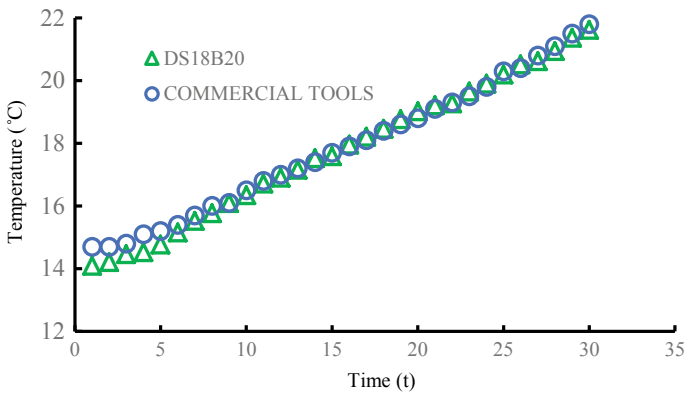
Fig. 6 Temperature measurement data of hot water using sensor DS18B20

3.3   PCM Temperature Profiles

PCM testing in the form of a 10% hydrated salt in water using a cold box was carried out for approximately 3 days. Figure 9 shows the temperature profile observed using a calibrated design monitoring device. This graph demonstrates the device's ability to record data up to almost two days of observation simultaneously through six sensors. From the results which can be seen in the graph, it can be said that the purpose of this study was fulfilled, meaning that the manual recording process and time constraints could be replaced by a more efficient and more accurate recording system [2, 3]. Figure 9 shows the temperature changes at six measurement points with the main focus of temperature changes in the PCM bottle (T6) as a medium that releases energy. As a medium for receiving energy, water was filled into a cup in the box (T1). This graph depicts the process of releasing
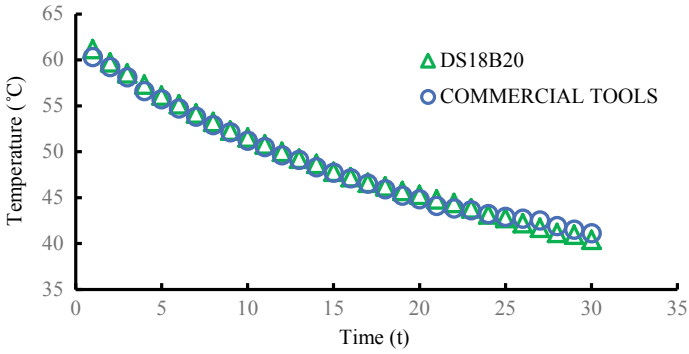
Fig. 7 Calibration curve for cooling process
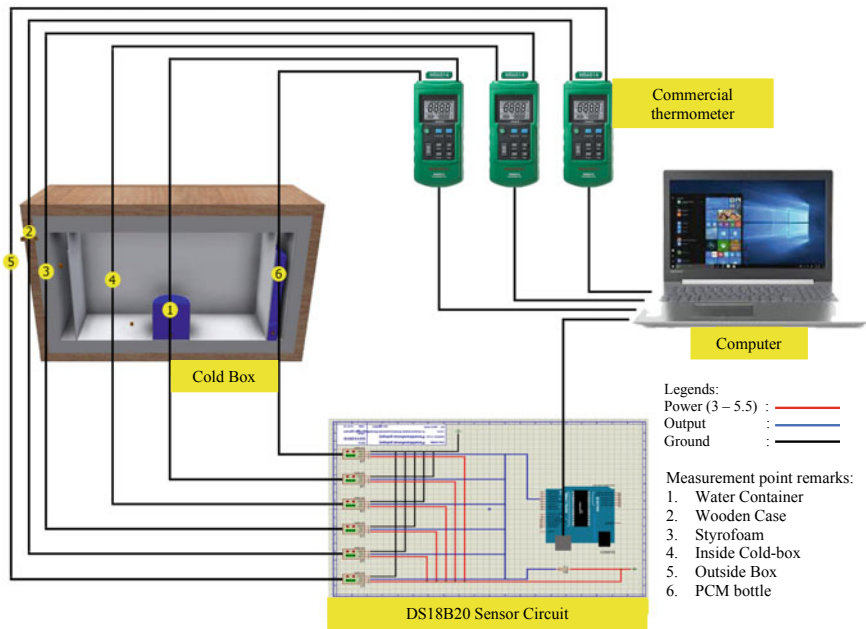
Fig. 8 Calibration curve for heating process

energy from the PCM which can be seen from the temperature increase since the beginning of the test (−10 °C). Meanwhile, the temperature of the water in the cup continued to decline, as evidence of energy absorption, from 22 to around 6 °C in the first 5 h. After five hours of experiment, there was temperature equilibrium between the PCM and the cooled medium. Furthermore, the temperature increased slowly after 12 h of testing until it reached the final temperature of around 25 °C.
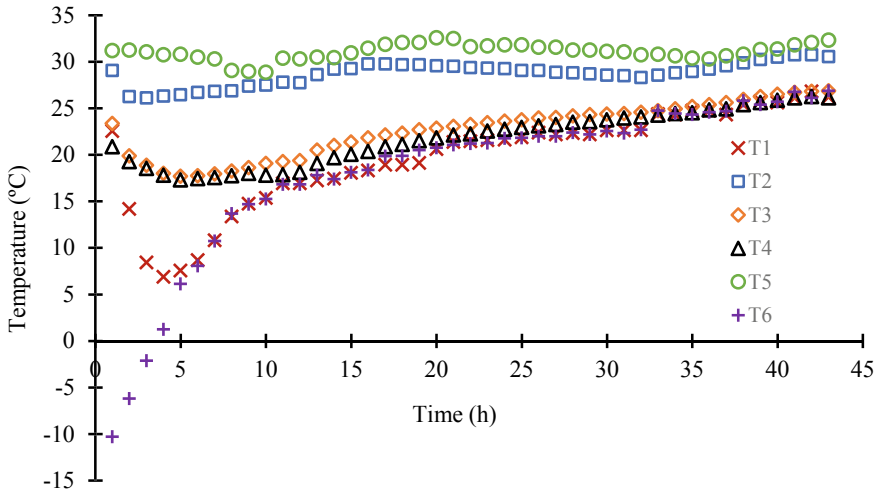
Fig. 9 Graph of the rate of change in temperature of a 10% hydrated salt

4　Conclusion

This study has succeeded in compiling the design of a temperature measuring device using DS18B20 sensor which is capable of recording and storing measurement result data automatically (data logger). The calibration result of the first DS18B20 sensor was 1.75, the second sensor was 0.98, the third sensor was 1.2, the fourth sensor was 1.21, the fifth sensor was 1.24, and the sixth sensor was 1.7. A temperature measuring device using DS18B20 sensor is capable of testing the temperature of the interior of 10% salt concentration for two days. Further research on calibration can be conducted by looking at the digital output (binary) of DS18B20 sensors and also looking at the accuracy, sensitivity, precision, and linearity to obtain more accurate results.

Appendix 1: The Main Program of the PCM Temperature Monitoring Device

```
//PENGATURAN SENSOR DS18B20
#include <OneWire.h>
#include <DallasTemperature.h>

const int PIN_DS18 = 3;

OneWire ds(PIN_DS18);
DallasTemperature sensor(&ds);

void setup()
{
  Serial.begin(9600);
  sensor.begin();

  Serial.println("CLEARDATA");
  Serial.println("LABEL,Time,suhul,suhu2,suhu3");
  analogReference(INTERNAL);

}
```

Appendix 2: The Output Setting Program

```
//MENAMPILKAN HASIL PENGUKURAN SUHU
void loop()

{
  sensor.requestTemperatures();
  float celciusA = sensor.getTempCByIndex(0);
  float celciusB = sensor.getTempCByIndex(1);
  float celciusC = sensor.getTempCByIndex(2);

  Serial.print("DATA,TIME,");
  Serial.print(celciusA);
  Serial.print(",");
  Serial.print(celciusB);
  Serial.print(",");
  Serial.print(celciusC);
  Serial.println(",");

  delay(1000);
}
```

References

1. Amri MFA (2014) Perancangan Alat Ukur Suhu dan Kelembaban Berbasis Mikrokontroler Atmega 16A dengan Menggunakan Sensor DHT11. Universitas Sumatera Utara
2. Gunawati NN, Sebayang K, Setiawan A (2019) Experimental investigation of a cold storage box with Aceh locally produced hydrated salt as phase change materials: effect of salt treatment IOP Conf. Ser Earth Environ, Sci, p 364
3. Gunawati, Dongoran AH and Setiawan A (2019) Evaluation on performance of cold storage box enveloped with phase change materials. J Phys Conf, Ser, 1242, 012023
4. Rozaq IA, DS NY (2017) Uji Karakterisasi Sensor Suhu DS18B20 Waterproof Berbasis Arduino Uno Sebagai Salah Satu Parameter Kualitas Air. Prosiding Prosiding Seminar Nasional Teknologi dan Informatika (SNATIF) Ke-4 Fakultas Teknik Universitas Muria Kudus (Kudus)

5. Sharma A, Tyagi VV, Chen CR, Buddhi D (2009) Review on thermal energy storage with phase change materials and applications. Renew Sustain Energy Rev 13:318–345
6. Mehling H, Cabeza F (2008) Heat and cold storage with PCM: an up to date introduction into basic and aplications. Springer, Berlin
7. Kadir A (2018) Arduino dan Sensor: Tuntunan Praktis Mempelajari Penggunaan sensor untuk Aneka Proyek Elektronika Berbasis Arduino ed Giovanny. Yogyakarta, Andi
8. Koestoer RA, Saleh YA, Roihan I (2019) A simple method for calibration of temperature sensor DS18B20 waterproof in oil bath based on Arduino data acquisition system. AIP Conf Proc 2062

Stress Analysis of the LN2 Storage Container on Head and Nozzles Using Finite Element Method

Asbar, Amir Zaki Mubarak, Muhardian Supanji, Irwansyah, and Irwansyah

Abstract Liquid nitrogen (LN2) container is a common pressure vessel used for storage in the fertilization industry. Due to it works at a design temperature of –196 °C and design pressure 1.02 MPa, the fluids may be evaporated if there is a leak in the pressure vessel. Mostly of vessel leaks are caused by stress either internal or external pressure. Leaks may occur by the significant stress concentration, particularly at vessel head nozzles. The objective of this study to analyze the maximum stress of LN2 storage tank head using finite element analysis. The LN2 container material is Stainless Steel 304 with yield strength 205 MPa. The initial stress simulation results carried out from three different locations of stress concentration at the head. Then the result was compared with analytical calculations. The result of stress analysis presents the maximum stress in the LN2 storage tank is 279.8 MPa. The result is not allowable due to it exceeds yield strength (σ_y) 205 MPa. Hence, the reinforcement strip in the nozzle model was applied. The maximum stress of LN2 container redesign presents 162.2 MPa. The results show that maximum stress concentration was in a safe condition.

1 Introduction

The liquid nitrogen (LN2) storage tank is a common pressure vessel found to store or transmit the fluids at different temperatures and pressure from ambient in the fertilizer plant. Pressure vessels are defined as containers for the containment of pressure, either internal or external. This pressure may be obtained from an external source, or by the application of heat from a direct or indirect source, or any combination sources [1]. The LN2 storage container was fabricated by complex

Asbar ($\boxtimes$) · A. Z. Mubarak · M. Supanji · Irwansyah
Department of Mechanical Engineering, Universitas Syiah Kuala, Banda Aceh 23111, Indonesia
e-mail: asbar@unsyiah.ac.id

Irwansyah
PT Pupuk Iskandar Muda, Krueng Geukueh, Aceh Utara PO. Box 021 Indonesia

geometric structures which is lead to some drawbacks [2–4]. Due to it works at a design temperature of −196 °C and design pressure 1.02 MPa, the fluids may be evaporated if there is a leak in the pressure vessel. Mostly of vessel leaks due to stress caused by either internal or external pressure. Despite the wall thickness, other factors like the effect of supports, types of end covers used for closing the vessel, nozzles, thickness variation, and external attachments like piping system caused uneven stress distribution in the pressure vessel. ASME Boiler and Pressure Vessel provide a large factor of safety at the geometrical discontinuity areas [5, 6]. Hechmer and Hollinger have studied stress behavior at the nozzle vessel intersected region and recommend to use the 3-D finite element models for studying the stress behavior of a nozzle-to-cylinder intersection structure [7, 8]. The stress distribution in a horizontal pressure vessel using finite element analysis has been studied [9]. The stress concentration usually among of the connection between the vessel and the piping system. Therefore, in this study, the maximum stress in the LN2 pressure vessel, at the head and nozzles were calculated and analyzed to get the safety design of the container.

2 Methods

In this study, the LN2 storage container fabricated by Toyo Engineering Corporation was used as a pressure vessel model, with vertical type and located outdoor. This type of pressure vessel consists of a shell, head, nozzle, support, and other components. Vessel head type is ellipsoidal with five (5) nozzles on the upper head and four (4) nozzles on the bottom head. The LN2 storage container specification is presented in Table 1 and the material properties are shown in Table 2. Then calculation refers to the ASME (American Society of Mechanical Engineers) Sect. VIII Div 1.

Analytical calculation of pressure vessel based on internal pressure calculation refer to ASME Section VIII Division 1. Shell with cylindrical type and a thin wall was calculated and analyzed. The thickness of the shell calculated using Eqs. 1 and 2.

Table 1 LN2 storage tank

Properties	
Fluid	Nitrogen cair
Location	Outdoor
Capacity	50 m^3
Operation pressure (P_o)	0.88 MPa
Design pressure (P_d)	1.02 MPa
Operation temperature (T_o)	−171 °C
Design temperature (T_d)	−196 °C
Corrosion factor (CA)	3
Welding efficiency (E)	0.85
Support type	Legs support

Table 2 Material properties of *Stainless Steel* type SA 240 Gr. 304 [10]

Property		
Young's modulus	203,000	MPa
Mass density	8000	kg/m^3
Yield strength	205	MPa
Tensile strength	515	MPa

$$t = \frac{PR_i}{2SE - 0.4P} \tag{1}$$

$$t = \frac{PR_i}{SE - 0.6P} \tag{2}$$

Stress on pressure vessel act by pressure in a longitudinal direction (longitudinal stress) and circular (circumferential stress). Longitudinal stress on the shell was calculated using Eq. 3 and circumferential stress calculated using Eq. 4.

$$\sigma_x = \frac{P(R_i - 0.4t)}{2Et} \tag{3}$$

$$\sigma_\phi = \frac{P(R_i + 0.6t)}{Et} \tag{4}$$

According to ASME Section VIII, to calculate maximum stress on the ellipsoidal head could be addressed on three points around the head. On the point x calculated using Eq. 5, at the center of the head using Eq. 6, and at the tangent line using Eq. 7. While equivalent stress which is the combination of longitudinal and circumferential stress was calculated using the distortion energy method or known well called Von Mises. Equivalent stress calculated using Eq. 8.

$$\sigma_x = \frac{PR_L}{2_t}, \text{dan } \sigma_\phi = \frac{PR_t}{t}\left(1 - \frac{R_L}{2R_m}\right) \tag{5}$$

$$\sigma_x = \frac{PR^2}{2_{th}}, \text{dan } \sigma_\phi = \sigma_x \tag{6}$$

$$\sigma_x = \frac{PR}{2_t}, \text{dan } \sigma_\phi = \frac{PR}{t}\left(1 - \frac{R^2}{2h^2}\right) \tag{7}$$

$$\sigma' = \sqrt{\sigma_x^2 + \sigma_\phi^2 - \sigma_x\sigma_\phi} \tag{8}$$

LN$_2$ Storage container model designed using Autodesk Inventor Professional 2020 software and analyzed using PC Desk computer Intel (R) Core i7, RAM 16 GB, as shown in Fig. 1.
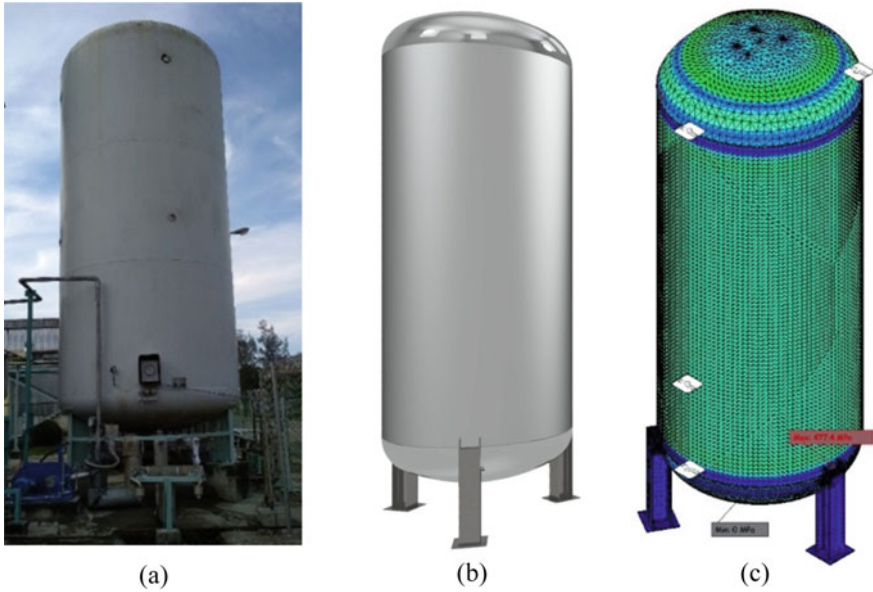
Fig. 1 LN$_2$ Storage container, **a** pressure vessel, **b** 3D model, **c** mesh model

3   Discussion

Stress analysis using an analytical approach was calculated to refer to ASME Section VIII. It employs to validate the result of pressure vessel model calculation, as shown in Fig. 2. Both approaches, computer simulation, and analytical calculation, even though shown differentiate results but it is not significant. It means that the developed model is acceptable for further analysis and calculation.

Then the maximum stress that occurred on the entire surface of the LN2 storage container was evaluated by simulating the model with software Autodesk Inventor Professional 2020. The result showed that stress distribution is concentrated on the bottom head of the vessel, as presented in Fig. 3. It indicates a nozzle presented a higher stress concentration 279.8 Mpa, see in Fig. 3a. This result is not acceptable

Calculated position at container head	Von Mises	
	Simulation	Analytic
1	79 Mpa	84,2 Mpa
2	100,1 Mpa	98,3 Mpa
3	59,4 Mpa	58,2 Mpa

(a)
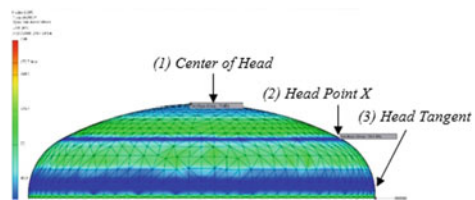
(b)

Fig. 2 Maximum stress concentration on vessel head, **a** comparison results, **b** simulation
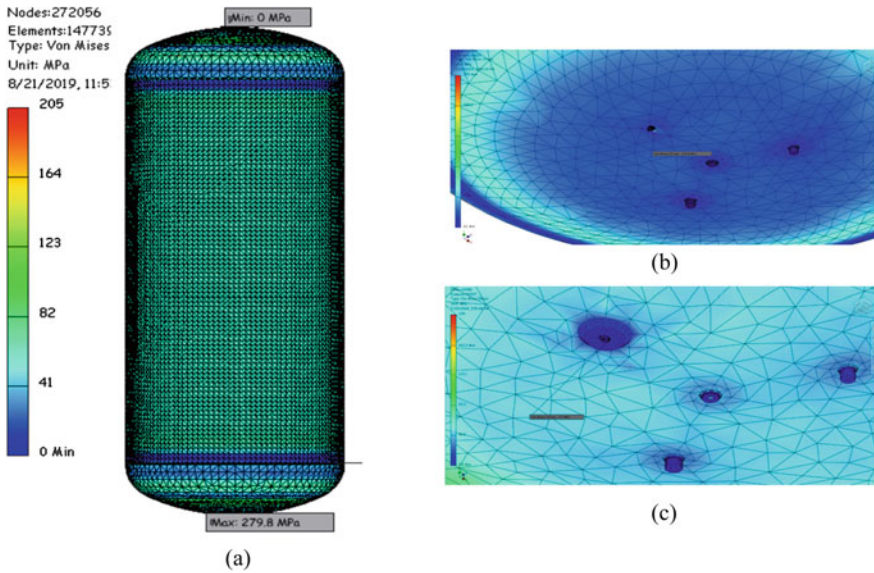
Fig. 3 Stress distribution on the LN2 storage, **a** the container, **b** head bottom, **c** nozzles

due to higher than allowable stress 205 MPa, whereas ($\sigma_{max} \leq \sigma_y$). For solution, the modified pressure vessel at initial design steps was conducted by adding extra reinforced strip around the nozzles, namely known as reinforcement factor (Rf), as presented in Fig. 3b, c.

After redesign by adding the reinforcement on the nozzle, the pressure vessel was restimulated to find the maximum stress concentration. It found that the redesigned model was given the maximum stress 162.2 MPa which is below the allowable stress 205 MPa ($\sigma_{max} \leq \sigma_y$). It means that the redesign LN2 storage container is acceptable, as presented in Fig. 4.

4   Conclusion

3D model of LN2 storage container was successfully generated and simulated. The equivalent stress of model simulation results was compared with the analytical approach which is not significantly different. The maximum stress at the nozzle bottom head 279.8 MPa, shows that the pressure vessel unsafe due to the results higher than yield strength material. Reinforcement (Rf) was employed as the extra at the nozzle. The result significantly improves 162.2 MPa, lower than yield strength 205 MPa ($\sigma_{MAX} \leq \sigma_y$). It can be concluded that the LN2 storage container design is safe.
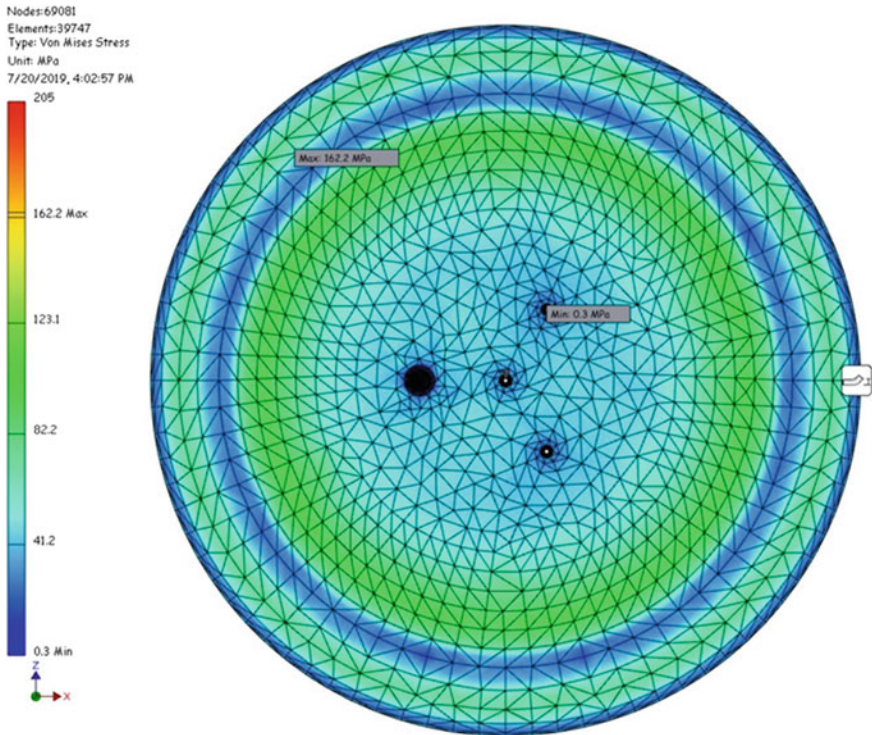
Fig. 4 Maximum stress after applied reinforcement at nozzles

References

1. Stewar M, Lewis OT (2013) Pressure vessels field manual: common operating problems and practical solutions. Elsevier Science
2. Seeli H, Dorapudi SH, Satish PV, Kumar SN (2016) Designing and analysis of cryogenic storage vessels. Int J Sci Eng Res 7(7)
3. PratikKumar P, Bhai B, Shah R (2014) Design and optimization of cryogenic storage vessel. Int J Eng Develop Res 3(1)
4. Khattak MA, Mukhtar A, Khan KA (2016) Common root causes of pressure vessel failures: a review. J Adv Res Appl Mech 21(1):22–37. Akademia Baru
5. ASME BPVC—Section VIII, Division 1: Rules for Construction of Pressure Vessels (2010)
6. ASME Section VIII—Division 2 Criteria and Commentary (2014)
7. Hollinger GL, Hechmer JL (1991) Phase 1 report: Three-dimensional stress criteria. New York, NY: PVRC. Grant 89-16 and 90-13
8. Hechmer JL, Hollinger GL (1998) 3D stress criteria e guidelines for application. Welding Research Council
9. Khan SMA (2010) Stress distributions in a horizontal pressure vessel and the saddle supports. Int J Press Vessels Pip 87:239–244
10. ASME (2015) Rules for Construction of Pressure Vessel Section VIII. Division 1. The American Society of Mechanical Engineers, New York, USA

Using QFD and FMEA to Improve Maintenance Effectiveness in a Petroleum Refinery

Fauzan Rahman, Mohamad Sazali Said, Azmi Hassan, Mohd Shahrizan Yusoff, and Surya Atmadyaya

Abstract A case study is reported which Improve the maintenance effectiveness by combines Quality Function Deployment (QFD) and Failure Mode and Effects Analysis (FMEA), QFD was used to identify the critical technical attributes which affect the customer satisfaction the most. FMEA was adopted to identify potential failure models and causes of critical manufacturing processes. Customer requirements (CRs) were obtained through Internal MMIP team. Analytic Hierarchy Process (AHP) selections was used to sort the importance of CRs and then compared to the technical attributes (TAs) in the House of Quality (HoQ). FMEA were used to analyse the Maintenance activity which resulted the relative solutions from High Risk Priority Number (RPN) indices failure models. By the integration of FMEA into QFD, a new maintenance management model developed and implemented, has increase by 116% Mean Time Between Maintenance and Decrease by 41% Number of Breakdown Maintenance Intervention, 47.6% Mean Time To Repair and 82% of maintenance cost or Rp. 5,754,791,630.00 lower compare to the same period in the previous year maintenance cost.

1 Introduction

Global demands over high-quality products in the manufacturing sector continue to increase. However, the future of competitiveness for any manufacturing companies are become more challenging due to the equipment's aging, equipment's addition and modification, upgrading technology, or expansion production unit are mandatory to be maintain to reduce downtimes, stoppages, breakdowns, and fail-

F. Rahman (✉) · M. S. Said · M. S. Yusoff · S. Atmadyaya
Manufacturing Section, Universiti Kuala Lumpur, Malaysian Spanish Institute, Kulim Hi-Tech Park, 09000 Kulim, Kedah, Malaysia
e-mail: fauzan.rahman@s.unikl.edu.my

A. Hassan
Electrical, Electronics and Automation Section, Universiti Kuala Lumpur, Malaysian Spanish Institute, Kulim Hi-Tech Park, 09000 Kulim, Kedah, Malaysia

ures to increase the reliability of a production system. The scheduling of maintenance activities may improve its productivity, efficiency, and quality [10]. Maintenance productivity aims to get the reduction of the maintenance cost by maximizing the maintenance performance [1].

In the Petroleum refinery, where this research implemented the 2018–2019 maintenance activity at the selected Critical equipment Hydroskimming Plant resume, show that there is 59 times cumulative maintenance breakdown during May 2018–June 2019 period, and then MTBM and MTTR analysis, the average duration in which at least one maintenance breakdown will be required in this system is 52 Days with the average repair duration is 21 days, and as the impact of those activity cost Rp. 7,014,206,497. The product quality strongly related to the maintenance quality which it also has a direct contribute to the cost reduction. The measurement of asset maintenance performance and its continuous control and evaluation is becoming critical through the outsourcing, separation of asset owners and asset managers, and complex accountability for the asset management [5]. However, the latest methodology for designing maintenance systems, i.e., no fully structured approach leading to an optimal maintenance system organizational structure with a defined hierarchy of authority and span of control; defined maintenance procedures and policies, etc. and currently still there is no method or model that universally accepted. Even if there are similar product organizations, but if the technology advancement and production size is different [5]. For this reason, maintenance systems are designed using experience and judgment supported by a number of formal decision tools and techniques [5] and the developed Maintenance models are typically valid solely for a specific industry. Analysis and implementation effort through a wider scope which considers other aspects within the manufacturing system should be carried out. This means is very potential to provide a more realistic picture of the Maintenance Effectiveness Implementation prospect in the manufacturing industries. Therefore, it is urgent to produce a creative solution to increase the maintenance effectiveness to achieve the reliability improvement. This study will focus on the problems that occurring the maintenance management which are coped by the QFD and FMEA combination.

2   Literature Review

Consumer requirements into an appropriate company requirements at each stage from research and product development is critical and QFD has the ability to translated it [4]. QFD helps designers to reveal the voice of customers (VOC), or customer requirements, to determine which engineering elements or product specifications are the most crucial. This prioritization helps designers to know which part of the product or process is the most beneficial to focus on during design, resulting a better acceptance [11]. So it can give a benefit for a new product development or current products improvement [2].

To identify potential failures of a product or service and then to determine the frequency and impact of the failure by using disciplined approach with FMEA. FMEA is an important method for preventive quality and reliability assurance. It involves investigation and assessment of all causes and effects of all possible failure modes of a product, from the earliest development phase [14]. For present study the equipment failure mode during normal operation and regular maintenance activity was analyse using FMEA. There are three indices that help to define the priority of failures: occurrence (O), severity (S) and detection difficulty (D). Occurrence is the frequency of the failure. Severity is the seriousness of the failure. Detection difficulty is the hardness to detect the failure before it reaches the customer. Risk Priority Number (RPN) is used to evaluate the risk level of a product's failure mode, and is determined by multiplication of the three failure mode indices:

$$\text{RPN} = O \times S \times D \tag{1}$$

QFD and FMEA are from different perspectives but tackling the same issue of customer satisfaction. Tanik [13] presented an integrated application of FMEA-QFD on a food package industry. FMEA analysis was helped the sales team for channeling these efforts in a better direction. The author also indicated that with the help of FMEA customer satisfaction is guaranteed by eliminating potential errors through the order handling process. Ginn introduced two schools of thought from Ford Motor Company with regards to the effective deployment of QFD and FMEA together in 1996. The first approach is applying QFD Phase 1 or Phase 2 followed by a full FMEA process. The second approach is arguably the ideal long-term solution, applying four-phase QFD with full support of an FMEA process. Based on the two thoughts, Ginn et al. [7] proposed a new model to push FMEA upstream and QFD downstream along the product development circle [7]. Programming model with a fuzzy linear to consider quality elements and parts/components risk analysis during the stage of new product development were developed by Chen and Ko [6]. Almannai [3] developed a joint QFD and FMEA model to choose the best alternative. Both QFD and FMEA were used to support the manufacturing decision-making process. This model combines two quality tools in a systematic way and forms a good decision tool because QFD has the ability to identify the most fit alternatives and FMEA has the ability to identify the associated risks with that alternative in design and implementation phases. For present study, QFD-FMEA a combined methodology was conducted to increase the maintenance effectiveness, first of all by introduce the critical of technical attributes using QFD while FMEA was used to reveal the critical failure modes during maintenance activity which has high level of RPN indices. Finally as the result of the analysis from QFD-FMEA combination, the Solutions and suggestions were delivered to improve current performance. The study plan and steps as shown in Fig. 1.
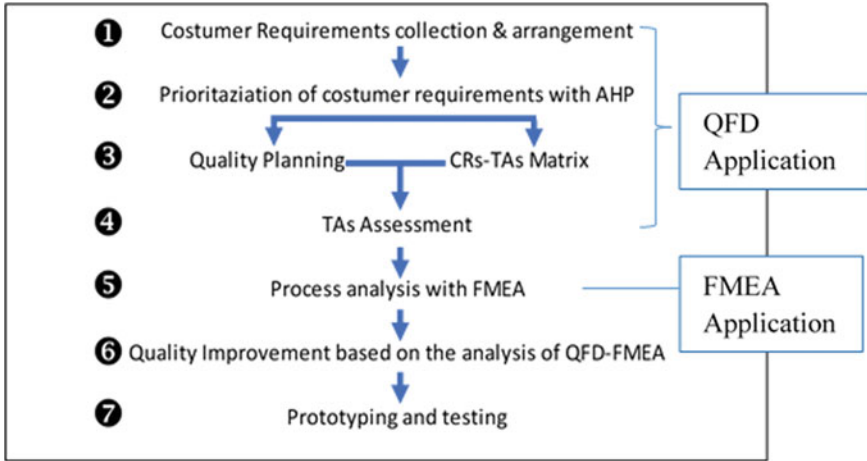
Fig. 1 Study plan

3 Methodologies

3.1 The Application of QFD

3.1.1 Customer Requirements (CRs) Collections

CRs were collected through Workshop Internal Maintenance Group Division (MMIP Team) as shown in Table 1.

Table 1 Customer requirements arrangement for the effective maintenance management

1st level	2nd level	3rd level
Effective maintenance	High maintenance productivity	Zero accident, high skilled people
	Good maintenance organization	Proven maintenance practice
	Easy maintenance control	Comply to procedure, well documented
	Accurate maintenance planning	Comply to scope of work, value added
	Accurate maintenance scheduling	Comply to work duration
	High availability of material and spare part	Minimum rework

3.1.2   Prioritization of Customer Requirements

AHP matrix was generalized based on the questionnaire data in Table 2. Importance rating for each customer requirement was calculated and listed in the last column of the AHP matrix. Satty [12] proposed a consistency index $CI = \frac{(\lambda_{\max} - n)}{(n-1)}$, the CRs for maintenance effectiveness was adopted to prioritize AHP with a 9-scale. Three main operations consisted under AHP: construction of hierarchy, analysis from priority and verifications consistency [8] as shown in Table 1. This hierarchy, can be obtained through applying Affinity Diagram. Then AHP-based questionnaire for the selected different CRs was designed to collect customers' preferences. For more information on AHP-based questionnaire please refer to Kahraman et al. [9] (Fig. 2).

The dimension of the matrix are n and $\lambda_{\max}$ and the maximal eigenvalue, respectively. When the consistent ratio is less than 0.1 the matrix is consistent [1]. Consistent ratio is the ratio of CI and RI, and which CI and RI are the consistency index and the random index, respectively.

3.1.3   Quality Planning Assessment

This team consisting of members from maintenance senior supervisors, maintenance area section heads, maintenance execution manager and human resource manager was established. Current and targeted level from companies related the maintenance effectiveness also decided to compared and analysed. Each customer requirement and the target level was set by the team, as value in Table 3. Target level/Current level resulted the Improvement ratio. Absolute importance value was taken from Importance rating × Improvement ratio. The percentage of the absolute importance value in the sum of total absolute importance values is Relative importance. The voice of customer give thought from the relative importance value.

3.1.4   Relationship Matrix CRs-TAs

Refer to the collected CRs and The internal target, 9 Zero Accident, High skilled people, Proven maintenance practice, Comply to procedure, Well documented, Comply to scope of work, Value added, Comply to work duration and Minimum rework. For CRs and TAs the Relationship matrix set up numerical values are 1, 3 and 5 as data shown in Table 4. To show the relationships strength (weak, moderate or strong), respectively. And no relationship indicate by the Blank cells.

Table 2 AHP matrix

CR's	Maint. productivity	Maint. organization	Maint. control	Maint. planning	Maint. scheduling	Material mgmt.	Importance rating
Maintenance productivity	1.0	7.0	5.0	3.0	3.0	9.0	0.4
Maintenance organization	0.1	1.0	0.3	0.3	0.3	3.0	0.1
Maintenance control	0.2	3.0	1.0	0.5	0.5	5.0	0.1
Maintenance planning	0.3	3.0	2.0	1.0	3.0	5.0	0.2
Maintenance scheduling	0.3	3.0	2.0	0.3	1.0	5.0	0.1
Mat'l and spare part mgmt.	0.1	0.3	0.2	0.3	0.2	1.0	0.0

With respect to *AHP priorities*, which criterion is more important, and how much more on a scale 1 to 9?

	A - wrt **AHP priorities** - or B?		Equal	How much more?
1	⦿ Maintenance Productivity	○ Maintenance Organization	○1	○2○3○4○5○6⦿7○8○9
2	⦿ Maintenance Productivity	○ Maintenance Control	○1	○2○3○4⦿5○6○7○8○9
3	⦿ Maintenance Productivity	○ Maintenance Planning	○1	○2⦿3○4○5○6○7○8○9
4	⦿ Maintenance Productivity	○ Maintenance Schedulling	○1	○2⦿3○4○5○6○7○8○9
5	⦿ Maintenance Productivity	○ Material & Sparepart Mgt	○1	○2○3○4○5○6○7○8⦿9
6	○ Maintenance Organization	⦿ Maintenance Control	○1	○2⦿3○4○5○6○7○8○9
7	○ Maintenance Organization	⦿ Maintenance Planning	○1	○2⦿3○4○5○6○7○8○9
8	○ Maintenance Organization	⦿ Maintenance Schedulling	○1	○2⦿3○4○5○6○7○8○9
9	⦿ Maintenance Organization	○ Material & Sparepart Mgt	○1	○2⦿3○4○5○6○7○8○9
10	○ Maintenance Control	⦿ Maintenance Planning	○1	⦿2○3○4○5○6○7○8○9
11	○ Maintenance Control	⦿ Maintenance Schedulling	○1	⦿2○3○4○5○6○7○8○9
12	⦿ Maintenance Control	○ Material & Sparepart Mgt	○1	○2⦿3○4○5○6○7○8○9
13	⦿ Maintenance Planning	○ Maintenance Schedulling	○1	○2⦿3○4○5○6○7○8○9
14	⦿ Maintenance Planning	○ Material & Sparepart Mgt	○1	○2○3○4⦿5○6○7○8○9
15	⦿ Maintenance Schedulling	○ Material & Sparepart Mgt	○1	○2○3○4⦿5○6○7○8○9

CR = 4.6% OK

Fig. 2 AHP questionaire

Table 3 Quality planning table

CR's	Importance rating	Current level	Target level	Improvement ratio	Absolute importance	Relative importance
Maintenance productivity	0.4	4.0	5.0	1.3	0.5	0.4
Maintenance organization	0.1	4.0	4.0	1.0	0.1	0.0
Maintenance control	0.1	3.0	4.0	1.3	0.2	0.1
Maintenance planning	0.2	3.0	5.0	1.7	0.3	0.3
Maintenance scheduling	0.1	3.0	5.0	1.7	0.2	0.2
Material and spare part management	0.0	4.0	4.0	1.0	0.0	0.0

Table 4 CRs–TAs two way dimensional table

CR's	Zero accident	High skilled people	Proven maintenance practice	Comply to procedure	Well documented	Comply to scope of work	Value added	Comply to work duration	Minimum rework	Importance rating CRs
Maintenance productivity	1.0	5.0				1.0		1.0	5.0	0.4
Maintenance organization		3.0	5.0		1.0				1.0	0.1
Maintenance control	3.0	5.0	1.0	3.0	3.0	3.0	3.0	1.0	5.0	0.1
Maintenance planning	3.0	3.0	1.0	5.0	1.0	5.0	1.0	3.0	3.0	0.2
Maintenance scheduling	5.0	3.0	1.0	3.0	1.0	5.0	1.0	5.0		0.1
Material and spare part management			1.0	1.0	5.0		1.0	3.0	3.0	0.0

3.1.5 Quality Designing

Technical attributes calculated to obtain the importance rating by the following equation:

$$T_j = \sum_{i=1}^{n} RW_i R_{ij} (1 \le i \le n, 1 \le j \le m)$$

n for CRs and m for technical attributes, ith row of customer requirement, the jth column of technical attribute where i, j, T_j, RW_i, R_{ij}, importance rating for the jth column of technical attribute, relative weight for the ith row of customer requirement.

Relationship strength of the ith row of customer requirement and the jth column of technical attribute [14]. Refer to the technical decision of Current operation level, target level and importance rating for every technical attribute, the target level of the matched technical attribute was determined. And then, critical technical attributes is the technical attribute with a high ranked, technical attributes which in range of category Need improvement their background would have colored in grey (Table 5).

3.1.6 House of Quality

The House of quality for the maintenance management as shown in Table 6. Based on the first phase of QFD analysis, key technical attributes, such as Zero Accident, High Skill People, Comply to Procedure, scope of Work, Work Duration and Minimum Rework were selected to be focused issue. Which has major impacts to the customer satisfaction of Maintenance Management.

3.2 FMEA Application

After result in QFD was obtained as the issue that need improvement, and then the main failure mode from the Maintenance Activity in Maintenance Management were predict by calculated the possibility of the incident and accident using FMEA. Maintenance management include Plant Reliability, Equipment Strategy, Redundant/Spare Equipment readiness, Energy consumption, Planned–Unplanned Maintenance Order and Rework Maintenance, etc. Then investigated the failure causes, severity, frequency of occurrence and assessed the difficulty of detection. with relatively high RPN indices several Failure modes were marked in grey, as shown in Table 7. In this case items with RPN index above 100 are taken as the focused item. As the result, in term to eliminate the possible failure modes or at least decrease its frequency of occurrence, recommendation for improvement action

Table 5 Quality designing

Technical attributes	Zero accident	High skilled people	Proven maint. practice	Comply to procedure	Well documented	Comply to scope of work	Value added	Comply to work duration	Minimum rework
Importance rating	2.1	4.0	0.8	1.9	0.9	2.6	0.7	2.0	3.5
Current company's level	5.0	5.0	2.0	5.0	3.0	5.0	4.0	4.0	3.0
Target level	7.0	6.0	4.0	6.0	6.0	6.0	5.0	6.0	6.0
Need improvement	IMPV	IMPV	MNT	IMPV	MNT	IMPV	MNT	IMPV	IMPV

Table 6 House of quality

	Zero accident	High skilled people	Proven maint. practice	Comply to procedure	Well documentd	Comply to scope of work	Value added	Comply to work duration	Minimum rework	Importance rating	Current level	Target level	Improvement ratio	Absolute Importance	Relative Importance
Maint. productivity	7.0	6.0	4.0	6.0	6.0	6.0	5.0	6.0	6.0	0.4	4.0	5.0	1.3	0.5	0.4
Maint. organization		3.0	5.0		1.0				1.0	0.1	4.0	4.0	1.0	0.1	0.0
Maint. control	3.0	5.0	1.0	3.0	3.0	3.0	3.0	1.0	5.0	0.1	3.0	4.0	1.3	0.2	0.1
Maint. planning	3.0	3.0	1.0	5.0	1.0	5.0	1.0	3.0	3.0	0.2	3.0	5.0	1.7	0.3	0.3
Maint. scheduling	5.0	3.0	1.0	3.0	1.0	5.0	1.0	5.0		0.1	3.0	5.0	1.7	0.2	0.2
Mat'l and spare part mgmt.			1.0	1.0	5.0		1.0	3.0	3.0	0.0	4.0	4.0	1.0	0.0	0.0
Importance rating	2.1	4.0	0.8	1.9	0.9	2.6	0.7	2.0	3.5						
Current company's level	5.0	5.0	2.0	5.0	3.0	5.0	4.0	4.0	3.0						
Target level	7.0	6.0	4.0	6.0	6.0	6.0	5.0	6.0	6.0						
Need improvement	IMV	IMV	MNT	IMV	MNT	IMV	MNT	IMV	IMV						

Table 7 The maintenance activity failure mode and effect analysis

No	Ops. failure	Failure mode	Sev	Failure cause	O	D	RPN index
1	Production capacity	Lack of plant reliability	7	Inappropriate processes	3	4	84
				Lack of maintenance quality	4	3	84
				Uncomplete maintenance service (material/spare part is not ready)	4	2	56
2	Maintenance strategy	Insufficient equipment strategy	7	Lack of capability	5	4	140
				Unclear role and responsibility	5	5	175
3	Critical equipment	Lack of redundant/ spare eqp readiness	7	Lack of maintenance quality	6	5	210
				Uncomplete maintenance service (material/spare part is not ready)	3	4	84
4	Energy consumption	Highly use and or release energy	5	Inappropriate processes	4	4	80
				Inadequate design	5	3	75
5	Maintenance activity	Unplanned maintenance order is high	6	Lack of PM compliance	8	6	288
				Lack of operator awareness	6	5	180
		Rework maintenance	5	Low quality of material	5	3	75
				Lack of workmanship internal/external	6	5	150

are suggested. Such as, the cause of Unplanned Maintenance Order is High is Lack of Preventive Maintenance Compliance and Lack of Operator Awareness. Suggestion were provided, such as standardized PM task list and improve the task list and the schedule accuracy so it will guide the technician activity and the operator schedule.

4   Discussion

By using QFD-FMEA analysis, the solution for improvement offered from technical attributes for maintenance activity, respectively.

4.1 Solutions for Technical Attribute Improvement

As listed in Table 6 several technical attribute were identified for improvement, such as Zero accident, high skill people, comply to procedure, comply to scope of work, comply to work duration and minimum rework. Solutions were given accordingly as shown in Fig. 3. The role of new maintenance management activity design as shown in Fig. 3. Therefore, The maintenance role clearer and more manageable.

To optimize the targets "Zero accident, High skill people & Minimum rework" the activity is Work progression sharing, knowledge sharing, learning from events, success story, and the task list which specifically design for each selected equipment is also expected as guide for junior technicians and minimize human error (30 m Meeting, Visual PM Program). And for "Comply to Procedure, Comply to Scope of Work & Comply to Work Duration" the activity is Basic equipment care by Plant Patrol, using critical equipment sharing dashboard, maintenance performance measurement and implementing engineering standard (Basic Equipment Care, Equipment Status Dashboard, Maint. Analysis Report, Workshop Mgmt).

Based on the discussion above, the maintenance management improvement program as proposed are summarized in Table 8.
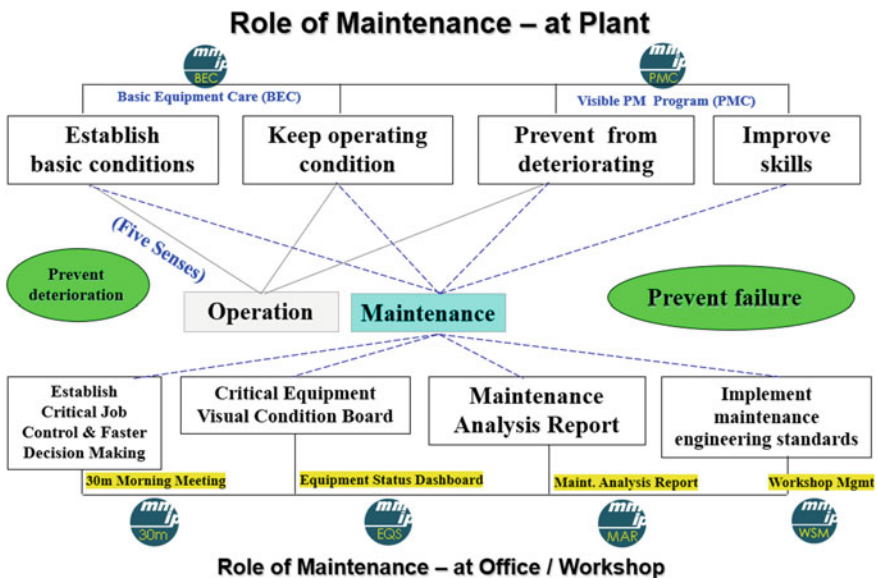
Fig. 3 Improvement of maintenance activity

Table 8 Improved results of technical attributes

Critical problems	Proposed solution	Effects
• Maintenance productivity	Activate a standard plant patrol	Increase maintenance productivity, early detection of unplanned repair
• Maintenance control	Top down cascade communication, standardize visual information board, standardize technical routine meeting and monthly report	Build togetherness, faster decision making, encourage frontline and raise up the technician and the operator awareness
• Maintenance planning and scheduling	Develop an accurate maintenance activity schedule at the critical equipments with a clear and fit maintenance task lists	Improve maintenance effectiveness, develop a better working culture, increase prevention rather than detection of any maintenance problem, a standard guidelines will make easier for junior technician to execute the maintenance activity

4.2 Solutions for Maintenance Effectiveness Improvement

Based on the Maintenance effectiveness analysis, as shown in Table 8 several items with high RPN indices were identified through FMEA application. Recommendation are given as shown in Table 9. The qualification ratio of maintenance effectiveness was increase and equipment reliability improve accordingly.

This case study was carried out in 2018 until 2020, in May 2018 to June 2019 February were compared with those in July 2019 to August 2020 in Table 10.

Several key items were exposed as the result of QFD-FMEA Analysis, such as Unplanned Maintenance order is High and Lack of PM Compliance, which highly impacted to customer complaints including maintainability as well as the

Table 9 Improvement strategy of maintenance management

Critical problems	Proposed solutions
Inappropriate maintenance strategy	Introduce a new maintenance management under maintenance execution
Unclear role and responsibility	Implement a new maintenance management model, with a detail and clear target and scope of work
Lack of PM compliance	Standardize PM task list schedule and evaluate the realization
Lack of maintenance quality in terms of critical equipments	Improve the accuracy PM
Lack of frontline awareness and workmanship	Encourage frontline, build togetherness by top down cascade communication

Table 10 Comparison chart of maintenance performance

No	Parameters	May 2018–June 2019	July 2019–August 2020		Value (%)	Desc.
1	Total maintenance intervention (events)	59 times	35 times	↓	41.0	The total maintenance intervention is reduced significantly
2	Mean time between maintenance (MTBM)	24 days	52 days	↑	116	MTBM increased drastically
3	Mean time to repair (MTTR)	21 days	11 days	↓	47.6	MTTR decreased significantly
4	Maintenance cost	Rp. 7,014,206,497	Rp. 1,259,414,867	↓	82	Maintenance cost decreased significantly

maintenance quality. Activate a standard Plant Patrol and Develop an Accurate Maintenance Activity Schedule at the Critical Equipment with a clear and fit maintenance task lists are proposed as the Improvement strategies. To ensure the study can capture a wider range of the customer satisfaction by using QFD and FMEA to explore problems from several point of views.

5 Conclusions

The QFD-FMEA combination, used as the methodology to answer the lack of maintenance management and to improve the maintenance effectiveness. QFD identify technical attributes, such as Zero Accident, High Skill People, Comply to Procedure, scope of Work, Work Duration and Minimum Rework were appears as critical issue which has highly impact to the costumer satisfaction. At the same time, FMEA analyze possible failure modes from the maintenance activity from the technical point of view. Recommended action were delivered accordingly. Significant result of maintenance effectiveness improvements achieved by using this method. the new maintenance management model has successfully developed and implemented, has increase by 116% Mean Time Between Maintenance and Decrease by 41% Number of Breakdown Maintenance Intervention, 47.6% Mean Time To Repair and 82% of maintenance cost or Rp. 5,754,791,630.00 lower compare to the previous year maintenance cost. but this method is required a big effort at the beginning, such as organized an event that can gather all senior supervisors and maintenance area section head to collect all common symptoms

under their area and then set the CR's. This hybrid QFD-FMEA worked effectively for improving the maintenance effectiveness.

References

1. Abdul-Rahman H, Kwan CL, Woods PC (1999) Quality function deployment in construction design: application in low-cost housing design. Int J Qual Reliab Manage 16(6):591–605
2. Akao Y, Mazur GH (2003) QFD: past, present, and future. Int Symp QFD 97:1–12
3. Almannai B, Greenough R, Kay J (2008) A decision support tool based on QFD and FMEA for the selection of manufacturing automation technologies. Rob Comput-Integr Manuf 24 (4):501–507
4. American Supplier Institute (1991) Quality function deployment: excerpts from the implementation manual for three-day QFD workshop. In: Transactions of the Third Symposium on Quality Function Deployment, pp 19–40
5. Ben-Daya M et al (2009) Handbook of maintenance management and engineering. Springer
6. Chen L-H, Ko W-C (2009) Fuzzy linear programming models for new product design using QFD with FMEA. Appl Math Model 33(2):633–647
7. Ginn DM, Jones DV, Rahnejat H, Zairi M (1998) The "QFD/FMEA interface". Eur J Innov Manage 1(1):7–20
8. Ho W (2008) Integrated analytic hierarchy process and its applications—a literature review. Eur J Oper Res 186(1):211–228
9. Kahraman C, Cebeci U, Ulukan Z (2003) Multi-criteria supplier selection using fuzzy AHP. Logistics Inf Manage 16(6):382–394
10. Kuschel T, Bock S (2019) Solving the weighted capacitated planned maintenance problem and its variants. Eur J Oper Res 272(3):847–858
11. Lamers TL et al (2007) Application of a modified quality function deployment method for MEMS, pp 159–168
12. Satty TL (1977) A scaling method for priorities in hierarchical structures. J Math Psychol 15 (3):234–281
13. Tanık M (2010) Improving "order handling" process by using QFD and FMEA methodologies: a case study. Int J Qual Reliab Manage 27(4):404–423
14. Xuguan T, Wei X (2018) Improving product quality based on QFD and FMEA theory—taking electrofusion joints as an example. In: International Conference on Computer Science and Information Engineering (ICCSIE 2018), CSP

Maintenance Strategy for Engine Oil 100-Ton Truck Using Taguchi Method at Coal Mining Company

Surya Atmadyaya, Mohamad Sazali Said, Azmi Hassan, Fauzan Rahman, and Iwan Susanto

Abstract The purpose of this thesis is to provide the best fit maintenance management alternative to assets owned by the company from the point of view of operational readiness. The nature of this topic is to determine the use of the reference maintenance management model, with several parameter adjustments for the implementation area at the plant and other critical operational assets. This research aims to the research is to analyze effectiveness engine oil drain interval and replacing engine oil filter to reduce contaminant on engine oil to meet acceptable level parameters as equipment manufacturing recommendation to meet target replacement 500 h using Taguchi Method. Based on the results of the analysis conducted, conclusions can be drawn (1) Oil formula factor and filter replacement have been proven to have a significant effect on all elements of the oil condition, wear metal, and additive response variables. The contribution of the oil formula factor in influencing the response was 33.33% and the contribution of the filter replacement factor in influencing the response was 66.66%. (2) The combination of factor levels that provide the most optimum results is an oil with a new formula and filter replacement is performed at 250 h. The alternative conditions that might be applicable in addition to the optimum conditions, namely oil with a new formula, but no filter replacement was performed at 250 h. (3) The average value of each element at the optimum conditions and alternative conditions compared with the applicable limit or standard, where the results can be concluded as (a) Optimum conditions: In the oil condition response variable, TBN falls into the caution category at 250 and 500 h, while OXI is normal. In the wear metal response variable Al, Cr, Fe, Pb, Cu, Sn are normal at the 250th and 500th hours. While the additive response variables, Zn, Pb, Mo are trending down but 2 other elements namely Mg and Ca have increased. (b) Alternative conditions: In the oil condition response

S. Atmadyaya (✉) · M. S. Said · F. Rahman · I. Susanto
Manufacturing Section, Malaysian Spanish Institute, Universiti Kuala Lumpur,
Kulim Hi-Tech Park, 09000 Kulim, Kedah, Malaysia
e-mail: atmadyaya.surya@s.unikl.edu.my

A. Hassan
Electrical, Electronics and Automation Section, Malaysian Spanish Institute,
Universiti Kuala Lumpur, Kulim Hi-Tech Park, 09000 Kulim, Kedah, Malaysia

variable, TBN falls into the caution category at the 250 and 500 h, while OXI is normal. In the *wear metal* response variable Al, Cr, Fe, Pb, Sn are normal at 250 and 500 h, but Cu is only normal at 250 h while at 500 h' critical category. While the additive response variable, P and B are trending down but 4 other elements namely Zn, Mg, Ca and Mo have increased.

1   Introduction

Effective integration of the maintenance function with the engineering functions and other production functions in the organization can help save large amounts of time, money, and other resources in managing needs, availability, maintenance, and performance problems. Maintenance is an important cost factor in the oil and gas industry, so research and development is an important area to focus on [4]. In order to reduce the risk and the consequences of unexpected shutdowns and enterprises in digital production, support must play a key role [11]. Industrial maintenance is recognized as a function that has a significant impact on the overall results of industrial companies and whose efficiency usually has great potential for improvement [10].

The responsibility of this unit ensures that material and spare parts are available in the right quality and quantity at the right time at minimal cost. In large or medium-sized organizations, this unit can be independent from the maintenance organization [1]. This proposal will make it possible to reduce not only the material losses of a single company, but also avoid a significant proportion of all the material losses that occur in transformation processes throughout a supply chain [3]. Maintenance research has been conducted to demonstrate better performance, cost reduction, and/or increased profitability, and to demonstrate profitability from maintenance based on circumstances [11].

Manufacturers look for opportunities to provide maintenance services in the service phase of the product life cycle to generate additional revenue and profit. Customers and end users expect to pay for product usage rather than full ownership [17]. The most important factor that can reduce engine performance and life is related to the friction and wear that is controlled by the engine oil system, monitoring the condition of the engine oil is getting more and more attention. Lubrication is a basic task in condition-based treatment. Lubricant analysis is useful for all critical equipment [15].

In order to implement the operating parameters and to achieve the best results, the Taguchi method is well known. It is a statistical and mathematical collection method for optimal system performance. To solve various kinds of industrial problems, this method is often used. One of the main benefits of using this method is a reduction in cost and time compared to a complete factorial design experiment [8].

2 Literature Review

The main purpose of care is to maintain the equipment, respond to its needs and get it running. However, in a business context, protection is not the goal [16]. Two key elements of a strategic maintenance management approach: "(1) maintenance management is a fundamental business activity that is essential to business continuity and success, and as such must be managed strategically. (2) Effective maintenance management must be based on a quantitative business model that integrates maintenance with other solutions such as production, etc." [7]. Operational level. Implementation at policy level transforms business priorities into a priority. Production equipment is used without a planned maintenance method [12]. Systematic maintenance replaces parts frequently to avoid stopping unexpected equipment, but increases the time associated with the cost of an inoperative and maintenance machine [9].

Gackowiec outlined three care strategies. Basically, the phases based on time intervals include pre-planned maintenance or fixed/planned timing adjustment, where the actions are predetermined [6]. Analyzing the components of the equipment provides a maintenance program for the machines. The second point is, in the said paper there is a precautionary measure or condition. In these cases, predicting reliance on a set of data and measurements to control the machines, to detect abnormal conditions and to avoid failures. Thirdly, the authors propose a correction or correction for failure. In general, these policies have steps and actions, which take place after the damage has occurred.

Considering the theories of TPM Production Product, two phases of comprehensive maintenance strategies: practical and also known as remedial remediation and applicable [18]. Practical approaches are aimed at repairs after a breakdown, while pre-designed tasks are intended to avoid these repairs and errors. A general classification of technical care policies such as breakdown or repair or running to ineffective maintenance, preventive maintenance, planned repairs, effective maintenance, conditional maintenance, planning maintenance [19].

Improved step-by-step analysis of the effective reduction of water thickness at each stage is achieved with the Taguchi method. In Taguchi's case, we think we're designing an engineering system—either a machine that does a specific job or a machine that produces. We use basic knowledge about the system and process phases for practical tests. We can skip all the extra efforts that would have gone into researching collaborations. With this, we can reduce the number of points. Taguchi divides data into two categories: regulatory causes, under our control and noise factors, which are not under our control, except during laboratory experiments [2].

Taguchi products can be found or scanned up. Small parts can be pulled by hand; large groups can come from dedicated algorithms. In general, arrays can be found online. The arrays are determined by the number of parameters (variety) and the number of positions (mean). This is also explained later in this article. Analysing the differences between the data collected from the Taguchi experimental design can be used to select new parameter values to improve performance

characteristics. Data from arrays can be evaluated by drawing data and performing a visual inspection, ANOVA, bin products and Fisher's accurate test, or Chi-squared test to assess significance [5].

Numerous studies have used Taguchi's method to improve surface quality (such as sharpness) for polishing process. Typically, the automatic polishing process consists of a number of steps that use different components such as the size of the coarse grain, the polishing processors, the supply chain, the polishing force and so on. ling. Tsai and Huang developed a self-organizing step-by-step design system that is compatible with the tool for selecting the best brightness levels for different lighting stages [13]. Another limiting factor is that Taguchi's methods do not work, so they do not fit into a dynamic process that changes as a simulation study. In addition, since Taguchi's methods work on quality design as opposed to fixing it for low quality, it is best used in the early stages of development process. After the various types of design have been mentioned, the implementation of the test plan may be cheaper [5] (Fig. 1).

3   Methodologies

3.1   Data Collection Method

The data of this research focuses on data taken from the results of the scheduling of engine lubricant oil inspection in the maintenance of mining equipment at a coal mine. The number of samples is 4300 samples from 171 units of 100T Haul Dump trucks, oil life of 250–500 h of operation from 100-ton truck engine.

3.2   Data Analysis

a. **Determine controllable factors and their initial level settings for inner orthogonal array**

When designing an experimental plan, the decision maker is primarily concerned with establishing the impacts associated with the various control conditions, and adjusting the condition so that it does not take into account the effects of noise.

b. **Determine the parameters of the adopted forecasting method for outer orthogonal array**

In Taguchi experiments, many external factors that are not built into the experiment influence their results. These fruits have a profound effect on the emergency, and they damage its stability. On the other hand, the performance of the forecast is

Fig. 1 Taguchi Method
Design of Experiments
(Fraley et al. 2020)
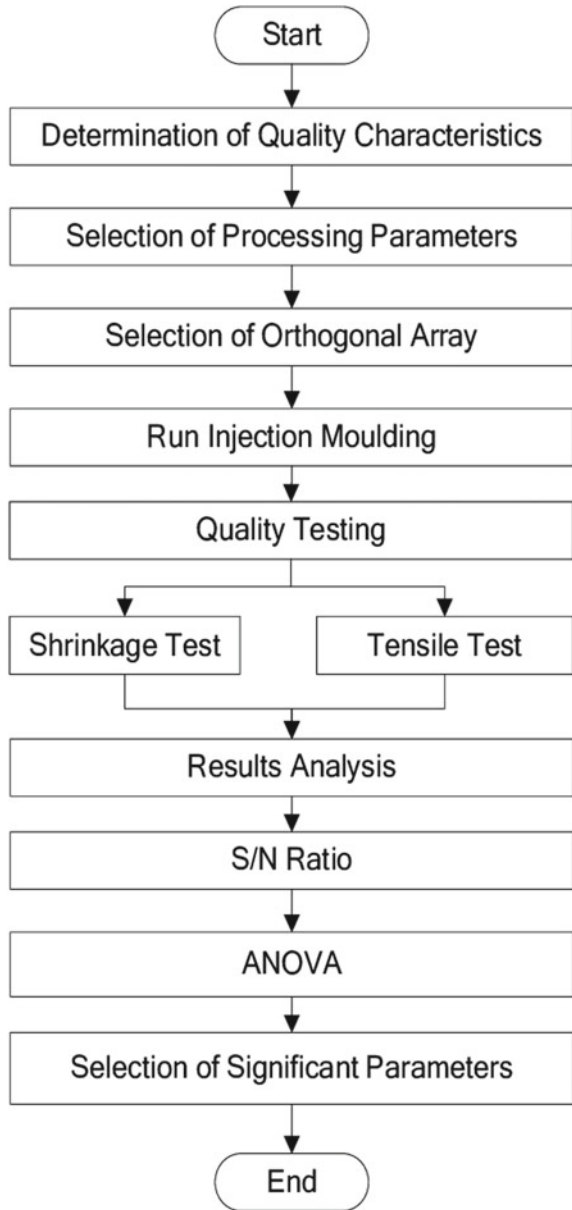
determined by the appropriate method of prediction. A particular process is affected by the phases of the accepted climate model. Studies have shown that different stages of predictive methods have different predictive results [14].

c. Using Taguchi method to evaluate controllable factors and levels

Taguchi's method reduces the cost of experiments by using orthogonal arrays to extract practical and sufficient information from a minimum of experimental data. By analysing the effects and co-operation of a variety of controlled factors, the use of an orthogonal team enables decision-makers to evaluate and position individual data in order to establish their high-level standards. In addition, orthogonal groups ensure a consistent result when different experiments perform design experiments.

d. Construction of an orthogonal design

In design experimentation, the correct choice of orthogonal sequence follows the liberal steps of a particular experiment. Thus, a parallel graph is used to indicate appropriate treatment and group status conditions. The current study focuses on three manageable factors and one interaction, thus accepting an internal orthogonal group to measure status levels.

e. Implementation of an experiment

In Taguchi method, controlled points are assigned to specific columns of the internal orthogonal component. Thus, the current study provides data time (factor A), length (factor B), and number of observed factors (factor C) in Columns 1, 2, and 4 of the internal orthogonal array, respectively. Each test will be repeated several times in different contexts of external prediction methods. In practice, these data can be assigned randomly to any of the arrays columns, as long as all components are included.

The Taguchi method recommends the use of the converted loss rate at the S/N rate to measure deviations from the approximate value to the S/N average for each level of p. ebetso is evaluated according to the S/N average rating and the S/N ratio corresponds to a high quality character regardless of class and the value is evaluated according to the S/N standard and the ratio The large S/N is accompanied by a good performance feature regardless of class and quality. After assigning appropriate level settings, the S/N analysis is needed to evaluate experiment results.

Smaller is the better characteristic S/N:

$$-10\log\frac{1}{n}\left(\sum y^2\right) \tag{1}$$

Nominal is the better characteristic S/N:

$$-10\log\frac{1}{n}\left(\sum \frac{\bar{Y}}{S_y^2}\right) \tag{2}$$

Larger is the better characteristic S/N:

$$-10\log\frac{1}{n}\left(\sum\frac{1}{y^2}\right) \tag{3}$$

where

$\bar{Y}$ is the average of the observed data variables

S_y^2 is variations of y

n is the number observed

$y1, y2,\ldots$ etc. is the result of experiments; and n, the number of repetitions (yi).

After obtaining further values by transforming the S/N Ratio of Response Variables into PCR-S/N Ratio, using the formula:

Smaller is the better characteristic:

$$n_j^i = -10\log_{10}\left[\frac{1}{l}\sum_{k=1}^{1}\left(y_{jk}^i\right)^2\right] \tag{4}$$

Nominal is the better characteristic:

$$n_j^i = -10\log_{10}\left[\frac{1}{l}\sum_{k=1}^{1}\frac{1}{\left(y_{jk}^i\right)^2}\right] \tag{5}$$

Larger is the better characteristic:

$$n_j^i = -10\log_{10}\left[\frac{\left(y_j^{-i}\right)^2}{\left(S_j^i\right)^2}\right] \tag{6}$$

The next step is the result of the PCR-S/N Ratio; we convert into TOP-SIS with the formula:

$$d^{i+} = \sqrt{\sum_{j=1}^{m}\left(C_j^i - C_j^+\right)^2} \tag{7}$$

f. **Ranking of selected factors**

ANOVA is performed to evaluate the critical performance of an assumed performance affecting product value a statistical variance of the data that can be calculated by measuring quantities such as degree of freedom, total square, difference ss, v and

part of the percentage of each point. Improvement in the process of coating and hardening of industrial ceramic ornaments using the Taguchi design process.

g. **Pooling of factors**

The conditional and diagnostic tasks described above can enable a researcher to combine one or more manageable items to reduce costs. It may be necessary to carry out some improvement process with the remaining details. Because the cost of the experiments controls the elimination of the process and the information, the combined data can produce satisfactory results. The test should be willing to compromise between the quality of the solution and the cost of the test, reflecting the phases of the system well.

h. **Optimization of factor level settings and construction of forecasting model**

After conducting some improvement experiments with remaining or updated items, we analysed the main outcome table to find the right test plan. It is important to identify the optimal conditions that improve the average response. These status settings are selected by analysing the final table of responses.

i. **Validation of experiment**

In the development of multiple products, the correct choice of system was evaluated with the help of the TOPSIS method. The correct installation steps were selected using the TOPSIS and AHP combination method on the Inconel 718 machine. The best lubricant is selected among a number of cosmetics using TOPSIS and AHP combined to convert EN31steel. The overall performance has been achieved for its operational activities in the success of the manufacturing company using the TOPSIS and AHP method. So the benefits of the TOPSIS and AHP methods are combined to achieve a flexible performance.

4   Discussion

4.1   *Estimated Average of Elements*

4.1.1   Estimated Results for Optimum Conditions

The optimum conditions, in this case, are based on the highest *PCR-TOPSIS* values obtained for each factor. It can be seen from Table 4.5 that the highest *PCR-TOPSIS* value is obtained at a combination of factor levels A_1, B_2 i.e. oil with a new formula, and filter replacement is done at 250 h.

a. **Estimation of Oil Condition Response Variables**

The estimated value of each element is carried out at 250 h and at 500 h. In calculating the average estimation of *oil condition* response variables for TBN and

OXI elements, the estimation calculation is based on the average sample data for each experiment/factor level combination.

The calculation of TBN and OXI elements at 500 h sample is done in the same way but the calculations are based on the average 500 h sample data in Table 1. The estimation results of the oil condition response variable are presented in Table 2 as follows.

b. **Estimation of Wear Metal Response Variables**

The estimated value of each element is carried out at 250 h and at 500 h. In calculating the average estimate of the wear metal response variable for the elements Al, Cr, Fe, Pb, Cu, and Sn, the estimation calculation is based on the average sample data for each experiment/factor level combination.

Element calculation Al, Cr, Fe, Pb, Cu, and Sn at 500 h sample is done in the same way but the calculations are based on the average 500 h (Table 3).

c. **Estimation of Additive Response Variables**

The estimated value of each element is carried out at 250 h and at 500 h. In calculating the estimated average of the *additive* response variables for the elements Zn, Mg, Ca, P, B, and Mo, the estimation calculation is based on the average sample data for each experiment/factor level combination (Table 4).

Element calculation Zn, Mg, Ca, P, B, and Mo at 500 h sample is done in the same way but the calculations are based on the average 500 h.

Table 1 TBN and OXI sample average data

Element	Type oil	Filter replacement	250 h sample average	500 h average sample
TBN (total base number)	New formula	Without filter replacement at 250 h	7,043	6,093
		With filter replacement at 250 h	7169	6.224
	Old formula	Without filter replacement at 250 h	6,988	6,075
		With filter replacement at 250 h	6,891	6,254
OXI (oxidation)	New formula	Without filter replacement at 250 h	14,333	16,667
		With filter replacement at 250 h	13,177	16,417
	Old formula	Without filter replacement at 250 h	13,000	14,583
		With filter replacement at 250 h	13,000	13,750

Table 2 Estimation of the value of oil condition response variables under optimum conditions

Element		Estimated average value of response variables under optimum conditions	
		250 h	500 h
Oil condition	TBN	7.1135	6.2363
	OXI	14.0208	16,2708

Table 3 Estimated value of *wear metal* response variables under optimum conditions

Element		Estimated average value of response variables under optimum conditions (new formula oil, filter replacement)	
		250 h	500 h
Metal wear	Al	2.1042	2.4583
	Cr	0.0208	0.3125
	Fe	96,250	17.125
	PB	0.5625	1.6667
	Cu	2.8958	0
	Sn	0.0417	0.0625

Table 4 Estimated value of *additive* response variables in optimum conditions

Element	Estimation of optimum conditions	
	250 h	500 h
Zn	1111.1667	1104.1458
Mg	9,7708	10.8125
Ca	3548.0208	3563.9792
P.	1100.5833	1076.5417
B	306.4792	273,2083
Mo	42.9167	42,1458

4.1.2 Estimation of Results in Alternative Conditions (New Formula Oil with No Filter Replacement)

Estimation of Oil Condition Response Variables

See Table 5.

Element		Estimated average value of response variables in alternative conditions	
		250 h	500 h
Oil condition	TBN	70,990	6.0813
	OXI	14.2292	16.8125

Table 5 Estimated value of *oil condition* response variables in alternative conditions

a. **Estimation of Wear Metal Response Variables**

The estimated value of each element is carried out at 250 h and at 500 h. In calculating the average estimate of the *wear metal* response variable for the elements Al, Cr, Fe, Pb, Cu, and Sn.

Element calculation Al, Cr, Fe, Pb, Cu, and Sn at 500 h sample is done in the same way but the calculations are based on the average at 500 h (Table 6).

b. **Estimation of Additive Response Variables**

The estimated value of each element is carried out at 250 h and at 500 h. In calculating the estimated average of the additive response variables for the elements Zn, Mg, Ca, P, B, and Mo, the estimation calculation is based on the average sample data for each experiment/factor level combination.

Element calculation Zn, Mg, Ca, P, B and Mo at 500 h sample is done in the same way but the calculations are based on the average 500 h (Table 7).

Element		Estimated average value of response variables in alternative conditions (new formula oil, filter replacement is available)	
		250 h	500 h
Metal wear	Al	1.9792	2.2917
	Cr	0.0625	0.3542
	Fe	9,953	19.2917
	Pb	0.8542	35,000
	Cu	4.1042	36.3542
	Sn	0.125	0.1875

Table 6 Estimated value of *wear metal* response variables in alternative conditions

Table 7 Estimated value of *additive* response variables in alternative conditions

Element	Estimation of optimum conditions	
	250 h	500 h
Zn	1067.4167	1101.3542
Mg	9,6458	10,6042
Ca	3431.8125	3531,1042
P.	1034.4167	1015,1250
B	309.9375	274.6250
Mo	40.9167	41.5208

4.2 Estimation Test Validation Results

If the estimation result is invalid, then the observation data will be used as consideration in concluding the estimated value at the optimum conditions for the Cu element at 500 h and the P element at 250 h has a significant difference when compared with the observations, so it can be said that the estimated value is invalid, whereas all values other estimates are valid. Therefore, for consideration of the decision, then for the Cu element at the 500 h and the P element at 250 h, the average data from observations is used because the estimation is invalid.

4.3 Comparison of Estimated Results for Optimum Conditions and Alternative Conditions

The average value of each element or response variable must also be compared again with the applicable quality standard or limit to see whether the average value of the element or response variable still meets the quality standard or limit (Table 8).

Although the estimated average value of the *oil condition* elements namely TBN and OXI in alternative conditions is higher, there is no difference in terms of compliance with applicable standards or limits. For wear metal elements in Table 10, it can also be seen that the estimated average value of *wear metal* elements in alternative conditions is higher. Mostly there is no difference in terms of compliance with applicable standards or limits except for Cu elements which even if using oil with a new formula, but if there is no filter replacement, the average Cu value is estimated to be quite high and into the critical category. As for the *addictive* elements in Table 11, it can also be seen that the estimated average value of the *wear metal* element in alternative conditions increases more than at 250 h at 500 h, this is natural because there is no filter replacement at 250 h, so that it causes in alternative conditions, the value of more additive elements does not meet the standard because it does not have a trending down pattern.

Table 8 Limit table

Category	Element	Normal	Caution	Critical
Wear metal	Cu	<9	10–11	> 11
	Fe	<22	23–28	> 28
	Cr	<1	1	> 1
	Al	<3	4	> 4
	PB	<3	3	> 4
	Sn	<3	4	> 4
Addictive	Zn	Trending down		
	Mg			
	Ca			
	P.			
	B			
	Mo			
Condition	TBN	> 5	<5	
	OXI	<20	20–25	> 25

5 Conclusions

Oil formula factor and filter replacement have been proven to have a significant effect on all elements of the oil condition, wear metal, and additive response variables. The contribution of the oil formula factor in influencing the response was 33.33% and the contribution of the filter replacement factor in influencing the response was 66.66%. The combination of factor levels that provide the most optimum results is an oil with a new formula and filter replacement is performed at 250 h. In this study, the researchers set alternative conditions that might be applicable in addition to the optimum conditions, namely oil with a new formula, but no filter replacement was performed at 250 h. The average value of each element at the optimum conditions and alternative conditions compared with the applicable limit or standard, where the results can be concluded as beircut. Optimum conditions: In the oil condition response variable, TBN falls into the caution category at 250 and 500 h, while OXI is normal. In the wear metal response variable Al, Cr, Fe, Pb, Cu, Sn are normal at the 250th and 500th hours. While the additive response variables, Zn, Pb, Mo are trending down but 2 other elements namely Mg and Ca have increased. Alternative conditions: In the oil condition response variable, TBN falls into the caution category at the 250 and 500 h, while OXI is normal. In the *wear metal* response variable Al, Cr, Fe, Pb, Sn are normal at 250 and 500 h, but Cu is only normal at 250 h while at 500 h critical category. While the additive response variable, P and B are trending down but 4 other elements namely Zn, Mg, Ca and Mo have increased.

References

1. Ben-Daya M (2009) Handbook of maintenance management and engineering. Springer, London
2. Davis R, John P (2018) Application of taguchi-based design of experiments for industrial chemical processes. Valter Silva, IntechOpen. https://doi.org/10.5772/intechopen.69501
3. Dierkes S, Siepelmeyer D (2019) Production and cost theory-based material flow cost accounting. J Cleaner Prod. June 2019
4. Eyoh J, Kalawsky RS (2018) Evolution of maintenance strategies in oil and gas industries: the present achievements and future trends. In: Presented at the FEAST International Conference on Engineering Management, Industrial Technology, Applied Sciences, Communications and Media (EITAC), London, UK, 28–29 July 2018
5. Fraley S, Oom M, Terrien B, Date JZ (2006) Design of experiments via Taguchi methods: orthogonal arrays. The Michigan chemical process dynamic and controls open text book, USA
6. Gackowiec P (2019) General overview of maintenance strategies—concepts and approaches. MAPE 2(1):126–139
7. Jasiulewicz-Kaczmarek M, Saniuk A, Nowicki T (2016) The maintenance management in the macro-ergonomics context. Adv Intell Syst Comput. 487:35–46
8. Thirumavalavan K, Karunamoorthy L, Padmanabhan KA (2019) Optimization of process parameters using taguchi technique in severe surface mechanical treatment of AA6061. Int J Eng Technol (IJET) 6(2), Apr–May 2014
9. Lee JH, Choi Y, Ann H, Jin SY, Lee S-Y, Kong JS (2019) Maintenance cost estimation in psci girder bridges using updating probabilistic deterioration model, sustainability, MDPI. Open Access J 11(23):1–19, Nov
10. Lopes I, Senra P, Vilarinho S, Sá V, Teixeira C, Lopes J (2018) Requirements specification of a computerized maintenance management system—a case study. Procedia
11. Lundgren C, Skoogh A, Bokrantz J (2018) Quantifying the effects of maintenance—a literature review of maintenance models. J Sci Direct Proc CIRP
12. Márquez AC, Díaz VGP, Fernández JFG, (eds) (2017) Advanced maintenance modelling for asset management: techniques and methods for complex industrial systems. Springer
13. Mohsin I, He K, Li Z, Zhang F, Du R (2020) Optimization of the polishing efficiency and torque by using taguchi method and ANOVA in robotic polishing. Appl Sci 10:824
14. Niska H, Hiltunen T, Karppinen A, Ruuskanen J, Kolehmaxinen M (2004) Evolving the neural network model for forecasting air pollution time series. Eng Appl Artif Intell 17:159–167
15. Raposo NHD, Farinha JMT, Ferreira LA, Galar D (2019) Reserve fleet indexed to exogenous cost variables. Transport 34(4):437–454
16. Relich M, Świć A, Gola A (2015) A knowledge-based approach to product concept screening. Adv Intell Syst Comput 373:341–348
17. Roy R, Stark R, Tracht K, Takata S, Mori M (2016) Continuous maintenance and the future—foundations and technological challenges. CIRP Ann 65:667–688
18. Sambrekar K, Rajpurohit VS (2019) Fast and efficient multiview access control mechanism for cloud based agriculture storage management system. Int J Cloud Appl Comput IJCAC 9 (1):33–49
19. Vishnu CR, Regikumar V (2016) Reliability based maintenance strategy selection in process plants: a case study. Proc Technol 25:1080–1087

Effect of Pineapple Leaf Fiber Volume Fraction with 157 BQTN-EX as a Matrix on the Tensile Strength of the Composite

Muhammad, Reza Putra, T. Hafli, and Asnawi

Abstract In this study, natural fiber-reinforced polymer composite materials were fabricated by hand lay-up method. The pineapple leaf fiber as reinforced composite has been investigated for tensile strength using Universal Testing Machine (UTM). The chemical treatment with soaking in 5 wt% NaOH solution and varying the type of fiber arrangement, the composite specimens have been made. The comparing of fibers fraction volume is restricted from 20, 30, and 40 vol.% with Unsaturated Polyester Resin (UPR), Yukalac 157 BQTN-EX Series as a total volume of the composite. The results showed that the fiber volume fraction ratio of 40% and unidirectional fiber orientation succeeded in increasing the tensile strength to 103.5 MPa.

Keywords Reinforced composite · Polyester · Pineapple · Hand lay-up

1 Introduction

Increased application of technology in composite materials have been fully leading on the composite-based naturally well as material reinforcement [1, 2]. Natural fiber has become an important commodity for economic matters and becomes a significant source of employment for developing countries. The natural fibers can be easily obtainable in many areas of tropical and available in the whole world. The characteristic of this composite are the properties of the fibers and the matrix was enabled to modified without reducing the functions and chemical properties of the materials itself. The development of natural reinforced composite has replaced the function of metal and carbon [1–3].

Study on the reinforced natural fibers as substitute glass fiber as composites had increased and got an opportunity to be mass-produced. However, the major

Muhammad (✉) · R. Putra · T. Hafli · Asnawi
Department of Mechanical Engineering, Universitas Malikussaleh, Jln. Batam no.1,
Bukit Indah, Lhokseumawe 24351, Indonesia
e-mail: muhammad.tm@unimal.ac.id

weakness of the natural fibers is the compatibility between the fibers and the matrix. Consequently, chemical treatment has been considered in modifying the properties of the surface of the fiber [2, 3]. One of the reinforced natural fibers is made from the leaves of a pineapple. It has been a lot of research with improvement through the properties of physical and mechanical fiber pineapple that are combined with polyester resin as a matrix [3].

In this research, the pineapple leaf will be used as a natural reinforced fiber. The term of composites also includes the materials that have a form of particles or layers. Volume fraction (in wt%) is the rule for mixing the volume of fiber and the volume of the matrix towards the total volume of the composite [4]. Usually, the term volume fraction refers to a large proportion (%) of the volume of reinforcing materials used in the manufacture of composites.

If the purpose of making a composite is strength, the reinforced fibers must have a larger aspect ratio when compared to the matrix [4, 5]. Obviously, the reinforced composite should be a component that is powerful to carry the load, and the reinforced fibers must have higher modulus elasticity. When the value of stiffness between matrix and reinforcement is critical, the load must able transferred from the matrix to the fibers if the composite was desirable with function with either [6]. Pineapple leaf fiber (PALF) which is relatively inexpensive and widely available, has been to potential composites with natural fiber strengthened [7].

Based on previous research, it's necessary to study the effect of volume fraction of pineapple leaf fiber with polyester matrix by comparing types of unidirectional and random fiber arrangement.

2   Experimental

2.1   Material

In this study, the materials of the natural composite of Pineapple Leaf Fiber (PALF) were obtained at the village in the district of Bener Meriah, Aceh. Unsaturated Polyester Resin (UPR), Yukalac 157 BQTN-EX Series with a density of 1.12 g/cm^3 at 25 °C from Justus Sakti Raya Company used as matrix and 1% catalyst methyl ethyl ketone peroxide (MEKP) used as a hardener of polyester. From the other research in the same field, the physical and chemical properties of natural fiber summarized as shown in Table 1.

2.2   Preparation of Specimens

The chemical used for the treatments of pineapple leaf fiber (PALF) was Sodium Hydroxide (NaOH) at a concentration of 5% of water volume. The process of

Properties	Pineapple leaf	References
Cellulose (wt%)	71.6	[8, 9]
Lignin (wt%)	5–12.7	[8, 9]
Hemicellulose (wt%)	4.58	[6, 8]
Microfibril angle (wt%)	14	[7, 8]
Density (g/cm$^{3)}$)	1.3	[8]
Tensile Strength (MPa)	150–1627	[9]

Table 1 The properties of pineapple leaf

making the fiber is done by way of soaking pineapple leaves in water that contains NaOH 5 wt% for 2 h. Then, the pineapple leaves are scratched in order to produce fiber. The fibers are dried at room temperature for 48 h [3]. Some of the fibers are cut into short fibers and others are cut out to the size of the test mold.

2.3 Methods

Comparison of volume between fiber and matrix in at 20, 30, and 40 vol.% of the composite. The composite materials have been made by a hand lay-up method. Composite fiber with unidirectional and random short fiber was created in the mold with dimensions of 24 × 14 × 3.2 mm. Specimens have been removed from the mold were cutting according to standard ASTM D638 [10] for tensile tests. The specimen test sample is repeated several times and the average results are taken to be discussed as the characteristic properties of the composite. Figure 1a, shows the device that has been used for tensile test, and Fig. 1b and c, show the shape of the composite specimen that has been made accordingly to ASTM D638.
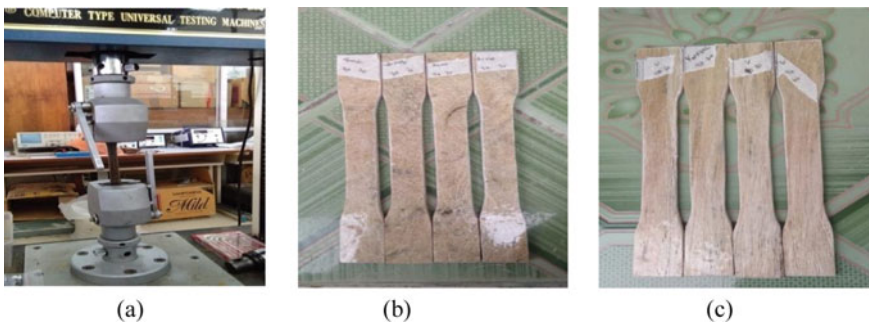
Fig. 1 **a** Universal testing machine (UTM), **b** random fiber test specimen, **c** unidirectional fiber test specimen

3   Results and Discussions

Has been achieved the results of tensile testing on reinforcement composites pineapple leaf fiber (PALF) with chemical treatment (5% NaOH) and optimization of fiber volume fraction of 20, 30, and 40 vol.%.

Figure 2 shows the relationship between the tensile strength of the differences in random fiber volume fraction. The results of the volume fraction of 20% random fiber arrangement have an average tensile strength value of 25.9 MPa. On the volume fraction of 30%, the average tensile strength only increased by 28.22 MPa. For fibers with 40% volume fraction, there was a significant increase in tensile strength above 40 MPa. This occurs since the greater the number of random fibers results in more bonds between the fibers and the matrix [11].

Figure 3 shows a tensile test specimen with a unidirectional fiber arrangement with a fiber volume fraction of 20, 30, and 40 vol.%. The average value of tensile strength increases more than 100% where the lowest value occurs at the fiber content of 20 vol.%, specifically 51.2 MPa. The highest tensile strength value was found in the fibers with a volume fraction of 40% is 103.5 MPa with an average tensile strength of 94.35 MPa.

The tensile strength increased of the reinforced composite was strongly influenced by the fiber arrangement and fiber volume from its comparison to the matrix [12]. The random arrangement did not significantly increase the tensile strength even with a large fiber volume (40%), While the unidirectional arrangement of the tensile plane showed significant strength results that exceeded twice than the random fibers with a minimum fiber volume fraction (20%).

Different types of pineapple leaves based on the sampling location and variations in chemical treatment also affected increased the tensile strength value. The bond between the fiber and matrix is more uniform across the surface of the fiber with chemical treatment [13]. The lower value of the tensile strength on this research, when compared with the previous studies, is due to the difficulty of obtaining a
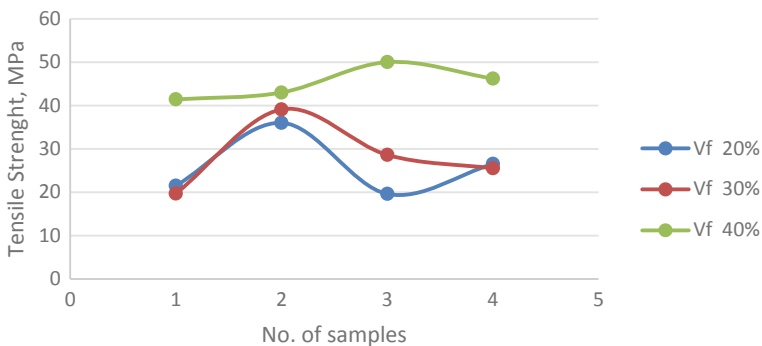

Fig. 2 Correlation between the tensile strength of composite PALF in a random arrangement with the difference in volume fraction
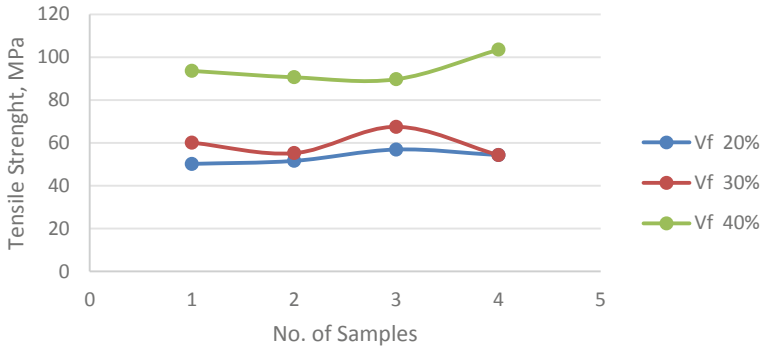
Fig. 3 Correlation between the tensile strength of composite PALF in a unidirectional arrangement with the difference of volume fraction

uniform dimension of natural fiber [14, 15]. To ensure the results of the tensile strength test, the specimen was taken in a microscopic image to see the shape of the fracture. Figure 4 shows the results of the microscopic picture on random fiber fracture and unidirectional arrangement at volume fraction 40%.

The fracture morphology of the two images in Fig. 4 shows different results. In random fibers, the fracture that occurs does not show a significant fiber effect. The fracture is shown in Fig. 4a shows the fracture of the brittle materials where the strength of the matrix was dominant. Figure 4b shows the shape of the fracture that extends in the direction of the pull, where the fracture results show the pull out of the fiber without visible voids in the bonds between the fibers and the matrix.

(a)　　　　　(b)
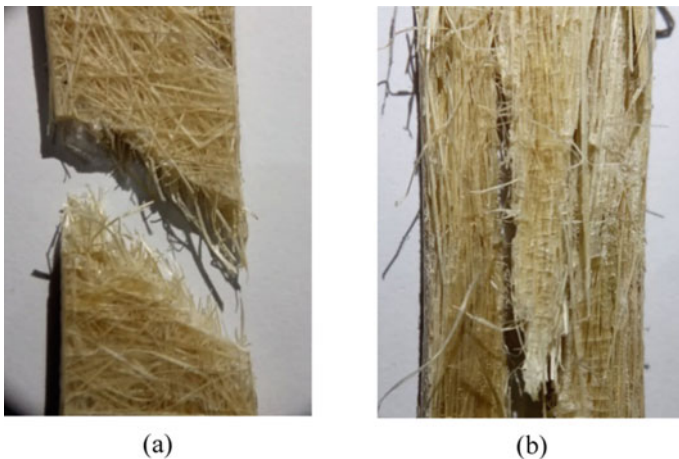
Fig. 4 Specimens after tensile test **a** fracture in random fibers, **b** fracture in unidirectional fibers

4   Conclusion

Pineapple fiber has been extensively studied with various techniques and compositions to achieved results as a reference for natural reinforced fiber. Research on the effect of chemical treatment with NaOH 5 wt% Pineapple leaf fiber showed that the ratio of fiber volume fraction and fiber direction orientation succeeded in increasing the tensile strength significantly up to 103.5 MPa. The selection of unidirectional fibers with a fiber volume fraction composition of 40% is highly recommended because it has an average tensile strength up to 94.35 MPa.

References

1. Asim M, Jawaid M, Abdan K, Ishak M (2017) Fiber Polym 18:940–947
2. Devi LU, Bhagawan S, Thomas (1997) J Appl Polym Sci 64(9):1739–1748
3. Suryani et al (2020) IOP Conf Ser: Mater Sci Eng 788:012038
4. Marliana M, Hassan A, Yuziah NM, Khalil AH, Inuwa I, Syakir M, Haafiz M (2016) Fiber Polym 17:940–947
5. Wan N, Jawaid M, Masri A, Khalil AS, Suhaily S, Mohamed RA (2012) J Polym Environ 20:404–411
6. Vlack Lawrence HV (2004) Elements of materials science & engineering. Addison-Wesley
7. Yusof Y, Nawi MN, Alias MSHB (2016) J Eng App Sci 11:4197–4202
8. Sanjay M, Yogesha B (2017) Mater Today: Proc 4:2739–2747
9. Yusoff RB, Takagi H, Nakagaito A (2016) Ind Crops Prod 94:562–573
10. ASTM D638-14, 2014 Standard Test Method for Tensile Properties of Plastics, West Conshohocken, PA
11. Akil H, Omar M, Mazuki A, Safiee S, Ishak ZM, Bakar A (2011) Rev Mater Des 32:4107–4121
12. Nirmal U, Hashim J, Ahmad MM (2015) Tribol Int 83:77–104
13. Jaafar J, Siregar JP, Piah MBM, Cionita T, Adnan S, Rihayat T (2019) J Polym Environ 26:4271–4281
14. Asim M, Jawaid M, Abdan K, Isaac (2016) J Bionic Eng 13:426–435
15. Panyasart K, Chaiyut N, Amornsakchai T, Santawitee O (2014) Energy Procedia 56:406–413

The Effect of Tool Angles on Welding Temperature in Friction Stir Lap Welding Process on AA1100 Aluminum Sheet

Suwarsono, Budiono, R. H. Hendaryati, and W. B. Wicaksono

Abstract Investigation of micro friction stir laps welding joints on aluminum AA1100 sheet, applying high rotation tool. This research aims to observe the effect of the tool angles on the temperature during the joining process. The parameters to be used are the traverse speed, the tilt angles during the welding process and the diameter of tool pin, the tool rotation speed of 33,000 rpm. The results of data analysis used multi variable analysis with Response Surface Methodology (RSM). There are 3 parameters (Tilt angle, Travers speed, Pin diameter) and 3 variances. Here it can be seen that the tool angle greatly affects the increase in welding temperature.

1 Introduction

The development of the industry is starting to consider aluminum as the main material in the production process. The need for aluminum plate in the industry is also getting higher. This is because aluminum and alloys are light metals which have high strength. Resistant to rust, a fairly good electrical conductor and of course lighter than iron or steel. Aluminum plate is widely applied in the industrial world such as in automotives, trains, airplanes, ships, and so on. This aluminum plate is very much needed in the industrial world, but has a problem with weldability. Therefore, it is necessary to have a suitable welding method to be able to join the aluminum plate so as to get the maximum welding strength.

Current technology various aluminum welding methods, including Friction Stir Welding (FSW). Friction Stir Welding is a solid welding method that was invented

Suwarsono (✉) · Budiono · R. H. Hendaryati · W. B. Wicaksono
Mechanical Engineering Department, University of Muhammadiyah Malang,
Jl. Raya Tlogomas No. 246, Malang 65144, Indonesia
e-mail: suwarsono@umm.ac.id

in 1991 at The Welding Institute (TWI) [1]. The FSW welding method itself has been widely used in the industrial world; automobiles, airplanes, ships, and so on. The Friction Stir Welding (FSW) method has a very simple working principle, utilizing the heat energy generated from the friction between the shoulder and the materials to be joined. This friction generates heat which causes the material to become plastic (solid state), allowing the tool to stir the materials so that it can joint [2].

There is no standardization regarding the parameters of Friction Stir Welding (FSW) according to metal thickness, metal type, welding speed, tool rotation speed and tool dimensions used. This becomes an obstacle to produce high quality of weld. Therefore it is necessary to experiment in Friction Stir Welding (FSW) on aluminium sheet to produce a good connection and have a high connection strength.

To find a suitable welding speed with a 0.4 mm aluminum plate, this research requires the traverse speed variable. The material tool used is HSS (High Speed Steel), with the dimensions of the tool, namely 4 mm shoulder diameter, pin diameter and pin length, while the type of connection used in this study is the lap welding connection.

In general, heat energy generated from material deformation and friction between the tool and the material. during the FSSW process, a very large axial force is applied, to produce deformation. Therefore, this process is very difficult when large CNC machines are not available or the process needs to be carried out in a location where it is not possible to carry a CNC machine. The FSSW hand tool mechanism cannot generate large axial forces. However, the high axial force cannot be maintained properly. Therefore, it is necessary to apply low axial force. Low axial force requirements allow the increases of high rotational tool speeds.

Previous research has investigated the relationship between the rotational speed of the FSW tools in terms of the microstructure and mechanical properties of the joints [3–6]. Zhang et al. [7] applied high rotational tool speed, and investigated the mechanical properties and microstructure. However, most of the researchers used a low rotational tool speed under 3000 rpm.

2   Material and Method

In this research, the aluminum material used is aluminum AA 1100. The chemical composition of aluminum AA 1100 is shown in Table 1.

Table 1 Chemical compositions of aluminium AA1100

%Si	%Fe	%Cu	%Mn	%Mg	%Ti	%Zn	%Ai	UTS (N/mm^2)	Elong (%)
0.14	0.56	0.08	0.01	0.01	0.01	0.02	99.08	119.5	10

2.1 Material

a. Material Preparation

Prepare the material welding object to be welded 2 plates AA1100 aluminum with a thickness of 0.4 mm. The specimen are cut to size length × wide = 75 × 50 mm (Fig. 1).

b. Tools Dimension

The tools material used are HSS, with shoulder diameter Ø 4 mm, pin length 0.6 mm and variate pin diameter Ø 1.5, Ø 2, Ø 2.5 mm (Fig. 2).
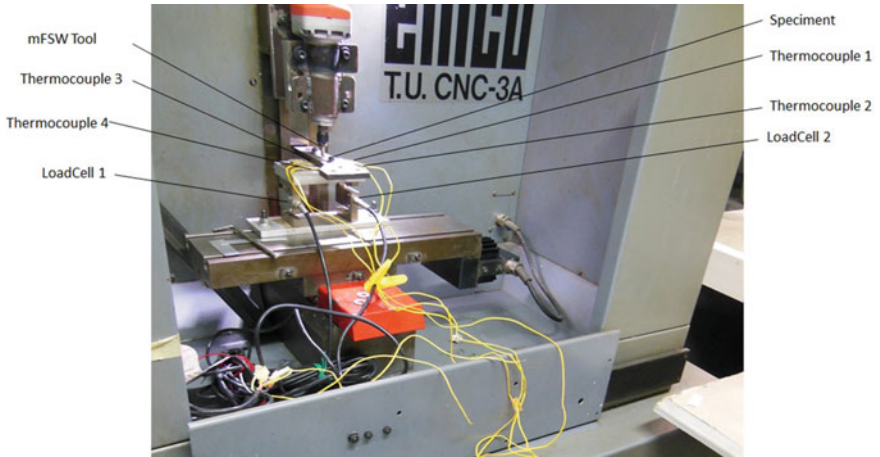
c. FSLW Steps
1. Installation of the hand grinder on a modified Emco 3A CNC machine with a stand (Fig. 3).
2. Installation of the FSW tool on the hand grinder, which has a rotating speed of 33000 rpm.
3. Installation of load cell to measure axial force.
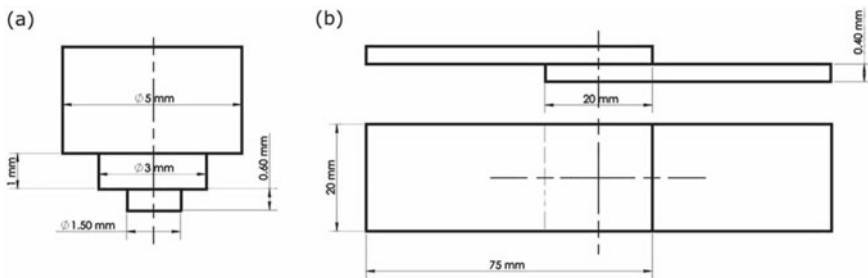
Fig. 1 Dimension of FSSW tool (**a**), and welding speciment (**b**)
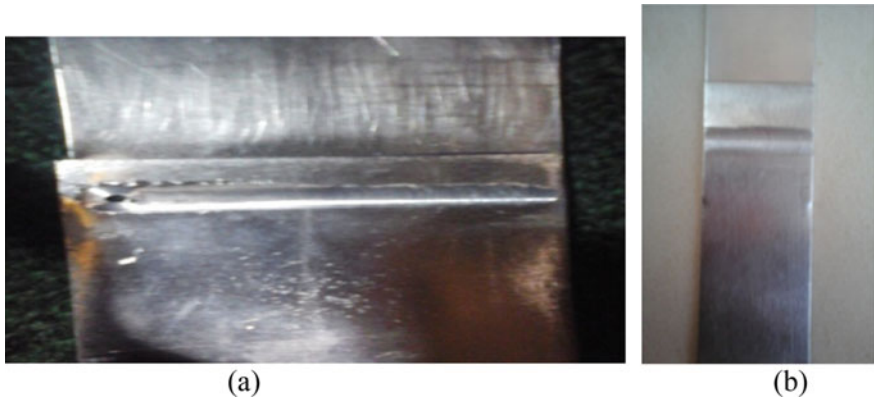
Fig. 2 Tools dimension of FSSW

Fig. 3 Installation of equipments

4. Prepare 2 plates AA1100 aluminium with a thickness of 0.4 mm, arranged an overlap of 20 mm.
5. Clamping the plate with a chuck so that the material does not shift during the welding process
6. Adjust the speed of the machine and the FSSW process (Fig. 4).

(a)   (b)

Fig. 4 FSSW Speciment **a** after welding **b** Speciment for tensile test

3 Analysis and Testing Techniques

Welding using the friction stir welding method is a welding that occurs in solid state joining by utilizing the friction of a rotating tool with another workpiece, so that it is possible to melt the stationary workpiece and eventually join together. In this welding experiment, the parameters to be analyzed are the aluminum temperature of Friction Stir Lap Welding (FSLW).

Table 2 Data of temperature measurement

| No.	Tilt angle (°)	ØPin (mm)	Feeding (mm/ mint)	Temperature rate (°C)				Center of weld
				T1	T2	T3	T4	
1	2	1.5	40	100.4	79.9	63.9	49.2	115.75
2	2	1.5	60	95.8	82.5	68.2	52.2	110.95
3	2	1.5	80	91.7	77.7	62.3	38.7	113.6
4	2	2	40	91	72.5	57.8	38	108.25
5	2	2	60	84.9	74.1	63.2	52.6	100.5
6	2	2	80	92.7	74.8	61	41	109.6
7	2	2.5	40	92.9	70	55.9	39.2	108.3
8	2	2.5	60	84.1	76.1	59.5	51.8	101.5
9	2	2.5	80	86.6	71.6	58.7	37.9	103.45
10	3	1.5	40	88.6	72.6	64.6	57.6	100.15
11	3	1.5	60	84.9	72.3	61.1	54.7	98.5
12	3	1.5	80	85.1	71.6	61	56.5	92.65
13	3	2	40	93.7	72.5	52.9	37.8	111.05
14	3	2	60	85.3	70.3	57.9	39.4	100.75
15	3	2	80	77.2	65.8	49.8	35.7	92.25
16	3	2.5	40	91.5	77	63	56.3	101.85
17	3	2.5	60	82.9	72.6	63.9	55.5	91.45
18	3	2.5	80	83.2	70.6	59.5	53.5	91.75
19	4	1.5	40	84.2	70.6	59.9	52.4	93.3
20	4	1.5	60	79.4	70.6	57.8	51	89.2
21	4	1.5	80	79.3	70.3	57.1	51.5	89.7
22	4	2	40	84.3	75.5	69.9	52.4	95.85
23	4	2	60	81.3	71.9	60	52.4	91.05
24	4	2	80	80	71.4	58.7	52.2	90.6
25	4	2.5	40	77.7	70.4	58.5	41.2	92.3
26	4	2.5	60	78.4	70.5	59.6	40	93.65
27	4	2.5	80	79.5	72.9	60	45.7	93.1
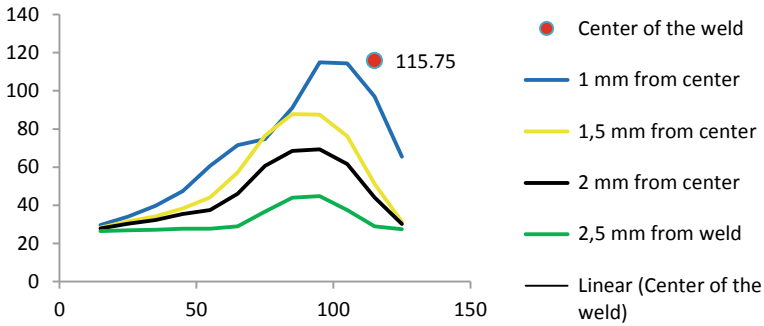
Fig. 5 Temperature distribution on FSLW

3.1 Result and Discussion

Response Surface Methodology (RSM) is statistical and mathematical techniques that are useful for analyzing the problem of several independent variables that affect the dependent variables of the response, and aiming at optimizing the response. Thus, the response surface methodology can be used by researchers to find a suitable approach function to predict future responses and determine the values of the independent variables that optimize the response.

Result of RSM method for Equation of the relationship between the variations made at the time of welding with the temperature f (Eq. 1).

$$
\begin{aligned}
Y_{\text{Temperature}} = {} & 99.68 - 8.18 \cdot A + 1.19 \cdot B + 0.40 \cdot C + 2.78 \cdot A \cdot B \\
& - 0.61 \cdot B \cdot C + 0.59 \cdot A \cdot C + 0.14 \cdot A^2 + 0.15 \cdot B^2 + 2.54 \cdot C^2
\end{aligned}
\tag{1}
$$

From Eq. 1, it can be seen that the parameter that has a major influence on temperature increase is "A" (tool tilt angle). Which is smaller tilt angle, will increase temperature significantly.

Effect of translation speed (feed rate) and tool Tilt angle (°) on the result of temperature (extrapolation) of the lap welding.

Figure 6 shows that the pin diameter with an angle affects the temperature of the Friction Stir Lap Welding (Fig. 7).

Effect of **translation speed** (feed rate) with **tool diameter variations** on the **temperature** results (extrapolation) in the lap welding connection method. It shows that the translation speed (feed rate) with an angle affects the temperature of the Friction Stir lap Welding.

Effect of translation speed (feed rate) with tool variations on the temperature results (extrapolation) in the lap welding connection method. Figure 8 shows that the higher translation speed (feed rate) with a lower tilt angle affects the increase of the FSLW temperature.
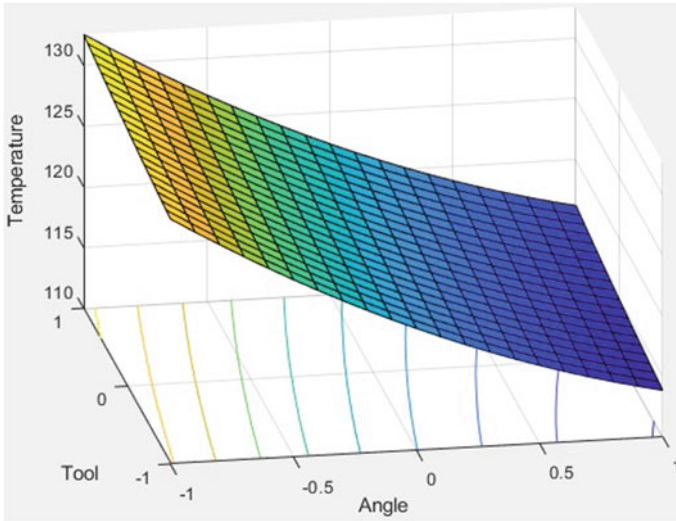
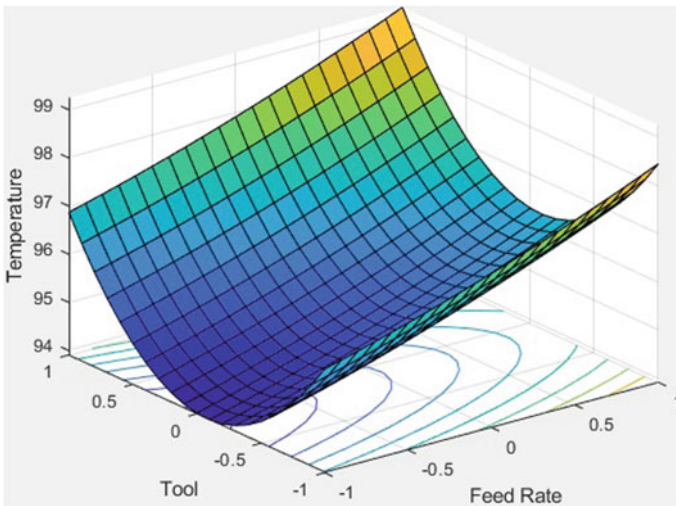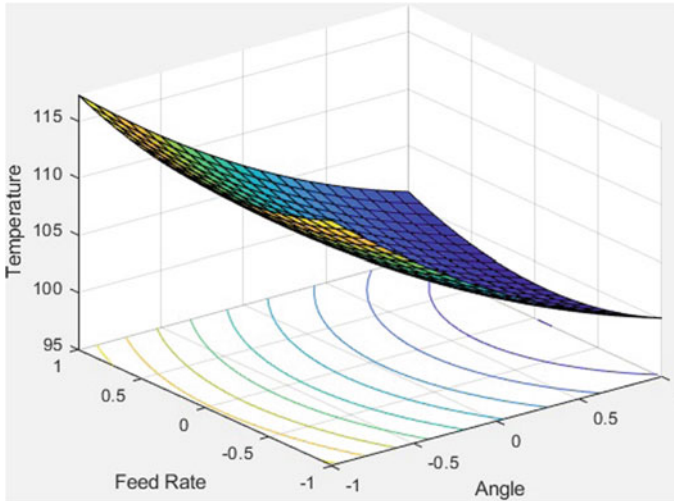**Fig. 6** The RSM relationship between the effect of translation speed and tilt angle on temperature

Fig. 7 Relation of **translation speed** (feed rate) with **tool diameter variations** on the **temperature**

Fig. 8 Relation of **translation speed** (feed rate) with **tool tilt angles** on the **temperature**

4 Conclusion

Based on the results of data processing and analysis, the following conclusions are obtained:

1. Parameter which greatly influences the temperature increase is the tool tilt angle. The smaller tilt angle will increase the temperature.
2. The changing of tool diameter variations has no temperature effect.
3. The increase in parameter will not be the same as the speed of tool translation (feeding) has an effect on increasing the temperature of the results of Friction Stir lap Welding (FSLW).
4. Future work will be more emphasized in the micro structure and axial force and transverse force.

References

1. Thomas WM, Nicholas ED (1997) Friction stir welding for the transportation industries. Mater Des 18(4):269–273
2. Chen CM, Kovacevic R (2003) Finite element modeling of friction stir welding - thermal and thermomechanical analysis. Int J Mach Tools Manuf 43(13):1319–1326
3. Baskoro AS, Kiswanto G, Budiono (2016) Numerical Model to Predict The Temperature of The Friction Stir Spot Welding Process. In: International Conference On Engineering and Applied Science

4. Baskoro AS, Nugroho AAD, Rahayu D, Suwarsono Kiswanto G, Winarto W (2013) Effects of welding parameters in micro friction stir lap welding of aluminum A1100. Adv Mater Res 789:356–359
5. Baskoro AS, Kiswanto G, Winarto W (2014) Effects of high speed tool rotation in micro friction stir spot welding of aluminum A1100. Appl Mech Mater 493:739–742
6. Suwarsono, Budiono, Baskoro AS, Kiswanto G (2019) Mechanical properties of friction stir lap welding (FSLW) on dissimilar aluminum sheet A1100 and A1050. In: AIP Conference Proceedings, p 030052, https://doi.org/10.1063/1.5098227
7. Wang D-A, Chao C-W, Lin P-C, Uan J-Y (2010) Mechanical characterization of friction stir spot microwelds. J Mater ProcessTechnol 210(14):1942–1948

Slow Pyrolysis of Areca-Nut Fibres in a-Pilot Scale Batch Reactor

Tuti Aryati, Akbar Williansyah, Zulnazri, and Adi Setiawan

Abstract Areca-nut fibers is one of agricultural residues which potentially can be converted into energy or fuel through thermochemical method. In this study, investigation on thermochemical process of areca-nut fibers was performed by preparing a pilot-plant pyrolysis reactor to find out product distribution of pyrolytic oil, tar and biochar. Pyrolysis test was carried out by feeding 1.5 kg of dried-areca-nut fibers and heated up to 400 °C. Another set of experiment was performed by dividing feedstock into three segments with supported stainless-steel wire-mesh to reduce feedstock piling-up effect. The temperature profiles and product distribution of both type of experiment was then compared in order to find out the best procedure for areca-nut fibers pyrolysis. The product distribution of areca nut fiber pyrolysis without trays were 34% for biochar, 15% for pyrolytic oil, 7% for tar and balanced with non-condensed gas. Meanwhile, the product distribution of pyrolysis process with trays was 32% for biochar, 16% for pyrolytic oil, 9% for tar and balanced with un-condensable gas. The result show that pyrolysis run with trays leads to the changes in product distribution and biochar quality. Supported trays are beneficial in improving the heat diffusion during the run and makes reaction temperature more stable.

T. Aryati
Postgraduate Program in Renewable Energy Engineering, Faculty of Engineering, Universitas Malikussaleh, Bukit Indah, Muara Satu, 24352 Lhokseumawe, Indonesia

A. Williansyah · A. Setiawan (✉)
Mechanical Engineering Department, Faculty of Engineering, Universitas Malikussaleh, Bukit Indah, Muara Satu, 24352 Lhokseumawe, Indonesia
e-mail: adis@unimal.ac.id

Zulnazri
Chemical Engineering Department, Faculty of Engineering, Universitas Malikussaleh, Bukit Indah, Muara Satu, 24352 Lhokseumawe, Indonesia

1   Introduction

In many countries, a number of studies have been devoted to investigate the potential utilization of agricultural wastes however profitable and technically feasible methods are still under development. A number of works have devoted recently for utilizing agroindustry-by-products including coffee-pulp [1, 2], leucaena leucocephala biomass [3] wheat bran [4], jute [5], areca-nut [6, 7] and many more. These biomass wastes can be directly used as fuel, however the combustion process cannot be maximized due to several factors, including high ash content, low density, non-competitive calorific value per unit volume, higher moisture contains and produces smoke [8].

In general, thermochemical process includes pyrolysis, gasification, combustion, liquefaction, and co-firing. In these processes, biomass is decomposed into smaller molecular weight compounds in the presence of heat. Among all the thermochemical process, pyrolysis has the potential to convert biomass into solids, liquids, and gases. Pyrolysis is the process that can be performed in an inert atmosphere and is highly affected by a variety of parameters such as heating rate, temperature, biomass composition, residence time, moisture content, particle size, and type of reactor [9]. This process is the initial stage of a series of processes in the gasification process, and it involves a complex physical chemical process as a change in operating conditions can affect the overall process.

Areca nut is known as palm species which is classified as a high-potential perennial crop. This tree is cultivated at a large scale to meet the need of raw materials for many sectors, such as the paint industry and chocolate manufacturing [10]. Matured areca nut fruit is harvested when reached full maturity and detached from the fruit bunch. Its color is commonly exhibiting brownish shades with coarse fiber. Actually, fiber is extracted from the fibrous part encapsulating the betel nut fruits which is mainly consisted of two types, i.e., fine and coarse fibers. The coarse fibers are composed of cellulose, hemicellulose, lignin, pectin and protopectin at varying compositions [11, 12]. Utilization of areca nut fiber reported in the literature are mostly focused on composite material development. Very limited work has been reported on the use of areca nut fibers as feedstock for pyrolysis process.

The objective of this investigation is to develop a simple pilot scale set-up and procedure for pyrolysis of areca nut fibers. Temperature changes during pyrolysis run and product distribution are the main parameter observed in this work. In order to optimize the performance of reactor, stainless steel wire mesh trays were installed inside the reactor and tested under similar condition to those run without trays.

2   Experimental Methods

The schematic of the experimental set up is shown in Fig. 1. This set-up consists of pyrolysis reactor, condenser, tar separator, gas burner and furnace. The mass of raw material fed into the reactor was 1.5 kg. A heat generator is needed to heat the

1. Reactor
2. Furnace
3. Tar separator
4. Condenser
5. LPG
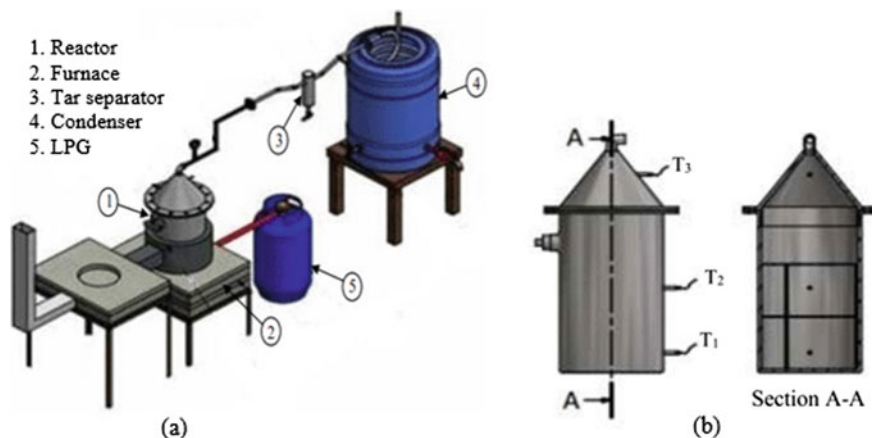
Fig. 1 **a** Slow pyrolysis experimental set-up, **b** Cross-sectional detail of segmented chamber

pyrolysis tube. In this experiment, the heat is generated from combustion of LPG. A burner was installed inside the furnace to heat up the reactor. The furnace was made of refractory bricks and cement. There is a valve installed after condenser for collecting most of pyrolytic oil and another valve installed under tar separator to collect tar-containing bio-oil.

As shown in Fig. 1b, the pyrolysis chamber was divided into three feedstock layers by two supported stainless-steel wire mesh. Each layer has one thermocouple to record the temperature changes in the pyrolysis chamber, where T_1 is the temperature of the bottom chamber of the tube, T_2 is the temperature of the middle of the chamber, and T_3 is the temperature of the top of the pyrolysis tube. K-type of thermocouple was used to observe the temperature changes during the pyrolysis process and to find out maximum temperature that can be achieved in the pyrolysis tube. A stop watch is used to record the length of time required for the pyrolysis process. In each experiment, the reactor was fed with 1.5 kg of areca nut fibers. The variables measured after the run include the mass of biochar, mass of pyrolytic oil (tar and liquid smoke).

3 Result and Discussion

Figure 2 shows that the temperature profiles recorded during the run without trays. It can be seen that the lower section of pyrolysis chamber has higher heating rate compared to those observed from middle and top section. After 30 min run, the valve of liquid product was firstly opened resulting a drop in temperature. At any run, when the valve is opened, the pressure in the pyrolysis camber is suddenly dropped and makes the pyrolysis temperature also dropped, but then it is increased
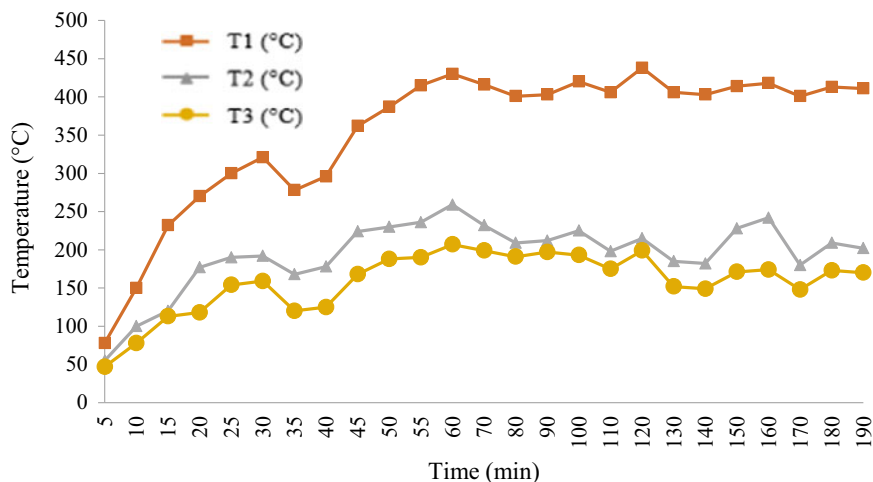
Fig. 2 Temperature profiles of pyrolysis process of areca nut fibers without trays

again. Once the maximum temperature reached 400 °C, the fire inside the furnace was adjusted to maintain the reaction temperature relatively constant at 400 °C.

Figure 3 shows temperature changes monitored during pyrolysis process of areca nut fibers with trays. This figure indicates that the temperature at the lower part of pyrolysis chamber was increased at a constant rate and relatively more stable compared to those observed from experiment without trays. Less drop in pressure was observed during this experiment indicating a positive effect on trays installation. Interestingly, a significant difference between T_1 and T_2 is shown in this figure where the average temperature of middle section was around 180 °C and bottom temperature (T_1) was about 400 °C. In term of top section temperature profiles, a significant difference can be observed between data in Figs. 2 and 3. This suggests that the use of trays leads to a decrease in temperature at the top section of chamber.

Figure 4 displays the images of biochar produced by using trays in comparison with those produced without trays. These images indicate differences in color between biochar from bottom layer, middle and top. The biochar from bottom part is darker compared to the others. Thus, the pyrolysis process was completely done. Whilst, in the middle and top section, the pyrolysis process was not 100% completed due to less heat diffused into this section. On the other hand, brownie colored biochar can be observed at any part of the image of biochar produced without tray (Fig. 4a). Indeed, the reaction time was set to 180–190 min. It seems that the residence time was not sufficient to complete thermal decomposition of 1.5 kg areca nut fibers.

Table 1 shows the average temperature and product distribution of pyrolysis without trays. In general, it is shown that the pyrolysis temperature greatly affects the distribution of the resulting products. The higher the temperature of the pyrolysis process, the less biochar and tar is produced. This is because the higher
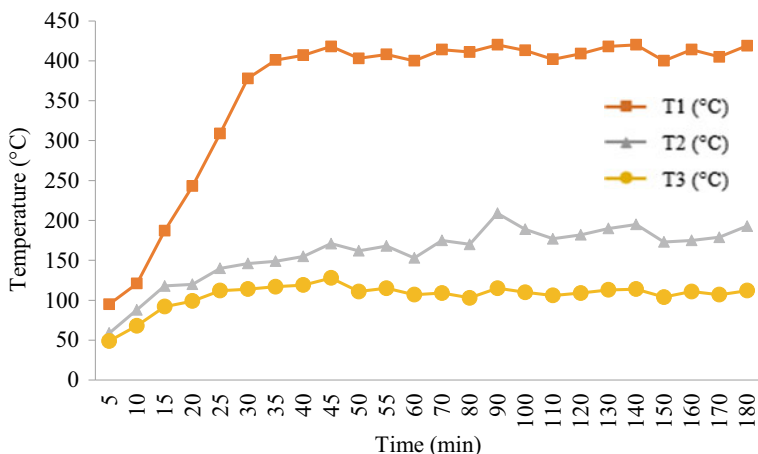
Fig. 3 Temperature profiles of pyrolysis process of areca nut fibers with trays

Fig. 4 The images of biochar produced: **a** without trays and **b** with trays

the reactor temperature, the faster the devolatilization process occurs, and carbon levels begin to decrease [13]. From this table, it can also be seen that the mass of biochar is 0.5 kg and the mass of tar is 0.11 kg. Conversely, the lower the operating temperature, the more biochar and tar produced from the pyrolysis process. The average of mass of biochar produced is 0.508 kg and the mass of tar is 0.111 kg.

Based on data of pyrolytic oil yield from pyrolysis without trays, it can be seen that the higher the pyrolysis temperature, the more bio-oil is produced. The yield of

Table 1 Average temperature and product distribution of pyrolysis without trays

No.	Raw material	Temperature (°C)			Mass of biochar ($m_{charcoal}$)	Mass of tar (m_{tar})	Mass of pyrolytic oil (m_{ls})	Un-condensed gas
	kg	Bottom (T_1)	Middle (T_2)	Top (T_3)	kg	kg	kg	
1	1.5	364.5	171.6	152.8	0.52	0.115	0.215	Balanced
2	1.5	352.4	193.5	157.8	0.5	0.11	0.23	Balanced
3	1.5	362.2	175.1	156.5	0.505	0.11	0.225	Balanced
Avg.	1.5	359.7	180.1	155.7	0.508	0.111	0.223	Balanced

Table 2 Average temperature and product distribution of pyrolysis with trays

No.	Raw material	Temperature (°C)			Mass of biochar ($m_{charcoal}$)	Mass of tar (m_{tar})	Mass of pyrolytic oil (m_{ls})	Un-condensed gas
	kg	Bottom (T_1)	Middle (T_2)	Top (T_3)	kg	kg	kg	%
1	1.5	387.2	164.9	119.4	0.477	0.12	0.255	45
2	1.5	363.4	166.2	103.9	0.482	0.13	0.25	43
3	1.5	363.1	159.8	106.0	0.495	0.155	0.235	42
Avg.	1.5	366.7	163.6	109.7	0.484	0.135	0.246	43

pyrolytic oil will increase with increasing temperature until a condition where the un-condensable gas production is higher so the temperature increase will further decrease the amount of pyrolytic oil production [14]. As seen in the table, the mass of pyrolytic-oil is 0.23 kg.

Table 2 summarized the average temperature and product distribution of pyrolysis with trays. It is shown that the pyrolysis temperature greatly affects the distribution of the resulting products. The higher the temperature of the pyrolysis process, the less biochar and tar is produced. The average mass of biochar and tar-containing oil respectively are 0.484 kg and 0.135 kg.

Nevertheless, in terms of pyrolytic oil formation from pyrolysis of areca nut fibers without trays, the higher the operational temperature of the pyrolysis, the more distribution of liquid smoke products will be. Meanwhile, the lower the operating temperature, the less oil is produced.

4   Conclusion

Investigation on the pyrolysis process of areca nut fiber has been performed with and without using trays in a pilot scale batch reactor. The result showed that the thermochemical conversion of areca nut fibers using trays (segmented reactor) leads to the changes in product distribution and biochar quality. The pyrolysis test without trays produces 34% biochar, 15% pyrolytic oil, 7% tar, and balanced with uncondensed gas. Meanwhile, the pyrolysis test with feedstock trays results in 32% biochar, 16% pyrolytic oil, 9% tar, and balanced with uncondensed gas. Installation of wire mesh trays helps in improving the heat diffusion during the run and makes reaction temperature more stable.

References

1. Janissen B, Huynh T (2018) Resources, Conservation & Recycling Chemical composition and value-adding applications of coffee industry by- products: A review Resour. Conserv Recycl 128:110–117
2. Setiawan A, Randa AG, Faisal, Nur T Bin and Rusdianasari (2020) Thermal decomposition of Gayo Arabica coffee-pulp in a segmented chamber. J Phys Conf Ser 1500
3. Wan Ibrahim WMH, Mohamad Amini MH, Sulaiman NS, Kadir WRA (2019) Powdered activated carbon prepared from Leucaena leucocephala biomass for cadmium removal in water purification process *Arab*. J Basic Appl Sci 26:30–40
4. Zhang Y, Song X, Xu Y, Shen H, Kong X, Xu H (2019) Utilization of wheat bran for producing activated carbon with high specific surface area via NaOH activation using industrial furnace. J Clean Prod 210:366–375
5. Khan JH, Marpaung F, Young C, Lin J, Islam MT, Alsheri SM, Ahamad T, Alhokbany N, Ariga K, Shrestha LK, Yamauchi Y, Wu KCW, Hossain MSA, Kim J (2019) Jute-derived microporous/mesoporous carbon with ultra-high surface area using a chemical activation process. Microporous Mesoporous Mater. 274:251–256
6. Chungcharoen T, Srisang N (2020) Preparation and characterization of fuel briquettes made from dual agricultural waste: Cashew nut shells and areca nuts. J Clean Prod 256:120434
7. Mishra RK, Mohanty K (2019) Pyrolysis of three waste biomass: Effect of biomass bed thickness and distance between successive beds on pyrolytic products yield and properties Renew. Energy 141:549–558
8. Haykiri-Acma H, Yaman S (2010) Production of Smokeless Bio-briquettes from Hazelnut Shell. Proceedings of the World Congress on Engineering and Computer Science 2:20–22
9. Mishra RK, Mohanty K (2018) Bioresource Technology Pyrolysis kinetics and thermal behavior of waste sawdust biomass using thermogravimetric analysis. Bioresour Technol 251:63–74
10. Srinivasa CV, Bharath KN (2011) Impact and Hardness Properties of Areca Fiber-Epoxy Reinforced Composites. J Mater Environ Sci 2:351–356
11. Yusriah L, Sapuan SM, Zainudin ES, Mariatti M (2014) Characterization of physical, mechanical, thermal and morphological properties of agro-waste betel nut (Areca catechu) husk fibre. J Clean Prod 72:174–180

12. Choudhury SU, Hazarika SB, Barbhuiya AH, Ray BC (2009) Natural Fiber Reinforced Polymer Biocomposites and Blends: Synthesis, Characterization and Applications The 17th International Conference on Composites Materials (Edinburgh), p 70
13. Basu P (2013) Biomass Gasification, Pyrolysis, and Torrefaction. Elsevier, Cambridge, MA, USA
14. Seri M, Putri FS (2017) Effect of Temperature, Time, and Water Content of Material on The Pyrolysis of palm Midrib Powder. J Tek Kim USU 6:35–40

Stress Analysis on an Automotive Lower Arm Steered on the Straight and Turning Roads

Wahyudin, Husaini, and T. E. Putra

Abstract This study aims to analyze the stress that occurred on an automotive lower arm made from the SAE 1513 carbon steel that was driven on a straight road as well as turning roads. The strain signals throughout 60s measured on the left lower arm were used as the loads in these analyses. The analysis results showed that the maximum stress occurred at the joint of the lower arm. These dynamic analyses also showed that the three types of roads provided almost the same stress. The clockwise road gave the highest stress value, which was 278.5 kPa, followed by the counter-clockwise road (277.9 kPa) and the straight road (277.7 kPa). The highest stress obtained when the car turns was the result of the load resting on the opposite side of the turn.

1 Introduction

The suspension system has a role in holding the weight of the car and isolating the car body from shocks when driving, as well as to maintain the interaction between the tire and the road surface. In a suspension system, there are several important components with their respective functions [1], one of them is the lower arm. As is known, the main function of the lower arm is to connect the suspension system to the mainframe of the car, to control the wheel movement, both up, down, back and forth as well as when the car turns [2]. Given this very important role, it is necessary to analyze the stress distribution that occurs in the lower arm when the car is driven on straight and turning roads.

Many studies have been conducted to analyze the stress on a lower arm. Singh [3] analyzed the stress in the lower arm which was subjected to statistical loads. In its application, this component receives dynamic loads from the road surface. In another study, Husin and Abdullah [4] provided a dynamic analysis on a lower arm.

Wahyudin · Husaini (✉) · T. E. Putra
Department of Mechanical Engineering, Universitas Syiah Kuala, Banda Aceh 23111, Indonesia
e-mail: husainiftm@unsyiah.ac.id

However, the load only came from a straight path. Road conditions are not only straight but also turn which can affect the failure of a lower arm.

Therefore, the aim of this study was to analyze the stress distribution on a lower arm due to the dynamic loads. These dynamic loads were derived from the strains received by the lower arm when steered on straight and turning roads. By knowing the stress on the lower arm due to road conditions, it can be identified the type of road that accelerates the failure of the component.

2 Material and Method

One of the recent studies on stress distribution analysis on the lower arm was carried out by Husaini et al. [5]. In that study, the front lower arm on the left side of the minibus made of the SAE 1513 carbon steel was given a static load of 3591 N. At the location of the maximum stress resulting from the load, a strain gauge was attached. The sensor functioned to measure the strains on the lower arm, when the car was driven on a straight, clockwise, and counter-clockwise road. The strain signals that were obtained has a duration of 60 s with a total data size of 30,000, as shown in Fig. 1.

In the dynamic analyses that were carried out in the current study, the strain signals in Fig. 1 were used as a load. The strain signals were converted into stresses using the Ramberg-Osgood equation [6], which is stated as follows.

$$\varepsilon = \frac{\sigma}{E} + \left(\frac{\sigma}{K'}\right)^{\frac{1}{n}} \tag{1}$$

where ε is the strain, σ is the stress, E is the material modulus of elasticity, K' is the cyclic strength coefficient, and n is the cyclic strain-hardening exponent. The values of the material modulus of elasticity, cyclic strain-hardening exponent, and cyclic strength coefficient were from Table 1. The stresses were then converted to forces using the following equation:

$$\sigma = \frac{P}{A_0} \tag{2}$$

where P is the force and A_0 is the cross-sectional area of the lower arm.

The forces that were obtained from Eq. 2 were entered into the finite element simulation. The lower arm model in this analysis was the same as the model in the research by Husaini et al. [5]. A model in finite element simulation is divided into smaller elements [7] to be analyzed with static and dynamic loads as well as linear and non-linear in the form of a mesh with boundary conditions and certain physical quantities [8]. T shape of the element used in this simulation was a 10-noded
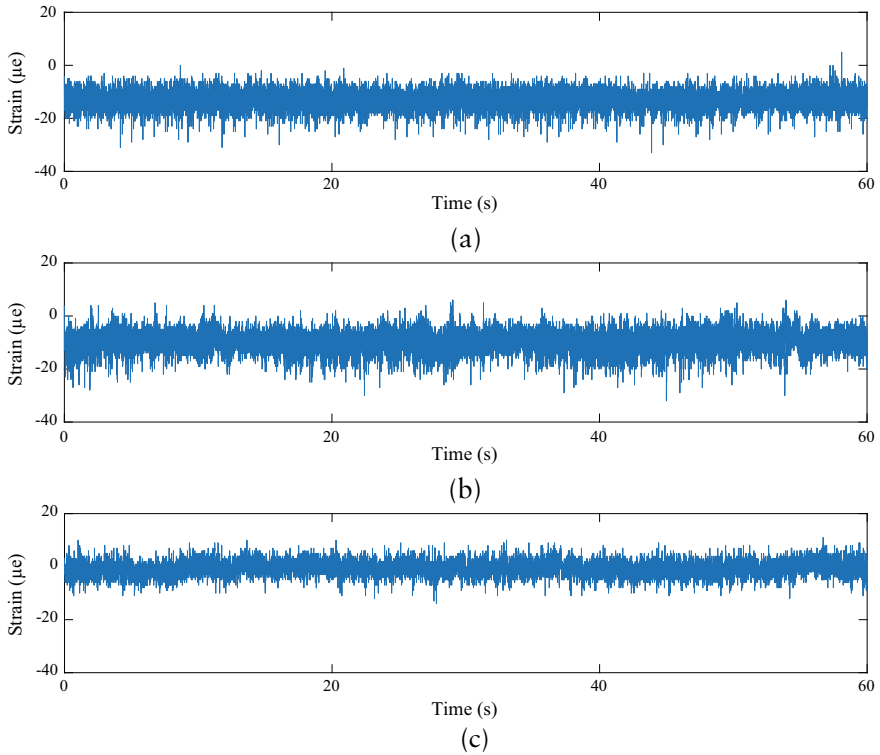
Fig. 1 Strain signals: **a** straight road, **b** clockwise road, **c** counter-clockwise road

Table 1 Mechanical properties of the SAE 1513 carbon steel [9]

Properties	Values
Ultimate tensile strength, S_u (MPa)	585
Material modulus of elasticity, E (GPa)	210
Yield strength (MPa)	450
Fatigue ductility coefficient, ε'f	0.4109
Fatigue strength exponent, b	−0.078
Fatigue ductility exponent, c	−0.5425
Fatigue strength coefficient, σ'_f (MPa)	1089
Cyclic strain-hardening exponent	0.1169
Cyclic strength coefficient (MPa)	978
Poison ratio	0.27–0.3

tetrahedral solid element. The mesh size used was 0.2 mm. The number of elements was 46.822 and 85.769 nodal after the meshing process was carried out. The meshing and boundary condition are shown in Fig. 2. A force was applied to the red part vertically upwards.

Fig. 2 Meshing and
boundary condition

Constraint
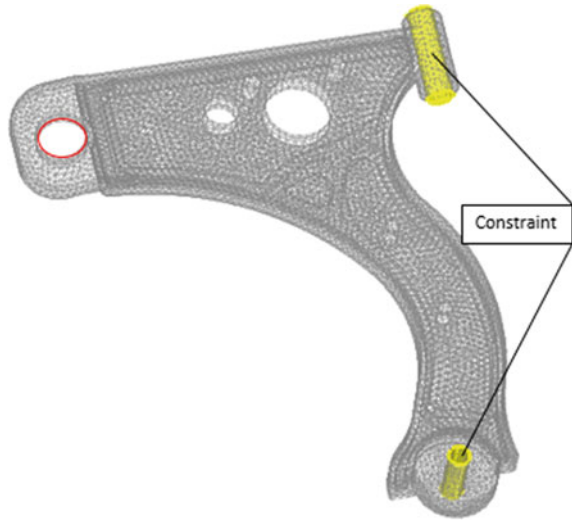
3 Results and Discussion

Figures 3, 4, 5, present the stress distributions for straight, clockwise, and
counter-clockwise roads, respectively. The critical area due to the three types of the
surface was at the same area, namely in the middle part near the small hole below
the component surface shown in red. This was similar to the results by Husaini et al.
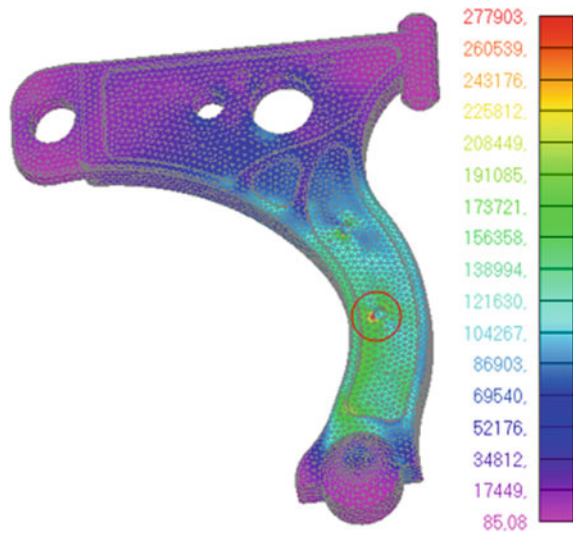[5, 10, 11]. However, the maximum stress values that occurred were different from

Fig. 3 Stress distributions
due to the straight road
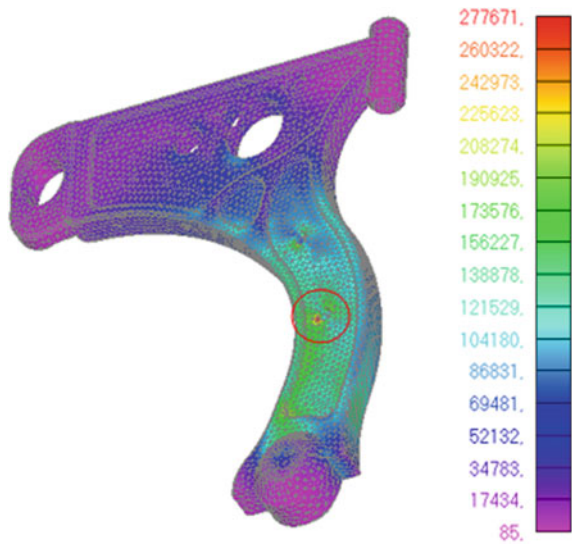
Fig. 4 Stress distributions
due to the clockwise road
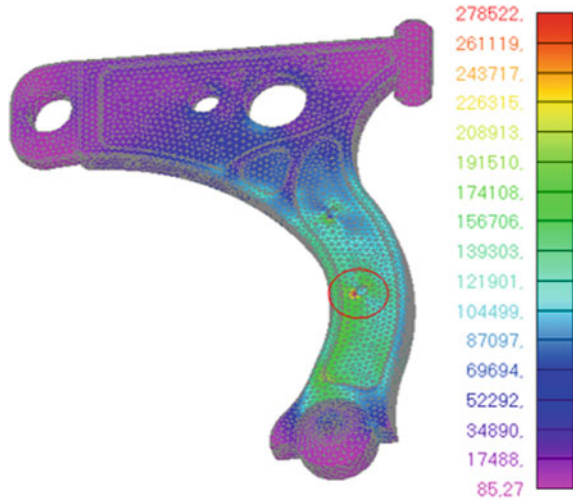
Fig. 5 Stress distributions
due to the counter-clockwise
road

the three road conditions. For straight road, the maximum stress was 277.7 kPa. The clockwise road gave the maximum stress of 278.5 kPa. The counter-clockwise road provided stress of 277.9 kPa. The turning roads provided greater stress than the straight road because when turning, the weight of the car was supported by one side. As a result, the lower arm on that side received a bigger load.

The stress values that occurred were still smaller than the yield strength of the SAE 1513 carbon steel, which was 450 MPa, as given in Table 1. They were

61.9% of the yield strength of the material. Even though they were small, these stresses can cause the failure of the lower arm because this component is subjected to continuous loads.

4   Conclusion

The aim of this study is to analyze the stress that occurs in the lower arm when the car was driven on straight and turning roads. The results showed that the turning roads provided greater stress than the straight road. The turning roads provided the stress of 278.5 kPa and 277.9 kPa, while the straight road provided the stress of 277.7 kPa. This is the result of the load resting on one side when the car turns.

References

1. Kadirgama RM, Noor K, M M Rejab M R M and Kesulai S A, MM (2009) Fatigue life prediction of lower suspension arm using strain-life approach. Eur J Sci Res 30(3):437–450
2. Arun Kumar S, Balachandar BV, K and Prem Kumar D K (2016) Analysis and optimization of lower control arm in front suspension system. Int J Chem Sci 14(2):1092–1098
3. Singh H, Bhushan G (2016) Finite Element Analysis of a Front Lower Control Arm of LCV Using Radioss Linear, July, pp 121–125
4. Husin Z, Rahman MM, Kadirgama K (2010) Prediction of Fatigue Life on Lower Suspension Arm. Mech Eng December, pp 100–116
5. Husaini PTE, Rizky MR (2020) Prediction of the Fatigue Life of the AISI 1513 Carbon Steel Lower Arm Based on Strain-Life Approach. IOP Conf Ser Mater Sci Eng 811:1
6. Ramberg W, Osgood WR (1943) (31)_Ramberg_1943.pdf.
7. Aykan M, Mehmet C (2009) Vibration fatigue analysis and multi-axial effect in testing of aerospace structures. Mech Sys Sig Proces 23:897–907
8. Putra TE, Husaini (2018) Identifying strain signal characteristics of automotive suspension system subjected to road surface vibrations. AIP Conf. Proc 1983
9. NCode G (2018) nCode International, Ltd., Sheffield. pp 1–3
10. Husaini PTE, Rizky MR, Akmal R, Hasanuddin I, Rizal M, Ali M (2020) Fatigue life assessments of the AISI carbon steel of a vehicle lower arm subjected to clockwise and counter-clockwise road strains. Defect Diffus Forum 402(1):45–49
11. Husaini, Putra TE, Ali N (2018) Int. J. of Auto Mech Eng 15:5251

Quality Improvement in a Multi-cavity Injection Moulding Process Using Response Surface Methodology

H. T. Toh and Adnan Hassan

Abstract Multi-cavity injection moulding process is challenging due to increasing complexity in design and higher precision requirement. Quality defects need to be addressed effectively and systematically. This paper reports an investigation based on a case study company producing consumable injection moulded parts for medical application. The current process suffers high reject rate due to excessive warpage and gate flash where the company lose about 17% of daily production. This has significantly effected the company's productivity. The objective of this study is to minimize warpage and gate flash of the injected moulded polyvinyl chloride (PVC) parts. Significant process parameters contributing to both warpage and gate flash defects are identified. The study also attempted to search for an optimum setting such that it could be used as a guide to concurrently improve the warpage and gate flash. A fractional factorial design and Response Surface Methodology (RSM) techniques were used. An optimum parameter setting is proposed through an overlaid contour plot that combine the two responses. The recommended feasible setting leading to an optimum performance are −1.6 for holding pressure and 0.6 for mould temperature (coded values). Practical validation indicates a significant reduction in rejection rate. This study shoud be further extended to refine the proposed regression model.

1 Introduction

Injection moulding is a common process for producing complex and precision plastic components. There has been an increasing demand for disposable plastic injected moulded devices in medical application to replace other material like steel, alloy, wood due to low cost and higher strength to weight ratio [1]. This process

H. T. Toh · A. Hassan (✉)
Department of Materials, Manufacturing and Industrial Engineering,
School of Mechanical Engineering, Faculty of Engineering,
Universiti Teknologi Malaysia, 81310 Johor Bahru, Malaysia
e-mail: adnan@utm.my; adnan@mail.fkm.utm.my

also common for production of polymer materials products of complex structure as found in high precision medical products. Such high precision medical production line may suffer high defects rates due to inconsistency of injection moulding process settings. Acheiving high quality moulded plastic parts remain challenging since the process is delicate and involved variety of variables. Generally, an injection moulding process requires an injection moulding machine and an injection mould. The injection moulding machine comprises a clamping unit, a mould assembly and an injection unit. Figure 1 illustrates schematic steps for an injection moulding process. An injection moulding cycle begins with plasticizing, mould close, injection, holding pressure, cooling and mould open phases.

There are five categories of process variables in injection moulding that are time, pressure, speed, temperature, and stroke [2]. Each of these categories can be further divided into their respective variables. For example, speed can be injection speed, screw speed, speed for mould close and open, among others. Example of temperature related process variables are melted temperature and mould temperature. Each of the process variable may interact with another variable and they cannot be independently isolated. An increase in melting temperature would lead to higher material viscosity which then influence the fill in, pressure and velocity. This characteristic might vary depending on raw materials and therefore it is important to understand the material behaviour as a result of process variable changes.

In some companies, trial an error method is still a common practice to acheive desirable process and product quality. Unfortunately, this approach is not sustainable and costly [1]. Researchers such as Attira and Alcock [4], Yang et al. [5], Eladl et al. [6], and Yizong et al. [1] have used designed of experiment (DoE) to evaluate the effect of process parameters in injection moulding processes on different responses. The challenge is to achieve high productivity while maintaining high quality production. To the best of our knowledge, there has been limited work focusing on optimization of precision injection moulding processes for medical components with focus on multiple quality defects optimisation.

This paper reports a study to improve process quality for a case study company, located in Johor Malaysia producing moulded injector known as connector, a
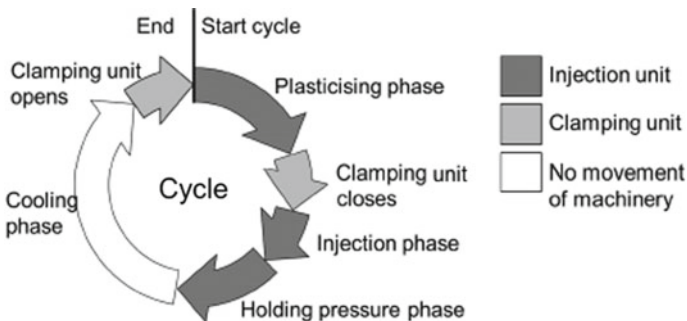
Fig. 1 Process steps in injection moulding of a plastic component [3]

consumable for dialysis device. The injection moulding machine was equipped with eight cavities. The current process setting resulted in high rejection rate due excessive warpage and gate flash defects where the company loss about 4000 units per day representing about 17% of daily production. This has negatively impacted on the company's productivity. The objective of the study was to identify significant process parameters contributing to both warpage and gate flash defects. We attempted to concurrently minimize these two quality characteristics. The second objective was to search for an optimum setting for both quality characteristics such that it could be used as a guide for process control. The rest of this paper is organized into five sections which are Methodology in Sect. 2, Results and Discussion in Sect. 3 and ends with a Conclusion in Sect. 4.

2 Methodology

The consumable connectors investigated in this study were produced using Sumitomo SE100D injection moulding machine. This was a 100-tonnage machine with VIP temperature controller unit attached for mould temperature control. The tooling was operated with semi-cold runner with runner and hot tip system. The moulding material was soft polyvinyl chloride (PVC) raw pallet material. The main product defects were physical warpage and gate flash.
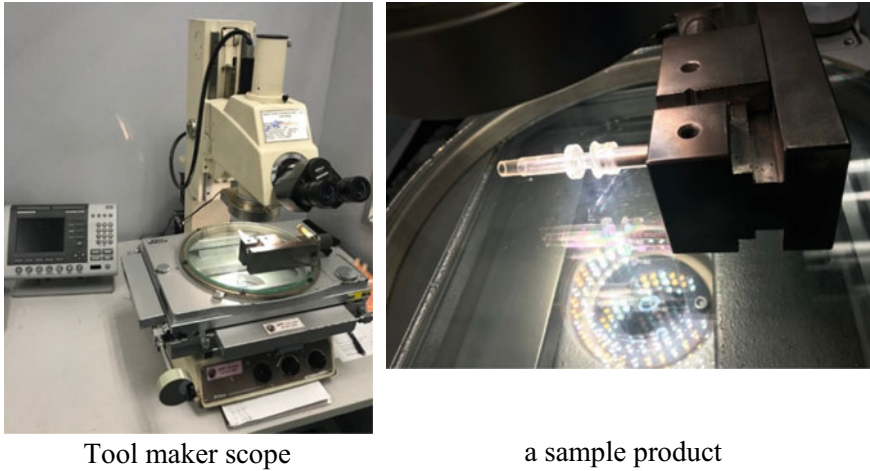
Figure 2 shows a tool maker microscope and a jig holding a sample product. The samples were measured using a tool maker microscope (TMS) to identify the distance of bend and gate flash height. Ideally, the warpage should be within 7.05 ±0.25 mm and the gate flash should not exceed 0.40 mm. The injection moulding process was operated in a controlled clean room environment. The machine was equipped with a special filtration unit to remove particulate matter. It was particularly important to consistently monitor the temperature and humidity in the clean room for this moulding process.

The study was implemented based on the following two phases: (i) characterisation phase, and (ii) optimisation phase. The characterisation phase involved the following steps:

a. Determine experimental variables and levels setting (parameter range) that could affect to the responses (warpage and gate flash).
b. Select the fractional factorial design of experimental plan (half factorial for 5 factors was selected).
c. Run the screening experiment and analyse results using ANOVA to identify significant factors.
d. Identify possible curvature in the response of each factor.

The process optimization using response surface methodology then proceed with the following steps:

Tool maker scope   a sample product

Fig. 2 Tool maker microscope and a jig holding a sample product

a. If curvature exist in the response, use central composite design (CDD), a response surface methodology (RSM). This method was used for modelling and analysing the process with the objective to optimize the responses.
b. Identify overlaid contour between two responses.
c. Predict an optimal ideal setting within the operating window.
d. Conduct confirmation run to validate the optimal parameter settings and the prediction model.

Statistical software Minitab 14 was used for data analysis. To comply with the case study company restriction, the numerical process setting presented here are in terms of coded values.

2.1 Experimental Design for Characterization Phase

Running all possible combinations to test the effect of all potential parameter is too costly and wasteful. A better approach is to use an analytical technique such as Taguchi Method or design of experiment (DoE) that could determine the relationship between factors affecting a process and the output of that process. Some researchers used Taguchi method to minimise the number of experiments [1, 7, 5]. However, this study adopted DoE and response surface methodology (RSM) since these methods are better approaches to study the effect and relationship of responses as argued by Montgomery [8].

   Five process factors namely injection speed (A), injection pressure (B), mould temperature (C) melt temperature (D) and holding pressure (E) were investigated. Injection speed determines the linear filling speed when injected material is in molten state. The correct injection speed is important and it depends on product geometry, material type and mould design. The rate of molten material flow into mould is also very much dependent on injection pressure applied. This filling process is one of the most important process cycles. Holding pressure time is the time when the screw is held almost stationary in the most forward position. Necessary holding pressure is applied to the molten material in order to pack it into the mould cavities during the early stages of material solidification. The selection selected holding time should apply just before the gate freezes off. Once the gate freezes off, any further pressure applied has no pack to the cavity. The melt temperature dependent on many process parameter and machine setting. Due to the proprietary restriction, only coded settings are presented in this paper as either (−1) for low level and (+1) for high level respectively. The two level for five factors of half factorial design (2^{5-1}) with resolution V resulted in 16 runs as shown in Table 1. The same design was applied to both warpage and gate flash responses, respectively. Each of the basic design was replicated two times for each response.

   For each production run, the machine runs for a stable 50 continuous full cycles. Samples were taken from three shots and replicated twice. Thus, a total of 768 pieces (3 shots × 8 cavities × 2 replicates × 16 runs) were taken, labelled, and measured. The measured samples were characterized through analysis of variance (ANOVA). If the ANOVA analysis shows significant curvature exists in the

Table 1 2^{5-1} half factorial experiment run design

Run	A	B	C	D	E = ABCD
1	−1	−1	−1	−1	+1
2	+1	−1	−1	−1	−1
3	−1	+1	−1	−1	−1
4	+1	+1	−1	−1	+1
5	−1	−1	+1	−1	−1
6	+1	−1	+1	−1	+1
7	−1	+1	+1	−1	+1
8	+1	+1	+1	−1	−1
9	−1	−1	−1	+1	−1
10	+1	−1	−1	+1	+1
11	−1	+1	−1	+1	+1
12	+1	+1	−1	+1	−1
13	−1	−1	+1	+1	+1
14	+1	−1	+1	+1	−1
15	−1	+1	+1	+1	−1
16	+1	+1	+1	+1	+1

process parameters, then Response Surface Methodology (RSM) would be applied to determine the optimum operating parameter for the process to minimize both that warpage and gate flash to all cavities.

2.2 Optimisation Phase with Response Surface Methodology

If there is a curvature in the relationship, then polynomial of higher degree must be used. RSM techniques would be an appropriate technique to optimize injection moulding process parameters [9]. The shape of response surface can be visualised when plotted on a three-dimensional space. It also provides contour plot which is a line of constant response when drawn in x_1 and x_2 plane. Each contour corresponds to a particular height of response surface. This will be helpful to study the result changes in the shape or height of response surface. In this study, Central Composite Design (CCD) was used to fit the second-order polynomial model which consist of 13 runs. Table 2 shows the design matric for the CCD made of cube points (nos. 1–4), 4 axial runs (nos. 5–8) and 5 centre points (nos. 9–13).

Then finally validation test was conducted to verify the optimal process parameter obtained

Table 2 CCD design metric

Std order	PtType	Blocks	Mold temp	Pack pressure
1	1	1	−1.00000	−1.00000
2	1	1	1.00000	−1.00000
3	1	1	−1.00000	1.00000
4	1	1	1.00000	1.00000
5	−1	1	−1.41421	0.00000
6	−1	1	1.41421	0.00000
7	−1	1	0.00000	−1.41421
8	−1	1	0.00000	1.41421
9	0	1	0.00000	0.00000
10	0	1	0.00000	−1.00000
11	0	1	0.00000	1.00000
12	0	1	−1.00000	0.00000
13	0	1	1.00000	0.00000

3   Results and Discussion

The experimental results of DoE responses for the multi-cavity moulding warpage and gate flash responses were analysed from the normal probability plots, main effect plots and residuals plots. The significant factors were identified, and the contour plots provide curvatures in the response surfaces. Finally, the overlay of warpage and gate flash responses indicates the optimum result.

3.1   DOE Characterization

3.1.1   Significant Factors for Warpage

The normal probability and standardized main effects plots of warpage for all respective eight cavities were analysed. The analysis revealed that each cavity gave varying significant effect and interaction. Figure 3 shows a sample of normal probability and main effect plots for cavity number 1. Since this study involved eight cavities, all the main effects and interactions need to be concurrently analysed. Table 3 consolidates the main effect and interactions of the eight cavities and reveals that only the main factor E (packing pressure) appears in all cavities.

3.1.2   Significant Factors for Flash

Similar analysis of significant main effect and interaction for all eight cavities was done for flash and the results are consolidated in Table 4. The table shows that the most significant main effect was attributed to factor C (mould temperature) where all eight cavities were sensitive to its setting.
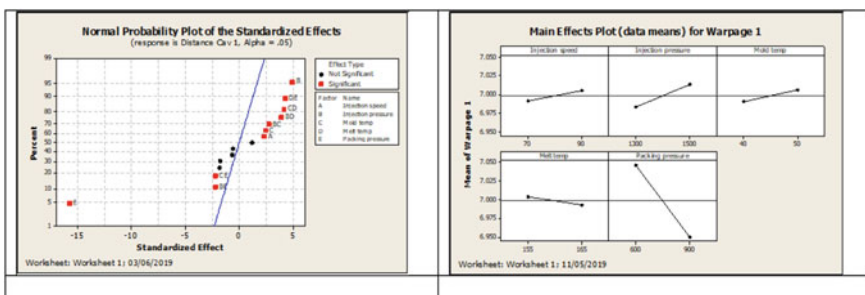
Fig. 3   Example of normal probability and main effect plots for cavity no. 1 for warpage

Table 3 Significant main effect and interaction for warpage

Cavity	A	B	C	D	E	AB	AC	AD	AE	BC	BD	BE	CD	CE	DE
1	/	/	/		/					/	/	/	/	/	/
2				/	/					/		/			
3	/	/	/	/	/	/				/	/				
4	/		/		/										
5	/	/	/	/	/		/					/	/		
6	/			/	/	/						/			
7	/	/	/	/	/		/					/	/		
8	/	/	/	/	/			/	/		/				/

Table 4 Significant main effect and interaction for flash

Cavity	A	B	C	D	E	AB	AC	AD	AE	BC	BD	BE	CD	CE	DE
1	/	/	/	/	/		/	/		/		/		/	
2	/	/	/				/	/				/			
3	/		/				/	/	/	/	/	/	/		
4	/		/				/	/	/	/	/	/	/		
5	/	/	/		/		/	/				/	/		
6			/												
7	/	/	/			/	/	/		/					
8		/	/	/	/		/	/		/	/	/	/		/

3.2 Analysis of Variance

To have more insight and interpretation of experimental result, analysis of variance (ANOVA) was performed on a warpage model to identify any curvature in the warpage response. All the cavities scored curvature test with P-value less than 0.05 except cavities 5 and 8. Since the majority of cavities demonstrated possible curvature existed in the model, we tentatively concluded that there was non-linearity in the warpage response and it should be modelled using RSM [10]. ANOVA was also conducted for the flash response and found that the curvature was significant for all outputs of all cavities except cavities 6 and 8. Only cavity 8 did not show any curvature in both warpage and flash. In general, it can be concluded both warpage and flash responses are non-linear in majority of the cavities with holding pressure (E) and mould temperature (C) having the most significant effects to all cavities. There are significant two-factor interations for some cavities. However, in selection of the main factors, we ignored the interation effects since they were widely inconsistent among the cavities, especially for warpage. As such, we selected holding pressure (E) and mould temperature (C) for further process optimzation using RSM.
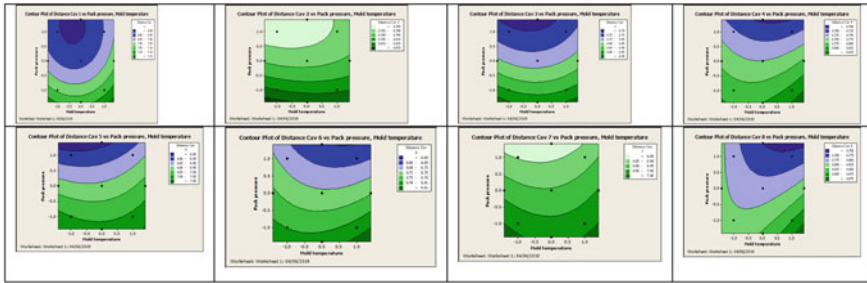
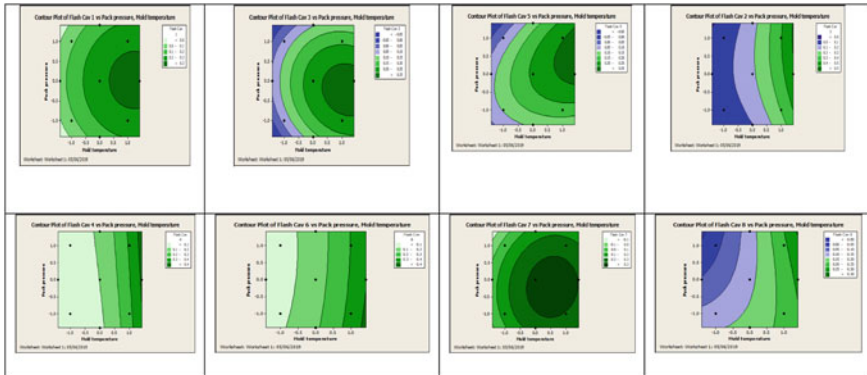**Fig. 4** Contour plots for warpage response at eight cavities

Fig. 5 Contour plots for flash response at 8 cavities

3.3 *Optimum Process Setting Through Response Surface Model*

Figure 4 presents the contour plots showing second order model (with interaction and main effects) which is twisted plane. In overall, it is observed that the holding pressure (E) at low level and mould temperature (C) at high level resulted in the best result (lowest warpage). Given that the holding pressure was the most significant factor to the warpage response where lower mould temperature resulted in a higher warpage. The results indicate that at low holding pressure with mould temperature at centre level can reduce the warpage.

Figure 5 shows the contour plot for the second response, flash. From the contour plots, it can be observed that mould temperature at low level and holding pressure at low level resulted in the minimum flash. However, there are contradiction between warpage and flash responses since the warpage required high level of mould temperature while flash required low level of mould temperature to achieve the optimum. We resolved these contradicting responses by using an overlaid contour plot to visually identify an area of compromise.
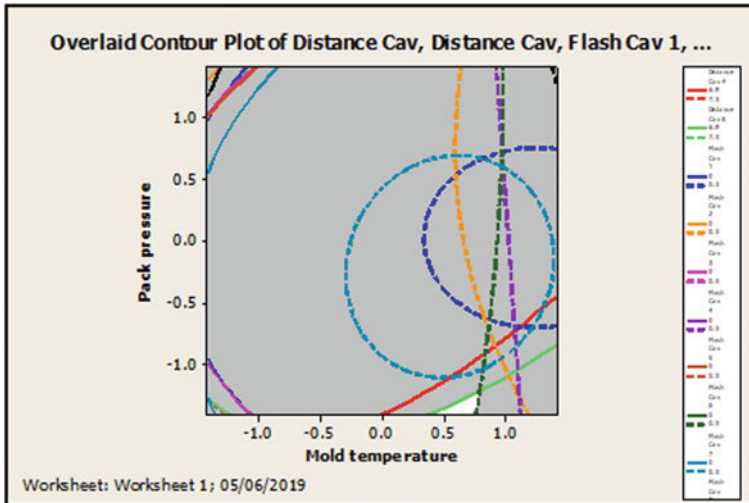
Fig. 6 Overlaid plot of warpage and flash responses for eight respective cavities

3.4 Optimal Overlaid Plot

Figure 6 shows the overlaid contour plot between two responses and the feasible region is shown in white colour. The predicted optimum value was selected where the pack pressure was at −1.6 and mould temperature was at 0.6 (coded values).

3.5 Confirmation Run

The confirmation of the predicted regression model is critical for both responses to ensure they are within the acceptable practical settings. In this study, the confirmation was more critical for warpage since the flash defects remained within the

Table 5 Predicted observation to actual test run

Cavity	Predicted warpage value	Actual warpage value
1	50.52408	7.10
2	−6.1339	6.85
3	4.17144	6.95
4	−13.4948	6.82
5	4.47934	7.02
6	−18.668	6.81
7	−26.1065	7.00
8	−8.576	6.82

acceptable level. An example of the regression model to predict the response warpage ($\hat{y}$) for cavity 5 is given in Eq. (1), where x_1 is the value of packing pressure and x_2 is the value of mould temperature.

$$\hat{y}_5 = 6.9107 + (0.01616)(x_1) + (-0.08224)(x_2) + (0.01824)(x_1^2) \quad (1)$$

Table 5 summarises the predicted warpage values compare to the actual warpage values. This findings suggest that there is a need to further improved the prediction model for some of the cavities since the difference between the predicted warpage and the actual warpage remain unsatisfactory. However, in the actual practical experiment the new recommended packing pressure (-1.6) and mould temperature (0.6), generally gave an improved overall performance and bring the warpage to an acceptable level (within the specification limits).

The preliminary results reported in this paper should be treated with precautions and more thorough investigations are needed before the above findings can be generalised.

4 Conclusion

This study proposes quality improvement for multi-cavity injection moulding process to reduce warpage and flash defects. The fractional factorial experimental design was applied to identify the key significant factors affecting the multi responses problem. The screening experiment using factorial experiments has revealed that two significant factors which are packing pressure and mould temperature. The CCD from RSM were used to optimize the process parameter settings. The optimization through RSM using overlaid method lead to optimal solution identification where the packing pressure setting should be at -1.6 and mould temperature should be at 0.6 (coded values). The confirmation run reveals that the proposed optimal parameters setting was able to meet the required specifications. This research provides reference for practitioners on the application of traditional DOE and RSM technique to address multi-cavities injection moulding process with multi responses. This study should be further extended to refine the formulation of prediction model. Interaction effects need to be thoroughly reconsidered in the analysis to obtain better prediction and more consistent performance among the cavities.

References

1. Yizong T, Ariff Z, Muhammad Khalil A (2017) Influence of processing parameters on injection molded polystyrene using Taguchi Method as design of experiment. Procedia Engineering 184:350–359
2. Thyregod P (2001) Modelling and monitoring in injection molding. PhD thesis. Technical University of Denmark
3. Müller E, Schillig R, Stock T, Schmeiler M (2014) Improvement of injection moulding processes by using dual energy signatures Procedia CIRP 17(Supplement C):704–709
4. Attia UM, Alcock JR (2010) Optimising process conditions for multiple quality criteria in micro-injection moulding. Int J Adv Manuf Technol 50(5):533–542
5. Yang Y-K, Shie J-R, Liao H-T, Wen J-L, Yang R-T (2008) A study of Taguchi and design of experiments method in injection molding process for polypropylene components. J Reinf Plast Compos 27(8):819–834
6. Eladl A, Mostafa R, Islam A, Loaldi D, Soltan H, Hansen H, Tosello G (2018) Effect of process parameters on flow length and flash formation in injection moulding of high aspect ratio polymeric micro features. Micromachines. 9(2):58
7. Sharma V, Goyal A, Sharma S (2015) Quality improvement of plastic injection molded product using doe and Taguchi techniques Int J Recent Adv Mech Eng 4(2):93–103
8. Montgomery DC (2019) Introduction to Statistical Quality Control (8th ed). Wiley
9. Jayakaran S, Jeevanantham AK (2018) Optimization of injection molding process to minimize weld-line and sink-mark defects using Taguchi based grey relational analysis. Mater Today: Proc 5(5):Part 2 12615–12622
10. Carley KY, Kamneva N, Reminga J (2004) Response surface methodology. CASOS Technical Report, Pittsburgh PA

Stress and Strain Analysis of the Traditional Boat *Jaloe Kayoh* Made of Composite Materials with Centered Loading Using the Finite Element Method

Akram Tamlicha, Samsul Rizal, Iskandar Hasanuddin, Adhittya Pahlevi, Nazaruddin, M. M. Noor, and Ichsan Setiawan

Abstract A composite material is a combination of two or more different materials between resin and fiber. The characteristic of this material is that it has a high level of corrosion resistance. This study aims to analyze the strength and durability of *Jaloe Kayoh* made of jute fiber polyester composite materials. Static analysis on *Jaloe Kayoh* is carried out through simulation or modeling using CAE-based software with the Finite Element Method (FEM), in static-general conditions. The parameters studied include the stress and strain values for centralized loading on the body of the boat with a minimum load of 650 N and a maximum load of 1950 N. The variations of the materials applied to *Jaloe Kayoh* include jute, jute-glass, jute-glass-jute, and fiberglass. *From* the simulation results on the 1950 N loading, the maximum stress is obtained by the jute-glass material with a value of

A. Tamlicha · S. Rizal · I. Hasanuddin
Doctoral School of Engineering Sciences, Universitas Syiah Kuala, Banda Aceh 23111, Indonesia

A. Tamlicha (✉) · S. Rizal · I. Hasanuddin (✉) · A. Pahlevi
Department of Mechanical and Industrial Engineering, Faculty of Engineering, University of Syiah Kuala, Banda Aceh, Indonesia
e-mail: akram@unsyiah.ac.id

I. Hasanuddin
e-mail: iskandarhasanuddin@unsyiah.ac.id

Nazaruddin
Department of Informatics, Faculty of Mathematics and Natural Sciences, University of Syiah Kuala, Banda Aceh, Indonesia

M. M. Noor
Faculty of Mechanical Engineering, University Malaysia Pahang (UMP), Gambang, Malaysia

I. Setiawan
Department of Marine Sciences, Faculty of Marine and Fisheries, University of Syiah Kuala, Banda Aceh, Indonesia

3.356×10^9 Pa. The greatest maximum strain by jute-glass material is with a value of 1.442×10^{-1}. The results of this study show that the four composite materials are categorized as good to be applied as the main material of the *Jaloe Kayoh*.

1 Background

The majority of Acehnese people who live in the coastal areas work as traditional fishermen [1–3]. The boats used by the fishermen are made of wood with a distinctive shape, known as the *jaloe kayoh*. Traditionally, the *jaloe kayoh* is made of wood as the main material. The wooden boat usually only lasts two to three years. Wood is a low-quality material that is easily degraded, but producers of the *jaloe kayoh* heavily depend on wood as the main material for the boats [1, 2].

One material that is not prone to degradation and decay is composite materials. Composite materials are materials that consist of two or more constituent materials at a macroscopic scale that are designed to have better performance and mechanical properties than the constituent materials independently [4]. Based on their origin, fibers can be divided into natural fibers and synthetic fibers. Natural fibers are good for the manufacture of various products. One of them is abaca fiber, which is used in composite panel products [5]. In this study, the natural fiber jute is used as the reinforcing material.

The development of CAD/CAE technology with features such as 3-Dimensional (3D) modeling and finite element simulation (FEM) has succeeded in reducing some of the problems or difficulties faced by the manufacturing industry. The machining process is a very important part of production in every production of the manufacturing industry [6, 7]. Software-based on CAD (Computer Aided Design) and CAE (Computer Aided Engineering) are an effective tool in creating and performing simulations with the Finite Element Method [8, 9]. Then, the stress and strain values obtained can be compared with the values from Finite Element Analysis (FEM) and the calculation of their material properties [10].

This study uses several variations of composite materials; they are jute, jute-glass, jute-glass-jute, and fiberglass as materials that are simulated against the *jaloe kayoh* design with the Finite Element Method (FEM). The strength and resistance levels of the materials are then analyzed. The parameters taken to express strength and resistance levels of the *jaloe kayoh* are the stress and strain values at the minimum loading variation of 650 N and the maximum loading of 1950 N which are distributed centrally on the body of the *jaloe kayoh*.

2 Literature Review

2.1 *Jute Fiber*

Jute fiber is a natural fiber that is commonly used as reinforcement in materials, that is classified as a green composite. Known under the scientific name Corchorus capsularis, it is a low-cost natural fiber with the maximum production volume in the world, at around 2.300×10^3–2.850×10^3 tons [11, 12]. Jute fiber has poor resistance to moisture, acids, and UV rays. On the other hand, its good texture and resistance to heat and fire make it a material that can be widely applied in industries such as textiles, construction, and automotive [13].

2.2 *The* Jaloe Kayoh

The *jaloe kayoh* is a small wooden boat from Aceh that is commonly used by the fishing community for fishing, water transportation, and pond maintenance see Fig. 1 [14].

2.3 *FEM (Finite Element Method)*

Finite Element Method (FEM) is a numerical science that can be applied to solve problems such as stress analysis on the structure and deformation of ships, vehicles, machines, building structures, and human body parts [15]. Analysis using FEM makes it possible to get the stress distribution in the analyzed model. The failure of a construct can be identified using this analysis and the precise point at which it is indicated or occurred. Thus, it is easier for engineers to modify or reinforce the construction that is identified as having a risk of damage or failure of construction.

Fig. 1 Acehnese traditional boat, the *Jaloe Kayoh* [14]

2.4 Stress

Stress is the quantity of the tensile force acting on the cross-sectional area of an object. The stress that occurs greatly affects the material properties of the object. If the load is static or changes relatively slowly with time and is applied uniformly over the cross-section or member surface, the mechanical behavior can be ascertained by a simple stress-strain test; this is most often done with metals at room temperature. There are three main ways in which loads can be applied: tensile, compressive, and shear. Voltage is defined by relation [16].

$$\sigma = \frac{F}{A_0} \tag{1}$$

2.5 Strain

The strain is defined as the change in the length of a material divided by the initial length due to the tensile and compressive forces on the material. The stress and strain relationships are no longer linear as the material reach the phase limits of its plastic properties. The strain is divided into two: engineering strain and true strain. Engineering strain is the strain calculated according to the dimensions of the original object (initial length). The amount of strain that occurs is calculated by dividing the elongation by the original length. The strain is defined by the relation [18].

$$\varepsilon = \frac{\Delta L}{Lo} \tag{2}$$

True strain can be calculated in stages (increment strain). The amount of strain is calculated on the actual dimensions of the object at certain times and not calculated based on the initial length of the dimensions of the object [16].

3 Methodology

3.1 Material

In this study, the materials used in the *jaloe kayoh* boat model are *jute, glass jute, glass jute*, and *fiberglass* which are formed through a lamination process, with the following mechanical properties as shown in Tables 1, 2, 3, and 4.

Table 1 *Jute* material mechanical properties [2]

Modulus young	(E)	84799 MPa
Poison ratio	(v)	0.38
Density	(ρ)	1409.443 (kg/m^3)

Table 2 *Jute glass* material mechanical properties [2]

Modulus young	(E)	28681 MPa
Poison ratio	(v)	0.29
Density	(ρ)	1456.077 (kg/m^3)

Table 3 *Jute glass jute* material mechanical properties [2]

Modulus young	(E)	295722 MPa
Poison ratio	(v)	0.32
Density	(ρ)	1504.491 (kg/m^3)

Table 4 *Fiberglass* material mechanical properties [2]

Modulus young	(E)	86129 MPa
Poison ratio	(v)	0.2
Density	(ρ)	2550.0 (kg/m^3)

3.2 Testing Procedure

3.2.1 Design

Before simulation was conducted, the design of the *jaloe kayoh* used CAD-based software. The length of the boat is 4398 mm, with a width of 1233 mm and a height of 596 mm (Fig. 2).

3.2.2 Application of Materials

In this simulation, four different types of materials are used, namely *jute, glass jute*, *glass jute*, and *fiberglass*, each of which is applied to the *jaloe kayoh* boat model.

3.2.3 Constraint

The stage of constraints used in the *jaloe kayoh* model is the coupling type. This stage aims to connect the reference point to the jaloe *kayoh body* so that later a concentrated load can be placed on the reference point (Fig. 3).
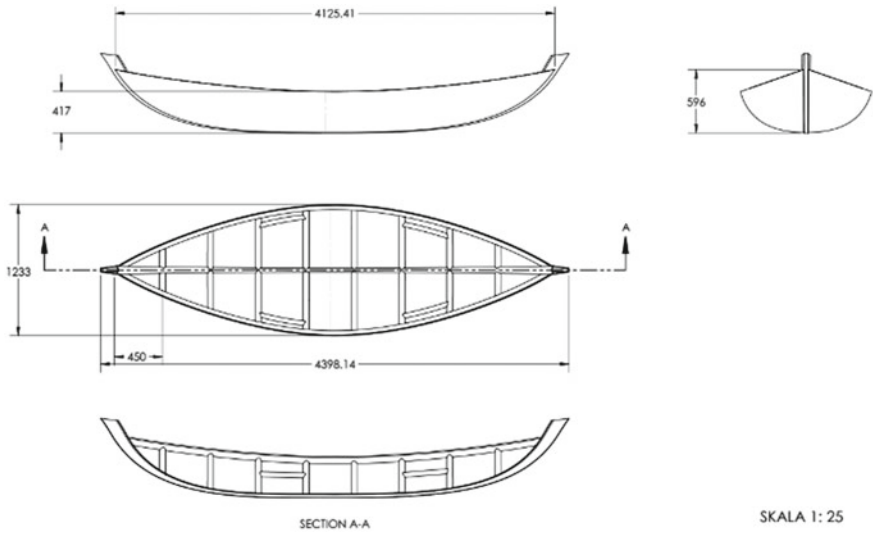
Fig. 2 *Jaloe Kayoh* dimensions (mm) [17]
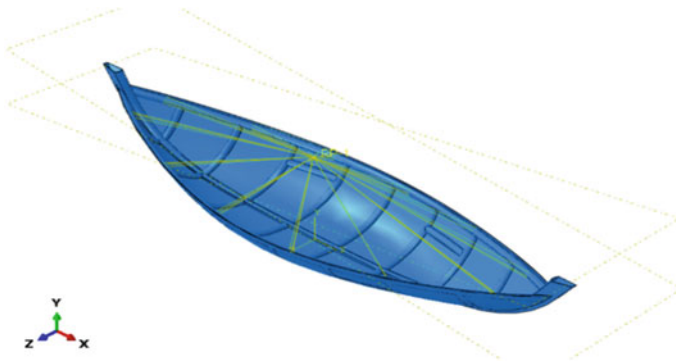
Fig. 3 *Constraint* results from the *jaloe kayoh* model

3.2.4 Determining the *Boundary Condition* and *Load*

In this study, the type of load given is *concentrated force* with a load variation of 650 N, 1300 N, and 1950 N. Furthermore, the type of support chosen (Fig. 4).

- *Boundary condition* 1 used the *ENCANSTRE* (U1 = U2 = U3 = UR1 = UR2 = UR3 = 0).
- *Boundary condition* 2 used *displacement/rotation* (U2 = U3 = UR1 = UR2 = UR3 = 0).
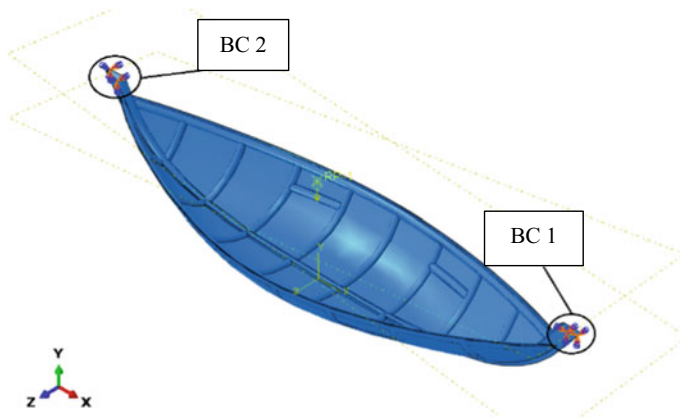
Fig. 4 Given *Load* and *boundary condition*

3.2.5 Meshing

The *meshing* stages carried out on the wooden *jaloe* model used a *tetrahedron mesh* type with a size of 7 mm (Fig. 5).

4 Results and Discussion

4.1 Stress Simulation

Stress analysis of the simulation using the Finite Element Method (FEM), the following results are shown in Fig. 6.

The maximum stress values that occur with variations in material and given load can be seen in Table 5.

4.2 Strain Simulation

Strain analysis of the simulation using the Finite Element Method (FEM) can be seen in Fig. 7.

The maximum strain values that occur with variations in material and given load can be seen in Table 6. The greatest maximum strain by jute-glass material is with a value of 1.442×10^{-1}.
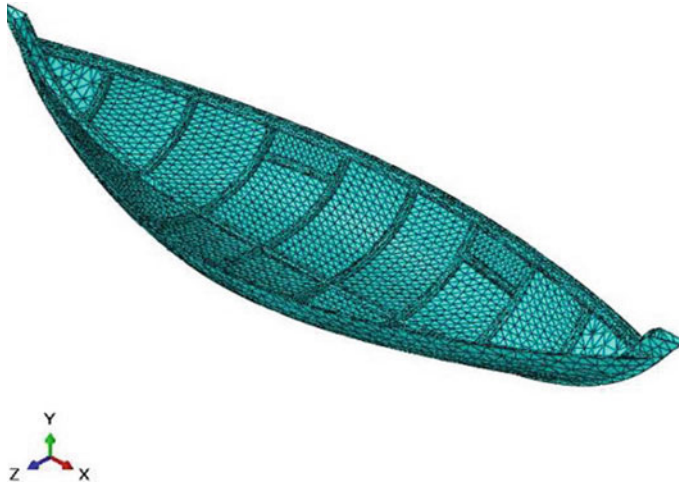
Fig. 5 Meshed model of the *jaloe kayoh* structure
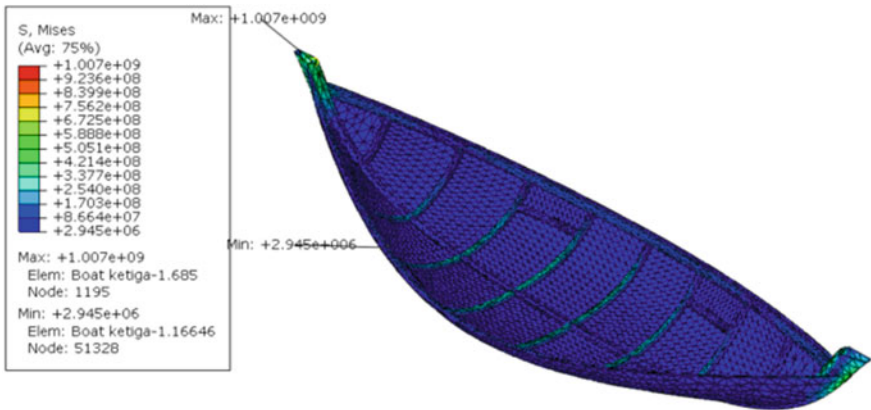
Fig. 6 Stress contours that occur in the jute-glass with a minimum load

Table 5 Stress simulation results

Material	Maximum stress (Pa)		
	650 N	1300 N	1950 N
Jute	8.601×10^8	1.796×10^9	2.844×10^9
Jute-glass	1.007×10^9	2.195×10^9	3.356×10^9
Jute-glass-Jute	8.718×10^8	1.766×10^9	2.684×10^9
Fiberglass	9.758×10^8	2.030×10^9	3.154×10^9
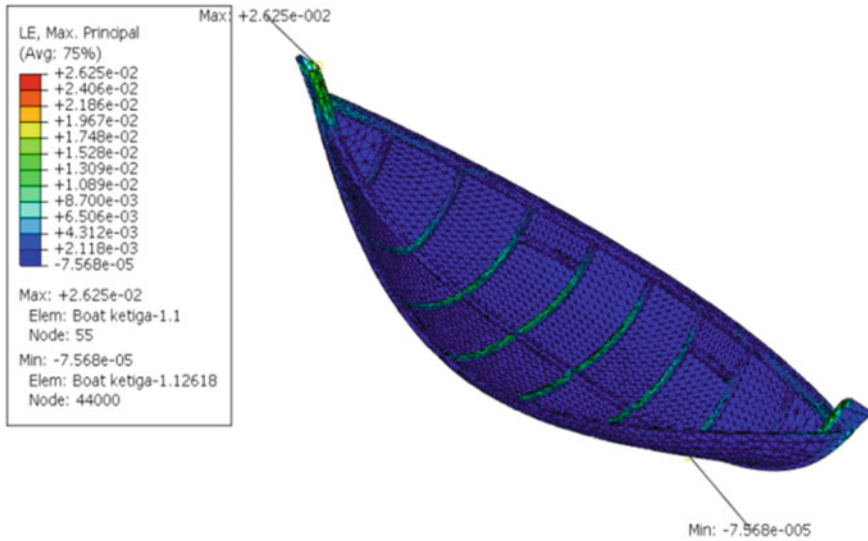
Fig. 7 Strain contours that occur in jute-glass with a minimum load

Table 6 Strain simulation results

Material	Maximum strain		
	650 N	1300 N	1950 N
Jute	1.130×10^{-2}	2.436×10^{-2}	3.870×10^{-2}
Jute-glass	2.625×10^{-2}	8.746×10^{-2}	1.442×10^{-1}
Jute-glass-Jute	2.384×10^{-3}	4.796×10^{-3}	7.233×10^{-3}
Fiberglass	8.859×10^{-3}	1.799×10^{-2}	2.724×10^{-2}

5   Conclusion

From the research that has been carried out through simulations using FEM, several conclusions can be drawn, including:

1. From static analysis with *concentrated force* on the *jaloe kayoh* using FEM, it is found that the jute-glass material produced the greatest maximum stress and strain values.
2. At a load of 650 N, the greatest maximum stress is found in the jute-glass material with a value of 1.007×10^9 Pa. The largest maximum strain is also found in the jute-glass material with a value of 2.625×10^{-2}. At a load of 1950 N, the largest value of the two parameters is also found in the jute-glass material with a maximum stress of 3.356×10^9 Pa, and a maximum strain of 1.442×10^{-1}.

3. The four composite materials that have been tested are found to be feasible and good alternatives for the use of wood as the main material for making the *jaloe kayoh* if the wall thickness is increased.

References

1. Akram I, Hasanuddin N, Syahril Z, Ahmad N (2018) A comparison in the structural strength between fiberglass and jute fiber in the traditional boat Jalo Kayoh using Finite Element Method. IOP Conf Ser Mater Sci Eng 523(1):012020
2. Akram I, Hasanuddin N, Putra R, Noor MM (2019) Mechanical behavior of hybrid glass fiber —jute reinforced with polymer composite for the wall of the Acehnese boat 'Jalo Kayoh'. IOP Conf Ser, Mater Sci Eng 523:012076
3. Nazaruddin N, Akram A, Hasanuddin I, Iqbal M, Kurniawan R, Putra R (2019) Mechanical properties of glass fiber reinforced polyester resin for use as the wall of the Acehnese boat 'thep-thep'. IOP Conf Ser Mater Sci Eng 523:012080
4. Pal B, Haseebuddin MR (2012) Analytical estimation of elastic properties of polypropylene fiber matrix composite by finite element analysis. J Adv Mat Phy Chem 2:23–30
5. Iqbal M, Aminanda Y, Firsa T, Ali M (2020) Bending strength of polyester composites reinforced with stitched random orientation and plain weave abaca fiber. IOP Conf Ser Mater Sci Eng 739:012078
6. Dirhamsyah M, Tadjuddin M, Udink A, Yusuf Z, Saiful HY (2019) The effect of cutting speed on dimension accuracy and burr development of high-speed micro drill process on aluminum. IOP Conf Ser, Mater Sci Eng 523:012074
7. Taha Z, Sah JMd, Passarella R, Ghazilla R, Ahmad N, Jen Y, Khai T, Kassim Z, Hasanuddin I, Yunus M (2009) A solar vehicle based on sustainable design concept. Proceedings of the IASTED International Conference on Solar Energy, SOE 2009:38–43
8. Liu XY, Dai GC (2007) Surface modification and micromechanical properties of jute fiber mat reinforced polypropylene composites. J Exp Polym Letters 1(5):299–307
9. Jauhari N, Mishra R, Thakur H (2015) Natural fiber reinforced composite laminates—A review. International Conference on Materials Processing and Characterization, proceeding, 2868–2877
10. Hasanuddin I, Husaini H, Syahrir MA, Sandy Yudha BZ, Akhyar A (2018) Stress and strain analysis from dynamic loads of mechanical hand using Finite Element Method. IOP Conf Ser, Mater Sci Eng 352:012017
11. Faruk O, Bledzki AK, Fink H-P, Sain M (2012) Biocomposites reinforced with natural fibers:2000-2010. Prog Polym Sci 37:1552–1596
12. Leonard Y, Mwaikambo LY, Ansell MP (2002) Chemical modification of hemp, sisal, jute, and kapok fibers by alkalization. J Appl Polym Sci 84:2222–2234
13. Fuqua MA, Huo S, Ulven CA (2012) Natural fiber reinforced composites. Polym Rev 52:259–320
14. Badan Statistik Provinsi Aceh (2015) Aceh in figures. BPS Provinsi Aceh
15. Hutton DV (2004) Fundamentals of finite element analysis. McGraw-Hill, New York
16. Callister WD (2007) Materials Science and Engineering an Introduction. Wiley, Hoboken

17. Ramadhan S, Rizal S, Hasanuddin I (2018) Static load comparison of Jalo Kayoh with composite and e-glass material variations using Finite Element Method. Universitas Syiah Kuala, Banda Aceh
18. Gomes A, Matsuo T, Goda K, Ohgi J (2007) Development and effect of alkali treatment on tensile properties of curaua fiber green composites. Compos B 38:1811–1820

Numerical Analysis of Traditional Aceh Fishing Boat with Various Scenario Loading and Hull Thickness, Manufacturing by Metal Plasma Cutting and Welding

Akhyar, Akram Tamlicha, Iskandar Hasanuddin, Yusrizal Muchlis, Amir Zaki Mubarak, Azwinur, Teuku Muhammad Yusuf, and Asbahrul Amri

Abstract Numerical analysis for the traditional Aceh fishing boat was studied with three loading scenarios, such as 2100, 3500, and 4200 N and four thickness variations are 3, 4, 5, and 6 mm. The analysis carried out involved stress, strain, and displacement on the low carbon steel St-37 alloy. This simulation aims to analyze the maximum stress, strain, and displacement of a traditional Aceh fishing boat with several variations in loading conditions and hull thickness. Then it is produced using CNC plate cutting techniques and assembled with welding techniques. The load is applied evenly to the lower half of the surface on a traditional Aceh fishing boat with the assumption boat receiving a pressure load from the water when it is placed above the water level. The results show are that the maximum load and strain are 340 MPa and 1.1×10^{-3} with third scenario loading conditions, the load is 4200 N which was applied to the simulation with a plate thickness of 6 mm. The maximum displacement was 4.76 mm in the third scenario loading conditions (the load applied is 4200 N), with a plate thickness of 2 mm.

Akhyar (✉) · A. Tamlicha · I. Hasanuddin · A. Z. Mubarak
Department of Mechanical Engineering, Universitas Syiah Kuala, Jln. Syech Abdurrauf no.7 Darussalam, Banda Aceh 23111, Indonesia
e-mail: akhyar@unsyiah.ac.id

Y. Muchlis
Department of Mechanical Engineering, Universitas Abulyatama, Banda Aceh, Indonesia

Azwinur
Department of Mechanical Engineering, Politeknik Negeri Lhokseumawe, Jl. Banda Aceh-Medan Km. 280 Buketrata, Lhokseumawe 24301, Indonesia

T. M. Yusuf
Consist Product Inc., Tanjong, Ingin Jaya, Kabupaten, Aceh Besar, Aceh 23116, Indonesia

A. Amri
Department of Industrial Engineering, Politeknik Aceh Selatan, Banda Aceh 23711, Indonesia

1   Introduction

Finite element analysis can be used to solve complex elasticity problems and structural analysis problems in various engineering. Stress analysis, strain, deformation, and other structural analysis can be done through this method. Several solutions have been analyzed, including the phenomenon of hydrogen-induced cracking in pipeline steel which has been analyzed using the finite element model. The results of experimental modeling and validation show that the crack propagation path can be predicted by the fracture mechanic approach [1]. Studies on the moment connection with the bolt on the end-plate have carried out finite element software through a cyclic-void growth model, the results show that the vibration mode has an important role in increasing damage to high-rise structures [2]. Finite element software analysis for thermal and mechanical simulations of single butt welding with several angle variations has been carried out on the St-37 material [3]. Toluene storage tank failures with varying capacities have been analyzed using Axisymmetric finite element analysis for the welding of tank roof fillets on St.37-2 [4]. Stress distribution and deformation were analyzed using the finite element method under various loading conditions [5]. Three-dimensional finite elements with a Goldak double ellipsoid heat source model were analyzed for the repair of the butt weld of two thin St 37 plates. The results obtained are finite element simulation can predict the residual stress in the initial welding and its repair [6]. Modeling of St 37 and St-70 plates of steel for three-dimensional I beam with a thickness of 3 mm has been analyzed through the finite element method to the elastic stress carried out on the X, Y, Z axes, the result is that the elastic stress of St 37 steel is higher than St 70 steel [7]. Simple three-dimensional numerical modeling on marine composite panels with the principle of damage mechanics using cyclic test data to obtain a reduction in modulus with damage has been carried out [8].

Stress distribution and bending behavior were analyzed for thin carbon fiber sandwich material for sailboat hull using the finite element method [9], and a composite hull response analysis with the finite element method has also been performed [10]. Finite element analysis was performed to predict the effect of shock pressure loading on the ring stiffened submersible hull [11], and the slope of the steering construction with several degrees of slope [12]. Optimization through ship structural analysis and design has been analyzed using elements to non-linear [13]. As well as optimization of the composite hull pressure design under 3 MPa hydrostatic pressure has been carried out at a depth of 300 m through the Tsai-Wu and Tsai-Hill failure criteria. The results show varying responses to variations in the angle of fiber orientation, and the total deformation increases linearly with increasing depth as expected [14].

Several methods/processes can be used in producing engineering products such as welding [15], casting [16–18], machining, and many other processes. The discussion of the process of removing vibration stress and heat treatment post welding by applying resonant vibrations has been observed in low carbon steel welding St.37 [15]. The effect of variations in shoulder rotation on the Friction Stir Welding (FSW) process has been analyzed through numerical simulations of welding joints in aluminum 5083 and 6061-T6. The simulation results of welding temperature distribution and reaching the maximum on the FSW weld metal due to shoulder rotation [19]. Multi-response analysis and optimization of the cutting speed, gas pressure, arc current, and stand-off distance to improve the quality characteristics of plasma arc cutting were investigated on the Monel 400 superalloy. The results obtained are that the optimal plasma arc cutting parameters consisting of cutting speed: 2400 mm/min, gas pressure: 3 bar, arc current: 45A, and stand-off distance: 2 mm are determined to obtain good quality [20].

The purpose of this simulation is to analyze the stress, strain, and displacement of a traditional Aceh fishing boat with several variations in loading and hull wall thickness. This FAE analysis will obtain the maximum value (for stress, strain, and displacement), as well as the area where the maximum number was formed in traditional Aceh fishing boats when load and thickness variations are applied. The results of the stress, strain, and displacement analysis are required to optimize the design and manufacturing of the traditional Aceh fishing boat.

2   Method and Parameters

This simulation has conducted stress, strain, and displacement analysis on a traditional Aceh fishing boat with three variations of the load number and four variations of wall thickness. This simulation has been carried out in the Computation Mechanic Laboratory at the Mechanical Engineering Department of Universitas Syiah Kuala. Currently, traditional Aceh fishing boats are produced with wood and fiberglass materials, and these boats are often used for fishing boats with a small size of around three GT (gross tonnage) in Aceh Province. The detailed dimensions of the boats include the length, width, and maximum height of the boats, which are 8717, 2062, and 2069 mm, respectively. The surface shape of the hull boat is wavy following the fluidity of the water. The schematic of the traditional Aceh fishing boat analyzed in this simulation is in more detail as shown in Fig. 1.

The material used in this study is low carbon steel St. 37 as shown in Table 1. The load given to the traditional Aceh fishing boat in this study is evenly distributed with four variations of the load magnitude as shown in Table 2. The loading scenario given in this simulation assumes the number of loads that work when loaded by passengers, machines, and other equipment when fishermen go to sea (with various load conditions). Meshing is carried out on the traditional Aceh fishing boat model using the tetrahedron mesh type. Figure 2 shows the conditions and location of the pedestal placement and the boundary conditions for static
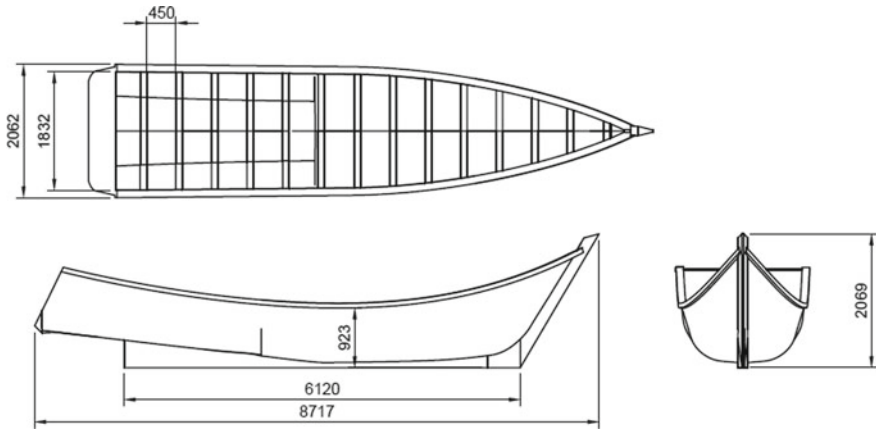
Fig. 1 Schematic upper, front, side views of traditional Aceh fishing boat

Table 1 Material properties of low carbon steel St. 37

Elastic (Young's tensile) modulus	69 GPa
Elongation	26%
Poisson's ratio	0.29
Shear modulus	75–80 GPa
Tensile strength	340–470 MPa
Yield strength	225–235 MPa
Density	2.7 g/cm^3

Table 2 Variation in loading conditions during the traditional Aceh fishing boat simulation

Loading Condition	Load Applied (N)
First loading condition	2100
Second loading condition	3500
Third loading condition	4200

loading, where the support chosen for boundary condition 1 is the type of pinch support (U1 = U2 = U3 = UR1 = UR2 = UR3 = 0) while the support for boundary condition 2 uses the type displacement/rotation (U2 = U3 = UR1 = UR2 = UR3 = 0). Furthermore, the simulation results have been manufactured through CNC plasma arc cutting technology for plate cutting and metal welding technology for assembling into a traditional Aceh fishing boat prototype.

3 Result Analysis

First scenario loading condition. The stress, strain, and displacement distributions with the variations in hull thickness given, they are 3, 4, 5, and 6 mm, respectively (as shown in Figs. 3, 4, 5, and 6). The results of the analysis show a maximum stress value

(a)

(b)

Fig. 2 **a** Boundary Conditions, **b** Load applied

(a)

(b)

(c)
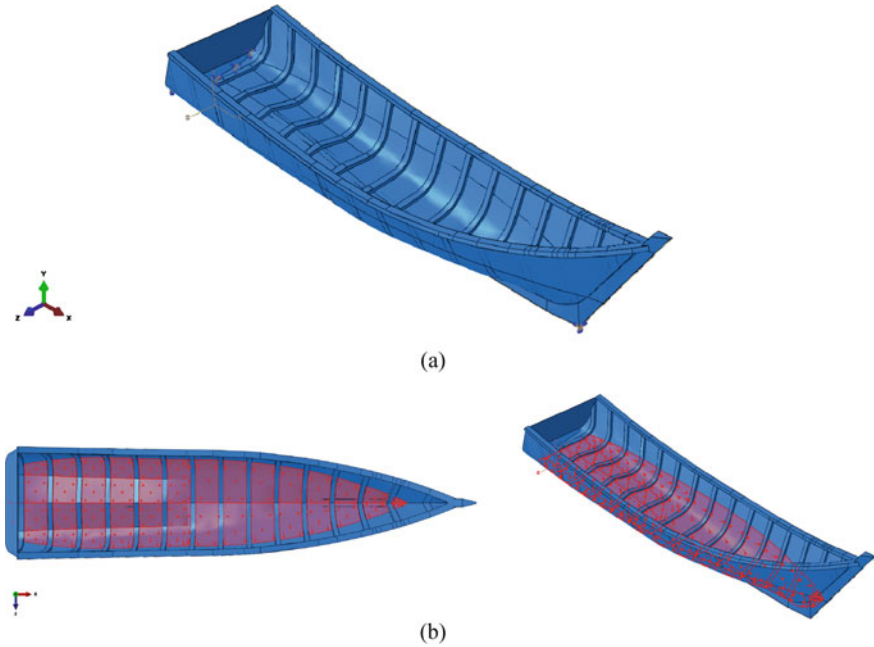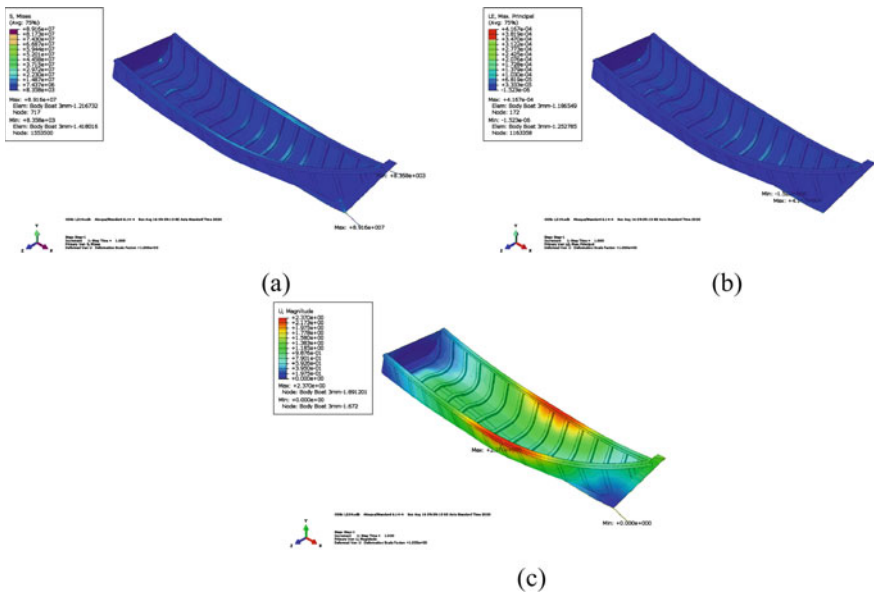
Fig. 3 Traditional Aceh fishing boat with 2100 N as loading application with 3 mm of plate thickness: **a** Stress, **b** Strain, and **c** displacement
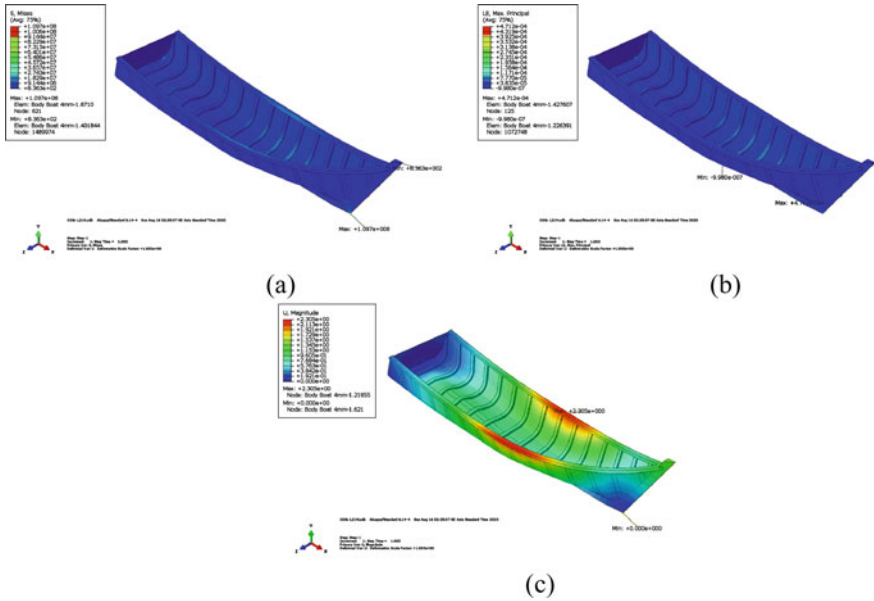
Fig. 4 Traditional Aceh fishing boat with 2100 N as loading application with 4 mm of plate thickness: **a** Stress, **b** Strain, and **c** displacement
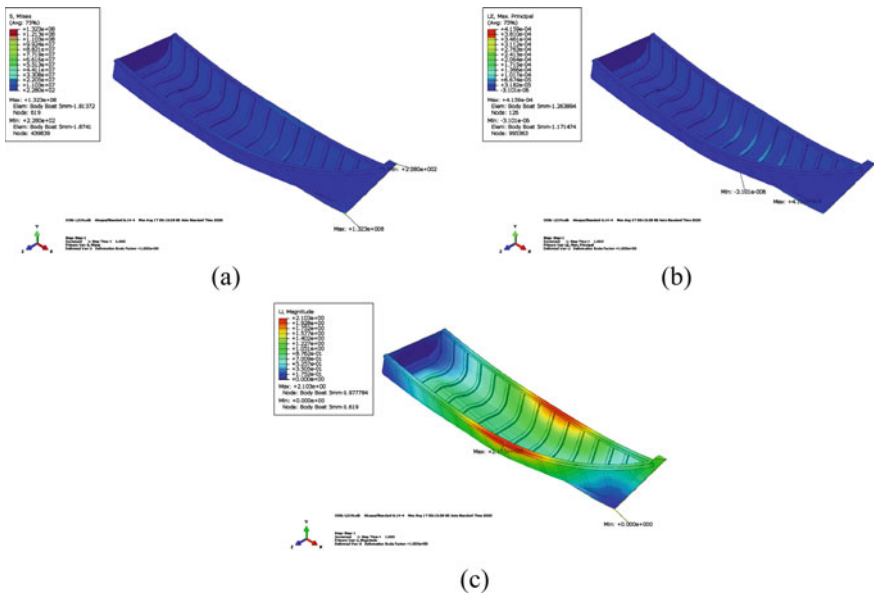
Fig. 5 Traditional Aceh fishing boat with 2100 N as loading application with 5 mm of plate thickness: **a** Stress, **b** Strain, and **c** displacement
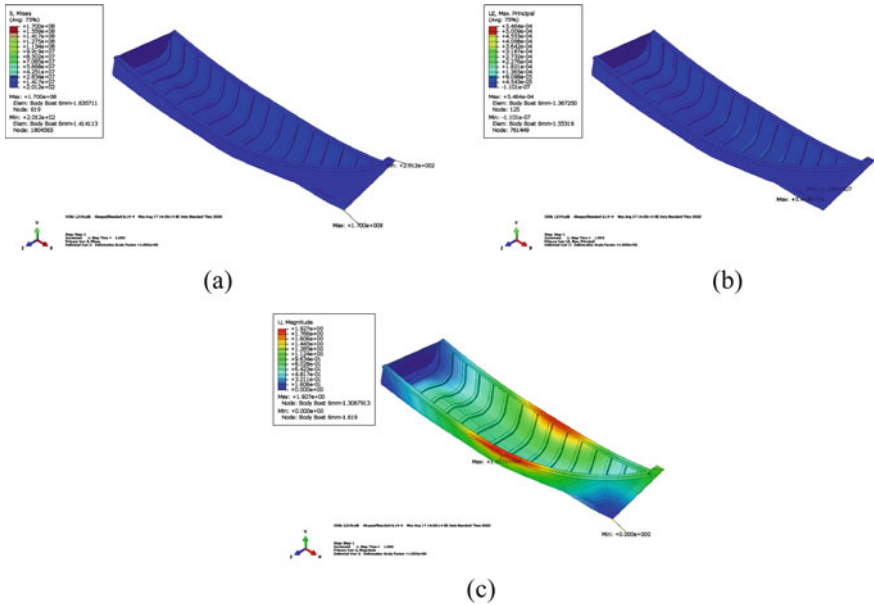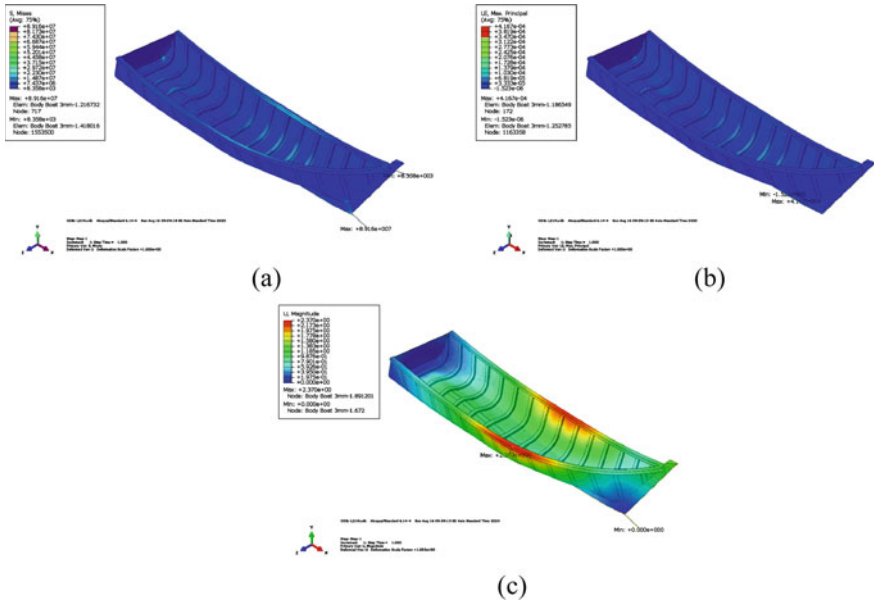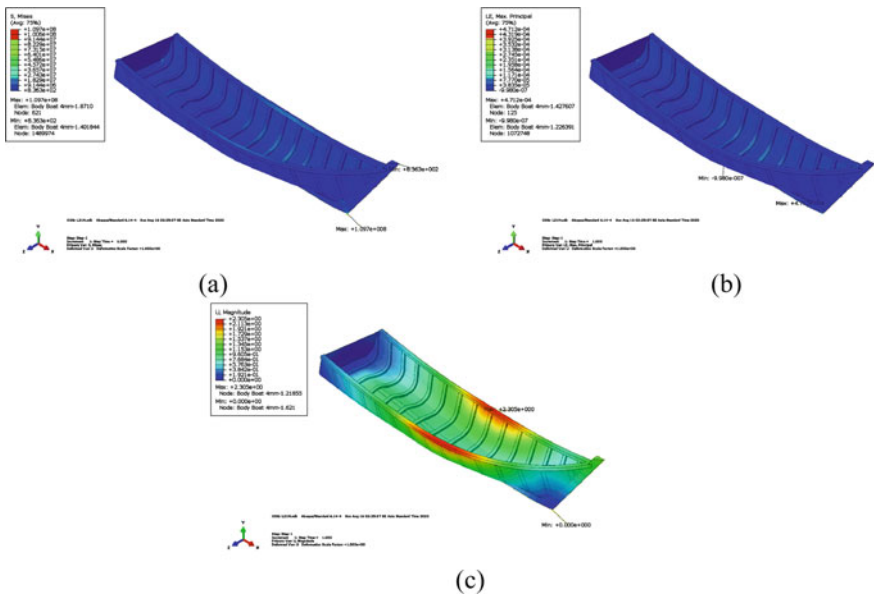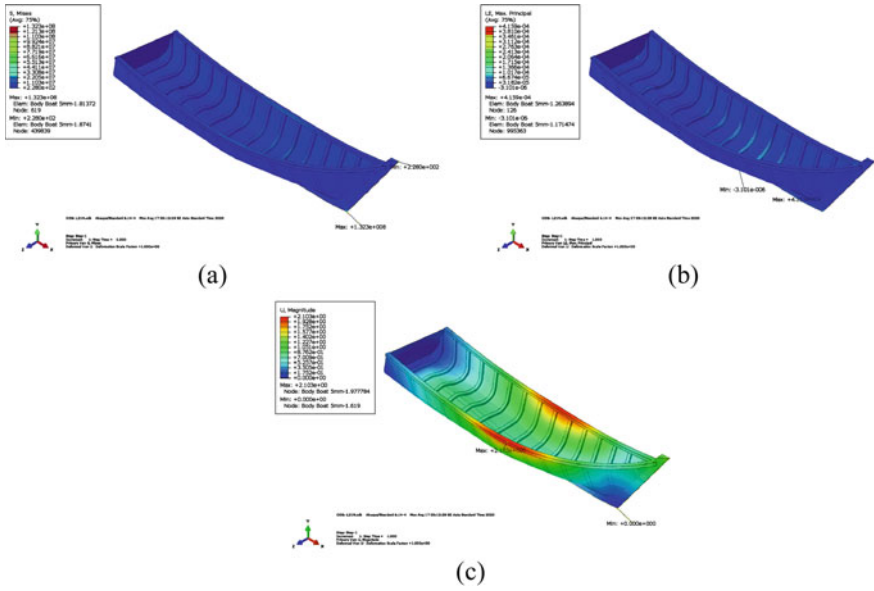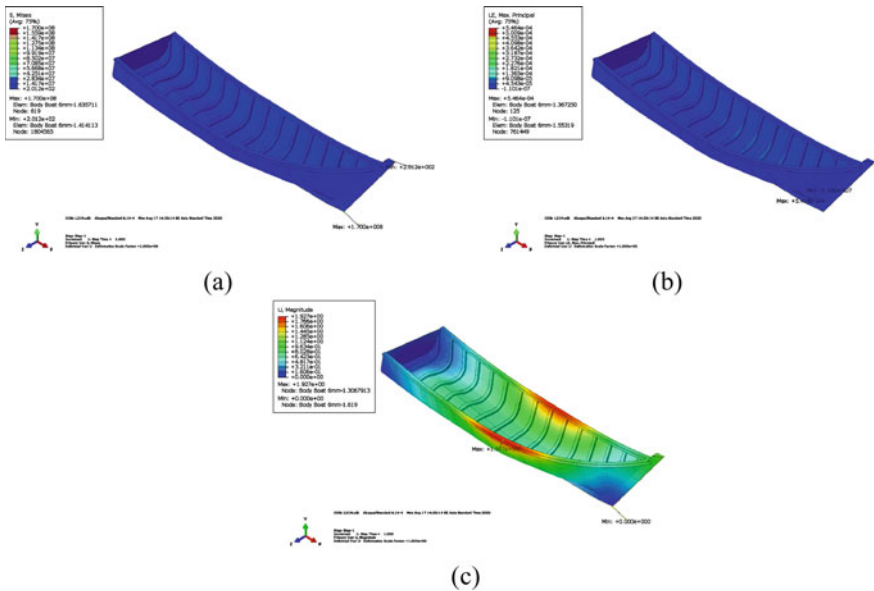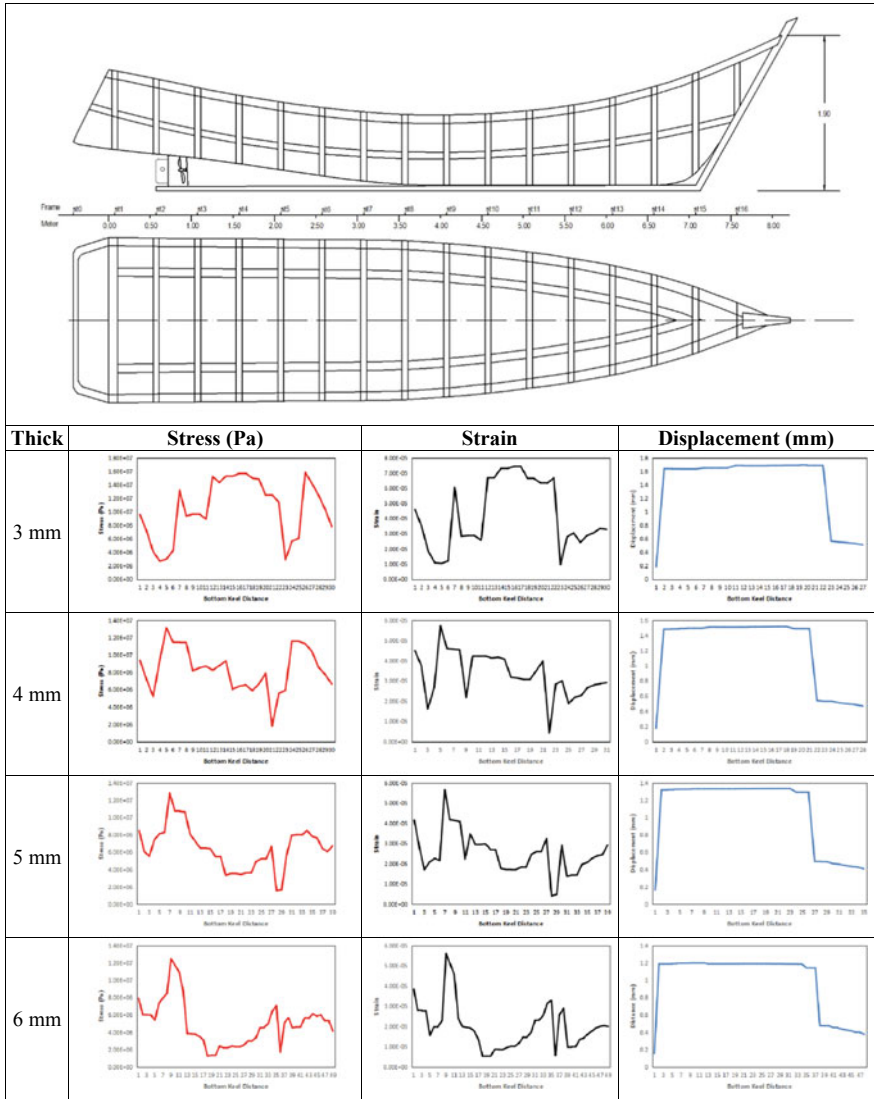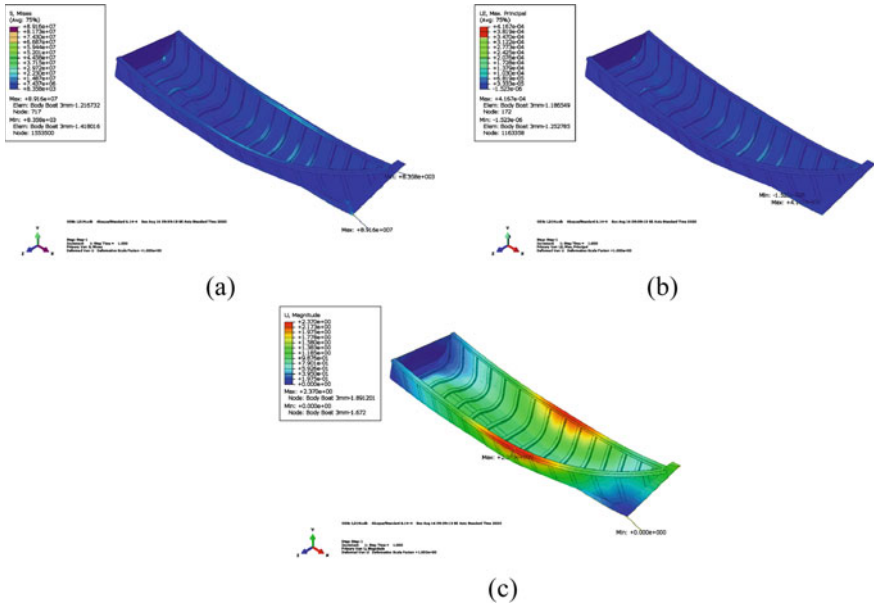
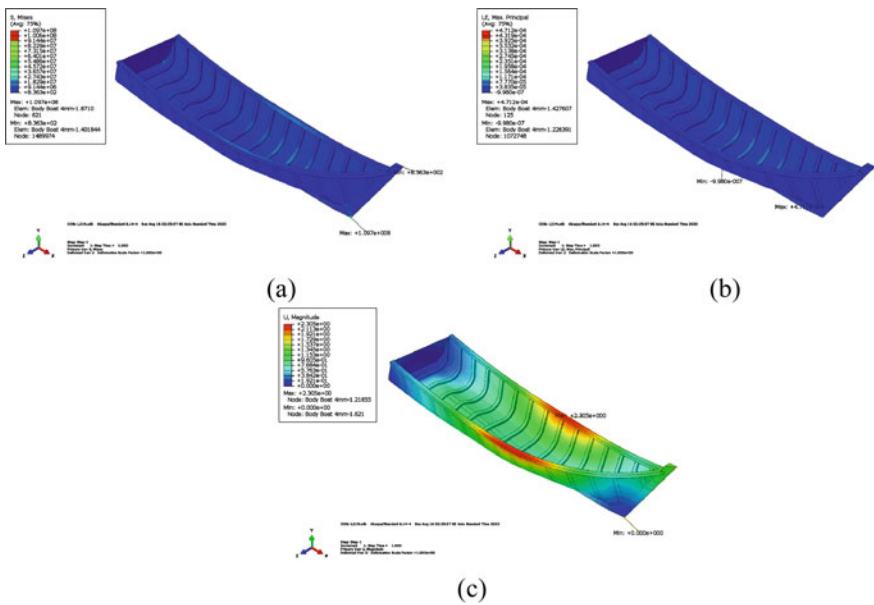Fig. 6 Traditional Aceh fishing boat with 2100 N as loading application with 6 mm of plate thickness: **a** Stress, **b** Strain, and **c** displacement

of 170 MPa with the location of the bottom keel at the front, the maximum strain of 5.46×10^{-4} with the location of the bottom keel at the front, and the maximum displacement of 2.37 mm with the location of the body draft upper midship. The distribution of stress, strain, and displacement along the bottom keel in the traditional Aceh fishing boat in the first scenario loading condition is shown in Fig. 7.

Second scenario loading condition. The stress, strain, and displacement distributions with the variations in hull thickness given of 3, 4, 5, and 6 mm, respectively (as shown in Fig. 8, 9, 10, and 11). The results of the analysis show a maximum stress number is 284 MPa with the location at the front bottom keel, the maximum strain of 9.12×10^{-4} with the location at the front bottom keel (6 mm of plate wall thickness), and a maximum displacement of 3.96 mm with the location of the body draft upper midship (3 mm plate wall thickness). The distribution of stress, strain, and displacement along the bottom keel of the traditional Aceh fishing boat under the second scenario loading condition, as shown in Fig. 12.

Third scenario loading condition. The distribution of stress, strain, and displacement with the variations in hull thickness given are 3, 4, 5, and 6 mm, respectively (as shown in Figs. 13, 14, 15, and 16). The results of the analysis show the maximum stress value is 340 MPa with the location at the front of the bottom keel, the maximum strain of 1.10×10^{-3} with the location at the front-bottom keel (6 mm of plate thickness), and a maximum displacement of 4.76 mm with the location of the body draft upper midship (3 mm of thickness). The distribution of
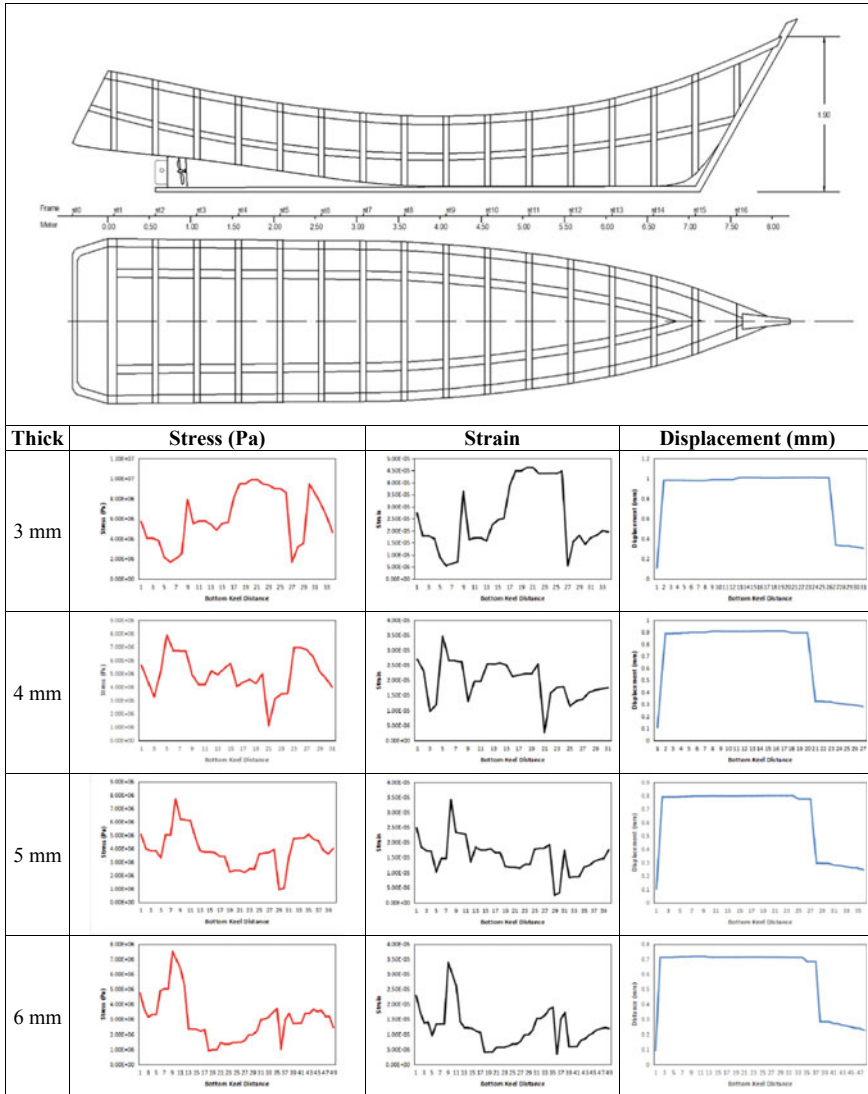
Fig. 7 Stress, strain, and displacement distribution along the mainframe of a traditional Aceh fishing boat with a load number is 2100 N

stress, strain, and displacement along the bottom keel in the traditional Aceh fishing boat in the third scenario loading condition is shown in Fig. 17.

Summary of simulation results of traditional Aceh fishing boat from three load variations and four thicknesses with maximum values. The location where the minimum stress, strain, and deformation is formed can be seen in Table 3. The results obtained are that the maximum load is 340 MPa and the maximum strain is

Fig. 8 Traditional Aceh fishing boat with 3500 N as loading application with 3 mm of plate thickness: **a** Stress, **b** Strain, and **c** displacement

Fig. 9 Traditional Aceh fishing boat with 3500 N as loading application with 4 mm of plate thickness: **a** Stress, **b** Strain, and **c** displacement
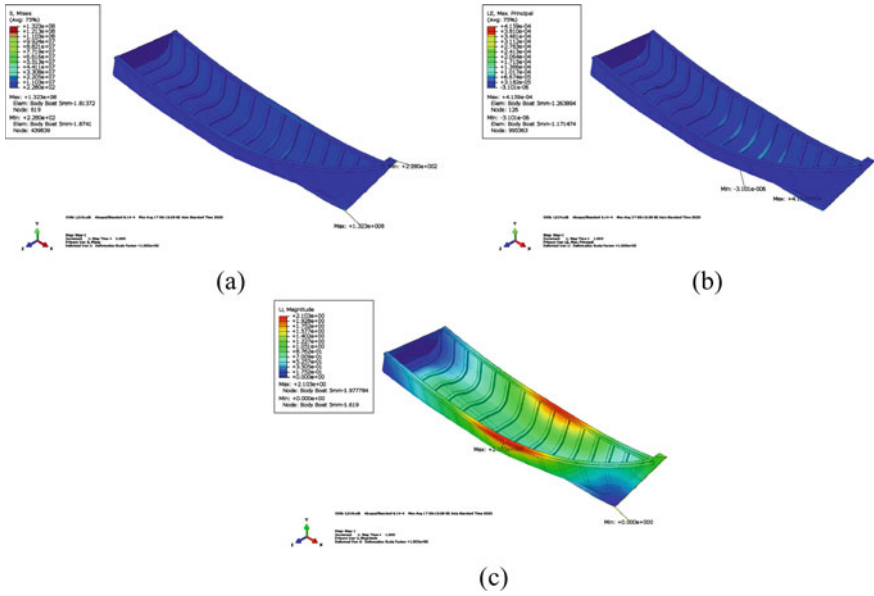
Fig. 10 Traditional Aceh fishing boat with 3500 N as loading application with 5 mm of plate thickness: **a** Stress, **b** Strain, and **c** displacement
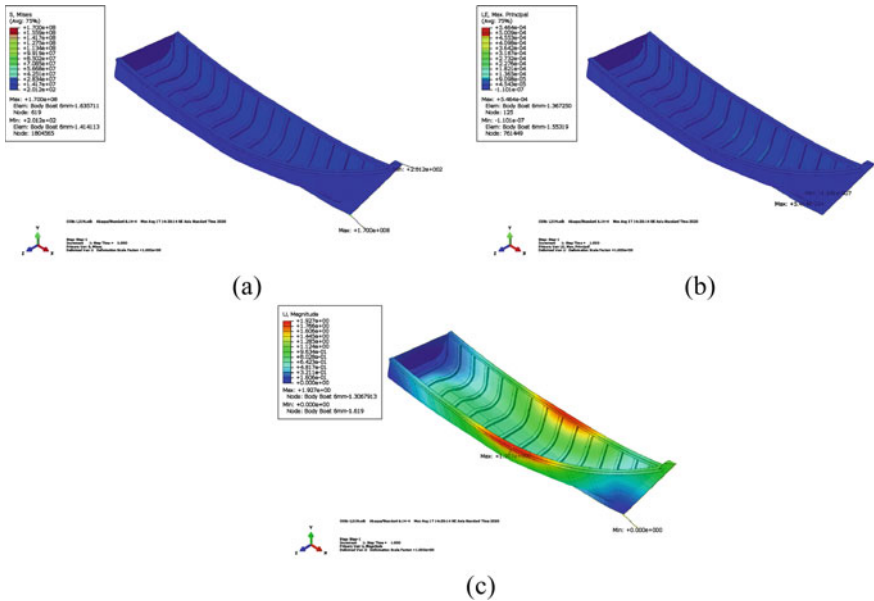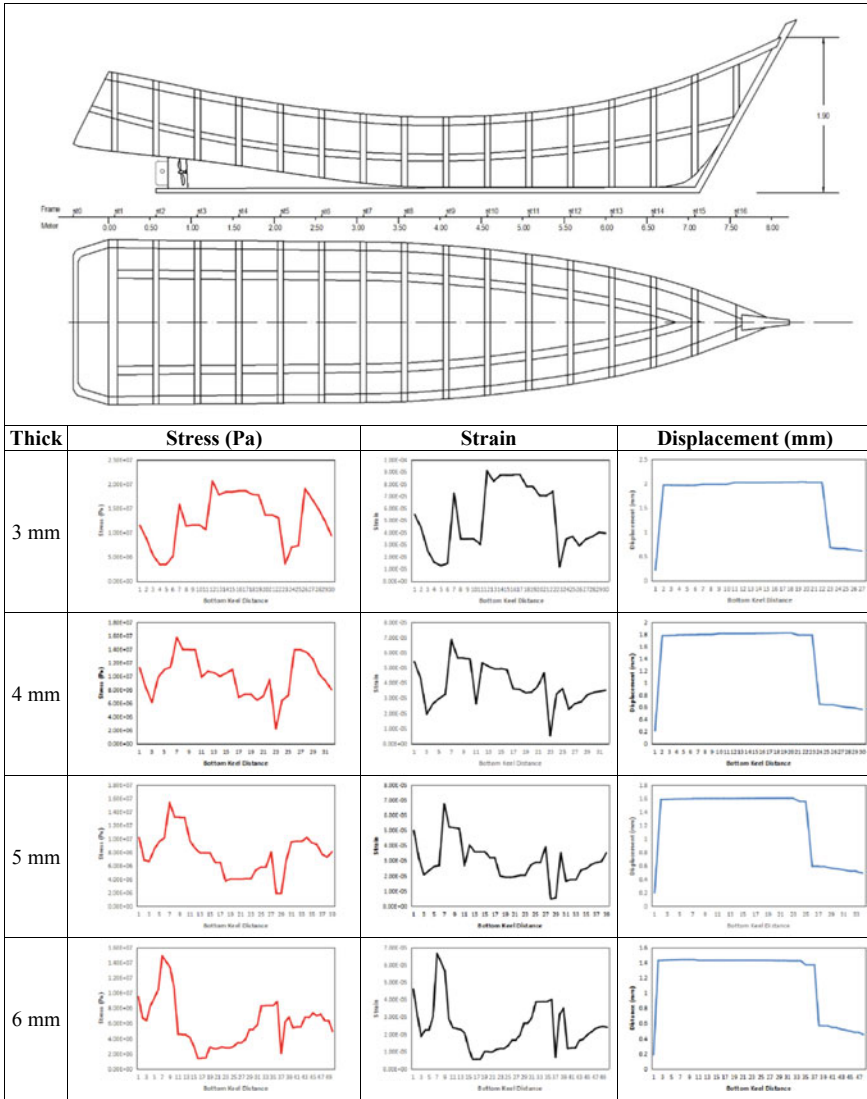

Fig. 11 Traditional Aceh fishing boat with 3500 N as loading application with 6 mm of plate thickness: **a** Stress, **b** Strain, and **c** displacement

Fig. 12 Stress, strain, and displacement distribution along the mainframe of a traditional Aceh fishing boat with a load number is 3500 N

1.1×10^{-3} with third scenario loading conditions (load 4200 N) with a plate thickness is 6 mm. The maximum displacement is 4.76 mm formed in the third scenario loading conditions (load 4200 N). The simulation results show that there is an increase in stress and strain with an increase in the loading value given in the simulation. However, the displacement value decreases with increases in the load applied to the boat structure. Furthermore, the thickness of the steel plate also

Fig. 13 Traditional Aceh fishing boat with 4200 N as loading application with 3 mm of plate thickness: **a** Stress, **b** Strain, and **c** displacement

Fig. 14 traditional Aceh fishing boat with 4200 N as loading application with 4 mm of plate thickness: **a** Stress, **b** Strain, and **c** displacement

Fig. 15 Traditional Aceh fishing boat with 4200 N as loading application with 5 mm of plate thickness: **a** Stress, **b** Strain, and **c** displacement

Fig. 16 Traditional Aceh fishing boat with 4200 N as loading application with 6 mm of plate thickness: **a** Stress, **b** Strain, and **c** displacement

Fig. 17 Stress, strain, and displacement distribution along the mainframe of a traditional Aceh fishing boat with a number load is 4200 N

affects the number of stress and strain produced from the simulation. The number of stress and strain increases with increasing thickness of the steel plate. Subsequently, the displacement value decreases with increasing thickness of the steel plate.

Traditional Aceh fishing boat manufacturing. Traditional Aceh fishing boat production has been carried out at the Material and Combustion Engineering Laboratory at the Mechanical Engineering Department of Universitas Syiah Kuala.

Table 3 Maximum stress, strain, and displacement with various loading conditions and different plate thicknesses

Scenario Loading Conditions	Plate thickness (mm)	Stress (MPa)		Strain		Displacement (mm)	
		Min.	Max.	Min.	Max.	Min.	Max.
First loading condition as 2100 N	3	8.36×10^{-3}	89.2	–	4.17×10^{-4}	–	2.37
	4	8.36×10^{-4}	110	–	4.71×10^{-4}	–	2.31
	5	2.28×10^{-4}	132	–	4.16×10^{-4}	–	2.10
	6	2.01×10^{-4}	170	–	5.46×10^{-4}	–	1.93
Second loading condition as 3500 N	3	1.40×10^{-2}	212	–	6.96×10^{-4}	–	3.96
	4	1.39×10^{-3}	183	–	7.87×10^{-4}	–	3.86
	5	3.8×10^{-4}	221	–	6.94×10^{-4}	–	3.52
	6	3.36×10^{-4}	284	–	9.12×10^{-4}	–	3.22
Third loading condition as 4200 N	3	1.67×10^{-2}	254	–	8.35×10^{-4}	–	4.76
	4	1.67×10^{-3}	220	–	9.45×10^{-4}	–	4.63
	5	4.56×10^{-4}	265	–	8.34×10^{-4}	–	4.23
	6	4.03×10^{-4}	340	–	1.10×10^{-3}	–	3.87
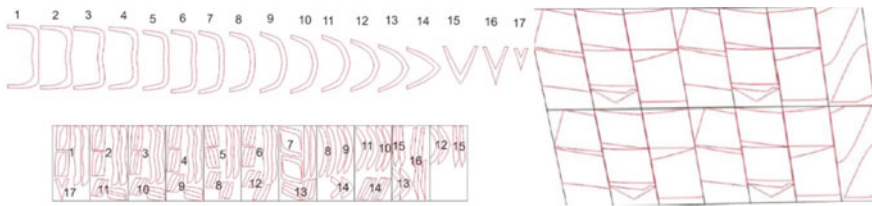
Fig. 18 Schematic of cutting a metal plate to be cut via CNC plasma cutting

Boat design is done using CAD software to produce working drawings and 3D design of a traditional Aceh fishing boat model. Furthermore, the model is cut using a CNC plasma arc cutting, the shape and cutting parts are as shown in Fig. 18. The pieces of low carbon steel plate are then assembled by welding techniques. The cutting and welding processes can be seen in Fig. 19.

4 Conclusions

Stress, strain, and displacement on traditional Aceh fishing boats with various loading variations have been analyzed through FAE simulations and are discussed in this paper. The results of this analysis will obtain the maximum and minimum values (for stress, strain, and displacement). The maximum stress obtained is 340 MPa and the maximum strain obtained is 1.1×10^{-3} with third scenario

Fig. 19 Manufacturing traditional Aceh fishing boat through metal cutting and welding processes

loading conditions (load 4200 N) and the plate thickness is 6 mm. The maximum displacement is 4.76 mm at third scenario loading conditions (4200 N load).

The location area that occurs on the traditional Aceh fishing boat for the three load variations applied for shows at the front bottom keel, this can be seen in the maximum stress and strain which is 6 mm of the hull thickness. Whereas the location of maximum displacement shows at the upper midship body draft with 3 mm of hull thickness, this occurs in the third loading scenario. The simulation results show the influence of increasing stress and strain on the loading variation applied to simulation. The number of stress and strain increases with the increasing number of the load. However, the displacement value decreases when the number of loads applied to boat structures increases. The thickness of the steel plate also affects the value of stress and strain produced. The number of stress and strain increases with the thickness of the steel plate, but the displacement value decreases with increasing thickness of the plate steel. So that it can be recommended to improve the traditional Aceh fishing boat design on the upper midship body draft, the improvements are intended for safety during boat applications at the ocean.

The results of the stress, strain, and displacement analysis are needed to optimize the design and manufacturing of traditional Aceh fishing boats. The manufacturing of traditional Aceh fishing boats goes through two processes. Specifically, metal cutting using a CNC plasma cutting then assembling it with a metal welding process. Generally, the hull traditional Aceh fishing boat was produced by wood, particularly for a size of about three GT. The change of material from wood to low carbon steel has been successfully analyzed numerically and manufactured through this study.

References

1. Mohtadi-Bonab MA, Mousavi H, Pourazizi R, Szpunar JA (2020) Finite element modeling of HIC propagation in pipeline steel with regard to experimental observations. Int J Hydrogen Energy 45(43):23122–23133. https://doi.org/10.1016/j.ijhydene.2020.06.054
2. Ghaderi M, Gerami M, Vahdani R (2020) Performance Assessment of Bolted Extended End-Plate Moment Connections Constructed from Grade St-37 Steel Subjected to Fatigue. J Mater Civ Eng 32(5):1–15
3. Ameen HA, Hassan KS (2010) Influence of Butt Welding Shapes Design on the Microstructure and Stresses of Low Carbon Steel. Eng & Tech J 28(15):5036–5047
4. Abo-Elkhier M, Muhammad K (2020) Failure analysis of an exploded large-capacity liquid storage tank using finite element analysis. Eng Fail Anal 110:104401. https://doi.org/10.1016/j.engfailanal.2020.104401
5. Akhyar H, Hasanuddin I, Farhan A (2019) Structural Simulations of Bicycle Frame Behaviour under Various Load Conditions. Materials Science Forum 961:137–147. https://doi.org/10.4028/www.scientific.net/MSF.961.137
6. Fadaei A, Mokhtari H (2015) Finite Element Modeling and Experimental Study of Residual Stresses in Repair Butt Weld of St-37 Plates. Transactions of Mechanical Engineering 39 (M2):291–307
7. Taskaya S, Zengin B, Kaymaz K, Askin M (2019) Elastic Stress Analysis of St 37 and St 70 Steels with Finite Element Method. Int J Mat Sci Appl 8(6):103–108
8. Johnson HE, Louca LA, Mouring S, Fallah AS (2009) Modelling impact damage in marine composite panels. Int J Impact Eng 36:25–39. https://doi.org/10.1016/j.ijimpeng.2008.01.013
9. Sathis Kumara S, Milwich M, Deopura BL, Plank H (2011) Finite element analysis of Carbon composite sandwich material with agglomerated Cork core. Procedia Engineering 10:478–483
10. Caramatescu A, Iulian Mocanu C (2019) Experimental and numerical evaluation of wave impact stress on a composite boat hull. Materials Today: Proceedings 12:440–445
11. Reddy AC (2017) Influence of Stiffeners on Strength of E-Glass/Epoxy Composite Submergible Hull Subjected to Shock Pressure Load using Finite Element Method. Materials Today: Proceedings 4:7507–7518
12. Nugroho A, Khaeroman, Nubli H, Prabowo AR, Yudo H (2020) Finite Element Based Analysis of Steering Construction System of ORCA Class Fisheries Inspection Ship. Procedia Structural Integrity 27:46–53. https://doi.org/10.1016/j.prostr.2020.07.007

13. Song HC, Kim T, Jang CD (2010) Structural design optimization of racing motor boat based on nonlinear finite element analysis. Inter J Nav Archit Oc Engng 2:217–222

14. Imran M, Shi D, Tong L, Waqas HM (2019) Design optimization of composite submerged cylindrical pressure hull using genetic algorithm and finite element analysis. Ocean Eng 190:106443. https://doi.org/10.1016/j.oceaneng.2019.106443

15. Kasim SY, Abttan NS (2018) Experimental Comparison Study on Stress Relief for Welded Low Carbon Steel (St 37) Bar by Vibration Mechanism and Heat Treatment Process. IOP Conf. Series: Materials Science and Engineering 454:1–7, https://doi.org/10.1088/1757-899x/454/1/012121

16. Akhyar H, Ali M, Ali N, Farhan A (2020) Effect of Different Gating Systems and Sand Mold Binder on the Cast-Quality of Bicycle Frame Produced through Sand Casting Method. Defect and Diffusion Forum 402:100–107. https://doi.org/10.4028/www.scientific.net/DDF.402.100

17. Ahmad F, Masri A (2019) Experiment on Hardness and Impact Strength of Recycled Aluminum Alloys by Metal Casting Process. Mat Sci Forum 961:65–72. https://doi.org/10.4028/www.scientific.net/MSF.961.65

18. Akhyar H, Iswanto PT, Malau V (2018) Non Treatment, T4 and T6 on Tensile Strength of Al-5.9Cu-1.9 Mg Alloy Investigated by Variation of Casting Temperature. Mat Sci Forum 929:56–62. https://doi.org/10.4028/www.scientific.net/MSF.929.56

19. Riswanda A, Sugianto H, Rizal KS (2020) Numerical Simulation of the Effect of Shoulder Rotation on the Tensile Strength of FSW Dissimilar Joints of Aluminum Alloy. Defect and Diffusion Forum 402:90–99. https://doi.org/10.4028/www.scientific.net/DDF.402.90

20. Ananthakumar K, Rajamani D, Balasubramanian E, Paulo Davimc J (2019) Measurement and optimization of multi-response characteristics in plasma arc cutting of Monel 400™ using RSM and TOPSIS. Measurement 135:725–737

A Simple Low-Cost Apparatus for of Single Fiber Tensile Strength Measurement

S. Sabri, Z. Fuadi, R. Kurniawan, I. Hajar, Samsul Rizal, and H. Homma

Abstract Concerns about environment impacts of synthetics fiber composites usages have led to various researches in Natural Fiber Composites (NFCs). Since various natural fibers are available worldwide, one of the issues in its application is the evaluation of mechanical properties of the fiber. In this study, we have designed a simple low-cost tensile test apparatus for evaluation of ultimate tensile strength of single natural fiber. The simple apparatus is built using a low-cost linear stage driven by a stepper motor. A cantilever spring is employed to measure the tensile force during the tensile test. The apparatus shows a good performance when used to evaluate the maximum tensile strength of single Abacafiber. However, the apparatus still has the limitation in that it has no feature to measure the fiber's elongation during the test. Nevertheless, the apparatus is considered useful for preliminary evaluation of the ultimate tensile strength of various single natural fiber.

Keywords Tensile test · Single fiber · Test apparatus · Ultimate tensile strength

1 Introduction

Natural Fiber Composites (NFCs) have been extracting attentions from many researchers because it could reduce the environmental impacts of synthetics fiber composites applications. NFCs have advantages such as [1] low density but high

S. Sabri
Doctoral School of Engineering, Postgraduate Study Program, Universitas Syiah Kuala, Banda Aceh 23111, Indonesia

Z. Fuadi (✉) · R. Kurniawan · S. Rizal · H. Homma
Department of Mechanical and Industrial Engineering, Universitas Syiah Kuala, Banda Aceh 23111, Indonesia
e-mail: zahrul.fuadi@unsyiah.ac.id

I. Hajar
Undergraduate Study Program, Department of Mechanical and Industrial Engineering, Universitas Syiah Kuala, Banda Aceh 23111, Indonesia

modulus and stiffness, renewable, low-production cost, low-hazard, produces low emission, and less abrasive. Natural fibres such as Ramie, Flax, Hemp, Jute, Sisal, and Abaca have been applied as natural reinforcing material in matrix composites and they have been showing promising results in various applications. Nevertheless, there are still various kinds of natural fibres available worldwide that are still unexplored which could have good properties for natural composite reinforced materials.

Among the most important factors in fiber selection for reinforcing material are the tensile strength and the interfacial shear strength. These two factors determine the performance of the composites since they decide the bonding strength between the fiber and the matrix. The interfacial shear strength of the fiber and the matrix have become the focus of several researchers previously [2–4].

Despite various kind of natural fiber availability, the mechanical properties of the fiber, such as tensile strength and interfacial shear strength, are still limitedly available. This is due to wide variation of fiber and matrixes selection as well as the limitation in the test equipment designated to natural fiber especially that for single fiber. The commonly available tensile test equipment is generally designed for high load so that they are less sensitive for evaluation of single fiber, which usually breaks at a tensile force less than 40 N [5].

In this study, we have designed a simple low-cost test apparatus for evaluation of the ultimate tensile strength of single natural fiber. The test apparatus is designed based on, although not fully complied to, ASTM-D3379-75; the standard test method for tensile strength and Young's Modulus for high modulus single filament materials. The objective of this study is to fabricate a simple and low-cost experiment set up to enable a simple and low-cost evaluation for the ultimate tensile strength of various single natural fiber. The apparatus is designed with flexibility to enable various modifications conducted to the main components for flexibility in the evaluation.

2 Apparatus Set-Up and Data Acquisition

2.1 Apparatus Set-Up and Components

The apparatus setup for the tensile test is given in Fig. 1. It consists of a linear guide equipped with a worm gear driven by a DC stepper motor. The linear guide has a maximum sliding distance of 150 mm. An x-y-z stage is installed on the linear guide stage. The x-y-z stage is installed for the alignment purpose of the single fiber specimen prior to the tensile test, controlled by micro meter screws. An L-shape bar base structure is installed on the x-y-z stage to support the specimen's holder. A cantilever beam is installed on the base.

In the tensile test, the specimen is positioned between two C-shape holders. The fiber specimen is mounted on a piece of paper using adhesive tape. Before the tensile
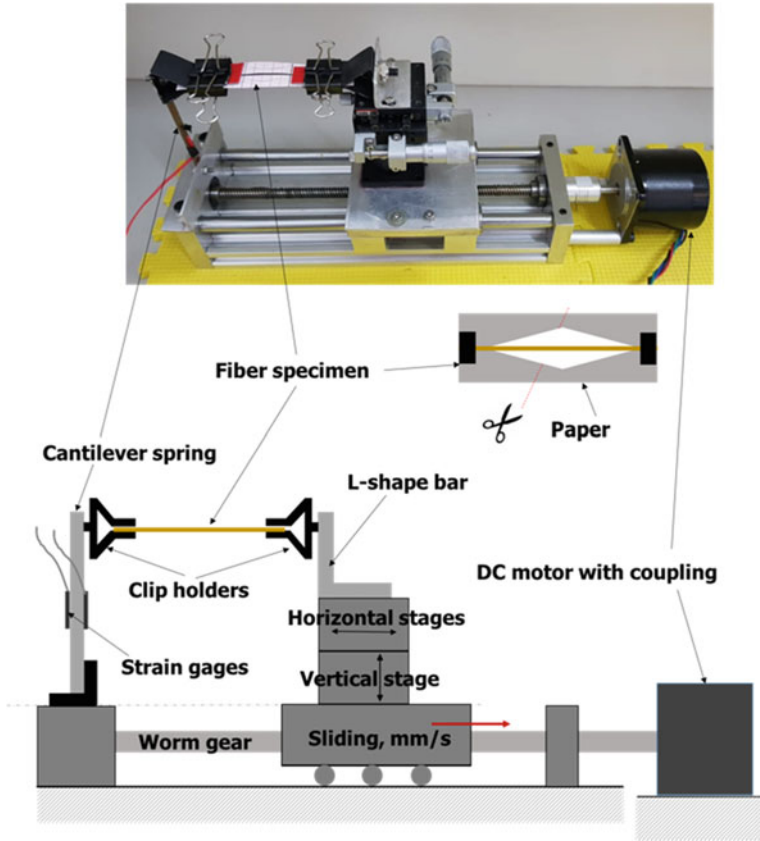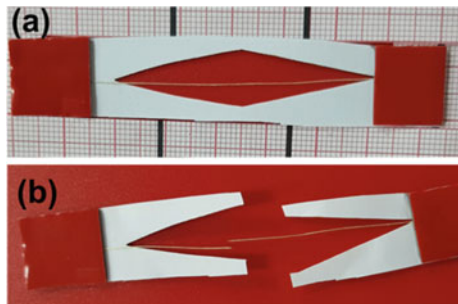
Fig. 1 The simple test apparatus for single fiber tensile test

Fig. 2 A single
fiber specimen before the test
(**a**) and after the test (**b**)

test, the paper is cut and the specimen is aligned horizontally by adjusting the x-y-z stages. A fiber specimen is shown in Fig. 2. Figure 2a shows the specimen before the tensile test and Fig. 2b shows that after the test showing broken fiber after subjected to tensile force.

The length of the specimen shown in Fig. 2 is 8 cm. Here, the gauge length of the fiber is 5 cm, which means that in the tensile test it is expected that the fiber will break at a location somewhere at ±2.5 cm from the centre. The designed apparatus allows the maximum gauge length of the specimen up to 15 cm.

The linear stage is moved in horizontal direction using the stepper motor by means of a worm gear shaft. The 12 V DC motor rotation is controlled by an Arduino controller through a Personal Computer (Fig. 3). The speed of linear stage is determined by the number of steps-per-second assigned to the stepper motor. The motor used in this setup allows the linear stage to slide at maximum speed of 50 mm/s without any load.

2.2 Data Acquisition

In order to record the tensile force data during a tensile test, a DAQ (Data Acquisition) system was built (Fig. 4). It consists of a pair of strain gauges, a cantilever beam, a bridge box, a strain amplifier, and a DAQ software installed on a PC. The data acquisition system is built based on Kyowa instrumentation system.

The cantilever beam (Fig. 5) is used to acquire the tensile force applied during the tensile test by means of the strain gauges. The beam is made of Copper-Zinc alloy, 2 mm thick, 4 mm wide, and 100 mm long. Two strain gauges, KFGS-1-120-C1-16 L1M2R made by Kyowa, were installed on the middle of the beam, 50 mm from the top. The beam is bolt-mounted on an L-shape bar mounted to the base.

The theoretical deflection of the cantilever beam is given in Fig. 6 for tensile force up to 15 N. The calculation was conducted by assuming that the length of the cantilever beam is 85 mm (from the edge of L-shaped bar to the specimen's mount)
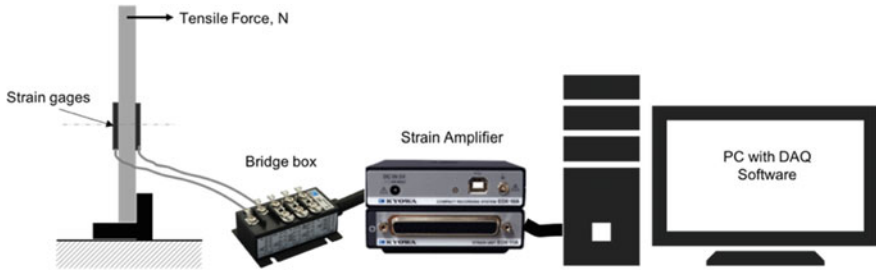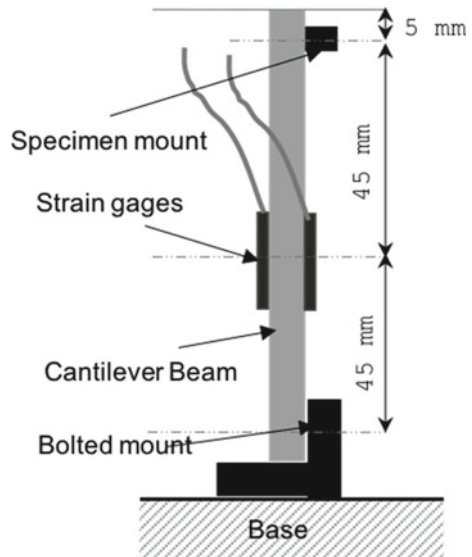

Fig. 3 Motor speed controller
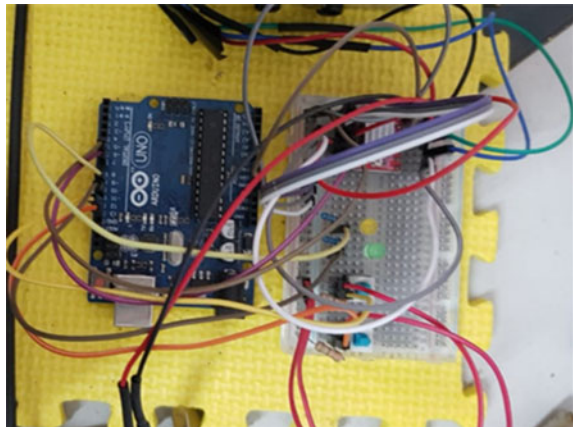
Fig. 4 Data acquisition components

Fig. 5 Cantilever beam

and the Young's Modulus value of the material is 117 GPa. The maximum deflection, δ_{max}, of the beam at tensile force of 15 N, which is the maximum designed load, is 2.46 mm with an angle of deflection of 2.48°. At the tensile force of 5 N, the maximum deflection, δ_{max}, is 0.82 mm.

Kyowa DCS100A Dynamic Data Acquisition Software is used for data acquisition. The allowable sampling frequency of the software is from 1 Hz to 10 kHz. The software allows the conversion of the recorded data, which is in the format of KS3 file, to a number of file formats such as CSV file which can later be processed by using spreadsheet or other data processing software.
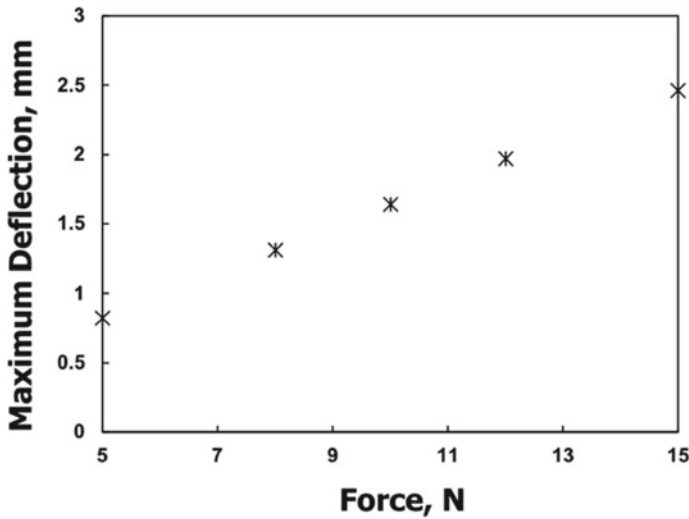
Fig. 6 Theoretical deflection of the beam

3 Results and Discussion

3.1 Load Calibration

One of the most important factors in a tensile test is the tensile force application. On this apparatus, the tensile force is achieved as the result of linear stage movement in horizontal direction, in which the value of the force is acquired by a pair of strain gages installed on the cantilever beam. Since the data acquired is the strain, it is necessary to establish a relationship between the strain, μm/m, and the force, N, for the particular cantilever beam. Figure 7 illustrates the method for tensile force calibration.

The method simply uses a bucket filled with water, in which the weight of the bucket depends on the volume of the water (Fig. 7). Three loads were used for the calibration; 3 N, 5 N, and 6.4 N. The load was measured by using a weight scale having a tolerance of 1 g. The result is given in Fig. 8. The three loads used resulted in strain of 140 μm/m, 234 μm/m, 306 μm/m for the respective load of 3 N, 5 N, and 6.4 N. Using this results, the relationship between the load, N, and the strain, μm/m, for the particular cantilever beam setting can be written as follows.

$$\text{Load}, N = 0.0208 * \text{Strain}\left(\frac{\mu m}{m}\right) \tag{1}$$

Therefore, Eq. 1 is the constant for the cantilever beam. In the tensile test, Eq. 1 is used to calculate the value of maximum tensile force at the fiber break-up using the acquired strain value.
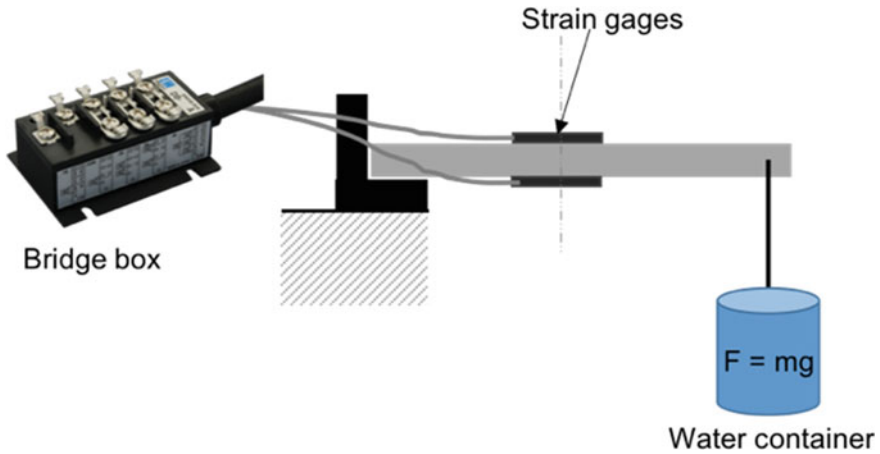
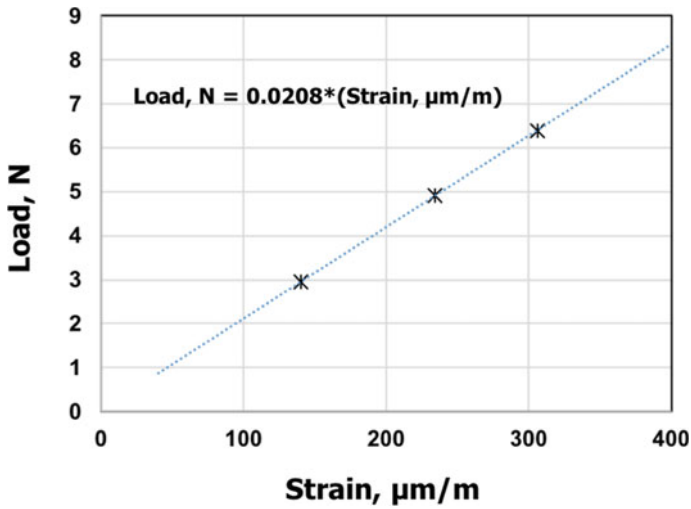**Fig. 7** Load calibration method

Fig. 8 Cantilever beam constant; relationship between strain and force

3.2 Strain vs. Time Relationship

A particular result of the tensile test is given in Fig. 9. It can be observed that the force application started after 2 s recording time. The tensile force increased linearly with time until reaching maximum at a strain value about 246 μm/m at 18.8 s. Thus, in this particular test, the time from fist tensile force application until break-up was about 16.8 s. This data was acquired with a sampling frequency of
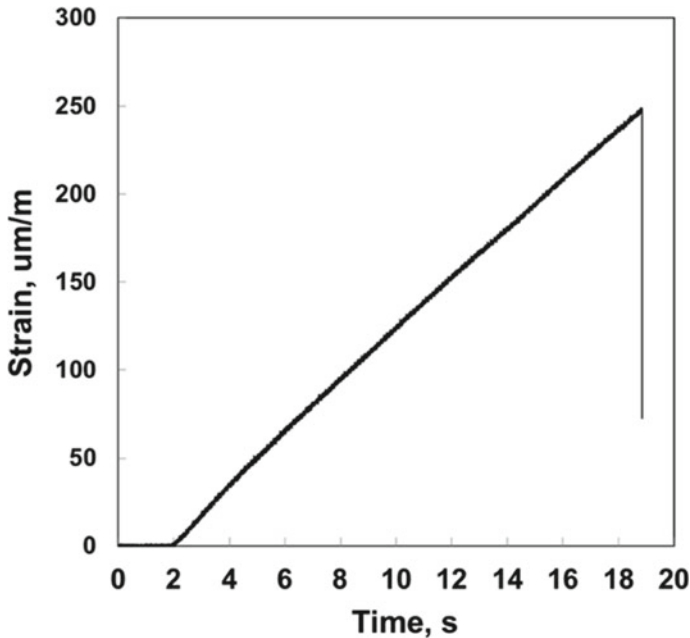
Fig. 9 A result of tensile test

1 kHz. The tensile force during this period can be obtained by using Eq. 1. For this case, the strain value of 246 μm/m is equal to a tensile force of 5.1 N.

The strain rate at which the data is recorded in Fig. 9 is 14.65 μm/m/s; equal to a loading rate of 0.3 N/s. Depending on the speed of the linear stage, which is controllable by motor rotation, the loading rate can be adjusted. However, the loading rate is decided by the stiffness of the cantilever spring and the speed of the linear stage. Figure 10 shows two tensile tests conducted at two different strain rates. For this particular apparatus, the maximum recommended loading rate is 1 N/s. Here, the loading rate more than 1 N/s is not recommended because it may cause a slippage in the stepping motor.

The strain rate or loading rate for the tensile test of single fiber is seldom discussed in literature. However, ASTM D3379-75 [6] indicated that the movable member should be driven to have a constant strain rate. Here, it is shown by Figs. 9 and 10 that constant strain rates were achieved.

3.3 Ultimate Tensile Strength

Single Abaca fiber were selected as specimens for evaluation of tensile strength using the designed apparatus. Five specimens were prepared with a gauge length of
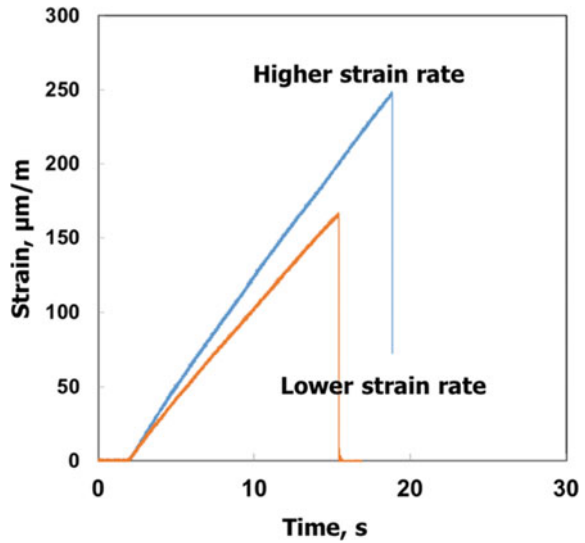
25 mm. The single fiber were randomly selected from an Abaca trunk. No additional treatments were applied to the fiber. The tensile tests were conducted with a loading rate of 0.3 N/s with a linear stage movement of 0.05 mm/s.

The results of the tensile tests are given in Fig. 11. Specimen No. 1 broke at a maximum strain of 248 μm/m equal to a maximum tensile force of 5.16 N. The maximum tensile forces for other four specimens are 5.26 N, 5.66 N, 5.84 N, and 6.3 N for respective specimen Nos. 2–4. It can be seen in Fig. 12 that all five tests were having a relatively similar loading rate.

The calculation of ultimate tensile strength of the fiber requires a microscopic evaluation of the cross-sectional area of each fiber. Due to large distribution of the cross-sectional area of the fiber along its longitudinal direction, some researchers used the average value of diameter which is evaluated for certain length [7]. For this particular case, the diameter of the single fibre was determined by evaluating the width of the fibre at break-up location. This assumption is taken because the break-up location tends to occur at the weakest part, which in this case the location where cross-sectional area is the smallest.

Figure 12 shows a single fiber at break-up location. Here, it is assumed that the fiber has a circular cross-section. Using this assumption, the single fiber shown in Fig. 12 has a diameter of 100 μm, which resulted in a cross-sectional area of 0.0082 mm^2. Using this value, the ultimate tensile strength of this particular fibre is calculated as 657 MPa.

Using similar assumption, the ultimate tensile strengths of the five specimens are given in Table 1. The maximum value of the tensile strength occurred for specimen No. 4, i.e. 1.012 MPa, while the smallest value occurred for specimen No. 3 with a value of 423 MPa. The value of the tensile strength may differ according to the method of determining the cross-section area of the fiber. Liu et al. [7] measured the
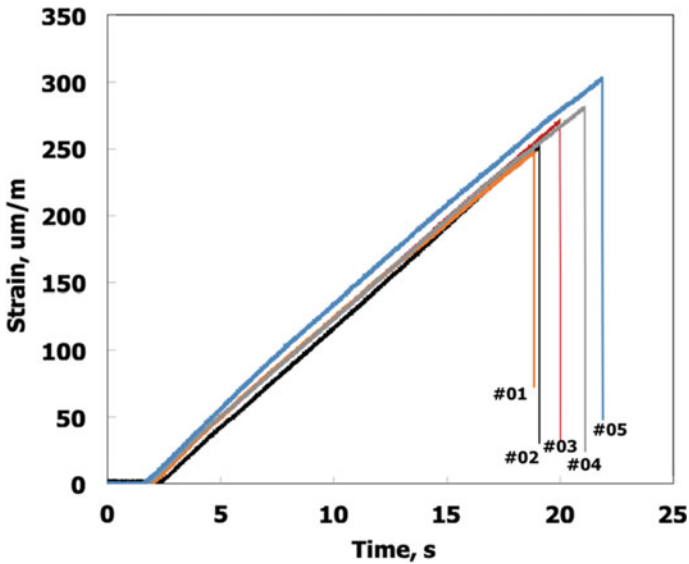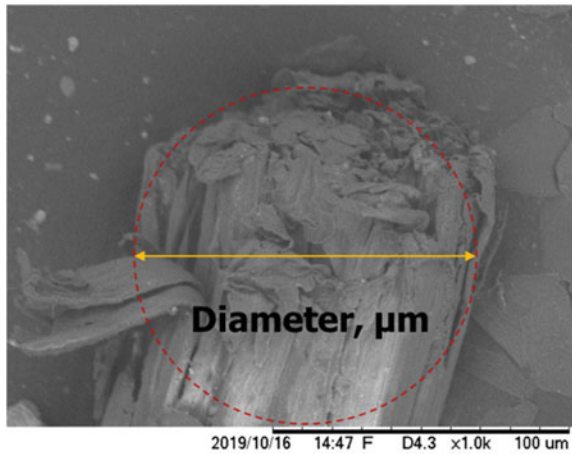
Fig. 11 Maximum strain at fiber break-up

Fig. 12 Assumption for diameter evaluation of the fiber

average diameter of the single fiber using optical observation at three locations. A more reliable result of the tensile strength value could be obtained by individual observation of the cross-section area at break-up point using three-dimensional high magnification optical microscope such as SEM in the axis normal to load application. However, conducting such analysis can be complicated and time consuming. Therefore, the exact value of the tensile strength of natural fiber depends not solely on the tensile test apparatus but also to the method used for cross-sectional area measurement.

Table 1 Maximum tensile strength of evaluated Abaca single fiber

Specimen no.	Strain max	Force max	Cross section area (mm^2)	Max. Tensile Strength, (MPa)
1	248	5.16	0.0082	657
2	253	5.26	0.0065	813
3	272	5.66	0.0134	423
4	281	5.84	0.0058	1.012
5	303	6.3	0.0121	519

In literatures, there are a wide range value of the tensile strength of Abaca single fiber. Among those are 717 MPa [4], 755 MPa [3], 955.7±299.7 MPa [8], and 500 MPa [9]. This wide variation of the tensile strength value and its margin of errors is caused by the randomness of the fiber's dimension, which is caused by the nature of its cultivation region as well as climates.

3.4 Limitation

The standard test method for tensile strength and Young's Modulus evaluation for high modulus single filament materials is described in ASTM-D3379-75 [6]. However, the test apparatus designed in this paper does not have full compliance to the standard's requirements. The limitation is that the system has no equipment for evaluating the elongation of the fiber during the tensile test. Therefore, the value of Young's Modulus for the evaluated fibre cannot be determined.

4 Conclusion

A simple experimental setup for tensile strength evaluation of single fiber has been designed in this study. The experiment setup uses a low-cost linear stage driven by a stepper motor controlled by an Arduino board. The data acquisition system is build using Kyowa instruments and data acquisition software. The performance of the tensile test apparatus was tested by using single abaca fibre. The results show that the fiber broke at a maximum tensile force between 5.16 N and 6.3 N, which resulted in ultimate tensile strength values from 423 MPa to 1.012 MPa.

The designed system has a limitation because it has no apparatus to measure the elongation of the fiber during the tensile test. Therefore, the value of Young's Modulus of the fiber cannot be calculated. Despite this limitation, such simple apparatus is considered having a good cost benefit for preliminary evaluation of the tensile strength of various single natural fiber.

References

1. Pickering KL, Efendy MGA, Le TM (2016) A review of recent developments in natural fibre composites and their mechanical performance. Compos A Appl Sci Manuf. https://doi.org/10.1016/j.compositesa.2015.08.038
2. Zhang Y, Li Y, Ma H, Yu T (2013) Tensile and interfacial properties of unidirectional flax/glass fiber reinforced hybrid composites. Compos. Sci. Technol. https://doi.org/10.1016/j.compscitech.2013.08.037
3. Cai M et al (2015) Influence of alkali treatment on internal microstructure and tensile properties of abaca fibers. Ind Crops Prod. https://doi.org/10.1016/j.indcrop.2014.11.048
4. Cai M, Takagi H, Nakagaito AN, Li Y, Waterhouse GIN (2016) Effect of alkali treatment on interfacial bonding in abaca fiber-reinforced composites. Compos. Part A Appl. Sci. Manuf. https://doi.org/10.1016/j.compositesa.2016.08.025
5. Cline J, Wu V, Moy P (2018) Assessment of the Tensile Properties for Single Fibers
6. ASTM (1989) Standard Test Method for Tensile Strength and Young' s Modulus for High-Modulus. ASTM Int, pp. 1–5
7. Liu K, Takagi H, Yang Z (2013) Dependence of tensile properties of abaca fiber fragments and its unidirectional composites on the fragment height in the fiber stem. Compos Part A Appl Sci Manuf. https://doi.org/10.1016/j.compositesa.2012.09.006
8. Symington MC, Banks WM, West OD, Pethrick RA (2009) Tensile testing of cellulose based natural fibers for structural composite applications. J Composite Mat. https://doi.org/10.1177/0021998308097740
9. Joseph S, Sreekala MS, Oommen Z, Koshy P, Thomas S (2002) A comparison of the mechanical properties of phenol formaldehyde composites reinforced with banana fibres and glass fibres. Compos Sci Technol. https://doi.org/10.1016/S0266-3538(02)00098-2

Three Dimensional Modeling Fractured Bone Reconstruction Using CT Scan Images

Irwansyah, Asbar, Redyarsa D. Bintara, Jiing-Yih Lai, and Pei-Yuan Lee

Abstract The medical three-dimensional model currently uses as an invaluable source of information to enhance clinicians in preoperative surgical planning. The favourable computer-aided design tool applied to improve the visualization quality of the medical model. In this study, the virtual reconstruction of proximal femur fractures with multi fragments was included. The mesh correction and smoothing algorithm also performed. The aim study is to analyze each step of the visualization digital model and their aspects that affect the accuracy and reproducibility. It found the complex fracture model took longer to reconstruct the virtual model. The beneficial approaches described in this study are not just limited to orthopaedic case, but also for many other fields of medicine.

1 Introduction

Three-dimensional (3D) virtual medical modeling has become state-of-the-art in preoperative surgical planning. The rapid growth of computer imaging technology transforms the traditional method from manual sketching to computerization. Generally, 3D-preoperative planning software assists the clinician to demonstrate a 3D medical model, diagnose malunity, and virtually planning before held in the theater room [1, 2]. The use of computer-preoperative planning also leading to

Irwansyah (✉) · Asbar
Department of Mechanical Engineering, Universitas Syiah Kuala, Banda Aceh, Indonesia
e-mail: irwansyah@unsyiah.ac.id

R. D. Bintara
Department of Mechanical Engineering, Universitas Negeri Malang, Malang, Indonesia

J.-Y. Lai
Department of Mechanical Engineering, National Central University, Taoyuan, Taiwan

P.-Y. Lee
Orthopedic Department, Show Chwan Memorial Hospital, Changhua, Taiwan

reduce surgical time and potential misinterpretations, as a consequence benefit is reducing the recovery time [3]. Computer-aided design (CAD) as a representative tool in engineering design and modeling is now being used extensively in medical modeling. Typically, a 3D bone model is constructed by extracting the boundary pixels of a bone structure on each slice of computed tomography (CT) images, following by bone segmentation, bone reduction, and implant fixation procedures. Precisely geometry to imitate the anatomic structure is the key to the successful treatment of bone fractures. Several 3D medical model reconstruction techniques were reported based on a 2D X-ray image and from CT images [4, 5]. However, the method which offers acceptable accuracy and appropriate local minima with fewer geometric errors still is debatable. The objective of this study is to describe and illustrate those aspects of each step of the virtual model reconstruction that affect the accuracy and reproducibility of the 3D medical models.

2   Methods

A patient's fractured femur data, intertrochanteric hip fractures with multi frag-ments AO/OTA 31-A2 were included in this study. The 3D femur model was developed prospectively, based on a CT scanned image using clinical CT images, 0.2 mm slice interval between two cross-sectional images, and size 512×512 pixels on each image. Thin-slice CT was saved in Digital Imaging and Communications in Medicine 3.0 format (DICOM, .dcm), and input into the pre-operative planning system for 3D model reconstruction. The system operates in a PC-based environment including virtual surgery simulation tools into a single computer program package (Intel® Core™ i5-4440 CPU, 3.1 GHz processor, 4 GB RAM, Windows 7 operating system) [6]. The system displays a 3D model with a volume rendering technique. A multi-region segmentation was employed by sep-arating bone tissue individually from surrounded tissues. Smoothing and imaging processes were performed by adjusting threshold values to reduce the error caused by imaging geometrical noises. The 3D medical model was converted to solid models and exported to a **.STL (STereoLithography) file. Triangulated-mesh formation and correction were finally performed to meet the desired virtual model for further stages either 3D modeling or 3D printing fabrication.

3   Results and Discussion

In this study, a series of femur multi-fragments were reconstructed and repositioned into their original anatomy position. The result of 3D modeling reconstruction is presented in Fig. 1.

CT images are imported to perform the segmentation by considering the mini-mum intensity value for bone and cortical bone tissues (Fig. 1a, b). The
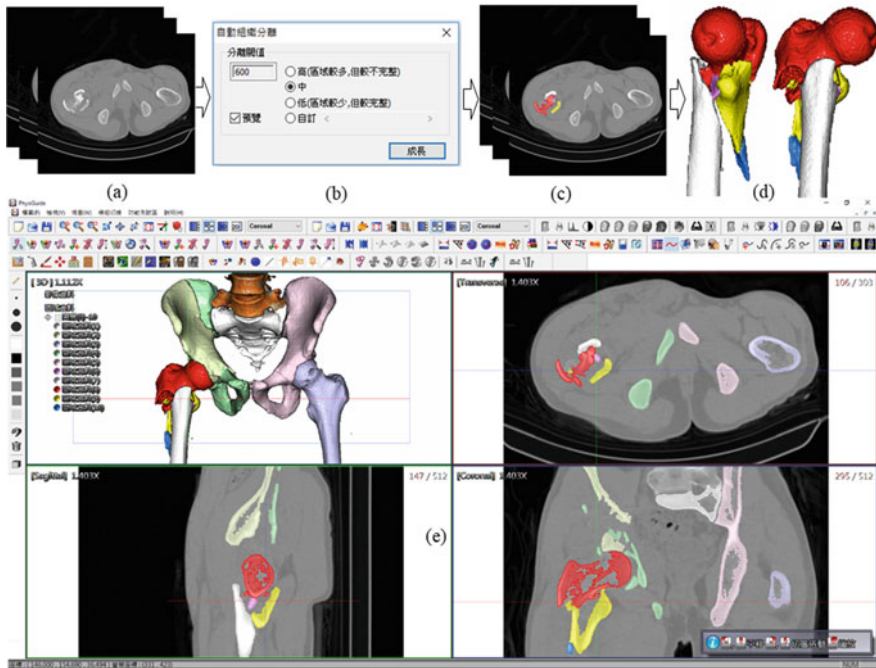
Fig. 1 Virtual fractured bone reconstruction modules, **a** CT-images, **b** GUI segmentation, **c** segmentation each images, **d** 3D fragments, and **e** 2D and 3D monitoring display

multi-region segmentation algorithm was employed to determine seed points automatically, then the region growing algorithm used to propagate regions simultaneously (Fig. 1c, d). Figure 1e depicts the screenshot after segmentation, whereas the interface displays 3D CT images where the pixels associated with each bone fragment are marked with different colors. The triangulated-meshes bone model formation is presented in Fig. 2. 3D meshes model was generated using the marching cubes algorithm. Smoothing and meshes correction was performed by adjusting the threshold value before converting the segmented model into a mesh model. The image processing approach was used to remove geometric errors for ready files in preoperative simulation and 3D printing fabrication.

The computation time for reconstructing a 3D femur AO/OTA 31-A2.2 was recorded 483 s, segmentation (134 s), and bone reduction (349 s). During segmentation, many unwanted noises and segmented artifacts can be accidentally captured. The erroneous data usually presents as the non-manifold vertices and folded poly-faces on the surface model, as presented in Fig. 3. Small poly-faces clusters within the model can also create problems when mesh correction and smoothing algorithms were applied. These drawbacks are necessary to be removed during the first stages of the process by using the mesh correction tool.
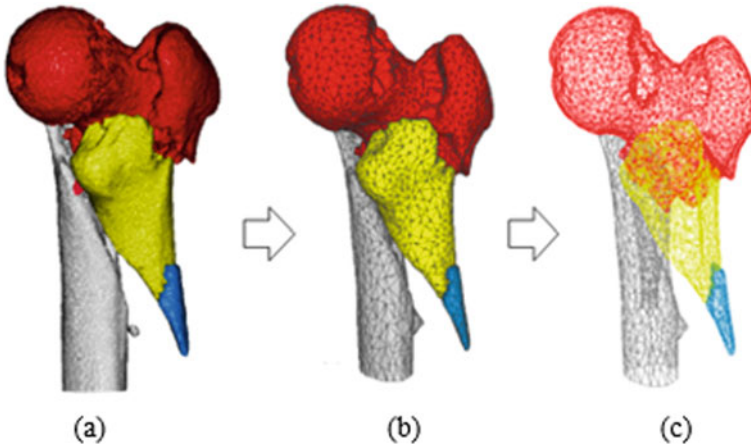
Fig. 2 Triangulated-mesh generation, **a** surface model of 3D fractured bone, **b** and **c** 3D model after the triangulated-meshes formation
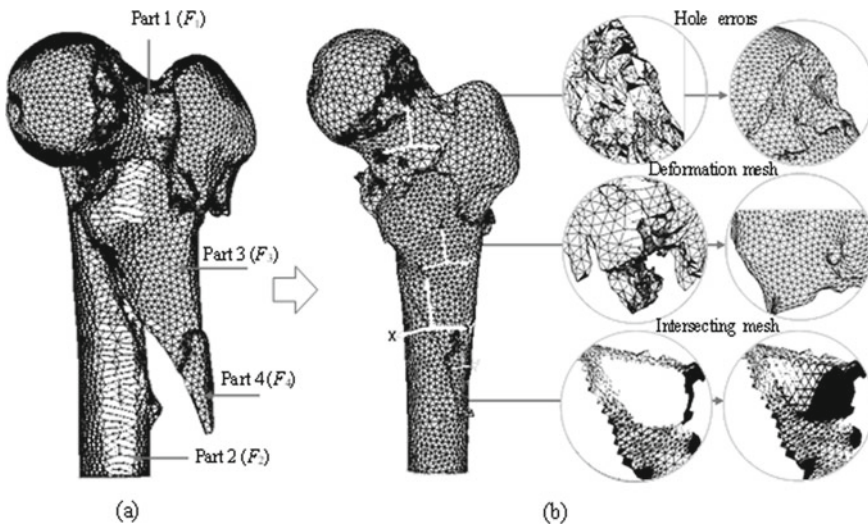
Fig. 3 The 3D Femur 31-A2.2. **a** A 3D model with four pieces of dissembled fragments, **b** assembled model and geometric defects correction on the surface model

The complexity of the microarchitecture of cancellous bone creates geometric erroneous during the model creation process. This difficulty of geometry occurs due to the complexity clusters of vertices and triangles nearby to one another. Holes defect can appear when the smoothing algorithm was performed to reduce the number of triangles in the mesh model. To create a water-tight model, the fill holes function in CAD software was used to fill the most simple holes in the mesh model.

However, mesh erroneous were still occurred when attempting to fix the complex holes, resulting in unrepresentative meshes. When this function fails to close a complex hole, the hole boundary can be simplified by break off the poly-faces into more manageable shapes for the further filling holes stage.

3D model smoothing surface strongly depends on the voxel size of the CT scan, size of the anatomy being modeled, number of fragments and level of complexity trabecular structure, and variety in a number of the poly-face mesh model. The Mesh model surface is made up of vertices that are connected by small triangles. Those triangles or poly-face count variety range, for a small tarsal bone (≤ 2000 faces) to upwards for a high-resolution scan of a skull ($\geq 5,000,000$ faces). The higher number of faces the greater the detail, as consequence high-resolution files require more computation to edit and visualize the meshes. Therefore, reducing the number of triangles early in the editing process is necessary, to minimize the processing times.

A balanced decision is required in reducing the number of polygons without losing important anatomical details. Several methods were used to reduce the number of poly-faces and vertices, and increase the uniformity of the mesh triangles [7–9]. A smoothing algorithm is used to optimize and smooth mesh quality by improving the consistency of edge lengths for each triangle that creates the appropriated meshes. Triangulated meshes have changed from a random configuration of tightly clustered triangles to a smooth and consistent mesh. Geometric erroneous and distance errors for each of the fragments before mesh correction were calculated. Facets number of fragment 1 before and after overlapping mesh removal and smoothing algorithm applied, 106,988 and 99,811, with a percentage different 6.94%. The maximum error and RMS error between two of fragment models are calculated 1.833 and 0.295 mm, respectively. The results for other fragments are shown in Table 1.

Discrepancy errors along the fragment boundaries have to be assembled as small as possible to facilitate bone adhesion. The measurement results of the gap and overlapping distance errors for the 3D femur model after modifying and smoothing, shown in Table 2. The histograms of the distance errors for both fragments showing that most of the errors are concentrated on the mean value. The percentage difference for each part of the bone model is calculated and the final model is deformed less than 2 mm from the original model. Figure 4 presents a 3D model

Table 1 Geometry errors before and after mesh-defect removing and smoothing

| Case	Fragments	Number of facts			Max. error	RMS error
		Before modified	After modified	Percentage different (%)		
Femur31-A2.2	Part 1 (F_1)	106.988	99.811	6.94	1.833	0.295
	Part 2 (F_2)	44.314	45.832	3.37	1.397	0.195
	Part 3 (F_3)	32.456	32.372	0.26	1.309	0.263
	Part 4 (F_4)	6.044	6.044	0.00	1.12	0.266

Table 2 Comparison of distance gap error 3D reduction before and after mesh defect removing

Case	Fragments	Position of measurement distance gap and overlap errors											
		1			2			3			4		
		A^a	B^b	Diff (%)	A^a	B^b	Diff (%)	A^a	B^b	Diff (%)	A^a	B^b	Diff (%)
Femur31-A2.2	F_1-F_2	1.97	1.52	25.79	3.01	2.23	29.77	2.53	1.98	24.39	1.95	1.46	28.74
	F_1-F_3	1.11	1.04	6.51	1.48	0.76	64.29	1.87	1.45	25.30	2.26	1.53	38.52
	F_2-F_3	2.26	1.44	44.32	2.66	1.83	36.97	2.4	2.48	17.01	1.79	1.65	8.14
	F_2-F_4	2.31	1.63	34.52	1.37	1.05	26.45	1.39	1.2	14.67	1.7	1.09	43.73
	F_3-F_4	2.94	2.63	11.13	2.02	1.78	12.63	1.52	1.38	9.66	2.14	1.97	8.27

[a] 3D model before optimizing and smoothing
[b] 3D model after optimizing and smoothing
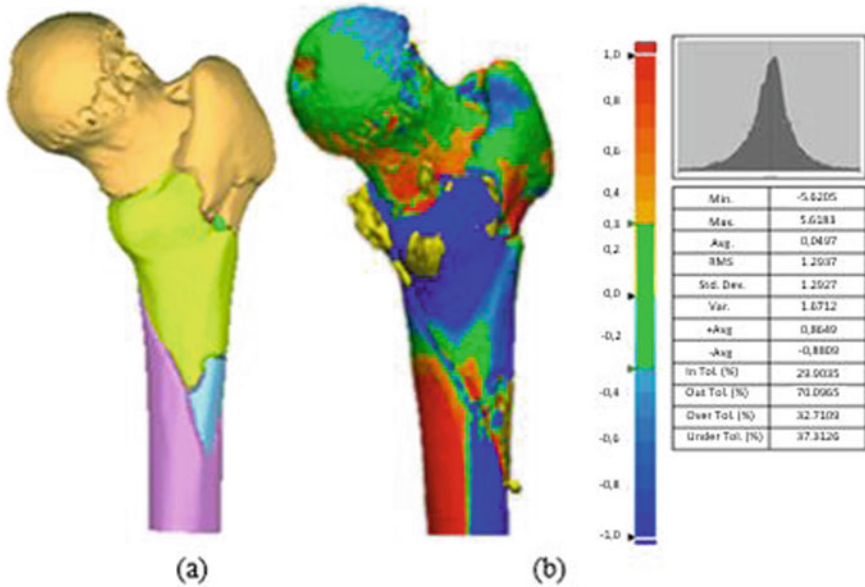
Fig. 4 Femur modeling, **a** model after mesh correction and smoothing **b** comparison original model before mesh correction

after mesh correction and smoothing compares to the original model before mesh correction and the 3D printed fabrication. Favier et al. [10] reported that a global error between non-smoothed meshes and smoothed meshes was ranged between 0.083 and 0.203 mm [10]. Thomas et al. [11] reported also that for a tibias case the alignment error of the reconstructed bone fragments was in the range of 0.03-0.4 mm [11].

It noticed that the many errors around the fragment boundary are collided and penetrated after bone reduction. The result clearly shows that applying the triangulated-mesh correction and smoothing algorithm can practically improve the quality of the 3D model for use in further stages, either simulation preoperative planning or fabrication 3D-printing.

4 Conclusion

This study proposes a comprehensive step to reconstruct the advanced visualization 3D model with more appropriate accuracy and reproducibility. The femur multi-fragments model was included and produced on average less than 10 min to digitally edit the CT scan. It found that a significant difficulty increase was observed in the number of fragments, segmentation time, reduction time, mesh editing time, and overall model built-up time. Therefore, the more complex the fracture, the

longer it took to create a model for 3D medical modeling. The beneficial proposed method is not only limited to femur fracture, but also other clinical cases of medical fields of study.

References

1. Lai JY, Yuanzhi Z, Zhang YZ (2018) Computer-Aided Preoperative Planning, and Virtual Simulation in Orthopedic Surgery: Ed. Pei G. Digital Orthopedics Springer, pp 281–306
2. Rodríguez JA, Entezari V, Iannotti JP, Ricchetti ET (2019) Pre-operative Planning for Reverse Shoulder Replacement: The Surgical Benefits, and Their Clinical Translation. Ann Joint 4:1–15
3. Atesok K, Galos D, Jazrawi LM, Egol KA (2015) Preoperative Planning in Orthopaedic Surgery Current Practice and Evolving Applications. Bull Hosp Jt Dis 73:257–268
4. Akkoul S, Hafiane A, Rozenbaum, O, et al (2017) 3D Reconstruction of the Proximal Femur Shape from Few Pairs of X-Ray Radiographs. Signal Proc.: Image Commun. 59, pp 65–72
5. Lee PY, Lai JY, Yu SA, Huang CY, Hu YS, Feng CL (2014) Computer-Assisted Fracture Reduction and Fixation Simulation for Pelvic Fractures. J Med Bio Eng, 368–376
6. Irwansyah I, Redyarsa DB, Lai JY, Essomba T, Lee PY (2018). Development of Mesh Defect Removal Algorithm to Enhance the Fitting of 3D Printed Parts for Comminuted Bone Fractures. J Med Bio Eng, pp 1–19
7. Green N, Glatt V, Tetsworth K, Wilson LJ, Grant CA (2016) A Practical Guide to Image Processing in the Creation of 3D Models for Orthopedics. Techniques in Orthopaedics 31 (3):153–163
8. Brandão J (2018) Mesh Simplification and Smoothing for Bone Fragment Models
9. Wang Y, Zheng J, Wang H (2019) Fast Mesh Simplification Method for Three-Dimensional Geometric Models with Feature-Preserving Efficiency. Scientific Programming, pp 1–12
10. Favier V, Zemiti N, Caravaca OM, Subsol G et al (2017) Geometric and Mechanical Evaluation of 3D-printing Materials for Skull Base Anatomical Education and Endoscopic Surgery Simulation-A First Step to Create Reliable Customized Simulators. PLoS ONE 12:1–16
11. Thomas TP, Anderson DD, Willis AR, Liu P, Frank MC, Marsh JL, Brown TD (2011) A Computational/Experimental Platform for Investigating Three-Dimensional Puzzle Solving of Comminuted Articular Fractures. Comp Methods Biomech Biomed Eng 14:263–270

FAE Analysis of Boat Propeller with Differences of Loading Conditions and Manufacturing by Casting Process

Iqbal, Nurdin Ali, Husni Husin, Akhyar, Khairil, and Ahmad Farhan

Abstract Finite Element Analysis (FEA) in this study was carried out on a boat propeller with five loading variations, such as 150, 300, 450, 600, and 800 MPa. The analysis carried out included stress, strain, and displacement on aluminum 8176 (AlFeSi) material. The purpose of this simulation is to analyze the maximum stress, strain, and displacement of the boat propeller with several loading variations. The process of manufacturing the propeller also has been carried out through metal casting techniques. The load is applied evenly to one side of the propeller surface with the assumption that it receives the pressure load from the water when the propeller rotates and the boat moves forward. The result is that the maximum stress and strain values are 70.03 MPa, 7.59×10^{-4} (respectively) at a load of 800 N, formed at the inner base of the propeller. The maximum displacement is 2.75 mm at the outer end of the propeller with a given load scenario of 800 N. Stress, strain, and displacement values in this simulation increase with the increasing load applied to the propeller. The production of boat propellers has been successfully implemented in this research by a gravity casting technique with permanent molding.

Keywords FAE Analysis · Boat Propeller · Differences of Loading Conditions · Casting Process

Iqbal · N. Ali · H. Husin · Akhyar (✉)
School of Engineering, Universitas Syiah Kuala, Banda Aceh 23111, Indonesia
e-mail: akhyar@unsyiah.ac.id

Iqbal
Department of Mechanical Engineering, Universitas Abulyatama, Banda Aceh, Indonesia

N. Ali · Akhyar · Khairil
Department of Mechanical Engineering, Universitas Syiah Kuala,
Jln. Syech Abdurrauf no.7 Darussalam, Banda Aceh 23111, Indonesia

H. Husin
Reaction Engineering and Catalysis Laboratory, Department of Chemical Engineering,
Universitas Syiah Kuala, Banda Aceh 23111, Indonesia

A. Farhan
Department of Physic Education, FKIP Syiah Kuala University, Darussalam,
Banda Aceh 23111, Indonesia

1   Introduction

Marine propellers are currently very interesting to discuss through design improvements, finite element analysis to improve better performance with various types of materials, such as metal alloys; plastics, glass and carbon composite materials; and metal matrix composites. Analysis of the propeller of a six-blade vessel through a finite element analysis has been discussed on the propeller of the composite for increased flexibility. The operating range can be increased from the cavitation inception point analysis [1]. The focus of using composite materials for marine propellers has been discussed in the review with various numbers of blades with fixed pitch. Apart from that, structural simulation, fluid mechanics, CFD, cavitation, wear test, and twist cocking are also reviewed in this study [2, 3]. The technology for producing composite propeller on a military ship has been carried through improving the design, manufacturing, and testing it directly at sea through FabHeli's Naval Research Group [4]. Stress, deformation, and strain analysis of composite torpedo blades have been discussed in a complex 3D model [5]. Numerical approaches, as well as validation at the ocean, have been carried out on metal and resin propellers. The simulation results show that the metal is considered to be more rigid and the resin variant shows measurable deformation, this is appropriate after field validation [6]. Carbon fiber propellers as an alternative to ship propellers have been produced and analyzed using FEM software, the direction of fiber orientation can improve the propeller hydrodynamic performance [7]. The independent adaptation behavior of composite marine propeller produced through fiber-reinforced plastic (FRP) has been observed under stable and unstable operating conditions, and the fluid-structure interactions were also analyzed. The results show that the significant efficiency of the composite propeller has been achieved [8]. Mechanical and vibration properties tested on marine propeller through two materials, they are CFRP (carbon fiber reinforced plastics) and NAB (nickel aluminum bronze casting) against cavitation erosion. The results showed that TLV is more resistant to cavitation erosion than FRP [9]. Three types of flexible propellers have been compared concerning the resulting thrust, flexion, cavitation stability, sound pressure level slip flow was also observed against the glass composite propellers [10]. Numerical simulations on submarine propellers have been carried out to predict underwater noise with several stages that have been observed. These stages include computational fluid dynamics (CFD) simulations for submarines and propellers, the transient response from submarines and propellers, thrust, and torque to calculate acoustic response [11].

Propeller analysis for the low draft ship has been simulated with data cross-section and pitch angle has been discussed through static structure and fatigue analysis of various material inputs [12]. The propeller fatigue analysis was evaluated against time over one revolution [13]. Analysis of ship propeller fatigue which is produced through the metal casting process has been successfully carried out using finite element software with two variations of shipload and hull load [14]. The implementation of the marine propeller model with a two-part validation approach,

namely a model for predicting the lifespan and comparing experimental and theoretical results has been discussed [15]. Stress and displacement analysis on bicycle frame through finite element analysis with several loading variation scenarios has been executed and produced by sand casting [16, 17]. Some other solutions through finite element simulations are the analysis of thermoplastic polyurethane elastomers at uniaxial stresses which have been analyzed by the classical strain energy density constitutive algorithm [18]. The ship propulsion system has been executed using finite element method software by considering the yield strength of the simulated material [19]. Investigations of metallic matrix nanocomposites (MMNCs) at uniaxial stress, three bending tests, and uniaxial compression have been studied by the finite element method [20]. Marine propellers can be produced through a metal casting process. The process of manufacturing a product using metal casting techniques can be done in several ways, including gravity casting [21], centrifugal casting [22], and high pressure die casting. Various types of molds can be used to produce boat propellers as well as various types of materials, one of which utilizes recycled metal alloys [23].

Prediction of the service life of ship propellers through heterogeneous models of materials. Porosity defects and inclusions from the metal casting were mapped through the finite element model. Besides that, the prediction of ship propeller fatigue was also carried out by integrated methods such as casting temperature and the gatting system was discussed [24]. The objective of this simulation is to analyze stress, strain, and displacement on boat propellers with various loading variations. This FAE analysis produces the maximum value (for stress, strain, and displacement), the location, and the area that occurs on the boat propeller when the load value variations are given. The results of stress, strain, and displacement analysis are needed to optimize the design and manufacturing of the boat propeller. The propeller production process through gravity casting techniques has been successfully carried out using a steel mold.

2   Method and Parameters

This simulation has performed stress, strain, and displacement analysis on the boat propeller with four load variations. This simulation has been carried out in the computation mechanic laboratory at the Mechanical Engineering Department of Universitas Syiah Kuala. Boat propeller with two blades and this propeller is often used for fishing boats with a low size of about three GT (gross tonnage) in Aceh Province. The length range of the two blades is 222 mm with a wavy surface following the fluidity of the water when the propeller rotates the pressure on the surface and then the boat can move. There is a hole for the placement of the shaft with a tapered hole with a small radius of 6.5 mm, a large radius of 9.77 mm, and an outer radius of 13 mm. The hole thickness for shaft fitting is as follows, on the straight side, it is 19 mm while the overall thickness is 32 mm. The schematic of the propeller analyzed in this simulation is more detailed as shown in Fig. 1.
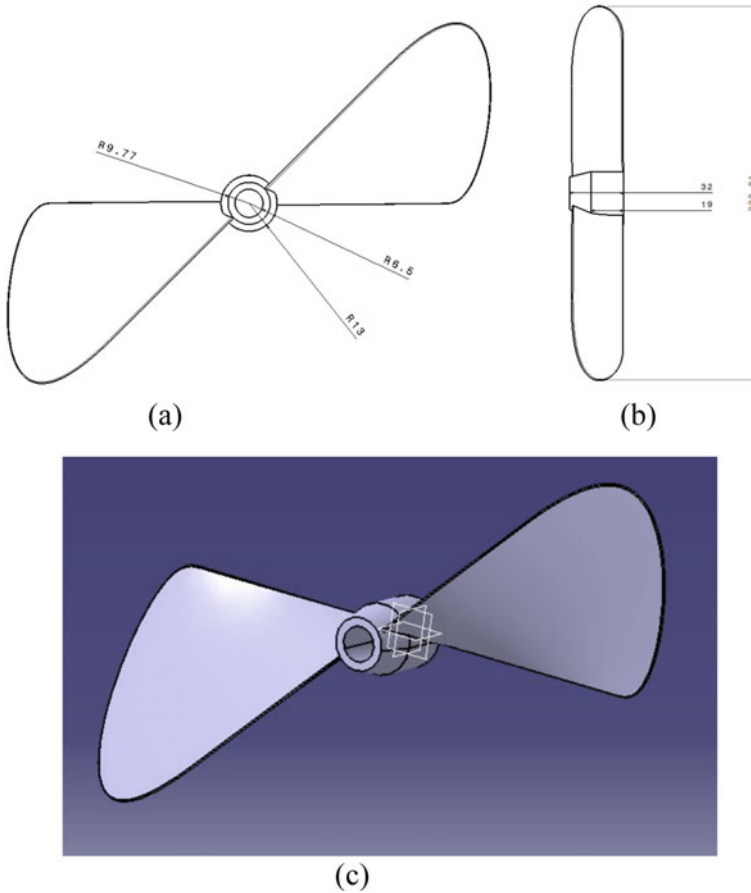
Fig. 1 Schematic of boat propeller: **a** upper view, **b** front view, and **c** 3D view

The material used in this study is aluminum 8176 (AlFeSi), its material properties are as shown in Table 1. The load given to the boat propeller in this study is evenly distributed with four variations of the load magnitude as shown in Table 2. The loading scenario given in this simulation assumes the amount of load needed to move the boat with various load and passenger conditions. Meshing is performed on a boat propeller model using a tetrahedron mesh type. Figure 2 shows the loading and boundary conditions, providing support for the boundary condition is displacement/rotation (U2 = U3 = UR1 = UR2 = UR3 = 0). Furthermore, the simulation results have been manufactured through metal casting technology, namely gravity steel mold casting.

Table 1 Material properties of aluminum 8176

Elastic (Young's Tensile) modulus	69 GPa	10×10^6 psi
Elongation at break	15%	
Fatigue strength	59 MPa	8.5×10^3 psi
Poisson's ratio	0.33	
Shear modulus	26 GPa	3.8×10^6 psi
Shear strength	70 GPa	10×10^3 psi
Tensile strength: ultimate (UTS)	160 MPa	23×10^3 psi
Tensile strength: yield (proof)	95 MPa	14×10^3 psi
Density	2.7 g/cm^3	

Table 2 Variations in loading conditions during the boat propeller simulation

Loading Condition	Load Applied (N)
First loading condition	150
Second loading condition	300
Third loading condition	450
Fourth loading condition	600
Fifth loading condition	800

(a)					(b)
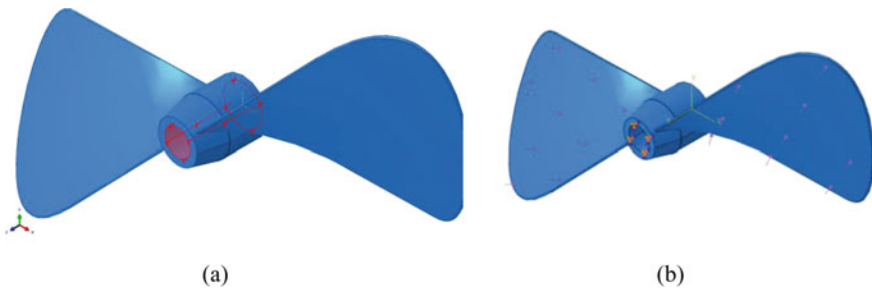
Fig. 2 a Boundary Conditions, **b** Load applied

3   Result Analysis

First scenario loading condition. Figure 3 shows the distribution of stress, strain, and displacement with the number of loads applied is 150 N. The simulation results show a maximum stress value of 13.14 MPa with a location at the inner base of the propeller, a maximum strain is 1.42×10^{-4} with a location at the inner base of the propeller and a maximum displacement is 0.52 mm with a location at the outer end of the propeller. Meanwhile, the minimum stress value is 3.84 MPa with a location at the outer end of the propeller at a load of 150 N.
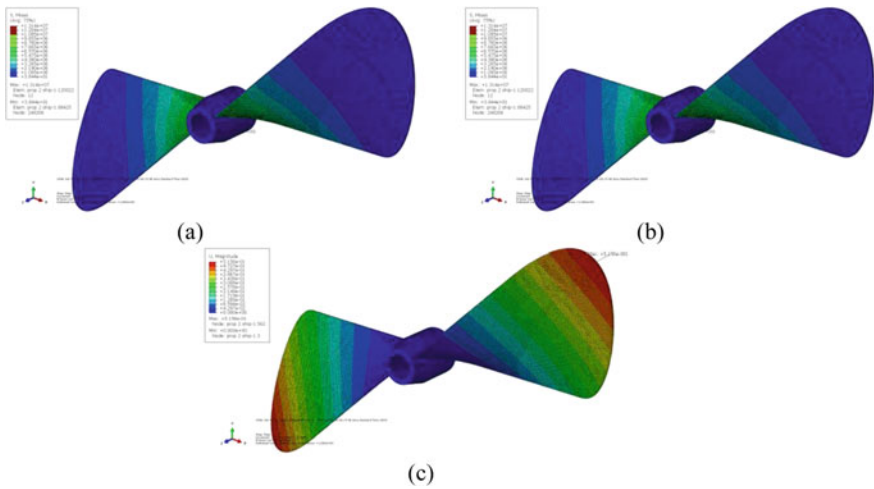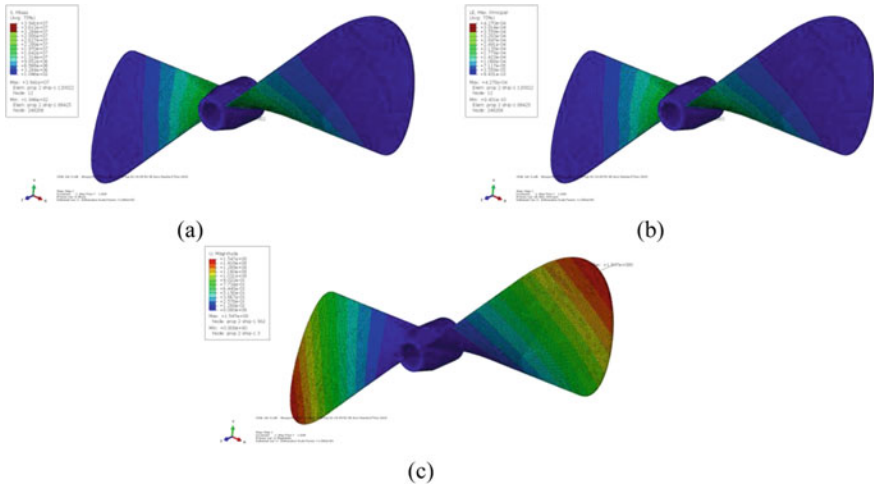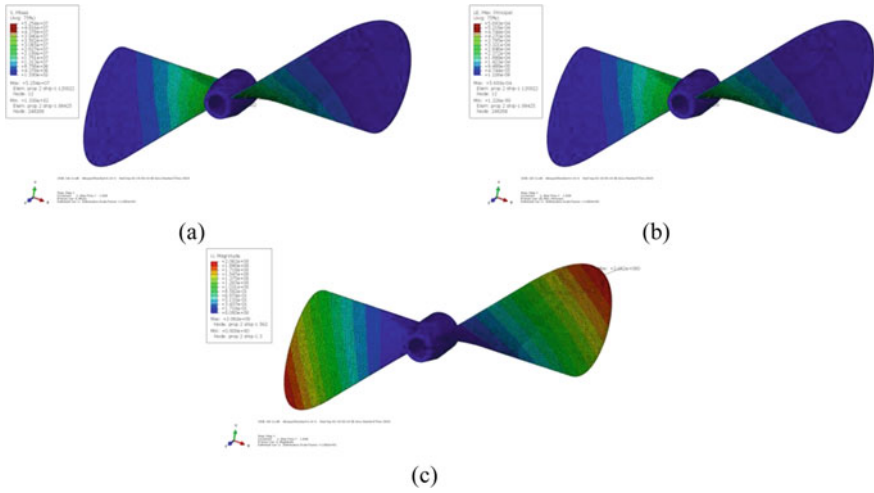
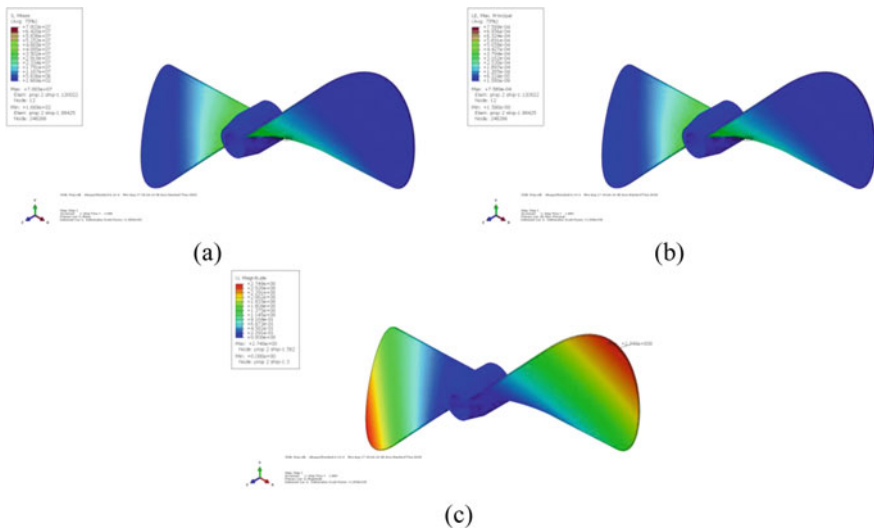**Fig. 3** Boat propeller with 150 N as loading application: **a** stress, **b** strain, and **c** displacement

Second scenario loading condition. Figure 4 shows the distribution of stress, strain, and displacement with the number of loads applied is 300 N. The analysis results show maximum stress is 26.28 MPa with a location at the inner base of the propeller, a maximum strain is 2.85×10^{-4} with a location at the inner base of the propeller and a maximum displacement of 1.03 mm with a location at the outer end of the propeller. The results of the analysis show a minimum stress value of 7.32 MPa with a location at the outer end of the propeller.
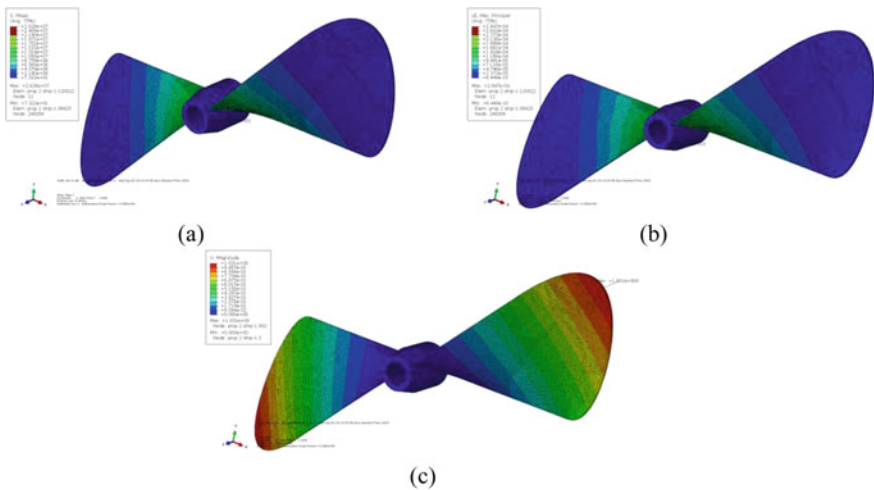
Fig. 4 Boat propeller with 300 N as loading application: **a** stress, **b** strain, and **c** displacement

Fig. 5 Boat propeller with 450 N as loading application: **a** stress, **b** strain, and **c** displacement

Third scenario loading condition. Figure 5 shows the distribution of stress, strain, and displacement with the number of loads applied is 450 N. The analysis results show a maximum stress value is 39.41 MPa with a location at the inner base of the propeller, a maximum strain is 4.27×10^{-4} with a location at the inner base of the propeller and a maximum displacement is 1.55 mm with a location at the outer end of the propeller. The results of the analysis show that the minimum stress value is 9.43×10^{-10} MPa with a location at the outer end of the propeller.

Fourth scenario loading condition. Figure 6 shows the distribution of stress, strain, and displacement with the amount of load applied is 600 N. The results of this simulation show a maximum stress value is 52.54 MPa with a location at the inner base of the propeller, a maximum strain is 5.69×10^{-4} with a location at the inner base of the propeller and a maximum displacement is 2.06 mm with a location at the outer end of the propeller. The simulation results show the value of the minimum stress value 1.23×10^{-9} MPa with a location at the outer end of the propeller.

Fifth scenario loading condition. The stress, strain, and displacement distribution as shown in Fig. 7, with the number of loads applied is 800 N. The analysis results show maximum stress value is 70.03 MPa with the location of the inner base of the propeller, the maximum strain is 7.59×10^{-4} with the location of the inner base of the propeller and the maximum displacement is 2.75 mm with the location at the outer end of the propeller. The analysis results show a minimum stress value of 1.67×10^{-2} MPa with a location at the outer end of the propeller.

The summary of the boat propeller simulation results from four loading variations with maximum and minimum values can be seen in Table 3 and Fig. 8. Boat propellers when operating in the water when moving the ship undergo hydrostatic

Fig. 6 Boat propeller with 600 N as loading application: **a** stress, **b** strain, and **c** displacement

Fig. 7 Boat propeller with 800 N as loading application: **a** Stress, **b** Strain, and **c** displacement

pressure on the front and rear surfaces, besides that the ship's propellers also bear hydrodynamic loads on both surfaces [5]. So that the design and analysis of this propeller are needed for optimal operation in water. High propulsion efficiency, minimum cavitation, low vibration level, and low noise are expected to be obtained from building models and FEA simulations before production [12]. The quality of metal casting products can be done by controlling the defects, one of which is by

Table 3 Location of maximum stress, strain, and displacement with different loading conditions

Scenario Loading Conditions	Stress (MPa)		Strain		Displacement (mm)	
	Min.	Max.	Min.	Max.	Min.	Max.
First loading (150 N)	3.84	13.14	–	1.42×10^{-4}	–	0.52
Second loading (300 N)	7.32	26.28	–	2.85×10^{-4}	–	1.03
Third loading (450 N)	9.43×10^{-10}	39.41	–	4.27×10^{-4}	–	1.55
Fourth loading (600 N)	1.23×10^{-9}	52.54	–	5.69×10^{-4}	–	2.06
Fifth loading (800 N)	1.67×10^{-2}	70.03	–	7.59×10^{-4}	–	2.75

adjusting the gating system and mold binder [17], as well as cooling the alloy rate by controlling the temperature during pouring [25]. The value of stress, strain, and displacement resulting from this finite element simulation on the boat propeller increases with increasing load scenarios.

Boat propeller manufacturing. Boat propeller production has been carried out at the Casting and Material Engineering Laboratory at the Mechanical Engineering Department of Syiah Kuala University. The mold used is a steel mold, and the propeller production process is through gravity casting techniques as shown in Fig. 9.

4 Conclusions

Stress, strain, and displacement on the boat propeller with various loading variations have been analyzed through FAE simulations. The conclusions from this simulation and propeller boat manufacturing are as follows:

1. The simulation of a fishing boat propeller on aluminum 8176 (AlFeSi) material with a finite element obtained the maximum stress, strain, and displacement values, are 70.03 MPa, 7.59×10^{-4}, and 2.75 mm, respectively in the fifth loading scenario (800 N).
2. The location of the maximum stress and strain is formed at the inner base of the propeller. Whereas the maximum displacement location is formed at the outer end of the boat propeller.
3. Stress, strain, and displacement values in the finite element simulation increase with the increasing of load scenarios.
4. Manufacturing boat propellers of the two-blade design in this work have been successfully produced by the gravity casting metal casting process on a metal mold.

(a)

(b)

(c)
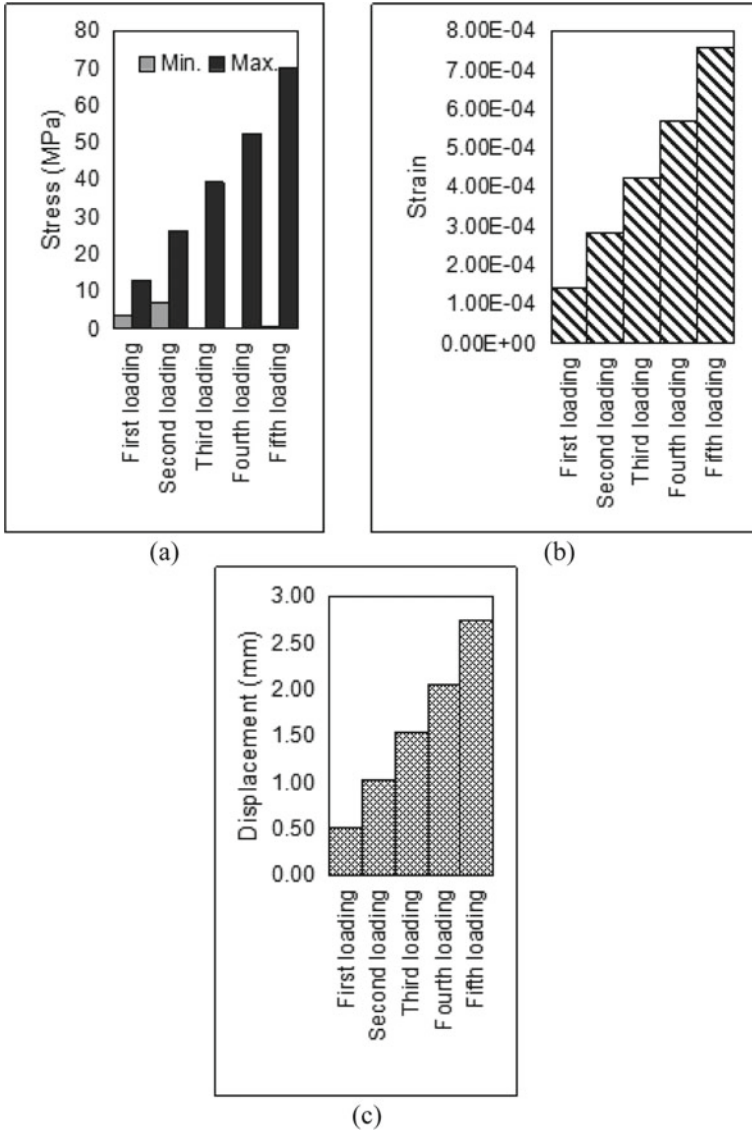
Fig. 8 **a** Stress min. and max., **b** strain max., **c** displacement max., with different loading conditions

Fig. 9 Manufacturing boat propeller through metal casting processes

References

1. Neeharika PD, Babu PS (2017) Design and analysis of ship propeller using FEA. South Asian J Eng Technol (SAJET) 2(1):74–77
2. Vardhana DH, Ramesh A, Reddy BCM (2019) A review on materials used for marine propellers. Mater Today Proc 18:4482–4490
3. Ligtelijn D (2017) Propeller design process, encyclopedia of maritime and offshore engineering. https://doi.org/10.1002/9781118476406.emoe061
4. Guillaume D, Samuel D, Franck B, Pol M, Frédérique LL (2019) Composite propeller in marine industry: first steps toward a technological breakthrough. In: OCEANS 2019—Marseille, Marseille, France, pp 1–6. https://doi.org/10.1109/OCEANSE.2019.8867439

5. Babu DK, Prasanth PSVRK (2018) Modeling and analysis of the submarine propeller by using various materials. Int J Appl Sci Eng Manage 7(4):18–24

6. Savio L, Sileo L, Ås SK (2020) A comparison of physical and numerical modeling of homogenous isotropic propeller blades. J Mar Sci Eng 8:1–22. https://doi.org/10.3390/jmse8010021

7. Kumar A, Lal Krishna G, Anantha Subramanian V (2019) Design and analysis of a carbon composite propeller for podded propulsion. In: Murali K, Sriram V, Samad A, Saha N (eds) Proceedings of the fourth international conference in ocean engineering (ICOE2018), Lecture Notes in Civil Engineering, vol 22. Springer, Singapore. https://doi.org/10.1007/978-981-13-3119-0_13

8. Motley MR, Liu Z, Young YL (2009) Utilizing fluid–structure interactions to improve energy efficiency of composite marine propellers in spatially varying wake. Compos Struct 90:304–313

9. Yamatogi T, Murayama H, Uzawa K, Mishima T, Ishihara Y (2011) Study on composite material marine propellers. JIME 46(3):43–53

10. Paik BG, Kim GD, Kim KY, Seol HS, Hyun BS, Lee SG, Jung YR (2013) Investigation on the performance characteristics of the flexible propellers. Ocean Eng 73:139–148. https://doi.org/10.1016/j.oceaneng.2013.09.005

11. Ying-San W, Yong-Sheng W, Shu-Ping C, Jian F (2012) Numerical prediction of propeller excited acoustic response of submarine structure based on CFD, FEM and BEM. J Hydrodynam 24(2):207–216. https://doi.org/10.1016/S1001-6058(11)60236-9

12. Surendra Rao R, Mohan S, Sawan Kumar G (2016) Determination of fatigue life of surface propeller by using finite element analysis. Int J Eng Sci Comput 6(8):2492–2503

13. Bertoglio C, Gaggero S, Rizzo CM, Viviani M (2014) Fatigue strength assessment of propellers by means of weakly coupled CFD and FEM analyses. In: Proceedings of the ASME 2014 33rd international conference on ocean, offshore and arctic engineering, OMAE2014, 8–13 June 2014, San Francisco, California, USA

14. Endramawan T, Sifa A, Dionisius F, Syah MI (2020) Lifetime simulation of traditional boat propellers using ansys. In: IOP conference series: materials science and engineering, vol 850, no 012041, pp 1–7. https://doi.org/10.1088/1757-899x/850/1/012041

15. Ezanno A, Doudard C, Moyne S, Calloch S, Millot T, Bellèvre D (2014) Validation of a high-cycle fatigue model via calculation/test comparisons at structural scale: application to copper alloy sandcast ship propellers. Int J Fatigue 74:38–45. https://doi.org/10.1016/j.ijfatigue.2014.12.008

16. Akhyar H, Hasanuddin I, Farhan A (2019) Structural simulations of bicycle frame behaviour under various load conditions. In: Materials science forum, vol 961, pp 137–147. https://doi.org/10.4028/www.scientific.net/MSF.961.137

17. Husaini A, Ali M, Ali N, Farhan A (2020) Effect of different gating systems and sand mold binder on the cast-quality of bicycle frame produced through sand casting method. In: Defect and diffusion forum, vol 402, pp 100–107. https://doi.org/10.4028/www.scientific.net/DDF.402.100

18. Wang Y, Luo W, Huang J, Peng C, Wang H, Yuan C, Chen G, Zeng B, Dai L (2020) Simplification of hyperelastic constitutive model and finite element analysis of thermoplastic polyurethane elastomers. Macromol Theory Simul 29(4):1–12. https://doi.org/10.1002/mats.202000009

19. Nubly MH, Yudo H (2017) Strength analysis of propeller shafting on orca class fisheries inspection boat using finite element method. Int J Civ Eng Technol (IJCIET) 89(10):1599–1610

20. Qiao Y, Liu J, Jia Y, Xu C, An L, Bai Y (2017) Study on coexistence of brittle and ductile fractures in nano reinforcement composites under different loading conditions. Int J Fract 204:205–224. https://doi.org/10.1007/s10704-016-0174-y

21. Akhyar H, Iswanto PT, Malau V (2018) Non treatment, T4 and T6 on tensile strength of Al-5.9Cu-1.9 Mg alloy investigated by variation of casting temperature. In: Materials science forum, vol 929, pp 56–62. https://doi.org/10.4028/www.scientific.net/MSF.929.56

22. Iswanto PT, Akhyar, Maliwemu EUK (2019) Fatigue crack growth rate of motorcycle wheel fabricated by centrifugal casting. Metalurgija 58(1–2):51–54
23. Farhan A, Akhyar, Ali M (2019) Experiment on hardness and impact strength of recycled aluminum alloys by metal casting process. In: Materials Science Forum, vol 961, pp 65–72. https://doi.org/10.4028/www.scientific.net/MSF.961.65
24. You K, Rao L, Bai X, Miao T (2020) An integrated analysis method of service life based on the 3D heterogeneous material model with casting defects. J Mater Eng Perform 29:4641–4651. https://doi.org/10.1007/s11665-020-04937-0
25. Akhyar H, Husaini (2016) Study on cooling curve behavior during solidification and investigation of impact strength and hardness of recycled Al–Zn aluminum alloy. Int J Metal Cast 10:452–456. https://doi.org/10.1007/s40962-016-0024-8

A Novel Analysis on Ethanol Droplets Heated by Electromagnetic Energy

Lukas Kano Mangalla and Hiroshi Enomoto

Abstract Utilizing bio-ethanol fuel in the internal combustion engine is recently developed for high performance combustion and emission reduction. The effect of electromagnetic heating on the ethanol droplets structure and distribution is the main focus of this analysis. An increasing temperature of the fuel can offer a potential solution for finer atomization and faster evaporation of droplets. The electromagnetic energy was used to heat the ethanol fuel before injected. Electromagnetic heating was generated by the magnetron of microwave and guided to the small chamber inside the LMI injector where the fuel pass-through. LMI is stand for Local-contact Microwave-heating Injector and developed in Combustion Laboratory of Kanazawa University Japan for cold start engine. The images of fuel injected from the LMI injector was visualized using a high-speed camera with halide back-light system. Laser scattering from He–Ne was used as an illuminating system for high-quality image purposes. An investigation on the droplet size and velocity distribution was analyzed using image processing software. The results of the analysis show that droplet fuel atomized finely and moved rapidly during heated by electromagnetic energy.

Keywords Spray velocity · Droplet size · Electromagnetic energy · Image processing · LMI system

1 Introduction

Spray characteristics of fuel play an important role in the performance and emission reduction of the internal combustion (IC) engine. Poor performances and high exhaust emission of the engine are the major problems related to the lack of spray

L. K. Mangalla (✉)
Engineering Faculty of Halu Oleo University, Kendari, Indonesia
e-mail: lukas.kano@uho.ac.id

H. Enomoto
College of Natural Science and Technology, Kanazawa University, Kanazawa, Japan

atomization and vaporization of the fuel. This phenomenon is more critical particularly when uses bio-component fuel such as bioethanol and biodiesel. Ethanol fuel has been widely recognized as an alternative for gasoline due to the higher octane number, oxygenated fuel, and high latent heat of vaporization that can run the engine with high power performance and lower emissions [1, 2]. However, some properties of the fuel such as lower volumetric energy density, higher latent heat of vaporization, and boiling point as well as high viscosity could be the main source problem especially for the cold start condition [3]. Vaporization of fuel must be good enough to ignite and burn faster in the combustion chamber to produce higher thermal efficiency and cleaner emissions of the combustion engine.

Improving atomization and evaporation ethanol fuel is remaining challenging in IC engine applications. Heating fuel flow inside the fuel injection system is one of the possible solutions to improve the spray characteristics under engine cold-start conditions [4]. The temperature of the fuel or surrounding gas of the fuel sprayed should be increased to accelerate fuel distribution and vaporization. Several studies have been performed technical solutions to improve the vaporization and atomization of fuel [5–9]. Enomoto and Iida [10] developed a new model of heating fuel flow, mainly ethanol or ethanol-gasoline blended, using a microwave heating energy system. An in-house injector development was used to heat fuel flow. The main aim of this system is to add some energy equivalent to the fluid flow inside the injector and this called Local-contact Microwave-heating Injector (LMI) system. The polarization of electromagnetic waves in this system can increase fuel temperature rapidly and lead to reduce SMD of droplet sprayed even in the early injection starting [11]. This advantage can offer the potential used of bio-ethanol fuel for cold start problem engines.

The effects of fuel heating using electromagnetic on the structure of the spray are the main concern of this analysis. Fuel heating is supposed to be a significant influence on the atomization and evaporation of ethanol.

2   Research Method

In this investigation, the spray droplets of ethanol from LMI system was visualized by using a high-speed camera and analyzed later on using post-processing images. High-magnification of images was produced with proper illuminating of incident light background from Halide Lamp. The productions of visualization images were captured during several injection interval of sprayed fuel. The structure of sprayed fuel is expected to be visualized and analyzed easily in this study.

The ethanol fuel was heated by microwave heating and then injected from an orifice nozzle diameter of 0.3 mm. Fuel injection was setting-up to the constant pressure of 0.3 MPa (Table 1), a typical operating pressure for the port fuel injection system. Fuel flow inside the injector was subjected to microwave energy produced from the magnetron of microwave heating. The imaging system was made using a high-speed camera with high quality of illumination

Table 1 Experimental condition

Conditions	Description
Fluid (material)	Ethanol
Injection pressure	0.3 MPa
Fuel temperature	293 K
Injection interval	5 ms over 200 ms
Heating duration	20 ms over 40 ms
Power input	60 W

Fig. 1 Experimental apparatus
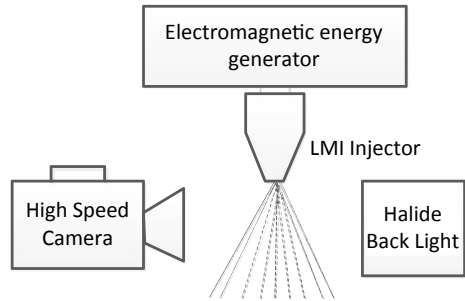
lamp. An experimental study was conducted in a state of the art of measurement devices. The injector was mounted vertical to the magnetron of the microwave generator and the schematic of this arrangement devices with an imaging system and droplet size measurement can be seen in Fig. 1.

2.1 Ethanol Fuel

The commercial grade of anhydrous ethanol (99.5% Ethanol) was used as the liquid fuel for the current study.

The temperature of the fuel was set around 293 K for the thermal condition of fuel during the experiment. Table 2 shows the typical properties of ethanol fuel compare with gasoline fuel. A composition of 100% ethanol was used in this study.

2.2 Injector and Heating Zone Geometries

A single hole of injector was developed for special purposes of studying the effect of microwave heating systems on the vaporization of the fuel. The schematic system of LMI system can be seen in Fig. 1. The injector has orifice diameter D = 0.3 mm and the heating zone has a diameter around 4 and 4 mm in length.

Table 2 Properties of ethanol compare with gasoline fuel

	Ethanol	Gasoline
Density (kg/m^3)	789	739
LHV (MJ/kg)	26.8	43.1
Stoichiometric Air/Fuel ratio	9	14.7
Latent heat vaporization (kJ/kg)	904	380–500
Boiling temperature (°C)	78.4	25–215
Research Octane Number (RON)	129	91

Source Matsumoto et al. 2010, SAE international [12]

Heating created inside the tip injector aims to generated heating of fuel flow by using a microwave heating scheme. This area is connected to the magnetron via coaxial cable as the passage of the electromagnetic wave.

The cover of the heating zone consists of metallic material that functions as an insulator for the electromagnetic wave. Fuel flow inside the system experiences heating generated by the polarization of the electromagnetic wave in ethanol fuel.

2.3 Experimental Conditions

The injector was designed specially to operate at lower injection pressure (0.3 MPa), the typical injection pressure for port fuel injection (PFI) engine. Electric power of 60 W was imposing into the microwave heating generator that operated at a constant frequency of 2.45 GHz. By this frequency, the electromagnetic wave can generate heating for ethanol flow. Control of heating and injection systems was formulated in a function generator system to provide the proper temperature distribution of fuel flow inside the heating area. The injection control system was arranged based on the engine rotation of 600 rpm at the normal operation. Heating control was adjusted for obtaining the proper temperature of the fuel generated inside the heating area.

2.4 An Image Analyze and Droplet Sizing Mechanism

In this paper, the results of spray distribution from both measurement devices and image analysis were explored. The droplet size distribution of the sprayed fuel can be one of the important characteristics between heated and non-heated fuel. Figure 6 shows the photograph of fuel sprayed at different view angles. The imaging system was assembled to show the spray characteristic of fuel under the different heating scheme: heated spray and non-heated spray. Droplet distribution was measured using Laser Diffraction of Spray Analyzer (LDSA) at each injection duration. Laser scattering from He–Ne was used as an illuminating system for

high-quality image purposes. The centerline of the measurement position was placed at 20 mm from the tip of the injector. The device can measure the SMD and droplet size distribution of sprayed fuel. Droplet size is one of the most important characteristic of the spray [13].

Optical system of fuel spray was carried out using high speed camera (PHOTORON FASTCAM SA5). For the appropriate analyzing system, the high speed camera and a source light were synchronized at 1/30,000 fps to produce imaging quality at 512×512 pixels. In order to optimize the imaging system the source light from metal halide lamp is coupled with the camera. The images captured in this system were analyzed in image processing software such as Image-J, Memrecam HXLink, and Photoshop.

For the purposes of determining spray angle and droplet size analyzed, the threshold value was adjusted to distinguish between background noise and fuel spray. Two angle view of imaging recorded, front and side view, were taken into account (Fig. 2). The different spray angle on the different view is due to the small deformation of the injector orifice during injection. The binarization of droplet sprayed was performed in Image-J to define the area of circularity edges of the images threshold. The droplet size of the spray was analyzed base on the basic concept of Sauter Mean Diameter (SMD).

Instead of direct measurement analysis, the image analysis of fuel sprayed was also performed. Figure 3 shows the description of binarization steps, an image processing, performed in the post image processing. The background noise of the images can be eliminated by subtracted the background and later the threshold value would be adjusted based on the mean of background pixels to leave a binary image. Subtracted background also makes the distance of background pixel become plate, thus, it can easily perform binarization of spray photos. The adjusting threshold number is critical for the droplet size analysis since it is related to the spatial area and diameter of droplets in the spray images.

3   Result and Analysis

Droplets spray of the LMI Injector were investigated in order to understand the effect of the heating generated by electromagnetic energy on the spray structure. During the injection of fuel, particle size and distribution formation of droplet sprayed were measured by LDSA. Spray characteristics were analyzed from the images captured with the high-speed camera.

In the preview study [11] on this device, the droplet size of spray, expressed as SMD, was reduced significantly in the heating fuel. The reduction of SMD in the early injection is due to the rapid increasing of fuel temperature after applying microwave heating into the fuel flow and this phenomenon is expected to enhance the vaporization rate of injected fuel into the combustion chamber.

Figures 4 and 5 compares the number of droplets and the number of pixels in the black area of the three different threshold numbers. Black images of the threshold
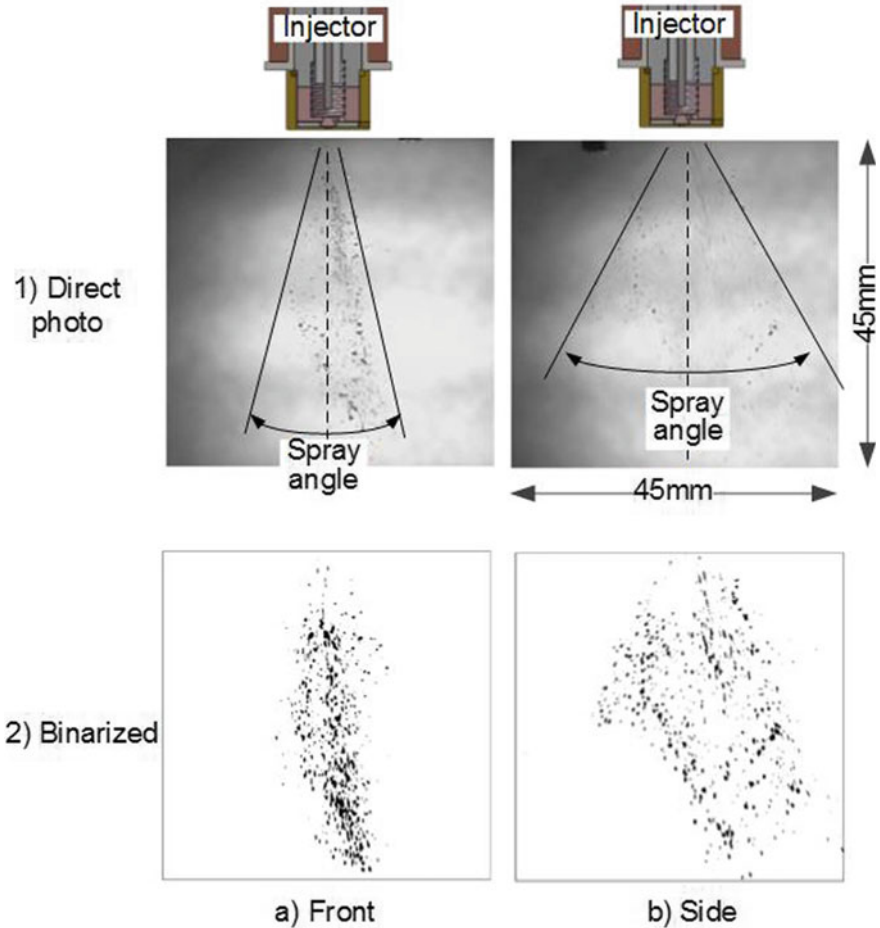
Fig. 2 Angle of view of the imaging system of fuel spray; **a** is the front view of sprayed fuel and **b** is the side view of spray, 90° from the front view

pictures can show the liquid area where the droplets are supposed to exist. The differences in the spray formation between heating and non-heating fuel were quantified from the calculation of droplet number and droplet diameter (SMD). In all threshold adjustment, it seems that the heated spray of the fuel has been significantly affected by the temperature of the fuel. However, it is not clear between injection timing and temperature effect. The images of spray cannot compare the spray pattern at the same timing injection. The penetration of the sprays is totally different between heating and non-heating spray.

SMD is the common parameter for expressing the diameter droplet in terms of the surface area of the spray [14]. The sizing information is presented in form of Sauter mean diameters (SMD) and calculated using expression [14, 15]: SMD is the
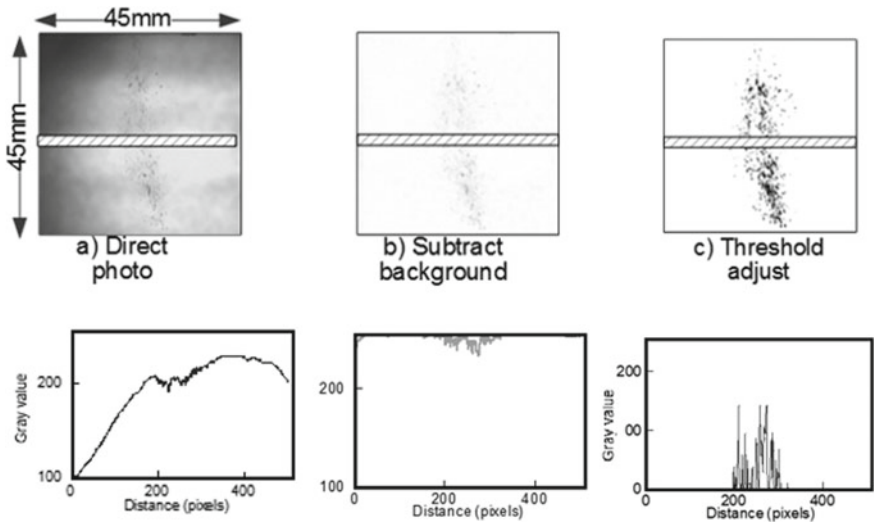
Fig. 3 Images analysis process steps
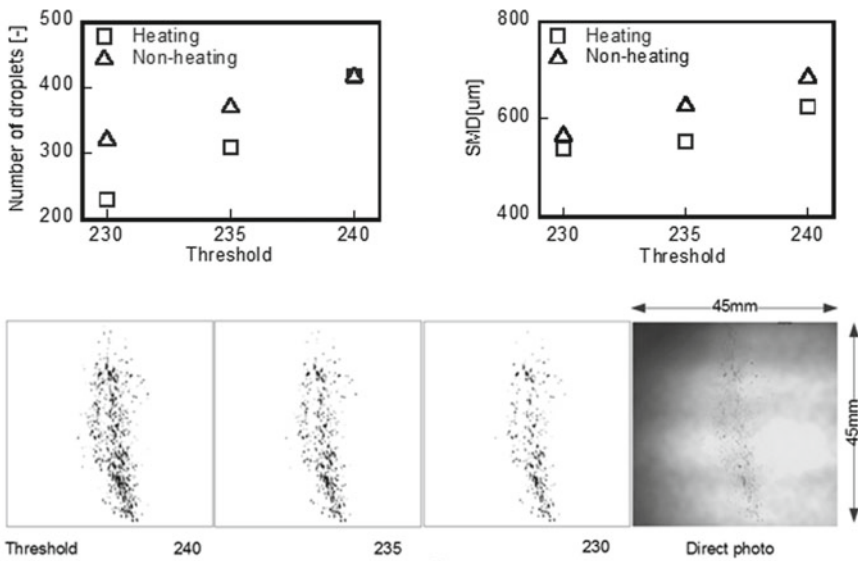
Fig. 4 Difference view of droplet images in the different threshold number

common parameter for expressing the diameter droplet in terms of surface area of the spray [14]. The sizing information is presented in form of Sauter mean diameters (SMD) and calculated using expression [14, 15]:
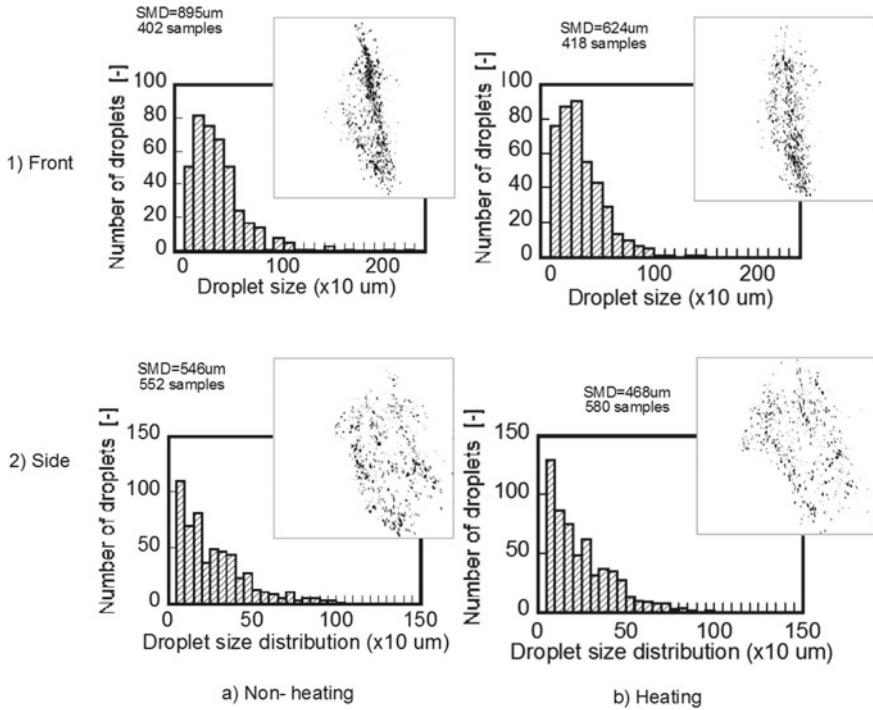
Fig. 5 Droplets view of heating and non-heating spray

$$SMD = \frac{\sum_0^n d_i^3}{\sum_0^n d_i^2} \tag{1}$$

where d_i is the droplet diameter of fuel sprayed, n is the number of particle inside the spray.

Figure 5 shows the distribution of SMD of injected fuel of the two different views. In the heating fuel spray, the frequency of smaller size droplets is higher than that in the non-heating spray. This indicates the finer droplet size can be produced by heating the fuel sprayed. High-temperature fuel will reduce the surface tension and viscosity and leads to reduce the size of the droplets of the spray [16]. The quantitative measurement of liquid spray is based on the edge detection on the images. The size of edges detection in this analysis was later converted to the droplet size of the spray.

In this experimental study, the images were captured on a high-speed camera, however, the quality of images produced still remains the structure of the unclear droplets due to the high speed moving of droplet. As the result, the edges of each droplet in the picture are unclear and the SMD of droplet became bigger. Further analysis of the imaging process is necessary. In image processing of injection, a watershed can help to divide areas of droplet spray (Fig. 6). Watershed on image
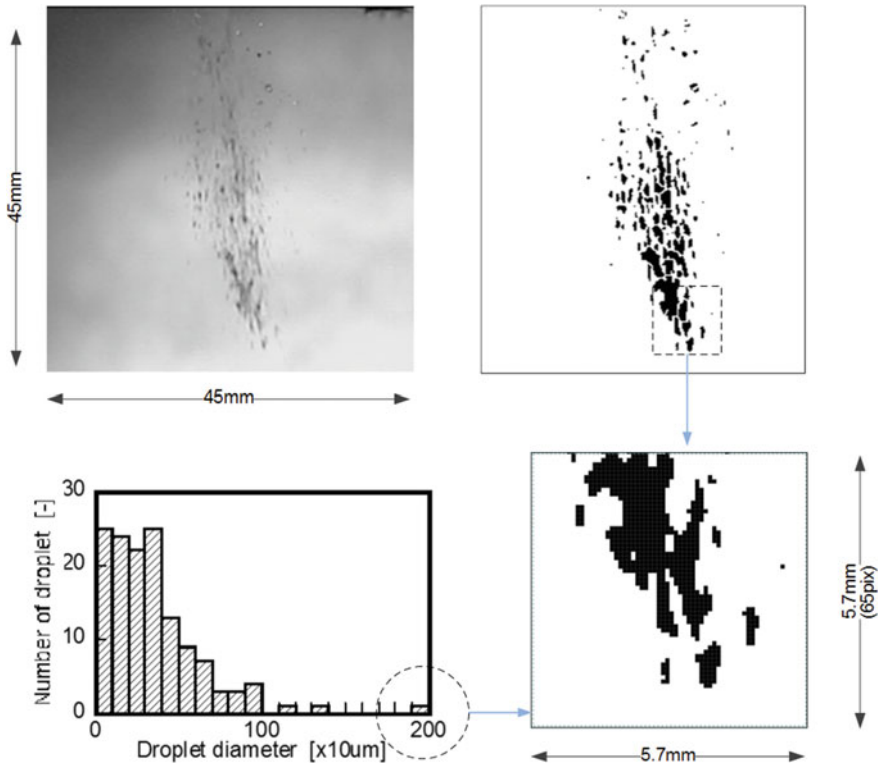
Fig. 6 Puffing of the overlapping droplets in the images and the effect on the droplets size and distribution

processing is a way of automatic separation or cut the particles that are touched. This step is important to convert objects overlapping in the images. In order to deeply understand the watershed effect on the images analysis, the watershed steps on the images of several sprays were considered.

Figure 7 shows a series of zooming (puffing) photograph in the tip of the ethanol fuel spray. This analysis is proposed to evaluate the liquid component in the spray dispersed into the small droplets. Figure 8 can show the effect of the watershed process on the image structure of fuel spray. Figure 8 shows the characteristic of this treatment in terms of SMD distributions. The bigger size of the droplet in the image can be separated by watershed into small droplet sizes and leads to reduce SMD of the spray.

Threshold images spraying provide clear information of spray structure between heated and non-heated fuel during the injection. In the heated spray, the liquid spray changes into the finer droplet in the short time which means the surface volume area became dispersion into several parts. The liquid fuel of heated spray at the specific location was completely changed into small droplets component in around 0.5 ms. A different characteristic of spray structure is showed in non-heated fuel. In the
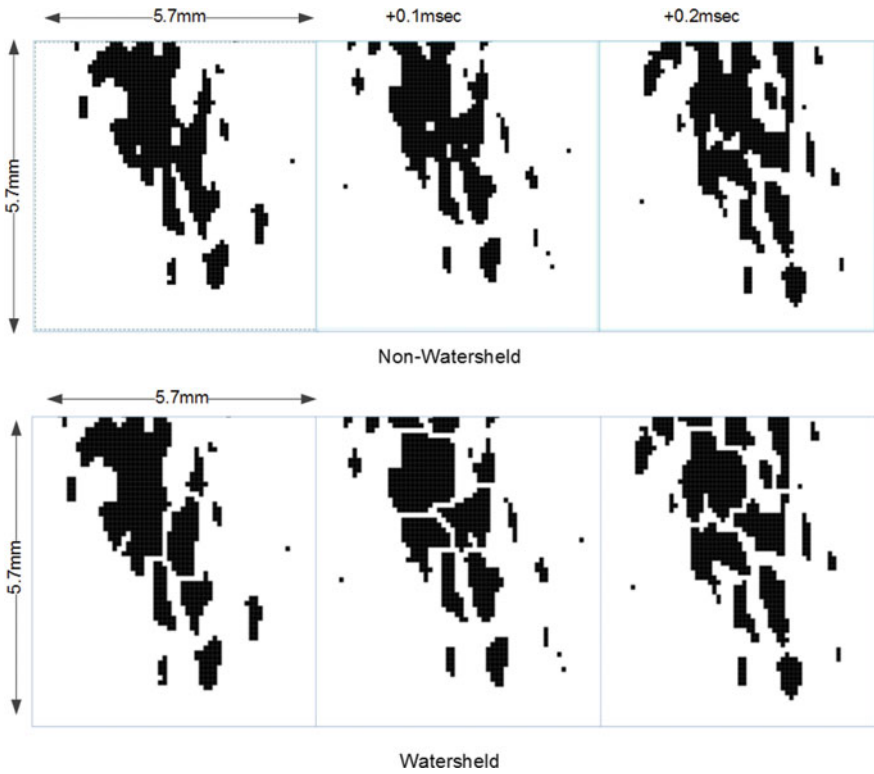
Fig. 7 Watershed on the images structure of the spray
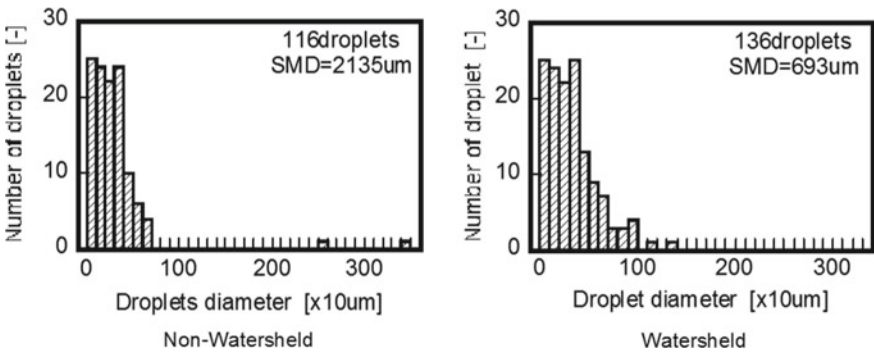
Fig. 8 Watersheld effect on the droplet size of fuel spray

histogram analysis of droplets size in Figs. 9 and 10, it clearly shows the trend of droplets distribution between heating and non-heating fuel. In the 0.5 ms the number of droplets in the heating spray becomes higher than non-heating spray.
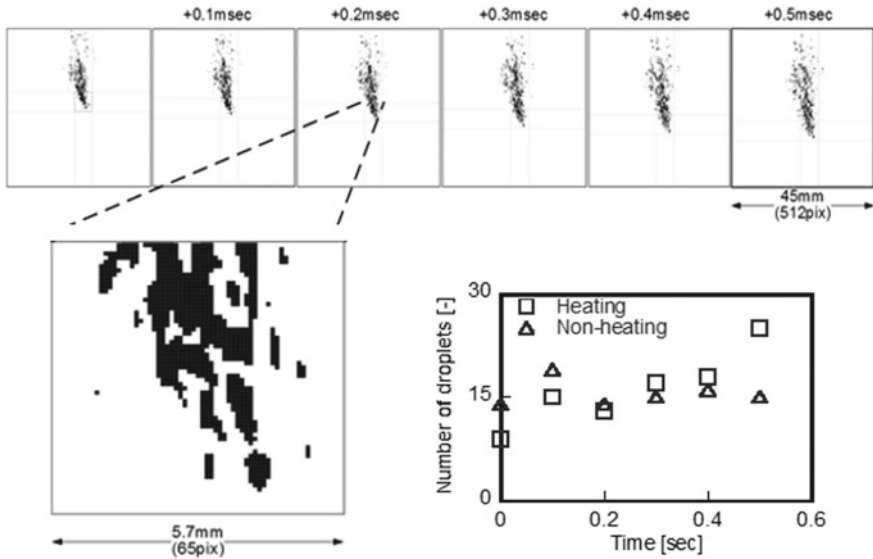
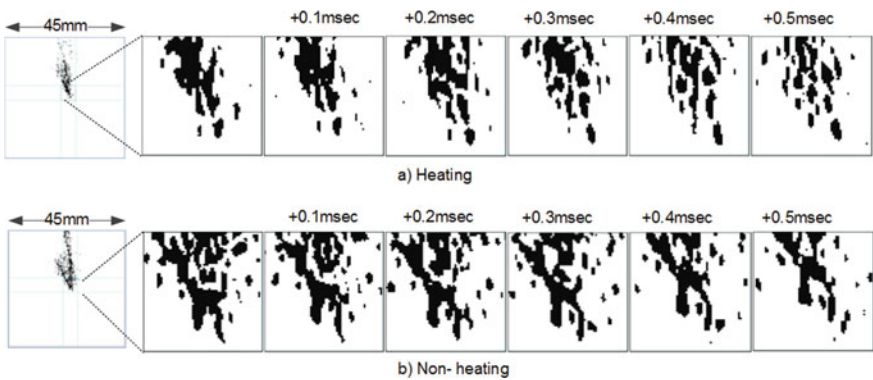**Fig. 9** Characteristic of the droplets during the injection

Fig. 10 Two different views of droplet structure in the different time of injection

Spray characteristics of the fuel injection can be affected also by the jet inertia force, viscous force, air drag force, and surface tension force [17]. Reynolds number and Weber number are the non-dimensional parameters that usually influence the spray structure. Changing the temperature of fuel sprayed can influence the Reynolds and Weber number parameters. Correlation between the fluid properties and velocity distribution of the spray is also considered in this study. This analysis aims to differentiate between the droplet velocity of the heating and non-heating fuel.
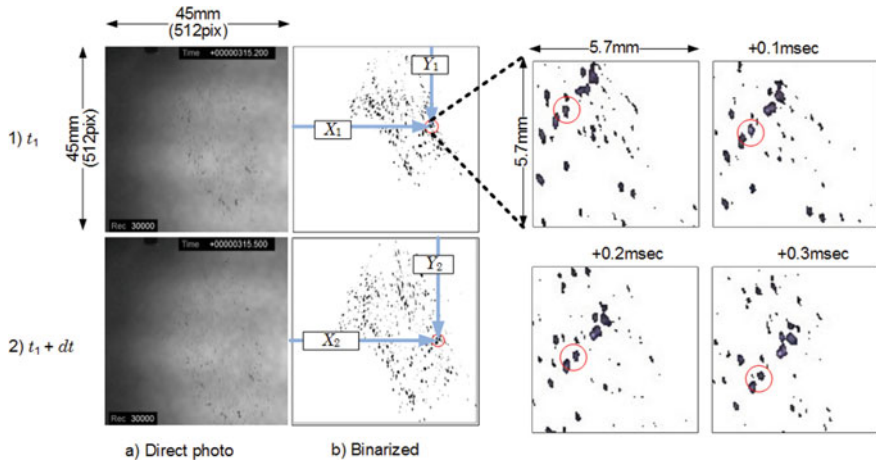
Fig. 11 The Spatial and temporal of droplet position in the images

Figure 11 describes the droplet position in each time exposure of droplets spray. In this analysis, the speed of droplets can be calculated from the images capture based on the frame information of the photos. The velocity of the droplet was calculated using the formula below [15]:

$$V = \sqrt{\frac{(Y_2 - Y_1)^2}{(X_2 - X_1)^2}} \frac{distance}{pixel} pfs \tag{2}$$

The images of spray consists of 512 pixel size and the *pfs* is frame size of imaging system (1/30.000 was used). Real distance of photos frame during experimental is 45 mm. In each image of spray analyzed, we were chosen 100 droplets to be considered and analyzed. The same process analysis was performed in the two different views, front and side view.

Figure 12 shows the velocity distribution between heating and non- heating fuel at two different views of spray. The averages velocity of droplets indicates the different droplet velocity under heated and non-heated fuel. In the front view, the average speed of non-heating droplets is 8.7 m/sec whereas in the heating fuel is 11.5 m/sec. The same trend appears in the side view where the velocity of heating fuel is higher than that of non-heating fuel. In heating fuel, the average velocity is 14.6 m/sec whereas, in non-heating fuel, the average velocity is 13.1 m/sec. These trends can explain the effect of temperature fuel on the droplet velocity. In the heated fuel the properties such as density and viscosity become changing and lead to change droplet velocity. The bigger the density the faster the droplets move.

The fuel heating process is sensitive to the position and size of the droplets distributions [18]. A strong correlation between heated fuel and the number of droplets in the spray images are observed, which describe the importance of heating
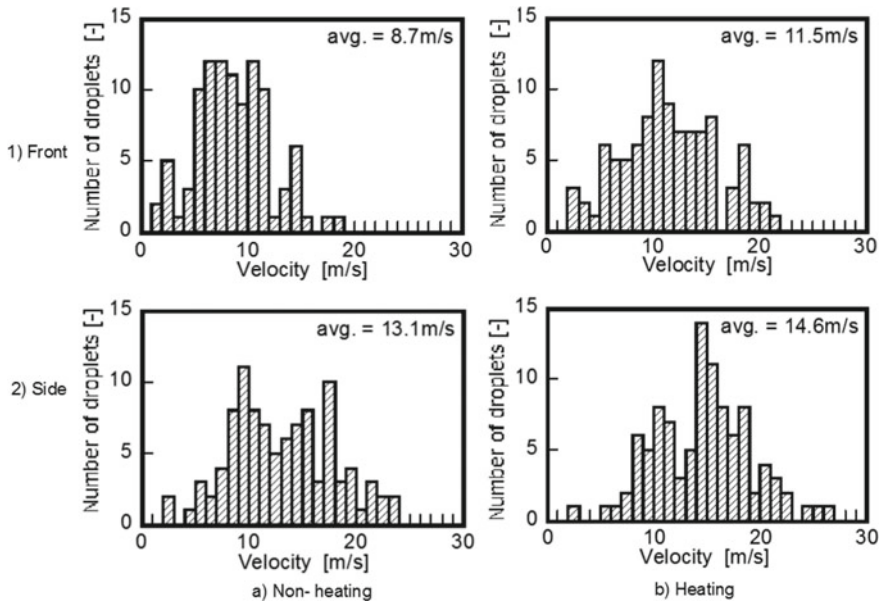
Fig. 12 Velocity analysis of droplets

effect on the atomization and vaporization of injected fuel [19–21]. For all images analyzed, it can be shown the effect of heating fuel on the spray structure. An increase in fuel temperature can increase the number of droplets. The increasing temperature also influences the movement of the droplets that are expected to improve the vaporization of fuel during injected into the combustion chamber.

4 Conclusion

An optical analysis was conducted to investigate the droplet characteristics of ethanol heated by LMI injector. According to the analysis results the following conclusion can be obtained:

– Droplets of the ethanol injected from LMI Injector tend to atomized finely which is expected to improve the evaporation of fuel.
– Velocity of the droplets increase also during heated by electromagnetic energy. This phenomena are expected to improve thermal efficiency of the internal combustion engine.

References

1. Zervas E, Montagne X, Lahaye J (1999) The influence of gasoline formulation on specific pollutant emissions. J Air Manag Assoc 49(11):1304–1314
2. Chen RH, Chiang LB, Chen CN, Lin TH (2011) Cold-start emissions of an SI engine using ethanol-gasoline blended fuel. Appl Therm Eng 31:1463–1467
3. Aleiferis PG, Pereira JS, van Romunde Z, Caine J, Wirth M (2010) Mechanisms of spray formation and combustion from a multi-hole injector with E-85 and gasoline. Combust Flame 157:735–756
4. Aleiferis PG, van Romunde ZR (2013) An analysis of spray development with Iso-octane, n-pentane, gasoline, ethanol and n-butanol from a multi-hole injector under hot fuel conditions. Fuel 105:143–168
5. Vasiliev LL, Burak VS, Kulakov AG, Mishkinis DA, Bohan PV (1999) Heat storage device for pre-heating internal combustion engines at start-up. Int J Therm Sci 38:98–104
6. Gumus M (2000) Reducing cold-start emission from internal combustion engines by means of thermal energy storage system. Appl Therm Eng 29:652–660
7. Zajdel A, Skorek J (2001) Evaluation of the influence of liquid fuel atomization on fuel consumption during heating of solids in a furnace. Energy 26:1135–1144
8. Kabasin D, Hoyer K, Kazour J, Lamers R, Hurter T (2009) Heated injector for ethanol cold starts. SAE International 2009-01-0615
9. Aleiferis PG, Pereira JS, Augoye A, Davies TJ, Cracknell RF, Richardson D (2010) Effect of fuel temperature on in-nozzle cavitation and spray formation of liquid hydrocarbons and alcohols from a real-size optical injector for direct injection spark ignition engine. Int J Heat Mass Trans 53:4588–4608
10. Enomoto H, Nozue H, Heida N (2014) Validation of heat-up effect on ethanol spray with local-contact microwave heating injector by using image analyses. Trans JSME 80(820). https://doi.org/10.1299/transjsme.2014tep0362. (In Japanesse)
11. Mangalla LK, Enomoto H (2013) Spray characteristics of local-contact microwave-heating injector fuelled with ethanol. SAE International Paper 2013-32-9126
12. Anand TNC, Mohan AM, Ravikhrisna RV (2012) Spray characteristic of gasoline-ethanol blends from a multihole port fuel injector. Fuel 102:613–623
13. Padala S, Le MK, Kook S, Hawkes ER (2013) Imaging diagnostics of ethanol port fuel injection sprays for automobile engine applications. Appl Therm Eng 52:24–37
14. Li G, Cao J, Li M, Quan Y, Chen Z (2012) Experimental study on the size distribution characteristics of spray droplets of DME/Diesel Blended Fuel. Fuel Process Tech 104:352–355
15. Mishra YN, Kristensson E, Berrocal E (2014) Reliable LIF/Mie droplet sizing in spray using structure laser illumination planar imaging. J Opt Express 22(4):4480–4492
16. Vicente J, Pinto J, Menezes J, Gaspar F (2013) Fundamental analysis of particle formation in spray drying. Powder Technol 247:1–7
17. Zeng W, Xu M, Zhang M, Zhang Y, Cleary DJ (2012) Macroscopic characteristics for direct-injection multi-hole sprays using dimensionless analysis. Exp Therm Fluid Sci 40:81–92
18. Sazhin SS, Kristyadi T, Abdelghaffar WA, Heikal MR (2006) Models for fuel droplet heating and evaporation: comparative analysis. Fuel 85:1613–1630
19. Matsumoto A, Moore WR, Lai M, Sheng Y, Foster M, Xie X, Yen D, Confer K, Hopkins E (2010) Spray characterization of ethanol gasoline blends and comparison to a CFD model for a gasoline direct injector. SAE International 2010-01-0601
20. Zhang M, Xu M, Zeng W, Zhang G, Zhang Y, Cleary DJ (2009) Characterization of methanol and ethanol sprays using mie-scattering and laser induced fluorescence under engine cold-start conditions. In: The 13th annual conference on liquid atomization and spray system-Asia
21. Oliveira ME, Franca AS (2002) Microwave heating of food stuffs. J Food Eng 53:347–359

CFD Investigation on Aerodynamic Characteristics and Performance of Windmill Aerator Type Savonius Four Blade

Darwin Harun, M. Dirhamsyah, Syarizal Fonna, Akhyar, Syifaul Huzni, and Muhammad Tadjuddin

Abstract The aeration process is a method of increasing dissolved oxygen levels in the water environment. One way to do this aeration process is by transferring oxygen into the water using a windmill aerator with a Savonius type windmill. These study aims are performance analysis that potential achieved of wind energy for the aerator system in carrying out its functions, a case study in Alue Kumba Village, East Aceh District. The method used is experimental testing on an aerator system that is placed in a four-meter high tower with a four-blade savonius windmill. The diameter and height of the blade are 56 and 82 cm, respectively, which serves to drive a single-acting type air pump with the diameter and height of 10 and 30 cm, respectively. The inhaled air is pumped into an air tank with 15 L capacity so that the air that leaves the water is continuous. The flow rate characteristics of the four-blade Savonius windmill with different heights at 2.5, 4, and 5.5 m will be discussed in this paper. Simulation using the finite element method will be analyzed using Computational Fluid Dynamic (CFD) software. The results of this study indicate that wind speed greatly affects the performance of the system. The highest wind speed recorded 8.98 m/s, which was seen on March 21, 2019, at 16.00 WIB (western Indonesian time) and wind power is 191.105 W. Some of the data recorded included the turbine power is 103.717 W, the intake air flow rate is 0.483 kg/min., the air pump power is 0.942 W, and the system efficiency is 1.17%.

Keywords CFD · Aerodynamic Characteristics · Windmill Aerator Type Savonius Four Blade

D. Harun (✉) · M. Dirhamsyah · S. Fonna · Akhyar (✉) · S. Huzni · M. Tadjuddin
Department of Mechanical Engineering, Universitas Syiah Kuala,
Jln. Syech Abdurrauf, No. 7 Darussalam, Banda Aceh 23111, Indonesia
e-mail: darwinmtir@unsyiah.ac.id

Akhyar
e-mail: akhyar@unsyiah.ac.id

367

1   Introduction

Wind energy is an alternative energy that is unlimited and easy to use. It is often used by humans to meet various needs such as electricity generation, rice milling in fields, irrigation, and aeration processes. The ease in utilizing wind energy makes humans always create new and creative ideas in the development of this energy utilization, such as in the aeration process. The aeration process is a process of increasing oxygen levels in the water which can be reached in two ways, namely by emitting water directly into the air, besides that by directly entering the air into the water so that it becomes small bubbles in the water. Gampong Alue Kumba, located in East Aceh District-Indonesia, is an area where almost three-fourths of the area is a stretch of fish and shrimp ponds, so this aeration process is something that is not uncommon in this area. Overall, the average wind energy potential in Indonesia is not large but based on surveys and wind data measurements that have been carried out since 1979, many areas are promising because they have annual average wind speeds of about 3.5–4.5 m/s [1]. In this condition, the wind turbine will work properly with a cut-in win speed is 3 m/s [2].

The Savonius wind turbine is one of the Vertical Axis Wind Turbine (VAWT) which has a cut-in win characteristic is easily rotates in low wind speed conditions, such as with wind speed in Indonesia conditions. The Savonius wind turbine has good self-starting so that it can rotate the rotor even though the wind speed is low, besides that the torque generated by the turbine is relatively high [3]. The vertical axis windmill is a type of windmill, whose main axis is arranged vertically perpendicular to the ground surface and the direction of the wind. Savonius type turbine in operation is to utilize drag force. This is because the resulting concave surface drag coefficient is greater than the convex surface. Therefore, the Savonius type has a relatively slow rotation ($\lambda \approx 1$) and has a low-efficiency Cp ≈ 1.5 until the maximum is Cp ≈ 2 [4].

Numerical simulation is needed to help a designer and engineer in predicting the parts of an engineering product before producing it. This simulation is necessary to reduce product failures. Several simulation and manufacture of various engineering product applications have been carried out, including numerical analysis of bicycle frames [5], simulation of hand prototypes through a kinematic model approach [6], different joints through welding simulations [7], review of turbine ventilator performance in Aceh by adding a bowl wind at the top of the wind turbine [8].

The purpose of this study is first to analyze the wind potential in Gampong Alue Kumba, Rantau Selamat District, East Aceh District-Indonesia, whether it can operate a windmill aerator with a Savonius windmill drive and a single-acting air pump as its air-producing component. Second, observing the highest wind speed, wind power, turbine power, airflow rate, pump power, and system efficiency from the results of field records. Third, observe the best height of the Savonius windmill to get the best wind speed. Fourth, comparing the simulation results with the field recording results on the performance of the four-blade Savonius windmill.

2 Method and Parameters

Simulations of aerodynamic characteristics have been carried out through computational analysis of computational fluid dynamics on the Savonius Four Blade aerator. In addition, a Savonius Four Blade type windmill aerator is built in our workshops. Field data collection to measure performance has been carried out in Alue Kumba Village, East Aceh District, Indonesia. This area is the target of our research to develop the community economy after the 2004 tsunami disaster [9]. Experiments and simulations in this study use Savonius four Blade windmills, with dimensions as shown in Fig. 1.

The simulation process begins designing the three dimensions of the Savonius four Blade Windmill. Furthermore, the meshing process in the form of tetra-mesh uses the top-up method on a part or area (volume) regularly, so that it can shorten
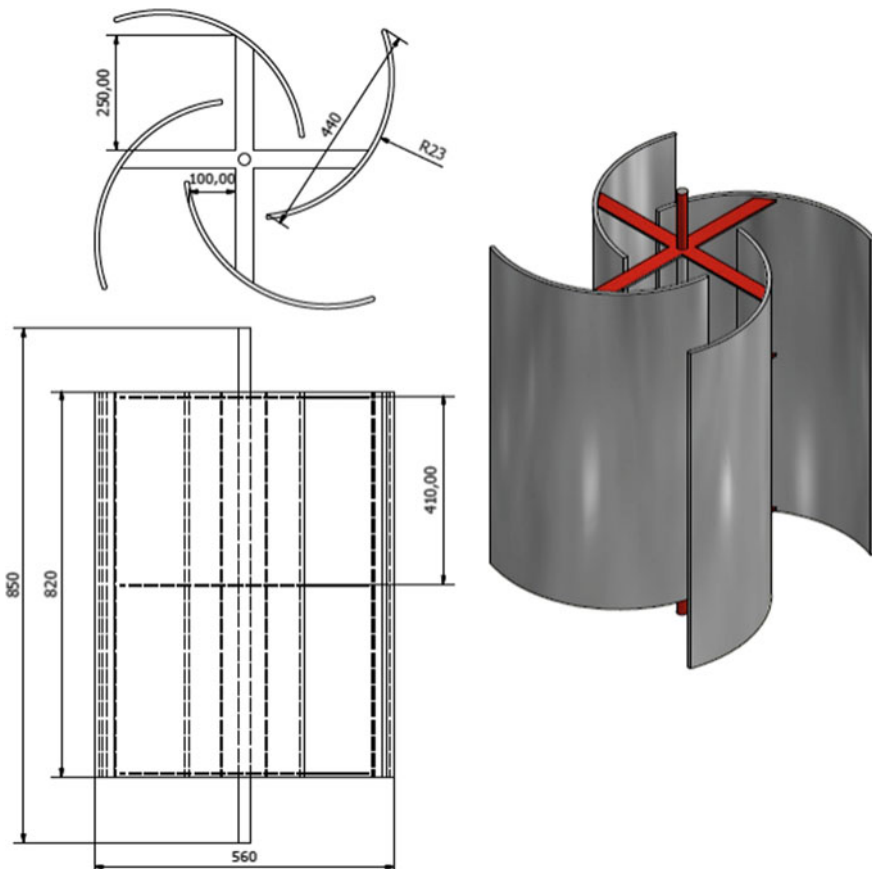
Fig. 1 The geometry of Savonius four Blade Windmill (in mm)
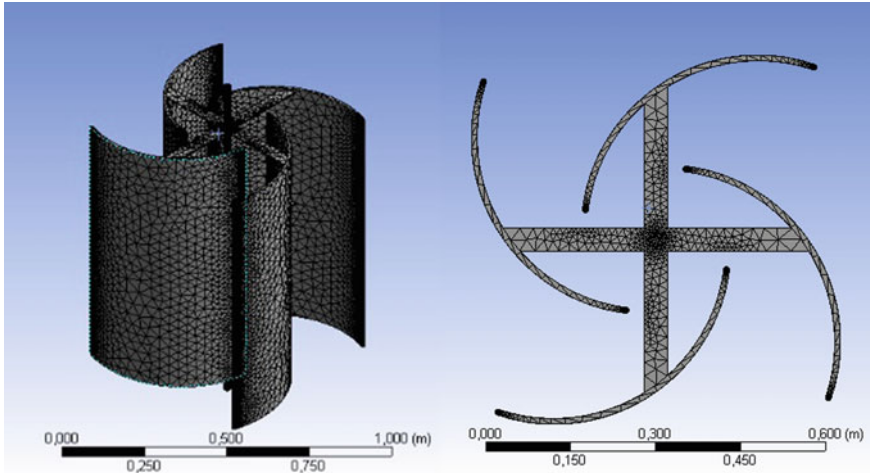
Fig. 2 Meshing Results

the calculation and convergence. The smaller the mesh size on an object, it more accurate in results. While the type of mesh used in the Savonius four Blade windmill is tetrahedral (Fig. 2). Schematic arrangement of the aerator system, as shown in Fig. 3. The placement of the measuring instrument in this experiment is as shown in Fig. 4.

Wind power can be determined by Eq. (1). The turbine mechanical power of the windmill is following Eq. (2). Analysis of the flow rate of air sucked by the pump (v_a) through Eq. (3), number of air pump power Eq. (4), aerator system efficiency Eq. (5). The power coefficient (Cp) is the ability of the windmill with the influence of the wind energy it receives. The number of the ratio between the converted mechanical power output from wind energy. Thus, the value of Cp is expressed by Eq. (6). The tip speed ratio states the ratio between the wind speed at the rotor tip and the wind speed through it. This tip speed ratio is varied and varies according to changing wind speeds. The tip speed ratio is expressed by Eq. (7), the TSR calculated by a derivative from the Torque calculation formula. Tip speed ratio and coefficient power are the main parameters in assessing the performance achievement value of a windmill. These two parameters are also linked in a curve that shows the relationship for each type of windmill rotor. Torque is a quantitative of the tendency for a force to cause or change the rotational motion of an object can be calculated with the Eqs. (8) and (9) [10].

$$p_o = \frac{1}{2} \cdot \rho.A.v_1^3 \tag{1}$$

$$p_t = \frac{1}{4} \rho A \left(v_1^2 - v_2^2\right)(v_1 + v_2) \tag{2}$$
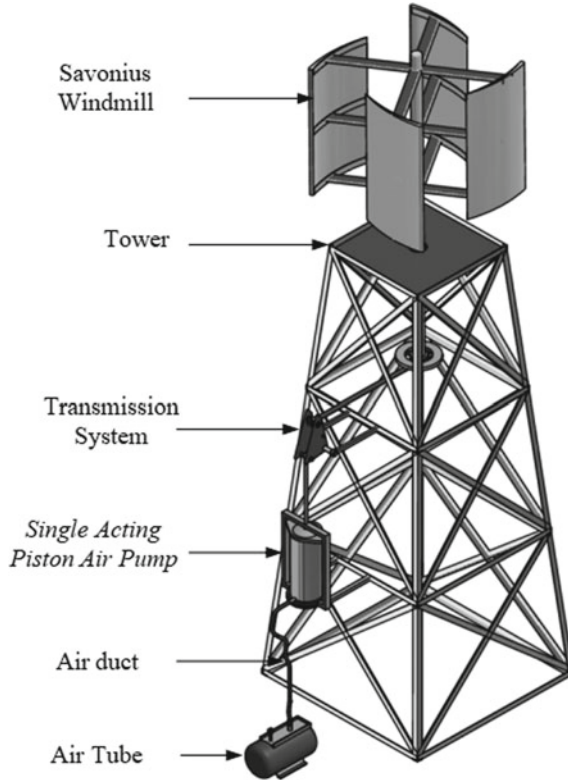
Fig. 3 Schematic of the aerator system

$$v_a = 2\frac{\pi}{4}.D^2.S.n.\eta_v.60 \tag{3}$$

$$N_{th} = 0.037.P_1.v_a.\frac{k}{k-1}\left\{\left(\frac{P_2}{P_1}\right)^{\frac{k-1}{k}}-1\right\} \tag{4}$$

$$\eta_{tot} = \frac{N_{th}}{p_o.\eta_{trans}} \times 100\% \tag{5}$$

$$C_p = \frac{P_t}{P_o} = \frac{\frac{1}{4}\rho A\left(v_1^2 - v_2^2\right)(v_1 + v_2)}{\frac{1}{2}.\rho.A.v_1^3} \tag{6}$$

$$\tau = \frac{v^2.R^3}{\lambda^2} = \lambda^2 = \frac{v^2.R^3}{\tau} = \lambda\sqrt{\frac{v^2.R^3}{\tau}} \tag{7}$$

(a)   (b)
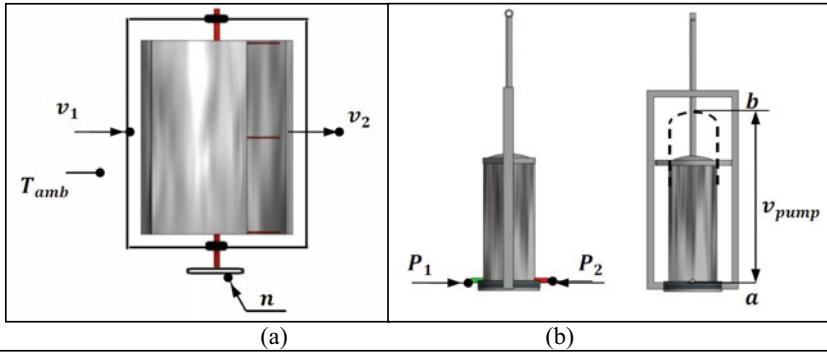
Caption:
- Wind speed before passing through the rotor of the mill (v_1)
- Wind speed after passing through the rotor of the mill (v_2)
- Windmill rotation speed (n)
- Air temperature (T)
- Air pump movement speed (v_{pump})
- Air pump intake/suction pressure (P_1)
- Air pump outlet/exhaust (P_1) pressure

Fig. 4 Placement of the measuring instrument: **a** in the windmill area, and **b** in the air pump

$$\tau = I.\alpha \tag{8}$$

$$\tau = \frac{v^2.R^3}{\lambda^2} \tag{9}$$

where:

P_o = wind power (Watt)
ρ = density of air (kg/m^3)
A = cross-sectional area of flow (m^2)
P_t = turbine power (Watt)
v_1 = velocity of air flow, before passing the rotor (m/s)
v_2 = velocity of air flow, after passing the rotor (m/s)
v_a = volume inhaled/air discharge (m^3/s)
S = step length (m)
D = piston diameter (m)
n = rotating rotation (rpm)
η_v = volumetric efficiency (81%)
N_{th} = air pump power (Watt)
P_1 = cylinder inlet pressure (kgf/cm^2)

P_2 = cylinder exit pressure (kgf/cm^2)

k = coefficient of gas left in the residual volume. For air ($k = 1, 4$)

η_{tot} = total aerator system efficiency (%)

P_o = wind power (Watt)

η_{trans} = transmission efficiency (%)

Cp = coefficient power

λ = tip speed ratio

τ = torque (kgf·cm).

3 Result and Discussion

3.1 Experiment

The investigations were carried out by experimental in the open air and not special treatment during data collection. The wind duration is only 5–10 s during data recorded, the data is taken every 30 min. Observation results will be obtained data on the effect of increasing and decreasing wind speed which is a form of energy produced by the wind on the performance of the aerator system. Table 1 is a

Table 1 Aerator system performance based on experimental data recording

| Time	Temperature (°C)	Wind speed		Windmill rotation (rpm)	Pump motion (m/s)	Pump pressure	
		V_1 (m/s)	V_2 (m/s)			P_1 (kg/cm^2)	P_2 (kg/cm^2)
09:00	29.10	1.52	0.5	–	–	–	–
09:30	29.20	2.10	0.22	–	–	–	–
10:00	30.80	1.32	0.3	–	–	–	–
10:30	31.10	4.43	1.72	85.12	3.5	−0.003	0.002
11:00	32.10	5.04	2.01	98.20	3.9	−0.004	0.003
11:30	33.00	4.90	1.08	93.20	3.7	−0.005	0.003
12:00	33.50	6.14	2.23	137.70	5.0	−0.007	0.006
12:30	33.80	6.79	2.85	159.70	6.3	−0.008	0.007
13:00	34.25	7.07	3.56	173.51	7.1	−0.006	0.004
13:30	33.50	6.01	2.01	118.80	4.5	−0.007	0.006
14:00	33.20	7.13	3.68	174.20	7.4	−0.012	0.011
14:30	33.20	7.36	3.86	189.25	8.6	−0.013	0.012
15:00	33.10	8.56	4.39	210.30	10.2	−0.013	0.012
15:30	32.80	8.34	4.22	200.98	9.6	−0.008	0.007
16:00	31.20	8.98	4.90	230.56	10.9	−0.014	0.013
16:30	30.30	7.22	3.50	179.14	7.7	−0.012	0.011
17:00	30.00	5.99	2.39	112.30	4.9	−0.008	0.007
17:30	29.03	4.97	2.48	95.52	3.9	−0.007	0.005
18:00	28.01	3.18	1.99	–	–	–	–
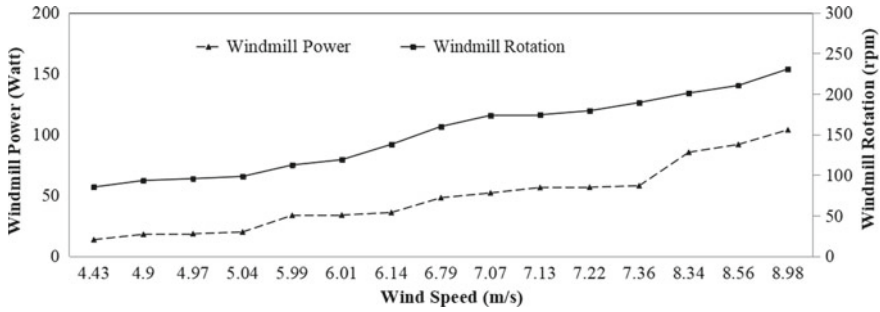
Fig. 5 The windmill rotation and windmill power are affected by wind speed

recapitulation of the performance of the aerator system that has been obtained from observing for three days.

Figure 5 shows windmill rotation versus wind speed and windmill power versus wind speed. Wind speed has a linear effect on windmills, this is caused by weather conditions around the pond that affect wind speed. The type of aerator system that develops in this experiment recorded the minimum wind speed is 3.03 m/s to operate the aerator system. Wind speed data from three days of observation shows that the wind energy around the fish-pond where the experiment was carried out has the potential to operate the windmill aerator. The aerator is used for the fish-pond aeration process so that the oxygen circulation in the water is good enough. From the results of the recording, it can be seen that at certain times an increase in wind speed exceeds the minimum limit in operating the aerator system so that the windmill power and rotation obtained also greater. The highest wind speed recorded is 8.98 m/s, producing a windmill rotation is 230.56 rpm, and the power windmill absorbed is 103.717 W.

Figure 6 shows that the wind speed influences the air pump, which is the airflow that is sucked by the pump and pump power. These two parameters have a relationship that is directly proportional to the increasing wind speed. The increasing
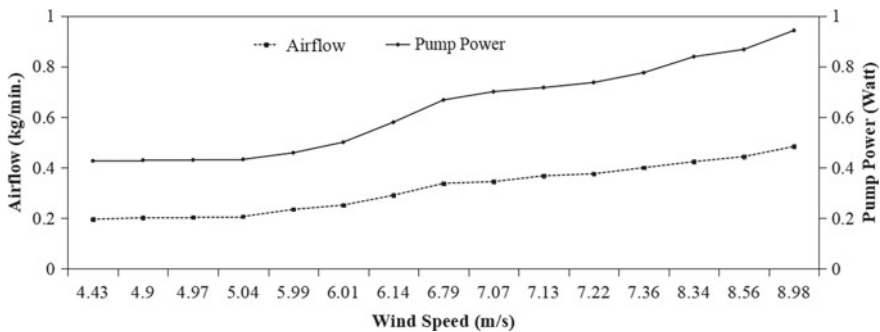
Fig. 6 Effect of wind speed on air pumps
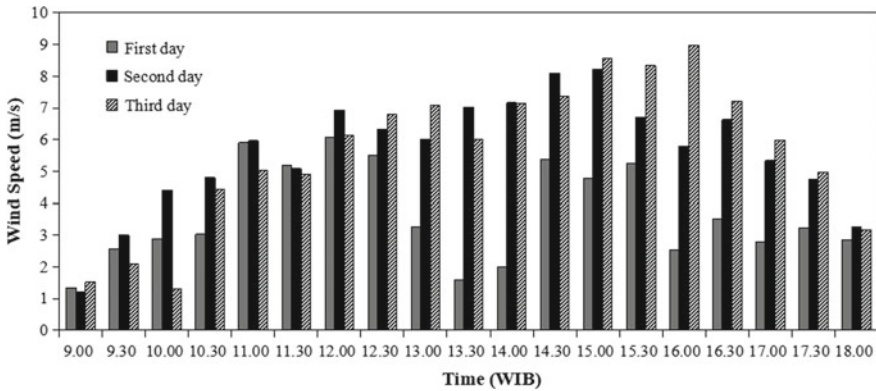
Fig. 7 Wind speed in the fish-pond area for three days of data collection
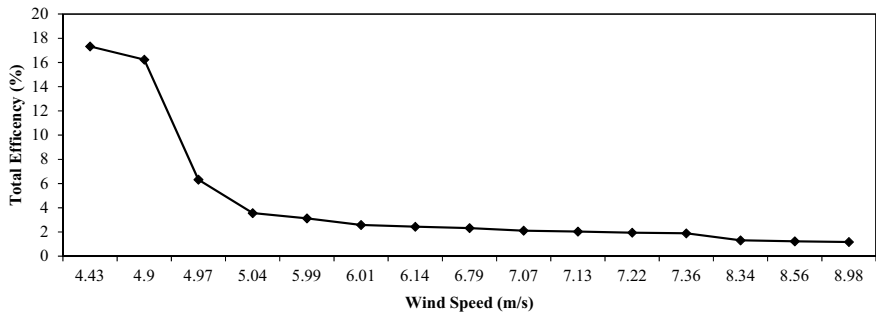

Fig. 8 Effect of wind speed on system efficiency

wind speed is followed by the enlarging airflow from the air pump and followed by the air pump power. There is a certainty between airflow and wind speed, airflow increases because the higher the rotation of the windmill makes the air pump (single-acting piston pump) will also rotate quickly. The increasing speed of air pump rotation makes the airflow that is sucked up by the pump higher.

Figure 6 shows the number of pump rotations increases with increasing wind speed, so the airflow will increase with increasing wind speed. The maximum airflow obtained is 0.483/minute with a wind speed of 8.98 m/s at 16.00 (Western Indonesia Time) and pump rotation is 230.56 rpm. Air pump power is influenced by the airflow that is sucked into the air pump in the aerator system. Related to Eq. 3, if the greater the air debit that is sucked and the pump power will also higher, it is 0.942 W with a wind speed of 8.98 m/s.

Figure 7 is the wind speed for three days of data collection in the area of the pond where the aerator system is installed. The wind speed during data collected on the first day tends to be lower than the next day, this is because on that day the

weather conditions are in a bad category, and there is light rain around the pond area. However on the second and the next day the wind speed (wind energy) tends to increase due to the sunny weather around the fish-pond. The maximum wind speed is obtained on the third day of data collection at 16.00, with a wind speed of 8.98 m/s.

Figure 8 shows the effect of increasing wind speed on the efficiency of the system achieved. The results are inversely proportional where that the increasing wind speed (v) the aerator system efficiency achieved decreases. Results of the efficiency of the aerator system will tend to increase with increasing wind speed, but this is contrary to the facts and results that have been obtained in the field. After analyzing, it occurs due to the lack of air pump power in balancing the kinetic energy of the wind which continues to increase. This is confirmed by Eq. 1, where the number of wind speed was third order means that the potential for wind energy to operate the aerator system greater. The pump power that is produced will never reach significantly high results due to the limited dimensions of the main components that exist in the air pump, such as the diameter of the cylinder is 10 cm, and the length of the air pump is 7 cm, this is indicated by the lack of airflow that is sucked up by the air pump. So with the increase in wind power, the air pump as a producer of air leading to the fish-pond is considered less effective in offsetting the number of wind energy available due to its limitations. Efforts to improve the efficiency of the aerator system can be done by enlarging the dimensions of important components in the air pump such as the cylinder diameter, piston connecting rod, and most importantly the length of the air pump. The length of the air pump gives a big enough effect on the airflow that is sucked by the pump. Rotations that continue to increase due to wind speed, can make the performance of air pumps achieve high results or at least the air pump used can offset the increase in wind energy that will move it in operating the aerator system in the fish-pond area.

Increasing the height of the windmill installation causes the number of the wind speed that passes through the Savonius four Blade windmill rotor will increase. Increasing the value of pressure, flow velocity, and turbulent kinetic energy can be seen in Fig. 9.

Figure 9a can be seen that the decrease in pressure of the Savonius four Blade Windmills and wind speed at height is 5.5 m windmill installation obtain optimal work compared to other heights. The pressure on the 5.5 m height of the windmill installation reaches the highest number (it is 110.42 Pa) with optimal distribution when passing through the windmill rotor so that it decreases to 40.37 Pa. Figure 9b can be seen that the flow velocity at the windmill is getting higher followed by the addition of the height of the windmill. Optimal flow velocity distribution is obtained at height of the windmill installation of 5.5 m because it is above the value of flow velocity at another height and has decreased by 8.9 m/s and then distributed to 5.16 m/s. Figure 9c shows that the highest of turbulent kinetic energy at the wind speed is 8.98 m/s (at the windmill installation of 5.5 m) because the flow velocity at the windmill installation of 5.5 m achieves the highest flow velocity. Increasing the flow velocity will increase the turbulent kinetic energy. The higher the turbulent number of kinetic energy, the greater the power generated [6].
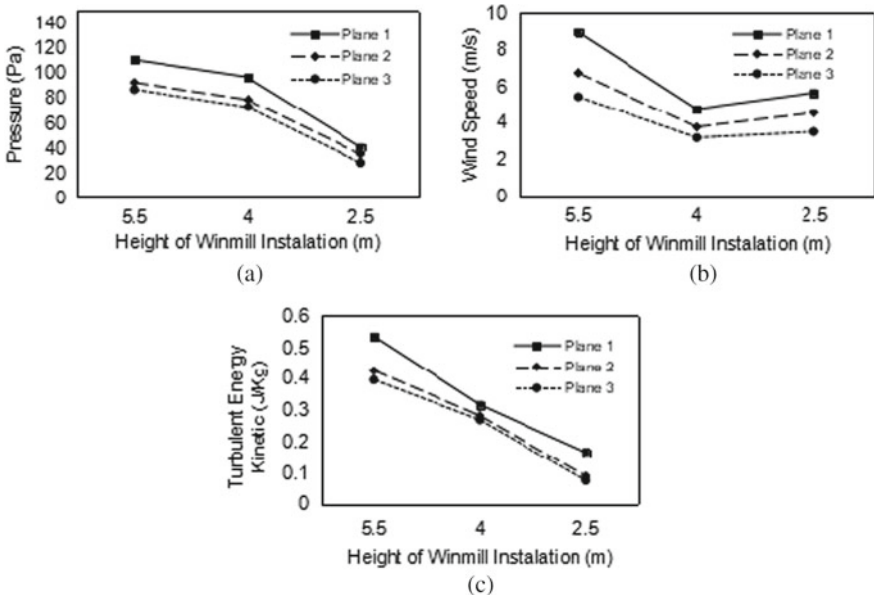
Fig. 9 **a** Pressure distribution, **b** wind speed, **c** turbulent kinetic energy on Savonius four Blade windmills

3.2 Simulation

The reddish color gradation in Fig. 10a, b shows that the inlet of the outer blade of the windmill is the part that has the most pressure. This is caused by the part being first struck by the fluid flow. The moment required is not too large because of the rotation caused by the initial moment [8].

The gradation of yellow in contour pressure is evenly distributed on the inside and outside of Savonius windmills. This shows that the fluid flow is well distributed. The velocity contour seen in Fig. 10c, d undergoes gradations of red and greenish at the inlet of the windmill blade but after that change to blue colors. This shows that the fluid flow passes through the windmill is directly forwarded to the center of the windmill and towards the blades of the outlet so that it can rotate the windmill, but the wind speed decreases due to the number of wind energy lost when the flow rate passes through the center of the windmill.

Figure 10e, f can be seen that at the blade of the windmill the inlet section has the largest turbulent kinetic energy, this can be seen from the gradation of color at the inlet blade up to the inside blade of the windmill. In the middle part of the Savonius windmill, the gradation of light blue color is expanding to the center of the windmill means the turbulent kinetic energy is more evenly distributed. But the windmill side of the outlet, only on the windmill blade which receives kinetic energy. This indicates that at each outer blade the windmill is able to convert flow velocity into turbulent kinetic energy.
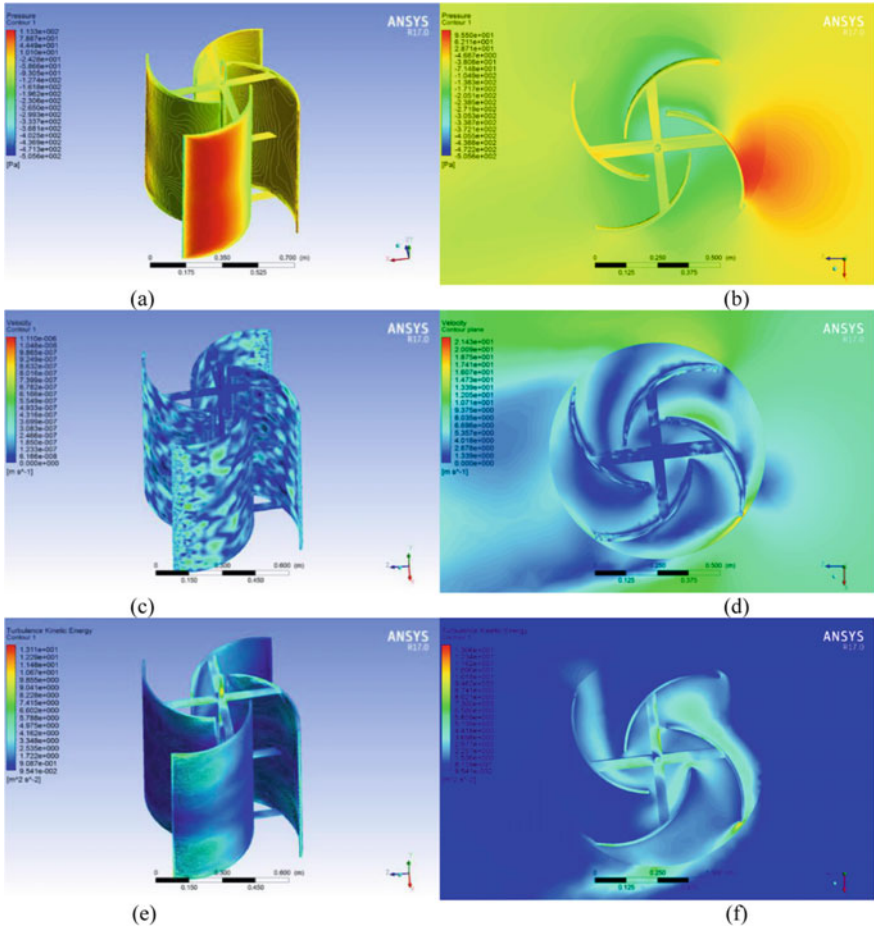
Fig. 10 Distribution of: **a** pressure distribution on the blade, **b** top view of pressure distribution, **c** velocity distribution on the blade, **d** top view of velocity distribution, **e** turbulence kinetic energy distribution on the blade, and **f** top view of the kinetic energy turbulence distribution

3.3   Simulation and Experiment

Simulation data obtained include pressure data, velocity, and turbulence kinetic energy, torque data can also be obtained, so that simulation data can be compared with experimental data, as can be seen in Fig. 11a. Figure 11b and c, they can be seen that the calculation of tip speed ratio and coefficient power (Cp) between experimental data and simulation data possess almost the same trend, particularly at 10.30, 12.30, and 16.00 WIB with a wind speed of 4.43, 6.79, and 8.98 m/s.
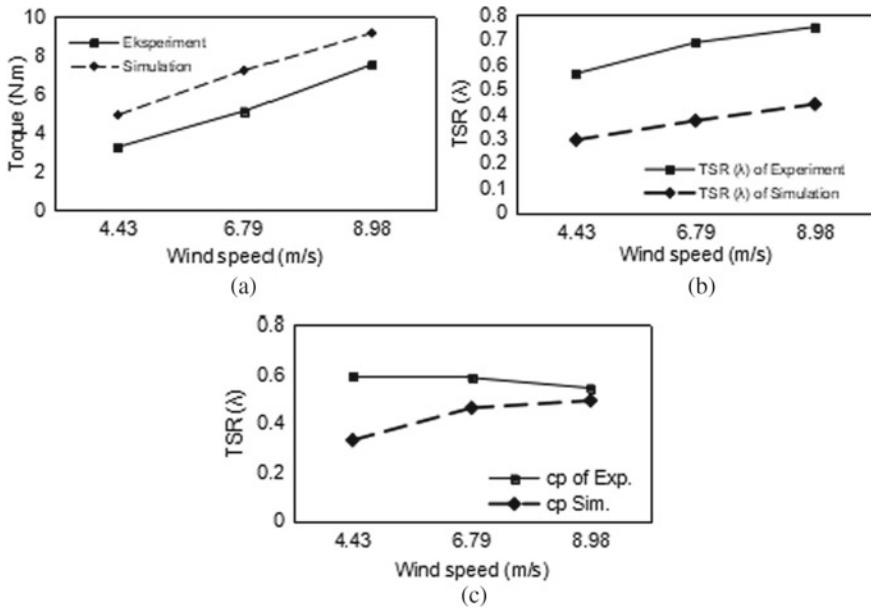
Fig. 11 Comparison between experiments and simulations for **a** torque, **b** tip speed ratio, and coefficient power

4 Conclusions

Based on the results of the study, it was concluded that the wind energy in Alue Kumba Village, Rantau Selamat District, East Aceh Regency was declared to have the potential to operate a windmill aerator with a Savonius windmill drive and a single-acting air pump as its air-producing component. The maximum wind speed is 8.98 m/s in sunny weather conditions. Only certain conditions, such as cloudiness and light rain, can make the wind speed significantly lower. However, even though it is cloudy, it is still possible to operate this windmill aerator because the minimum wind speed required is 3.03 m/s. The highest wind speed is 8.98 m/s, produces wind power of about 191.105 W, turbine power is 103.717 W, the airflow is 0.483/minute, air pump power is 0.942 W, and system efficiency is 1.17%.

The performance results obtained are that the average wind energy is higher, which shows the results that tend to increase with increasing speed, such as the rotation of the windmill, the power of the turbine, the power of the pump, and also the air flow rate. In contrast to the system efficiency which tends to decrease with increasing wind speed, due to the limitations of the air pump in terms of the dimensions of the main components of the air pump such as cylinder diameter, piston rod, and also the stride length. So that with the increase in existing wind power, the air pump is less able to keep up with the available energy. So that efforts can be made to increase system efficiency or at least compensate for the amount of

wind energy by reconstructing the air pump by enlarging the dimensions of its main components so that the resulting performance is more optimal.

The height of 5.5 m is the best altitude with the highest wind speed of 8.98 m/s. The simulation results that have been carried out on the Savonius four-blade windmill show that at an altitude of 5.5 m it produces better performance compared to other heights. The pressure distribution value is 110.42 Pa, the flow velocity is 8.98 m/s, and the turbulent distribution of kinetic energy is 0.535 J/Kg. The simulation results also show that at an altitude of 5.5 m the largest torque value is 8.41 Nm.

References

1. Susandi A (2006) Potensi Energi Angin dan Surya di Indonesia. Meteorologi ITB, Bandung. (In Indonesia)
2. Rizal Bintang S (2014) Uji Performansi Turbin Angin Sebagai Penggerak Aerator di Tambak Udang, Departemen Teknik Mesin, Fakultas Teknik, Universitas Sumatera Utara. (In Indonesia)
3. Sargolzay J (2007) Prediction of the power ratio in wind turbine savonius rotors using artificial neural networks. Int J Energy Environ 2(2)
4. Imanuel M (2012) Performansi Turbin Angin Savonius Dengan 3 Sudu Untuk Menggerakkan Pompa, Departemen Teknik Mesin, Fakultas Teknik, Universitas Sumatera Utara. (In Indonesia)
5. Akhyar, Husaini, Hasanuddin I, Ahmad F (2019) Structural simulations of bicycle frame behaviour under various load conditions. In: Materials science forum, vol 961, pp 137–147. https://doi.org/10.4028/www.scientific.net/MSF.961.137
6. Husaini, Hasanuddin I, Sandi-Yudha BZ, Akhyar H (2018) Stress analysis on mechanical hand prototype with kinematics model approach and performance tests. In: AIP conference proceedings 1983, p 030001. https://doi.org/10.1063/1.5046236
7. Riswanda, Akhyar, Sugianto, Kadir H, Rizal S (2020) Numerical simulation of the effect of shoulder rotation on the tensile strength of FSW dissimilar joints of aluminum alloy. In: Defect and diffusion forum, vol 402, pp 90–99. https://doi.org/10.4028/www.scientific.net/DDF.402.90
8. Harun D, Zulfadhli, Akhyar H (2018) Investigation of turbine ventilator performance after added wind cup for room exhaust air applications. In: IOP conference series: materials science and engineering, vol 352, p 012011. https://doi.org/10.1088/1757-899X/352/1/012011
9. Farhan A, Akhyar H (2017) Analysis of tsunami disaster map by geographic information system (GIS): Aceh Singkil-Indonesia. In: IOP conference series: earth and environmental science, vol 56, p 012002. https://doi.org/10.1088/1755-1315/56/1/012002
10. Hau E (2006) Wind Turbine Fundamental, Technologies, Applications, Economics, 2nd edn. Springer, Berlin, Heidelberg, Germany, pp 81–89

The Influence of Triple Tube Heat Exchanger as a Liquid Collecting System on Bio-oil Production by Pyrolysis Process

Nasruddin A. Abdullah, Zainal Arif, Suheri, Nazaruddin, and Hamdani Umar

Abstract Indonesia with its abundant natural wealth and waste that has the potential to become a bioenergy barn and other chemical substances. Bio-oil is one of the products which can be obtained from the biomass originated from waste and forestry production. Pyrolysis is one way to produce bio-oil that can be used as fuel to generate electricity, chemical compound, and preservatives. Many variables influence the product in the pyrolysis process. Triple tube heat exchange is the type of condenser that can be used to collect the liquid from pyrolysis vapor. Jati Belanda (Guazuma ulimfolia Lamk) is a feedstock with a size <0.707 mm with an average moisture content of 7 wt% (dry). The reaction temperature used 500 °C with heating supply 1500 W, reaction zone heater set at 150, and 250 °C. Cooling water at ambient temperature is used to absorb the heat with an inner and outer cooling flow, also a combination of both inner and outer cooling flow. The maximum liquid smoke yield was obtained on reaction zone heater 150 °C with the inner and outer cooling flow, which is 49 wt%. The triple tube heat exchanger absorbs the maximum heat from the vapor until 35.77 W. The more expanse condensation area will produce a more liquid amount.

1 Introduction

Indonesia, as an agricultural country that has many rice fields, farms, and forestry. In general, the most available biomass in Indonesia is wood, sawdust, and farm products; such as the waste from the oil palm industry, maize, sugarcane, agricultural products; rice husks. Data statistics Ministry of Environment and Forestry

N. A. Abdullah (✉) · Z. Arif · Suheri · Nazaruddin
Department of Mechanical Engineering, Faculty of Engineering, Universitas Samudra, Kota Langsa 24416, Indonesia
e-mail: nasruddin@unsam.ac.id

Z. Arif · H. Umar
Department of Mechanical Engineering, Universitas Syiah Kuala, Darussalam, Banda Aceh 23111, Indonesia

2015 from the year 2011–2015 the production of wood chips in Indonesia in 2011 was 1,864,142 m^3 and in the year 2015 amounted to 25,856,152 m^3. This data shows that wood waste always increases from year to year [1]. Wood waste and plant material need to be used for more beneficial substances. *Guazuma ulimfolia* Lamk. That also known as Jati Belanda is available in a large amount, especially in Indonesia, and this type of wood can be used as furniture, and also it can be converted into a liquid product. The decomposition of chemical compounds from biomass is obtained in the form of liquid smoke or bio-oil. Liquid smoke is produced from the decomposing biomass into pyrolysis vapor and condenses into a liquid. The biomass containing hemicellulose, cellulose, lignin, and other carbon compounds. In general, the raw material from wood consists of about 50% cellulose, 25% hemicellulose, and 25% lignin [2].

Bio-oil is obtained from the vapor condensation of the pyrolysis process using a liquid collecting system. Pyrolysis is a thermochemical method for decomposing chemical compounds by heating on raw materials without involving oxygen inside. Pyrolysis is divided into four steps, starting from the evaporation of water, then followed by decomposition of hemicelluloses, cellulose, and the latter of lignin composition. Hemicellulose and cellulose pyrolysis occur between 180 and 350 °C which produces carboxylic acids and carbonyl components while the new lignin will be polarized at 300–500 °C and produce phenols [2–4]. The main variables affecting product yield and liquid smoke characteristics are temperature, heating rate, the particle size of raw material, pyrolysis atmosphere, vapor residence, and the composition of biomass [3]. The liquid collecting system is a heat exchanger device which can be used as liquefaction from the vapor phase into a liquid phase. The working principle of the liquid collecting system is the same as the heat exchanger [5]. A vapor chamber has been used to utilize rapid cooling [6]. The heat exchanger is a device that functions to absorb thermal energy (enthalpy) between two or more fluids at different temperature conditions in the thermal contact state [7], here is a need to enhance the effectiveness of double tube heat exchanger as a liquid collecting system on pyrolysis of the wood material to improve the liquid product quantity [8]. A modified version of a double tube heat exchanger is created to cover the disadvantages of the double tube heat exchanger and to increase the quantity of the liquid that produces from the pyrolysis process. A triple tube heat exchanger is made to improve the heat transfer rate through an additional flow passage and a larger heat transfer area per unit length. Little investigations have studied the thermal performance of the triple tube heat exchanger [9–11].

Many papers investigate and analyzed the type of reactor [12], pyrolysis type [13], sweeping gas [14], but still, few were discussed about the use of the triple tube heat exchanger as a liquid collecting system on the pyrolysis process. In this paper, we investigate the influence of the triple tube heat exchanger as a liquid collecting system for producing bio-oil. The feedstock used in this paper is Guazuma ulimfolia Lamk wood from a local carpenter.

2   Materials and Methods

2.1   Material and Sample Preparation

The material as a feedstock to produce bio-oil is the waste wood from the local carpenter, the type of wood was Guazuma ulimfolia Lam, also known as Jati Belanda. The material was prepared by shredded into small pieces, then sieved into size 25 mesh so the particle size will be <0.707 mm. The sieved material must be dried below 10% of moisture content; 200 grams of raw material was fed into a reactor with density 0.248 gr/cm^3. The feedstock from Guazuma ulimfolia Lamk presented in Fig. 1.

2.2   Experimental Setup

Laboratory scale of a tubular fixed-bed reactor with base material SS316L. The reactor was equipped with an electric heater and installed in the system. The volume of the reactor is 1.065 cm^3. Proportional Integral and Deferential (PID) controller was connected to a heater to control the reactor temperature at 500 °C. In the process, there is no sweeping gas injected into the system. The voltage regulator was installed to control the heating rate of the feedstock. An electric heater was also installed at the reaction zone to vary the vapor temperature; a PID controller was connected to the heater at the reaction zone to prevent early condensation [15]. A thermocouple type K was placed at the outside wall of the reaction zone as a reference temperature of PID. The voltage regulator was connected to the reaction zone heater to control the heating supply to the heater. Figure 2 showed the experimental setup for investigation in this research.

To condense the hot pyrolysis vapor, a triple tube heat exchanger as a liquid collecting system (LCS) was made from SS304L the ambient temperature of cooling water flowed into LCS to reduce hot fluids which generated in the reactor. The dimension of the triple tube heat exchanger showed in Table 1. The feedstock
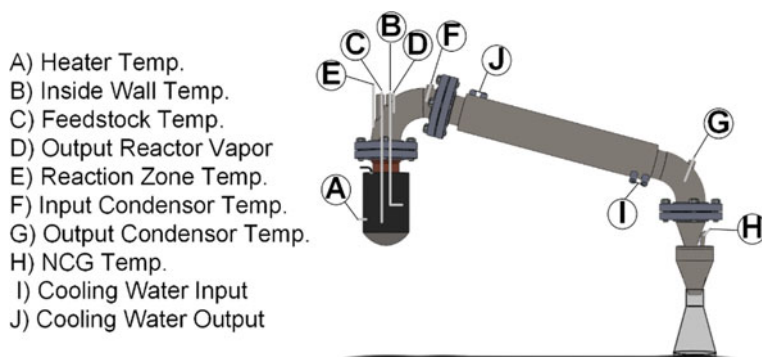

Fig. 1 Guazuma ulimfolia Lamk wood as feedstock
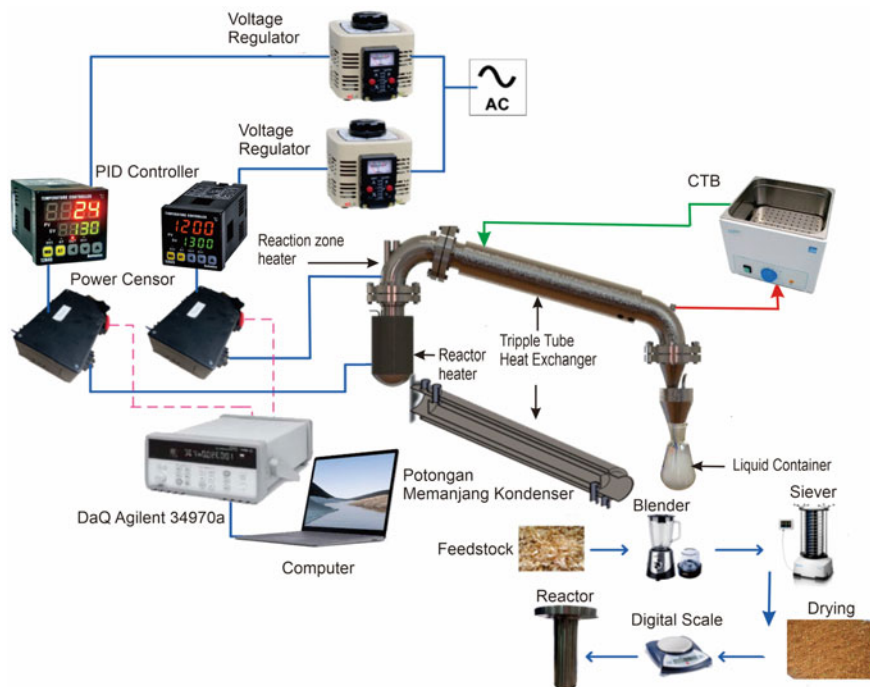
Fig. 2 Experimental Setup

Table 1 The dimension of the triple tube heat exchanger

Geometrical Characteristics	Inner Tube	Intermediate Tube	Outer Tube
Outer diameter (mm)	48.3	88.9	114.3
Inner diameter (mm)	42.7	82.8	108.2
Wall thickness (mm)	2.8	3.1	3.0
Length (mm)	550.0	660.0	600.0
Tube material	SS304L	SS304L	SS304L

was converted into vapors, which were condensed in the LCS and to be a bio-oil, through the condenser and all of the liquid will be collected in the collection tank, meanwhile, the non-condensable gas (NCG) will be through the gas outlet above the collection tank.

Thermocouples were placed at several points to investigate the temperature as shown in Fig. 3. Mass balance for non-condensable gas was calculated based on the total mass of feedstock which subtracted by weighing the product of liquid and solid yield. The product yield was calculated according to the following equation [16]:

A) Heater Temp.
B) Inside Wall Temp.
C) Feedstock Temp.
D) Output Reactor Vapor
E) Reaction Zone Temp.
F) Input Condensor Temp.
G) Output Condensor Temp.
H) NCG Temp.
I) Cooling Water Input
J) Cooling Water Output

Fig. 3 Thermocouple position

$$\text{Liquid yield}\,(\%) = (\text{liquid weight})/(\text{feed weight}) \times 100\%, \tag{1}$$

$$\text{Solid yield}\,(\%) = (\text{solid weight})/(\text{feed weight}) \times 100\%, \tag{2}$$

$$\text{Ash/char yield}(\%) = 100\% - (\text{liquid yield} + \text{solid yield}). \tag{3}$$

The maximum liquid yield was investigated according to the operational variables of the triple pipe heat exchanger. The heat absorbed in the heat exchanger calculated using Eq. (4).

$$\dot{Q}_n = \dot{m}_n c_n (T_{n_o} - T_{n_i}) \tag{4}$$

where $\dot{Q}_n$ is the heat absorbed in the heat exchanger, $\dot{m}_n$ is the mass flow rate of cooling water, c_n is the heat capacity of cooling water and $T_{n_o} - T_{n_i}$ is the mean of temperature deferent of cooling water input and output.

2.3 Experimental Variation

The reaction temperature was maintained at 500 °C, and this temperature was controlled by PID. The voltage regulator controls the electric supply to the heater at 1500 W. This power supply will create the heating rate from 5 to 7 °C/minute. The variation of temperatures at the reaction zone is 150 and 250 °C. Those variation temperatures as a way to obtain the different performance of the heat exchanger with the different heat gain. The vapor temperature influences the product yield [17]. In this experiment, the cooling water flow was divided into three types, which are inner, outer, and outer combined with the inner annulus cooling system. In the

condenser, the heat of the vapor was absorbed by cooling water and its phase was changed into the liquid. The temperature variation was used to determine the effect of cooling water flow to produce maximum liquid.

3 Result and Discussion

3.1 Product Yield

The product yield consists of the liquid, ash, and non-condensable gas. The liquids were condensed in the heat exchanger correspondent to each boiling point of the compound. The maximum liquid oil as called bio-oil was 49 wt% obtained with the combination flow, inner and outer at vapor temperature 150 °C as shown in Table 2, compared to the other research, the liquid yield 46 wt% using a double pipe as condenser and camphor wood as feedstock [15], 35–45 wt% at reaction temperature 300–700 °C [18], and 35–42.5 wt% using a heat pipe fin L-shaped condenser [17]. The increasing of liquid yield not significant because of the condensable gas in the volatile at those cooling water temperature are limited. The higher temperature produces more gases in consequence of second decomposition [19]. Figure 4 shown the stacked bar of product yield due to the cooling water flow in the triple tube heat exchanger and vapor temperature at (a) 150 °C and (b) 250 °C.

3.2 Heat Absorbed by Cooling Water in the Heat Exchanger

Table 3 shows the heat absorbed by cooling water in the heat exchanger. The maximum heat absorbed by a heat exchanger with combination flow, which is inner and outer flow, both vapor temperature at 150 and 250 °C as well, the more expanse condensation area will produce more liquid amount. The maximum heat absorbed was occurred at vapor temperature 250 °C for inner and outer flow correspondent to the high temperature and extensive area of heat transfer in the heat exchanger.

Table 2 Product yield due to the type of condenser

Vapor Temperature	Cooling flow (wt%)	Liquid (wt%)	Ash (wt%)	NCG (wt%)
150	Inner	47.0	30.5	22.5
	Outer	47.5	31.5	21.0
	Inner and Outer	49.0	7.5	43.5
250	Inner	46.0	25.0	29.0
	Outer	46.5	26.5	27.0
	Inner and Outer	47.0	13.5	39.5
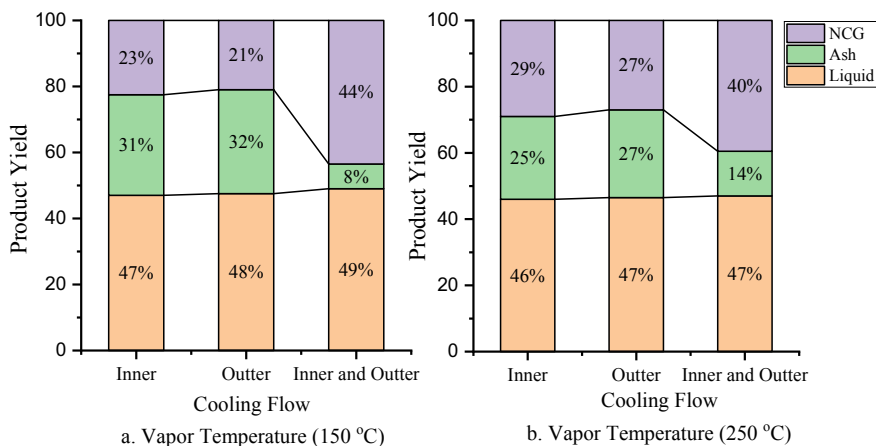
Fig. 4 Total product yield due to the type of cooling water flow

Table 3 Heat absorbed by cooling water in the heat exchanger

Description	Vapor temperature 150 °C			Vapor temperature 250 °C		
				Flow		
	Inner	Outer	Inner and Outer	Inner	Outer	Inner and Outer
Mass flow (kg/s)	0.08	0.08	0.08	0.08	0.08	0.08
Cp (J/kg K)	4188	4188	4188	4188	4188	4188
Cooling water in (°C)	30.35	31.46	29.92	31.45	32.09	27.66
Cooling water out (°C)	30.37	31.48	30.02	31.49	32.17	27.77
Delta T (°C)	0.02	0.03	0.10	0.05	0.08	0.11
Heat absorbed (W)	6.76	8.16	33.18	14.44	24.46	35.77

4   Conclusion

Triple tube heat exchanger affected the product yield in the pyrolysis process. The maximum liquid yield is 49 wt% with Jati Belanda (Guazuma ulimfolia Lamk) as feedstock, particle size <0.707 mm, average moisture content of 7 wt% (dry), the reaction temperature 500 °C, heating supply 1500 W, vapor temperature at 150 °C, and the ambient temperature of cooling water with a combination of inner and outer flow. The triple tube heat exchanger absorbs the maximum heat from the vapor until 35.77 W.

References

1. Kehutanan KLHD (2015) Statistik Kementerian Lingkungan Hidup Dan Kehutanan Tahun 2015. Kementrian Lingkungan Hidup dan Kehutanan
2. Šimko P (2005) Factors affecting elimination of polycyclic aromatic hydrocarbons from smoked meat foods and liquid smoke flavorings. Mol Nutr Food Res 49:637–647
3. Ramakrishnan S, Moeller P (2002) Liquid smoke: product of hardwood pyrolysis. Fuel Chem Div Preprints 47:366
4. Abdullah NA, Novianti A, Hakim II, Putra N, Koestoer RA (2018) Influence of temperature on conversion of plastics waste (polystyrene) to liquid oil using pyrolysis process. In: IOP conference series: earth and environmental science: IOP publishing, p 012033
5. Bridgwater AV (2012) Review of fast pyrolysis of biomass and product upgrading. Biomass Bioenerg 38:68–94
6. Hasnan A, Putra N, Septiadi WN, Ariantara B, Abdullah NA (2017) Vapor chamber utilization for rapid cooling in the conventional plastic injection molding process. Int J Technol 8:690–697
7. Luo G, Suto T, Yasu S, Kato K (2000) Catalytic degradation of high density polyethylene and polypropylene into liquid fuel in a powder-particle fluidized bed. Polym Degrad Stab 70:97–102
8. Abdullah NA, Putra N, Hakim II, Koestoer RA (2017) A review of improvements to the liquid collection system used in the pyrolysis process for producing liquid smoke. Int J Technol 8:1197–1206
9. Gomaa A, Halim M, Elsaid AM (2016) Experimental and numerical investigations of a triple concentric-tube heat exchanger. Appl Therm Eng 99:1303–1315
10. Gomaa A, Halim M, Elsaid AM (2017) Enhancement of cooling characteristics and optimization of a triple concentric-tube heat exchanger with inserted ribs. Int J Therm Sci 120:106–120
11. Radulescu S, Negoita IL, Onutu I (2012) Heat transfer coefficient solver for a triple concentric-tube heat exchanger in transition regime. Rev Chim (Bucharest) 8:820–824
12. Bridgwater A (1999) Principles and practice of biomass fast pyrolysis processes for liquids. J Anal Appl Pyrolysis 51:3–22
13. Marshall ASJ, Wu PF, Mun SH, Lalonde C (2014) Commercial application of pyrolysis technology in agriculture. In: 2014 Montreal, Quebec Canada, July 13–July 16, 2014: American society of agricultural and biological engineers, p 1
14. Kim P, Weaver S, Labbé N (2016) Effect of sweeping gas flow rates on temperature-controlled multistage condensation of pyrolysis vapors in an auger intermediate pyrolysis system. J Anal Appl Pyrolysis 118:325–334
15. Abdullah NA, Tila J, Hakim II, Putra N, Koestoer RA (2018) An experimental study of the vapor temperature in the reaction zone for producing liquid from camphor wood in a non-sweeping gas fixed-bed pyrolysis reactor. Int J Technol 9:1236–1245
16. Ly HV, Kim S-S, Choi JH, Woo HC, Kim J (2016) Fast pyrolysis of Saccharina japonica alga in a fixed-bed reactor for bio-oil production. Energ Conver Manag 122:526–534
17. Abdullah NA, Tila J, Hakim II, Koestoer RA, Putra N (2020) Influence of feedstock particle size from Merbau Wood (Intsia bijuga) on bio-oil production using a heat pipe fin L-shaped condenser in a pyrolysis process. Eng J 24:261–271
18. Park J, Lee Y, Ryu C, Park Y-K (2014) Slow pyrolysis of rice straw: analysis of products properties, carbon and energy yields. Biores Technol 155:63–70
19. Ly HV, Kim S-S, Woo HC, Choi JH, Suh DJ, Kim J (2015) Fast pyrolysis of macroalga Saccharina japonica in a bubbling fluidized-bed reactor for bio-oil production. Energy 93:1436–1446

Experimental Study of Thermoelectric Cooler Box Using Heat Sink with Vapor Chamber as Hot Side Cooling Device

Adi Winarta, I. Made Rasta, I. Nyoman Suamir, and I. G. K. Puja

Abstract Thermoelectric refrigeration system is considered environmentally friendly because it does not use refrigerants which have huge potential for damaging the ozone layer. In this experimental work, a vapor chamber heat sink was used to absorb heat at the hot side of Peltier module of the cooler box. The cooler box has 215 mm × 175 mm × 130 mm of inner dimension. The performance of cooler box is analysed for each different current supplies to the thermoelectric module. The result shows that increasing the current result in larger temperature difference of the hot and the cold side, increase the cabin temperature, decrease the COP of the cooler box. The experimental result also stated that highest COP with 500 ml of water within the cooler box is 0.72.

Keywords Thermoelectric · Cooler box · Vapor chamber · COP · Thermoelectric refrigerator

1 Introduction

Refrigeration is the mechanism of decrease space temperatures to a level that is lower than its environment. There are at least eight types of refrigerant systems. Among them are vapor-compression, absorption, thermoelectric (TEC), air-standard, steam jet, solar, thermo acoustic and metal hydride refrigeration [1].

A. Winarta (✉) · I. M. Rasta · I. N. Suamir
Mechanical Engineering Department, Politeknik Negeri Bali, Jalan Raya Kampus Bukit, Kuta Selatan, Bali 80364, Indonesia
e-mail: adi.winarta@pnb.ac.id

I. G. K. Puja
Mechanical Engineering Department, Sanata Dharma University, Yogyakarta, Indonesia

The most popular refrigeration system is vapor compression (VC). It is not surprising due to its highest efficiency compare with others systems. Unfortunately, the majority of refrigerants used by the vapor compression system still contained chlorine which causes global warming and thinning of the ozone layer [1].

Thermoelectric is one of the solutions to reduce the detrimental effects of the refrigerants used in vapor compression system. However, not every application would be fit with thermoelectric characteristics as a refrigeration system. But in certain applications such as military, medical industries, aerospace, and instrumentation, thermoelectric might be preferred over any other system. Due to less noise and fewer mechanical moving parts, accurate temperature control, compact design, and low-cost maintenance [2, 3]. Thermoelectric also can be supplied with direct current power which can be generated from any renewable energy source which could increase its efficiency [4].

Many studies had been published concerning the evaluation of thermoelectric refrigeration performances, in the past years. Most of the studies have been conducted to increase the efficiency of the thermoelectric system as a cooling device or refrigerator. Min and Row [5] studied the performance of several types of coolers that used a thermoelectric system and compared it with a vapor compression system. They found not only the performance characteristic of thermoelectric but further improvement may be possible with reducing contact resistance, fixing the thermal design, and making a realistic model. Dai et al. [6] studied the thermoelectric refrigerator with solar cell driven. They showed the refrigerator's COP was maintained at about 0.3 under conditions suitable with cabin temperatures ranging from 5 to 10 °C. Vián and Astrain [7] experimented with increasing the performance of thermoelectric refrigeration using a heat exchanger based on the thermosiphon principle for the hot and cold sides. Their device successfully increases the C.O.P of the thermoelectric refrigerator. Jugsujinda et al. [8] studied the thermoelectric cooler box with 0.022 m^3 cabin volume. They could decreased the cabin temperature from 30 to -42 °C in 60 minute using 3.5 A of electric current to Peltier module. The COP of thermoelectric was 0.22 for the supply power of 40.46 W. Gökçek et al. [4] experimentally studied mini-channel water as the cooling device of thermoelectric hot side. They reported that increased the flow rate of water to mini-channel decrease the inner temperature of the cold side. Mirmanto et al. [8] used two different types of heat sink units on the hot side of thermoelectric cooler box to improved the system performance. Their result stated the experimental COP increase with time for COP increases sharply for while and then get flat as long as the device operation. They also stated that heat sink fan is more reliable if the energy consumed became a consideration. Mirmanto et al. also studied about the position of Peltier module at the thermoelectric cooler box with the effect COP from its position variation. Their box was 0.004891 m^3 in volume and made from 50 mm of Styrofoam. The also put a 360 ml of water as a cooling loads. They result stated that Peltier module which attached at the side wall of cooler box giving the best performance. Lertsatitthanakorn et al. studied the performance of thermoelectric air cooling using the vapor chamber [9]. Their result shows that vapor chamber increase the system performance up to 32.2% compare with conventional heat sink.

In thermoelectric refrigeration, cooling device usually applied as thermal management for the hot side of TEC. One method to improve thermoelectric cooling performance is to maximize the absorption of heat released at the hot side. Better performance of TEC was achieved if the temperature of hot side can be reduced to desired level with the use of heat pipe [10]. Many researches also had been performed with many passive device such as heat pipe, thermosyphon as a cooling device [7, 10–12].

Vapor chambers plates are other types of passive device cooling which is one of the heat pipe family [13–15]. Vapor chamber generally used to collect heat from flat and larger area sources of heat transfer. Vapor chambers are generally used for high heat flux applications due to its characteristic as a latent passive cooling. It has unique or genuine two-dimensional spreading area from other conventional heat pipe like tubular pipe.

Many types of heat sink, includes active and passive, have been investigated by many researchers to achieved the maximum cooling at thermoelectric refrigeration [4, 7, 9, 10, 16]. However, very few work have been conducted with the vapor chamber as a thermoelectric hot side cooler, especially for the cooler box. To the author best knowledge there is no study performed using vapor chamber in thermoelectric cooler box yet. Therefore, the objective of the research was to find the performance of thermoelectric cooler box using vapor chamber as the cooling device of the hot side.

2   Method and Material

To study the vapor chamber as a cooling device of hot side thermoelectric, a cooler box was built made from polyurethane and has a thickness of 40 mm. Configuration of experimental test of thermoelectric cooler box is shown in Fig. 1. It is composed of a cooler box with thermoelectric module unit, data acquisition unit for temperature logging, power supply units for thermoelectric module and fans, a power meter for electricity power measurement. The inner dimension of the cooler box was approximate 215 mm × 175 mm × 130 mm with the thermoelectric module inserted at the top of the box. Peltier module TEHC1-12710 for cooling from ®Thermonamic was used as a cooling device for the cooler box. It has dimensions of 40 mm × 40 mm × 3.6 mm. Seeback coefficient, thermal conductivity and internal resistance of thermoelectric are 0.00023 V/K, 1.5 W/m °C, 1.25 Ω, respectively. The vapor chamber heat sink used in this experiment was supplied from Dongguan Awind Electronic Technology Co., Ltd. The device dimension was approximately 90 mm × 90 mm × 2.4 mm exclude the heat sink which embedded into one part as shown in Fig. 2. An extender used between the hot side of TEC and vapor chamber which made from copper block with a dimension of 40 mm × 40 mm × 35 mm. The cooper block dimension is 40 mm × 40 mm × 35 mm A cold sink with a dimension of 90 mm × 90 mm × 20 mm was clamped tight at the cold side of TEC using the bolt and nut structure. Two DC axial fan were used at the top of vapor
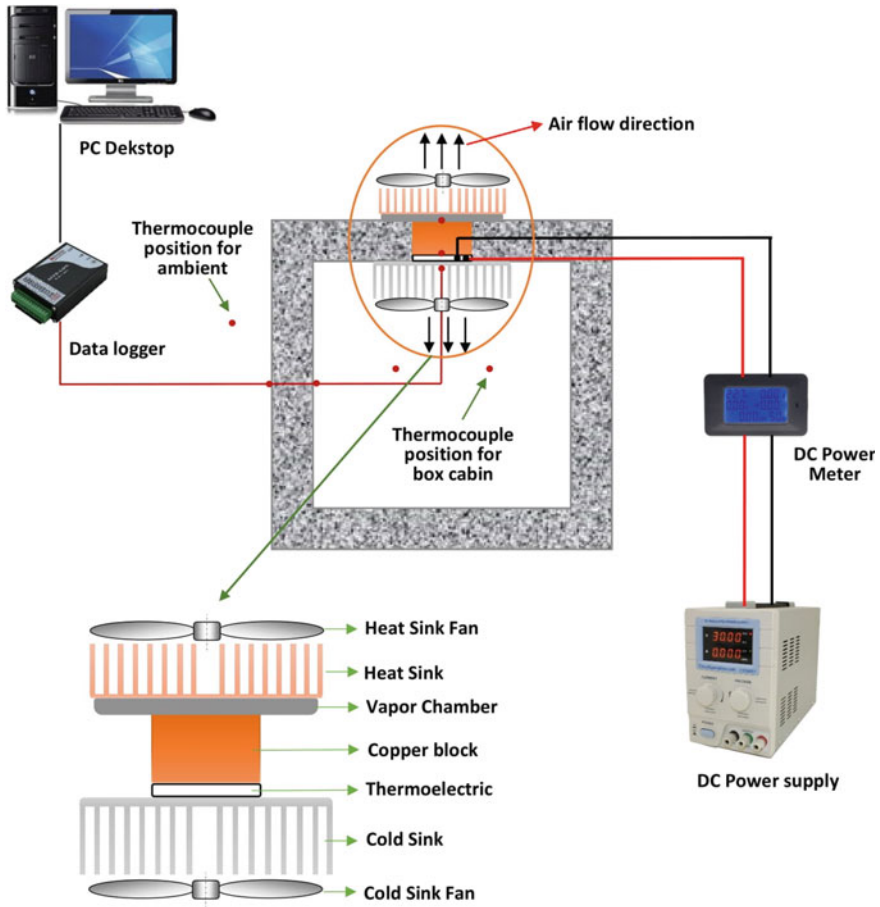
Fig. 1 Schematic of experimental setup

chamber and the bottom of cold sink to increase the convective heat transfers. This fan has a dimension of 90 mm × 90 mm × 24 mm and operates at 12 V/0.15 A. Thermal paste with 1.97 W/m °C of thermal conductivity was used to minimize all the contact resistance between vapor chamber with heat sink, thermoelectric module, cold sink and copper block. The DC power flows to the thermoelectric module was measure using PZEM-017 power meter with measurement error of 1%. The DC power supplied for both fans was handle by ®Sanfix DC power regulator. Type-K thermocouples (accuracy ± 0.5 °C) was used to measure all the temperatures and connecting it with data acquisition from National Instrument (NI 9213 and NI 9274). Thermocouple positions are displayed in Fig. 1 with the red dots. Temperature data were record with data acquisition software and store on a desktop PC.

The goal of this study was to inspect the cooling performance (COP) of thermoelectric cooler box using vapor chamber as the hot side cooling device. Test were performed at five different currents: 4, 5, 6, 7 and 8 A. The test was carried out
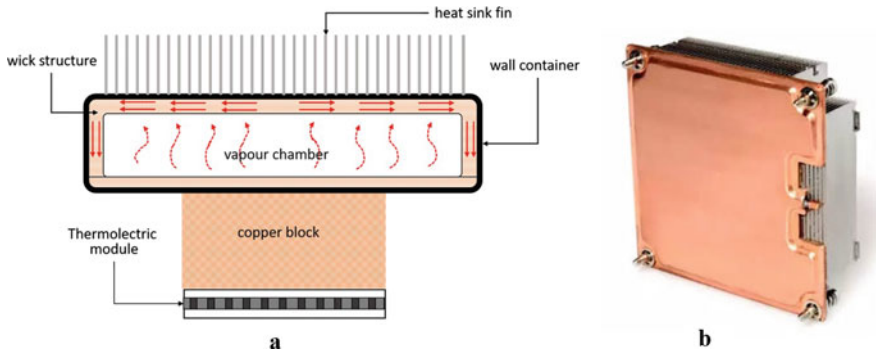
Fig. 2 Vapor chamber, **a** structure of inner side, **b** attached with heat sink

by supplying voltage to the thermoelectric and fan then observing the resulting temperature data. The effect of current supplied to the Peltier module which using a vapor chamber is investigated. Such as temperature of the hot and cold side of TEC, cabin temperature, temperature of vapor chamber evaporator, ambient temperature and inner and outer wall temperature of cooler box, and thermoelectric and fan power supplied. The ambient temperature was set constant around 25 °C using air conditioning.

The calculation of COP using the following expression [4, 17]:

$$COP = \frac{\dot{Q}_T}{P_{total}} \tag{1}$$

where $\dot{Q}_T$ (watt) is total rate of refrigeration load of thermoelectric cooler box and calculated from expression below:

$$\dot{Q}_T = \dot{Q}_a + \dot{Q}_c + \dot{W}_{inner\,fan} \tag{2}$$

$\dot{Q}_T$ is consist of the heat transfer of air inside the cabin box ($\dot{Q}_a$) and heat flow through the walls ($\dot{Q}_c$) entering the cabin inside the cooler box. $\dot{W}_{inner\,fan}$ also calculated as part of refrigeration load using its rate of electrical power consumption [4]. The power consumes of cooler box indicated by P_{total} (watt), which is express in following equation:

$$P_{total} = P_{vc\,fan} + P_{TEC} \tag{3}$$

$\dot{Q}_a$ is the heat transfer of air within the cabin. The rate of heat transfer was calculated based on the air property using the following equations:

$$\dot{Q}_a = \frac{dE}{dt} = m_a c_{p,a} \frac{dT}{dt} \tag{4}$$

E is the energy (J), $\dot{Q}_a$ is the air heat transfer rate (watt), m_a is the mass of air (kg), $c_{p,a}$ is the specific heat of air (J kg^{-1} K^{-1}), $dT.dt^{-1}$ is the temperature gradient per unit time. $\dot{Q}_c$ calculated using Eq. (5) below;

$$\dot{Q}_c = A \cdot U \cdot (T_{amb} - T_{cabin}) \tag{5}$$

where A is the total heat transfer surface of cooler box (m), U is the overall heat transfer coefficient, T_{cabin} is the average temperature of refrigerated space (Fig. 1) and ambient temperature T_{amb}. The calculation of overall heat transfer coefficient is using Eq. (6) below.

$$U = \frac{1}{\frac{1}{h_{int}} + \frac{L}{k_{wall}} + \frac{1}{h_{ext}}} \tag{6}$$

The heat transfer coefficient at cold sink was calculated using correlation given by Parmelee and Huebscher [4, 7]. The equation is given below as (7) and (8).

$$Nu = 0.664 \cdot Pr^{1/3} \cdot Re^{1/3} \tag{7}$$

$$\begin{bmatrix} 0.6 \leq Pr \leq 50 \\ Re < Re_{x,c} \approx 5 \times 10^5 \end{bmatrix} \tag{8}$$

3 Results and Discussion

Table 1 provides the power information given for each variation of the current supply to the TEC module. Figure 3 shows the cold and hot side temperature of thermoelectric due to the effect of different supply current. Increasing the current supply to the thermoelectric module result in an increase in temperature hot side and a reverse effect on the cold side temperature. The cold side lowest temperature

Table 1 Variation of supplied current to the TEC module

Current (amp)	Voltage (V)	Power (W)
4	6.75	27
5	8.4	42
6	10.4	62.5
7	13	91.6
8	14.87	119
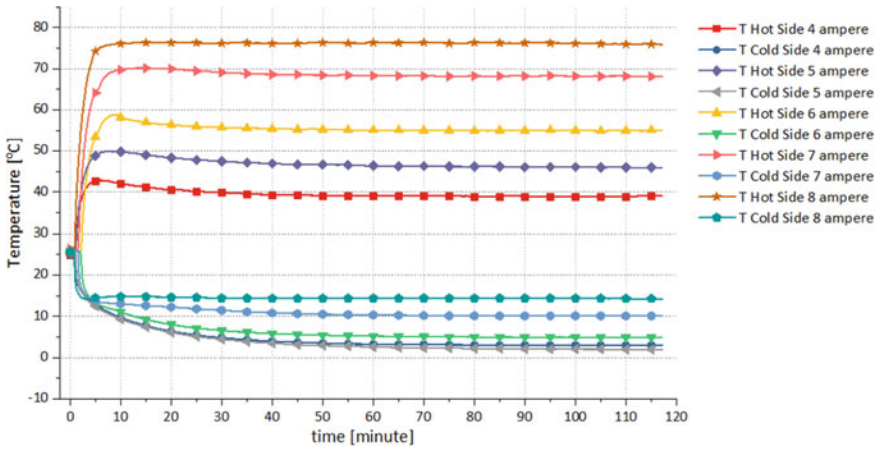
Fig. 3 Temperature of hot and cold side of TE versus times for each current supplied
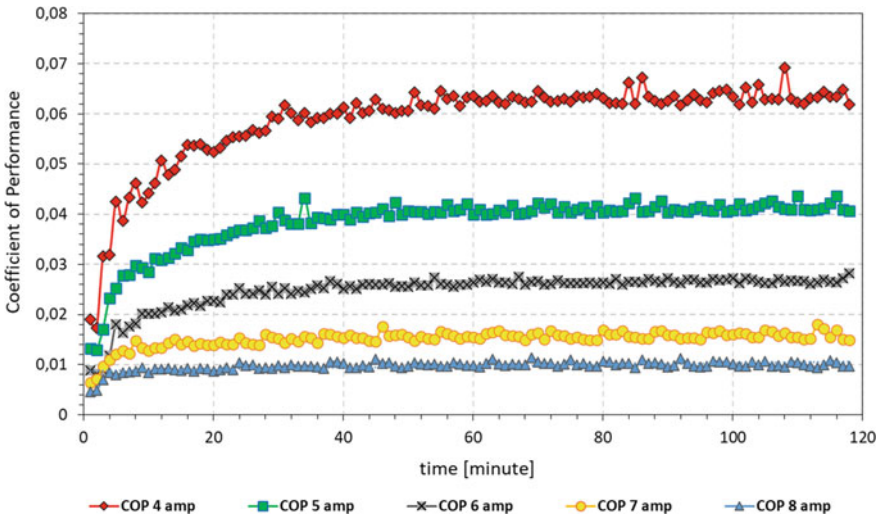
Fig. 4 Variation of COP due to different current supplied to the TE Cooler Box

1.94 °C achieved by 5 A of current supply. Meanwhile, the highest hot side temperature 75.92 °C was found on a current supply of 8 A. Increase the supply current enlarge the temperature difference between the hot side and the cold side which would decrease the cooling capacity of the thermoelectric module.

The COP versus time which calculated using Eq. 1 for each different current is shown in Fig. 4. All COP values showed almost similar trends. The graph increases at an early stage and gradually stable after around 60 minutes. This trend agrees with result that had been showed by Mirmanto et al. [11]. The $\dot{Q}_c$ component in Eq. 2

increases due to an elevation of the temperature difference between the cabin and the environment during the cooling period. Therefore the COP value increases with respect to cooling time until the cabin temperature reaches a steady-state condition. A current supply of 4 A has the highest average COP value which is about 0.0588. Increases the current to the module result in a decrease in COP. This is due to more heat that had to be rejected out from the hot side of the Peltier module. Resulting in larger of TEC temperatures different and lower cooling capacity.

Figure 5 shows the cabin temperatures of cooler box for each different current. The lowest cabin temperature was achieved by 5 A current which is around 5.94 °C. Meanwhile, for 8 A current result in cabin temperature around 17.36 °C. In fact for the refrigerator purpose, the temperature achievement for 4 A, around 6.73 °C was quite successful if we consider energy consumption which is only 27 W. At higher current supply, more than 6 A, did not give appropriate cooling for the requirement of cooler box. Therefore, we may conclude that lower current gives a more efficient cooling performance in terms of energy and achievement of temperature.

To enrich the analysis, the additional load was added and tested only for 4 A current supply, which the highest performance of the preceding test. The additional load, 500 ml tap water, also to test the response of cooler box from regenerated object. The temperature trends of cooler box using 500 ml of water depicted at Fig. 6a. The heat transfer rate for the product load is calculated using the following equation:

$$\dot{Q}_w = \frac{dE}{dt} = m_w c_{p,w} \frac{dT}{dt} \tag{9}$$
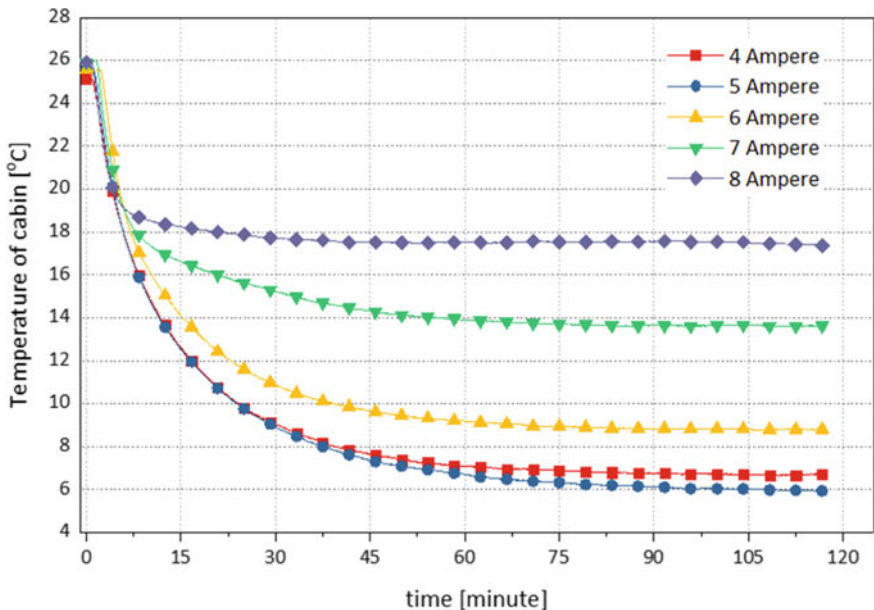
Fig. 5 Cabin temperature variation due to different current supplied
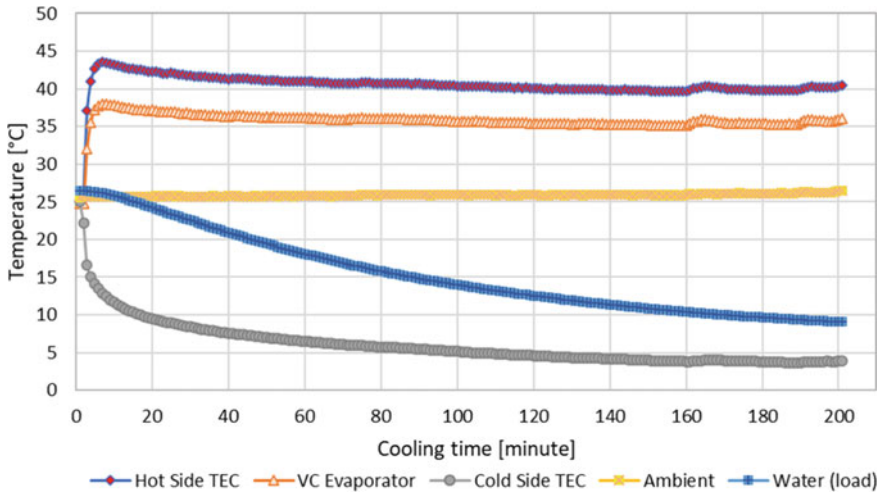
Fig. 6 Temperature trends of TE Cooler box **a** without water as cooling load **b** with 500 ml water

where m_w is the mass of water, $c_{p,w}$ is specific heat of water. Figure 6 shows the period time of water cooling around 200 min from 26.4 °C until 9.09 °C. This may look quite well if considering the non-use of the dangerous refrigerant that may be harmful to the environment.

With the data from cooler box with additional water load, the comparison was made between a cooler box with and without 500 ml of load for the same current supply. Cooler box with and without water load will be referred to as "load" and "no-load" as shown in Fig. 7. The COP calculation with load was derived from
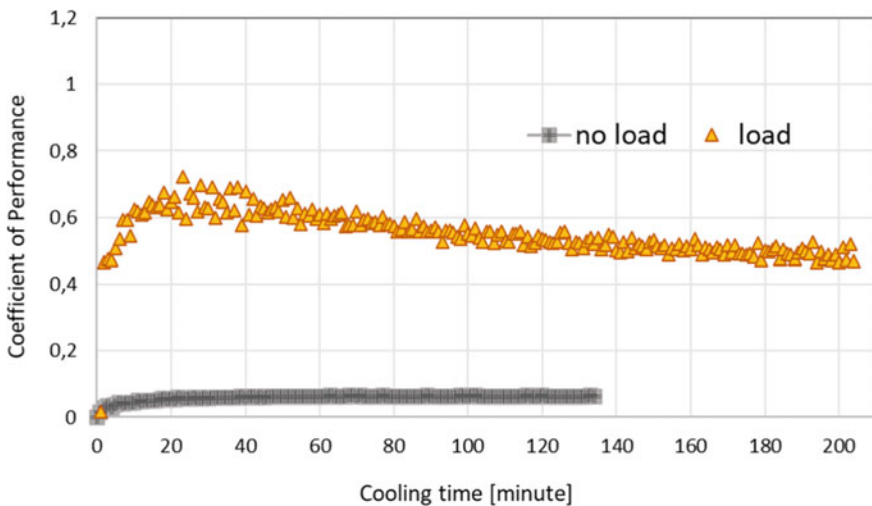
Fig. 7 COP comparation between cooler box with load (500 ml of water) and no load

recalculation of Eq. 1. The total refrigeration load ($\dot{Q}_T$) was add with heat transfer rate from water ($\dot{Q}_w$) from Eq. 9. Adding water as product load will increases significantly the performance ratio of cooler box. The COP trend also still agrees with the result that had been stated by Mirmanto et al. [11]. But also the magnitude is close to the results given by Martinez and Astrain et al. [10, 18]. The highest and average COP of cooler box with product load was 0.72 and 0.55 respectively. An enormous different between load and no-load COP is due to the very large specific heat difference between water and air (water 4180 J/kg and air 1007 J/kg at 15 °C). Therefore, the additional water load will increase the total absorbed heat by the cold side of thermoelectric module ($\dot{Q}_T$).

4 Conclusion

In the present study, thermoelectric cooler box using vapor chamber as a cooling device has been experimentally investigated. The vapor chamber with heat sink was used to absorb the heat from the hot side of thermoelectric module. The experimental data shows that increasing the current supply of thermoelectric result in higher temperature difference between the hot and the cold side, increase the cabin temperature, decrease the experimental COP of the cooler box. A current supply of 4 A has the highest average COP value which is about 0.0588. The experimental result also stated that if the 4 A current tested with additional 500 ml of water within the cooler box then the COP becomes 0.72.

References

1. Dincer I, Kanoglu M (2010) Refrigeration systems and applications. Wiley Online Library
2. Enescu D, Virjoghe EO (2014) A review on thermoelectric cooling parameters and performance. Renew Sustain Energ Rev 38:903–916
3. Liang K, Li Z, Chen M, Jiang H (2019) Comparisons between heat pipe, thermoelectric system, and vapour compression refrigeration system for electronics cooling. Appl Therm Eng 146:260–267
4. Gökçek M, Şahin F (2017) Experimental performance investigation of mini channel water cooled-thermoelectric refrigerator. Case Stud Therm Eng 10:54–62
5. Min G, Rowe D (2006) Experimental evaluation of prototype thermoelectric domestic-refrigerators. Appl Energ 83(2):133–152
6. Dai Y, Wang R, Ni L (2003) Experimental investigation and analysis on a thermoelectric refrigerator driven by solar cells. Sol Energy Mater Sol Cells 77(4):377–391

7. Vián J, Astrain D (2009) Development of a thermoelectric refrigerator with two-phase thermosyphons and capillary lift. Appl Therm Eng 29(10):1935–1940
8. Jugsujinda S, Vora-ud A, Seetawan T (2011) Analyzing of thermoelectric refrigerator performance. Proc Eng 8:154–159
9. Lertsatitthanakorn C, Tipsaenprom W, Rungsiyopas M (2014) Improvement of cooling performance of a thermoelectric air cooling system using a vapor chamber heat sink. J Electron Mater 43(6):1554–1559
10. Astrain DE, Vian J, Domınguez M (2003) Increase of COP in the thermoelectric refrigeration by the optimization of heat dissipation. Appl Therm Eng 23(17):2183–2200
11. Mirmanto M, Sayoga I, Sutanto R, Alit I, Nurchayati N, Mulyanto A (2018) Experimental cooler box performance using two different heat removal units: a heat sink fin-fan, and a double fan heat pipe. Front Heat Mass Trans (FHMT) 10
12. Riffat S, Ma X (2004) Improving the coefficient of performance of thermoelectric cooling systems: a review. Int J Energ Res 28(9):753–768
13. Winarta A, Putra N, Bakhtiar F (2017) Thermal performance of oscillating heat pipe with ethanol/methanol for heat recovery application design. Int J Therm Sci 7(4):1268
14. Winarta A, Putra N, Sumirat I (2018) A preliminary investigation on visualization of oscillating heat pipe with non-destructive test. In: IOP conference series: earth and environmental science, vol 105, no 1, p 012074. IOP Publishing Ltd
15. Winarta A, Putra N, Koestoer RA, Pamitran AS, Ibnu I (2019) Heat transfer performance of oscillating heat pipe with ethanol and methanol working fluid with different inclinations for heat recovery application. J Adv Res Fluid Mech Therm Sci 57(2):148–157
16. Midiani L, Subagia I, Suastawa I, Sapteka A, Winarta A (2020) Preliminary investigation of performance and temperature distribution of thermoelectric cooler box with and without internal fan. In: Journal of physics: conference series, vol 1450, p 012088
17. Mirmanto M, Syahrul S, Wirdan Y (2019) Experimental performances of a thermoelectric cooler box with thermoelectric position variations. Int J Eng Sci Technol 22(1):177–184
18. Martinez A, Astrain D, Rodriguez A, Aranguren P (2016) Advanced computational model for Peltier effect based refrigerators. Appl Therm Eng 95:339–347

The Application of *R* Software as a Statistical Tool for Mechanical Data Clustering

A. Saputra, H. Sofyan, and T. E. Putra

Abstract The purpose of this research is to implement *R* software in developing a correlation between wavelet coefficient and fatigue life utilizing Fuzzy *C*-Means. The fatigue-based strain data were simulated at the range between 200 to 2000 με through the application of constant and variable amplitudes with the mean values of negative, zero, and positive. The wavelet transforms involved were the 4th, 12th, 20th, and 30th orders of the continuous and discrete Daubechies wavelets as well as the Morlet wavelet. Meanwhile, the fatigue life was determined by Coffin-Manson, Morrow, and Smith-Watson-Topper models. *R* software with fclust package estimated 3 clusters as the optimum numbers with 1.5 as the fuzzifier value. Hereafter, the result showed that there was a negative correlation between the wavelet coefficient and fatigue life. The strongest correlation was between the 20th order of the discrete Daubechies wavelet and the Coffin-Manson model, i.e. −0.623 with the determination coefficient of 0.388. According to the results, it can be concluded that the software can be applied for clustering mechanical data. Therefore, it is recommended for mechanical engineering applications, involving complex and bigger data.

1 Introduction

One of the most common failures in engineering caused by stress concentration from cyclic loads is called fatigue. Therefore, it is important to predict fatigue life so engineers can prevent failure. Unfortunately, the prediction value is still far from the actual value because of its complexion and the long process between crack initiation, propagation, and fracture of a component.

A. Saputra · H. Sofyan
Department of Statistics, Universitas Syiah Kuala, Banda Aceh 23111, Indonesia
e-mail: edi@unsyiah.ac.id

T. E. Putra (✉)
Department of Mechanical Engineering, Universitas Syiah Kuala,
Banda Aceh 23111, Indonesia

In order to address this problem, signal processing approaches particularly the wavelet transforms have been applied in fatigue analyses. According to previous studies, the 4th [1], 12th [2], 20th [3], and 30th [4] orders of the Daubechies wavelet gave remarkable results. Since 2010, the Morlet wavelet has been used as well [5] and has been applied for many mechanical signals [6, 7] since it gave a better result [8]. Earlier results showed that those wavelet transforms have a solid correlation with fatigue life. Hence, the Fuzzy C-Means (FCM) was used to develop the correlation between them [9, 10].

However, the correlations in those studies were resulted from a simple developed algorithm without considering the optimum number of clusters and the fuzzifier. Thus, the results of the clustering and the estimation of the correlation can be maximized with a proper package. Therefore, the purpose of this study is to implement fclust package provided in R software to determine the best number of clusters and to cluster data with FCM in developing the correlation between wavelet coefficient and fatigue life. R software is a language in statistical programming introduced by Ross Ithaka and Robert Gentlemen, two professors from University of Auckland, New Zealand, in 1966 [11]. The software is based on the S programming language developed by Bell Laboratories [12].

2   Materials and Method

In this study, fatigue-based strain data were developed consisting of constant and variable amplitudes with negative, zero, and positive mean values. Each strain data has a range of 200, 400, 600, 800, 1000, 1200, 1400, 1600, 1800, and 2000 με. Therefore, sixty strain data were generated in total. The examples of the strain data for constant and variable amplitudes for the range of 200 με, respectively, are shown in Figs. 1 and 2.

Furthermore, the wavelet coefficient of each strain data was determined. The wavelet coefficient WC of the Continuous Wavelet Transform (CWT) is expressed by [13]:
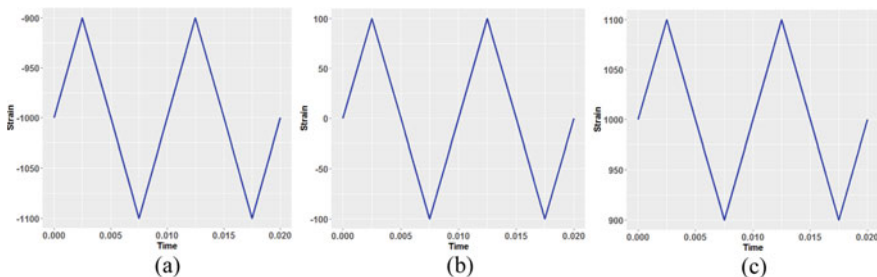
Fig. 1 Constant amplitude strain data with the mean value: **a** negative, **b** zero, **c** positive
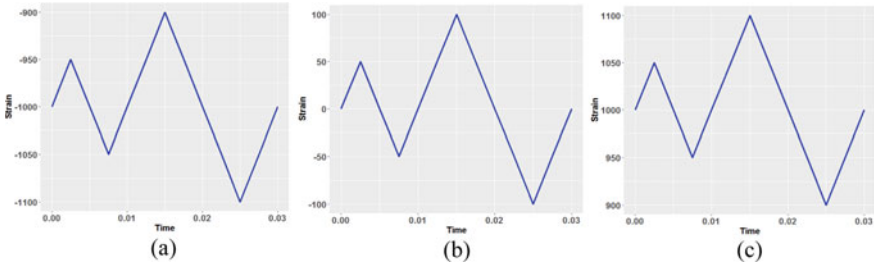
Fig. 2 Variable amplitude strain data with the mean value: **a** negative, **b** zero, **c** positive

$$WC_{(p,q)} = \frac{1}{\sqrt{p}} \int\limits_{-\infty}^{+\infty} F_{(t)} \Psi\left(\frac{t-q}{p}\right) dt \tag{1}$$

The wavelet coefficient *WC* of the Discrete Wavelet Transform (DWT) is obtained from the discretization of the CWT, which is:

$$WC_{(p,q)} = \frac{1}{\sqrt{2^p}} \int\limits_{-\infty}^{+\infty} F_{(t)} \Psi\left(\frac{t-2^p q}{2^p}\right) dt \tag{2}$$

where *p* is the scale index, *q* is the time-shifting, *F* is the strain data, ψ is the mother wavelet, and *t* is the time. The mother wavelets involved were the Morlet wavelet [14, 15] in the CWT as well as the Daubechies wavelet [13] analyzed in the CWT and the DWT.

The fatigue life was determined based on the strain-life approach. The common models in this approach are the Coffin-Manson [16, 17], Morrow [18], and Smith-Watson-Topper (SWT) [19], respectively, as described in the following equations:

$$\varepsilon = \frac{\sigma'_f}{E}(2N_f)^b + \varepsilon'_f(2N_f)^c \tag{3}$$

$$\varepsilon = \frac{\sigma'_f - \sigma_{\text{mean}}}{E}(2N_f)^b + \varepsilon'_f(2N_f)^c \tag{4}$$

$$\sigma_{\text{max}}\varepsilon = \frac{\sigma'^2_f}{E}(2N_f)^{2b} + \sigma'_f\varepsilon'_f(2N_f)^{b+c} \tag{5}$$

where ε is the strain amplitude, σ'_f is the fatigue strength coefficient, *E* is the material modulus of elasticity, N_f is the number of cycles, *b* is the fatigue strength exponent, ε'_f is the fatigue ductile coefficient, *c* is the fatigue ductile exponent, σ_{mean} is the mean stress, and σ_{max} is the maximum stress amplitude.

Table 1 Mechanical properties of the SAE 5160 carbon steel [22]

Mechanical properties	Values
Ultimate tensile strength, S_u (MPa)	1584
Material modulus of elasticity, E (GPa)	207
Fatigue strength coefficient, σ'_f (MPa)	2063
Fatigue strength exponent, b	−0.08
Fatigue ductility exponent, c	−1.05
Fatigue ductility coefficient, ε'_f	9.56

Strain-based fatigue life assessments are usually associated with the Palmgren-Miner rule [20, 21] to determine the cumulative fatigue damage D of a loading block as described by:

$$D = \sum \left(\frac{n_i}{N_f}\right) \tag{6}$$

where n_i is the number of applied cycles. For the simulation purposes, the material used was the SAE 5160 carbon steel, where its properties are shown in Table 1.

The tool used in this research was R software with fclust package, providing a common toolbox for clustering data with a fuzzy algorithm [23]. It has been rewritten in C++ language to increase its computational efficiency. Another advantage of this software is the utilization of cluster validity index to select the optimum number of clusters automatically. The FCM is one of the clustering methods to clarify a data's similarity to every cluster [24]. This method represents the resemblance between data with each cluster using a function called membership function. Thus, every data will have a membership degree in every cluster. Therefore, the membership degree that is close to zero implies less similarity between the cluster and the data, and the data with a membership degree close to one indicates a great similarity between the cluster and the data [25]. After classifying the strain data with the FCM algorithm, the correlations between wavelet coefficient and fatigue life were developed. The strain data were then visualized using a scatter diagram for every wavelet transform and strain-life model.

3 Results and Discussion

In order to cluster data with the FCM, the number of clusters needs to be obtained beforehand. Thus, the fclust package was used to determine the optimum number of clusters (c) with three different fuzzifier (w), i.e. 1.5, 2.0, and 2.5. Table 2 provides the optimum number of clusters according to the validation index in fclust package [23], showing a different optimum number of clusters with different fuzzifier.

Table 2 Validation index in fclust package

| Index	c	w	Value
The partition coefficient	3	1.5	0.915
The classification entropy	3	1.5	0.159
The modified partition coefficient	3	1.5	0.872
The Xie-Beni	2	2.5	0.045
The fuzzy silhouette width	2	2.5	0.885

According to the partition coefficient, the classification entropy, and the modified partition coefficient, the optimum number of clusters was 3 with 1.5 as the fuzzifier value. However, the other indexes, i.e. the Xie-Beni and the fuzzy silhouette width showed that 2 as the optimum number of clusters and 2.5 as the fuzzifier value. Therefore, the number of clusters used was 3 with 1.5 as the fuzzifier value.

Figures 3, 4 and 5 scatter diagrams between the wavelet coefficient and the fatigue life. The figures consisted of 10 segments in cluster 1, 10 segments in cluster 2, and 40 segments in cluster 3. The correlations obtained were a negative correlation, which means if the wavelet coefficient was high, then the fatigue life was low. On the contrary, if the wavelet coefficient was low, then the fatigue life was high.

For the Coffin-Manson model, the strongest correlation was the 20th order of the discrete Daubechies wavelet, i.e. −0.623 with the determination coefficient of 0.388, whilst the weakest correlation was the 30th order of the continuous Daubechies wavelet, i.e. −0.320 with 0.103 as the determination coefficient. The 20th order of the discrete Daubechies wavelet also affected the Morrow model with the correlation of −0.618 and the coefficient of determination equal to 0.382. On the other hand, the Morrow model less affected by the 30th order of the continuous Daubechies wavelet, with the correlation was −0.317 and the determination coefficient of 0.100. The SWT model displayed a similar pattern to the other two models. The 20th order of the discrete Daubechies wavelet has a major effect on the model, where the correlation was equal to −0.569 with 0.324 as the determination coefficient. However, the 30th order of the continuous Daubechies wavelet has a minor effect on the model, where the correlation was −0.280 with the determination coefficient of 0.078. Even though the determination coefficients were low, indicating that the wavelet coefficient has a low impact on fatigue life, the wavelet coefficient still can be used as an early indicator in predicting fatigue life.
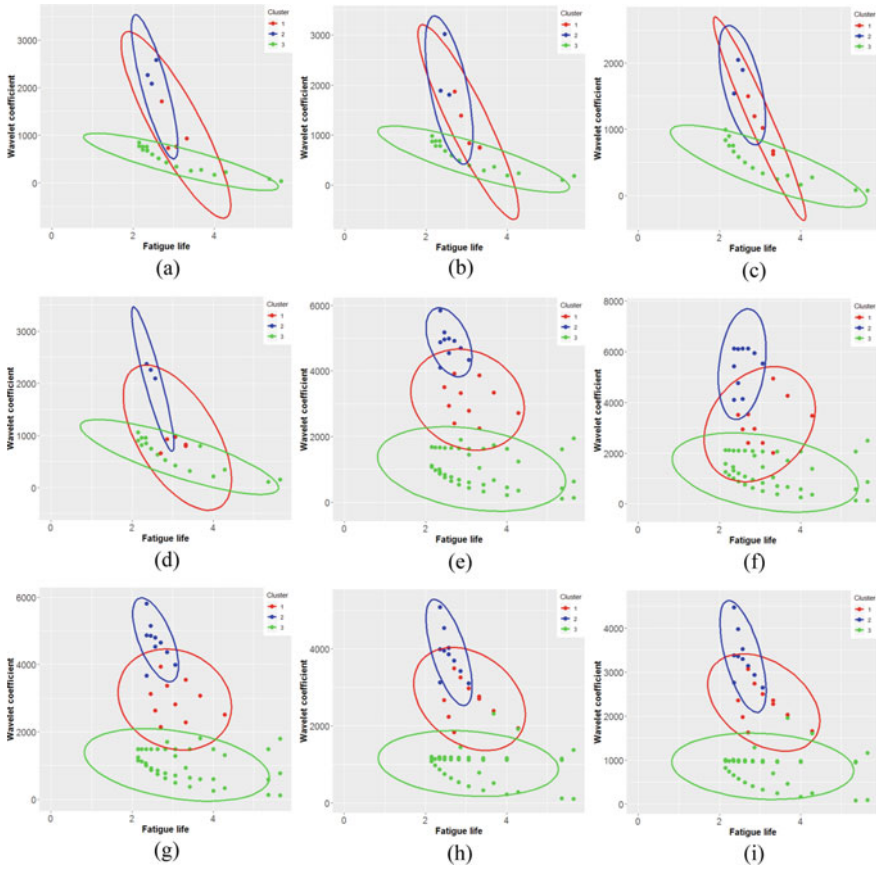
Fig. 3 Scatter diagrams of the Coffin-Manson model and the wavelet coefficients: **a** the 4th order of the discrete Daubechies wavelet, **b** the 12th order of the discrete Daubechies wavelet, **c** the 20th order of the discrete Daubechies wavelet, **d** the 30th order of the discrete Daubechies wavelet, **e** the continuous Morlet wavelet, **f** the 4th order of the continuous Daubechies wavelet, **g** the 12th order of the continuous Daubechies wavelet, **h** the 20th order of the continuous Daubechies wavelet, **i** the 30th order of the continuous Daubechies wavelet
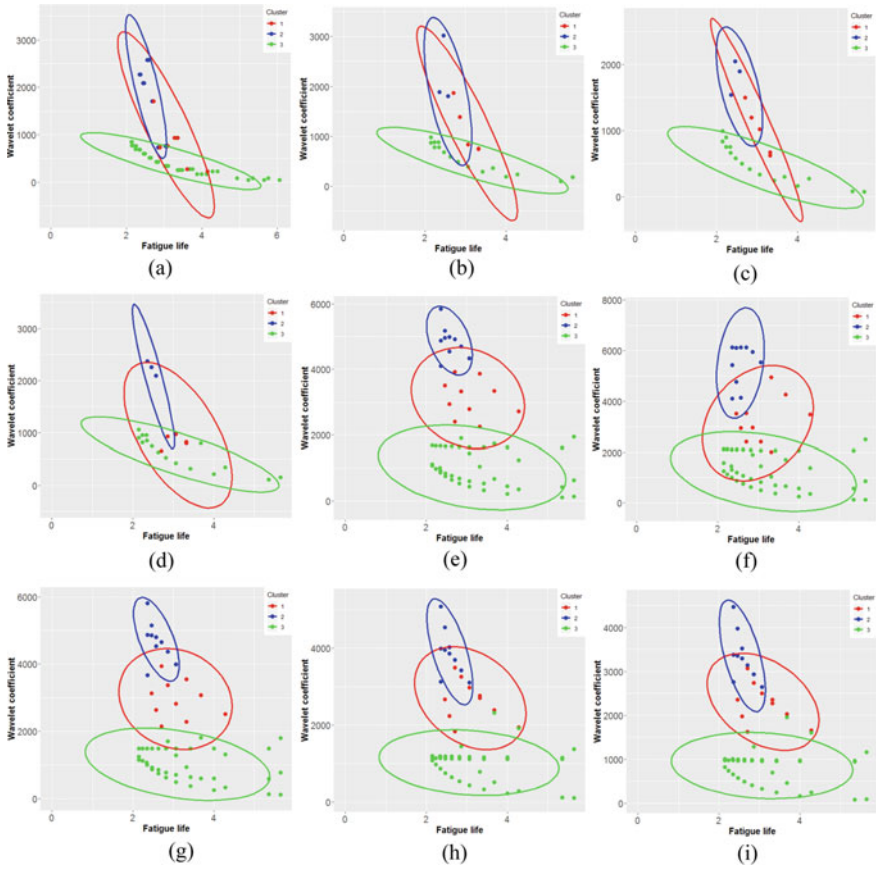
Fig. 4 Scatter diagrams of the Morrow model and the wavelet coefficients: **a** the 4th order of the discrete Daubechies wavelet, **b** the 12th order of the discrete Daubechies wavelet, **c** the 20th order of the discrete Daubechies wavelet, **d** the 30th order of the discrete Daubechies wavelet, **e** the continuous Morlet wavelet, **f** the 4th order of the continuous Daubechies wavelet, **g** the 12th order of the continuous Daubechies wavelet, **h** the 20th order of the continuous Daubechies wavelet, **i** the 30th order of the continuous Daubechies wavelet
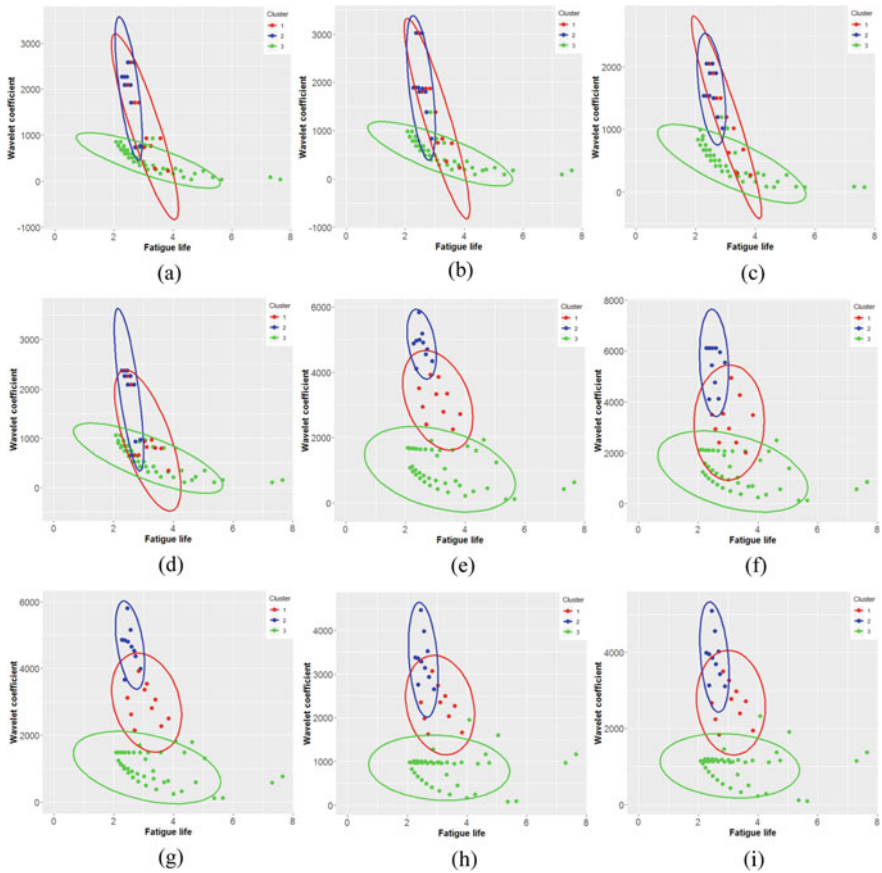
Fig. 5 Scatter diagrams of the SWT model and the wavelet coefficients: **a** the 4th order of the discrete Daubechies wavelet, **b** the 12th order of the discrete Daubechies wavelet, **c** the 20th order of the discrete Daubechies wavelet, **d** the 30th order of the discrete Daubechies wavelet, **e** the continuous Morlet wavelet, **f** the 4th order of the continuous Daubechies wavelet, **g** the 12th order of the continuous Daubechies wavelet, **h** the 20th order of the continuous Daubechies wavelet, **i** the 30th order of the continuous Daubechies wavelet

4 Conclusion

R software as one of the statistical tools was utilized to estimate the correlation between the wavelet coefficient and the fatigue life. The strongest correlation was found with the 20th order of the discrete Daubechies wavelet. The correlation coefficients and the determination coefficients, respectively, were −0.623 and 0.388 for the Coffin-Manson model, −0.618 and 0.382 for the Morrow model, as well as −0.569 and 0.324 for the SWT model. The results showed that the software has the capability to solve problems of mechanical data, specifically in developing the correlation between the wavelet coefficient and the fatigue life.

References

1. Abdullah S, Sahadan SN, Nuawi MZ, Nopiah ZM (2008) Fatigue road signal denoising process using the 4th order of Daubechies wavelet transform. J Appl Sci 8:2496–2509
2. Abdullah S, Choi JC, Giacomin JA, Yates JR (2006) Bump extraction algorithm for variable amplitude fatigue loading. Int J Fatigue 28(7):675–691
3. Sahadan SN, Abdullah S, Nuawi MZ, Nizwan CKE (2008) Analysis of Daubechies wavelet for fatigue time history using the Parserval's energy theorem. In: International conference on mechanical and manufacturing (ICME)
4. Oh CS (2001) Application of wavelet transform in fatigue history editing. Int J Fatigue 23 (3):241–250
5. Putra TE, Abdullah S, Nuawi MZ, Nopiah ZM (2010) Wavelet coefficient extraction algorithm for extracting fatigue features in variable amplitude fatigue loading. J Appl Sci 10 (4):277–283
6. Husaini, Putra TE, Ali N (2018) The Morlet wavelet transform for reducing fatigue testing time of an automotive suspension signal. In: AIP conference proceedings, vol 1983
7. Putra TE, Abdullah S, Schramm D (2020) Effect of cycle amplitude removal of fatigue strain loadings associated to signal energy characteristics. Eng Fail Anal 116
8. Nopiah ZM, Abdullah S, Baharin MN, Putra TE, Sahadan SN, Willis KO (2011) Comparative study on data editing techniques for fatigue time series signals. Adv Mater Res 146–147:1681–1684
9. Abdullah S, Putra TE, Nuawi MZ, Nopiah ZM, Arifin A, Abdullah L (2010) The Morlet wavelet analysis for fatigue feature clustering. WSEAS Trans Math 5(9):345–354
10. Husaini, Putra TE, Ali N (2018) Fatigue feature clustering of modified automotive strain signals for saving testing time. Int J Automot Mech Eng (IJAME) 15(2):5251–5272
11. Sofyan H, Jumila, Rahayu L (2018) The application of *R* and ArcGIS software as a learning media to estimate the return period of the destructive earthquake in Aceh areas using maximum likelihood method. J Phys Conf Ser 1088
12. Fox J, Leanage A (2016) R and the journal of statistical software. J Stat Softw 73
13. Daubechies I (1992) Ten lectures on wavelets society for industrial and applied mathematics
14. Morlet J, Arens G, Fourgeau E, Giard D (1982) Wave propagation and sampling theory—part I: complex signal and scattering in multilayered media. Geophysics 47:203–221
15. Morlet J, Arens G, Fourgeau E, Giard D (1982) Wave propagation and sampling theory—part II: sampling theory and complex waves. Geophysics 47:222–236
16. Coffin Jr LF (1954) A study of the effects of cyclic thermal stresses on a ductile metal. Trans ASME 76:931–950
17. Manson SS (1965) Fatigue: a complex subject—some simple approximation. Exp Mech 5:193–226
18. Morrow J (1968) Fatigue design handbook society of automotive engineers
19. Smith KN, Watson P, Topper TH (1970) A stress-strain function for the fatigue of materials. J Mater JMLSA 5:767–778
20. Palmgren A (1924) Die Lebensdauer von Kugellagern. Zeitschrift VDI 68:339–341
21. Miner MA (1945) Cumulative damage in fatigue. J Appl Mech 67:A159–A164
22. nCode (2018) GlyphWorks nCode International, Ltd

23. Ferraro MB, Giordani P, Serafini A (2019) fclust: an *R* package for fuzzy clustering. R J 11
24. Zadeh LA (1965) Fuzzy sets information and control 8:338–353
25. Bezdek JC, Ehrlich R, William F (1984) FCM: the fuzzy *C*-means clustering algorithm. Comput Geosci 10:191–203

Optimization of Struvite Batch Crystallization Reactor for Recovery Process from Urea Fertilizer Plant Wastewater

R. Ulfa, I. Machdar, S. Suhendrayatna, and Y. Yunardi

Abstract The present paper reports removal of ammonium nitrogen concentration from a urea fertilizer plant wastewater through struvite crystal ($NH_4MgPO_4.6H_2O$) formation. The aim of this research was to obtain the optimum conditions of mole ratio, pH value, and crystallization time in NH_4^+–N recovery by producing slow release fertilizer material (struvite crystal). In this work, a source of Mg and P was magnesium chloride ($MgCl_2$) and potassium dihydrogen phosphate (KH_2PO_4) solution, respectively. Experiment was designed in a batch crystallizer-reactor at different mole ratio of Mg^{2+}, NH_4^+, and PO_4^{3-}. The reactor volume was 500 ml equipped with an agitator. The study was conducted at a room temperature. The effect of $Mg^{2+}:NH_4^+:PO_4^{3-}$ mole ratio was studied, it was found that at a molar ratio of $Mg^{2+}:NH_4^+:PO_4^{3-}$ (1:1:1) and pH of 9, the ammonium removal was obtained around of 90.48%. Recovery for NH_4^+ increased with increasing Mg^{2+} concentration. The removal achieved around 93.66% at the ratio $Mg^{2+}:NH_4^+:PO_4^{3-}$ of 1.2:1:1. Moreover, the obtained struvite crystals were analyzed using a SEM to indicate that the shape and the size of struvite crystal.

1 Introduction

One of the environmental problems caused by domestic or industrial activities is a problem related to ammonia. Increased ammonia content in water can cause phitoplactone which is often called eutrophication [1, 2]. The method that has been applied for reducing ammonia nitrogen from industrial waste is through physical, chemical, and biological treatment [3–5]. The physical-chemical treatment process

R. Ulfa (✉) · I. Machdar · S. Suhendrayatna · Y. Yunardi
Doctoral Program, School of Engineering, Universitas Syiah Kuala, Banda Aceh 23111, Indonesia
e-mail: ulfa1996@mhs.unsyiah.ac.id

R. Ulfa · I. Machdar · S. Suhendrayatna · Y. Yunardi
Department of Chemical Engineering, Universitas Syiah Kuala, Banda Aceh 23111, Indonesia

produces a fairly good level of pollutant reduction and this method is widely used by the urea fertilizer industry in Indonesia which generally uses ammonia striping tower. It is known that this system is unstable if the ammonia content in the waste fluctuates. This is because the system depends on the distribution of waste in the tower and wind speed. In addition, ammonia released into the air causes odor pollution around the plant. Biological processes generally require relatively low costs, because they do not or require only a few additional chemicals. However, biological processes generally last relatively long because leachate contains substances that are difficult to degrade biologically, often even containing components that are toxic to microorganisms [5]. It is a great challenge to find methods to encourage ammonia removal from wastewater to produce valuable materials and simultaneously improve the quality of wastewater [6].

Struvite precipitation is one of the physical-chemical methods that can be used to reduce levels of ammonium nitrogen from wastewater [1, 7]. Struvite precipitation process is carried out with the help of precipitant chemicals containing Mg^{2+} and PO_4^{3-}. Ammonium reaction with Mg^{2+} and PO^{3-} forms precipitates in the form of struvite crystals ($MgNH_4PO_4.6H_2O$). This precipitation process is also affected by several factors, including the molar ratio $[Mg^{2+}]:[NH_4^+]:[PO_4^{3-}]$. The minimum is 1:1:1, this proves that the molar concentration plays an important role in the removal of ammonium, and the addition of excess magnesium 1.2:1 can increase ammonium removal [8], pH (range 7–12), reaction time (15–30 min), and operating methods [9]. Many studies have investigated the feasibility of N-recovery through struvite precipitation from the laboratory to the pilot scale and the existing full-scale struvite crystallization techniques all advertise high recovery efficiency (80–95%) [7, 10].

Struvite is relatively easy to dry and handle to provide potential as a slow release fertilizer [11], and the solubility of struvite is around 0.018 g/100 ml at 25 °C, sruvite as a fine mineral, not washed with water flow so that it can be used as fertilizer in flood areas [12]. Studies using agro-industrial wastewater show that struvite can be a very useful fertilizer containing almost all major macronutrients (N, P, Mg, K) and other important secondary macronutrients, such as Na and Ca [13].

This study aims to evaluate the efficiency of ammonium removal from urea fertilizer plant wastewater through the production of struvite crystals, by adding potassium dihydrogen phosphate and magnesium oxide as external sources of phosphorus and magnesium respectively at various molar ratios and base pH variations. Economic evaluations of the applied processes were also reported and the characteristics of the struvite crystal dry product was analyzed by SEM.

2   Methodology

2.1   Characteristic of Wastewaster

The wastewater as low cost source ammonium nitrogen (NH_4^+) supplied from a urea fertilizer plant located in Aceh Province, Indonesia, with the composition as

Table 1 Characteristics of urea fertilizer plant used as a source of ammonium

Parameter	Value (mg/L)
NH_3–N	1053
COD	878
TSS	89.34
Oil	305.35
TKN	2376
Urea	3744.2
PO_4	7.80

shown in Table 1. Magnesium chloride hexahydrate ($MgCl_2 \cdot 6H_2O$) as Mg^{2+}, potassium dihydrogen phosphate (KH_2PO_4) as PO_4^{3-}, and potassium hydroxide (KOH). All chemical reagents were bought from Merck with analytical grade. Struvite crystal forms according to the following reaction:

$$Mg^{2+} + NH_4^+ + PO_4^{3-} + 6H_2O \rightarrow MgNH_4PO_4 \cdot 6H_2O \tag{1}$$
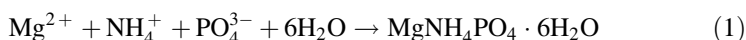
Taking into account the very low solubility of struvite (pKs = 12.6), it can be completely separated from the liquid phase.

2.2 Struvite Precipitation Process

The experiments was made applying a lab-scale crystallization batch system of capacity 500 ml at ambient temperature with the mixed reactant stirred operated at 120 rpm. Struvite precipitation was carried out at Mg^{2+}:NH_4^+:PO_4^{3-} molar ratio. In particular, three molar ratios (i.e., 1:1:1, 1.2:1:1 and 1:1:1.2) were investigated. The pH measurements are made with pH meter Portable and pH is adjusted either with KOH solutions (pH 8, 9 and 10). Experiments for struvite precipitation were present. Firstly, add $MgCl_2$ and KH_2PO_4 to raw wastewater. Secondly, the reaction solution was agitated by magnetic stirrers for 60 min, and than adjust pH was kept constant during experiments by addition of 1 N KOH. Thirdly, filter the reaction solution with Whatman filter paper 0.45 µm. Lastly, the product struvite was filtered, oven dried 24 h at 50 °C [14] struvite should be dried at a temperature between 30 and 50 °C to avoid mass loss and phase transformation, and than carried out weight and characteristics analysis of struvite product.

2.3 Analytical Methods

The concentration of NH_4^+–N in the supernatant was analyzed by UV-vis spectrophotometer (Shimadzu UV-1700). Supernatants were analyzed for residual ammonium nitrogen in the struvite precipitation process by means of analyze the

filtrate quantity of 5 ml with 5 min interval sampling time of reactant solution with addicting reagent nessler (K_2HgI_4) 1 ml and sodium potassium tartrat tetrahydrat ($C_4H_4KNaO_6.4H_2O$) 1 drop for remaining concentration of NH_4^+–N. The characteristics of struvite product were observed by SEM (JEOL JSM 6510) and FTIR (Shimadzu IR Prestige21). After each experiment, the supernatants and the precipitates were analysed for M, N and P to check the consistency of experimental results and all balances closed within acceptable limits [15, 16].

3 Results and Discussions

3.1 Efficiency of Ammonium Removal

The urea fertilizer plant wastewater used has an initial NH_4^+ concentration high enough, which is 547 ± 513. Figure 1 shows the ammonium removal efficiency at various molar ratios ($Mg^{2+}:NH_4^+:PO_4^{3-}$) and pH. pH is one of the parameters used in this study because the activity of NH_4 and PO_4 ions is influenced by pH. NH_4 will be volatilized to NH_3 at a pH greater than 9 [8, 17]. The pH range used in this study was between 8 and 10. Ammonium removal occurred significantly at pH 9 and 10 at each molar ratio used. The removal efficiency of NH_4^+ at various molar ratios and pH ranges between 93.66 ± 81.58%. The highest removal efficiency of NH_4^+ concentration occurred at a molar ratio of 1.2:1:1 and pH 9 of 93.7% with a final NH_4^+ concentration of 34.65 mg/l. The removal efficiency of NH_4^+ concentration at a ratio of 1:1:1 at pH 9 is 90.48% with a final NH_4^+ concentration of 50.51 mg/l. The removal efficiency of NH_4^+ concentration at a ratio of 1:1:1.2 at pH 9 is 86.37% with a final NH_4^+ concentration of 70.01 mg/l. The selection of the best molar and pH ratio is based on the highest efficiency of NH_4^+ concentration reduction. With the highest elimination rate of NH_4^+, it is expected that the acquisition of struvite is higher and the quality of processed wastewater is better. The best selected molar ratios are 1.2:1:1 and pH 9. The same research results obtained [18] that the removal of ammonium by deposition of struvite occurs at pH 7 to 10, and the removal efficiency increases pH from pH to 10.

Along with an increase in the molar ratio, the removal efficiency also increases [19]. The results of this study also show that the addition of magnesium can increase the removal of ammonium in the urea fertilizer industrial wastewater. Previous studies also showed that the addition of excess magnesium concentrations can increase the removal of ammonium and phosphate [7, 8]. Decreased ammonium concentration in solution gives an indication of the formation of struvite. It was found that the rate of reduction of ammonium in the bulk solution was stable after 30 min in all the experiments investigated [20].
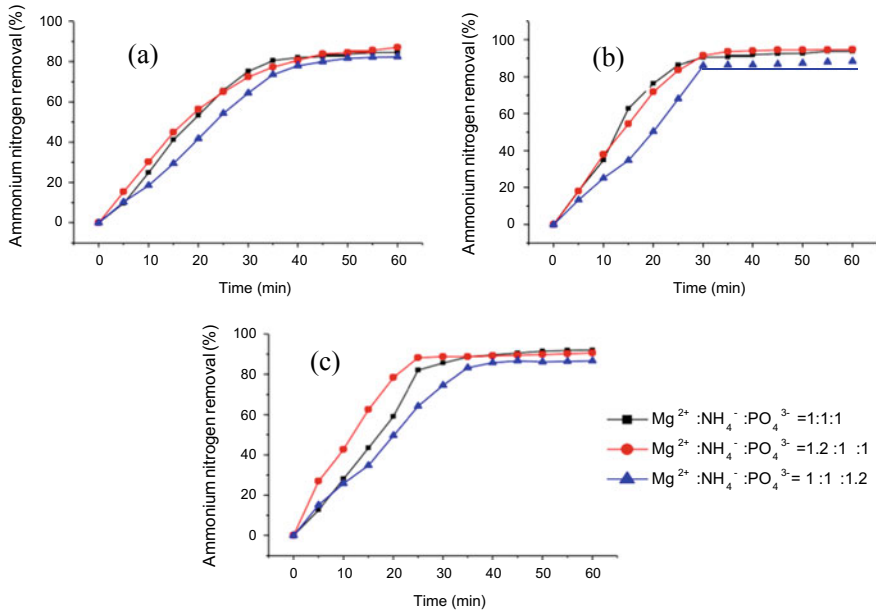
Fig. 1 The ammonium nitrogen removal measured in the experiments. **a** pH 8; **b** pH 9; **c** pH 10

3.2 Amount of Struvite Product Obtained

Increased pH causes more deposition to form due to strong and perfect ionic bonds which are influenced by the ph ion activity of ammonium and phosphate [21]. The molar ratio also has an important role in amount struvite crystal was obtained [22]. Based on chemical reactions, the minimum molar ratio of struvite precipitation is $Mg^{2+}:NH_4^+:PO_4^{3-} = 1:1:1$ with the chemical reaction in press (1).

The number of products weighs in grams. struvite crystals obtained by compilation had been done in an oven at 50 °C for 24 h. The results of research on struvite production showed optimal weight at pH 9 (Fig. 2). The increase in the value of struvite at pH 8 to pH 9 is caused by the activity of ions in the solution which more easily form crystals that produce salt so that the resulting sediment is also increasing [21], decrease in product when pH 10 is due to the pH will tend to form $Mg(OH)_2$ therefor reducing the availability of Mg ions which can reduce the productivity of struvite crystal formation [18]. As regards the amount of struvite precipitated, Fig. 2 shows the theoretical and experimental amount of dried struvite produced per 500 ml of ammonia wastewater at each investigated molar ratio value. Theoretical struvite is the amount of precipitate that one would expect on the basis of ammonia removals shown in Fig. 1, whereas the experimental struvite is the amount of precipitate actually weighed during the tests. Looking at Fig. 2, it is possible to note that the amount of struvite produced increases with the increase in
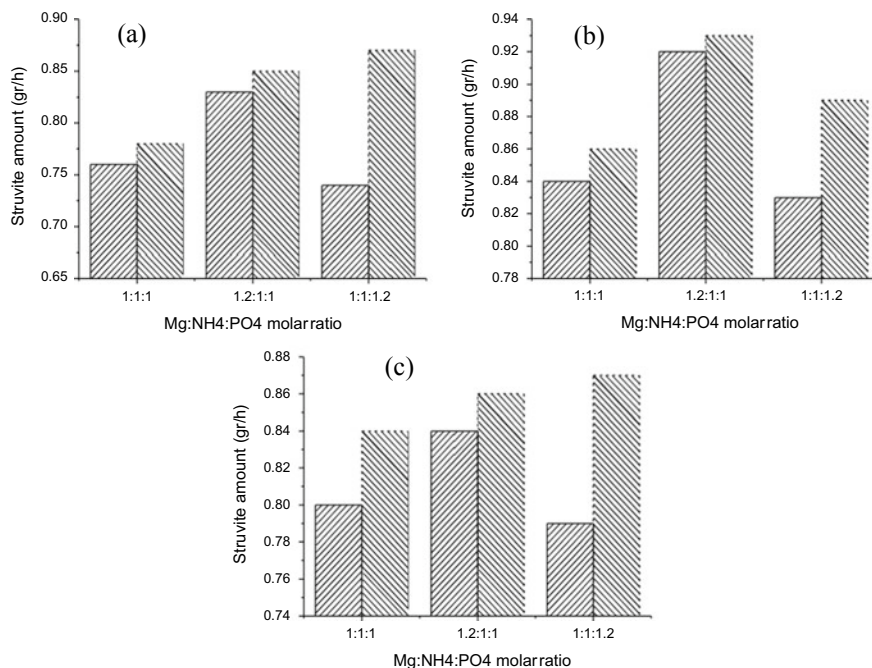
Fig. 2 Experimental and theoretical amount of struvite for each are investigated molar ratio and ph **a** pH 8; **b** pH 9; **c** pH 10. [▨] experimental amount; [▨] theoretical amount

the molar ratio (i.e. from 0.86 gr at the stoichiometric molar ratio to 0.93 gr/1.5 l of ammonia wastewater at a molar ratio of 1.2:1:1) because of the increased quantity of removed ammonia. In addition, this figure highlights a difference between the theoretical and experimental struvite values, probably due to the presence in the latter of other precipitates. This is because when taking samples for ammonia removal analysis using a UV-vis spectrophotometer, filtering is first done with filter paper so that the sediment does not enter the solution to be analyzed.

3.3 Product Characterization

Struvite produced from this research is in the form of white crystalline powder consisting of the same concentrations of magnesium, ammonium, and phosphate combined with six water molecules (Fig. 3).

SEM (Scanning electron microscope) analysis of struvite products (solution pH 9 and $Mg^{2+}:NH_4^+:PO_4^{3-}$ = 1.2: 1: 1 molar ratio) can be seen in Fig. 4. Struvite products have round stems with irregular structures. Formation of similar struvite

Fig. 3 Struvite precipitation from the experiment

Fig. 4 SEM of crystal struvite product
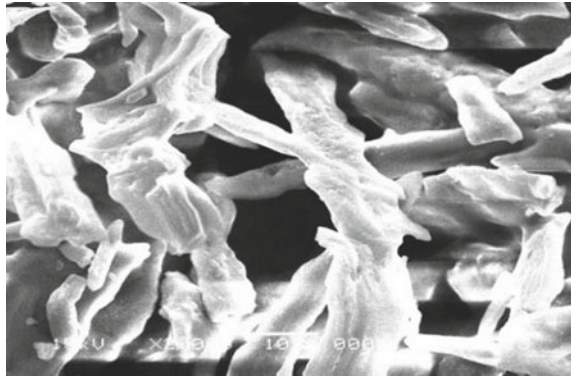
crystals has been reported by Le Corre et al. [23] using synthetic liquids in pilot scale reactors, and its size was irregular (2.5–5 μm length).

4 Conclusions

Struvite precipitation process using $MgCl_2$ and KH_2PO_4 as ammonium precipitant sourced from urea fertilizer industry wastewater is influenced by the precipitated molar ratio and pH value. The result obtained $Mg:NH_4:PO_4$ molar ratio of 1.2:1:1 and pH 9 is required for a satisfactory ammonia removal (i.e. 93.7%), by getting struvite products 0.92 gr. The struvite produced was characterized by confirmed the formation of struvite.

References

1. Yetilmezsoy K, Ilhan F, Kocak E, Akbin HM (2017) Feasibility of struvite recovery process for fertilizer industry: a study of financial and economic analysis. J Clean Prod 152:88–102
2. Thant Zin MM, Kim DJ (2019) Struvite production from food processing wastewater and incinerated sewage sludge ash as an alternative N and P source: optimization of multiple resources recovery by response surface methodology. Process Saf Environ Prot 126:242–249
3. Karabelas AJ et al (2001) Water and materials recovery from fertilizer industry acidic effluents by membrane processes. Desalination 138:93–102
4. Yang Y (2017) ScienceDirect Concentration of nitrogen as new energy source from wastewater. In: The 15th international symposium on district heating and cooling by electrodeionization assessing feasibility of using the heat temperature function for a long-term. Energy Procedia 142:1421–1426
5. Chung Y, Son D, Ahn D (2018) Nitrogen and organics removal from industrial wastewater using natural zeolite media, 127–134
6. Ulfa R, Machdar I, Yunardi Y, Rinaldi W, Jauharlina J (2020) Residence time distribution study in laboratory scale struvite crystallization reactor with online conductivity measurement residence time distribution study in laboratory scale struvite crystallization reactor with online conductivity measurement. In: IOP conference series: materials science and engineering, vol 845
7. Di Iaconi C, Pagano M, Ramadori R, Lopez A (2010) Nitrogen recovery from a stabilized municipal landfill leachate. Bioresour Technol 101:1732–1736
8. Rahman MM, Liu YH, Kwag JH, Ra CS (2011) Recovery of struvite from animal wastewater and its nutrient leaching loss in soil. J Hazard Mater 186:2026–2030
9. Rahman MM et al (2014) Production of slow release crystal fertilizer from wastewaters through struvite crystallization—a review. Arab J Chem 7:139–155
10. Britton A et al (2005) Pilot-scale struvite recovery from anaerobic digester supernatant at an enhanced biological phosphorus removal wastewater treatment plant. J Environ Eng Sci 4:265–277
11. Li B et al (2019) Phosphorous recovery through struvite crystallization: challenges for future design. Sci Total Environ 648:1244–1256
12. Lee JE, Rahman MM, Ra CS (2009) Dose effects of Mg and PO4 sources on the composting of swine manure. J Hazard Mater 169:801–807
13. Taddeo R, Honkanen M, Kolppo K, Lepistö R (2018) Nutrient management via struvite precipitation and recovery from various agroindustrial wastewaters: process feasibility and struvite quality. J Environ Manage 212:433–439
14. Darwish M, Aris A, Puteh MH, Abideen MZ, Othman MN (2016) Ammonium-nitrogen recovery from wastewater by struvite crystallization technology. Sep Purif Rev 45:261–274
15. Çelen I, Türker M (2001) Recovery of ammonia as struvite from anaerobic digester effluents. Environ Technol (United Kingdom) 22:1263–1272
16. Rafie SE, Hawash S, Shalaby MS (2013) Evaluation of struvite precipitated from chemical fertilizer industrial effluents. Pelagia Res Libr Adv Appl Sci Res 4:113–123
17. Wang J, Burken JG, Zhang X, Surampalli R (2005) Engineered struvite precipitation: impacts of component-ion molar ratios and pH. J Environ Eng 131:1433–1440
18. Ariyanto E, Sen TK, Ang HM (2014) The influence of various physico-chemical process parameters on kinetics and growth mechanism of struvite crystallisation. Adv Powder Technol 25:682–694
19. Warmadewanthi, Liu JC (2009) Recovery of phosphate and ammonium as struvite from semiconductor wastewater. Sep Purif Technol 64:368–373
20. Machdar I et al (2018) Ammonium nitrogen removal from urea fertilizer plant wastewater via struvite crystal production. In: IOP conference series: materials science and engineering, vol 358

21. Shaddel S, Ucar S, Andreassen JP, Sterhus SW (2019) Engineering of struvite crystals by regulating supersaturation—correlation with phosphorus recovery, crystal morphology and process efficiency. J Environ Chem Eng 7:102918
22. Moragaspitiya C, Rajapakse J, Millar GJ (2019) Effect of Ca: Mg ratio and high ammoniacal nitrogen on characteristics of struvite precipitated from waste activated sludge digester effluent. J Environ Sci (China) 86:65–77
23. Le Corre KS, Valsami-Jones E, Hobbs P, Jefferson B, Parsons SA (2007) Struvite crystallisation and recovery using a stainless steel structure as a seed material. Water Res 41:2449–2456

Image Processing, Symbolic PDE Computing, and FEA: A Simulation Study of Stress Distribution in Heterogeneous Material

Israr Bin M. Ibrahim, Syarizal Fonna, and Ramana M. Pidaparti

Abstract Heterogenous material modeling is typically used in analysis of composite materials and microstructures. Heterogenous materials present difficulty in FEA (Finite Element Analysis) modeling due to irregularity of constituent's shape. In this study, we demonstrate a method utilizing image processing and symbolic PDE (Partial Differential Equation) FEA to model heterogenous materials. We validated our results with ANSYS, a well-known FEA modeling tool. The stress distribution from our model agree well with result from ANSYS. The results show that the peaks of stress occur in the interface. The results suggest that the topology of the constituent may influence the stress accumulation.

Keywords Heterogeneous materials · Image processing · Symbolic PDE · Finite element analysis · Automated differential equation solving · Linear elasticity

1 Introduction

In many engineering cases, materials exhibit heterogeneity, that is, their material constants (e.g. Young's modulus, conductivity) are not distributed uniformly. The heterogeneity can be continuous or discrete. In the first case, the material constants are typically defined as a function of space [1–3]. In the latter, the material constants are modeled as stepwise function over the domain of the body, such as in the case of microstructure [4–6]. The computational models then proceed to solve the elasticity problem as usual through numerical methods such as FEA.

I. B. M. Ibrahim (✉) · S. Fonna
CCRG Lab, Mechanical Engineering Department, Universitas Syiah Kuala, Banda Aceh 23111, Indonesia
e-mail: israrbmi@gmail.com

R. M. Pidaparti
DICE Lab, College of Engineering, University of Georgia, Athens, Georgia 30602, USA
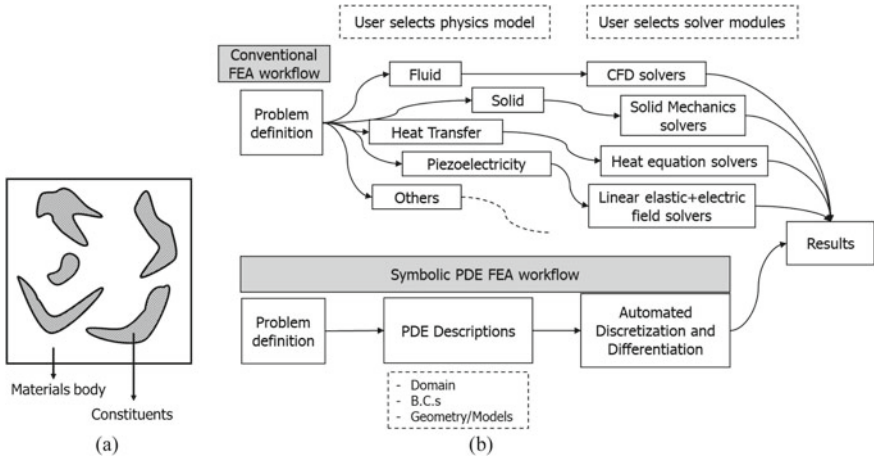
Fig. 1 a Illustration of materials with discrete heterogeneity, **b** workflow of conventional FEA and symbolic PDE FEA

However, difficulty arises when generating FEA model and mesh due to irregularity of constituent's shape. Figure 1 shows an illustration of irregular constituents that can be found in microstructure [7]. Image processing tools enable one to import and convert the images into a vector and then into a mesh model. However, technical difficulties might arise when switching mesh definition formats to comply with FEA and 3D modeling software requirements.

In this study, we developed algorithm to seamlessly perform image processing, generate model and mesh, and carry out FEA through symbolic PDE modeling. Symbolic PDE and automated differential equation solving have seen a rising interest in recent years as various numerical software products have offered these as built-in features or are built around these features. The most well-known are FlexPDE [8], Wolfram Mathematica [9], MATLAB [10], Project FEniCS (open source) [11] and COMSOL [12]. Symbolic PDE modeling allows physics modeling through user-defined equations and constitutive relationships, and modeling of multi-physics systems through explicitly stating multiple governing PDEs.

This is especially beneficial when modeling phenomena where the governing equations, the coupling schemes or constitutive relationships are not available in traditional FEA software (such as problems in biomechanics, complex fluid or involving multi-physics). Figure 1 illustrates the workflow of FEA. Conventionally, in an FEA task, users must determine the physics model of their problem in order to select the appropriate solver modules available in their FEM software of choices. However, problem arises when the case needs combination of physics or user-defined constitutive equations, or even user-defined PDEs. In symbolic PDE modeling, the environment allows users to define PDEs and constitutive equations of their choices.

2 Methods

2.1 The Algorithm

The method is depicted in Fig. 2. The algorithm takes any 2D image, such as image obtained from microscopy techniques (e.g. SEM). The image processing consists of binarizing the image, removing small elements (if necessary, with a threshold of pixel size) and converting it into vector graphics. The algorithm then identifies regions to distinguish discrete constituents of the materials. This is done based on domain of each curve that defines the vector of the graphics elements. Lastly, mesh is generated to approximate the shape.

   The subject of this study is heterogeneous materials with two discrete constituents (the model can be extended for more than two constituents). Hence, the PDE and constitutive relationships needed are based on linear elasticity, which is explained in the next section. The material properties would be Young's modulus, assigned to each constituent (that is defined as region as explained earlier). The algorithm was developed using Wolfram Mathematica 12 utilizing its image processing, algorithmic shape generation, mesh generation, symbolic PDE, FEA and various plotting features.
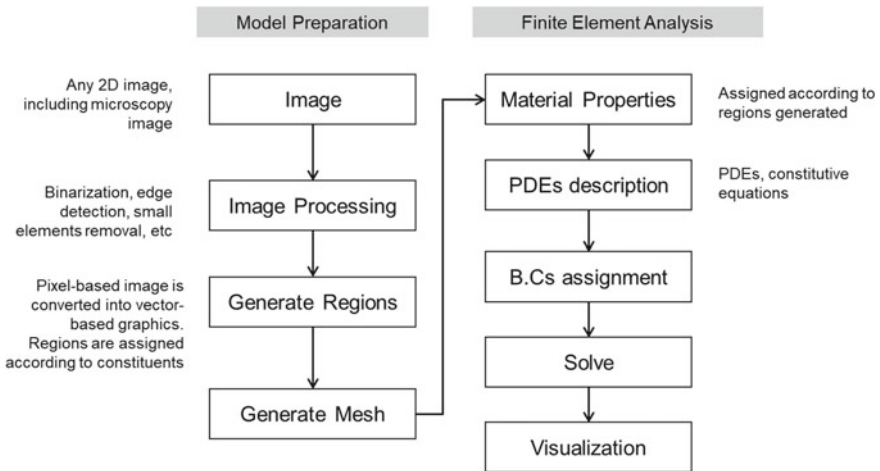
Fig. 2 Algorithm developed to overcome difficulties in translating images with irregular constituent shapes into an FEA models

2.2 Elasticity Model

The symbolic PDE requires developer to build model from the ground up. The elasticity model is built based on linear elasticity. The governing equation is Cauchy momentum equation (for static problem and without body force),

$$\nabla \cdot \boldsymbol{\sigma} = 0 \tag{1}$$

where ∇ is divergence operator, $\boldsymbol{\sigma}$ is stress tensor. For planar stress problem in cartesian coordinate, Eq. (1) reduces to,

$$\frac{\partial \sigma_{xx}}{\partial x} + \frac{\partial \sigma_{xy}}{\partial y} = 0 \tag{2}$$

$$\frac{\partial \sigma_{xy}}{\partial x} + \frac{\partial \sigma_{yy}}{\partial y} = 0 \tag{3}$$

In linear elasticity, small strain is typically used and defined as,

$$\epsilon = \frac{1}{2}\left(\nabla \mathbf{u} + (\nabla \mathbf{u})^{\mathrm{T}}\right) \tag{4}$$

where ϵ is strain tensor, ∇ is divergence operator, $\mathbf{u}$ is displacement field. Equation (4) yields description of small strain as,

$$\epsilon_{xx} = \partial u_x / \partial x, \tag{5}$$

$$\epsilon_{yy} = \partial u_y / \partial y \tag{6}$$

$$\epsilon_{xy} = \frac{1}{2}\left(\frac{\partial u_x}{\partial y} + \frac{\partial u_y}{\partial x}\right) \tag{7}$$

Hooke's law state that,

$$\boldsymbol{\sigma} = \mathbf{C}\epsilon \tag{8}$$

where $\mathbf{C}$ is stiffness tensor. For isotropic linear elastic material, the constitutive relationship for each tensor element is established and can easily be found in basic continuum mechanics literature, such as [13]. For plane stress, the constitutive relationships are,

$$\begin{bmatrix} \sigma_{xx} \\ \sigma_{yy} \\ \sigma_{xy} \end{bmatrix} = \frac{E}{1 - v^2} \begin{bmatrix} 1 & v & 0 \\ v & 1 & 0 \\ 0 & 0 & \frac{1-v}{2} \end{bmatrix} \begin{bmatrix} \epsilon_{xx} \\ \epsilon_{yy} \\ 2\epsilon_{xy} \end{bmatrix} \tag{9}$$

where E is Young's modulus and v is Poisson's ratio. Substituting constitutive relations (6) and governing Eqs. (2) and (3) gives coupled PDE,

$$\frac{\partial}{\partial x}\left(C_{11}\frac{\partial u_x}{\partial x} + C_{12}\frac{\partial u_y}{\partial y}\right) + \frac{\partial}{\partial y}\left(C_{33}\left(\frac{\partial u_x}{\partial x} + \frac{\partial u_y}{\partial y}\right)\right) = 0 \tag{10}$$

$$\frac{\partial}{\partial x}\left(C_{33}\left(\frac{\partial u_x}{\partial x} + \frac{\partial u_y}{\partial y}\right)\right) + \frac{\partial}{\partial y}\left(C_{12}\frac{\partial u_x}{\partial x} + C_{11}\frac{\partial u_y}{\partial y}\right) = 0 \tag{11}$$

where $C_{11} = \frac{E}{1-v^2}$, $C_{12} = \frac{Ev}{1-v^2}$, $C_{33} = C_{11}\frac{(1-v)}{2}$, u_x and u_y are displacement component in direction x and y of cartesian coordinate, respectively. Based on Eqs. (7) and (8), the computational model seeks to solve displacement field u_x and u_y.

The algorithm at first solve Eqs. (7) and (8) to obtain displacement fields, u_x and u_y, as functions in terms of cartesian coordinates, x and y. Then, strains can be calculated according to Eqs. (5–7), and stresses according to Eq. (9). Other derived quantities such as Von Mises and principal stresses can then be calculated as,

$$\text{Von Mises stress}: \sigma_v = \sqrt{\frac{1}{2}\left(\sigma_{xx} - \sigma_{yy}\right)^2 + 3 \cdot \sigma_{xy}^2} \tag{12}$$

The model was developed using Wolfram Mathematica 12 utilizing its symbolic PDE FEA capabilities. Displacement field, u_x and u_y, were defined as function data type. Then, subsequent operation (Eqs. (5–13)) were directly coded as are. The geometrical model is generated from 2D image, which is then converted into FEA mesh. This algorithm allows direct FE analysis on microscopy images of solid materials (e.g. from SEM) that are typical in materials science research.

2.3 Heterogeneous Model and Mesh

To demonstrate the capability of the model, a simulation of two-phase material is presented. The model is a 15×6.4 μm rectangular elastic body with an elliptical constituent in the center, as illustrated in Fig. 3a. Each region (termed Ω_1 and Ω_2) of the body has its own Young's modulus. Hence, the Young's modulus is a function of cartesian coordinate ($E(x, y)$). Since in this case the heterogeneity is discrete by nature, $E(x, y)$ is a piecewise equation,
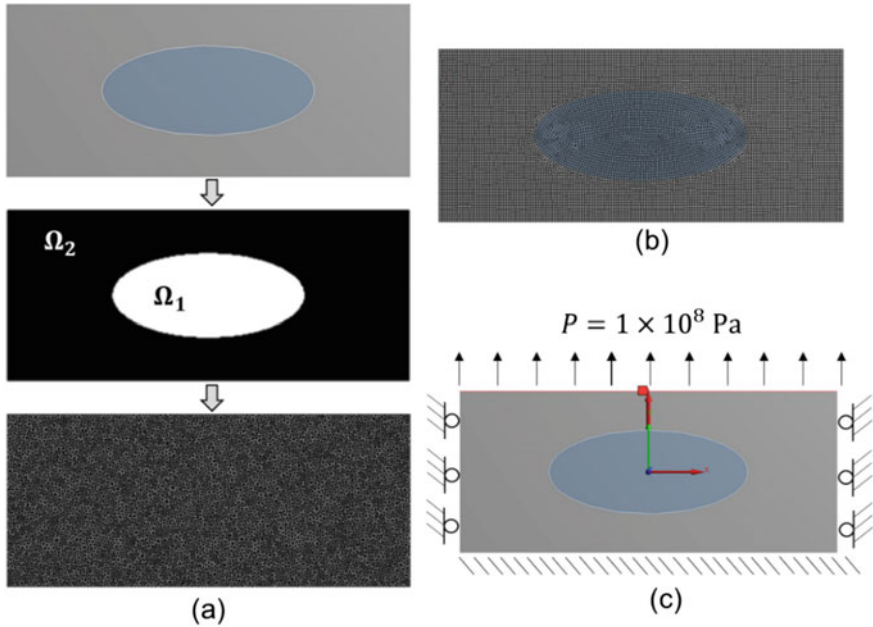
Fig. 3 a An FEA mesh generated from an image: Top: the original image, a model of heterogenous material with a constituent in the center. The model is 15 by 6.4 μm. Middle: image processing generates two distinct domains, termed Ω_1 and Ω_2 as indicated by the labels. Bottom: the mesh generated for symbolic PDE FEA. **b** Mesh for ANSYS model. **c** Boundary conditions of the problems. The material is pulled from the top

$$E(x, y) = \begin{cases} E_1, (x, y) \in \Omega_1 \\ E_2, (x, y) \in \Omega_2 \end{cases} \tag{13}$$

The boundary conditions are shown in Fig. 3c. The same model was also used for simulation using ANSYS Workbench 11. The meshes of both models are shown in Fig 3(a) and (b). The number of elements is 15,082 triangular elements for the symbolic PDE model, and 9840 triangular and rectangular elements. The Young's modulus for Ω_1 is 1.84 MPa, while Ω_2 2 MPa. Poisson's ratio for both constituents is 0.29.

3 Results and Discussion

3.1 Deformation

When a linear elastic body is pulled from one side, it is expected that the material deforms linearly in the direction of pull. Due to the heterogenous nature of the

elastic body in the study case, it is expected that some alteration of linear defor-
mation will occur around the interface of the two phases.

Figure 4 shows displacement visualization for the problem stated in Fig. 3. It
can be seen that the body deforms linearly from top to bottom, as expected when it
is pulled from the top part of the body. However, there is a slight interruption to the
linear pattern at some point close to the center as indicated by the arrow in Fig. 4.
This is the point where the two constituents meet, or the interface. In a homoge-
neous elastic body, the deformation would continue linearly without interruption.
But the heterogenous nature of this elastic body alters the deformation as expected.

Figure 4 also shows displacement distribution obtained from Ansys. The slight
interruption of linear deformation pattern can also be found in Ansys's result, as
indicated by arrow. The displacement distribution, as well as its range of values,
from our symbolic PDE model agrees well with that of Ansys.

3.2 Stress Distribution

Due to heterogenous nature of the elastic body, it is expected to find accumulation
of stress in the interface of two constituents. Figure 5a shows stress (Von Mises)
distribution from the symbolic PDE model. The peaks of the stress can be found in
the interface of the two constituents, as expected. Interestingly, the peaks of stress
are located on the right and left side of constituent Ω_1, the side perpendicular to the
location of the load source (top). Whether there is geometrical relationship between
location of interfacial stress accumulation with regard to load location is a matter
for further investigation.

Figure 5a also shows stress distribution from ANSYS simulation for the same
problem. It is shown that distribution of stress, as well as range of stress values,
from symbolic PDE model agrees well with ANSYS's. To compare the stress
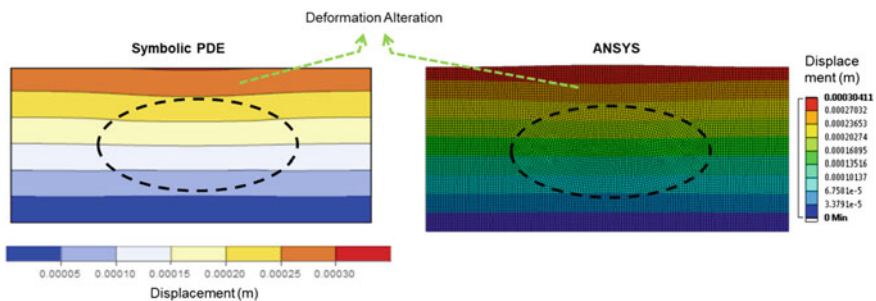
Fig. 4 Displacement distribution from the symbolic PDE model (left) and ANSYS (right). The
constituent Ω_1 is indicated by dashed ellipse. Deviation of deformation can be observed around the
interface region of constituent Ω_1 and Ω_2. The distribution and range of values from both models
agree well
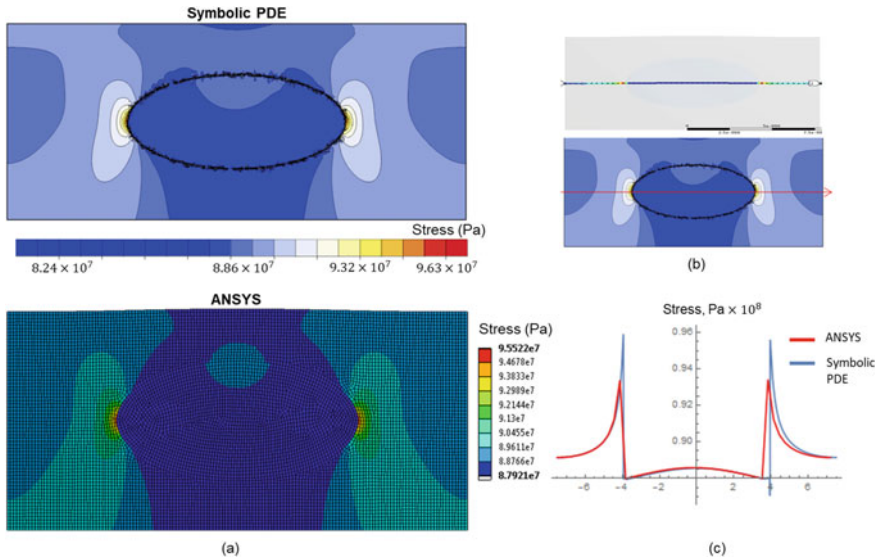
Fig. 5 a Stress distribution from symbolic PDE model (top) and ANSYS (bottom). Peak stress values (stress accumulation) occur in the interfacial region. **b** Stress values along indicated line were obtained from ANSYS (top) and symbolic PDE model (bottom). **c** The plot of stress values along lines in (**b**). The values from symbolic PDE model agree with ANSYS's

values from the two computational models quantitatively, stress values along a horizontal line that crosses the center of the body were obtained. The line is shown in Fig. 5b. The quantitative values were plotted in Fig. 5c. It is shown that the stress values from the two computational models are a good fit. The slight discrepancy may come from the mesh distribution of the two models, and/or the finite element formulation itself (e.g. the symbolic PDE store solutions as functions while ANSYS as array of real numbers).

4 Conclusion

Heterogeneous materials present distinct difficulty in simulation and modeling due to irregularities in shape and materials properties. On another hand, machine learning has become ubiquitous in today's computational software. In addition, symbolic programming for PDE formulation has become a current trend in numerical software.

In this study, an algorithm is presented that seamlessly combine image processing and symbolic PDE FEA simulation to resolve difficulty with modeling heterogenous materials. To demonstrate the capability of the model, a simulation of linear elastic body with two constituents is presented. In heterogenous elastic body

under load, it is expected that the interface would interrupt the deformation and accumulate stress. Simulation results show that deformation along the body is altered the interface region, as expected. The stress distribution indicates that stress accumulates at the interface. It is also shown that the results from symbolic PDE FEA model agrees very well with ANSYS's, qualitatively and quantitatively.

References

1. Michalak B, Wirowski A (2012) Dynamic modelling of thin plate made of certain functionally graded materials. Meccanica 47(6):1487–1498. https://doi.org/10.1007/s11012-011-9532-z
2. Van Long N, Quoc TH, Tu TM (2016) Bending and free vibration analysis of functionally graded plates using new eight-unknown shear deformation theory by finite-element method. Int J Adv Struct Eng 8(4):391–399. https://doi.org/10.1007/s40091-016-0140-y
3. Burlayenko VN, Sadowski T (2020) Free vibrations and static analysis of functionally graded sandwich plates with three-dimensional finite elements. Meccanica 55(4):815–832. https://doi.org/10.1007/s11012-019-01001-7
4. Lv J, Song C, Zheng Y, Zhang H (2020) Extended multiscale finite element method based on polyhedral coarse grid elements for heterogeneous materials and structures. Mater Today Commun 24:101142. https://doi.org/10.1016/j.mtcomm.2020.101142
5. Du C, Ying Z, Jiang S (2010) Extended finite element method and its application in heterogeneous materials with inclusions. IOP Conf Ser Mater Sci Eng 10:12083. https://doi.org/10.1088/1757-899x/10/1/012083
6. Jansson J, Olofsson J, Salomonsson K (2019) On the use of heterogeneous thermomechanical and thermophysical material properties in finite element analyses of cast components. IOP Conf Ser Mater Sci Eng. 529:12076. https://doi.org/10.1088/1757-899x/529/1/012076
7. Pidaparti RM, Ibrahim IBM, Graceraj PP, Yang Y, Rao AS (2020) Computational investigation of interface stresses in duplex structure stainless steels. J Mater Eng Perform 29(6):3895–3905. https://doi.org/10.1007/s11665-020-04877-9
8. P. S. Inc (2020) FlexPDE 7
9. Wolfram Research I (2020) Mathematica, Version 12. Champaign, Illinois: Wolfram Research, Inc
10. The MathWorks I (2020) MATLAB 2020b. Natick, Massachussets
11. Alnæs MS et al (2015) The FEniCS project version 1.5. Arch Numer Softw 3(100). https://doi.org/10.11588/ans.2015.100.20553
12. AB C (2020) COMSOL Multiphysics® v. 5.4. Stockholm, Sweden
13. Chaves EWV (2013) Notes on continuum mechanics. Springer, Netherlands

The Effect of Filter Size Rating and Oil Operating Hour on Hydraulic Oil Contamination Control Using a Developed off Board Filtering System

Iwan Susanto, Muhammad Al-Hapis Abdul Razak, Azmi Hassan, Surya Atmadyaya, and Tumianto

Abstract This paper presents the experiment results to identify the contamination control with hydraulic oil used over 250 tons of Hitachi hydraulic excavator works on coal mining operations. The nature of this topic is to analyze the effectiveness off-board filtering systems by using different sizes of micron rating filters in a specific time interval to reduce Particles Contaminant PC06 and PC14 in hydraulic oil. Based on the analysis results, conclusions can be drawn (1) The SNR value on the filter factor reaches optimal at level 2, a combination of Filter B (2×10 μm and 2×8 μm). At the time factor, it comes optimal at level 1 (1000 h) so that the combination of filter and time that can optimize (minimize) the PC06 content in the oil is to use filter B and 1000 h. (2) There is no significant effect of the filter, time, and interaction factors on PC14. The SNR value on the filter factor reaches optimal at level 2 using Filter B (2×10 μm and 2×8 μm). At the time factor, it comes optimal at level 1 (1000 h) so that the combination of filter and time that can optimize (minimize) is to use filter B and time 1000 h. (3) There is a significant effect of the factor filter on V100. There is a substantial effect of the time factor on V100. There is no influence on the interaction between factors on V100. The proportion of each factor's contribution to the V100 response, filter factor has an effect of 14.926%, the time factor has an impact of 10.868%, and the filter inter-action factor and time affect 0.17%.

I. Susanto (✉) · M. A.-H. Abdul Razak · S. Atmadyaya · Tumianto
Manufacturing Section, Universiti Kuala Lumpur Malaysian Spanish Institute, Kulim
Hi-Tech Park, 09000 Kulim, Kedah, Malaysia
e-mail: Iwan.susanto@s.unikl.edu.my

A. Hassan
Electrical, Electronics and Automation Section, Universiti Kuala Lumpur Malaysian Spanish
Institute, Kulim Hi-Tech Park, 09000 Kulim, Kedah, Malaysia

1 Introduction

The attention to repair and maintenance strategy is to keep changing over time as advances in technology and rapidly growing research, and this makes become more efficient and reliable. In the early days of production, the maintenance method was to "fix the issue after it has a problem". The reason is simple because the machines were used in production, and demand was not very high. Thus, make the equipment down could not be avoided. This type of maintenance is called a corrective maintenance repair [1].

Maintenance costs can be an important part of the organization's profit. In practice, maintenance costs can take up 2–10% of corporate revenue and reach 24% in the transport industry. Modern management considers maintenance a key component in achieving the production process and high-quality products while maintaining the necessary equipment and reliability of machinery as required in modern times. Automation, simple and flexible production processes, "lean production" and "just-in-time" operation [2].

Referring to Singh et al. [3] in hydraulic oil contamination, the previous study proved if the oil can cause wear and tear on parts of the Hydraulic system. That study analyzed if about 70% of hydraulic system failures are caused by not clean oil. A detailed analysis reveals that the main cause of damage to pumps, valves, and actuators is contamination. Contamination that occurs in the system can damage the components' surface or stop the movement of moving parts, causing system damage. Another study by Marko Orošnjak [4] regarding hydraulic contamination control in condition-based maintenance systems stated that there would be three fundamental steps of CBM related to contamination in hydraulic systems where first is data acquisition, the second is data processing, and the last one decision making to decide necessary actions to prevent failure in the future. That is why contamination control for hydraulic oil in a machine is really important.

The cleanliness of hydraulic oil affects system performance in general, such as the cylinder's response, the inner parts of the components, impact on movement and pressure, component stability, environmental impact, energy loss caused by the effects of the contamination of the oil. The effect of lack of hydraulic power for working or, in some cases, to avoid unnecessary breakdown, a proper form of maintenance strategy must be implemented to meet the machine's requirements [4]. Oil Monitoring and Schedule Oil Sampling plays an important role in ensuring equipment can be operated optimal without disruption from oil-related issues, especially in hydraulic systems. The maintenance team and engineers should understand equipment performance, cycles, cleanliness and contamination controls, operating environment, operating system temperature, and oil characteristics to predict and evaluate the process. The reason because oil contamination can destroy the mechanism in many ways.

A study was carried out in the past to measure contamination particles' level of hydraulic oil in the system while the machine is operating (Onboard system), Ng et al. [5]. But at this experimental process aims to analyze the correlation of filtering

size and oil operating hour effect in reducing contaminants on hydraulic oil at acceptable level parameters as equipment manufacturing recommendation by using a developed Off Board Filtering system, instead of On Board with particles counters.

Hydraulic equipment is constantly improving, resulting in a higher power and faster response rate while at the same time maintaining energy efficiency. The issue is based on hydraulic drive development and control, error detection systems, and Predictive Maintenance (PdM) for contamination control.

Contamination in the hydraulic system will harm the performance and service life of the hydraulic equipment; it can cause system failures, which include:

a. Deterioration in performance: this is due to the interaction between contaminant particles that can damage the two moving surfaces, causing aeration, abrasive wear, and corrosion.
b. Intermittent: temporary resistance caused by contaminants that occur in the poppet movement or valve spool, which functions to open and close the oil flow in the systems.
c. Severe damage that occurs due to the presence of a few large particles or a large number of small particles causing a jamming of moving parts.

Once hydraulic oil is contaminated with pollutants either from inside or outside the system, this can cause a system failure. In general, there are three main sources of contaminants in a hydraulic system.

a. Internal contaminants, which can come from manufacturing, assembling, and testing hydraulic components.
b. External contamination often occurs due to inadequate system sealing or inadequate filtration of the oil reservoir air caps. Machines used in the mining industry tend to have high levels of silicon, dirt, and water in the hydraulic system. Contamination can also occur during maintenance, especially when refilling hydraulic oil if environmental contamination is not considered.
c. The resulting contamination, also known as abrasion, is caused by contact with hydraulic components during use and cannot always be avoided [5].

The International Standards Organization (ISO) has developed a code system for convenience in discussing the cleanliness level of a fluid. The system reports on particles at two important size categories (>5 μm and >15 μm). This system of reporting oil cleanliness can have a better impact on managing the life of hydraulic components. Particle Count (PC), which is used for hydraulic system oil samples, is one of two tests in the Scheduled Oil Sampling (SOS) Services program that looks at particles. Unlike Wear Rate Analysis, Particle Count detects metallic and non-metallic particles from 2 to 100 μm [6].

Fluid cleanliness can be measured by taking fluid samples from various machine compartments. Particle Contaminants (PC) are typically measured by particle counters. The number of particles in fluids is expressed in "ISO (International Organization for Standardization)" ratings. It is Standard classifies fluid cleanliness

by the number and size of particles in 1 ml of fluid. It measures particle size in μm (microns) and reports the resulting count in three code ranges X, Y and Z. The three code range defines the size and distribution of particles in 1 millilitre of fluid:

a. The first code range, X, represents the number of particles equal to or larger than 4 μm per millilitre of fluid.
b. The second code range, Y, represents the number of particles equal to or larger than 6 μm per millilitre of fluid.
c. The third code range, Z, represents the number of particles equal to or larger than 14 μm per millilitre of fluid [6].

The three code range follows "ISO 4406" definitions and is used for liquid fuels such as diesel and gasoline. The two code system, for example, "ISO-/16/13", is used for certain lubricant systems. In the two code system, the first number is the number of particles equal to or larger than 4 μm per millilitre of fluid. This number is not required and may be represented by a dash (−). The second number (Y) and the third number (Z) follow "ISO 4406" definitions [6]. For hydraulic oil in this study reports, the Y and Z codes where it represents by

a. PC06 represents the number of particles equal to or larger than 6 μm per millilitre of fluid with the normal specification limit, which is <2500 particle count (ISO Code 18).
b. PC14 represents the number of particles equal to or larger than 14 μm per millilitre of fluid with a normal specification limit, which is <320 particle count (ISO code 15).

Other than oil contamination, the viscosity of the oil also has an important role in ensuring the hydraulic system working properly. Viscosity is a temperature-dependent characteristic of lubricants that describes how the oil will flow. Viscosity is usually measured at 100 °C (V100). At high operating temperatures, a lubricant must be able to maintain appropriate film thickness. If the viscosity becomes too low, wear will occur within the compartment. If viscosity is too high, the oil will not flow to areas needing lubrication.

The Taguchi approach involves reducing operational variables with a robust experimental design. The purpose of this method is to produce a high-quality product at a lower cost to the manufacturer. Taguchi's experimental technique includes the use of orthogonal groups to organize the phases that affect the process and the conditions in which they should differ [3]. This method uses orthogonal arrays that use a small number of experiments to extract complete information about functional components. These test products are generally selected based on trade between the price (time or materials) of the test and the accuracy of the results [7].

The Taguchi method allows for the analysis of different phases without much higher experiments. For example, a process of 8 types, each with three countries, would require 6561 (3^8) trials to test all kinds. However, only 18 experiments are needed using Taguchi orthogonal arrays, or less than 3% of the original number of experiments. In this way, it allows for identifying critical conditions that significantly impact the quality of the process so that further tests can be performed, and invalid conditions can be ignored [8].

2 Methodologies

Methodologies on the research will be described as follow:

2.1 Data Collection Method

The data on this research is taken from hydraulic oil inspection to maintain mining equipment at a coal mine in Indonesia. The number of samples is taken from four excavators 250 tons of Hitachi, where each of them used eight samples of hydraulic oil reports from SOS's laboratory to be analyzed.

2.2 Data Analysis

The variables used in the analysis consisted of two types of variables, namely the response variable and the independent variable. The response variable used is a variable that indicates the quality of the oil. In this case, three response variables were chosen, namely:

a. PC06, with the normal specification limit, is <2500, where smaller is better characters.
b. PC14, with normal specification limit, is <320, where smaller is better characters.
   The Signal to Noise Ratio (SNR) of two above variables (PC06 and PC14) will be measured as follow;

$$\text{Smaller is the better characteristic} \quad \text{SNR:} -10\log\frac{1}{n}\left(\sum y^2\right) \quad (1)$$

c. V100, with normal specifications >7, so it has larger is better characters.
   The Signal to Noise Ratio (SNR) of V100 variables will be measured as follow;

$$\text{Larger is the better characteristic} \quad \text{SNR:} -10\log\frac{1}{n}\left(\sum \frac{1}{y^2}\right) \quad (2)$$

n　　　　is the sample observed
y1, y2, … is the data results

While the independent variables in this analysis are the variables used to optimize the quality of oil, and each has two levels, namely:

Table 1 Factor and level used	Level	X1 (Filter)	X2 (Time)
	1	A	1000
	2	B	2000

a. Filter (X1), which consists of the level filter set A (4 × 10 μm filters) and filter set B (2 × of 10 μm and 2 × of 8 μm filters).
b. Time (X2), which consists of levels 1000 (interval hour) and 2000 (interval hour).

The following is a summary of the factors and levels used (Table 1):

Based on the available data, this analysis uses eight data for each combination of factor levels X1 and X2. The data taken is data from the first time the oil is used (after the oil is changed) until it is replaced again. Eight data were taken because there were eight data, which made it possible to have the same number of replications for each level combination. Data are presented in Tables 2, 3, 4 and 5.

Table 2 Experiment data EX78—using filter set A with an interval of 1000 h	Sample ID	PC06	PC14	V100
	EX78_1	1273	153	7.52
	EX78_2	2495	116	7.34
	EX78_3	2208	107	7.18
	EX78_4	2629	268	7.58
	EX78_5	2183	320	7.38
	EX78_6	3414	228	7.36
	EX78_7	3203	373	7.34
	EX78_8	3089	356	7.47

Table 3 Experiment data EX55—using filter set A with an interval of 2000 h	Sample ID	PC06	PC14	V100
	EX55_1	1271	70	7.36
	EX55_2	565	141	7.26
	EX55_3	611	265	7.35
	EX55_4	641	235	7.14
	EX55_5	5243	474	7.3
	EX55_6	4836	326	7.33
	EX55_7	3557	317	7.49
	EX55_8	3989	294	7.38

Table 4 Experiment data EX64—using filter set B with an interval of 1000 h

Sample ID	PC06	PC14	V100
EX64_1	887	95	7.63
EX64_2	682	145	7.47
EX64_3	1003	101	7.48
EX64_4	2396	233	7.59
EX64_5	1996	147	7.47
EX64_6	1993	245	7.43
EX64_7	2199	165	7.47
EX64_8	2429	210	7.46

Table 5 Experiment data EX65—using filter set B with an interval of 2000 h

Sample ID	PC06	PC14	V100
EX65_1	3794	102	7.47
EX65_2	3335	429	7.31
EX65_3	1957	226	7.41
EX65_4	1594	105	7.44
EX65_5	4230	402	7.41
EX65_6	3741	203	7.61
EX65_7	2468	227	7.14
EX65_8	4726	373	7.49

3　Discussion

Results of the experimental on analyzing particles contamination using Off Board Filtering System are as follow:

3.1　Taguchi Analysis of PC06 Response

3.1.1　Orthogonal Array on PC06 Response

The analysis used two factors that are thought to influence the response (PC06), namely Filter (X1) and Hour (X2), where each factor has two levels. This analysis used an orthogonal array of 4 experiments with eight repetitions for each experiment (a combination of factors on each level). The orthogonal arrangement design, as follows: x = experiment = 4, n = sample observed = 8, a = factor level X1 = 2, b = factor level X2 = 2.

Table 6 SNR on PC06 response

No.	Set filter (X1)	Time interval (X2)	Y bar	S/R ratio for PC06
1	A	1000	2561.750	−68.440
2	A	2000	2589.125	−70.116
3	B	1000	1698.125	−65.233
4	B	2000	3230.625	−70.616
Average			2519.906	−68.601

3.1.2 Signal to Noise Ratio (SNR) on PC06 Response

SNR measures the level of performance and also the obscurity of the output quality characteristics. The higher the performance as measured by the higher SNR is the same as, the smaller the loss (Table 6).

3.1.3 ANOVA on PC06 Response

The results of the ANOVA analysis can be explained as follows (Table 7).

From the P-value, it is known that there is no effect of filter factors on PC06 at the significance level of $\alpha = 5$ and 10%. While the time factor has a significant effect on PC06 at the significance level $\alpha = 10\%$.

3.1.4 Large Factor Contributions

The proportion of each factor's contribution to the response: Filter factor has an effect of 0.184% on PC06. The time factor has an impact of 9.061% on PC06. The filter interaction factor and time have an effect of 8.436% on PC06.

Table 7 ANOVA on PC06 response

CF	DOF	SS	V	F ratio	F (0.95; DOF1; DOF2)	P Value	%C
X1	1	98679.031	98679.031	0.062	4.196	0.804	0.184
X2	1	4866420.031	4866420.031	3.082	4.196	0.090	9.061
X1 * X2	1	4530802.531	4530802.531	2.869	4.196	0.101	8.436
Error	28	44211927.125	1578997.397				
Total	31	53707828.719					

Table 8 Response SNR on PC06

Level	X1	X2
1	−69.278	−66.836
2	−67.925	−70.366
Delta	1.353	3.530
Optimal	2	1
Rank	2	1
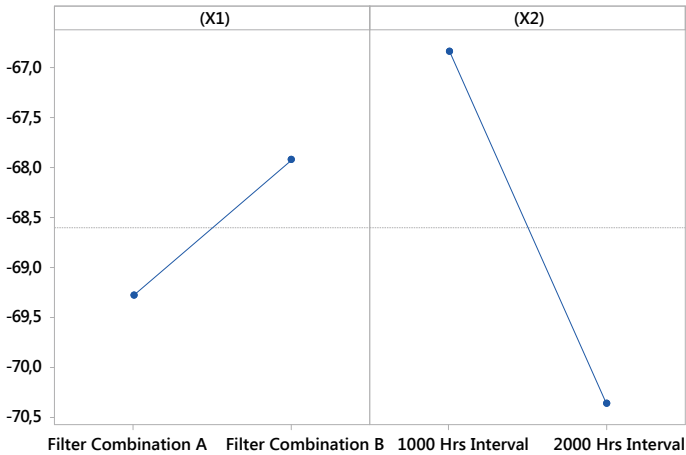
Fig. 1 Average SNR response on PC06

3.1.5 Response SNR on PC06

The effect table calculation is by calculating the SNR average value at each level of each corresponding factor (Table 8).

The design that produces the best SNR value is the design with filter B (level 2) and 1000 h (level 1) (Fig. 1).

The SNR value on the filter factor reaches optimal at level 2 (Filter B), and at the time factor, it comes optimal at level 1 (1000 h) so that the combination of filter and time that can optimize (minimize) the PC06 content in the oil is to use filter B and 1000 h.

3.1.6 PC06 and SNR Predictions

The prediction of the value of PC06 in oil will be carried out if the optimal design is used, filter B with 1000 h. The prediction results are as follows:

$$\widehat{y} = \overline{X1}_B + \overline{X2}_{1000} - \overline{y}_{...} = 2074.406$$

The average PC06 oil content is 2074.406.

3.2 Taguchi Analysis of PC14 Response

3.2.1 Orthogonal Array on PC14 Response

The analysis used two factors that are thought to influence the response (PC014), namely Filter (X1) and Hour (X2), where each factor has two levels. This analysis used an orthogonal array of 4 experiments with eight repetitions for each experiment (a combination of factors on each level). The orthogonal arrangement design, x = experiment = 4, n = sample observed, a = factor level, X1 = 2, b = factor level, X2 = 2.

3.2.2 Signal to Noise Ratio (SNR) on PC14 Response

(See Table 9).

3.2.3 ANOVA on PC14 Response

The results of the ANOVA analysis can be explained as follows (Table 10).

From the *P*-value, it is known that there is no effect of filter, time, and interaction factors on PC14 at the significance level of $\alpha = 5$ and 10%.

Table 9 SNR on PC14 response

No	Set filter (X1)	Time interval (X2)	Y bar	S/R ratio for PC14
1	A	1000	240.125	−48.296
2	A	2000	265.250	−49.218
3	B	1000	167.625	−44.905
4	B	2000	258.375	−49.098
Average			232.844	−47.879

Table 10 ANOVA on PC14 response

CF	DOF	SS	V	F ratio	F(0.95; DOF1; DOF2)	P-value	%C
X1	1	12600.781	12600.781	1.092	4.196	0.305	3.396
X2	1	26854.031	26854.031	2.328	4.196	0.138	7.236
X1 * X2	1	8613.281	8613.281	0.747	4.196	0.395	2.321
Error	28	323024.125	11536.576				
Total	31	371092.219					

3.2.4 Large Factor Contributions

The proportion of each factor's contribution to the response: Filter factor has an effect of 3.396% on PC14. The time factor has an impact of 7.236% on PC14. The filter interaction factor and time have an effect of 2.321% on PC14.

3.2.5 Response SNR on PC14

The effect table calculation is by calculating the SNR average value at each level of each corresponding factor.

The design that produces the best SNR value is the design with filter B (level 2) and 1000 h (level 2) (Fig. 2).

The best SNR value is the design with filter B (level 2) and 1000 h (level 1). Also, from Table 11, a graph of the average SNR for PC14 responses can be
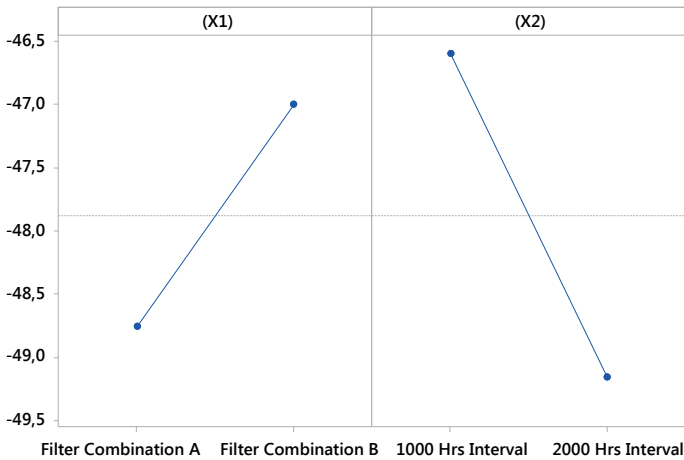
Fig. 2 Average SNR response on PC14

Table 11 Response SNR on PC14

Level	X1	X2
1	−48.757	−46.600
2	−47.002	−49.158
Delta	1.755	2.557
Optimal	2	1
Rank	2	1

compiled using Software R.1000 so that the combination of filter and time that can optimize (minimize) the PC14 content in the oil is to use filter B and a time of 1000 h.

3.2.6　PC14 and SNR Predictions

Furthermore, the prediction of the value of PC14 in oil will be carried out if the optimal design is used, namely, filter B with 1000 h.

$$\widehat{y} = \overline{X1}_B + \overline{X2}_{1000} - \overline{y}_{...} = 2184.031$$

The average of PC14 is 2184.031.

3.3　Taguchi Analysis of V100 Response

3.3.1　Orthogonal Array on V100 Response

The analysis used two factors that are thought to influence the response (V100), namely Filter (X1) and Hour (X2). Each factor has two levels. This analysis used an orthogonal array of 4 experiments with eight repetitions for each experiment (a combination of factors on each level). The orthogonal arrangement design, x = experiment = 4, n = sample observed = 8, a = factor level, X1 = 2, b = factor level, X2 = 2.

3.3.2　Signal to Noise Ratio (S/R) on V100 Response

The higher the performance as measured by the higher SNR is the same as, the smaller the loss (Tables 12 and 13).

Table 12 SNR on V100 response

No.	Set filter (X1)	Time interval (X2)	Y bar	S/R ratio for V100
1	A	1000	7.396	17.377
2	A	2000	7.326	17.295
3	B	1000	7.500	17.500
4	B	2000	7.410	17.392
Average			7.408	17.391

Table 13 ANOVA on V100 response

CF	DOF	SS	V	F ratio	F(0.95; DOF1; DOF2)	P-value	%C
X1	1	0.070	0.070	5.645	4.196	0.025	14.926
X2	1	0.051	0.051	4.110	4.196	0.052	10.868
X1 * X2	1	0.001	0.001	0.064	4.196	0.802	0.170
Error	28	0.349	0.012				
Total	31	0.471					

3.3.3 ANOVA on V100 Response

There is a significant effect of the factor filter on V100 at the significance level $\alpha = 5\%$. Also, with the level of $\alpha = 10\%$, there is a significant effect of the time factor on V100. At the significance level $\alpha = 5$ and 10%, there is no influence on the interaction factors on V100.

3.3.4 Large Factor Contributions

The proportion of each factor's contribution to the response: Filter factor has an effect of 14.926% on V100. The time factor has an effect of 10.868% on V100. The filter interaction factor and time have an impact of 0.17% on V100.

3.3.5 Response SNR on V100

The effect table calculation is by calculating the SNR average value at each level of each corresponding factor (Table 14).

The design that produces the best SNR value is the design with filter B (level 2) and 1000 h (level 2) (Fig. 3).

Table 14 Response SNR on V100

Level	X1	X2
1	17.336	17.439
2	17.446	17.344
Delta	0.110	0.095
Optimal	2	1
Rank	1	2
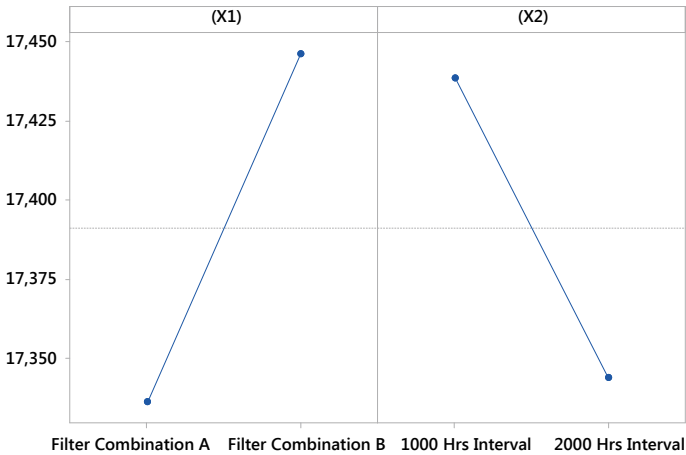
Fig. 3 Average SNR response on V100

The SNR value on the filter factor reaches optimal at level 2 (Filter B). At the time factor, it comes optimal at level 1 (Time 1000) so that the combination of filter and time that can optimize (minimize) the V100 content in the oil is to use filter B and time 1000 h.

3.3.6 V100 and SNR Predictions

The prediction of the value of V100 in oil will be carried out if the optimal design is used, namely, filter B in 1000 h. The prediction results are as follows:

$$\hat{y} = \overline{X1}_B + \overline{X2}_{1000} - \bar{y}_{...} = 7.495$$

The average of V100 content in the oil is 7.495.

4   Conclusions

There is no effect of filter and interaction factors on PC06 at the significance level of $\alpha = 5\%$ and $\alpha = 10\%$. The proportion of each factor's contribution to the PC06 response, filter factor has an effect of 0.184%, the time factor has an impact of 9.061%, and the filter interaction factor and time have an effect of 8.436%. The SNR value on the filter factor reaches optimal at level 2 (Filter B). At the time factor, it comes optimal at level 1 (1000 h) so that the combination of filter and time that can optimize (minimize) the PC06 content in the oil is to use filter B and 1000 h. The average PC06 oil content is 2.074406.

There is no effect of filter, time, and interaction factors on PC14 at the significance level of $\alpha = 5$ and 10%. The proportion of each factor's contribution to the PC14 response: filter factor has an effect of 3.396%, the time factor has an effect of 7.236%, and the filter interaction factor and time have an impact of 2.321%. The SNR value on the filter factor reaches optimal at level 2 (Filter B). At the time factor, it comes optimal at level 1 (1000 h) so that the combination of filter and time that can optimize (minimize) the V100 content in the oil is to use filter B and time 1000 h. The prediction of the value of PC14 in oil is an average of 2184.031.

There is a significant effect of the factor filter on V100 at the significance level $\alpha = 5\%$. Also, with a significance level of $\alpha = 10\%$, there is a significant effect of the time factor on V100. The proportion of each factor's contribution to the V100 response, filter factor has an impact of 14.926%, the time factor has an effect of 10.868%, and the filter interaction factor and time affect 0.17%. The average of V100 content in the oil is 7.495.

There is a potential opportunity to use a combination of time factor A (1000 h.) with filter set B (2ea of 10 mm and 2ea of 8 mm) to improve hydraulic oil usage hour in the future, and this will also impact maintenance strategy in managing a fleet of equipment which uses a large quantity of oil for their hydraulic system.

References

1. Ayo-Imoru RM, Cilliers AC (2018) A survey of the state of condition-based maintenance (CBM) in the nuclear power industry. Ann Nucl Energy 112:177–188
2. Ben-Daya M, Duffuaa SO, Raouf A, Knezevic J, Ait-Kadi D (2009) Handbook of maintenance management and engineering
3. Singh M, Lathkar GS, Basu SK (2012) Failure prevention of hydraulic system based on oil contamination. J Inst Eng (India) Ser C 93(3), 269–274
4. Marko Orošnjak TP, Jocanović M, Karanović V, Novak AH (2017) Using contamination control in condition based maintenance of a hydraulic system
5. Ng F, Harding JA, Glass J (2017) Improving hydraulic excavator performance through in line hydraulic oil contamination monitoring. Mech Syst Signal Process 83:176–193

6. Caterpillar (2017) Caterpillar machine fluids recommendation, pp 141–143
7. Mohsin I et al (2020) Optimization of the polishing efficiency and torque by using Taguchi Method and ANOVA in robotic polishing. Appl Sci 10(3):824
8. Stephanie Fraley MO, Terrien B, Zalewsk J (2020) Design of experiments via Taguchi Methods—Orthogonal Arrays

A Study on the Effect of Chimney Roof Angle Towards Temperature Uniformity on Multilevel Dryer

Ratna Sary and Ahmad Syuhada

Abstract One way to improve the drying capacity is by using multilevel drying equipment system and fuel energy. The use of multilevel dryer in the drying chamber particularly remains divergent temperature. In this regard, a non-uniform drying air temperature correspondingly decreases the drying quality. Large temperature variations can be overcome by inhibiting the rate at which hot air escapes from the drying chamber. Such formulated investigation can be performed by reducing the angle of the chimney roof. In this research-based paper, the researchers will therefore turn the attention towards the effect of the chimney roof angles on the temperature uniformity in the multi-stored drying chamber. Such drying machine is equipped with combustion chamber, start-up, hot gas flow, multi-stored drying chamber and exhaust chimney of residual hot air. The chimney roof tested varies on angles 15°, 25° and 35°, respectively. The findings disclosed that the angle of chimneys is 15° which results in a more uniform drying chamber temperature.

1   Introduction

To improve the capacity of the dryer, it can be performed with a multilevel drying machine system and fuel energy for drying energy [1, 2] as it has been mostly conducted. Beyond the use of multilevel drying chamber, there is still divergent among multilevel temperatures in the drying chamber. Once the difference has occured, the air temperature in the drying chamber will result in less quality drying products [3–9].

Large temperature variations in multilevel dryer are caused by fluid flow that occurs by natural convection. To avoid such obvious issue, it can be performed by inhibiting the rate at which hot air escapes from the drying chamber as reducing the slope of the chimney roof angle [10].

R. Sary · A. Syuhada (✉)
Mechanical and Industrial Engineering Department, Faculty of Engineering,
Universitas Syiah Kuala, Banda Aceh, Indonesia
e-mail: ahmadsyuhada@unsyiah.ac.id

With regard to this issue, the foregoing illustration refers as the background for the researchers to study the effect of the slope of the chimneys towards the temperature uniformity on the multilevel dryer. To investigate the matter, the present project is carried out to figure out to what extent the influence of the slope of chimney roof angle towards the temperature uniformity in the drying chamber. As well, the present study also focuses on the effect of initial steering on the temperature distribution in the heating duct.

Drying equipment system of hot gas flows generated from a fuel combustion engine naturally leads to the drying chamber. This drying equipment is equipped with combustion chamber, start-up, hot gas flow, multi-storey drying chamber and exhaust chimney of residual hot air.

2 Research Methodology

2.1 Method

This research-based paper numerically examines the effect of the slope of the chimney roof angle towards temperature uniformity in the drying chamber. In this paper, temperature distribution test is performed in the drying chamber with no drying object.

2.2 Test Equipment

The equipment for testing is designed in such a way as shown in Fig. 1. Multi-storey drying tools are equipped with a combustion chamber, start-up, hot gas flow, multi-storey drying chamber and exhaust chimney for residual hot air.

Combustion Chamber
The primary function of the combustion section is to burn fuel for drying heat energy. This combustion chamber measures 100×100 cm, the bottom measures 150×150 cm and the total height is 75 cm.

Start-up
The start-up is made in the shape of a *V* with an angle of 30° Unperforated, serves for hot gas divider from the combustion process which will be supplied into the drying chamber through the heater duct. This initial guide is placed above the combustion chamber.

Heating Duct
The heating/directing channel functions as a distributor and divider of hot gas from the combustion chamber to the drying room [10–12]. This hot gas distribution occurs because there is a hole from the connection of the heating duct to the drying

Information:

1. Combustion Chamber
2. Unperforated start-up
3. Heating duct
4. Drying Chamber and Shelf
5. Hot air chimney from drying
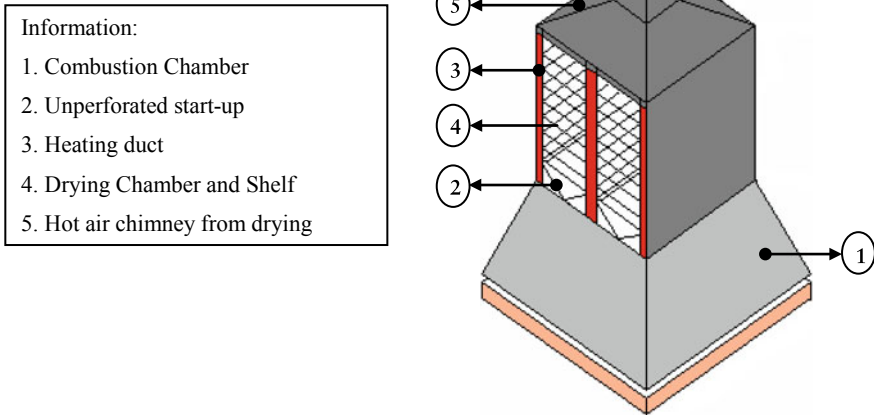
Fig. 1 Schematic design of drying machine

chamber. The number of these connecting holes is equal to the number of levels or drying shelf, for this test, there are 7 levels within this shelf with heating duct is $5 \times 95 \times 95$ cm.

Drying Chamber/Shelf

The drying chamber is the place to put down the drying object during drying. The drying chamber has dimensions of $100 \times 100 \times 100$ cm. With 2 drying chamber flows whilst the shelf here functions to place the material to be dried, this drying shelf is placed two in the path of the drying room. Each path of this drying chamber is placed 7 shelves, each shelf measures $92 \times 40 \times 3$ cm with a distance of 10 cm, respectively.

Drying Chamber/Shelf

The chimney of hot air exhaust from the drying residue serves as an output for the mixture of hot air and steam from the drying results. The dimensions of the bottom are as the same as the dimensions of the drying chamber 100×100 cm and at the top it is reduced to size $30 \times 30 \times 30$ cm. In this test, the slope of the chimney roof varies from angles 15°, 25° and 35°, respectively.

2.3 Variable Observed

The variable observed is the temperature distribution at several points on the drying equipment. In this respect, measurement points is defined in Fig. 2. There are six chimney on the drying equipment. Each chimney has two different measurement
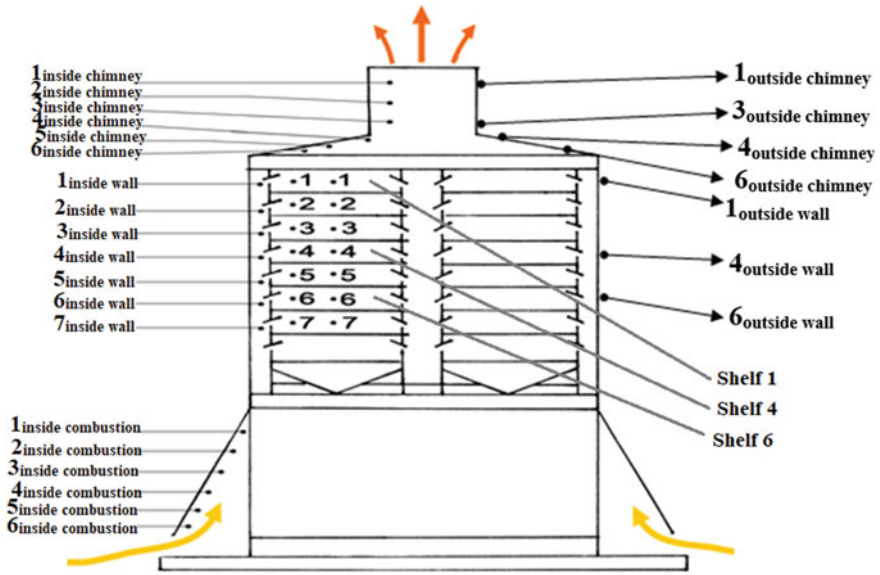
Fig. 2 The temperature distribution at several points on the drying equipment

point which are outside and inside measurement points. We take just 1, 3, 4 point from outside chimney and 1, 4, 6 from outside wall to see how different temperature distribution from dryer are.

3 Result and Discussion

Based on the test results and measurements obtained in this line of research, the temperature distribution of hot gas flows of the drying equipment has been received. Measuring the temperature of the drying equitment for 2–3 h with an interval of 15 min.

In this test, the findings of temperature distribution are based on the result of influencing each other between parts of the dryer, that are:

1. The temperature in the guide flow
2. The temperature in the drying chamber
3. The temperature at the chimney.

3.1 The Influence of the Start-up on the Temperature Distribution of the Dryer

The effect of the non-perforated start-up is notably real especially in the heating duct and the drying chamber.

3.1.1 The Influence of the Start-Up on the Temperature Distribution of the Guide Flows (Inside Wall)

The results of temperature distribution measurements are shown in Fig. 3. It describes the temperature distribution that occurs in the guide flows. At the beginning of heating, the drying equipment distributes the temperature of the hot gas between the drain point 6 ($6_{inside\ wall}$) and the end of the flow point 1($1_{inside\ wall}$) show a significant difference. This is because the heat at point 6 and 5 is more in the drying chamber which is still low in temperature. After the temperature of the 1, 2 and 3 shelves has increased, the temperature in the heating duct has increased, this occurs after 80 min of heating the dryer.

This happens because of the influence of the start-up on the temperature distribution pattern in the guide flows. This start-up has function to divide the hot gas from the combustion of fuel in the combustion chamber to the heating duct. In this regard, most of the heat energy from the combustion product is entered into the drying chamber through the heating channel divided by the starting guide.

With this start-up, the temperature distribution in the heating duct remains irregular. This temperature distribution irregularity is due to the flow pattern of hot gas in the channel in which the speed and temperature are always changing at each measurement point. Because the hot gas from the combustion of the fuel goes into the room resulting in high flow turbulence.
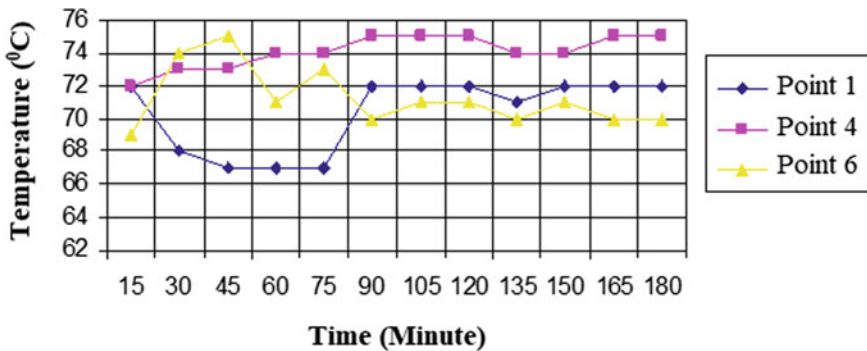
Fig. 3 Temperature distribution of the inside wall with chimney angle 15°
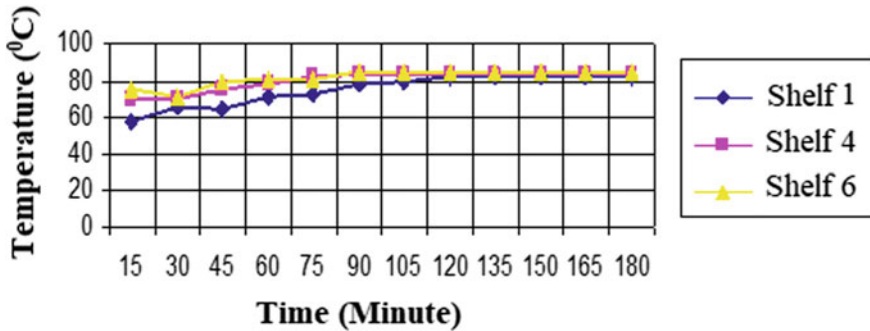
Fig. 4 The temperature distribution in the drying chamber 5 cm from the hot flow wall with chimney angle 15°

3.1.2 The Influence of the Start-Up on the Temperature Distribution of the Drying Chamber

The effect of the start-up on the temperature distribution in the drying chamber at the measuring point 5 cm from the heating duct with the chimney roof angle 15°. Figure 4 shows the temperature distribution pattern in the drying chamber. From Fig. 4, we can figure out that the temperature uniformity between shelf 1 to shelf 6 is achieved after heating 90 min, which is when the heating gradient temperature between shelf 1 and shelf 6 reaches 4–7 °C. After 120 min of heating, the flow pattern is somewhat stable so that the temperature gradient between shelf 1 and shelf 6 reaches 2–3 °C. Such obvious hardness is good enough to be applied to a drying system because the drying time is between 5–12 h, depending on the object and water content of the desired drying results.

3.1.3 The Effect of Start-up on Temperature Distribution in Chimneys (Inside Chimney)

The effect of the start-up on the temperature distribution in the drying chamber at the measuring point 5 cm from the heating duct with the chimney roof angle 15°. Figure 5 shows the temperature distribution pattern in the drying chamber. From Fig. 5, we can figure out that the temperature.

3.2 The Effect of Chimney Angle on Temperature Distribution

The measurement results show that the temperature distribution in each flow influences the slope angle 15°, 25° and 25°, respectively. In this regard, the size of
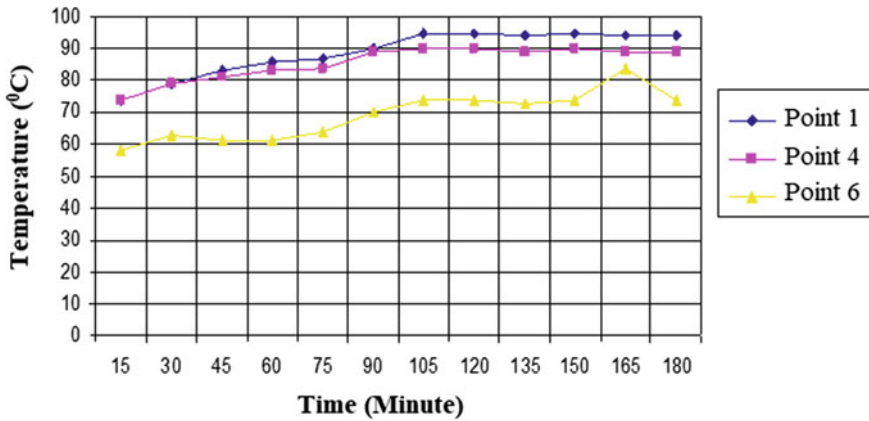
Fig. 5 The temperature distribution at the chimney with angle 15°

the slope of the chimney roof angles of flue gas mainly determines the flow pattern and temperature distribution either in the guide or heater, drying chamber or even in the chimney.

3.2.1 Effect of Chimney Angle on Temperature Distribution in Heating/Guide Flows

With the start-up of temperature distribution in the heater or steering flows with a slope of the roof angle 15° is somewhat regular and a laminar flow pattern. However, it notably differs from the angle of roof slope 25 and 35°, where the temperature distribution is irregular and the flow pattern is slightly turbulent.

From the test results of the third distribution on the chimney roof angle, the temperature gradient between shelf 1 and shelf 6 is obtained after 120 min process of heating the drying chamber. Whilst, the slope of the roof angle 15° with a temperature gradient reaches 2–3 °C, and in turns, the slope of the roof angle 25° with a temperature gradient reaches 4–5 °C and the slope of the roof angle 35° with and the temperature gradient reaches 6–7 °C.

3.2.2 Effect of Chimney Angle on Temperature Distribution in Drying Chamber

With the start-up of temperature distribution in the heater or steering flows with a slope of the roof angle 15° is somewhat regular and a laminar flow pattern. However, it notably differs from the angle of roof slope 25° and 35°, where the temperature distribution is irregular and the flow pattern is slightly

Fig. 6 The chimney angle to the temperature distribution in the drying chamber at position 5 cm from the wall
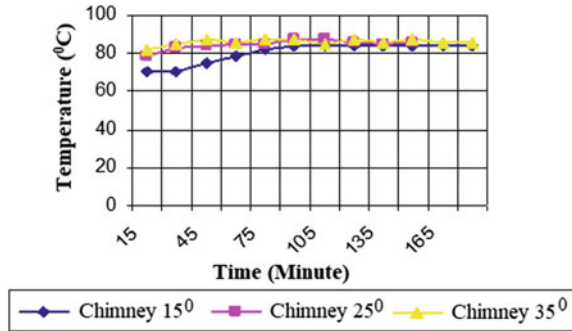
a. Measuring position 5 cm from the heater

Figure 6 shows the results of measuring the temperature distribution in the drying chamber with measurement position 5 cm from the heating wall with variations in the roof slope's angle 25° and 35°.

Figure 6 demonstrates that at the beginning of heating, the temperature distribution is slightly different between the angular values of the roof. Following the process, however, once it reaches 100 min, the temperature distribution in the three variations of the angular magnitude tends to be indistinguishable. Such obvious trend is due to this warming has reached steady. Thus, before steady, the influence of the angle of chimneys affects the temperature distribution in the drying chamber at the measuring point 5 cm from the heating wall.

b. Measuring position 25 cm from the heater

Figure 7 discloses the temperature distribution on shelf 4 which is a measuring distance of 25 cm from the heating flow wall for the three chimney angles. The temperature gradient in the three types of chimneys is smaller than the measurement position of 5 cm from the heating flow wall, this occurs because the
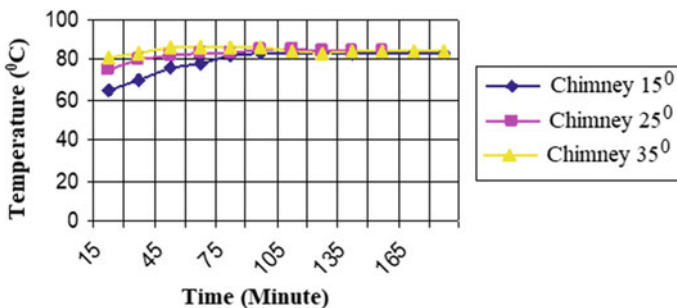
Fig. 7 The chimney angle to the temperature distribution in the drying chamber at position 25 cm from the wall
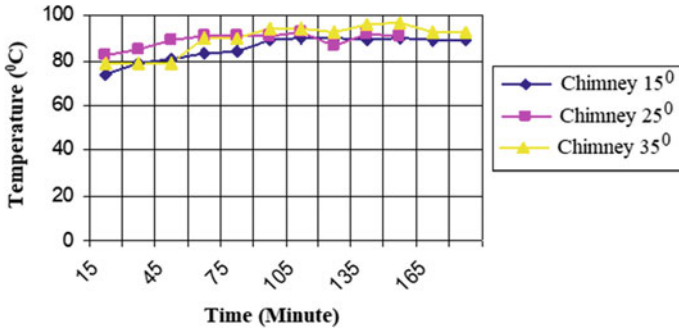
Fig. 8 Temperature distribution at point 4 on the chimney

movement of hot gas in this position is more stable due to the measurement position remains far from the inlet in the heating flows wall and the temperature uniformity of the three chimneys is also faster, that is, 75 min of initial heating.

3.2.3 Effect of Chimney Angle on Temperature Distribution in Chimney

Figure 8 shows the temperature distribution at the three types of chimney roof angles at point 4. From these two figures we can highlight that the type of hot gas flow is less laminar, and thus, the temperature distribution in those three types chimneys is less regular.

3.3 Discussion

In an effort to select the optimal chimney slope angle for the application, the drying equipment is determined by the level of dryness of the drying temperature in the drying chamber. As covers, such formulated temperature uniformity depends on the smallest feasible temperature difference between the lowest shelf and the top shelf in the drying chamber. From the measurement results, the temperature distribution in the drying chamber is measured at 2 positions on each shelf, namely at point 5 cm from the wall and at point 25 cm or at the center point of the drying chamber. The distribution of the measured temperature occurs in the drying chamber for three slope angles of the chimney, it is found that the chimney with angle 15° can produce a regular temperature distribution, the temperature gradient that occurs is small at the beginning of heating and after stability is achieved the temperature distribution becomes uniform on each shelf in drying chamber.

The distribution of the measured temperature in the drying chamber is at 25 cm from the outer wall of the heating flows with the chimney roof angle 15° that the uniformity of the temperature between the shelf 1–6 with the initial guide is not perforated is achieved after heating 90 min, which is at preheating the gradient temperature between the shelf 1 and 6 reaches 2–3 °C. As well, the slope of the roof angle 15° with temperature gradient reaches 2–3 °C. This small temperature difference is due to the slope of the chimney roof angle which can inhibits hot air from residual drying of the drying chamber. And therefore, the temperature of the residual hot air increases in the room after going through shelf 6. This causes the shelf temperature of 6, 5, 4 gets increase as well.

For the chimney slope of the roof angle 25°, the resistance to hot air flow is smaller than that of the chimneys on angle 15°. This is what becomes the temperature gradient of the roof angle slope of 25°, greater than the chimneys on angle 15°, which is 4–5 °C. The closely identical thing also occured to the chimney slope angle 35°, the resistance of hot air flow is smaller than the chimney slope of 35°. And therefore, the slope of the roof angle is 35° and its temperature gradient reaches 6–7 °C.

4   Conclusion

The smaller the chimney slope of a multi-tiered dryer, the more uniform the temperature distribution in the drying chamber will be. The 15° angle roof chimney is more uniform in temperature distribution than the 25° and 25° roof angle chimney. The temperature distribution at the center position is more uniform among the shelves in the drying chamber. The smaller the chimney slope angle, the greater the chimney outflow drag, therefore it makes the uniformity of temperature distribution in the drying chamber higher.

References

1. Syuhada A, Sary R (2006) Kaji Karakteristik Distrbusi Temperatur dan Perpindahan Panas pada Peralatan Pengeringan Bertingkat. Prosiding SNTTM V, UI, 21–23 November 2006
2. Hasan ME, Syuhada A, Hamdani (2012) Kaji Ekperimental Karakteristik Pengeringan Ikan Bandeng Pada Alat Pengering Berbahan Bakar Gas, vol 1, no 2. http://www.jurnal.unsyiah.ac.id/JTM/
3. Hatta M, Syuhada A, Fuadi Z (2019) Sistem Pengeringan Ikan Dengan Metode Hybrid. J Polim 17(1)
4. Sary R, Syuhada A (2019) Study of fish drying process using multilevel shelves with wood fuel. In: Prosiding SNTTM XVIII. 9–10 Oktober 2019, Ke-5

5. Beigi M (2016) Energy efficiency and moisture diffusivity of apple slices during convective drying. J Food Sci Technol 36(1):145–150. https://doi.org/10.1590/1678-457X.0068
6. State O (2014) Evaluation of a cabinet dryer developed for cassava chips. Int J Appl Agric Apic Res 10(1–2):10–20
7. Abeen R, Aijaz T, Gul K (2015) Drying kinetics of potato using a self-designed cabinet dryer. Cogent Food Agric 1(1):1–5. Food Science & Technology. Research Article. https://doi.org/10.1080/23311932.2015.1036485
8. Setyawan EY, Siagian P, Widodo B, Prihatmi TN, Suwandono P, Siagian L, Gultom T (2018) Performance of turmeric dryer cabinets with Lpg fuel using temperatur control and air speed. IOP Conf Ser Mater Sci Eng 420:012044. https://doi.org/10.1088/1757-899X/420/1/012044
9. Putra RN, Ajiwiguna TA (2017) Influence of air temperatur and velocity for drying process. Procedia Eng 170:516–519. https://doi.org/10.1016/j.proeng.2017.03.082
10. Syuhada A (2000) Heat (Mass) Transfer characteristics in rectangular serpentine channels with a sharp turn. Nagoya University
11. Syuhada A, Hirota M, Fujita H, Araki S, Yanagida Y, Tanaka T (1998) Heat/mass transfer in serpentine flow passage with rectangular cross-section. In: Proceedings of international syposium on advanced energi conversion syistems and related tech, Nagoya, pp 304–305
12. Syuhada A, Hirota M, Fujita H, Araki S, Yanagida Y, Tanaka T (2001) Heat (mass) transfer in serpentine flow passage with regtangular cross-section. Int J Energy Convert M 159–166

The Effect of Hardening on Mechanical Properties of Low Alloy Steel Grinding Media

Husni Usman, Syarizal Fonna, Syifaul Huzni,
Teuku Irvan Ramadhan, and Tommy Octaviantana

Abstract The influence of hardening on mechanical properties of the low alloy steel grinding balls was investigated. The as received low alloy steel samples were austenitized at 950 °C for three different austenitization times and then quenched in oil media. Spectrometer was used to determine the chemical composition of as received alloy steel and optical microscope was used to observe microstructural features. Hardness and Charpy impact tests were performed to measure mechanical properties of the alloy steel samples. The results showed hardness profiles of the as-received steel ball considerably varied from surface to the center. The steel ball exhibited poor hardenability with the thin hardened band at the surface. Compared with the Rockwell hardness of the as received steel samples, the hardness of the as quenched steel at 30 min austenitization time increased while the impact energy decreased. At the higher time, the hardness of as quenched sample decreased, whereas the impact energy remained unchanged. Samples austenitized at 950 °C for 30 min. would obtain a maximum hardening and can be used as a baseline for further tempering process.

1 Introduction

In mining industries, there are two main operating costs related to grinding mills operation, namely energy consumption, mill liner and grinding media wear [1, 2]. Grinding mills represent up to 40% of the direct total operating costs of mineral

H. Usman (✉) · S. Fonna · S. Huzni · T. I. Ramadhan
Laboratory of Materials Engineering, Department of Mechanical and Industrial Engineering,
Faculty of Engineering, Universitas Syiah Kuala, Jl. Syech A. Rauf 7, Banda Aceh 23111,
Aceh, Indonesia
e-mail: husmanphd@unsyiah.ac.id

T. Octaviantana
PT. Nusa Halmahera Minerals, Gosowong Gold Mine, Halmahera Utara,
Maluku Utara, Indonesia

459

processing. The cost of grinding media and liner wear itself is approximately 15–25%.

The design of liner and materials of construction include important factors in the efficiency of the operating cost of the grinding operation, i.e. power consumption per tonne of ore ground and liner life. Due to incorrect liner designs, the grinding media would fall down on the liner rather than on 'the toe of the charge', resulting in less efficient energy utilization, poor grinding, and high maintenance costs [3–5]. Even though liners used in large SAG (semi-autogenous) mills are without both of porosity and casting defect, improper liner design could also make grinding media impact directly on the liner, resulting in impact liner fracture and grinding media damage.

The increased height of fall of such grinding balls in larger SAG mills results in severe impact between the grinding balls and also between the balls and the mill liners. As there are steel balls up to 150 mm in large SAG mills, it is suggested to utilize tougher steels that exhibit good resistance to wear and high energy impact as well. Cost required in replacing new liners in tumbling mills continuously increases. Therefore, despite cost of liners the tendency to use them with the best service life becomes increasingly interesting and attempts to increase liner life are continuously investigated in operating mills.

Different alloys, such as austenitic manganese steels, Ni-Cr white cast iron, high-Cr white iron, and high-carbon Cr–Mo steels are frequently applied to manufacture mill liners for tumbling mills [3]. High impact strength alloys, such as manganese or chrome-molybdenum steels are generally used for liner materials. Alloys with large amounts of chromium and molybdenum have better abrasion-resistance. For low impact, highly-abrasive wear zones, such as end liners, white iron have been in use as a material of choice. High carbon chrome-moly steels are currently considered as the main materials used for SAG mill liners. The alloys produced vary with either different carbon or chrome contents.

The wear rate of grinding media was dependent on a complex interaction of factors including microstructure, hardness ratio of ball to mineral, slurry pH, oxygen potential, and mineral slurry chemistry, such as presence of sulfides [6]. Grinding media hardness affected wet grinding efficiency. Generally, media wear under wet grinding was much higher than that under dry grinding.

The hardening capacity of a steel depends mostly on the carbon content and, somewhat, on the amount of alloying elements and austenite grain size [7]. If the carbon content of martensite increases, its hardness would increase. As a quenched steel contains retained austenite, the hardness of a quenched steel is not the same as the hardness of martensite crytals. The hardness of a steel quenched from austenite temperatures reaches its maximum at a carbon concentration of 0.8–0.9% C and then decreases.

The martensitic stainless steel grinding balls could be heat treated to provide microstructures at their surfaces which ranged from 100% austenite to basically all martensite [8]. Wear rate of grinding ball consisting fully of hard martensite increased under an oxygen environment. The balls that was furnace-cooled and the

ice-water-quenched balls would produce combined microstructures of soft austenite and hard martensite and thus, result in less wear under an oxygen atmosphere.

Changing the austenitization temperature of a high carbon steel could obtain variations in Interlamellar spacing [9]. Hence, hardness and strength increased and followed a Hall-Petch relationship with the interlamellar spacing ($S^{-1/2}$). However, percent elongation and toughness, as well as the wear rate decreased and unfollowed the relationship with the interlamellar spacing of the samples

Moreover, the effects of austempering and martempering processes using salt bath quenching media on wear resistance and impact toughness of Cr–Mo steels was studied and the results were compared with compressed air quench [10]. The samples austempered for 2 h exhibited the best impact toughness and the samples martempered for 2 h showed the highest values of wear resistance. The austempered and martempered specimens quenched in salt bath demonstrated a better combination of wear resistance and toughness than compressed-air quenched specimens.

According to the investigation of the differences in microstructure, hardness, abrasion and impact toughness of steel media from different manufacturing sources, it was observed abrasive wear has a tendency to be dependent on media hardness for grinding media with a chromium content of less than 0.7% and independent of hardness for media with chromium content bigger than 0.75% [11]. Hardness and abrasion wear are slightly interrelated to the chemical composition. Charpy impact energy strongly depends on the carbon content and alloy steels with carbon content more than about 0.2% would produce a brittle fracture at room temperature.

The proper heat treatment needs to be explored to produce low alloy steel grinding media with better mechanical properties and wear resistance. In this work, the effect of hardening on mechanical properties of low alloy steel was investigated.

2 Materials and Methods

The 100.75 mm-diameter grinding ball that was received from a mining company, is shown in Fig. 1. The low alloy steel was melted using induction furnace and cast into sand mold. Because of insufficient information on the heat treatment of the as-received grinding ball, it is believed that after casting it was followed by quenching using compressed air. A wire electro discharge machine (EDM) cutting tool was used to cut the as-received steel grinding media into examination and mechanical testing specimens. Spectrometer was used to determine the chemical composition of the as received alloy steel.

The metallographic samples were prepared according to the standard ASTM E3-01 [12]. The mounted sample was polished by a sequence of 100, 320, 600, 1000, 1200, and 2000-grit silicon carbide papers and was finished by vibratory-polishing using an aqueous suspension of 0.01-μm alumina. The polished specimen was then etched in a solution of 2% nital at room temperature to reveal
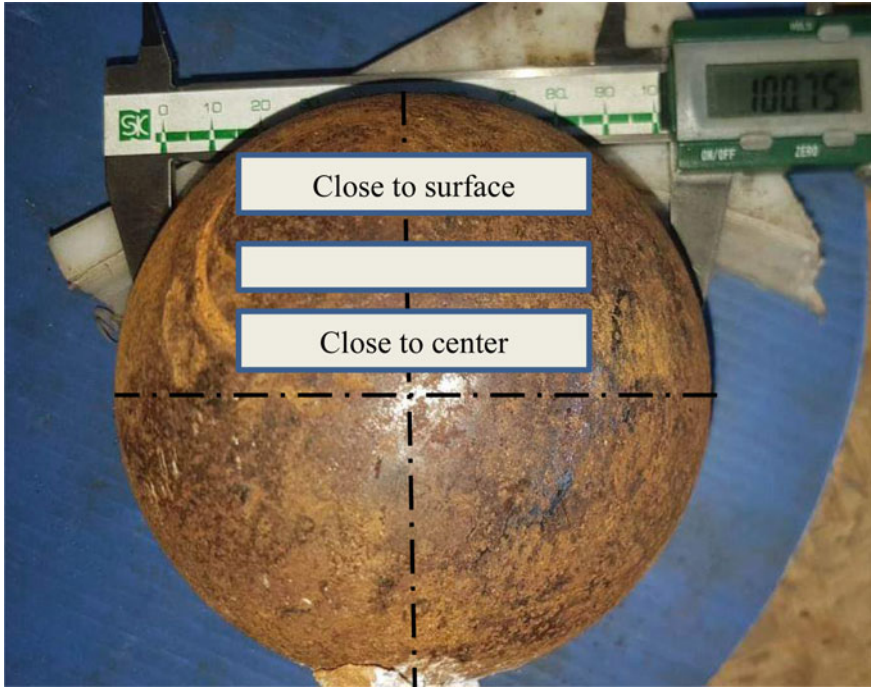
Fig. 1 As received 100.75 mm diameter low alloy steel grinding ball showing the locations where Charpy test samples were cut from using EDM wire cutting

microstructure and grain boundaries. Optical microscope was used to observe microstructural features.

Figure 2 shows the heat treatment cycles of quenching and tempering. The samples were austenitized at 950 °C (the temperature was determined in accordance with the previous research [10]) for the different austenitization times: 30, 60 and 90 min. Then, they were quenched in oil media and were followed by tempering. Both as quenched and as tempered specimens were also prepared for microstructural examination and mechanical tests.

A Rockwell hardness test was performed in accordance with ASTM standard E 18-03 [13] using a Rockwell type hardness tester. A Rockwell C scale with a load of 150 kg that employed a diamond point (Brale indenter) was used. A Vickers micro-hardness test was also carried out to measure traverse hardness as a function of distance from surface of the ball. The results of Vickers hardness (VH) was then converted into Rockwell hardness (HRC) in accordance with ASTM E 140-02 [14]. Impact Charpy test was done in accordance with ASTM E23-02 [15].
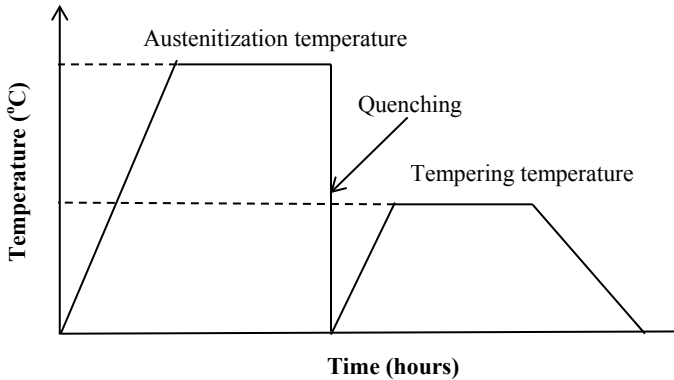
Fig. 2 Heat treatment cycles of quenching and tempering

3 Results and Discussion

3.1 Chemical Analysis

Table 1 gives the chemical composition of as-received low alloy steel that was used in this research. In terms of carbon content, the steel is classified as a high carbon steel (high carbon steels containing 0.55–1.00% C) and includes hypo-eutectoid steel. The addition of alloying elements such as chromium, molybdenum, manganese, as well as high carbon content have been intended to improve hardenability and wear resistance [7]. The sulfur and phosphor contents (impurity elements) are acceptable for the cast alloy steel.

The content of manganese is still acceptable. On the other hand, high content (>2% Mn) would increase tendency to cracking and distortion during quenching. Chromium was added as a medium carbide former that is hard and wear-resistant. It would enhance hardenability, abrasion resistance in high-carbon grades. Molybdenum is obvious carbide former. It can produce secondary hardening during the tempering of quenched steels and also increases the creep strength of low-alloy steels at elevated temperatures.

Table 1 Chemical composition of as received low alloy steel

Element	C	Mn	Si	Cr	Ni	Mo	S	P	Fe
%weight	0.61	0.78	0.28	0.95	0.06	0.01	0.003	0.005	Bal.

3.2 Microstructure

Figure 3 shows optical microscope images examined at near surface, half radius, and in core of the low alloy steel ball. The microstructure at near surface consists of mixed martensite and bainite (Fig. 3a and b). According to the measured hardness as shown in Fig. 5, the steel ball was quenched but with lowered hardenability (ability of the steel to form martensite across the section of the steel media by quenching).
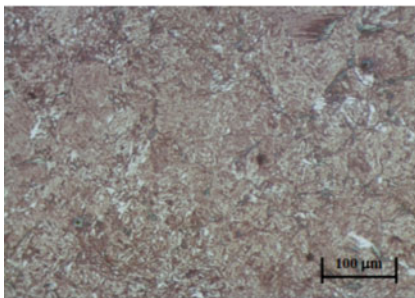
(a) near surface of the ball (200x)   (b) near surface of the ball (700x)
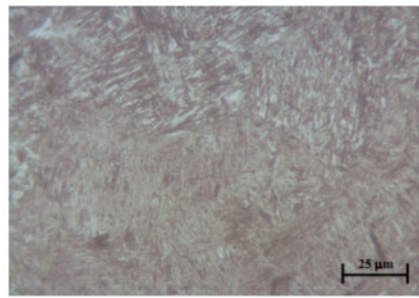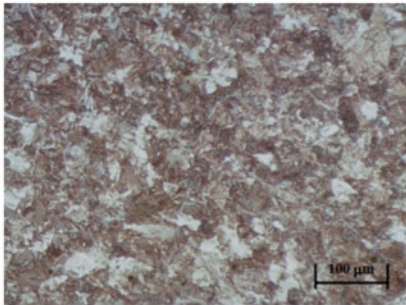
(c) half radius of the ball (200x)   (d) half radius of the ball (700x)
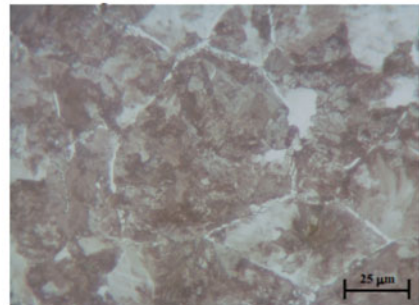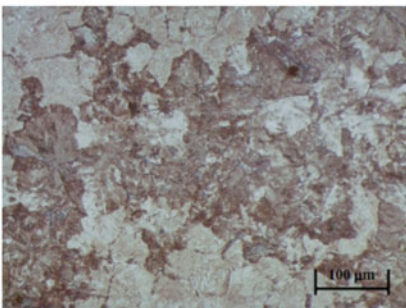
(e) in core of the ball (200x)   (f) in core of the ball (700x)
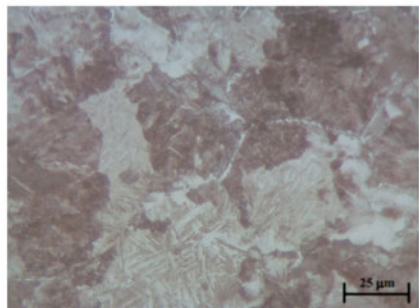
Fig. 3 Optical microscope images of as-received low alloy steel ball examined at near surface, half radius, and in core of the steel ball. Etchant: 2% nital

　　The microstructure in the half radius of the steel ball shows some martensite/ bainite along with pearlite (Fig. 3c and d). The precipitation of pro-eutectoid ferrite at grain boundaries has probably occurred during hardening (Fig. 3d). As shown in Fig. 3e and f, pearlite with ferrite along prior austenite grain boundaries is observed across most of remaining ball.

　　The optical microscope images of as quenched samples after being austenitized at 950 °C for the austenitization times of 30, 60, and 90 min. are shown in Fig. 4. The microstructures of all the samples are composed of martensite with different orientations and small inclusions of irregular shapes. The brighter areas found in Fig. 4 could be retained austenite.

3.3　Mechanical Properties of Low Alloy Steel

Table 2 provides the results of Rockwell hardness measured at near surface of the as received low alloy steel. Hardness profiles of the steel ball, which was measured from the surface to the center of the steel ball, are presented in Fig. 5 as well.

(a) 30 min.

(b) 60 min.

(c) 90 min.
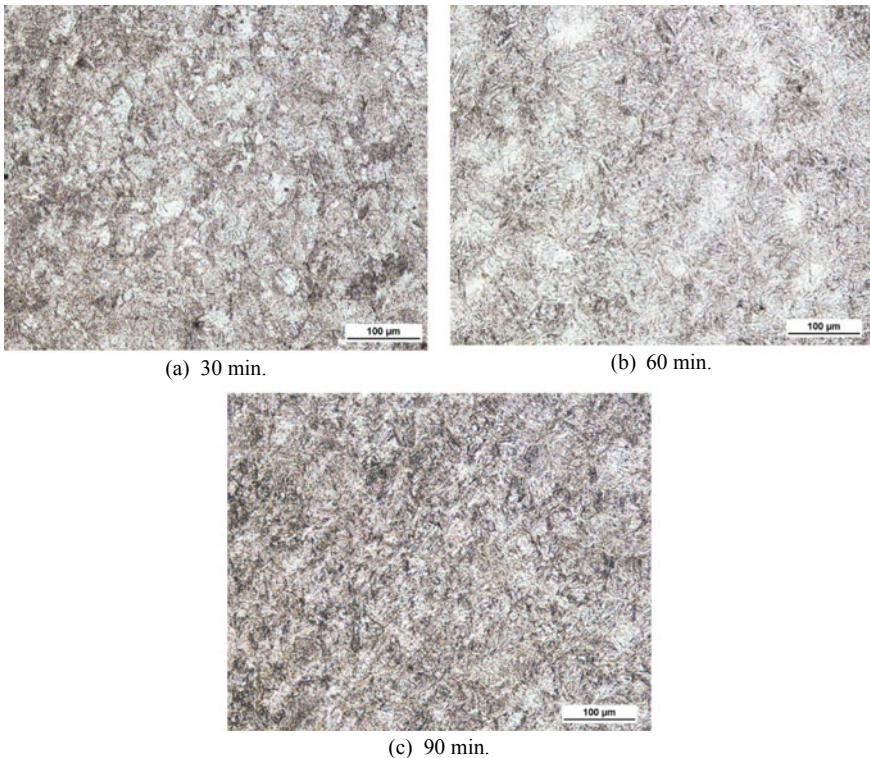
Fig. 4 Optical microscope images of as-quenched low alloy steel ball after austenitized at 950 °C for the different holding times and oil-quenched. Etchant: 3% nital

Table 2 Rockwell hardness at near surface of the as received low alloy steel

Testing	1st	2nd	3rd	4th	5th	Average
HRC	54.0	53.9	54.2	52.8	54.1	54.0
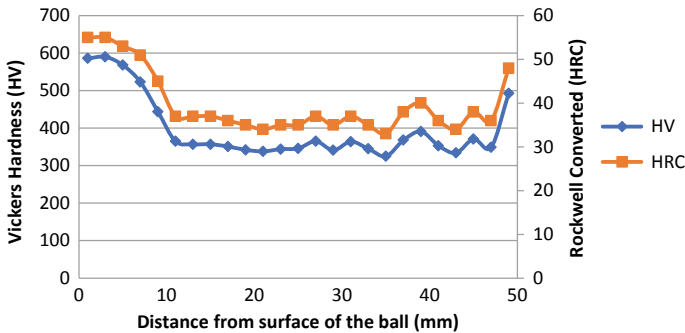
Fig. 5 Hardness profiles of as received steel ball as a function of distance from surface of the ball

Compared with the average Rockwell surface hardness, hardness profiles considerably vary from surface to the center. Hardness profiles of the steel ball reflected the microstructure with only about 5 mm thick showing Vickers hardness near 600 HV (55 HRC). Most of the cross section of steel ball had a Vickers hardness below 400 HV (35 HRC). This indicates that heat treatment was improperly done and thus, the steel ball exhibited poor hardenability with the thin hardened band at the surface. Additionally, the high carbon content of steel ball could produce low hardenability during heat treatment [16, 17].

The results of Charpy impact energy or the impact toughness of the as received steel ball based on the specimen location (shown in Fig. 1) within the steel ball are shown in Fig. 6. The impact energy of all the tests is independent of location. The fracture surfaces of the tested Charpy specimens clearly displayed brittle fracture. Moreover, according to the brittle fracture criteria, the impact energy of the steel ball is below the brittle fracture impact energy of 20 J. Therefore, the fracture mode of the steel ball was found to show brittle fracture.

The as-received steel samples were austenitized at 950 °C for three different austenitization times and then oil quenched. The average Rockwell hardness and impact energy of the as-quenched samples are shown in Fig. 7. Compared to the as received steel, at 30 min austenitization time the Rockwell hardness of the as quenched steel increases while the impact energy decreases. If holding time at quenching temperature is increased to 60 min, the hardness and impact energy of the as quenched steel decreases. At a higher time of 90 min, the Rockwell hardness of as quenched sample is lower than that of the as received one, whereas the average impact energy remains unchanged.
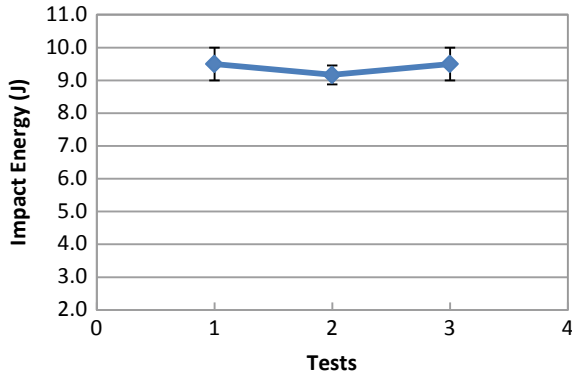
Fig. 6 The impact energy of the as-receieved low alloy steel balls based on specimen location within the steel media
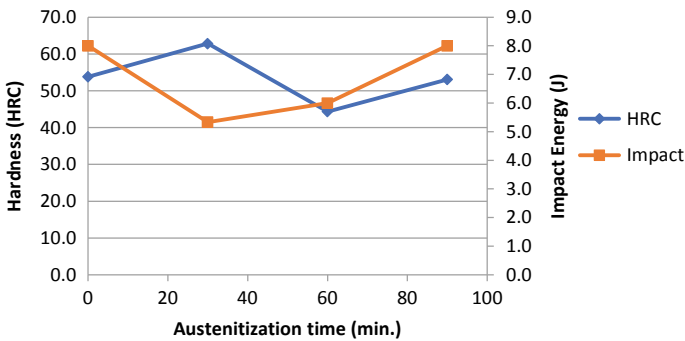
Fig. 7 Rockwell hardness and impact energy of the as-quenched samples after being austenitized at 950 °C for different austenitization times

It is generally accepted that hardness has an inverse relationship with impact toughness. If hardness of the steel decreases, impact energy would increase. The effects of the heat treatment cycles of quenching and tempering on microstructure and mechanical properties will be performed on further research. It is expected that the heat treatment of hardening and followed by tempering would lead to a better combination of impact energy and hardness.

4   Conclusion

The microstructure of the as received grinding ball at near surface composed of mixed martensite and bainite. Pearlite with ferrite along prior austenite grain boundaries was observed across most of remaining ball. The microstructures of all

the as quenched samples are typically composed of martensite with many different orientations.

Hardness profiles of the as-received steel ball considerably varied from surface to the center. Hardness profiles of the steel ball reflected the microstructure with only about 8 mm shell showing Vickers hardness near 600 HV. Most of the cross section of steel ball had Vickers hardness below 400 HV. The steel ball exhibited poor hardenability with the thin hardened band at the surface.

Compared with the Rockwell hardness of the as received steel samples, the hardness of the as quenched steel at 30 min. holding time increased while the impact energy decreased. At higher holding time, the hardness of as quenched sample decreased, whereas the impact energy remained unchanged. It can be concluded that samples austenitized at 950 °C for 30 min. would obtain a maximum hardening and can be used as a baseline for further tempering process.

References

1. Curry JA, Ismay MJL, Jameson GJ (2014) Mine operating costs and the potential impacts of energy and grinding. Miner Eng 56:70–80
2. Wills BA, Finch JA (2016) Wills' mineral processing technology: an introduction to the practical aspects of ore treatment and mineral recovery. Elsevier Ltd., Oxford
3. Powell M, Smit I, Radziszewski P, Cleary P, Rattray B, Eriksson K, Schaeffer L (2006) Selection and design of Mill liners. In: Kawatra SK (ed) Advances in comminution. SME, Englewood, Colorado, pp 331–376
4. Usman H, Taylor P, Spiller DE (2017) The effects of lifter configurations and mill speeds on the mill power draw and performance. In: AIP Conference Proceedings, vol 1805, no 050001
5. Usman H, Fonna S, Thalib S (2020) A review on current mill liner design and performance. In: IOP conference series materials science and engineering, vol 931, no 012016
6. Moore JJ, Perez R, Gangopadhyay AK, Eggert JF (1988) Factors affecting wear in tumbling mills: influence of composition and microstructure. Int J Miner Process 22:313–343
7. Sverdlin AV, Ness AR (2007) Effects of alloying elements on the heat treatment of steel. In: Totten GE (ed) Steel heat treatment handbook. Taylor & Francis Group, USA, pp 166–211
8. Jang JW, Iwasaki I (1988) Effect of martensite and austenite on grinding media wear. Wear 122:285–299
9. Modi OP, Mondal DP, Prasad BK, Singh M, Khaira HK (2003) Abrasive wear behaviour of a high carbon steel: effects of microstructure and experimental parameters and correlation with mechanical properties. Mater Sci Eng A 343:235–242
10. Shaeri MH, Saghafian H, Shabestari SG (2012) Effect of heat treatment on microstructure and mechanical properties of Cr–Mo steels (FMU-226) used in mills liner. Mater Des 34:192–200
11. Sabih A, Radziszewski P, Mullany I (2017) Investigating grinding media differences in microstructure, hardness, abrasion and fracture toughness. Miner Eng 103–104:43–53
12. ASTM E3-01: Standard practice for preparation of metallographic specimens. American Standard for Testing Materials, West Conshoocken, PA, pp 1–8, 03.01 (2001)

13. ASTM E18-03 (2003) Standard test methods for Rockwell hardness and Rockwell superficial hardness of metallic materials. American Standard for Testing Materials, West Conshoocken, PA, pp 116–129, 03.01 (2003)
14. ASTM 140-02: Standard hardness conversion tables for metals relationship among brinell hardness, vickers hardness, rockwell hardness, superficial hardness, knoop hardness, and scleroscope hardness. American Standard for Testing Materials, West Conshoocken, PA, 03.01 (2002)
15. ASTM E23-02a: Standard test methods for notched bar impact testing of metallic materials. PA: American Standard for Testing Materials, West Conshoocken, 3.01 (2003)
16. Elwazri AM, Wanjara P, Yuea S (2005) The effect of microstructural characteristics of pearlite on the mechanical properties of hypereutectoid steel. Mater Sci Eng A 404:91–98
17. Eshghian R, Abbasi M (2017) Wear and failure analysis of semi-autogenous grinding mill liners. J Fail Anal Prev 17:340–348

Fly Ash Utilization in Rigid Pavement Construction

F. M. Suryani, Samsul Rizal, Abdullah, and M. Isya

Abstract Fly ash is a waste byproduct from burning coal in electric power generating plants. The tendency of abundant coal waste not optimally utilized leads to a serious environmental problem in the future. One of the management that can be applied is utilizing this waste as civil engineering building materials. Previous studies have recommended the use of residual materials, especially fly ash, as a substitute in the concrete mixture. Based on this background, we evaluated the effectivity of fly ash substitution in lightweight concrete as a material in rigid pavement construction based on the compressive strength requirements at 28 days of age. This study used a mixture of Portland cement type I and foam to produce lightweight concrete with a specific gravity of 1.2. As much as 15% of the total mixture will be substituted using fly ash obtained from a power plant. The results showed that the lightweight concrete produced from this mixture had a compressive strength of 139 kg/cm^2. Accordingly, in addition to be a great contribution in overcoming these coal-waste-related environmental concerns and a cost-effective method, 15% fly ash substitution in concrete mixture can be taken into consideration in obtaining lightweight concrete that fulfils the general specification criteria for the cement-treated subbase (CTSB).

F. M. Suryani (✉) · Abdullah · M. Isya
Civil Engineering Department, Engineering Faculty, Universitas Syiah Kuala, Darussalam, Banda Aceh 23111, Indonesia
e-mail: fitrika_mitasuryani@unsyiah.ac.id

S. Rizal
Mechanical Engineering Department, Engineering Faculty, Universitas Syiah Kuala, Darussalam, Banda Aceh 23111, Indonesia

1 Introduction

The road is a very vital infrastructure of moving life in various aspects. Roads can be made from a variety of forming materials, including flexible and rigid pavement. In order for the pavement construction to function properly, the roads must be managed in a patterned and structured manner. This process includes activities beginning with the planning stage by considering internal and external factors and influences such as the ability of the materials and vehicles that will use them, including natural factors [1].

At the time of construction, the focus between planning and implementation needs to be the focus so that road strength and reliability can be achieved. Once it is opened to traffic and roads are starting to function, management needs to be directed towards performance monitoring activities so that the service life of the plan can be achieved and roads can survive more reliably and have longer construction service times. Pavement performance is a function of its relative ability to serve the amount of traffic flow in a certain period of time according to the design age. For maximum pavement performance, the foundation support under the concrete slab must be strong and uniform [1].

One of the important variables in road pavement design is the material that forms the layers of the pavement components [2]. Rigid pavement requires higher costs than flexible pavement [3]. Initial cost of rigid pavement is reduced by replacing cement by fly ash at some percentage or by using other alternatives [4]. Fly ash is a waste produced of the coal combustion processed for power generation. Therefore, this study aimed to assess the effect of fly ash material substitution in lightweight concrete mixtures.

2 Literature Review

2.1 Rigid Pavement

Rigid pavement structures, also called cement concrete pavements, can be implemented in conditions of poor subgrade bearing capacity (small, such as 2% in size) or relatively large traffic loads [5] (Fig. 1).
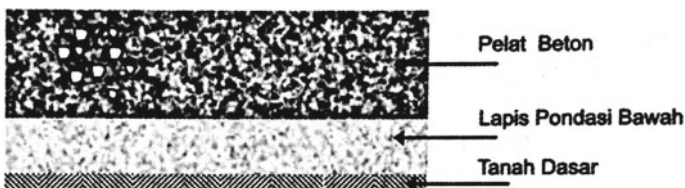
Fig. 1 Rigid pavement structures [5]

2.2 Rigid Pavement with Cement-Treated Subbase (CTSB)

In rigid pavement, one of the foundation layers is the binder sub-base, which is known as the cement-treated subbase (CTSB). One of the CTSB is the stabilization of the grained material with the binder grade according to the design, to ensure the strength of the mixture and its resistance to erosion. The binder can be cement, lime, fly ash or crushed slag [5].

The planning of the CTSB mixture must provide a comparison of the aggregate composition, with several levels of cement and optimum moisture content that gives results in accordance with the expected concrete quality [5]. Requirements for the unconfined compressive strength of Class B Cement Aggregate Foundation (CTSB) in the age of 7 (seven) days is 35–45 kg/cm^2 [6]. Meanwhile, for mixed planning, the minimum mix strength at 28 days should not be less than 75 kg/cm^2 [5].

2.3 CTSB Element

The CTSB consists of several elements, namely:

- Cement. The cement used for CTSB is ordinary Portland Cement in accordance with the requirements of SII 0013-77 "Cement Portland" or AASHTO M 85 (Portland Cement type I).
- Water. Water used for mixing, treating or other uses, must be free from oil, acid salts, alkalis, sugars, herbs or other substances that harm the final product.
- Aggregates. The aggregate for CTSB must be free of clays, dirt, organic elements or other harmful elements. The aggregate requirements to be used for CTSB must meet the requirements in Table 1 [5].

2.4 Lightweight Concrete

Based on SNI 03-3449-1994, structural lightweight concrete is a concrete that uses lightweight aggregate, or a mixture of lightweight-coarse aggregate and natural sand as a substitute for lightweight fine aggregate, and meets the requirements for compressive and flexural strength with the maximum weight of 1850 kg/m^3.

Table 1 The lists of specimen manufacture for each test

Tests	Specimen	Fly ash percentage (%)	Concrete age (days)	Quantity
Compressive strength	Cylinder 15 cm × 30 cm	15	28	3
Total				3

The flexural strength of air-dry lightweight concrete ranges from 70 to 90%, compared to the general concrete of the same compressive strength. Nevertheless, if being exposed continuously to a certain level of moisture, these two types would have the same level of flexural strength [7].

The development of lightweight concrete at Universitas Syiah Kuala (Unsyiah) began in 2006. Unsyiah has been able to produce lightweight concrete with structural quality (compressive strength value >17 mPa). Various qualified products using lightweight concrete as a material have been invented [8]. Lightweight concrete is classified into low density concrete (content weight less than 50 pcf (800 kg/m^3)), medium strength concrete (content weight ranging from 60 to 80 pcf (960–1360 kg/m^3) and compressive strength between 1000 and 2500 psi (6.89–17.23 MPa)) and structural concrete (content weight ranging from 90 to 120 pcf (1440–1920 kg/m^3) and equal compressive strength to the general concrete) [9].

In general, concrete is obtained from a mixture of Portland cement, water and aggregate, while for lightweight concrete, the constituent materials depend on its type. Lightweight concrete is a mixture of cement, water, air, and foam produced from foam agents. Production of lightweight concretes is generally done by adding air bubbles into the concrete mixture or by using lightweight aggregates, such as clay and pumice [10].

2.5   Fly Ash

Aggregate, based on the processing technique, is divided into natural aggregates, first-processed aggregates and artificial aggregates. Artificial aggregate is a mineral filler (particles with a size less than 0.075 mm) obtained from the by-products of cement factories and stone crushing machines. Fly ash is a material that has the characteristics of small and fine grains with a grayish color and can be obtained from the residue of coal burning [11]. Fly ash with good quality can increase the strength of concrete in the long term [12]. Fly ash has very fine grains, which pass the sieve No. 325 (45 millimicrons) 5–7% in specific gravity between 2.15 and 2.8 g/cm^3 [11].

According to the ASTM C 618-05, fly ash is classified into:

- Class C, with more than 10% CaO component, is produced from burning coal with a carbon content of ±60%.
- Class F, with less than 10% CaO component, is produced from burning anthracite coal at a temperature of 1560 °C
- Class N, namely natural pozolan or combustion products classified into diatomic soil, opaline chertz and shales, tuff and volcanic ash which are processed with or without burning [13].

2.6 Compressive and Flexural Strength

Compressive strength illustrates the concrete quality. According to SNI 03-1974-1990, concrete compressive strength is the amount of load per unit area that causes the concrete specimens to collapse when loaded with a certain compressive force generated by a compressive testing machine [14]. Flexural strength is the ability of concrete placed on two positions to withstand the force given in the direction perpendicular to the axis of the specimen until collapsed which is stated in Mega Pascal (MPa) force per unit area. The concrete flexural strength affects its ability to overcome the initial cracks before being loaded [15].

3 Materials and Methods

3.1 Materials

The specimens used in this study was made from a mixture of lightweight concrete and fly ash material. The percentage of fly ash in the mixture was 15%. The cement used was Portland cement type I and the fly ash was obtained from a power station. The fly ash was preheated and sieved through No.200 sieve before the density was measured. The water-cement ratio was 0.5 and the specific gravity was 1.2. The manufacture of cylindrical specimens with a diameter of 15 cm and a height of 30 cm were intended for compressive strength test. Other equipment used included press loading machine with 100 Tf capacity, balance, filter, concrete mixer, compressive strength testing device and foam generator (Figs. 2, 3 and 4).

Fig. 2 Type I Portland cement

Fig. 3 Fly ash

Fig. 4 Fly ash in the power station

3.2 Methods

3.2.1 Specimen Manufacture and Maintenance

The specimen manufacture was carried out at the Construction and Building Materials Laboratory of the Civil Engineering Department, Unsyiah in the following procedure.

- Preparation and measure of the materials according to the predetermined proportion of the mixture.
- Substitution of fly ash material in the amount of 15% of water and cement mixture.
- Addition of the mixture into the foam produced by the generator in the concrete mixer until well blended.
- Adjustment of the concrete mixture on the mold and formation of the concrete cast.
- Treatment of the concrete was carried out after hardened.
- Removal of the concrete cast from the mold to be put under immersion.

3.2.2 Compressive Strength Test

The specimens were tested at the age of 28 days of concrete after immersion. Before doing the test, it was confirmed that the specimens were dried, weighed and measured. The test was carried out by giving loads until the specimens were destroyed.

4 Results

The compression strength value obtained was as follows.

Table 2 shows the average value of the compressive strength was 139 kg/cm^2. Based on the literature, for mixed planning, the minimum mix strength at 28 days should not be less than 75 kg/cm^2 [5]. In this study, the specific gravity of the cement used was 1.2. The results indicate that the quality of lightweight concrete with a substitution of fly ash at 15% percentage at the age of 28 days has fulfilled the compressive strength requirements. In normal and lightweight concrete, higher concrete age increases the concrete quality [16].

The result was considered noteworthy because the specific gravity of lightweight concrete tested was very small compared to that of normal concrete which reaches 2.4. In addition to this, 15% of the mixture consists of fly ash material, a byproduct that is not the constituent materials of concrete. In spite of this substitution, the

Table 2 The compression strength values

Specimen	Compression strength		
	(N/mm^2)	(kg/cm^2)	
		Unit	Average*
1	13.33	135.98	139 $\pm$ 3.45
2	13.55	138.26	
3	13.99	142.76	

*The data is presented as mean $\pm$ SD

compressive strength of the lightweight concrete produced still fulfilled the requirements for the unconfined compressive strength of cement-treated subbase (CTSB) in the age of 28 days. Therefore, it revealed that the method of utilizing fly ash as a substitution in the concrete mixture was applicable. This practice also indicated a potential way in reducing the amount of concrete usage, thus cutting down the initial cost needed in rigid pavement construction.

5   Conclusions

In summary, this study suggests that fly ash substitution in 15% of the lightweight concrete can be taken into consideration in the purpose of obtaining lightweight concrete that fulfils the general specification criteria for the cement-treated subbase (CTSB). Additionally, this method also leads to a significantly lower cost required in road construction. Furthermore, utilizing fly ash as a new material in engineering field is influential in the management of coal-waste-related environmental problems. We propose that further research is required to identify the effect of substituting fly ash in higher specific gravity the lightweight concrete mixture in order to improve the quality as well as cost-effectiveness of the concrete produced.

References

1. Agah HR, Rarasati AD (2010) Pemeliharaan dan Perbaikan Konstruksi Jalan Lentur. Yayasan Badan Penerbit Pekerjaan Umum PT. Mediatama Saptakarya, Jakarta
2. Hardiyatmo HC (2015) Pemeliharaan Jalan Raya. Gadjah Mada University Press, Yogyakarta
3. Direktorat Jenderal Bina Marga (2017) Manual Desain Perkerasan Jalan. Direktorat Jenderal Bina Marga, Jakarta
4. Mohod M, Kadam K (2016) Comparative study on rigid and flexible pavement: a review. IOSR J Mech Civ Eng 13:84–88
5. Saodang H (2005) Konstruksi Jalan Raya: Perancangan Perkerasan Jalan Raya. Penerbit Nova, Bandung
6. Direktorat Jenderal Bina Marga (2018) Spesifikasi Umum 2018 untuk Pekerjaan Konstruksi Jalan dan Jembatan. Direktorat Jenderal Bina Marga, Jakarta
7. Direktorat Pekerjaan Umum (1994) Tata Cara Rencana Pembuatan Campuran Beton Ringan dengan Agregat Ringan (SNI 03-3449-1994). Direktorat Pekerjaan Umum, Bandung
8. Abdullah B, Fonna S (2007) Pengembangan Beton Ringan Mutu Tinggi dengan dan Tanpa Serat. Unsyiah, Banda Aceh
9. Winter G, Nilson A (1993) Perencanaan Beton Bertulang. PT. Pradnya Paramita, Jakarta
10. Gunawan P, Prayitno S, Warsino W (2015) Pengaruh Penambahan Serat Polyethylene pada Beton Ringan dengan Teknologi Gas terhadap Kuat Tekan, Kuat Tarik Belah dan Modulus Elastisitas. e-Jurnal Matriks Tek. Sipil 679–87
11. Wardani S, Prabandiyani R (2008) Pemanfaatan Limbah Batubara (Fly Ash) untuk Stabilisasi Tanah Maupun Keperluan Teknik Sipil Lainnya dalam Mengurangi Pencemaran Lingkungan. J Fak Tek Univ, Diponegoro, p 1
12. Nugraha P, Antoni (2008) Teknologi Beton. Penerbit Andi, Yogyakarta

13. ASTM International (2005) ASTM C 618–05: Standard Specification for Coal Fly Ash and Raw or Calcined Natural Pozzolan for Use in Concrete. ASTM, West Conshohocken
14. Badan Standarisasi Nasional (1990) Metode Pengujian Kuat Tekan Beton (SNI 03-1974-1990). Badan Standarisasi Nasional, Jakarta
15. Badan Standarisasi Nasional (1997) Metode Pengujian Kuat Lentur Normal dengan Dua Titik Pembebanan (SNI 03-4431-1997). Badan Standarisasi Nasional, Jakarta
16. Badan Standarisasi Nasional (2002) Metode Pengujian untuk Mengukur Nilai Kuat Tekan Beton pada Umur Awal dan Memproyeksikan Kekuatan pada Umur Berikutnya (SNI 03-6805-2002). Badan Standarisasi Nasional, Jakarta

Feature Variations on the Cartesian 3D Print Machine Using Vibration and Sound Signal Readings

M. Dirhamsyah, Hammam Riza, Fenda Dwi Ariefianto, Udink Aulia, and Mohd. Zaki Bin Nuawi

Abstract Condition monitoring is analyzing the condition of a machine with the running process and to find out indications of failure to develop during the running process of the machine by several means of monitoring. In this study, using vibration and sound signals to a Cartesian 3D Print machine. The study was conducted by testing 5 (five) samples of adaptive manufacturing process feature movement. Obtained in the form of results by processing signal analysis with wavelets and Fast Fourier Transform (FFT). In the readout the vibration signal is more identifiable than the sound signal and it is easy to group the signal from the adaptive manufacturing process movement. In this monitoring, cylindrical features can be easily recognized based on the changing characteristics of every 12000 rows of data. Meanwhile, various prismatic features have the same characteristics and still have not received condition monitoring analysis.

Keywords Condition monitoring · 3D print · Vibration and sound

1 Introduction

Currently, the use of 3D printing machines has been widely used in the manufacturing world. 3D printers (three-dimensional) were first introduced to the Indonesian market in 2013. 3D printing technology that has become widespread is known as Additive Manufacturing (AM) and Fused Deposition Modeling (FDM) or also known as Fused Filament Fabrication (FFF) [1]. As the development of

M. Dirhamsyah (✉) · F. D. Ariefianto · U. Aulia
Faculty of Engineering, Universitas Syiah Kuala, Banda Aceh, Indonesia
e-mail: mdirhamsyah@unsyiah.ac.id

H. Riza
Agency for the Assessment and Application of Technology, Central Jakarta, Indonesia

Mohd.Z. B. Nuawi
Faculty of Engineering and Built Environment, Universiti Kebangsaan Malaysia,
Bangi, Malaysia

Adaptive Manufacturing grows, a number of challenges continue to occur along with its development, especially in the field of Non-Destructive Evaluation/ Non-Destructive Testing (NDE/NDT) techniques for monitoring and measuring the lifetime of Adaptive Manufacturing equipment [2].

During the 3D Print machine process, the addition of the first layer sometimes gets a failure where the ink or 3D print filament does not come out through the nozzle which has many suspicions of nozzle failure or blockage, such as the heatbed is too close to the nozzle, has residual filament in the nozzle which is temperature-treated different, clogs in the tubes, print speed and others that require condition monitoring activities.

Condition monitoring is monitoring the condition of the engine to see changes that occur during the engine running so that it knows indications of developing failure. 3D printing machines have limited condition monitoring techniques, such as minimizing nozzle clogging failures [3]. To obtain high quality manufacturing results, direct product monitoring conditions are important as maintenance of FFF machines under normal conditions [4].

Meanwhile, in Samin's research [5] Fast Fourier Transform (FFT) was carried out to display the latent signal in the time domain in the machining process. Wavelet transform has been used successfully for strain signal editing [6] and previously Abdullah [7] succeeded in filtering and shortening the testing time for strain signal. In this 3D Printing Condition Monitoring study, using *FFT* signals and wavelet morlet to apply the extraction algorithm from continuous signal sources of vibration and sound.

So from this background some problems were formulated, namely in the form of monitoring the condition of the features and the type of movement on the 3D Printer machine, although the limitation of the problem was using Polylactid Acid (PLA) filament ink. The aim is to produce signal characteristics based on time domain and frequency domain and the benefits of getting readings from vibration and sound signals so that they can obtain a data base for signal grouping.

2   Research Methods

The systematics used in this research is in the form of having 5 features with three trials. This flow chart can be seen in Fig. 1.

2.1   Specimen Design

In the data analysis process, the test material preparation process is carried out using the Autodesk Inventor application to create a 3D STL file with dimensions in millimeters as follows (Fig. 2 and 3):
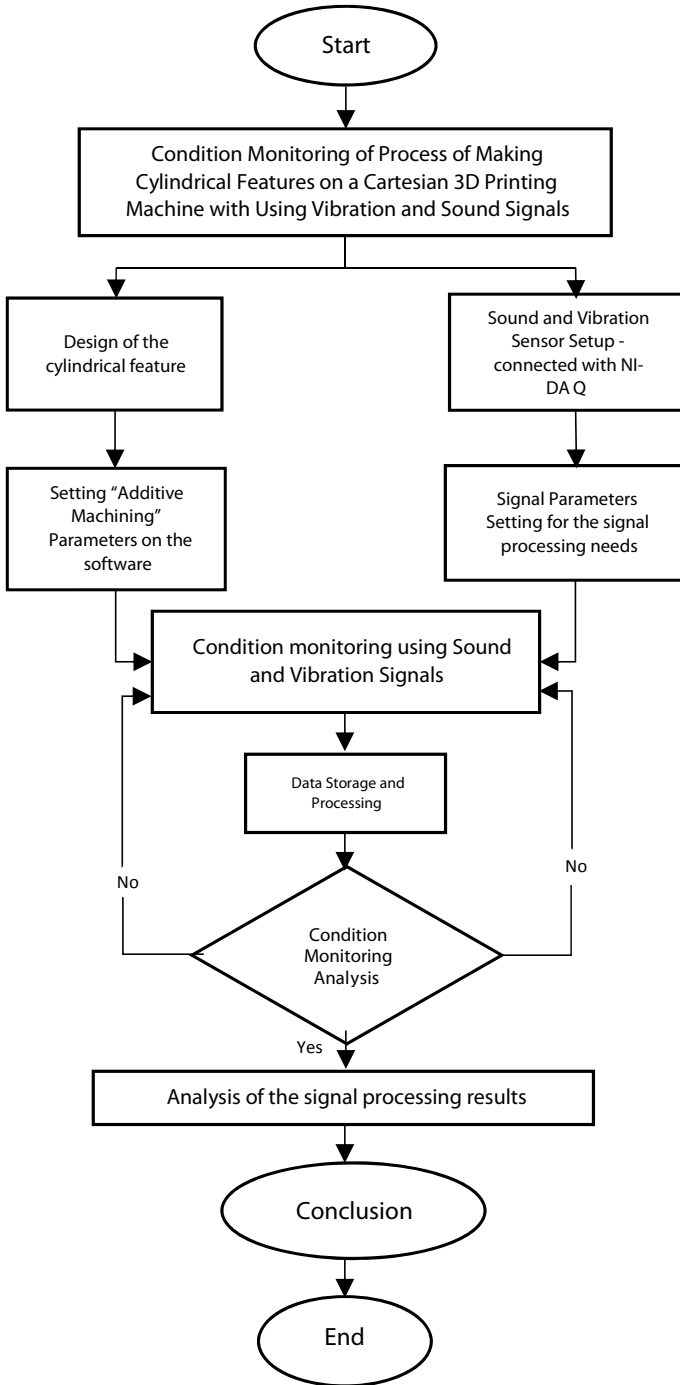
Fig. 1 Research flow for the condition monitoring of process of making cylindrical features on a Cartesian 3D printing machine with using vibration and sound signals

Fig. 2 The cylindrical
feature design
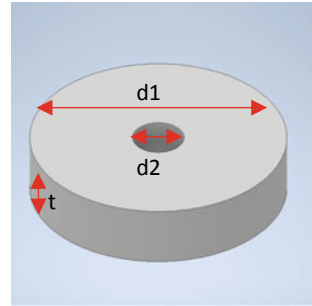
Fig. 3 The prismatic
feature design
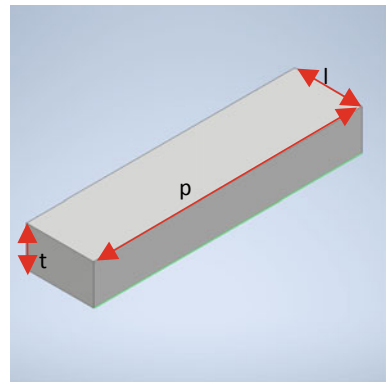
1. *Feature* cylindris: $d1 = 2.5$, $d2 = 12.5$, and $t = 3$
2. *Feature* prismatic: $p = 20$, $l = 5$, and $t = 3$.

2.2 Research Testing Tool Settings

The features state monitoring test uses the Creality CP-01 Cartesian 3D print engine
(Fig. 4).

Process signal analysis using sensors in the form of vibration and sound taken
with Ni DAQ 9254 4 Channel, microphone Bruel & Kjaer Type 2671
No. 2373246 and an accelerometer and a computer for the analysis process carried
out in the Reverberation Chamber at the Engineering Faculty, Universiti
Kebangsaan Malaysia with the equipment setup as shown in Fig. 5.

Fig. 4 Printer creality CP-01 [8]

2.3   3D Print Operation Parameters

The setting stage for machining parameters in the Ultimaker Cura application is carried out with the specifications in Tables 1, 2 and 3.

2.4   Data Analysis

Data analysis was performed using MATLAB and using pseudo-code to obtain time domain, frequency domain, and wavelet morlet (Table 4).

Variations of 5 (five) features (cylindrical, horizontal, vertical, diagonal \ and diagonal /) obtained raw data of ±8,500,000 (eight million five hundred thousand) sample data within 6 min then cut a total of 7,000,000 (seven million) sample data (Zo) with a time of 280 s. While the observation cluster is carried out with a total of 1,000,000 (one million) sample data (Z1). In the grouping of zone 1, there are 7 observation zones. Each zone will be analyzed the frequency and wavelet morlet with the pseudo-code in Table 5 as follows.

3   Results and Discussion

The results obtained from the 5 features of the reading of vibration and sound signals in the first sample with Zo are as follows (Figs. 6 and 7).

Fig. 5 Experimental setup
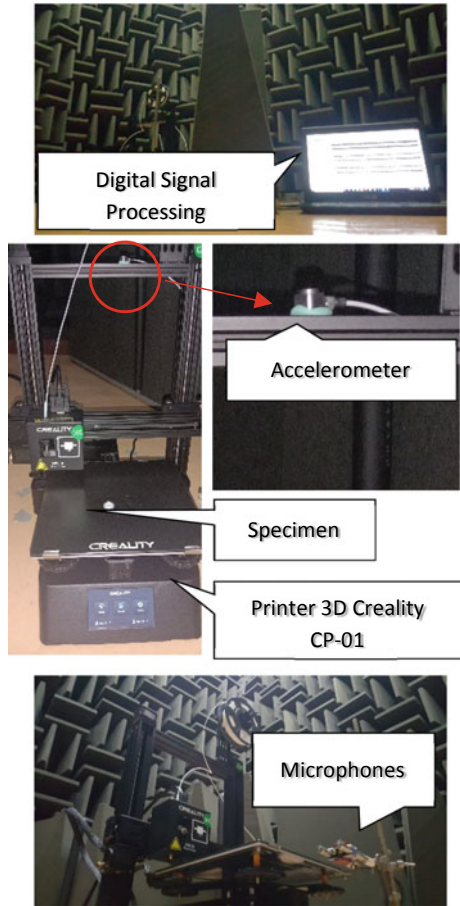
Table 1 3D print operation parameters 3D-print as machining parameters

Type	Value
Material	PLA
Extruder temperature	210 °C
Nozzle diameter	0.4 mm
Layer thickness	0.2 mm
Density	20%
Filling pattern	Grid
Filling feed rate	30 mm/s
Speed travel	100 mm/s

Source Shenzhen eSun Industrial Co., LTD, product manual global 3D printing resources platform, 3D printing material

Table 2 Specification printer cartesian [8]

Model	CP-01
Type	3D Laser, CNC, FDM
Material (frames)	Aluminium extrusion
Platform board	Aluminium alloy, Aluminium base
Nozzle diameter	0.4 mm
Nozzle temperature	0–260 °C
Product forming size	200 * 200 * 200 mm
Layer thickness	0.1–0.4 mm
LCD screen	Yes
Print speed	10–80 mm/s
Bed temperature	21–100 °C

Source Shenzhen eSun Industrial Co., LTD, product manual global 3D printing resources platform, 3D printing material

Table 3 Specification of filamen PLA [8]

Filament diameter	1.75 mm
Print temperature	190–210 °C
Bed temperature	No Heat (60–80)
Density	1.25 g/cm^3
Heat distortion temp	56 °C, 0.45 Mpa
Melt flow index (g/10 min)	5 (190 °C/2.16 kg)
Tensile strength	65 MPa
Elongation at break	8%
Flexural strength	97 MPa
Flexural modulus	3600 MPa
IZOD impact strength	4 kJ/m^2

Source Shenzhen eSun Industrial Co., LTD, product manual global 3D printing resources platform, 3D printing material

Obtained in the form of movement of G28 in vibration and sound signals by cutting 500,000 (five hundred thousand) data as an example result in signal grouping (Figs. 8 and 9).

In the testing, it was found that the additive motion characteristics of cylindrical products have signal characteristics that are significantly different from the filling signal for prismatic products which can be graphically seen in Figs. 10, 11, 12, 13, and 14.

The result of signal processing obtained in this test is that there is a significant difference in signal features that are significant from the horizontal cylindrical and prismatic features. The horizontal prismatic features appear to be the same due to the uniformity of filler filling at 135º and 45º.

Table 4 Product of 3D Print results and every sample of sound and vibration data collection

Printer cartesian CP-01			
Feature	Sample		
	I	II	III
(a) Cylindris			
(b) Horizontal			
(c) Vertikal			
(d) Diagonal \			
(e) Diagonal /			

Table 5 Pseudo-code data raw *FFT* and wavelet morlet

```
load filename.txt
x= filename;
N=length(x);
fs=25600;
T=1/fs; ts=N/fs;
t=[ts/N:ts/N:ts];
% FFT
k=[0:N-1]; f_k =(fft(x)); f_k = abs (f_k);
w=k*(1/ts);
% Pseudo-code energy
x= filename; N=length(x);
fs=25600;
T=1/fs; ts=N/fs; t=[ts/N:ts/N:ts];
%  morletwavelet
ccfs=cwt(x,2:2:128,'morl');
l=ccfs(:); N=length(l); [Y,F,T,P]
=spectrogram(l,gausswin(256),120,256,fs,'yaxis');
for i=1:length(T)
   for j=1:length(F)
      NewData(j)=P(j,i);
   end
   UE2Hz(i)=sum(NewData);
End
```

4   Conclusion

In adaptive manufacturing conditions monitoring with a variety of features on the Cartesian 3D Print machine using vibration and sound signals is obtained

- Vibration and sound signals using FFT and Wavelet Morlet can be used to obtain differences in the characteristics of the resulting signal.
- Vibration and sound signals have the same characteristics for all prismatic feature conditions.
- G28 movement can be easily monitored using vibration and sound signals.
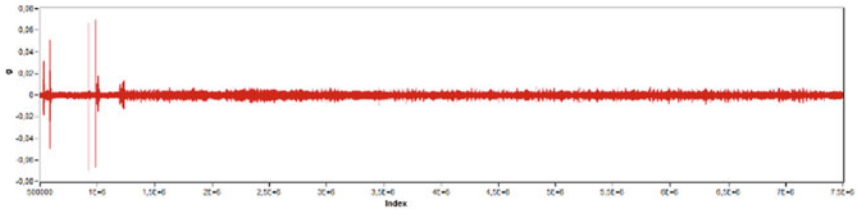
a. Cylindrical
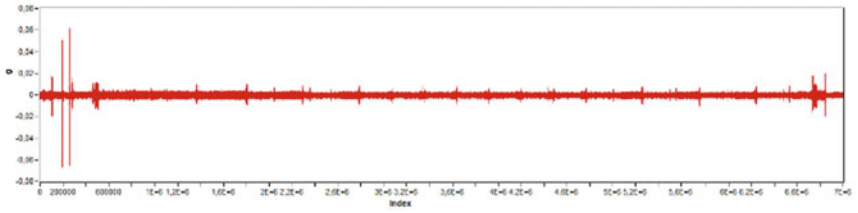
b. Prismatic horizontal
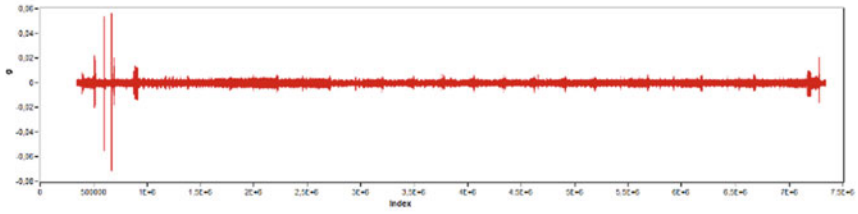
c. Prismatic vertical
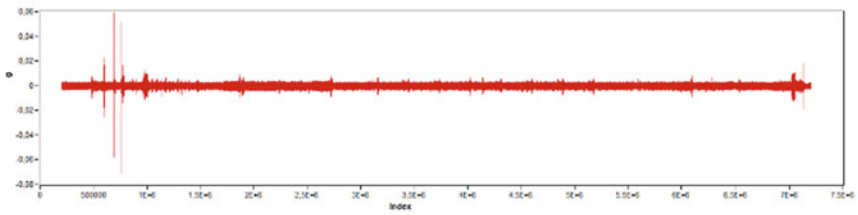
d. Prismatic diagonal \
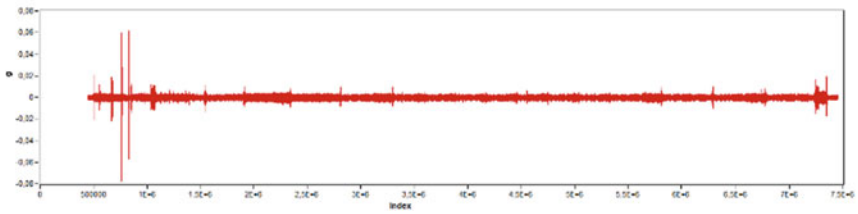
e. Prismatic diagonal /

Fig. 6 Vibration signal on various features using Zo 7.000.000 sample data
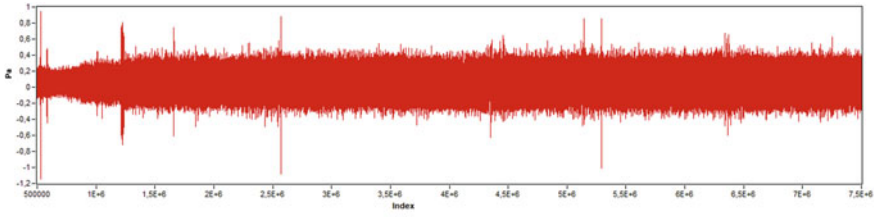
a. Cylindris
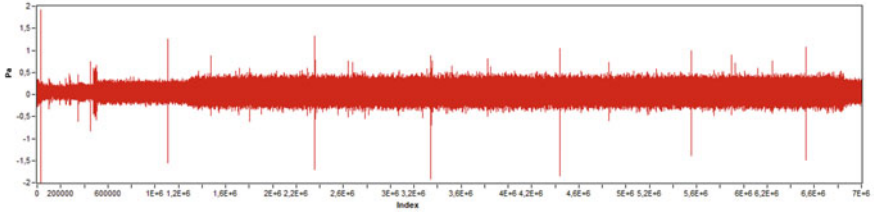
b. Prismatic horizontal
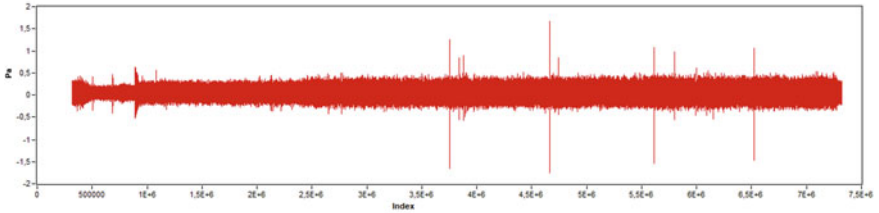
c. Prismatic vertical
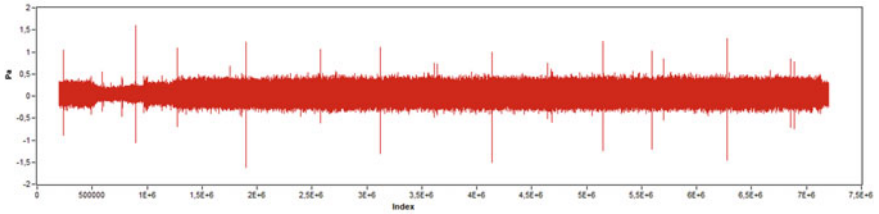
d. Prismatic diagonal \
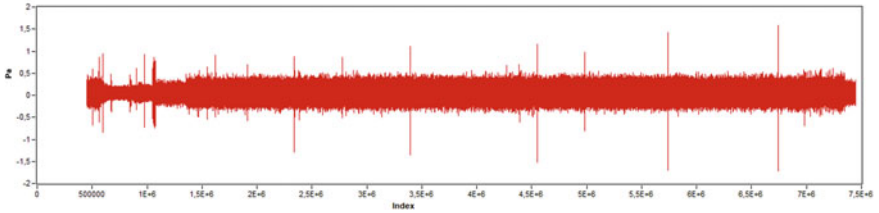
e. Prismatic diagonal /

Fig. 7 Sound signal on various features using Zo 7.000.000 sample data
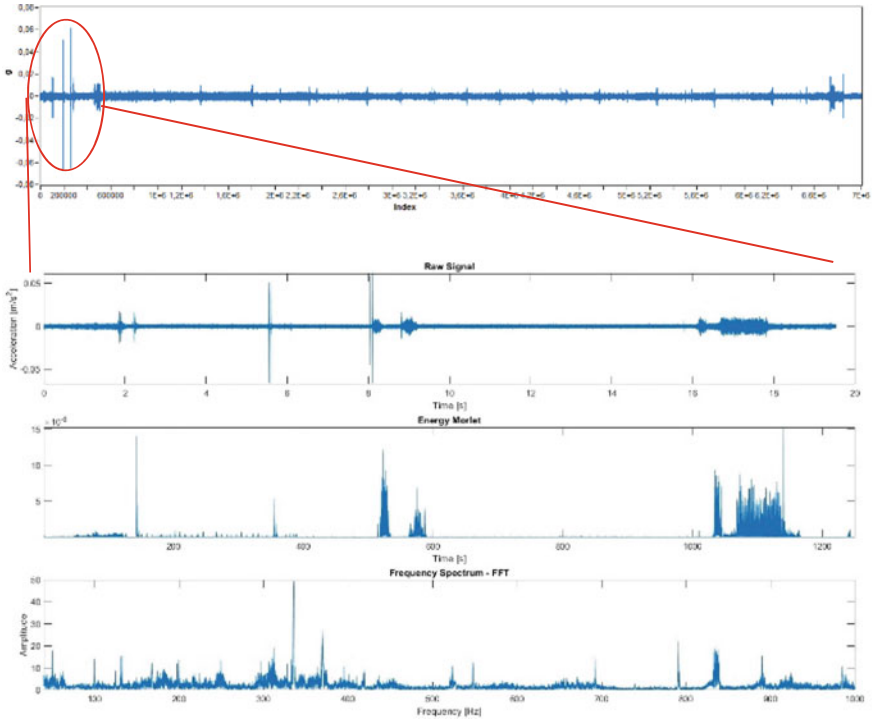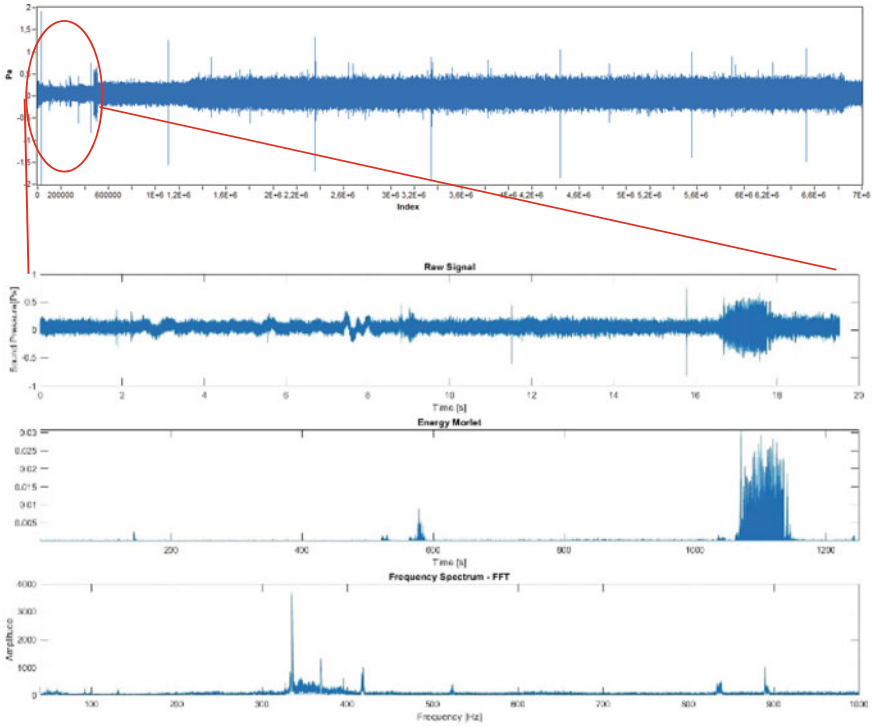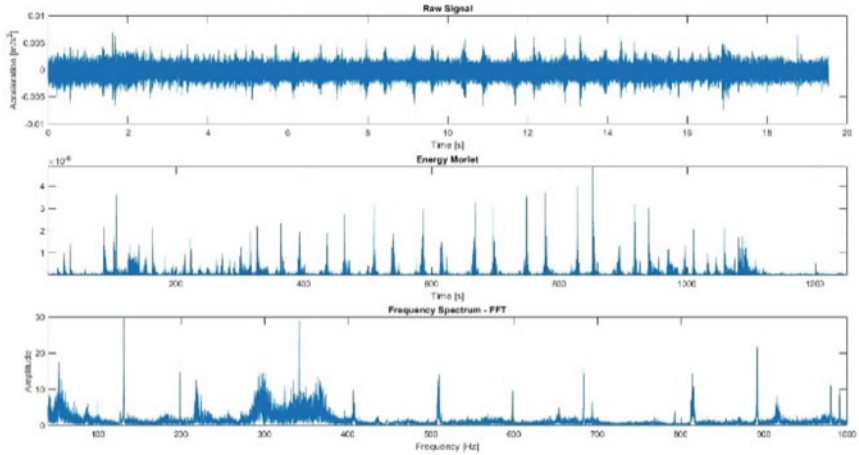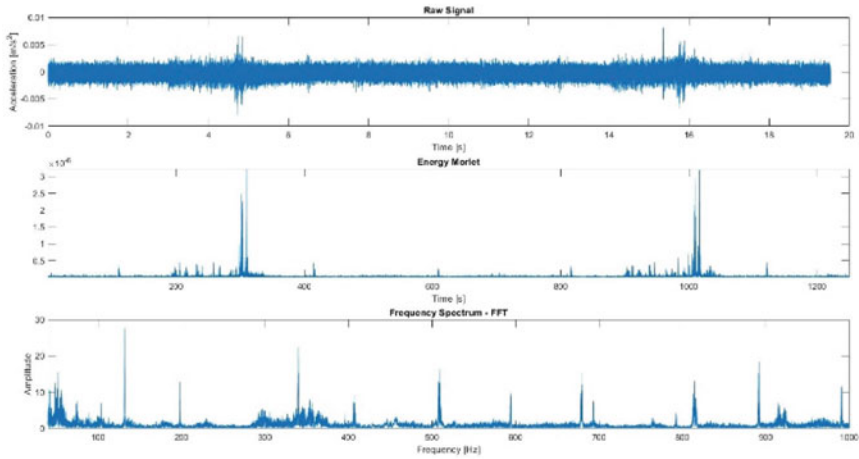
Fig. 8 G28 movement using vibration signals

Fig. 9 G28 movement using sound signals

a. Cylindrical 3 using Zo form sample

b. Horizontal 1 using Zo form sample

Fig. 10 Cylindrical and prismatic vibration signals signatures for time domain, frequency, and wavelet morlet
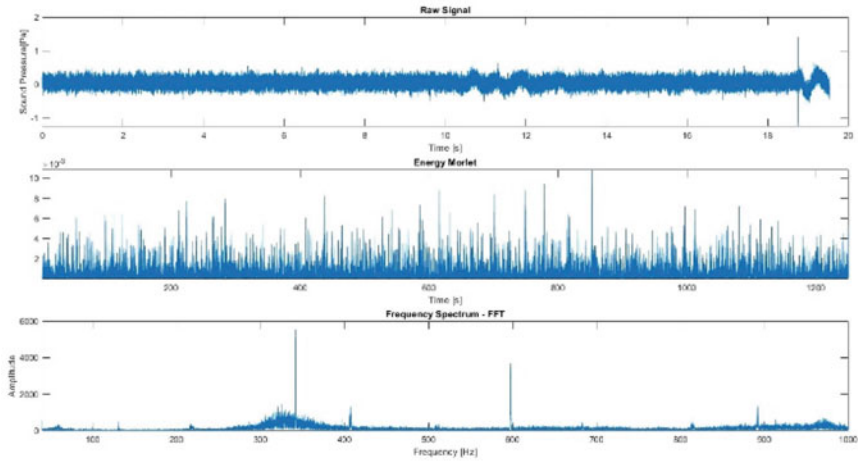
a. Cylindrical 3 using Zo form sample
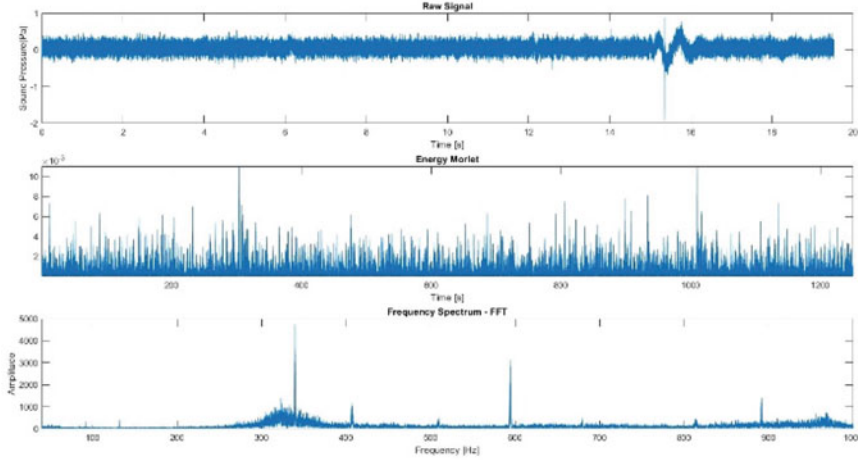
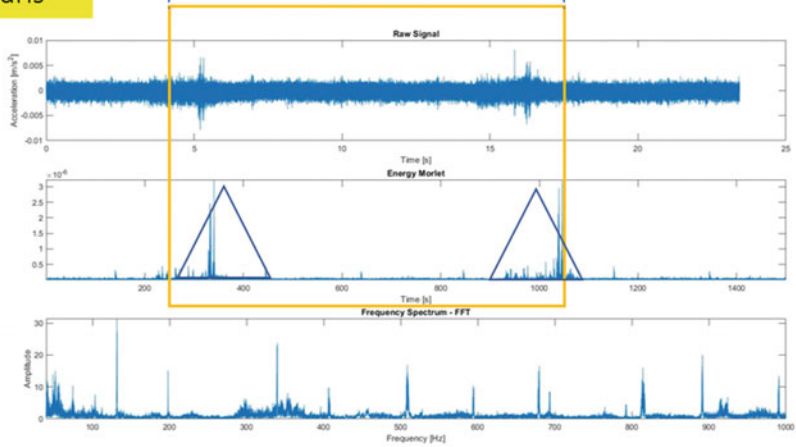b. Horizontal 1 using Zo form sample

Fig. 11 Cylindrical and prismatic vibration signals signatures for time domain, frequency, and wavelet morlet
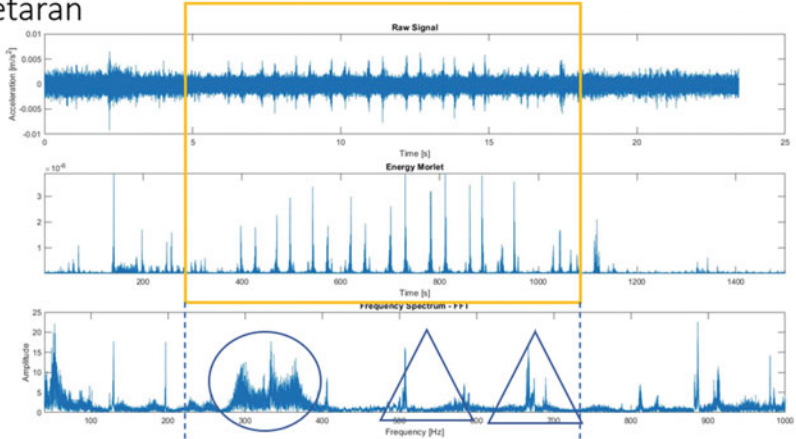
Fig. 12 Vibration signal to the cylindrical features of sample 1 and prismatic horizontal sample 1
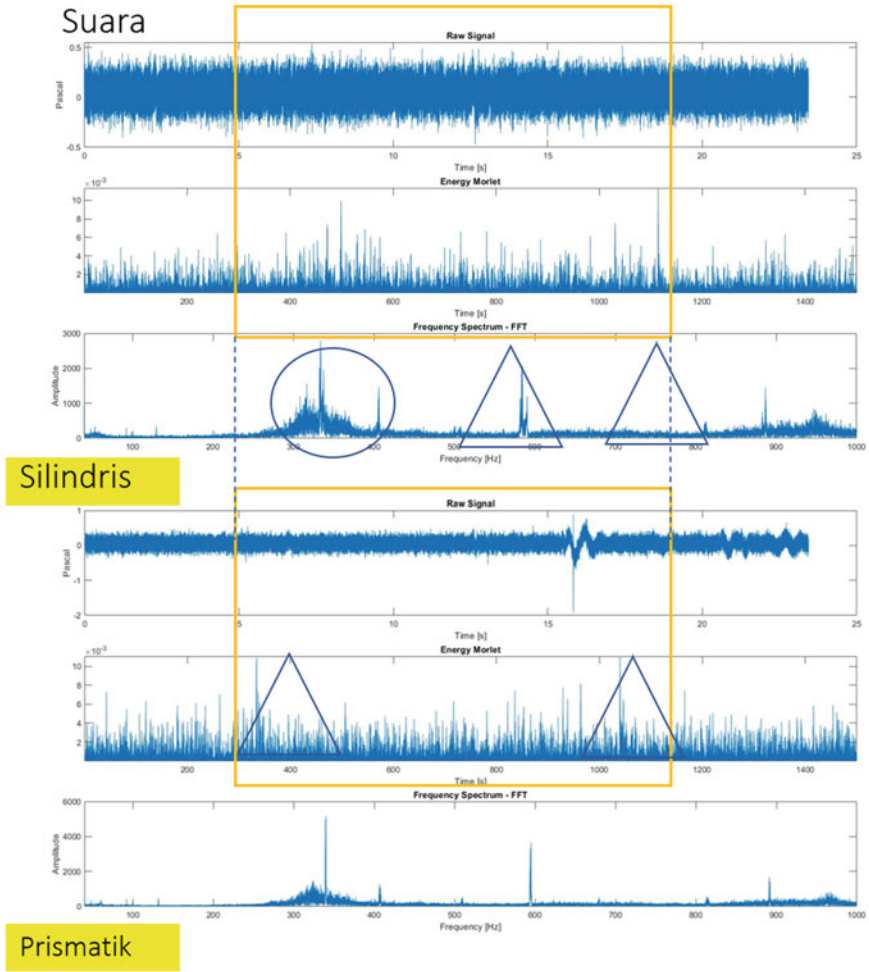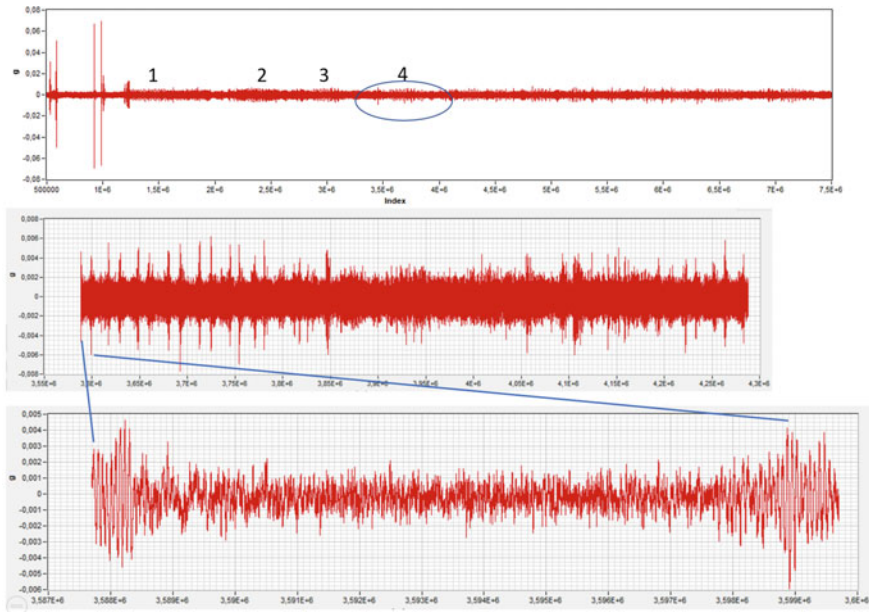
Fig. 13 Sound signal to the cylindrical features of sample 1 and prismatic horizontal sample 1

Fig. 14 The cylindrical feature vibration signal samples 1 12000 lines of data

- Condition monitoring of the prismatic feature variations of the 3D Print engine with vibration and sound signals can be recognized and still requires other means of monitoring conditions.
- Artificial intelligence can be used to speed up smart clustering.

References

1. Pranzo D, Larizza P, Filippini D, Percoco G (2018) Extrusion-based 3D printing of microfluidic devices for chemical and biomedical applications: a topical review. Micromachines 9(8). https://doi.org/10.3390/mi9080374
2. Yoon J, He D, Van Hecke B (2014) A PHM approach to additive manufacturing equipment health monitoring, fault diagnosis, and quality control. PHM 2014 Proc Annu Conf Progn Heal Manag Soc 2014:732–740
3. Tlegenov Y, Hong GS, Lu WF (2018) Nozzle condition monitoring in 3D printing. Robot Comput Integr Manuf 54:45–55. https://doi.org/10.1016/j.rcim.2018.05.010
4. Monitoring I, Sensors V (2019) In-situ monitoring and diagnosing for fused. Sensors 19:1–18
5. Samin R, Nuawi MZ, Haris SM, Ghani JA (2019) Stability analysis of regenerative vibration in turning operation using I-kaz3DTM signal processing approach. J Phys Conf Ser 1262(1). https://doi.org/10.1088/1742-6596/1262/1/012029
6. Sahadan SN, Abdullah S, Nuawi MZ, Nizwan CKE (2008) Analysis of Daubechies wavelet for fatigue time history using the Parserval's Energy Theorem. In: International conference on mechanical and manufacturing. Johor, Malaysia

7. Abdullah S, Choi JC, Giacomin JA, Yates JR (2006) Bump extraction algorithm for variable amplitude fatigue loading. Int J Fatigue 28(7):675–691
8. https://creality3d.shop/collections/new-arrival/products/creality3d-cp-01-3-in-1-modular-3d-printer. Access on 3 Mei 2020

The Development of Two Wheel Mobil Robot: Generated Path Using Simulation and Actual Path of Mobile Robot Are Compared

T. Firsa, Muhammad Tadjuddin, Iskandar, and Syahriza

Abstract This paper shows a mobile robot movement whose is gotten from the best predetermined path is derived from simulation. The robot movement is programmed on a simulated bordered floor, and the trajectory is optimized before the program is downloaded to the mobile robot. This paper describes the development of a two wheel mobile robot. The kinematics and dynamic model of the mobile robot are created and simulated using MATLAB. The experiment is conducted to compare the differences between the simulated path and the actual path. The calculations and the strategies in the simulation, the path is almost similar compared to the actual mobile robot path. The program helps the user to start the programming and optimize it to obtain the best trajectory and position of a mobile robot.

1 Introduction

An industrial robot can only handle objects in front of it. Most industrial robots are fixed in their position, their space is limited by the maximum extension of their linkages. The objects are taken and brought by the robot and, taken away by conveyors and other mechanical device. To overcome these problems caused by the limited extend a robot arm, a wheeled robot is preferred. A wheeled robot has mobility and flexibility in movement and performing a task.

There are some major wheel catagory. They differ widely in kinematics, and therefore the choice of wheel type has a substatial effect on the overall kinematics of the mobile robot. The choice of wheel types for a mobile robot is strongly linked to the choice of wheel arrangement, or wheel geometry. The mobile robot designer must consider these two issues simultaneously when designing the locomotion mechanism of a wheeled robot [1]. The variety of wheeled robot types are one-wheeled vehicles, two-wheeled vehicles (bicycles), Front steering wheels for

T. Firsa (✉) · M. Tadjuddin · Iskandar · Syahriza
Department of Mechanical and Industrial Engineering, Universitas Syiah Kuala,
Jl. Tgk. Syech Abdurrauf No. 7 Darussalam, Banda Aceh 23111, Indonesia
e-mail: teuku.firsa@unsyiah.ac.id

steering, Rear driving wheels, Front wheels for both driving and steering, Steering mechanism of a wheel loader used in construction and mining industry as well two wheel mobile robot using a differential speed steering.

The turning of the differential steering robot can be controlled by providing a different angular velocity to the wheel (by changing the speed of each motor). The term differential steering comes from the fact that the turning radius of the robot is a function of the ratios of the wheel.

In the previous published paper the robot movement is programmed, simulated and path will be optimized with manipulate the velocity and acceleration before the program is downloaded to the real mobile robot [2].

This paper describes the development of a two wheeled mobile robot. The kinematics and dynamic model of the mobile robot movement are programed and simulated using MATLAB. MATLAB is a data-manipulation software package that allows data to be analyzed and to visualize by using existing functions and user-designed programs. MATLAB is a numerical computing environment with programming language that is used to program the path of the mobile robot [3, 4]. The path was gotten from then downloaded to the actual mobile robot. The advantage of this method is that we can see and verify the motion before actually running. this method can also reduce the time taken for image processing. The actual and simulated trajectory in [2] are compared and analysed.

During the robot movement, it is calculated that the error would appear especially when the robot is moving in curvature. The error appear due to friction between wheel and floor as well as slip and skid of the robot movement. However, this was not taken into consideration.

2 Kinematics and Dynamics of Mobile Robot

The robot's position and orientation as a function of the movement of its wheels is referred to as a kinematics approach. while the causes of motion is study in a dynamics approach [5]. Manipulating the actuator is the process of causing an autonomous robot running. The forces of robot movement must be applied to the mobile robot in order to produce motion. The study of motion in which these forces are modeled is known as dynamics, whereas kinematics is the study of the mathematics of motion without considering the forces that affect the motion.

There are 3 parameters involved in the mobile robot kinematics when it is moving on a horizontal plane. The Cartesian coordinates give the instantaneous position and the orientation of the mobile robot (x, y) as a reference point of the robot fixed on the floor, the heading angle of the robot (θ), and the absolute position is represented by the function (x, y, θ) [6].

2.1 Kinematics

Kinematics of this mobile robot discusses the acceleration, linear velocity and the differential steering system included in rounding a corner, the derivation and straight line movement.

2.1.1 Control Input for Mobile Robot

Figure 1 illustrates the robot movement. Each wheel has the same radius of R_w, and the wheels have a distance of l. The control inputs of the robot are:

Angular velocity of motor on left wheel: ω_l (rad/s)
Angular velocity of motor on right wheel: ω_r (rad/s)

ω Angular velocity of the center of the mobile robot
R_c The radius of the instantaneous curvature.

Whereas, Fig. 2 shows the robot is moving pivot which the speed of two wheels are at the same but different direction.
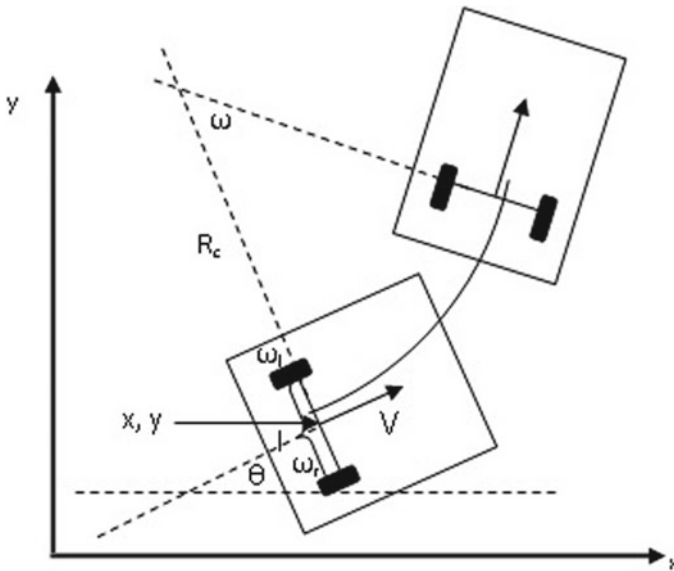

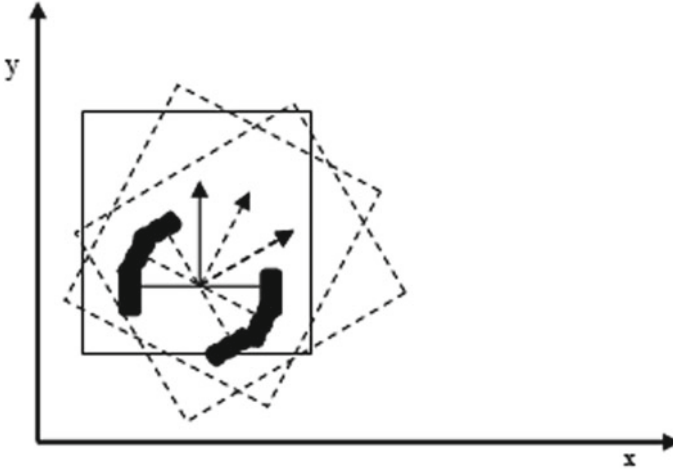**Fig. 1** Differential of a steering robot

Fig. 2 Robot moving pivot

2.1.2 Instantaneous Curvature and Linear Motion

An instantaneous curvature occurs when $\omega_r > \omega_l$. Figure 1 shows the instantaneous curvature of such a robot. The angular velocities of the center of the robot is:

$$\omega = \frac{R_w}{l\eta}(\omega_r - \omega_l) \tag{1}$$

The linear velocity of mobile robot is:

$$v = \frac{R_w}{2\eta}(\omega_l + \omega_r) \tag{2}$$

So that the radius of the instantaneous curvature is given by

$$R_c = \frac{v}{\omega} \tag{3}$$

From equation [2], the position of the robot is given by

$$\dot{x} = \frac{R_w}{2\eta}(\omega_l + \omega_r)\cos\theta \tag{4}$$

$$\dot{y} = \frac{R_w}{2\eta}(\omega_l + \omega_r)\sin\theta \tag{5}$$

2.2 Dynamics

The dynamics of a robot is related to masses, inertias and acceleration of the loads. In dynamic, to accelerate a mass, force or torque is required to act on it. To have much desired acceleration and velocity of robot, it is necessary to have actuators that are capable of exerting enough vastly forces and torques to move. Otherwise, the mobile robot may not be moving fast enough, and thus it will lose its positional accuracy. To have how strong each actuator must be, it is necessary to determine the dynamic relationships that manage the robot motions. These equations are the torque, inertia and angular acceleration relationships. Based on these equations and considering the external loads on the robot, it is possible to calculate the largest loads to which the actuators may be subjected and thereby design the actuator to be able to send the necessary torques, [7].

In general, the dynamic equations can be used to find the motion equations mechanisms by knowing the forces and torques. The desired accelerations of the robot can be determined. These equations are also utilized to identify the effects of different inertial loads depending on the desired accelerations.

2.2.1 Lagrangian Mechanics

Lagrangian mechanics is based on the differentiation of the energy terms with respect to the system's variables and time. The lagrangian method is relatively simple to use. The Lagrangian mechanics is based on the following two generalized equations, one for linear motions, and one for rotational motions [7].

$$L = K - P \tag{6}$$

where:

L   Lagrangian
K   Kinetic energy
P   Potential energy

The relation between the angular acceleration of each wheel and the torque applied is obtained from Eq. [8], using the following relation:

$$T = \frac{\partial}{\partial t}\left(\frac{\partial L}{\partial \dot{\theta}}\right) - \frac{\partial L}{\partial \theta} \tag{7}$$

where:

T   The summation of all torques in a rotational motion,
θ System variables

2.2.2 Mobile Robot Dynamic

The mobile robot dynamic equation using Lagrangian formulation as following derived,

$$L = K - P$$

where,

$$K = \frac{1}{2}MV^2 + 2\left(\frac{1}{2}I\dot\omega^2\right)$$
$$L = \frac{1}{2}MV^2 + \frac{1}{2}mr^2\dot\omega^2$$

(8)

Replacing value at Eq. (6) on Eq. (6), the Lagrangian expression is obtained:

$$T = \frac{1}{8}Mr^2\left(\dot\omega_l^2 + \dot\omega_r^2\right) + \frac{1}{2}mr^2\dot\omega^2$$

(9)

where,

T   Torque from 0 to max velocity (NM)
M   Mass of robot (N)
m   Mass of wheel (N)
r   Radius of wheel (m)

$$P = F V$$

(10)

3   Design of the Chassis

The mobile robot's characteristics, number of wheels, materials, structure etc., are first designed by using Pro-Engineer software (wildfire). It is one of the world's most widely used computer Aided Design (CAD) software. It is a powerful part modeling, easy 2D and 3D geometry creation environment. The mobile robot chassis in this thesis is designed based on the L-shape plate that is available and easily found in the market. Figure 4.1 and 4.2 show the chassis of a mobile robot being assembled. The height of the base plate form from the floor is 460 mm, the length is 404 mm and the width is 395 mm (Fig. 3).
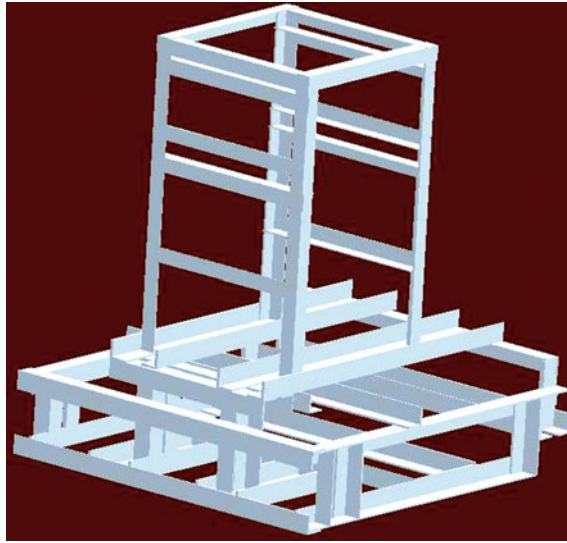
Fig. 3 The whole platform without components

4 Mobile Robot Modeling

Figure 4 shows the mobile robot model with the basic parameters used in the system. The body of robot is considered to be square with mass M, with two wheels of radius R_w and a mass m of each. The right wheel rotates at an angular speed of $\omega_l = \dot{\theta}_l$, and the left at $\omega_r = \dot{\theta}_r$. Each wheel is connected to an independent DC motor by using a gear system of the ratio 15:1.
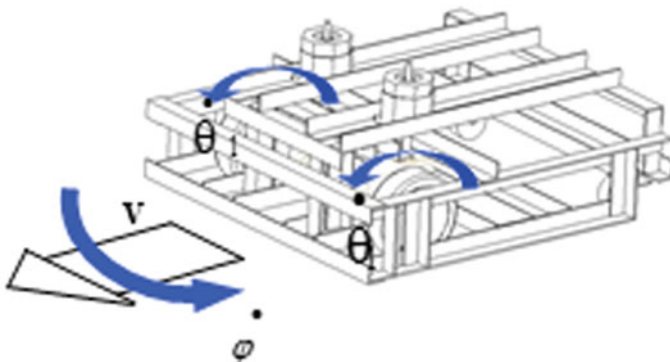

Fig. 4 The robot model (showing the main dynamic parameter)

4.1   Robot Kinematics

The kinematics for the robot relates the state or posture of the machine, with the angular displacement of each wheel. Figure 5 shows the kinematic model of a differential steering robot when it is turning a curvature. In this case, the angular velocity of the right wheel is faster than the left wheel, so that the mobile robot will turn to the left. The mobile robot has a gear box to reduce the speed and increase the torque as shown in Fig. 6. In this paper, the ratio of the gears is as follows:

$$\eta = \frac{R_w}{R_m} \gg 1$$

where: $R_w = 15$, $R_m = 1$

So, $\eta = 15/1$

The kinematics equations of (11) and (12) show the relation between the angular speed of the wheel and rotational and tangential speed of the robot with the gear ratio is taken into account.

In this example, it is assumed that the angular velocity of the right wheel and the left wheel are different. The angular velocity of the center of the robot is given by:
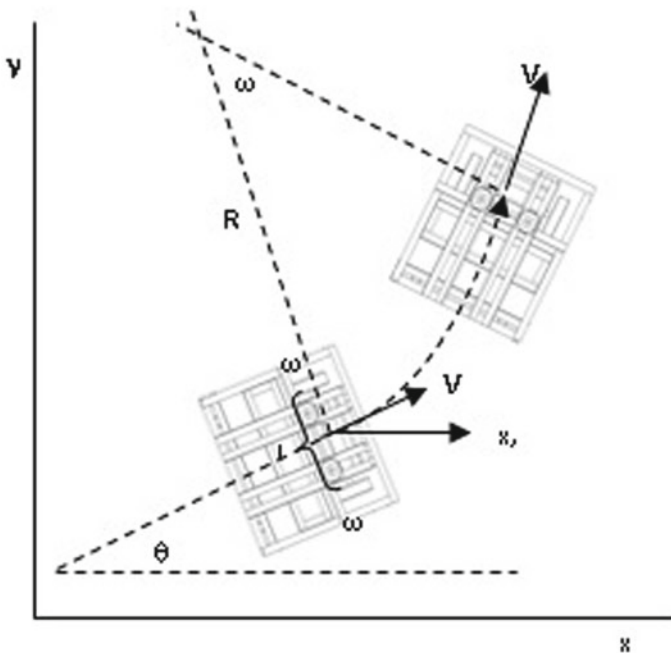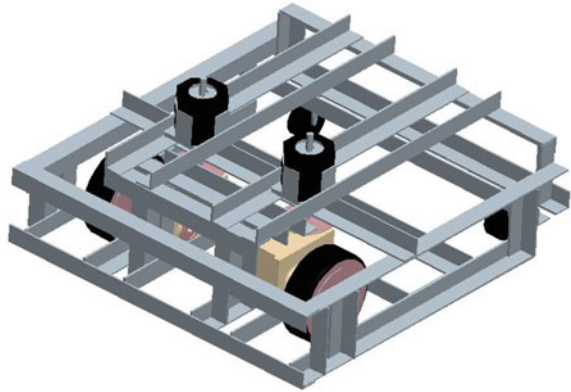

Fig. 5 The kinematic model of differential steering robot

Fig. 6 Base chassis assembled with motor, gear box and wheel

$$\omega = \frac{R_w}{l\eta}(\omega_r - \omega_l) \tag{11}$$

where,

$R_w = 0.05$ m

$L = 0.269$ m

$\omega_r = 500$ rpm $= 52.33$ rad/sec (assumed)

$\omega_l = 200$ rpm $= 20.933$ rad/sec (assumed)

$\omega = \frac{0.05}{0.269 \times 15}(52.33 - 20.933)$

$\omega = 0.377$ rad/sec

The linear velocity of robot is:

$$v = \frac{R_w}{2\eta}(\omega_l + \omega_r) \tag{12}$$

$$v = \frac{0.05}{2 \times 15}(20.933 + 52.33)$$

$$v = 0.147 \, \text{m/s}$$

The velocity at x and y position is as follows:

$$\dot{x} = \frac{R_w}{2\eta}(\omega_l + \omega_r)\cos\theta$$

$$\dot{y} = \frac{R_w}{2\eta} (\omega_l + \omega_r) \sin \theta$$

where, θ is as input for initial orientation of the robot (see Fig. 5).

4.2 Robot Dynamics

The dynamic equation of the robot is related to the torque which is applied to the wheels, considering the mass inertia of the different elements in the model. These equations can be deduced by using the Lagrangian formulation, which is based on the calculation of the energy of the system. The total energy of the robot can be calculated as the sum of the kinetic energy of the body and the kinetic energy of each wheel. The potential energy is not used as the robot is considered to move on a single level plane.

Using Eq. (7), the torque required is given by

$$T = \frac{\partial}{\partial t} \left(\frac{\partial L}{\partial \dot{\theta}} \right) - \frac{\partial L}{\partial \theta}$$

$$T = \frac{1}{8} M r^2 \left(\ddot{\theta}_l + \ddot{\theta}_r \right) + \frac{1}{2} m r^2 \ddot{\theta}$$

where,

$\ddot{\theta} = \alpha$ = acceleration of wheel

$$\alpha = \frac{\omega_f - \omega_i}{t}$$

where, $\omega_{fl} = 62.8$ rad/s, $\omega_{fr} = 62.8$ rad/s, t = 10 s

$$\alpha_l = \frac{\omega_{fl} - \omega_{il}}{t}$$

$\alpha_l = 6.28$ rad/sec^2

$\alpha_r = 6.28$ rad/sec^2

$$T = \frac{1}{8} M r^2 (6.28 + 6.28) + \frac{1}{2} m r^2 6.28$$

where,

M = 15 kg = 147.15 N
m = 1 kg = 9.81 N
r = 0.05 m

$$T = \frac{1}{8} 147.15 \times (0.05)^2 (6.28 + 6.28) + \frac{1}{2} 9.81 \times (0.05)^2 6.28$$

So, the maximum required torque from 0 to maximum velocity required is: $T = 0.655$ Nm

The maximum torque can be reached in the specifications of motor is 1 Nm.

$$F = C_r \, mg$$

where,

Cr = 0.02

F = 0.02 × 15 × 9.81

F = 2.943

So,

$$v = \frac{0.05}{2 \times 15}(62.8 + 62.8)$$

$v = 0.209$ m/s (maximum velocity)

P = 2.943 × 0.209

P = 0.616 W (power required).

5 Development of Mobile Robot

The making of robot mechanical and electrical is a complex task. The good software cannot overcome lack robot design including mechanical design. Thus, potentially weak points in robot design must be eliminated. Such weak points include structural deformation, gear backlash, and poor bearing clearance, friction, thermal effects, and poor connection of transducer. The chassis of the robot is manually made; most of the structure is simplified. Mounting the motor on the gearbox and wheel conducted with high accuracy of alignment due to misalignment need extra torque to start up and turn the wheel.

The ratio of gear box 1:15 is chosen because of it could increase torque of the robot, whereas the rubber wheel with diameter 30 mm is selected using the existing component in market and it is assumed type and size are suitable. Figure 6 shows the mechanism designs of motor gear box and wheel assembled into the base chassis. This design has been used as a reference to build the actual mobile robot frame.

The chassis is made from L-shaped aluminum for lightness but strength. Each aluminum L-shaped is riveted together for rigidity. The design and actual mobile robot is shown Fig. 7.
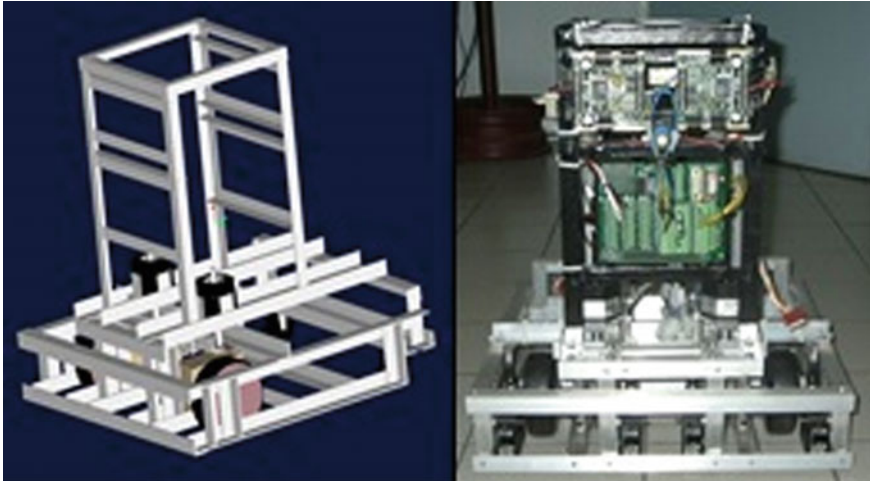
Fig. 7 CAD model and actual mobile robot

The robot is an integrated mobile robot system with the proximity sensor and other electronic devices. The body of mobile robot is supported by four wheels of which the two front rubber wheels is driven by a stepper motor of 39 W.

6   Simulation Results

The user can enter the desired motion. The program will generate the coordinates as shown in Table 1. Moreover, all dimensions of the robot modeling and environment in simulation are similar to the real one.

In Table 1 above, with th = 0.000 deg and y = 0.000 the robot moves in straight line because there is no orientation. At the 11th step, theta begins to increase. This means the robot is turning along a curvature.

The combination of the speed between motor 1 and motor 2 along a curvature with different radius can be seen in Table 2.

In Table 2 above, the radius of turning curvature of a robot depend on the different between the speeds of two motors. It can be seen in row number one (motor1 = 100 rpm, motor2 = 300), the radius obtained is 0.268. Base on the graph below, we can conclude that the incremental value of the radius is constant (Fig. 8).

Table 1 The mobile robot trajectory as x, y, and θ

X coordinate	y coordinate	Orientation (θ)	Remark
0.000000	0.000000	0.000000	Goes straight
0.174533	0.000000	0.000000	
0.349066	0.000000	0.000000	
0.523599	0.000000	0.000000	
0.698132	0.000000	0.000000	
0.872665	0.000000	0.000000	
1.047198	0.000000	0.000000	
1.221730	0.000000	0.000000	
1.396263	0.000000	0.000000	
1.570796	0.000000	0.000000	
1.570796	0.000000c	0.000000	
1.745329	0.000000	22.304833	Turning curve
1.906803	0.066241	44.609665	
2.031055	0.188811	66.914498	
2.099490	0.349367	89.219331	
2.101868	0.523884	111.524164	
2.037833	0.686246	133.828996	
1.916967	0.812155	156.133829	
1.757358	0.882772	178.438662	
1.582890	0.887527	200.743494	
1.419671	0.825710	223.048327	

Table 2 The radius for curve turning of the robot

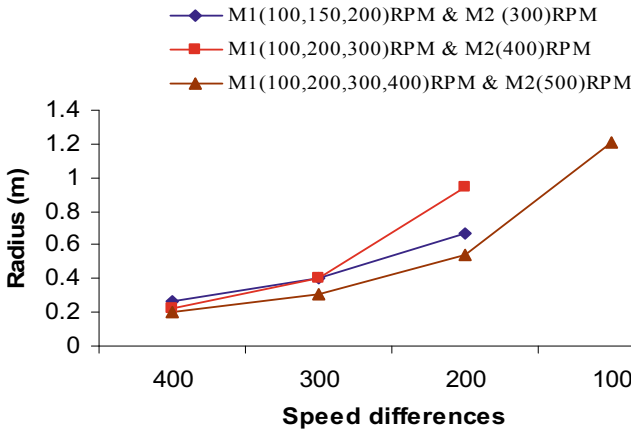| No	Motor 1 (rpm)	Motor 2 (rpm)	Radius (m)
1	100	300	0.268
2	150	300	0.4025
3	200	300	0.672
4	100	400	0.222
5	200	400	0.402
6	300	400	0.941
7	100	500	0.199
8	200	500	0.312
9	300	500	0.536
10	400	500	1.210

**Fig. 8** The incremental value of radius

7   Experiment Results

The desired path is simulated by using MATLAB and the output is shown in the graph with (x, y) coordinates. This graph shows the path of the mobile robot with respect to time. The next position and orientation of the mobile robot is always based on the previous position and may be formulated as vectors in mathematical terms. Finally, the simulation will generate the codes for the mobile robot's program.

The simulation results as MINT programming codes will be used for running the actual mobile robot movement (data positioning trajectory of the real robot will be captured by using a digital video camera, thus, the trajectory will be a coordinate for x and y position in 2 dimensional).

In case of a two driven wheeled mobile robot, the auxiliary wheels do not affect the absolute position. The auxiliary wheel is not critical to the position estimation and, hence, it is not considered in this thesis. Subsequently, for this reason, we assume that the simplified mobile robot consists of only two wheels with the axis connecting these wheels.

**Fig. 9** Test setup
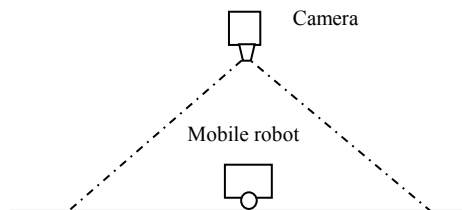
7.1 Comparison Graphs

The mobile robot was run with the codes that are generated by simulation. A test area where the floor is leveled and gridded for easier position measurement was close. Figure 9 shows the test setup. In the experiment the actual robot moving a straight line and a curvature which is recorded by a video camera.

Several tests are done to the actual robot with the same speed and different speed and they are compared to the path obtained from simulation as shown in Figs. 10, 11, 12 and 13.

7.2 Position and Curvature Errors

The error in each figure was determined and is recorded into Table 3 as the linear error and the curvature error. Here, the error is the difference between the actual and the desired coordinates (simulation path) in meter. The linear error refers to the difference when the wheels are driving at the same speed. Whereas, the curvature error refers to the difference when both wheels are at different speeds.

The table shows the coordinate of the linear error is smaller than the curvature error. A few factors affect the motion of the robot such as friction on the wheel and surface, power lost in transmission, skid and slip.
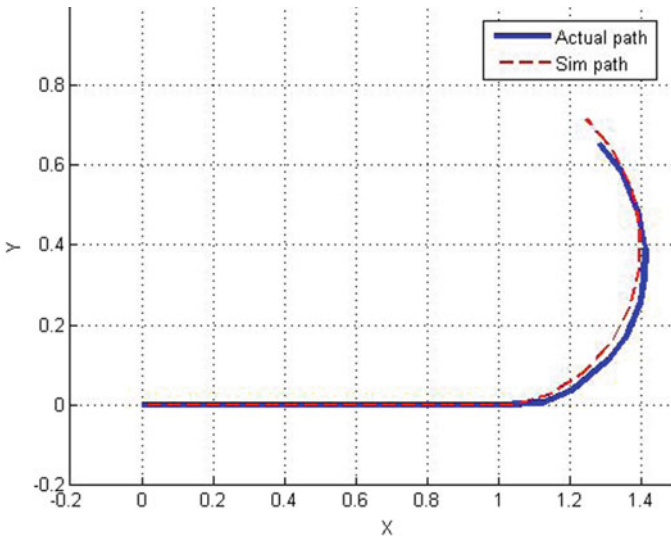
Fig. 10 The actual robot's and simulation path for moving a linear and curvature with 0.268 m radius
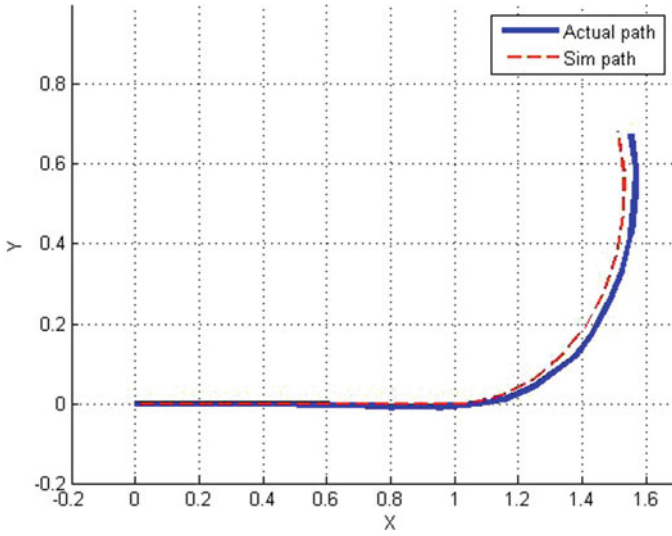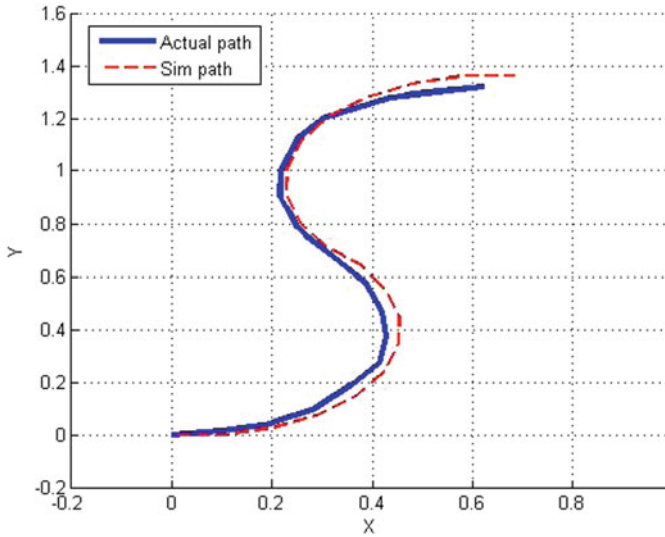
Fig. 11 The actual robot's and simulation path for moving a linear and curvature with 0.4025 m radius
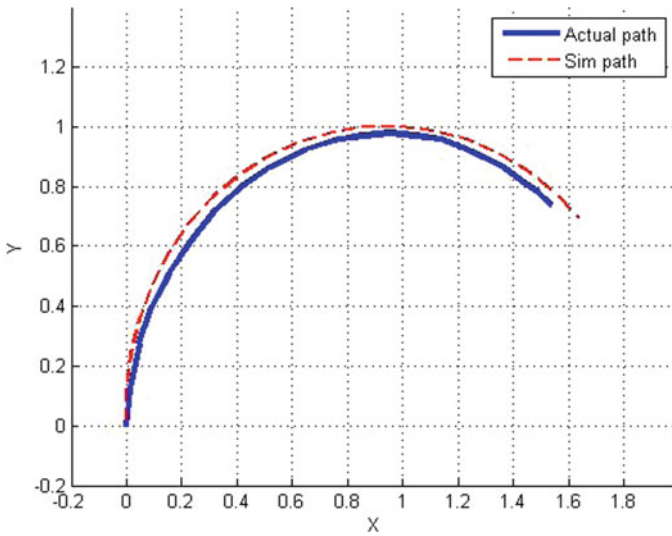
Fig. 12 The actual robot's simulation path for moving curvature with 0.914 m and 0.672 m radius

However, based on the calculations and the strategies in the simulation, the path is almost similar compared to the actual mobile robot path with errors is less than 0.978%.

Fig. 13 The actual robot's simulation path for moving curvature with 0.402 m and 0.268 m radius

Table 3 Errors for significant level of the deferential speed between the wheels (duration, $t = 20$ s, gear ratio = 1:15)

Test	Left motor RPM straight & curvature	Right motor RPM straight & curvature	Linear error, e_l/m (x, y)	Linear error, e_l/% (x, y)
1	300 & 100	300 & 300	(0.0094, 0)	(0.873, 0)
2	300 & 150	300 & 300	(0.0299, 0.0030)	(0.922, 0)
3	300 & 200	300 & 300	(0.0657, 0.0058)	(0.815, 0.662)
4	500 & 100	500 & 500	(0.0065, 0)	(0.840, 0)
5	500 & 200	500 & 500	(0.0325, 0.0030)	(0.871, 0.361)
6	500 & 300 (45°)	500 & 500	(0.0233, 0.0083)	(0.872, 0.882)
7	500 & 300 (90°)	500 & 500	(0.0025, 0.0307)	(0.452, 0.819)
8	200 & 300	400 & 100	–	–
9	400 & 300 (90°)	300 & 200	–	–
Test	Left motor RPM straight & curvature	Right motor RPM straight & curvature	Curvature error, e_c/m (x, y)	Curvature error, e_c/% (x, y)
1	300 & 100	300 & 300	(0.0383, 0.0187)	(0.969, 0.787)
2	300 & 150	300 & 300	(0.0729, 0.0365)	(0.801, 0.801)
3	300 & 200	300 & 300	(0.0973, 0.0125)	(0.933, 0.4716)
4	500 & 100	500 & 500	(0.0526, 0.0069)	(0.97, 0.863)

(continued)

Table 3 (continued)

5	500 & 200	500 & 500	(0.0477, 0.0068)	(0.975, 0.840)
6	500 & 300 (45°)	500 & 500	(0.0264, 0.0076)	(0.978, 0.969)
7	500 & 300 (90°)	500 & 500	(0.0372, 0.0949)	(0.772, 0.957)
8	200 & 300	400 & 100	(0.0244, 0.0117)	(0.877, 0.909)
9	400 & 300 (90°)	300 & 200	(0.0803, 0.0045)	(0.749, 0.907)

8 Conclusion

Based on comparison between the linear and curvature movement, the curvature error is bigger than the linear error. A few factors affecting the motion of the robot such as friction on between wheels and surface, power lost in transmission, skid and slip. however it was not considered in this research. Based on the calculations and the strategies in the simulation, the path or trajectory is almost similar compared to the actual mobile robot path.

Moreover, the program helps the user to start the programming and optimize it to obtain the best trajectory and position of a mobile robot.

References

1. Goris K (2005) Autonomous mobile robot mechanical design. Vrije Universiteit Brussel
2. Teuku F, Tadjuddin M, Iskandar S (2016) Path Generated and Optimized of Mobile Robot using Simulation, SNTTM-BKSTM, ITB Bandung
3. http://en.wikipedia.org/wiki/MATLAB, 04/02/2006
4. MATLAB Help Navigator (2005) Introduction: what is MATLAB?. Version 7.04.365 (R14)
5. Lucas GW (2001) A tutorial and elementary trajectory model for the differential steering system of robot wheel actuator. The Rossum Project volunteers
6. Furukawa T. Robot design. Lecture 3: kinematic fundamentals. School of Mechanical and Manufacturing
7. Niku SB (2001) Introduction to robotics: analysis, systems, application. Prentice-Hall, New York
8. Groover MP et al (1978) Industrial robotics: technology, programming, and application. McGraw-Hill, NewYork

Study of the Sound Absorption Characteristics of Abaca and Coconut Coir Fibers

T. Firsa, Muhammad Tadjuddin, M. Iqbal, and R. Syah Putra

Abstract Abaca and coconut coir fibers which are natural fibers able to be as damping material effectively. Those fibers availability in Aceh are abundant and the price are relatively cheaper compared to other types of dampers material. This research aims to determine the level of sound absorption of abaca and coconut coir fibers. Tests are carried out in the Reverberation Room, which refers to ISO—354: 2003 regarding standard measurements with reverberation space methods. The temperature and humidity in the room without air conditioning respectively is 32.0 0 C and 89.6%. The calibration of the microphone is 113.7 dB at a frequency of 1 kHz with sensitivity—27.3 dB. The measurements were made using Real Time Analyzer 140 with a filter band 1/3 octave, frequency range 125–6.3 kHz. Type of sound used in the research was White Noise and Pink Noise. Based on the test results show that the Abaca fiber test sample with a test sample area of 1.21 m^2 has a maximum absorption coefficient at low frequency (160–250 Hz) which is 0.93 (93%) at a frequency of 200 Hz and minimum at low frequencies (125–500 Hz) which is 0.17 (17%) at 315 Hz. The coefficient values tend to be stable at intermediate frequencies (1000–3150 Hz) ranging between 0.26 and 0.47 (26–47%). While the coconut fiber test sample has a maximum absorption coefficient at high frequencies (1600–6300 Hz) at 0.84 (84%) at 2000 Hz and a minimum at low frequencies (125–500 Hz) at 0.12 (12%) at 250 Hz. The absorption coefficient value of coconut coir tends to be stable at medium frequencies (800–1250 Hz) ranging between 0.14 and 0.33. So the sound energy that occurs in coconut coir is 14–33% of the total energy that comes.

T. Firsa (✉) · M. Tadjuddin · M. Iqbal · R. S. Putra
Department of Mechanical Engineering, Universitas Syiah Kuala,
Jl. Tgk. Syech Abdurrauf No. 7 Darussalam, Banda Aceh 23111, Indonesia
e-mail: teuku.firsa@unsyiah.ac.id

1 Introduction

Sound absorbing material is able to absorb sound from a sound source. This sound absorbing material is used to control the noise. Noise can cause psychological and biological effects for people, such as decreased comfort, concentration, and can also cause stress that effect to heart working system, circulatory system or respiratory circulation. In addition, this can also interfere with verbal communication, it can even lead to reduced ability of hearing or permanent damage to the sense of hearing.

Sound is a wave that has general wave characteristics, namely when it meets a surface it can be reflected, absorbed and also transmitted. Porous materials can absorb sound energy more than other materials, because with the presence of pores, sound waves can enter the material. Sound energy is absorbed by materials that are converted into another form of energy, usually converted into heat energy. The ratio between the sound energy absorbed by a material with the sound energy coming to a surface of the material is called the absorption coefficient [1].

The way to reduce sound pollution/noise levels in a building is to use sound absorbers or acoustic materials that absorb or reduce sound so that noise can be reduced. The material is a special material whose function is to absorb at a certain frequency. The material must be soft, porous and fibrous, it is believed to be able to absorb sound energy that hits it. Based on the three characteristics of the abrasive material, natural fibers were chosen, namely abaca banana fiber and coconut coir fiber [2].

Abaca banana fiber are a natural fiber known in the world which is used as material for clothing, paper or other uses. Abaca fiber has good ductility, is not brittle and is not easily torn or broken. Abaca fiber also has a very good and shiny texture that can reflect light. Abaca fiber is a natural source that can be renewed and very easy to cultivate. Abaca fiber has buoyancy and resistance to damage in salt water [3].

In paper [4] mentioned the Fiber Reinforced Polymer (FRP) composite made from polyester resin matrix and abaca fiber.

Ordinary banana fiber, the fronds are very thin and soft so that the strength is very low and easy to break. "The Abaca banana (*klutuk in Java language*) fiber has better strength compare to ordinary banana fibre. This banana fiber is usually used for weft yarn, while other fibers are used as a solution to strengthen the weave [5].

Coconut coir is a natural fiber. Long ago, this material was used in traditional building construction, in clothing, and even frequently as a source of energy. Coconut coir fiber is one of the most lignocellulosic fibers. It is not brittle, is amenable to chemical modification, is non-toxic and biodegradable [6].

Sound absorbers or acoustic materials are special materials that are made and function to absorb sound at certain frequencies. Sound absorbing materials can be classified as follows: porous materials, such as fiber boards, soft stucco, and mineral wools, which have the basic characteristics of a cellular network with interconnected pores. Panel or membrane material is an efficient low frequency absorber,

such as: wood panels, hardboard, gypsum boards. Cavity resonators, are sound absorbers consisting of a number of enclosed air bounded by a solid wall and connected by a narrow gap in the surrounding space, where the waves dock. Porous materials are the most frequently used because porous materials are relatively cheaper and lighter than other types of absorbers [7].

In general, absorbent materials are naturally resistive, fibrous, porous or in special cases are active resonators. When sound waves hit the absorbent material, the sound energy is partially absorbed and converted into heat. The sound will enter the material through the pores. The sound will hit the particles in the material, then the particles are reflected to other particles, and so on so that the sound is confined in the material [8].

The purpose of this study was to determine the level of sound absorption and the coefficient value of abaca banana fiber and coconut coir fiber on sound frequency. To determine and compare the level of sound absorption and the coefficient value of the abaca banana and coconut fiber material, it was carried out by using the drone field approach in a drone room.

2   Sound

Sound wave propagation is caused by stretching of air particles moving outward due to pressure drift. This is almost the same as the spreading of a water wave over the surface of the pond from a point a rock is dropped on the pond. The air particles that carry on the sound waves will not change their normal position.

The speed of propagation of sound waves at room temperature of 680 F (200C) is about 1,130 ft/s (344 m/s). If a sound wave has a collision on a material, it is likely that the sound wave will be deflected, absorbed, diffused, deflected, hummed, and forwarded.

3   Sound Absorption

Sound absorption coefficient is the efficiency of sound absorption of a material at frequency. The sound absorption coefficient of a surface is the sound energy absorbed, or not reflected, by the surface. This unit is stated in the letter Geek a. Value ranges from 0 to 1; for example at 500 Hz when an acoustic material absorbs 65% of the incoming sound energy and reflects 35% of it, then the sound absorption coefficient of this material is 0.65. The sound absorption coefficient can change depending on the angle of incidence of the sound wave at a material with a certain frequency. The coefficient values are averaged over all incident angles at a certain frequency (random arrival).

The sound absorption of a surface is measured in sabins, formerly known as open-window units. One sabin represents a surface of 1 ft^2 (or 1 m^2) that has an

absorption coefficient of α = 1.0. Surface absorption is obtained by multiplying the surface area in ft^2 (or m^2), by the sound absorption coefficient.

It is standard practice to list the sound absorption coefficient values at the representative of the standard frequencies covering the most important parts of the audio range, namely at 125, 250, 500, 1000, 2000, 4000, and 8000 Hz or 128, 256, 512, 1024, 2048, 4096, and 8192 Hz [9].

4 Reverberation Room Method

This method used to determine the sound power level of a sound source is the drone field method. This method is done in a room designed to have reflective walls with a sound absorption coefficient less than 0.06. This space is called the Reverberation Room. In a drone room, sound energy will be completely diffused into the room so that the sound pressure level at all points in the room is ideally the same. Determination of the sound power level using the drone room method is carried out by measuring the reverberation time and sound pressure level in the drone room [10].

The coefficient of measurement using this method is done in the Reverberation Room. The drone room is a room that is designed to cover all walls, floors and ceilings with a material that is very hard and almost non-porous so that all the sound that comes can be fully reflected back, even reflected repeatedly. Thus, the votes will travel in all directions with the same quantity and probability. With this condition, the reverberation space is assumed to be a diffuse field.

For the value of α in the drone chamber, the data required is the reverberation time of the empty drone (T1) and the time of reverberation in the drone chamber with the test sample (T2).

There are three equations to calculate the reverberation time as follows:

1. Sabine Equation

$$T_{60} = \frac{55.3V}{c\left[\sum_{i=1}^{n} s_i a_i\right]} \tag{1}$$

2. Norris—Eyring Equation

$$T_{60} = \frac{55.3V}{c\left[\sum_{i=1}^{n} s_i\right] In(I - \bar{a})} \tag{2}$$

Where,

$$\bar{a} = \frac{\sum_{i=1}^{n} s_i a_i}{\sum_{i=1}^{n} s_i} \tag{3}$$

3. Millington—Sette Equation

$$T_{60} = -\frac{55.3V}{\left[c\sum_{i=1}^{n} s_i In(I - a_1)\right]} \tag{4}$$

The equation used in this study is the Sabine equation. The absorption coefficient of Sabine is calculated under conditions of long reverberation times, namely by measuring the reverberation time in a drone chamber without a sample (T1) and with a sample (T2). Suppose the surface area of the sample S_b with the absorption coefficient α to be searched for. The calculation is done in the drone room with a total wall area of S_T which has an absorption coefficient of α_o.

$$T_1 = \frac{55.3V}{cS_T a_0} \tag{5}$$

$$T_2 = \frac{55.3V}{c[S_b a + (S_T S_b)a_o]} \tag{6}$$

From Eqs. (5) dan (6), the coeffisien α can be as follows:

$$a = a_o + \frac{55.3V}{cS_b}\left[\frac{I}{T_2} - \frac{I}{T_1}\right] \tag{7}$$

5 Experiment Method

The experiment was carried out in several stages, starting from obtaining the ISO standard information used for the test. The preparation of the experiment object (sample) also needs to describe in this method. In additional to experiment sample it is needed to detail set up the drone room due to it is affect to the test results. Finally, in this method is described the experiment steps.

5.1 Testing Standards

This test is done using the international standard ISO—354: 2003 (Measurement of Sound Absorption in a Reverberation Room), which is testing samples in the drone room to obtain reverberation time (RT60) and then processed to obtain an absorption coefficient (α). Measurements are made at various frequencies because the reverberation time and absorption coefficient of a sample have different values for each frequency. Other influencing factors are temperature, drone chamber humidity, drone chamber volume, and surface area of the test sample.

5.2 Preparation of Test Samples

The test sample of fibers are arranged in a mold and pressed, then the fibers that have been pressed are sewn so that the fibers do not come off easily and can take the form of natural panel fibers without any mixture. This sample has a length of 1 m, a width of 1 m with fiber thickness is about 15.75 mm. The test sample shows at Fig. 1.

5.3 Drone Room Set up

The drone room was setup includes measuring room temperature (32 °C) without Air Conditioning, room humidity (89%). The room dimensions are: Length (5.6 m), Width (3.9 m), High (3.3 m) and room volume (72.1 m^3). Detail drone room set up shows at Figs. 2, 3 and 4.

5.4 Experimental Steps

The experimental steps for determining the reverberation time (Reverberation Time RT60) which refer to the ISO Standard—354: 2003 are as follows:

a. Determining the measurement point in the drone room.
b. Placing the microphone and speaker at the predetermined measurement point position with a minimum distance of 1 m from the source and the wall of the room as shown in Fig. 3.
c. Measuring the temperature and humidity of the hum using the Center 310 Series Humidity Temperature Meter.
d. Calibrating the microphone using calibrator 1251 at SPL 113.7 dB, frequency 1000 Hz and sensitivity −27.3 dB.
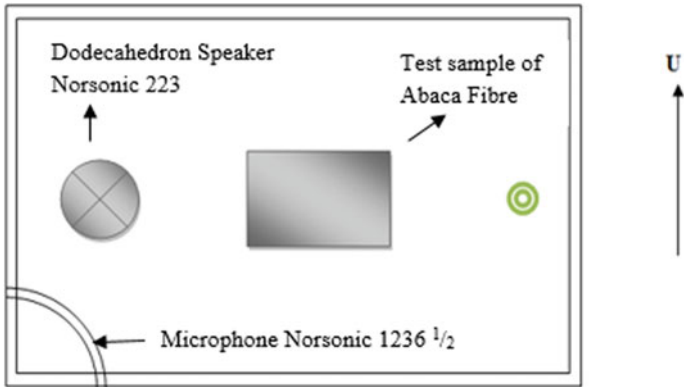

Fig. 1 The test sample of fibers

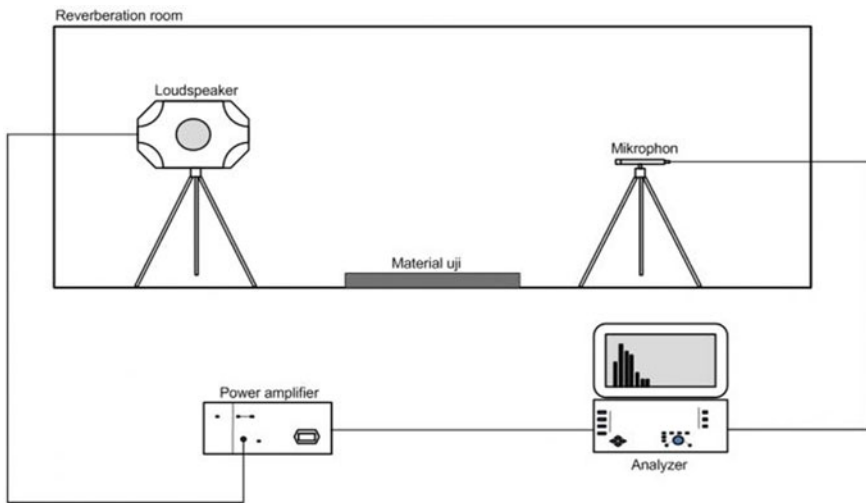**Fig. 2** Sketch of time measurement point of drone (RT) with test sample

Fig. 3 Illustration of measurement kit

e. Measuring Background Noise Level (has been done by Vipac Engineer and Scientists Singapore).

f. Measuring the empty space drone time (without test sample) and record the RT30 value for each frequency that appears on the Real Time Analyzer screen. This test was carried out five times without changing the setup of the tools and the position of the materials in the drone chamber.

g. Measuring the time of space reverberation with the test sample (Abaca Banana Fiber) and record the RT30 value of each frequency that appears on the Real

Fig. 4 Drone room set up

Time Analyzer screen. This measurement is carried out five times without changing the tool setup and the position of the materials in the drone chamber.

h. Calculating the average value of the RT30 free space and with the test sample, then calculating the RT60 value and finally calculating the absorption coefficient value of the test sample using the Sabine equation.

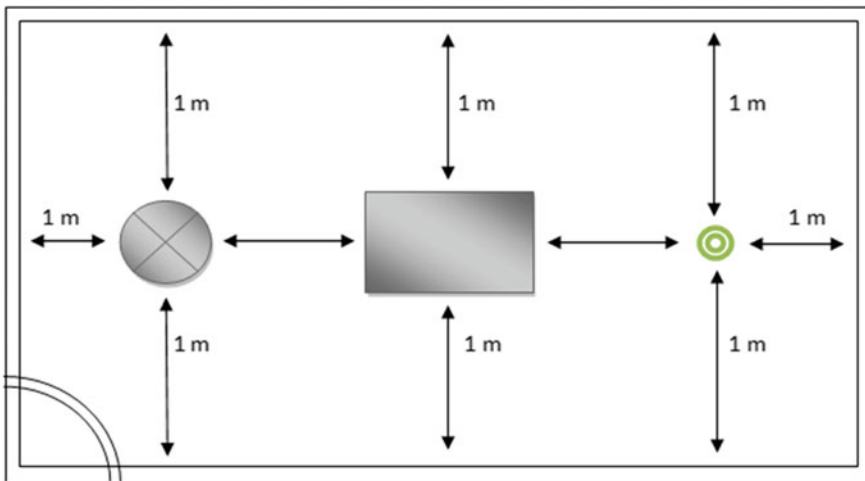The detail dimension of equipment distance of experiment shows at Fig. 5.

Fig. 5 The dimension of equipment distance in drone room during experiment

6   Results

Measurement of the absorption coefficient value on the entire surface of the drone chamber material needs to be done before conducted the experiment using a test sample (abaca fiber). According to ISO—354: 2003, acoustic materials must have the lowest possible sound absorption coefficient and a maximum value of 0.06 in an empty state. In this experiment, measurements have been carried out by Vipac Engineers and Scientists Singapore, whose coefficient results are 0.04. From the results of this measurement, it is also obtained the background noise level (BNL), empty space reverberation time (T1) and space reverberation time with the test sample (T2).

After determining the volume of the test room (V) is 72.1 m^3, the speed of sound propagation in the drone chamber (c) is 347.14 m/s, the surface area of the test sample (S_b) is 1 m^2, then the absorption coefficient (α_o) of the abaca fiber material have been calculated on certain frequency. The Norsonic 140 Real Time Analyzer meter used can only calculate up to RT30, while to calculate the absorption coefficient we need the value of RT60. To get RT60 values, RT30 only needs to be

Tabel 1 RT30 and RT60 measurement results of abaca and coconut fibres

Frekeunsi (Hz)	RT30			RT60		
	TI empty room (s)	T2 Abaca fiber (s)	T2 coconut fibre (s)	TI Empty room (s)	T2 Abaca Fiber (s)	T2 coconut Fibre (s)
125	2.07	2.13	2.05	4.14	4.26	4.10
160	2.16	2.34	2.40	4.32	4.68	4.80
200	2.35	2.25	2.08	4.70	4.50	4.16
250	3.43	2.83	3.20	6.86	5.66	6.40
315	3.50	3.15	3.26	7.00	6.30	6.52
400	4.44	3.56	3.47	8.88	7.12	6.94
500	4.10	3.36	3.57	8.20	6.72	7.14
630	3.93	3.39	3.18	7.86	6.78	6.36
800	4.04	3.25	3.68	8.08	6.50	7.36
1000	3.72	3.14	3.80	7.44	6.28	7.60
1250	4.01	3.26	3.19	8.02	6.52	6.38
1600	4.08	3.15	3.48	8.16	6.30	6.96
2000	3.94	2.94	3.69	7.88	5.88	7.38
2500	3.56	2.71	3.49	7.12	5.42	6.98
3150	3.13	2.43	3.12	6.26	4.86	6.24
4000	2.58	2.20	2.67	5.16	4.40	5.34
5000	2.25	1.95	2.40	4.50	3.90	4.80
6300	2.13	1.86	2.12	4.26	3.72	4.24
Average	3.30	2.77	3.05	6.60	5.54	6.09

considered that RT60 is 2 times RT30. The following is a table of RT30 measurements and the results of RT60 calculations. The detail result shows at Table 1.

Based on Table 1 above, measurement of the sound absorption coefficient in the drone room of Abaca and Coconut Fibers which results in reverberation time.

Figure 6 shows that in the empty space, the average RT60 value is 6.60 s and with the abaca fiber test sample the RT60. There is a difference between the free space and the one using the abaca fiber test sample. In a graphs, it can be seen that some of the sound is absorbed in the drone chamber.

In Fig. 6, is also shows the average RT60 value is 6.60 s and with the abaca fiber test sample the RT60 value drops to 5.54 s. the gaps is about 1,06 s. It means that some of the sound energy absorption has occurred in the drone room by the fiber so that accelerates the pulverization process of the sound pressure level by 60 dB.

In Fig. 7 can be seen the difference between the empty space RT60 with the Abaca Banana Fiber test sample and the Coconut Coir Fiber test sample. In the empty space the average RT60 value is 6.60 s and with the Abaca Abaca Banana fiber test sample the RT60 value drops to 5.54 s, while with the RT60 coconut fiber sample it drops to 6.09. This means that some of the sound energy has been absorbed in the reverberation chamber by the abaca and coconut coir fibers, thereby accelerating the pulverization process of the sound pressure level by 60 dB.

6.1 Absorption Coefficient

The method used to find the absorption coefficient value is the drone space method where the objective is to get the RT60 value, namely the empty space (T1) with the test sample (T2). The RT60 value is then entered into the Sabine equation:
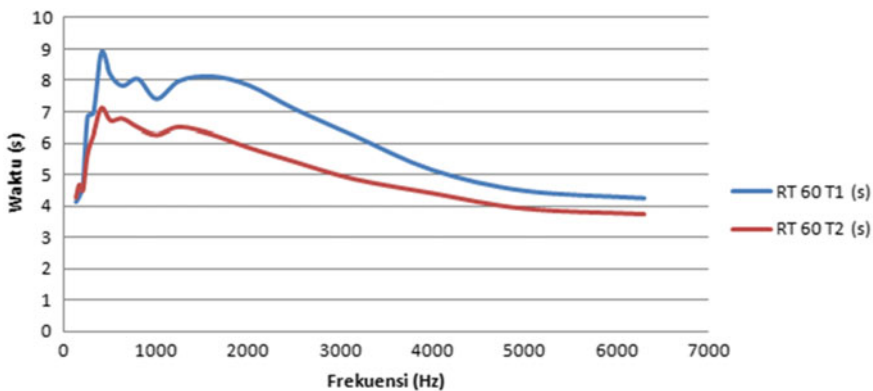

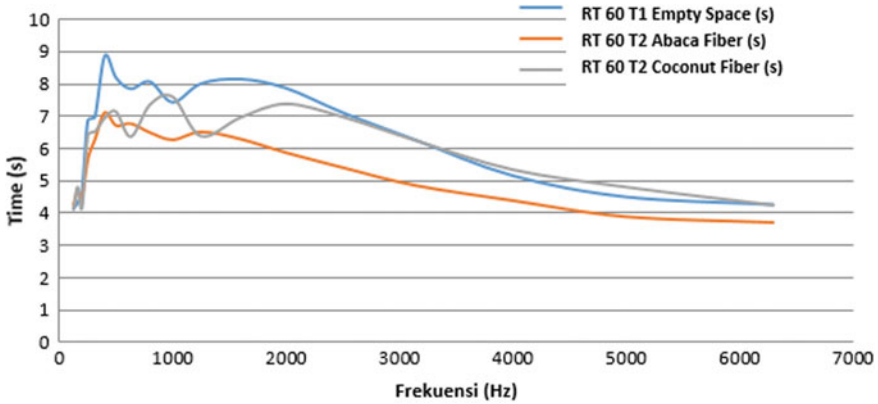**Fig. 6** Abaca fiber reverberation time 60 dB (RT60)

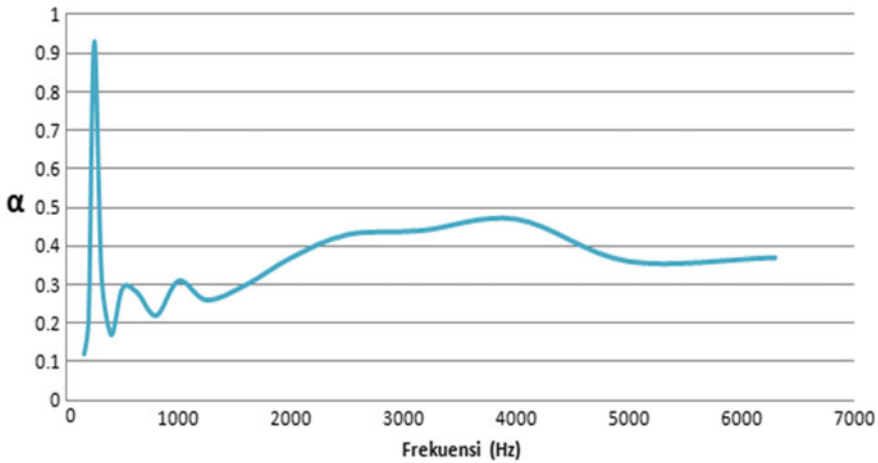**Fig. 7** Comparison between abaca and coconut fiber reverberation time 60 dB (RT60)

Fig. 8 Abaca fiber absorption coefficient value

$$\alpha = \alpha_o + \frac{55.3V}{cS_b}\left[\frac{1}{T_2} - \frac{1}{T_1}\right]$$

From the calculation results using formula above, the absorption coefficient value fluctuates at different frequencies, especially at low frequencies, below is the table and graph of the absorption coefficient (α) obtained from the calculation results. The detail absorption coefficient value (fluctuates) can be seen at Figs. 8 and 9.

From the graph above, it can be explained that the absorption coefficient of abaca fiber from the Pink Noise sound source shows that the maximum absorption occurs
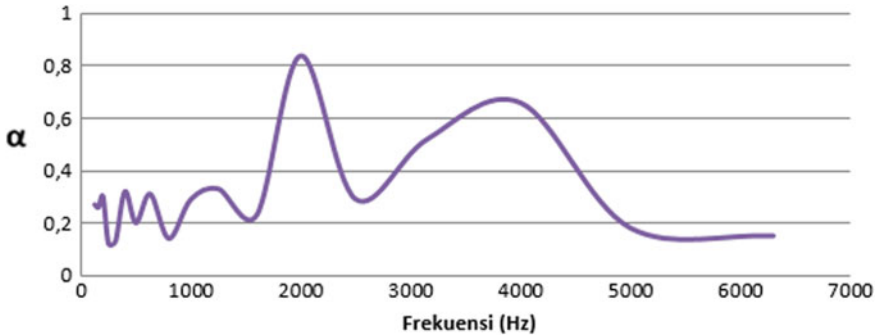
Fig. 9 Coconut fiber absorption coefficient value

at low frequencies (160–250 Hz), namely 0.93 at 200 Hz and the minimum at low frequencies (125–500 Hz) which is 0, 17 at 315 Hz. The graph tends to be stable at intermediate frequencies (1000–3150 Hz), with absorption coefficient values ranging between 0.26 and 0.47.

Meanwhile, the absorption coefficient of coconut coir shows below that the maximum absorption occurs at high frequencies (1600–6300 Hz), namely 0.84 at 2000 Hz and the minimum at low frequencies (125–500 Hz) which is 0.12 at 250 Hz. The graph tends to be stable at medium frequencies (800–1250 Hz), with absorption coefficient values ranging between 0.14 and 0.33.

7   Conclusion

Based on the test results data, data analysis and characteristic graphs, the following conclusions can be drawn:

1. The absorption coefficient of abaca banana fiber and coconut coir fiber fluctuates at different frequencies.
2. The maximum value at low frequencies (160–250 Hz) is at 0.93 at 200 Hz, meaning that at this frequency 93% of the sound energy is absorbed by abaca banana fibers, while the maximum value of coconut coir fibers at high frequencies (1600–6300 Hz) namely at 0.84 at 2000 Hz, meaning that at this frequency 84% of the sound energy is absorbed by the coir fiber.
3. The minimum value at low frequencies (125–500 Hz) is 0.17 at 315 Hz, meaning that only 17% of the total sound energy is absorbed by the abaca banana fiber at this frequency. Meanwhile, the minimum value of coconut coir occurs at low frequencies (125–500 Hz), namely at 0.12 at 250 Hz, meaning that only 12% of the total sound energy is absorbed by the coir fiber at this frequency.

4. The absorption coefficient value of abaca banana fiber tends to be stable at medium frequencies (1000–3150 Hz) ranging between 0.26 and 0.47. In other words, in the frequency range, the absorption of sound energy that occurs is 26–47% of the total incoming energy. Meanwhile, the absorption coefficient value of coconut coir tends to be stable at medium frequency (800–1250 Hz) ranging between 0.14 and 0.33. So the sound energy that occurs in coconut coir fibers is 14–33% of the total energy that comes.

5. The average absorption coefficient of abaca banana fiber for the frequency range 125–6.3 kHz is 0.38 or 38%. While the average absorption coefficient of coconut coir for the frequency range 125–6.3 kHz is 0.30 or 30%.

References

1. Eriningsih R, Widodo M, Marlina R (2014) Manufacturing and characterization of sound absorbers from natural fiber raw materials. Textile Arena 29(1)
2. Khotimah K, Soeprianto H (2015) Sifat Penyerapan Bunyi Pada Komposit Serat Batang Pisang (SBP)–Polyester. J Penelit Pendidik IPA 1(1)
3. Suantara D, Oktaviani E (2015) The utilization of coconut fiber and abaca fiber as raw materials for particle board. Textile Arena 30(1)
4. Iqbal M, Aminanda Y, Firsa T, Ali M (2019) Bending strength of polyester composites reinforced with stitched random orientation and plain weave abaca fiber. In: IOP conference series: materials science and engineering, vol 739
5. Maimunah N (2006) Utilization of banana fiber as material for textile handicrafts in the weaving and creative handicraft company of Pekalongan. Dissertation Sebelas Maret University
6. Suardana NPG, Lokantara IP (2011) Jae Kyoo Lim. Influence of water absorption on mechanical properties of coconut coir fiber/poly-lactic acid biocomposites, materials physics and mechanics 12(2):113–125
7. Khotimah K, Susilawati S, Soeprianto H (2014) Banana fiber composite (SBP)—epoxy as a sound absorbent material. Nat B 2(4):322–326
8. Hayat W (2013) The effect of density on sound absorption coefficient of particle board of pineapple leaf fiber (Ananas Comosus L Merr). Pillar of Physics 1(1)
9. Kahorika IMG, Astika IM, Lokantara IP (2012) Design of sound absorbers based on coconut filter fibers and measurement of sound absorption coefficients. Department of Mechanical Engineering, Faculty of Engineering, Udayana University
10. Ufri F (2010) Study of sound absorption characteristics in straw test samples (STRAWBALE). USK, Banda Aceh

Correction to: Proceedings of the 2nd International Conference on Experimental and Computational Mechanics in Engineering

Akhyar

Correction to:
Akhyar (ed.), *Proceedings of the 2nd International Conference on Experimental and Computational Mechanics in Engineering*, Lecture Notes in Mechanical Engineering,
https://doi.org/10.1007/978-981-16-0736-3

The original version of the book was inadvertently published with incorrect author names in chapters 15 and 44. The names have been corrected and details of the changes have been provided below:

Chapter "The Effect of Atmosphere Media on Temperature and Mass of Torrefacted Coffee Beans":

M. Faisal has been changed to Faisal

Chapter "Fly Ash Utilization in Rigid Pavement Construction":

Nasruddin A. Abdullah has been changed to Abdullah

The correction chapters and the book have been updated with changes.

Correction to: Experimental Study of Thermoelectric Cooler Box Using Heat Sink with Vapor Chamber as Hot Side Cooling Device

Adi Winarta, I. Made Rasta, I. Nyoman Suamir, and I. G. K. Puja

Correction to:
Chapter "Experimental Study of Thermoelectric Cooler Box Using Heat Sink with Vapor Chamber as Hot Side Cooling Device" in: Akhyar (ed.), *Proceedings of the 2nd International Conference on Experimental and Computational Mechanics in Engineering,* **Lecture Notes in Mechanical Engineering,** **https://doi.org/10.1007/978-981-16-0736-3_37**

The chapter "Experimental Study of Thermoelectric Cooler 15 Box Using Heat Sink with Vapor Chamber as Hot Side Cooling Device" was published with an incorrect Acknowledgement text, which has now been corrected in the chapter.

The updated version of this chapter can be found at
https://doi.org/10.1007/978-981-16-0736-3_37

C3